Crystallography Reports, Vol. 49, No. 3, 2004, pp. 327–342. Translated from Kristallografiya, Vol. 49, No. 3, 2004, pp. 391–406.

CRYSTAL CHEMISTRY

Dedicated to the 60th Anniversary of the Shubnikov Institute of Crystallography of the Russian Academy of Sciences

Theoretical Crystal Chemistry of Phosphates: Topological Analysis and Classification of Suprapolyhedral Ensembles of Orthophosphates and Their Analogues $M_x(TO_4)_y$

G. D. Ilyushin* and V. A. Blatov**

** Shubnikov Institute of Crystallography, Russian Academy of Sciences, Leninskiĭ pr. 59, Moscow, 119333 Russia*
e-mail: ilyushin@ns.crys.ras.ru
*** Samara State University, ul. Akademika Pavlova 1, Samara, 443011 Russia*
Received February 18, 2003

Abstract—Geometrical and topological analysis of the orthotetrahedral phases $M_x(TO_4)_y$ (73 phosphates and 31 arsenates) was carried out using the TOPOS 3.2 program package. The coordination sequences $\{N_k\}$ of *T* nodes were used as the classification parameters of topologically different *MT*O frameworks. The crystal structures were analyzed within the first 12 coordination spheres of *T* nodes and were assigned to 43 topological types. It was found that only 14 types are common to the structures of phosphates and arsenates, whereas 29 types are unique, of which 21 types characterize phosphates, and 8 types characterize arsenates. The average lengths of the bonds ⟨P–O⟩ and ⟨As–O⟩ are 1.54(3) and 1.69(2) Å, respectively. The hierarchical ordering of the crystal structures was carried out using the concept of a polyhedral microensemble (PME). The revealed local regions of the crystal structures (which provide the basis for the classification) are *T*-PMEs with invariant PO_4 and AsO_4 tetrahedra. Such *T*-PMEs provide the geometric interpretation of coordination sequences of *T* nodes. For orthophosphates and their analogues, the suprapolyhedral level of organization of the crystal structures as a whole was taken into account for the first time. In this case, the PO_4 and AsO_4 tetrahedra are considered as invariant particles serving as templates for the condensation of any geometric types of the MO_n polyhedra.

INTRODUCTION

Theoretical crystal chemistry of phosphates has long been based on concepts and methods developed by Bragg for analysis of silicate structures [1–3]. A universal classification by types of tetrahedral *T*,O radicals is used in virtually all generalizations for phosphates in crystal chemistry [4–13]. Liebau [2] distinguished about 60 topologically different radicals in 786 silicates (minerals and synthetic phases).

According to Bragg's classification, the number of subclasses governed by the number of topologically different *T* radicals is much smaller for phosphates than for silicates. This circumstance is due to the difference between silicon and phosphorus atoms in corresponding oxides from the viewpoint of crystal chemistry. Unlike the silicate tetrahedra $Si(OH)_4$, one of the vertices of the orthotetrahedron H_3PO_4=$P(OH)_3O$ cannot be shared with the O vertex of another tetrahedron in the case of mutual condensation. As a consequence of this behavior during condensation, the following P,O radicals occur in the crystal structures of phosphates [3]: PO_4 orthotetrahedra, $\{PO_3\}_n$ finite chains (n = 2, 3, 4, or 5), PO_3 infinite chains, $\{PO_3\}_n$ rings (n = 3, 4, 5, 6, 8, 10, and 12), ribbons with 8*T* rings, and sheets consisting of 14*T*, 8*T* + 12*T*, or 8*T* + 16*T* rings.

The data on the crystal chemistry of phosphates were surveyed and generalized in reviews and studies, which were published in the period of 1966–1998 [4–11]. The structures of divalent phosphates were reviewed in [12]. The data on the structural types of rare-earth phosphates were reported in [13, 14]. The corresponding data on rare-earth arsenates were reviewed in the monograph [14]. The structures of the phosphates Li_3PO_4, Na_3PO_4, and Ag_3PO_4 and their solid solutions, which are ionic conductors, were considered in the monograph [15].

In the structural mineralogy of phosphates, orthophosphate compounds are of particular importance, because all phosphate minerals belong to this class of compounds [3, 7–11]. In addition, as will be demonstrated below, the family of orthophosphates is more structurally informative (characterized by a diversity of topological types) compared to orthosilicates [16] and orthosulfates [17]. The uniqueness of orthophosphates

1063-7745/04/4903-0327$26.00 © 2004 MAIK "Nauka/Interperiodica"

is emphasized by the existence of the chemically simple compound $AlPO_4$, for which more than 20 topological types of tetrahedral structures are known (see the *Atlas of Zeolite Structure Types* [18]). It should be noted that only three of these topological types are analogous to the simplest SiO_2 structures and (like silicates) are also characterized by high- and low-temperature modifications [19].

The following two classification schemes are presently used for 3D (framework) structures of phosphates:

(i) a universal classification (according to Bragg) by tetrahedral radicals [3];

(ii) a special classification developed for orthophosphate minerals, i.e., for structures containing octahedrally coordinated divalent M(2+) and trivalent M(3+) atoms [7–10, 20, 21].

Phosphates are classified by topological types of clusters consisting of the linked M octahedra [7–10] or clusters consisting of two octahedra and two M_2T_2 tetrahedra [20, 21]. In the latter case, a method for separating these clusters in 3D framework structures remains to be developed [11, 20, 21].

The degree of the chemical and crystallographic complexity of the known silicates is virtually equivalent to that of phosphates. This circumstance gives rise to the problem of comparing such large groups of structures with each other. However, in Bragg–Liebau's classification scheme [1, 2], all compounds belong to the same groups regardless of the chemical rank R_{chem}, which is equal to the number of chemically different atoms in their compositions. The hierarchical ordering in any group cannot be specified, because all other components of the structure, except for the T,O radicals, are excluded from the consideration. To solve modern problems of crystal chemistry, all chemical components of the structures should be taken into account. For example, the chemical rank (number of components) and the degree of integration interactions between components, which is controlled by the long-range order, complementary coupling, and the existence of feedback, are the basic system concepts in the simulation of self-organization processes in crystal-forming systems [22, 23].

In [16], the structural organization of orthosilicates was analyzed at the suprapolyhedral level, where all the structure-forming components (with any geometric types of the MO_n polyhedra and sets of compositions of the M polyhedra) were considered; i.e., the analysis was carried out at a level higher than the T level (used in the Bragg–Liebau classification [1, 2]) or M level (used in Moore's classification [7–10]). A consideration of the topology of coupling of the M polyhedra in the first coordination (polyhedral) sphere of the orthotetahedra made it possible to classify silicates by types of structure-forming MT ensembles.

The methodology of topological analysis of silicates, taking into account the characteristic features of the chemical composition and structures of orthophosphates (arsenates) used in [16, 24], is considered below.

THEORETICAL CONSIDERATION

Method of Coordination Sequences

In 1979, Meier and Moeck [25] suggested a classification of tetrahedral frameworks of zeolites based on sets of n numbers $\{N_k\}$ called *coordination sequences* (CSs). This classification employs the method of representing frameworks as 3D networks (graphs), which was developed by Wells [26]. The chemical rank of all structures was reduced to $R_{chem} = 1$. For T atoms, CSs were calculated up to the fifth coordination sphere ($n = 5$). In addition, Meier and Moeck [25] used the CSs of crystallographically different T atoms in a framework to determine their topological equivalence. Thus, the equality of CSs for T atoms indicated the presence of an additional "topological" symmetry of the framework. The results of [25] led to a new line of investigation of the properties of CSs for T atoms in zeolites [26–29]. Presently, the CSs for T atoms are considered as one of the most important topological characteristics of zeolites [18] and were calculated up to $n = 10$.

The advantages of using CSs [16] in the classification of framework compounds of any composition and structure result from the following factors:

(i) the unambiguity of calculations of CSs;

(ii) the simplicity of comparing and the possibility of ordering CS sets in the hierarchical classification;

(iii) the possibility of combining the local and global approaches to the description of crystal structures; in spite of the fact that CS is determined for a finite (local) structural fragment, the equality of the sets $\{N_k\}$ for the corresponding framework-forming atoms of the substructures to be compared within 3–5 coordination spheres is, as a rule, indicative of global isomorphism [17].

The method of coordination sequences was used [17] for the development of a generalized scheme for crystallochemical analysis and classification. In this scheme, a crystal structure as a whole is represented as a reduced graph, which completely retains the bond system of the structure. The isomorphism of the reduced graphs of two frameworks to be compared is indicative of their equivalence; therefore, such frameworks can be assigned to the same topological type or topological family. The isomorphism of two crystal structures is determined by comparing CSs for all crystallographically nonequivalent atoms present in these structures. One should also take into account the possible existence of a topological symmetry for crystallographically nonequivalent atoms, which manifests itself in the equality of their sets $\{N_k\}$ and in the fact

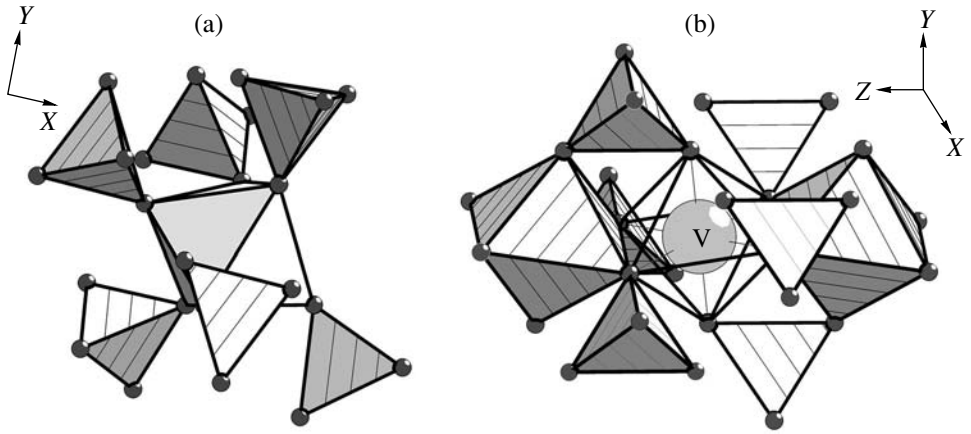

Fig. 1. *M*-PMEs in the (a) $Sb_2(PO_4)_3$ and (b) VPO_4 structures.

that these atoms belong to the same topological sort [17].

Methods of Analysis of the Structural Organization of Orthostructures: Relationship between Geometry and Topology and Levels of the Structural Organization of MT Orthostructures

The mathematical method of coordination sequences providing strict classification criteria (sets of topological indices) does not account explicitly for the dependence of the topological properties of structures on the limitations associated with the characteristic features of the chemical compositions and geometry of the simplest polyhedral building units (BUs) MO_n and TO_4.

Let us consider the methodology of the synthesis of the topological and geometric properties of *MT* orthostructures, which takes into account three levels of their organization; namely, atomic (chemical), polyhedral, and suprpolyhedral [16, 24].

At the atomic level, the most important classification parameters are the characteristics of point models of *MT* orthostructures; among them, the number and symmetry of Wyckoff positions in fundamental regions of space groups and stoichiometric ratios for the *M*, *T*, and O atoms.

In the general case, the stoichiometric formulas $M_aT_bO_c$ of *MT* orthostructures are characterized by the fixed *c*/*b* ratio of 4. The chemical formulas of all such oxygen-containing orthophases can be obtained by enumerating the oxidation states of *M* atoms. For the fixed oxidation state of *T* atoms (for orthophosphates, $\xi_T = 5$), we can write the following formula for the *a* and *b* indices of the interacting hypothetical electrically neutral polyhedral particles of the same type:

$$a[M(m+)(OH)_m] + b[P(5+)O(OH)_3].$$

After the transformation of these particles into an oxide form, we can write

$$M_pPO_4 \ (p = a/b, m = 3/p).$$

If the oxidation state of *M* atoms is limited to a range of $\xi_M = 1–3$, the parameter *p* in the chemical formulas of orthostructures of phosphates and arsenates [*T* = P(5+), As(5+)] may be equal to 3, 1.5, or 1. Correspondingly, the composition of orthostructures varies in the series of $M(1+)_3PO_4$, $M(2+)_3(PO_4)_2$, and $M(3+)PO_4$. A few examples of phosphate structures with *M* atoms in the mixed-valence state are considered below.

At the polyhedral level, the MO_n polyhedra and TO_4 tetrahedra, which serve as framework-forming BUs, are identified. At this stage of analysis, chemical compounds are assigned to a particular class of *MT* orthostructures.

At the suprapolyhedral level, *MT* frameworks are classified by the CSs of atoms, and polyhedral clusters consisting of several BUs are selected.

Such polyhedral ensembles are suprapolyhedral invariants of the topological type to which the crystal structure is related [16]. These ensembles are used as the basis for a search for representatives of this topological type in other classes of orthostructures (silicates, sulfates, etc.). The *MT* framework can be described by different symmetry groups and lattice parameters and can be characterized by different distortions of the geometry of coordination polyhedra. However, the framework connectivity, which is represented mathematically as CSs and geometrically as suprapolyhedral invariants (clusters), remains the same in all phases belonging to the corresponding topological type.

In this study, we use the following algorithm of the hierarchical construction of suprapolyhedral invariants.

First sublevel. For each of the MO_n and TO_4 polyhedra in the unit cell, all polyhedra of the structure directly connected with the polyhedron considered are taken into account. Only the following two alternative

Table 1. Classification of phosphates and arsenates $M(1+)_3TO_4$ by topological and structural types

Topological type, no.	Number of *T*-PMEs	Structural type	Name of mineral or modification	Space group	*CC**
Ag_3PO_4 (1)	1	Ag_3PO_4			14000
		Ag_3AsO_4	low-temperature phase	$P\bar{4}3n$	76969
Li_3PO_4 (2)	1	Li_3PO_4	γ modification	$Pmnb$	79427
Li_3PO_4 (3)	1	Li_3PO_4			10257
		Li_3AsO_4	α modification	$Pmn2_1$	75927
Na_3PO_4 (4)	1	Na_3PO_4		$P\bar{4}2_1c$	33718
Tl_3PO_4 (5)	1	Tl_3PO_4			60780
		Tl_3AsO_4		$P6_3$	407561

* Herein, the Collection Codes of the compounds in the ICSD are given.

compositions of the resulting *M* and *T* suprapolyhedral invariants are possible:

(i) $[MO_n]$–$\{[MO_n]_i, [TO_4]_j\}$ (because *M* polyhedra, generally, can form contacts with each other, Figs. 1a and 1b);

(ii) $[TO_4]$–$\{[MO_6]_i\}$ (according to the definition of orthostructures).

Therefore, at the first sublevel, suprapolyhedral invariants are polyhedral microensembles (PMEs) [16, 24] constructed based on *M* or *T* nodes, and their geometric shapes are unambiguously determined by a set of the *i* and *j* indices. After the construction of PMEs and determination of the topological characteristics of the *M* and *T* nodes in 3D networks, it is important to establish their nonequivalence, i.e., to assign these nodes to different topological types.

When classifying *MT* orthoframework structures with the use of CSs, it is particularly essential to determine the minimum number of topologically different *M* or *T* nodes in the frameworks under consideration and to find out how many CSs (and for which types of nodes) are required for an unambiguous identification of the framework. Therefore, a set of CSs for the framework atoms is the most important classification criterion at this sublevel.

Second and higher sublevels. For each PME of the first level (PME-1), BUs located in the next polyhedral sphere are taken into account. This consideration gives rise to PMEs of the second level (PMEs-2). The formation of more complex PMEs of the third, fourth, and higher sublevels from the PMEs of lower sublevels can be considered analogously. In this study, we restrict ourselves to the first sublevel of structural and topological analysis of PMEs; i.e., we consider only PMEs-1 (hereinafter, the index indicating the number of the sublevel will be omitted for brevity).

Polyhedral microensembles make it possible to directly visualize the CSs $\{N_k\}$ with $k = 1 - n$ for *M* and *T* nodes (Figs. 1a–1c). Depending on the level of calculation, PMEs reflect the topology of bonds in crystal-forming *MT* precursors and their spatial correlations (generally, at $n \geq 6$). In the orthostructures under consideration, the sequence $\{N_k\}$ for any atom reflects the number of cations or anions alternating it its coordination spheres. For example, the *T*-PME composition of an orthostructure can be coded as follows:

$$\{4(O), N_2(M), N_3(O), N_4(M + T), N_5(O), \ldots\},$$

where the symbols in parentheses indicate the chemical compositions of the coordination spheres.

Like in the classification of orthostructures of silicates [16], it is convenient to choose invariant *T* nodes as the central atoms in PMEs of orthophosphates, because these nodes possess the following important classification properties:

(i) the number of crystallographically different *T* nodes in orthostructures of the main families is minimum compared to the *M* and O nodes, by which is meant their minimum density in the *MT*O networks $M(1+)_3PO_4$, $M(2+)_3(PO_4)_2$, and $M(3+)PO_4$ (in zirconosilicates, only *M*-MPEs possess this property [24]);

(ii) only *M* atoms are involved in the second coordination sphere of *T* atoms.

EXPERIMENTAL

In the present study, we carried out crystallochemical analysis of the large family of orthophosphates M_pPO_4 (minerals and synthetic phases) and of the structurally and chemically related family of orthoarsenates M_pAsO_4, whose detailed classification has been unavailable. A comparative analysis and classification of the compounds were performed using the modified TOPOS 3.2 program package [30, 31]. The algorithm of analysis includes the following steps.

The creation of a database of crystal structures of phosphates and arsenates with the rank $R_{chem} = 3$. At this stage, chemically and crystallographically different compounds containing P and O atoms or As and O atoms were taken from the Inorganic Crystal Structure

Table 2. Classification of phosphates and arsenates $M(2+)_3(TO_4)_2$ by topological and structural types

Topological type, no.	Number of *T*-PMEs	Structural type	Name of mineral or modification	Space group	*CC*
$Ba_3(PO_4)_2$ (6)	1	$Ba_3(PO_4)_2$		*R m*	69450
		$Sr_3(PO_4)_2$			404438
		$Pb_3(PO_4)_2$			28053
		$Ca_3(PO_4)_2$			200202
		$Ba_3(AsO_4)_2$			69449
$Ca_3(PO_4)_2$ (7)	12	$Ca_3(PO_4)_2$	α Modification	$P\,2_1/a$	923
$Cd_3(AsO_4)_2$ (8)	2	$Cd_3(AsO_4)_2$		$P\,2_1/c$	14257
$Cd_3(PO_4)_2$ (9)	6	$Cd_3(PO_4)_2$	β Modification	$P\,2_1/c$	63548
$Cd_3(PO_4)_2$ (10)	2	$Cd_3(PO_4)_2$		*C m c a*	20202
$Co_3(AsO_4)_2$ (11)	2	$Co_3(AsO_4)_2$	High-temperature phase	$P\,2_1/c$	59000
$Co_3(AsO_4)_2$ (12)	2	$Co_3(AsO_4)_2$		$P\,2_1/c$	23547
		$Ni_3(AsO_4)_2$	Xanthiosite		63709
$Co_3(PO_4)_2$ (13)	1	$Co_3(PO_4)_2$		$P\,2_1/n$	38259
		$Mg_3(PO_4)_2$	Farringtonite	$P\,2_1/c$	31005
		$Zn_3(PO_4)_2$	γ Modification	$P\,2_1/n$	34303
		$Zn_3(AsO_4)_2$	β Modification	$P\,2_1/c$	404229
$Co_3(PO_4)_2$ (14)	1	$Co_3(PO_4)_2$		$P\,2_1/b$	9850
		$Fe_3(PO_4)_2$	Sarcopside	$P\,2_1/c$	72049
		$Mg_3(PO_4)_2$		$P\,2_1/b$	9849
		$Ni_3(PO_4)_2$		P 2_1/c	4269
$Cr_3(PO_4)_2$ (15)	4	$Cr_3(PO_4)_2$		$P\,2_1\,2_1\,2_1$	406829
$Cu_3(AsO_4)_2$ (16)	1	$Cu_3(AsO_4)_2$	Lammerite	$P\,2_1/a$	201733
$Cu_3(AsO_4)_2$ (17)	2	$Cu_3(AsO_4)_2$		$P\,2_1/c$	24198
		$Zn_3(AsO_4)_2$	α Modification		404199
$Cu_3(PO_4)_2$ (18)	1	$Cu_3(PO_4)_2$		$\cdot P\,\bar{1}$	68811
		$Cu_3(AsO_4)_2$			63057
$Fe_3(PO_4)_2$ (19)	2	$Fe_3(PO_4)_2$	Graftonite	$P\,2_1/c$	79906
$Hg_3(PO_4)_2$ (20)	2	$Hg_3(PO_4)_2$		$P\,2_1/c$	4273
		$Hg_3(AsO_4)_2$		$P\,2_1/c$	72527
$In_3(PO_4)_2$ (21)	1	$In_3(PO_4)_2$		$I\,\bar{4}\,3\,d$	66831
$Mg_3(PO_4)_2$ (22)	4	$Mg_3(PO_4)_2$		$P\,\bar{1}$	84710
$Mn_3(PO_4)_2$ (23)	6	$Mn_3(PO_4)_2$		$P\,2_1/c$	23541
$Ni_3(AsO_4)_2$ (24)	1	$Ni_3(AsO_4)_2$		*C m c a*	63708
$Pb_3(PO_4)_2$ (25)	1	$Pb_3(PO_4)_2$		*C* 2/*c*	66379
$Sn_3(PO_4)_2$ (26)	2	$Sn_3(PO_4)_2$		$P\,2_1/c$	966
$Zn_3(PO_4)_2$ (27)	1	$Zn_3(PO_4)_2$	α Modification	*C* 2/*c*	27554
$Zn_3(PO_4)_2$ (28)	2	$Zn_3(PO_4)_2$	β Modification	$P\,2_1/c$	24192

Database (ICSD, released as of January 2001) using the TOPOS program package. Of the total number of structure solutions present in the ICSD (588 and 150 compounds containing *M*, P, and O atoms or *M*, As, and O atoms, respectively), we chose anhydrous compounds whose structures were completely established, have no statistically disordered atoms, and contain only the TO_4 tetrahedral groups (*T* = P or As). In addition, we excluded two orthophosphates and two orthoarsenates of monovalent mercury containing Hg–Hg bonds (in

Table 3. Classification of phosphates and arsenates $M(3+)TO_4$ by topological and structural types

Topological type, no.	Number of *T*-PMEs	Structural type	Name of mineral or modification	Space group	*CC*
$AlPO_4$(quartz) (29)	1	$AlPO_4$	Berlinite	$P\,3_12$	33742
		$FePO_4$			201795
		$GaPO_4$			30881
		$AlAsO_4$	Alarsite		67228
		$GaAsO_4$			50674
$AlPO_4$(cristobalite) (30)	1	$AlPO_4$		$I\bar{4}$	24511
		$AlAsO_4$			24512
		$BAsO_4$			26891
		$AlPO_4$		$C\,2\,2\,2_1$	16651
		$GaPO_4$			16652
$AsPO_4$ (31)	1	$AsPO_4$		*P n m a*	31879
$FeAsO_4$ (32)	1	$FeAsO_4$		$P\,2_1/n$	73978
$CrPO_4$ (33)	1	$CrPO_4$	β Modification	*C m c m*	62159
		$InPO_4$			16618
		$TiPO_4$			82283
		$TlPO_4$			16619
		VPO_4			82285
		$InPO_4$	β Modification	*P n m a*	85579
		$CrAsO_4$	β Modification		62132
		$TiPO_4$		$P\,2_1/m$	72714
		$MnAsO_4$		$P\,2_1/n$	73489
$CrPO_4$ (34)	2	$CrPO_4$	α Modification	*I m m a*	60836
		$RhPO_4$			74726
$BiAsO_4$ (scheelite) (35)	1	$BiAsO_4$	Tetrarooseveltite	$I\,4_1/a$	30636
$BiPO_4$ (36)	1	$BiPO_4$	High-temperature phase	$P\,2_1/m$	60522
		$SbPO_4$			62977
		$SbAsO_4$			23316
$CePO_4$ (37)	1	$CePO_4$	Rhabdophane	$P\,6_2\,2\,2$	31563
		$LaPO_4$			31564
		$NdPO_4$			31565
$CePO_4$ (huttonite) (38)	1	$CePO_4$	Monazite	$P\,2_1/n$	79748
		$EuPO_4$			79752
		$GdPO_4$			79753
		$LaPO_4$			79747
		$NdPO_4$			79750
		$PrPO_4$			79749
		$SmPO_4$			79751
		$BiPO_4$			67987
		$BiAsO_4$	Rooseveltite		27199
$DyPO_4$ (zircon) (39)	1	$DyPO_4$	Xenotime	$I\,4_1/a\,m\,d$	79756
		$ErPO_4$			79758
		$HoPO_4$			79757
		$LuPO_4$			79761
		$ScPO_4$			74483
		$TbPO_4$			79755
		$TmPO_4$			79759
		YPO_4			79754
		$YbPO_4$			79760
		$DyAsO_4$			200228
		$LuAsO_4$			2506
		$TbAsO_4$			200230
		$YAsO_4$	Chernovite		24513
		$DyAsO_4$		*I m m a*	200229

Table 4. Phosphates and arsenates containing mixed-valence *M* atoms in the mixed-valence state; classification by topological and structural types

Topological types	$N\ TO_4$	Structural type	Space group	*CC*
		M(1+), *M*(2+)		
Cu_2PO_4 (40)	2	Cu_2PO_4	$P\ \bar{1}$	80181
		M(2+), *M*(3+)		
$Cr_7(PO_4)_6$ (41)	3	$Cr_7(PO_4)_6$	$P\ \bar{1}$	73261
		$Fe_7(PO_4)_6$		20765
		M(4+), *M*(5+)		
$Nb_2(PO_4)_3$ (NASICON) (42)	1	$Nb_2(PO_4)_3$	$R\ \bar{3}\ c$	65658
$Sb_2(PO_4)_3$ (43)	2	$Sb_2(PO_4)_3$	$P\ 2_1/n$	72735

the Hg_2 groups and Hg_3 rings). Of 26 structural types of the $AlPO_4$ family, only types topologically analogous to SiO_2 (cristobalite and quartz), which are absent in the *Atlas of Zeolite Structure Types* [18], were included in the classification. A total of 73 phosphates and 31 arsenates were studied.

For each structure, the adjacency matrix was calculated and BUs were selected using the AutoCN program [30]. At this stage, cation–anion interactions were considered for the "main" faces of the Voronoi–Dirichlet polyhedra of the atoms characterized by the solid angles $\Omega \geq 5\%$ of the total solid angle of 4π steradian. The adjacency matrices were calculated using the method of intersecting segments and the Slater system of atomic radii.

The statistical processing of the bond lengths for the PO_4 and AsO_4 orthotetrahedra was performed using the StatPack program [30]. Only those structures that were established with an accuracy of $R_f \leq 5\%$ and published after 1970 were considered. As a result, 86 independent PO_4 tetrahedra and 28 independent AsO_4 tetrahedra were included in calculations, and 344 P–O bonds and 112 As–O bonds were analyzed.

The sequences $\{N_k\}$ for the *MT*O representations of each structure were calculated, and their topologies were compared using the IsoTest program [30].

ANALYSIS OF THE TOPOLOGY OF CRYSTAL STRUCTURES

Classification of Topological Types by Main Families

Our study demonstrated that 104 crystal structures of phosphates and arsenates belonging to 50 structural types are distributed over 43 topological types. Most of these types (39) belong to three main families $M(1+)_3PO_4$, $M(2+)_3(PO_4)_2$, and $M(3+)PO_4$ (Tables 1–4).

The $M(2+)_3T_2O_8$ family is characterized by the largest number of topological types (23), which is almost one-half of their total number. Fifteen chemically different *M*(2+) atoms, which form the series Mg–Ca–Sr–Ba, Zn–Cd–Hg, Cr–Mn–Fe–Co–Ni–Cu, Sn, Pb, and In (the oxidation state +2 is atypical of the latter element), are involved in the structural formation.

The $M(3+)TO_4$ family. Phases with the simplest *T* : *M* stoichiometry of 1 : 1 belong to 11 topological types. The crystal structures are formed with the participation of the *M* atoms in the characteristic oxidation state 3+, such as B–Al–Ga–In–Tl and Sc–Y–La…Lu, and also with the participation of the Ti, V, Cr, Mn, Fe, Cu, Rh, and As–Sb–Bi atoms (in the lower oxidation state).

The $M(1+)_3TO_4$ family. Five types of phases were revealed with the maximum content of *T* atoms: *T* : *M* = 1 : 3. These compounds are formed with the participation of the *M* atoms, for which the oxidation state 1+ is the most typical (Li, Na, Ag, and Tl).

The $M(m+)$–$M(m+1+)$–*T*–O family. In four topological types of structures, the mixed-valence state of atoms was revealed. This state is typical of the Cr(2+/3+) and Fe(2+/3+) atoms (in $M_7(PO_4)_6$) and Cu(1+/2+) atoms in Cu_2PO_4 and is rather rare for Nb(4+/5+) and Sb(4+/5+) in $M_2T_3O_{12}$.

Systematics and Characteristic Features of the Topology of T-PMEs

In Tables 5–7, the structural types are classified by the number of topologically different *T*-PME types into three groups (with one, two, and more *T*-PMEs). In each group, the structural types are hierarchically ordered according to the first members of the CSs for *T* atoms. When ordering the *T* nodes in structures with several topological sorts of *T*-PMEs, the corresponding values of N_k were averaged for different *T*-PMEs. The ordering numbers of the *T* atoms correspond to those used in the structure solutions. It was found that the number of topological sorts of *T*-PMEs in the orthostructures (Tables 5–7) varies from 1 to 12.

Table 5. Coordination sequences for *T* atoms in the structures of orthophosphates and arsenates with one topological sort of *T*-PMEs

Topological type	*CC*	Coordination number of *M*	Atom *T*	Coordination sequence N_k (k = 1–12)											
				1	2	3	4	5	6	7	8	9	10	11	12
Series with N_2 = 3.4															
$AsPO_4$	31879	3	P(1)	4	3	6	6	18	9	15	12	33	15	24	18
$AlPO_4$	24511	4	P(1)	4	4	12	12	36	24	60	42	108	64	148	92
$AlPO_4$	33742	4	P(1)	4	4	12	12	36	30	84	52	124	80	196	116
$Nb_2(PO_4)_3$	65658	6	P(1)	4	4	20	16	44	26	112	66	152	70	268	150
Series with N_2 = 5															
$FeAsO_4$	73978	5	As(1)	4	5	19	18	50	39	111	75	179	113	276	169
Series with N_2 = 6															
$Zn_3(PO_4)_2$	27554	4	P(1)	4	6	16	19	46	47	95	74	149	128	234	169
$CrPO_4$	62159	6	P(1)	4	6	26	24	64	56	154	96	226	152	368	216
$CePO_4$	31563	8	P(1)	4	6	32	30	88	68	184	124	308	196	476	294
$DyPO_4$	79756	8	P(1)	4	6	36	34	92	62	180	122	300	182	444	266
$BiPO_4$	60522	8	P(1)	4	6	36	38	118	86	230	150	378	234	566	338
Series with N_2 = 7															
$Cu_3(PO_4)_2$	68811	4–5	P(1)	4	7	23	28	64	61	132	107	208	168	322	239
$Co_3(PO_4)_2$	38259	5–6	P(1)	4	7	24	27	62	61	134	106	204	174	343	246
$Co_3(PO_4)_2$	9850	6	P(1)	4	7	27	37	85	81	179	146	293	237	448	337
$CePO_4$	79748	9	P(1)	4	7	42	42	126	94	251	167	420	266	630	379
Series with N_2 = 8															
$Cu_3(AsO_4)_2$	201733	4–6	As(1)	4	8	30	36	82	76	171	146	285	221	438	333
$BiAsO_4$	30636	8	As(1)	4	8	44	42	112	84	228	150	376	240	568	342
Series with N_2 = 9															
$Ni_3(AsO_4)_2$	63708	6	As(1)	4	9	33	36	80	76	173	141	271	217	431	314
$In_3(PO_4)_2$	66831	8	P(1)	4	9	40	50	125	116	260	221	455	359	698	524
Series with N_2 = 10															
$Pb_3(PO_4)_2$	66379	9–10	P(1)	4	10	49	60	149	135	304	253	512	391	769	578
$Ba_3(PO_4)_2$	69450	10–12	P(1)	4	10	54	68	181	161	367	302	615	469	925	692
Series with N_2 = 12.13															
Li_3PO_4	10257	4	P(1)	4	12	25	44	67	96	130	170	214	264	319	380
Li_3PO_4	79427	4–5	P(1)	4	12	26	46	73	106	145	190	243	302	365	434
Ag_3PO_4	201361	4	P(1)	4	12	28	50	76	120	172	218	284	344	448	546
Tl_3PO_4	60780	5	P(1)	4	12	28	53	92	131	176	236	305	374	443	527
Na_3PO_4	33718	4–7	P(1)	4	13	34	64	108	166	242	330	443	561	707	857

Classification of Topological Types of Structures by the Number of Topological Types of T-PMEs

The $M(1+)_3TO_4$ and $M(3+)TO_4$ families include the topologically simplest structures. Thus, all topological types of the structures from the M_3TO_4 family (five types) and almost all types of MTO_4 (11 types) are characterized by the simplest topology with one type of *T*-PME. Two topological types of *T*-PMEs were found only in the $CrPO_4$-type structures.

The $M(2+)_3T_2O_8$ family. Of 23 structural types, nine phases contain one *T*-PME and nine phases have two topologically different *T*-PMEs. This family includes four structural types characterized by the most complex topology, namely, with four (two structural types), six, and twelve types of *T*-PMEs.

The $M(m+)$–$M(m+1+)$–T–O family. Of four types containing *M* atoms in the mixed-valence state, one compound, $Nb_2(PO_4)_3$, has a topologically simple

Table 6. Coordination sequences for *T* atoms in the structures of orthophosphates and arsenates with two topological sorts of *T*-PMEs

Topological type	*CC*	Coordination number of *M*	Atom *T*	Coordination sequence N_k (k = 1–12)											
				1	2	3	4	5	6	7	8	9	10	11	12
$Sb_2(PO_4)_3$	72735	6	P(3)	4	4	20	16	44	28	124	72	164	76	292	162
			P(1, 2)	4	4	20	17	48	28	120	70	160	76	296	163
$CrPO_4$	60836	6	P(2)	4	5	22	23	60	48	134	99	228	147	356	235
			P(1)	4	6	24	24	60	52	144	106	254	166	384	236
$Sn_3(PO_4)_2$	966	4–7	P(2)	4	6	22	25	59	64	146	126	251	20	390	298
			P(1)	4	6	25	29	66	65	140	127	260	20	392	294
$Zn_3(PO_4)_2$	24192	5, 6	P(2)	4	6	24	30	69	66	143	121	252	201	390	307
			P(1)	4	8	29	34	80	73	158	134	268	219	412	314
$Cu_3(AsO_4)_2$	24198	5, 6	As(1)	4	7	25	29	70	66	140	119	241	198	369	274
			As(2)	4	8	28	31	72	72	151	121	244	198	372	282
$Fe_3(PO_4)_2$	79906	5, 6	P(2)	4	7	26	34	78	71	154	128	264	216	397	303
			P(1)	4	8	30	34	76	73	160	134	269	218	410	307
$Hg_3(PO_4)_2$	4273	5–7	P(1)	4	7	29	39	97	91	201	174	353	272	523	391
			P(2)	4	8	32	40	96	91	204	168	336	271	521	393
$Cd_3(AsO_4)_2$	14257	5, 6, 8	As(2)	4	7	29	40	103	97	206	180	366	291	558	423
			As(1)	4	8	32	41	96	93	208	172	346	283	540	414
Cu_2PO_4	80181	3–6	P(2)	4	8	23	29	58	66	117	117	210	194	301	267
			P(1)	4	8	24	33	67	72	124	120	199	192	313	281
$Co_3(AsO_4)_2$	59000	5, 6	As(1)	4	8	29	32	76	72	151	129	262	210	392	296
			As(2)	4	8	30	34	77	77	163	131	266	214	397	304
$Co_3(AsO_4)_2$	23547	6	As(1)	4	7	27	34	77	75	165	140	280	218	420	324
			As(2)	4	9	33	39	87	80	173	148	291	222	430	332
$Cd_3(PO_4)_2$	20202	6–8	P(1)	4	8	32	40	96	92	208	176	362	302	586	426
			P(2)	4	8	34	44	107	99	216	183	373	289	561	443

structure (with one type of *T*-PME). In the *MT* framework of this compound, the *M* octahedra share only vertices with the *T* tetrahedra. Three other orthophosphates have *T*-PMEs of two types each, and one orthophosphate ($Cr_7(PO_4)_6$) is characterized by *T*-PMEs of three types.

Structures with One Type of T-PMEs

Table 5 gives the hierarchical classification of 25 topological types belonging to different families, which contain one topological type of *T*-PMEs. The structures are divided into eight groups according to the range in which the number of *M* atoms on the *T*-PME surface varies. The number of *M* atoms on the surface of the *T* tetrahedron (N_2) varies from 3 to 13, except for $N_2 = 11$. All the types of *T*-PMEs with the above-mentioned values of N_2 are shown in Fig. 2. Examples of selected polyhedral *T*-PMEs containing the *M* polyhedra with coordination numbers from 3 to 9 are shown in Fig. 3.

The total differentiation of 23 out of 25 topological types takes place in the third coordination sphere. As for the remaining two types, a high topological symmetry was found (the CSs are identical up to the fifth coordination sphere) for the $AlPO_4$ phases containing the BU tetrahedra. The latter types are topologically analogous to the SiO_2 frameworks (the structures of cristobalite and quartz).

As mentioned above, the values of N_3 correspond to the number of oxygen atoms bound to the *M* atoms located on the *T*-PME surface. In the topological types under consideration, the minimum value of N_3 (6) corresponds to the O atoms present in the environment of three As atoms with a coordination number of 3, and $N_3 = 12$ corresponds to the O atoms belonging to four isolated Al tetrahedra, which surround the central P tet-

Table 7. Coordination sequences for *T* atoms in the structures of orthophosphates and arsenates with three or more topological sorts of *T*-PMEs

Topological type	*CC*	Coordination number of *M*	Atom *T*	Coordination sequence N_k (k = 1–12)											
				1	2	3	4	5	6	7	8	9	10	11	12
$Cr_7(PO_4)_6$	73261	5, 6	P(1)	4	6	26	28	70	60	151	111	254	177	382	256
			P(3)	4	7	28	28	70	60	153	111	250	181	398	258
			P(2)	4	7	28	28	73	62	150	111	252	177	394	264
$Mg_3(PO_4)_2$	84710	5–7	P(4)	4	7	28	34	80	76	170	147	306	250	480	360
			P(2)	4	8	30	37	91	84	180	157	326	257	485	369
			P(3)	4	8	32	36	86	86	181	153	312	249	494	379
			P(1)	4	8	33	40	90	91	196	162	329	263	512	385
$Cr_3(PO_4)_2$	406829	5, 6	P(2)	4	7	28	35	79	75	163	143	293	224	424	321
			P(4)	4	8	28	32	76	76	162	135	269	211	414	318
			P(3)	4	8	30	31	69	75	167	133	267	217	413	320
			P(1)	4	9	32	32	74	75	164	138	274	218	416	326
$Mn_3(PO_4)_2$	23541	5, 6	P(5)	4	7	28	34	80	80	168	143	299	243	467	370
			P(6)	4	7	28	35	83	81	170	145	302	241	471	372
			P(4)	4	7	29	37	86	89	188	163	337	255	499	394
			P(1)	4	8	29	39	92	87	195	166	321	268	518	387
			P(3)	4	8	29	39	93	87	188	160	325	264	509	389
			P(2)	4	8	30	39	91	82	178	153	315	260	495	376
$Cd_3(PO_4)_2$	63548	5–7	P(3)	4	7	28	35	84	83	173	148	313	254	486	380
			P(2)	4	7	28	36	87	84	177	153	324	258	499	391
			P(1)	4	7	29	37	90	93	196	169	345	264	533	417
			P(5)	4	8	30	41	99	92	200	170	342	277	538	410
			P(6)	4	8	31	42	98	87	193	168	336	272	516	392
			P(4)	4	8	31	42	99	93	207	176	350	285	545	408
$Ca_3(PO_4)_2$	923	6–9	P(11)	4	7	33	42	100	90	196	176	369	288	556	427
			P(12)	4	8	30	37	94	90	204	171	356	291	564	424
			P(10)	4	8	31	36	93	91	211	177	354	292	565	426
			P(6)	4	8	31	38	97	93	210	174	342	282	563	423
			P(2)	4	8	31	40	104	96	214	179	357	297	580	428
			P(8)	4	8	32	37	87	86	197	173	364	285	552	415
			P(4)	4	8	32	37	88	87	192	168	360	282	552	421
			P(3)	4	8	32	43	104	91	204	180	376	287	550	428
			P(5)	4	8	33	38	89	88	201	170	346	276	554	421
			P(7)	4	8	34	40	92	88	202	170	350	279	532	407
			P(9)	4	8	35	39	92	92	208	182	375	295	575	435
			P(1)	4	8	35	41	95	96	215	180	374	301	604	455

rahedron in the modifications of $AlPO_4$. The maximum value of N_3 (54) listed in Table 5 corresponds to the O atoms of ten BaO_n polyhedra on the surface of the *T* tetrahedron in the $Ba_3(PO_4)_2$ structure.

Structures with Two Types of T-PMEs

Table 6 gives the classification of 11 topological types with two types of *T*-PMEs. The number of *M* atoms on the *T*-PME surface varies within a narrower

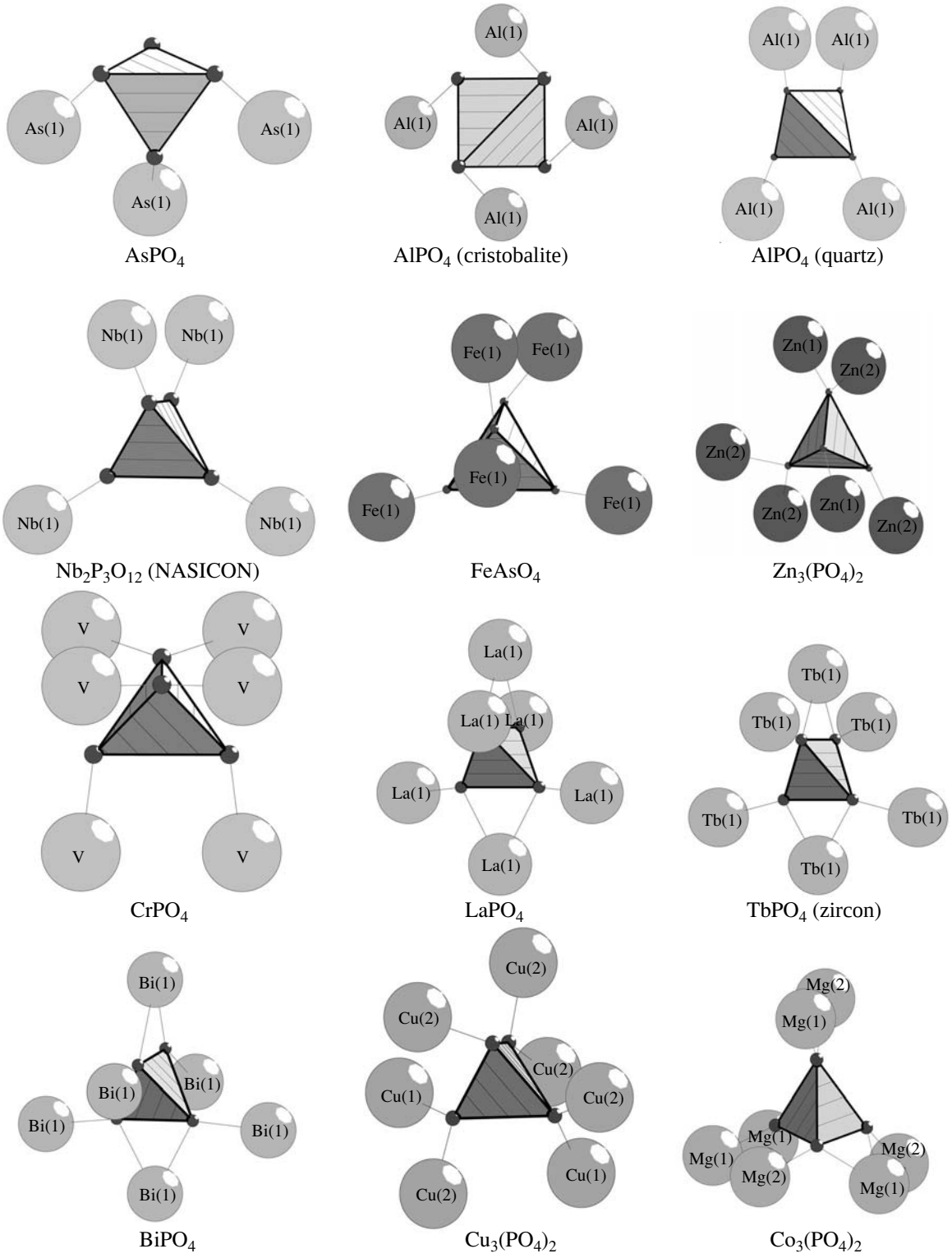

Fig. 2. *T*-PMEs in the crystal structures of uninodal orthophosphates and arsenates.

range (N_2 = 4–9) compared to that observed for the phases with one type of *T*-PMEs.

The phosphorus atoms in the $Sb_2(PO_4)_3$ structure are characterized by the minimum indices $\{N_1, N_2\} = \{4, 4\}$. The framework of this phosphate, like that of $Nb_2(PO_4)_3$ (Table 5), is formed of the octahedra and tetrahedra with shared vertices and its topology is identical to that of the Li-containing superionic conductor $Li_3Fe_2P_3O_{12}$ [32]. It should be noted that it this the only

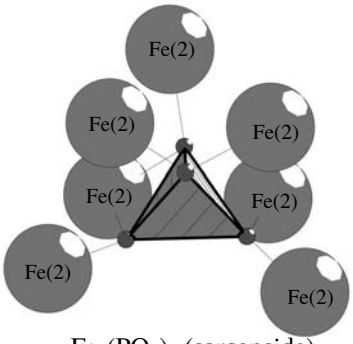

$Fe_2(PO_4)_2$ (sarcopside)

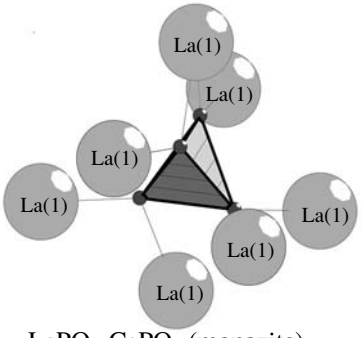

$LaPO_4$-$CePO_4$ (monazite)

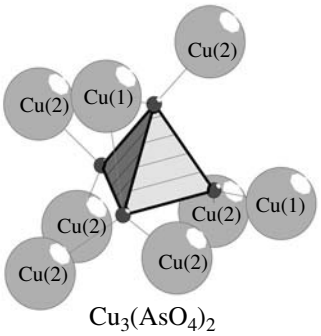

$Cu_3(AsO_4)_2$

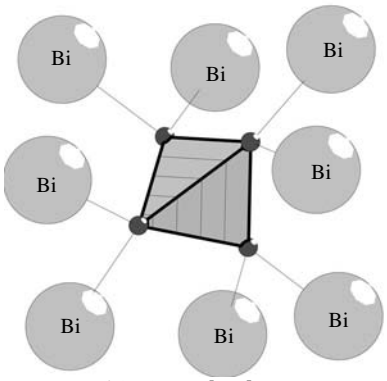

$BiAsO_4$ (scheelite)

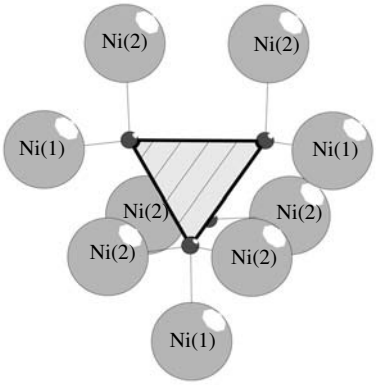

$Ni_3(AsO_4)_2$

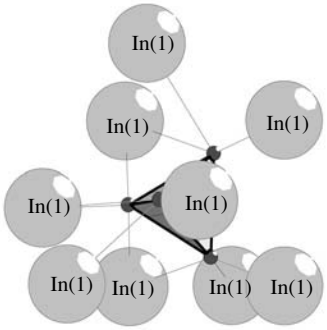

$In_3(PO_4)_2$

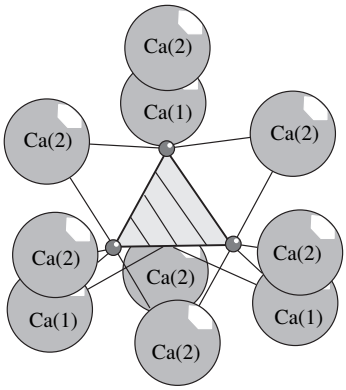

$Ca_3(PO_4)_2$

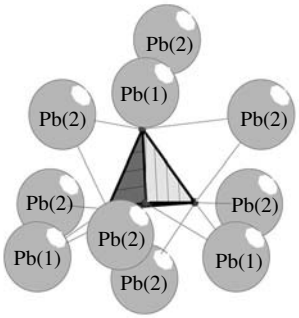

$Pb_3(PO_4)_2$

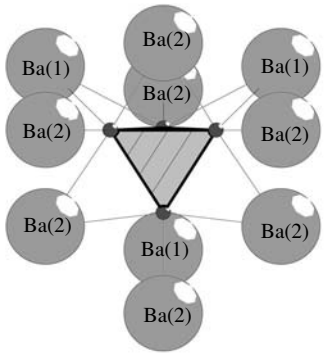

$Ba_3(PO_4)_2$

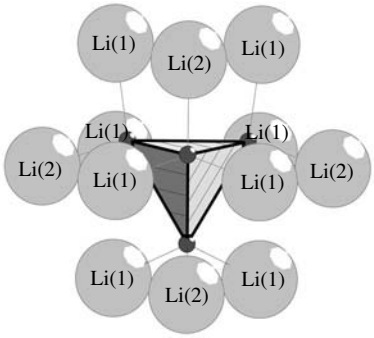

Li_3PO_4 (low-temperature modification)

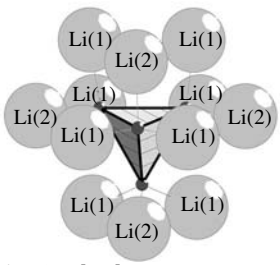

Li_3PO_4 (high-temperature modification)

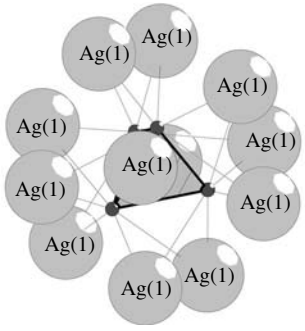

Ag_3PO_4

Fig. 2. (Contd.)

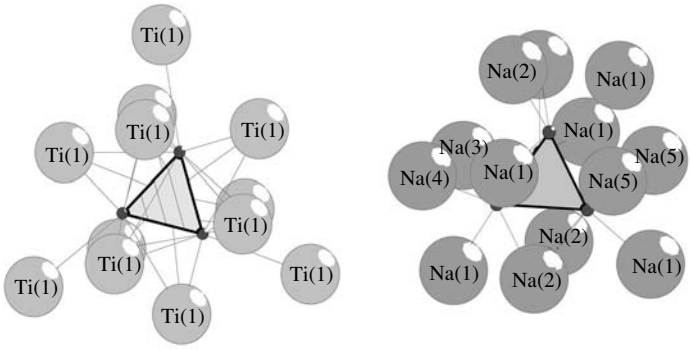

Tl_3PO_4 Na_3PO_4

Fig. 2. (Contd.)

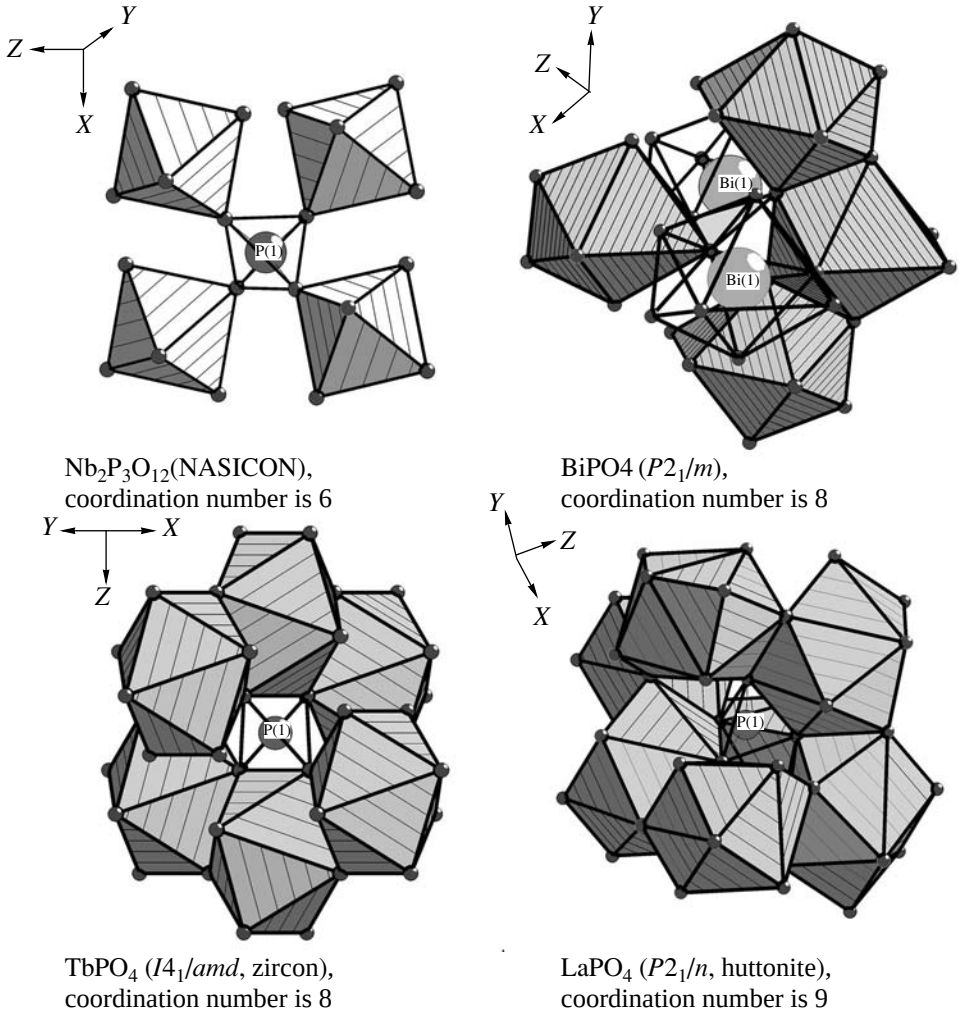

$Nb_2P_3O_{12}$(NASICON), coordination number is 6

BiPO4 ($P2_1/m$), coordination number is 8

$TbPO_4$ ($I4_1/amd$, zircon), coordination number is 8

$LaPO_4$ ($P2_1/n$, huttonite), coordination number is 9

Fig. 3. Examples of polyhedral *T*-PMEs containing *M* polyhedra with the coordination numbers from 6 to 9.

example in this group of compounds under consideration where crystallographically different *T* atoms belong to the same topological type.

The most characteristic sets of indices $\{N_1, N_2\}$ = {4, 7}, {4, 8} and {4, 8}, {4, 8} were found for four and three topological types, respectively.

Table 8. Topological types of MPO_4 and $MAsPO_4$ containing M atoms with the coordination number of M atoms of 9 or 8*

Type	Coordination number	La	Ce	Bi	Pr	Nd	Pm	Sm	Eu	Gd	Tb	Dy	Ho	Y	Er	Tm	Yb	Lu	Sc
		Phosphates																	
ZIR	8	–	–	–	–	–	–	–	–	–	+	+	+	+	+	+	+	+	+
HUT	9	+	+	+	+	+	+	+	+	+	+*c**	+*c*	–	–	–	–	–	–	–
*P*6222	8	+	+	–	–	+	–	–	–	–	–	–	–	–	–	–	–	–	–
*P*21/*m*	8	–	–	+**	–	–	–	–	–	–	–	–	–	–	–	–	–	–	–
		Arsenates																	
ZIR	8	–	–	–	–	–	+*c*	+*c*	+*c*	+*c*	+	+	+*c*	+	+*c*	+*c*	+*c*	+	+*c*
HUT	9	+*c*	+*c*	+	+*c*	–	–	–	–	–	–	–	–	–	–	–	–	–	–
SHE	8	–	–	+	–	–	–	–	–	–	–	–	–	–	–	–	–	–	–

* Reference data were taken from [14]. The $M(3+)$ atoms in the upper row are arranged in decreasing descending order of the unit-cell volumes of the compounds. The topological types are denoted as proposed in the study [24].

** High-temperature phase.

In all structures, the total differentiation of the topology of the coordination spheres of T atoms occurs already in the third coordination sphere, except for $Sb_2(PO_4)_3$. In the structure of this compound, the topologically nonequivalent phosphorus atoms have equal values of $\{N_k\}$ at k = 1–3.

Structures with Three or More Types of T-PMEs

Table 7 lists six topological types of orthophosphates. Five of these types belong to the $M_3T_2O_8$ family, and only one type has a unique stoichiometric composition ($M_7P_6O_{24}$). It should be noted that only one structural type has two representatives, namely, the $M_7(PO_4)_6$ family (M = Cr or Fe) with three types of T-PMEs. The compounds $Mn_3(PO_4)_2$ and $Cd_3(PO_4)_2$ with six types of T-PMEs have similar structures. The structural types from the $M_3T_2O_8$ family with M = Mg or Cr (containing four types of T-PMEs) and with M = Ca (containing 12 types of T-PMEs) are unique.

The number of M atoms on the T-PME surface (N_2) varies from 6 to 9. For all T-PMEs in the structures of the $M_3T_2O_8$ family, the number of M atoms on the surface varies from 7 to 9. It should be noted that the differentiation of some types of T-PMEs in $Cr_7(PO_4)_6$, $Mn_3(PO_4)_2$, and $Ca_3(PO_4)_2$ occurs only after the fourth coordination sphere.

Comparison of the Structural Types of Orthophosphates and Orthoarsenates

On the basis of the data listed in Tables 1–7, the following differences in the topology of the structures of the orthophosphate and orthoarsenate phases can be revealed:

(i) 21 types are characteristic of orthophosphates;

(ii) eight types are characteristic of orthoarsenates;

(iii) 14 types are common to orthophosphates and orthoarsenates.

The structures of orthoarsenates are crystallographically simpler than those of orthophosphates. Thus, eight unique structural types of arsenates and 14 types of arsenates isostructural with phosphates have only one or two different types of T-PMEs, unlike 3, 4, 6, and 12 types of T-PMEs for phosphates.

A substantially larger number of structural types of phosphates (21) is associated with a larger diversity of structural modifications, which are particularly characteristic of phosphates belonging to the $M_3T_2O_{12}$ family. The phosphates $Zn_3(PO_4)_2$ and $Mg_3(PO_4)_2$ have three modifications each: **I** with $C2/c$, **II** with $P2_1/c$, and **III** with $P2_1/c$ (farringtonite) for the former phosphate and **I** with $P2_1/n$ (farringtonite), **II** with $P2_1/b$ (sarcopside), and **III** with $P\bar{1}$ for the latter phosphate. The phosphates $Fe_3(PO_4)_2$, $Co_3(PO_4)_2$, and $Cd_3(PO_4)_2$ have two modifications each. Among arsenates, the dimorphism was found only for $Co_3(AsO_4)_2$ and $Cu_3(AsO_4)_2$.

Analysis of the structures of five topological types of the phases with the simplest stoichiometric composition MTO_4 (the coordination number of M is 8 or 9) (Table 8) led to the following conclusions:

(i) a decrease in the size of the TO_4 tetrahedron, on passing from arsenates to phosphates, leads to the expected shift of the boundary of the structural transition huttonite ⟶ zircon (according to [16], HUT ⟶ ZIR) to smaller sizes of the rare-earth atoms;

(ii) phosphates of early rare-earth elements belong to another structural type (sp. gr. $P6_222$), which is not observed for arsenates;

(iii) for Bi(3+) atoms, which are large in size, the differences in the sizes of the tetrahedra manifest them-

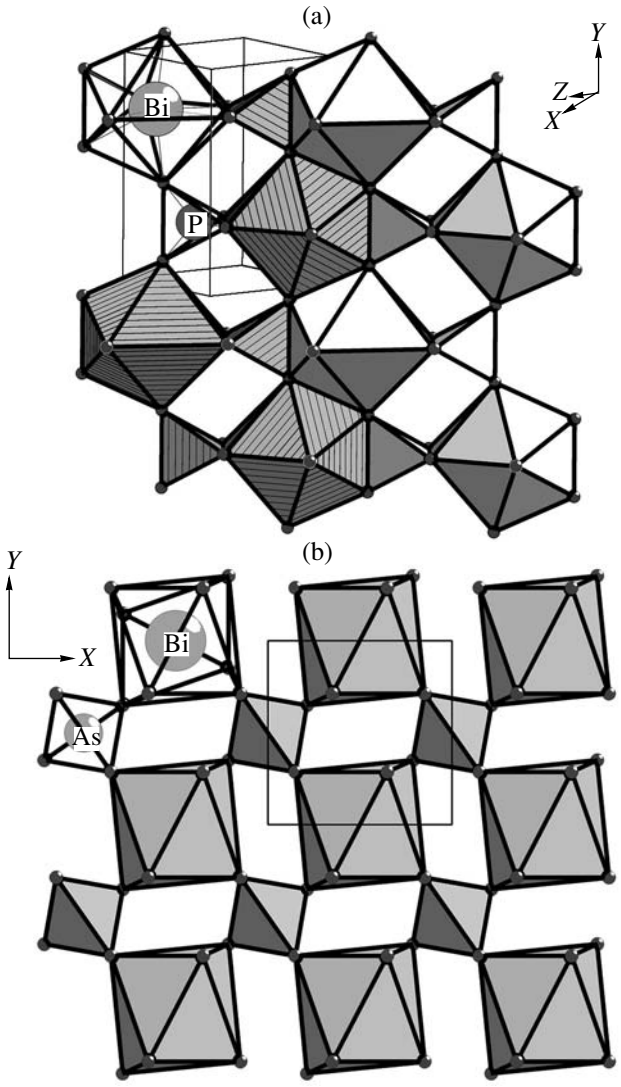

Fig. 4. Fragments of the (a) $BiPO_4$ and (b) $BiAsO_4$ structures.

selves in the crystallization of scheelite-type arsenate (SHE [16]), in which the AsO_4 polyhedra do not share edges with the BiO_8 polyhedra (Fig. 4a), and phosphate (sp. gr. $P2_1/m$), in which shared edges are present (Fig. 4b).

The average bond lengths for the PO_4 and AsO_4 tetrahedra are 1.54(3) Å (P–O) and 1.69(2) Å (As–O). In addition to the above-considered effect of the size of the PO_4 and AsO_4 tetrahedra both on the shift of the boundary of the HUT ⟶ ZIR phase transition and the formation of topologically different structural types (characteristic only of phosphates or arsenates), the geometric characteristics of the tetrahedra can be used to precisely estimate the differences in the bond lengths of the terminal and bridging O atoms in diorthophosphates and arsenates (i.e., in the O_3T–O–TO_3 groups) as well as in any other structures of condensed phosphates and arsenates.

CONCLUSIONS

The classification scheme proposed by us differentiates the largest classes in the Bragg classification and allows one to solve topical problems of crystal chemistry related to the simulation of self-organization processes of crystal-forming systems. Primarily, a large number of orthostructures of phosphates (and arsenates) were divided into subsets with equal chemical ranks of complexity. Then, the structures were differentiated and arranged in order of increasing crystallochemical complexity by the number of topologically different *T*-PMEs. The numbers of the *M* polyhedra, which form the local region of a periodic 3D orthostructure together with the TO_4 tetrahedra, were determined, and their geometric types were identified. By going from the consideration of the simplest building units (tetrahedra and *M* polyhedra) to the analysis of invariant suprapolyhedral clusters using the theory of graphs for their representation, one, in fact, synthesizes the Pauling and Wells models of crystal structures.

ACKNOWLEDGMENTS

This study was supported by the Russian Foundation for Basic Research, project no. 02-02-16861.

REFERENCES

1. W. L. Bragg, Z. Kristallogr. **74**, 237 (1930).
2. F. Liebau, *Structural Chemistry of Silicates* (Springer, Berlin, 1985).
3. D. Yu. Pushcharovskiĭ, *Structural Mineralogy of Silicates and Their Synthetic Analogs* (Nedra, Moscow, 1986).
4. F. Liebau, Fortschr. Mineral. **42** (2), 266 (1966).
5. D. E. C. Corbridge, Top. Phosphorus Chem. **3**, 57 (1966).
6. D. E. C. Corbridge, *The Structural Chemistry of Phosphorus* (Elsevier, Amsterdam, 1974).
7. P. B. Moore, Neues Jahrb. Mineral., Abh., No. 1, 163 (1970).
8. P. B. Moore, Neues Jahrb. Mineral., Abh. **120**, 205 (1974).
9. P. B. Moore, in *Second International Congress Phosphorous Compound Proceeding, Boston, 1980* (Inst. Mondial du Phosphate, 1980), p. 105.
10. P. B. Moore, *Crystallochemical Aspects of the Phosphate Minerals*, Ed. by J. O. Nriagu and P. B. Moore (Springer, Berlin, 1984), p. 155.
11. F. C. Hawthorne, Miner. Mag. **62** (2), 141 (1998).
12. G. A. Nord and P. Kierkegard, Chem. Scr. **15** (1), 27 (1980).
13. K. K. Palkina, Neorg. Mater. **18** (9), 1413 (1982).
14. K. I. Portnoĭ and N. I. Timofeeva, *Oxygen Compounds of Rare-Earth Elements* (Metallurgiya, Moscow, 1986).

15. A. K. Ivanov-Shitz and I. V. Murin, *Ionics of Solid State* (S.-Peterb. Gos. Univ., St. Petersburg, 2000), Vol. 1.
16. G. D. Ilyushin, B. A. Blatov, and Yu. A. Zakutkin, Acta Crystallogr., Sect. B: Struct. Sci. **58** (6), 948 (2002).
17. V. A. Blatov, Acta Crystallogr., Sect. A: Found. Crystallogr. **56**, 178 (2000).
18. *Atlas of Zeolite Structure Types*, 4th ed., Ed. by W. M. Meier *et al*. (Elsevier, London, 1996).
19. A. Wells, *Structural Inorganic Chemistry* (Clarendon Press, Oxford, 1984; Mir, Moscow, 1987), Vol. 2.
20. F. C. Hawthorne, Acta Crystallogr., Sect. A: Found. Crystallogr. **39**, 724 (1983).
21. F. C. Hawthorne, Z. Kristallogr. **192**, 1 (1990).
22. J.-M. Lehn, *Supramolecular Chemistry: Concepts and Perspectives* (VCH, Weinheim, 1995; Nauka, Novosibirsk, 1998).
23. G. D. Ilyushin and L. N. Dem'yanets, *Model of Matrix Assembly of Crystal Structures* (Nauka, Moscow, 2002), p. 82.
24. G. D. Ilyushin and B. A. Blatov, Acta Crystallogr., Sect. B: Struct. Sci. **58** (2), 198 (2002).
25. W. M. Meier and H. J. Moeck, J. Solid State Chem. **27**, 349 (1979).
26. A. F. Wells, *Three-Dimensional Nets and Polyhedra* (Interscience, New York, 1977).
27. L. Stixrude and M. S. T. Bukowinski, Am. Mineral. **75**, 1159 (1990).
28. M. O'Keeffe, Acta Crystallogr., Sect. A: Found. Crystallogr. **51**, 916 (1995).
29. R. W. Grosse-Kunstleve, G. O. Brunner, and N. J. A. Sloane, Acta Crystallogr., Sect. A: Found. Crystallogr. **52**, 879 (1996).
30. V. A. Blatov, A. P. Shevchenko, and V. N. Serezhkin, J. Appl. Crystallogr. **33**, 1193 (2000).
31. V. A. Blatov and V. N. Serezhkin, Russ. J. Inorg. Chem. **45** (Suppl. 2), S105 (2000).
32. G. D. Ilyushin and L. N. Dem'yanets, *Germanates of Tetravalent Metals* (VINITI, Moscow, 1989).

Translated by T. Safonova

Crystallography Reports, Vol. 49, No. 3, 2004, pp. 343–352. Translated from Kristallografiya, Vol. 49, No. 3, 2004, pp. 407–417.

DIFFRACTION AND SCATTERING OF IONIZING RADIATIONS

To the Memory of Z.G. Pinsker

HRTEM Simulation in Determination of Thickness and Grain Misorientation for Hydroxyapatite Crystals

E. I. Suvorova*, P. A. Stadelmann, and P.-A. Buffat****

** Shubnikov Institute of Crystallography, Russian Academy of Sciences, Leninskiĭ pr. 59, Moscow, 119333 Russia*
e-mail: suvorova@ns.crys.ras.ru
*** Centre Interdisciplinaire de Microscopie Electronique, EPFL Lausanne, Switzerland*
Received June 16, 2003

Abstract—High-resolution transmission electron microscopy (HRTEM) and HRTEM simulation by the Bloch wave method (JEMS) are used to determine the structure and thickness of micro- and nanocrystals of biominerals and hydroxyapatite grown from aqueous solutions. It is established that thin (from one to several lattice parameters) crystals, including hydroxyapatite in mineralized biological tissues, are usually formed in low-temperature (up to 40°C) solutions. Relatively thick (up to several tens of lattice parameters) crystals grow only in high-temperature (~95°C) aqueous solutions. HRTEM simulation showed that crystals with a thickness exceeding one lattice parameter consist of nanograins misoriented with respect to one another along various directions within an angle of 0.7°. © *2004 MAIK "Nauka/Interperiodica".*

INTRODUCTION

Comparative characterization of the structure and morphology of hydroxyapatite crystals precipitated as a result of the chemical reaction between calcium and phosphate ions in aqueous solutions under various conditions is important for understanding the mechanisms of crystal growth, including biomineralization and optimization of technology of production of synthetic biomaterials. High-resolution electron microscopy (HREM) allows one to study material structures on the nanometer scale using fast Fourier transform (FFT) of images. The respective diffractograms (FFT) contain the information on the crystal lattice and sample orientation. Simulation of HRTEM images for the known crystal lattice and the zone axis allows one to determine the sample structure on the subnanometer scale and its dimensions along three directions, which, in turn, allows one to follow the mechanism of crystal growth.

The characteristic feature of hydroxyapatite (HAP) morphology is the pronounced shape anisotropy—thin crystalline plates are elongated in the [0001] direction. Two plate parameters (length and width) can readily be determined from the electron microscopy images, whereas the third parameter—crystal thickness—cannot be determined directly and accurately from micrographs. Thus, all attempts to determine the minimum dimension by orienting a crystal with its large face rigorously parallel to the beam have failed, because crystals in this position acquire a considerable charge, and crystal irradiation induces sample drift and deformation. Therefore, one has to determine the thickness on an "in-plane" oriented crystal. The use of thickness contours, stereopairs, and convergent-beam electron diffraction patterns [1, 2] in the thickness range of several nanometers (characteristic of precipitated hydroxyapatite crystals) is not possible either. Analysis of the intensities of X-ray energy-dispersion spectra [3] cannot help either, because of possible lattice distortion caused by radiation damage produced by a focused beam.

Thus, one of the most informative and least destructive methods of determination of the thickness of thin HAP crystals is HRTEM simulation and the subsequent comparison of the simulated images with the known experimental data for their best fitting at the set thickness of the object. Earlier [4–6], we applied this method for determining thickness in the identification of calcium phosphate crystals. However, simulation of some images or some regions of these images gave no satisfactory agreement with the experimental data because of the high sensitivity of crystals to irradiation with electrons, crystal bending, and block structure, which considerably hindered the rigorous orientation of the zone axis. All these difficulties required the introduction of new parameters in image simulation and, first of all, a parameter that would describe the deviation of the crystal orientation from the zone axis associated with possible grain misorientation or crystal bending. Thus, in addition to the three necessary parameters (crystal structure, sample thickness, and defocus), one has also to take into account crystal orientation (both its amplitude and azimuthal angle). For attaining better agreement between the calculations and experiment, we also

1063-7745/04/4903-0343$26.00 © 2004 MAIK "Nauka/Interperiodica"

took into consideration a possible drift and vibrations of the sample. The correction for astigmatism was introduced directly in the process of electron microscopy investigation.

The present study demonstrates good possibilities of the modified simulation software for description of rather complicated situations arising in the interpretation of HRTEM images of large multiatomic unit cells with a large number of light atoms, such as $Ca_{10}(OH)_2(PO_4)_6$. The estimates of small thickness (one lattice parameter) of as-grown crystals and the subnanostructure determined show that attempts to establish the growth mechanism of thin crystals by studying their morphology and structure using HRTEM images are quite justified, as they allow one to work at a near-atomic level.

MATERIALS AND METHODS

Hydroxyapatite crystals were precipitated from dilute aqueous solutions as a result of the chemical reaction between calcium chloride and potassium dihydrophosphate at pH = 5.5–7.5 and various rates of mixing the initial solutions in the temperature range T = 25–95°C [4–6]. Precipitated crystals were washed in distilled water, dried, and transferred onto copper grids preliminarily coated with carbon films for further electron microscopy study. No additional thinning was used, because the crystals were sufficiently thin for electron diffraction analysis and obtaining high-quality HRTEM images.

Biosamples (mineral precipitates on cardiac valves) were prepared in the same way as the samples synthesized in aqueous solutions. The samples of bone tissues (bovine limbs and pieces of broken bones from various parts of the human spine) were washed for several days in the sodium chloride solution and dried. Then, the samples, about $2 \times 2 \times 2$ mm in size, were filled up with epoxy resin so that it penetrated the sample pores. Using the method of ultramicrotomy and a diamond knife, we obtained thin (50–70 nm) slices of the solidified composite thus prepared. It should be noted that, to avoid possible artifacts in electron diffraction analysis and interpretation of HRTEM images, none of the indicated samples was stained or coated either with carbon or metal film.

The samples were studied on a Philips CM300UT FEG high-resolution electron microscope. The images were obtained with the aid of a CCD Gatan797 camera (1024×1024 pixel $\times$ 14 bit). The experimental images were quantitatively processed using the Digital Micrograph 3.6.1 computer program.

Electron diffraction patterns and HRTEM images were analyzed and interpreted based on their simulation using the Java Electron Microscopy Simulation (JEMS) software [7] for hexagonal hydroxyapatite crystals (sp. gr. $P6_3/m$) with the lattice parameters a = 0.942 nm and x = 0.688 nm [8].

JEMS SIMULATION OF HRTEM IMAGES

JEMS [7] is a multifunctional software designed for simulating HRTEM images (by the multislice and Bloch-wave methods), single-, polycrystal, and convergent-beam electron diffraction patterns (within the frameworks of both kinematical and dynamical theories), transfer functions for all the types of electron microscopes, and constructing crystallographic models of various substances in both direct and reciprocal spaces, stereographic projections, and three-dimensional images. In comparison with the earlier EMS simulation software [9], the recent version, written in the Java language for a new user's graphic interface, allows one to vary any sample or image parameter at any moment. Setting the necessary parameters, it is possible to observe, e.g., the changes in HRTEM images in real time. An important advantage of JEMS is the high speed of computations and new possibilities for interpreting results associated with sample drift, vibrations, tilt, astigmatism, and image shift. In studies of the compositions of multiphase systems, JEMS allows one to analyze electron diffraction patterns and identify the constituent phases in a large number of compounds simultaneously. Thus, in order to confirm the presence of the hydroxyapatite phase, each electron diffraction pattern obtained was compared with 15 calculated diffraction patterns of different modifications of calcium phosphate.

We used JEMS to simulate electron diffraction patterns, HRTEM images, and their diffractograms. The procedure of simulation of HRTEM images consisted in the following. First, we input into the program the following parameters of the microscope used (e.g., of a Philips CM300UT FEG microscope):

—accelerating voltage 300 kV,

—spherical-aberration coefficient 0.65 mm,

—chromatic-aberration coefficient 1.2 mm,

—resolution at a 45-nm-Scherzer defocus of 0.17 nm,

—divergence of the electron beam (half-illumination angle) 0.8 mrad, and

—deviation from the focus distribution 4.0 nm.

The parameters for simulating images, namely, the initial defocus, the step in the defocus variation, the set of defocus values, the dimensions of the simulated images along the x and y directions, and the level of random noise were set directly in the process of simulation; the number of iterations determined the crystal thickness.

JEMS allows one to study the effect of the incident-beam tilt either by displacing the objective-lens aperture or by tilting the sample. In the present study, we assumed that the incident beam is normal to the sample surface and considered only the effect of the beam deviation from the zone axis. The crystal tilt in the JEMS program is described by positioning the Laue circle center (CLC) in the reference system of reflection indi-

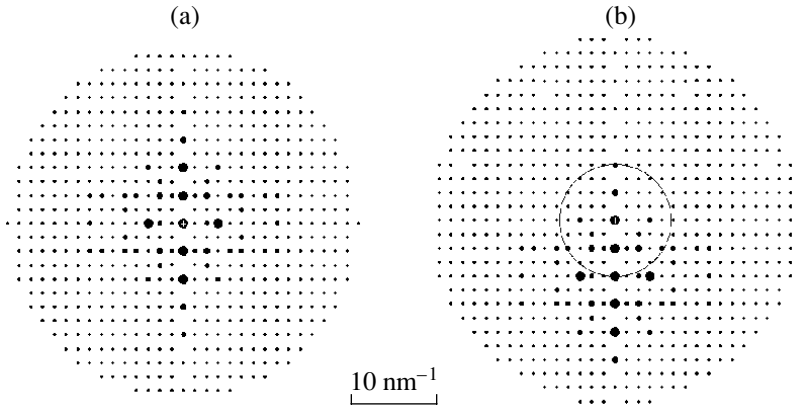

Fig. 1. Effect of the sample tilt on the electron diffraction pattern: (a) sample is oriented rigorously (no tilt) along the [100] zone axis, (b) sample is tilted at an angle of 0.66° to the [100] direction, with the CLC being located at the point with the coordinates 0, 0, –4.02. The closest zone axis is [60, 0, –1].

ces that can be both integral, coinciding with the reflection coordinates, or fractional. To distinguish the reflection indices from the CLC coordinates, the latter are separated in the JEMS program by commas, whereas the negative values are preceded by a minus sign and negative reflection indices are indicated by bars. In Fig. 1a, the CLC lies at 0, 0, 0 with the circle radius tending to zero for the exact setting of the axis zone. Figure 1b shows that the crystal orientation is close to the zone axis [100]: the crystal is tilted by an angle of 0.66° to the [001] direction; in this case, the CLC coincides with the $00\bar{4}$ reflection with the coordinates 0, 0, –4.02 and the radius equal to $g_{00\bar{4}}$. In this example, we used a hydroxyapatite crystal lattice.

Sample drift and vibrations are usually induced by the charge and radiation damages of a crystal and produce a considerable effect on the contrast of the HRTEM images at the given thickness and defocus. We used the advantage of the JEMS program when studying this effect by introducing numerical values of drift and vibrations along various directions during simulation in order to attain the best possible correspondence between the observed and calculated images. However, it should be noted that the effect of a crystal tilt is considerably more pronounced than all the other possible effects—image shift and sample drift and vibrations, and, therefore, at the first stages of simulation, we took into account only the crystal tilt and, if necessary, introduced into consideration all the remaining parameters at the following stages.

MEASUREMENTS OF THICKNESS OF THIN CRYSTALS

Crystals synthesized in solutions. Thin platelike hydroxyapatite micro- and nanocrystals up to 0.5 μm in length were obtained by precipitation in low-temperature (<40°C) solutions. We shall show that the thickness of such crystals usually do not exceed three hydroxyapatite lattice parameters.

The series of HRTEM images of $[\bar{1}100]$-oriented hydroxyapatite crystal calculated for various values of thickness and defocus by the Bloch wave method are shown in Fig. 2a. Roman numeral I indicates the images simulated for the exact position of the zone axis with no allowance made for vibrations, II indicates the images calculated for crystals misoriented with respect to the zone axis by 0.81°, with the CLC being located at the point with the coordinates 0, 0, –0.5, and, finally, images III were calculated with due regard for the sample tilt and vibrations along the *y* axis with the amplitude 0.06 nm. The comparison of all the calculated images with the experimentally obtained image in Fig. 2b showed that it was absolutely necessary to take into account the tilt and vibrations of the sample while estimating its thickness. The best agreement was attained for the image calculated for a 0.8-nm-thick crystal with the defocus 45 nm, at the 0.81° tilt to the $[\bar{1}100]$ zone axis, and the vibration amplitude 0.06 nm. It is seen that the ideal (I) and real (III) images considerably differ.

Table 1. Conditions for simulating HRTEM images of hydroxyapatite crystals and attaining the best possible match of the calculated image to the experimental micrograph shown in Fig. 3b

Region	CLC	Tilt angle, deg
T_0	Without tilt, drift, and vibrations	
t_1	(0, 0.04, –2.82)	0.47
t_2	(0, 0, –4)	0.66
t_3	(0, 0.04, –2.79)	0.46
t_4	(0, 0.04, –4.61)	0.76

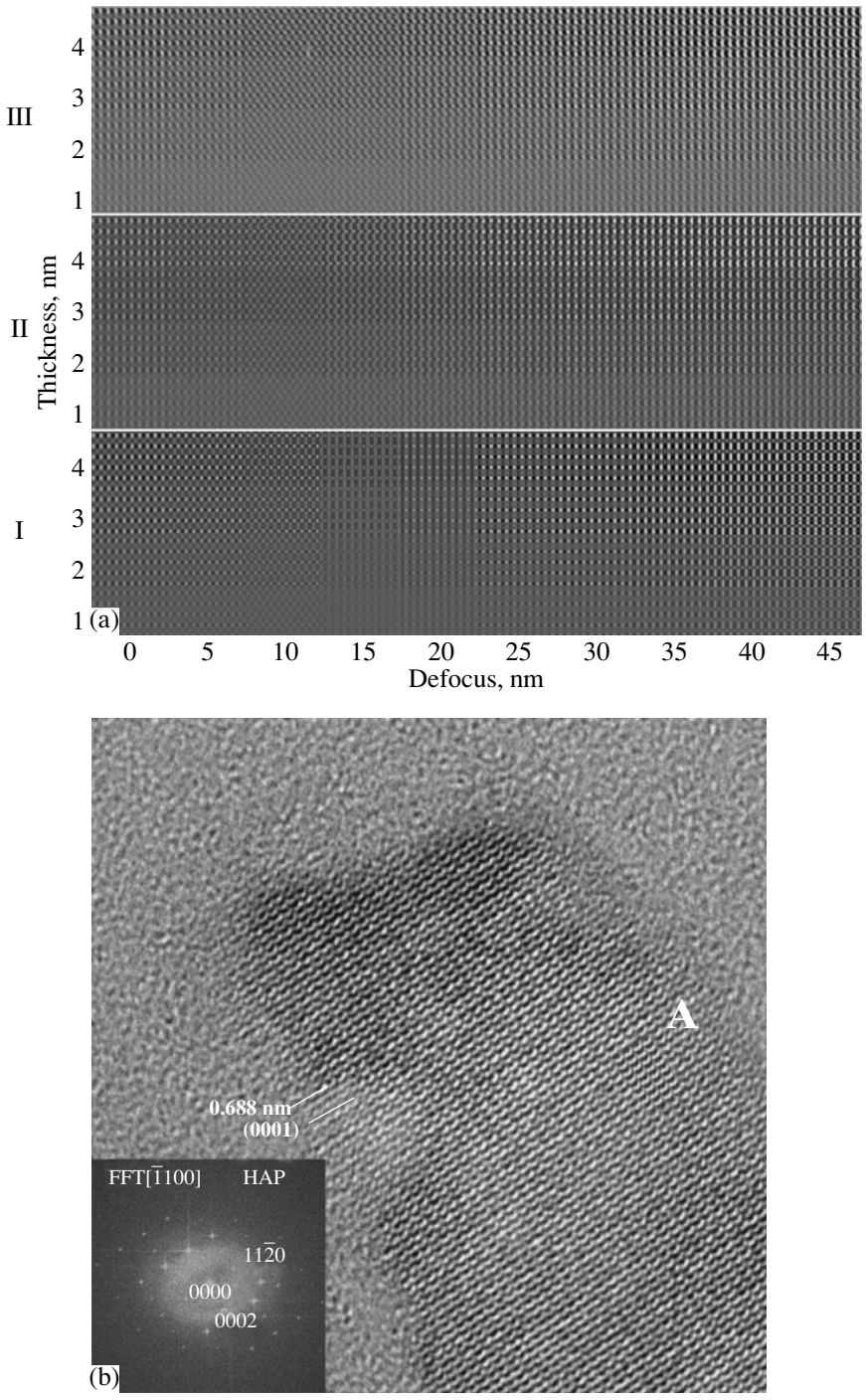

Fig. 2. (a) Images of a hydroxyapatite crystal calculated at the orientation close to [$\bar{1}$100] at defocus ranging from 0 to 45 nm and thickness ranging from 1 to 4 nm. (I) Simulation at the exact orientation (without sample tilt and vibrations), (II) simulation of the crystal images for a sample tilted by an angle of 0.81° to the [$\bar{1}$100] zone axis (CLC coordinates are 0, 0, – 5). (III) simulated images of a crystal tilted to an angle of 0.81° (CLC with coordinates 0, 0, –5) to the [$\bar{1}$100] zone axis and a vibration amplitude of y = 0.06 nm; (b) HRTEM image of a thin hydroxyapatite microcrystal with the zone axis close to the [$\bar{1}$100] direction and the simulated image (inset A) obtained at a defocus of 45 nm and a crystal thickness of 1.0 nm, which illustrates the influence of the 0.81° tilt to the [$\bar{1}$100] axis along the [000$\bar{1}$] direction and the sample vibrations with the amplitude x = 0.06 nm.

(a)

Conditions / Thickness, nm	Without tilt, vibrations, and drift	Tilt: CLC (0, 0, –4) angle 0.66°	Tilt: CLC (0, 0, –4) + vibrations (x = 0.085 nm, y = 0.052 nm) + drift [0.02 nm/s]
4.0 (5 unit cells)	d/nm 4.5 t/nm 4	d/nm 4.5 t/nm 4	d/nm 4.5 t/nm 4
3.2 (4 unit cells)	d/nm 4.5 t/nm 3.2	d/nm 4.5 t/nm 3.2	d/nm 4.5 t/nm 3.2
2.5 (3 unit cells)	d/nm 4.5 t/nm 2.5	d/nm 4.5 t/nm 2.5	d/nm 4.5 t/nm 2.5
1.5 (2 unit cells)	d/nm 4.5 t/nm 1.5	d/nm 4.5 t/nm 1.5	d/nm 4.5 t/nm 1.5
0.8 (1 unit cell)	d/nm 4.5 t/nm 0.8	d/nm 4.5 t/nm 0.8	d/nm 4.5 t/nm 0.8

(b)

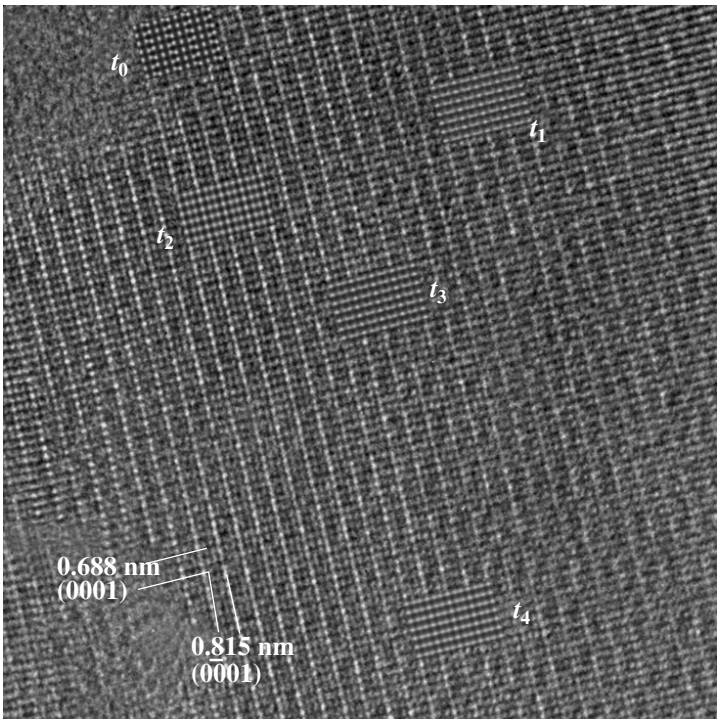

Fig. 3. (a) Series of simulated images of hydroxyapatite crystals with the $[2\bar{1}\bar{1}\,0]$ zone axis obtained at a defocus of 45 nm in the thickness range from 0.8 to 4.0 nm (from one to five unit-cell parameters); (b) HRTEM image of a thin hydroxyapatite crystal grown in low-temperature solution. The t_1–t_4 insets show the calculated images for the $[2\bar{1}\bar{1}\,0]$ zone axis, defocus 45 nm, and thickness 1.5 nm (two unit-cell parameters). The simulation conditions and the misorientation angles are indicated in Table 1. Simulating the images, we took into account vibrations with the amplitudes x = 0.085 and y = 0.052 nm and the sample drift 0.02 nm/s.

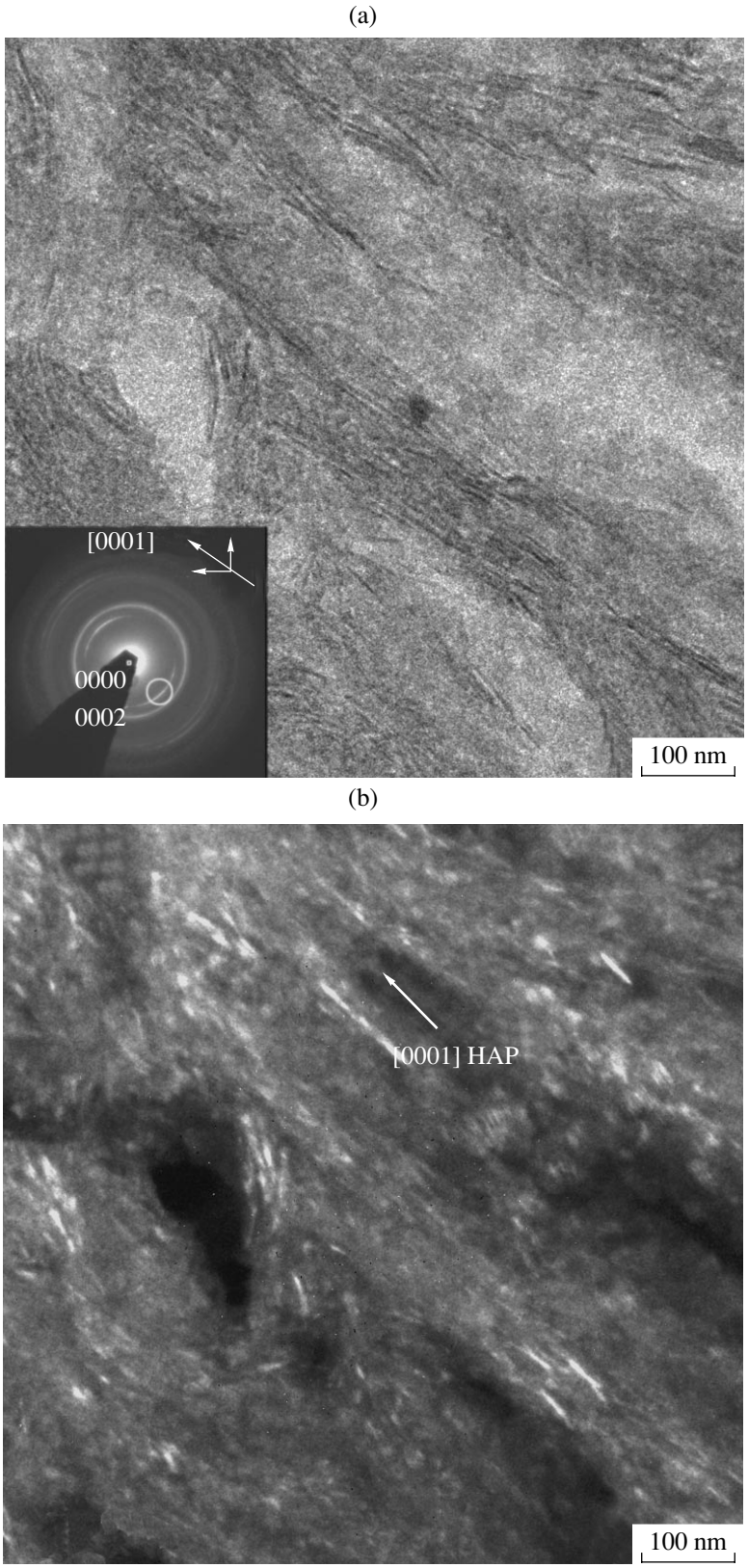

Fig. 4. (a) Bright- and (b) dark-field images of a sample of bone tissue. White circle shows the 0002 reflection in which the dark-field image was obtained.

Figure 3a shows a series of images of a hydroxyapatite crystal obtained along the $[2\bar{1}\bar{1}0]$ direction. The images were simulated for thickness ranging from 0.8 to 4.0 nm (i.e., from one to five unit-cell parameters) at the defocus 45 nm. The left-hand column in Fig. 3a shows the images calculated for the exact zone axis without any sample tilt, drift or vibrations. The middle column shows the images from a sample tilted by an angle of 0.66° to the [0001] direction, which corresponds to the CLC position at the point with the coordinates 0, 0, –4 ($000\bar{4}$ reflection), and, finally, the right-hand column shows the images calculated with due regard for small drift and vibrations of the sample. This series of calculated images was compared with the region A_2 of the experimental micrograph in Fig. 3b. The best agreement was achieved for 1.5- and 2.5-nm-thick crystals with due regard for their drift and vibrations along the *x* and *y* directions. The successive simulation of various regions of this image along the same [0001] direction showed the maximum 0.76° tilt (inset A4) to the $[2\bar{1}\bar{1}0]$ axis (Table 1). The result obtained indicated that the crystal was bent along the [0001] direction. For comparison, in the upper left-hand corner, the image simulated for the ideal case (no tilt, drift or vibrations) is shown.

Biological hydroxyapatite crystals. We expected that the thickness of hydroxyapatite crystals formed in living organisms would not exceed the thickness of these crystals synthesized in low-temperature solutions. This assumption was confirmed by simulated images.

The bright- (Fig. 4a) and dark-field (Fig. 4b) images of bone tissues showed that nanocrystals in the sample are textured along the [0001] direction coinciding with the direction of collagen fibers, with the angle of nanocrystal misorientation attaining values of ±30°. The dark-field image obtained in the 0002 reflection (Fig. 4b) clearly shows that the length of hydroxyapatite crystals on the collagen fibers from bone tissues is less than 15 nm. Simulated HRTEM images of individual hydroxyapatite crystals from bone tissues gave a thickness equal to one unit-cell parameter. Figure 5 shows the HRTEM image of one of these crystals along the $[2\bar{1}\bar{1}0]$ direction (determined from the diffractogram) and the corresponding calculated image (inset A) for the assumed thickness 0.8 nm, defocus 45 nm, and tilt angle to the $[2\bar{1}\bar{1}0]$ axis of about 0.11° along the $[01\bar{1}0]$ direction.

The crystals of mineral precipitates formed on cardiac valves were randomly orientated in agglomerates, which is confirmed by the ring electron diffraction pattern in Fig. 6 and were up to 0.5 μm in length. All these facts make these samples similar to precipitates formed in aqueous solutions, but different from the samples of bone tissues. Thus, crystallization of hydroxyapatite

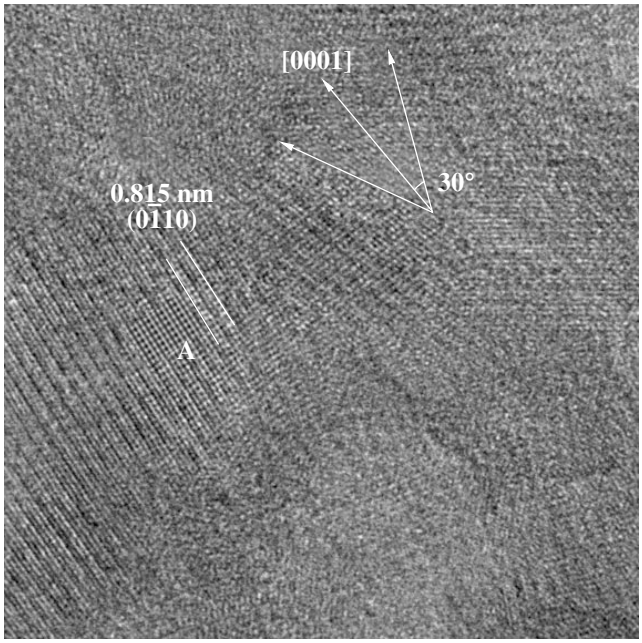

Fig. 5. HRTEM images of hydroxyapatite nanocrystals from a sample of bone tissue. The images (inset A) were simulated at the defocus 45 nm and the crystal thickness 0.8 nm, and the crystal was tilted by 0.11° to the given direction. The arrows on the micrograph indicate the angular scatter in the texture, ±30°, consistent with the corresponding electron diffraction pattern.

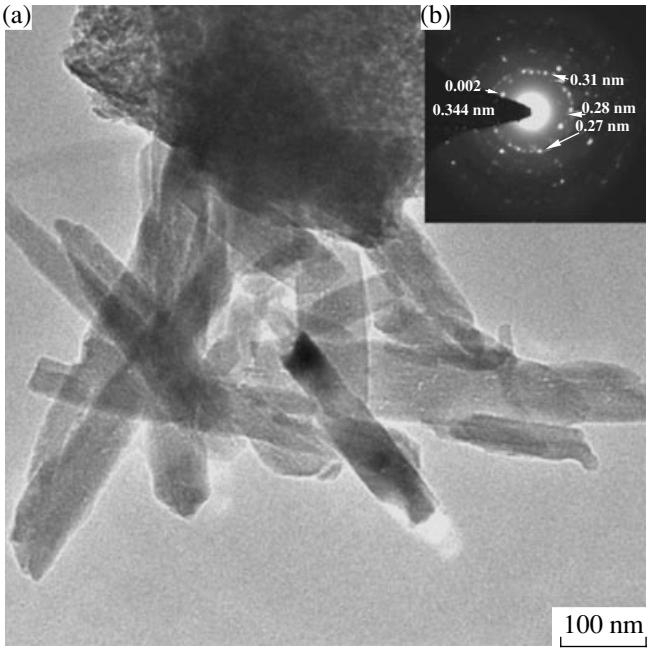

Fig. 6. (a) Hydroxyapatite crystals precipitated on the cardiac aortic valve and (b) the corresponding electron diffraction pattern.

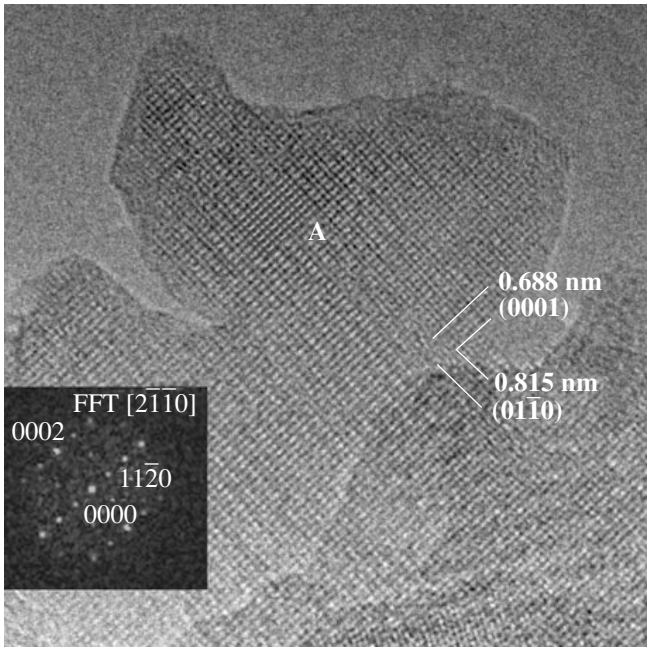

Fig. 7. Hydroxyapatite crystals precipitated on the cardiac aortic valve: HRTEM image and the corresponding diffractogram and the simulated image (inset A) obtained at the [2$\bar{1}\bar{1}$0] zone axis, the defocus 45 nm, the thickness 0.8 nm, the tilt angle to the [2$\bar{1}\bar{1}$0] direction 0.23°, sample vibrations x = 0.085 nm and y = 0.052 nm, and sample drift 0.02 nm/s.

crystals from aqueous solutions can be considered an adequate model of pathological mineralization on cardiac valves [10]. The common characteristic is the crystal thickness, which does not exceed three lattice parameters. Figure 7 shows an HRTEM image with the zone axis close to the [2$\bar{1}\bar{1}$0] direction, defocus 45 nm, crystal thickness 0.8 nm, tilt angle to the [2$\bar{1}\bar{1}$0] direction 0.23°, amplitudes of sample vibration x = 0.085 and y = 0.052 nm, and sample drift 0.02 nm/s.

THICKNESS AND STRUCTURE OF "THICK" HYDROXYAPATITE CRYSTALS

The thickness of relatively thick (up to several tens of nanometers) hydroxyapatite crystals that usually formed in high-temperature (up to 95°C) aqueous solutions considerably exceeds the thickness of crystals precipitated in low-temperature solutions. Figure 8a shows a thick hydroxyapatite crystal and its electron diffraction pattern taken along the [$\bar{1}$100] zone axis. The crystal length is about 1 μm, and its width is about 250 nm. The analysis of the corresponding HRTEM image was made for the crystal part indicated by a light square.

Simulation was started with the construction of a series of images in the "defocus-thickness" coordinates, with the thickness ranging from 1 to 100 nm and defocus ranging from 0 to 60 nm for a rigorously oriented [$\bar{1}$100] hydroxyapatite crystal. We selected from this series only the images with defocus close to the Scherzer value and, when necessary, simulated the image for a crystal whose orientation deviated from the exact zone axis of the sample. The results obtained are presented in Fig. 8b. It is seen that the thickness of the crystal edge equals 1 nm, i.e., one lattice parameter along this direction (inset t_1 in Fig. 8b). Moving from the edge to the crystal center (from t_1 to t_{10}), we successively determined sample thickness up to a value of 46 nm, which corresponded to 46 unit-cell parameters of a hydroxyapatite crystal. Table 2 lists the crystal thickness determined in the direction from the crystal edge to its center and, also, the directions and the values of deviations of nanograins from the [$\bar{1}$100] zone axis during crystal growth.

Table 2. Thickness change in the direction from the edge of the crystal to its center and nanograin misorientation in a hydroxyapatite crystal shown in Figs. 8a and 8b

Region	Thickness, nm	Defocus, nm	CLC coordinates	Tilt angle, deg
t_1	1.0	34 ± 3	(000)	0
t_2	2.0	34 ± 3	(0.88, 0.88, –1.86)	0.37
t_3	7.5	31 ± 3	(0.76, 0.76, 1.46)	0.30
t_4	15	34 ± 3	(0.80, 0.80, 1.75)	0.34
t_5	23	22 ± 3	(0.60, 0.60, –1.51)	0.29
t_6	35	32 ± 3	(1.48, 1.48, –0.99)	0.34
t_7	39	103 ± 3	(–0.52, –0.52, 1.22)	0.24
t_8	43	123 ± 3	(–0.52, –0.52, 1.22)	0.24
t_9	46	128 ± 3	(–0.52, –0.52, 1.22)	0.24
t_{10}	46	161 ± 3	(–2.20, –2.20, 0.47)	0.53

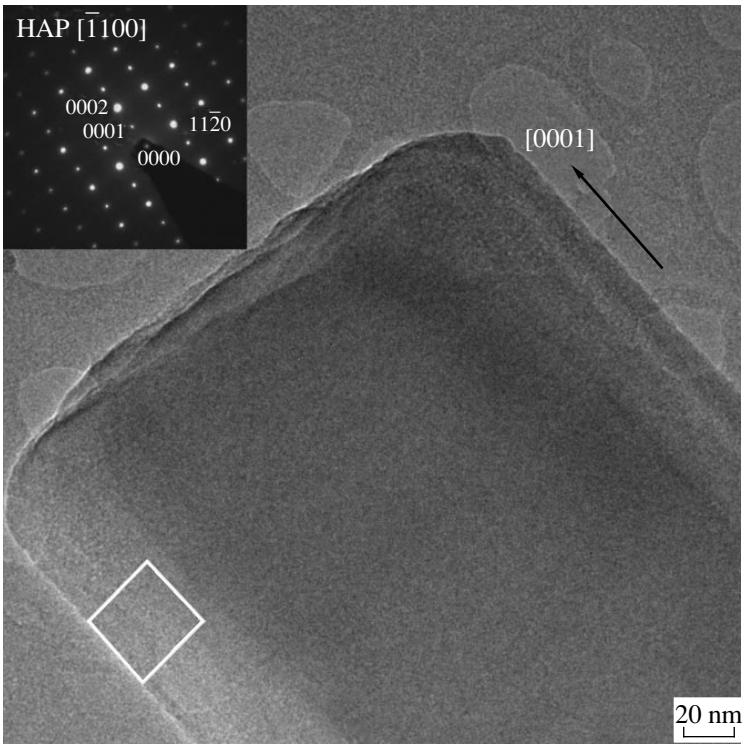

Fig. 8. Electron-microscopy image of a thick hydroxyapatite crystal and the corresponding electron diffraction pattern obtained along the [$\bar{1}$100] zone axis.

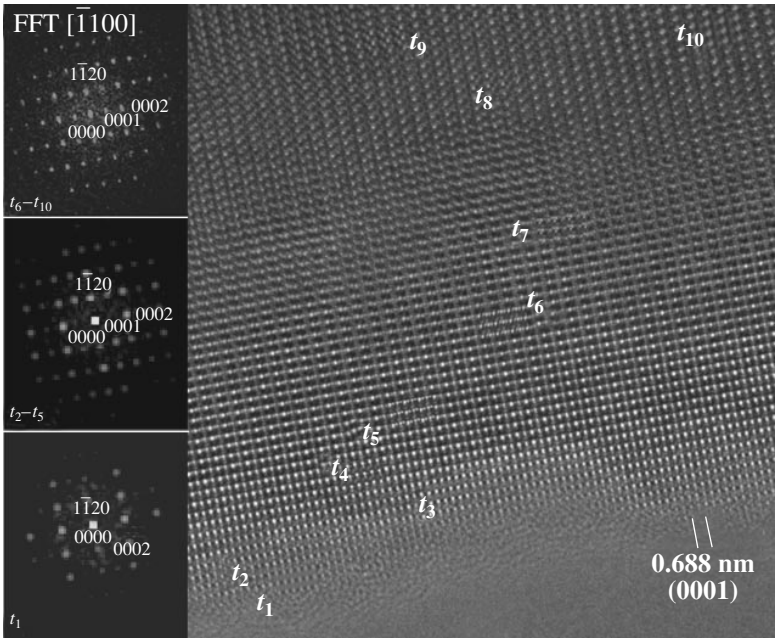

Fig. 9. The region shown by a white square yields the HRTEM image that is simulated in order to determine the crystal thickness. HRTEM image along the [$\bar{1}$100]. Three diffractograms in the left-hand side of the figure correspond to the thickness t_1 = 1 nm, t_1–t_5 to thickness ranging from 2 to 23 nm, and t_6–t_{10}, to thickness ranging from 35 to 46 nm. Insets t_1–t_{10} show simulated images, with the conditions of their simulation being indicated in Table 2.

Three diffractograms in the left-hand part of Fig. 8b were obtained from the successive parts of the crystal having different thickness and containing the same crystallographic information as the electron diffraction pattern shown in Fig. 2a. Attention must be paid to the absence of the forbidden 0001 reflection on the diffractogram t_1 obtained from the thinnest part of the sample, whereas two other diffractograms, as well as the electron diffraction pattern, show this reflection. The absence of the 0001 reflection for the thinnest part of the crystal is consistent with the extinction rules for diffraction patterns of hydroxyapatite crystals in the kinematical approximation. At the same time, high intensities of the forbidden reflections observed for thicker portions of the crystal cannot be explained by double diffraction of the sample thus oriented or by nonideal packing of atomic planes.

It should be noted that agglomeration is less characteristic of relatively large crystals than of thin nanocrystals. Moreover, thick crystals preserve their structure under an electron beam for a longer time. Therefore, there was no necessity to take into account the shift and vibration effects in the simulated images of thick crystals, whereas making allowance for these effect is absolutely necessary for thin micro- and nanocrystals.

CONCLUSIONS

High-resolution transmission electron microscopy and image simulation form an efficient method of determining thickness of thin crystals and crystals formed in living organisms. More precise results can be obtained by the conventional method of simulating a number of images at the set thickness and defocus with due regard for the effects associated with the sample tilt (deviation from the exact position of the zone axis) and its drift and vibrations. Simulation of individual nanoregions of crystals and determination of their misorientation with respect to one another yields information on the structure at the subnanometer level and the mechanism of crystal formation. The following characteristics of crystals synthesized from low-temperature aqueous solutions and crystals formed in living organisms are established. In both cases, crystal thickness does not exceed three unit-cell parameters, whereas the crystals formed in high-temperature solutions can have thickness up to several tens of nanometers.

ACKNOWLEDGMENTS

The authors are grateful to Prof. E. Lundager Madsen from the Chemistry Department of the Royal Veterinary and Agricultural University, Denmark, and Prof. V.V. Klechkovskaya from the Shubnikov Institute of Crystallography of the Russian Academy of Sciences, Moscow, for fruitful discussions and to D. Laub from the Center Interdisciplinaire de Microscopie Electronique, EPFL, Lausanne, Switzerland, for her help in preparation of samples of bone tissues. The study was supported by the Russian Foundation for Basic Research, project no. 01-02-16176.

REFERENCES

1. *Electron Microscopy of Thin Crystals*, Ed. by P. B. Hirsch, A. Howie, R. B. Nicholson, D. W. Pashley, and M. J. Whelan (Plenum, New York, 1965; Mir, Moscow, 1968); D. B. Williams and C. B. Carter, *Transmission Electron Microscopy: A Textbook for Materials Science* (Plenum, New York, 1996).
2. D. C. Joy, A. D. Romig, Jr., and J. I. Goldstein, *Principles of Analytical Electron Microscopy* (Plenum, New York, 1986).
3. P. A. Buffat, J.-D. Ganiére, and P. Stadelmann, *Evaluation of Advanced Semiconductor Materials by Electron Microscopy*, Ed. by D. Cherns (Plenum, New York, 1990).
4. E. I. Suvorova and P.-A. Buffat, J. Microsc. **196**, 46 (1999).
5. E. I. Suvorova and P.-A. Buffat, Eur. Cells Mater. **1**, 27 (2001); http://www.eurocelmat.org.uk.
6. E. I. Suvorova and P.-A. Buffat, Kristallografiya **46** (5), 796 (2001) [Crystallogr. Rep. **46**, 722 (2001)].
7. M. I. Kay, R. A. Young, and A. S. Posner, Nature **204**, 1050 (1964).
8. P. Stadelmann, http://cimewww.epfl.ch/people/Stadelmann/jemsWebSite/jems.html.
9. P. Stadelmann, Ultramicroscopy **21**, 131 (1987).
10. E. I. Suvorova and P. A. Buffat, J. Biomed. Mater. Res. **63**, 424 (2002).

Translated by L. Man

Crystallography Reports, Vol. 49, No. 3, 2004, pp. 353–356. Translated from Kristallografiya, Vol. 49, No. 3, 2004, pp. 418–421.

DIFFRACTION AND SCATTERING OF IONIZING RADIATIONS

To the Memory of Z.G. Pinsker

Energy Dependence of the Reliability Factor in Electron Crystallography

V. L. Vergasov and S. V. Nikolaeva

Shubnikov Institute of Crystallography, Russian Academy of Sciences, Leninskiĭ pr. 59, Moscow, 119333 Russia

e-mail: snikolaeva@yandex.ru

Received July 1, 2003

Abstract—The region of the global minimum of the reliability factor is established for a ⟨111⟩ oriented Si crystal with thickness z ranging within $200 < z < 250$ Å at an energy of $E = 100$ keV. The value of this minimum allows one to perform structural analysis for a dynamically scattering specimen within the framework of the kinematical theory of diffraction. It is established that the formation of this region is provided by a small number of densely filled Bloch states. Theories of direct and back quasi-kinematical diffraction are developed. It is shown that the crystal under study can be brought into the region of quasi-kinematical diffraction by varying the accelerating voltage of the beam. The criteria are formulated that should be satisfied in this case. © *2004 MAIK "Nauka/Interperiodica".*

The physical basis that underlies the structural determination by the methods of electron crystallography is the first Born approximation of the scattering theory, in which an object is considered as a weak perturbation of an incident electron beam. In application to scattering from periodic structures, this approximation is called the kinematical theory of diffraction [1, 2] and the amplitude of the gth diffraction beam, Ψ_g, is proportional to the corresponding Fourier component V_{0g} of the crystal potential

$$\Psi_g \sim \frac{V_{0g}}{|\mathbf{K}_0|} z, \tag{1}$$

where $\mathbf{K}_0$ is the wave vector of the incident beam and z is the object thickness.

In this case, the knowledge of diffracted-beam intensities $I_g = |\Psi_g|^2$ allows one to solve the inverse problem of the scattering theory, i.e., to determine the potential of the scattering object $V(\mathbf{r}) = \sum_g V_{0g} \exp\{2\pi i \mathbf{g}\mathbf{r}\}$.

In electron diffraction analysis, this Fourier analysis is performed mathematically, whereas, in high-resolution electron microscopy (HREM), it is performed directly in a microscope. As a result, one can observe the projection of the atomic structure of an object, $V(\rho) = \bar{V}(\mathbf{r})_z$. We believe that it is useful to combine electron diffraction analysis and HREM: electron diffraction analysis yields information on the absolute V_{0g} values, whereas HREM provides information about their phases [3].

The applicability condition of the first Born approximation, a weak perturbation of an incident beam, is the requirement that the intensity I_0 of the incident beam be much higher than the intensities of all the diffracted beams, $I_0 \gg I_g$. Then, assuming that I_0 equals unity, we arrive at the inequality

$$\left|\frac{V_{0g}}{K_0} z\right| \ll 1, \tag{2}$$

which imposes severe restrictions on the problem parameters and, in particular, on crystal thickness.

For the conventional energy of incident electrons used in experiments, $E = K_0^2 \sim 100$ keV, the thickness of an object should not exceed several tens of angstroms, i.e., the crystal thickness should not exceed ten unit cells. Violation of this condition makes inequality (1) invalid; in other words, the kinematical theory of diffraction becomes inapplicable and the description of the transmitted electron beam requires rigorous solution of the wave equation. In fact, this solution is the dynamical theory of diffraction. In this case, the amplitude of the diffracted beam, Ψ_g, depends on the whole

1063-7745/04/4903-0353$26.00

Parameters of electron Bloch waves in a ⟨111⟩ Si crystal at E = 100 keV and N = 61

Serial number of the Bloch wave, j	1	2	3
Excitation amplitude, ψ_0^j	0.88	0.47	0.04
Transverse energy, $E_\perp^j$, eV	–24.46	9.60	97.22

set of the Fourier components $\{V_{0g}\}$, which makes the solution of the inverse problem of scattering rather problematic. A HREM image, in this case, no longer corresponds to the potential distribution in the crystal.

Under real experimental conditions, the thickness of a studied object is a barely controlled parameter. Therefore, the question arises whether the results of the respective structural determination are reliable or not. The parameter that determines the answer to this question is the so-called reliability factor R,

$$R = \frac{\sum_g \left| |V_{0g}^{\text{exp}}| - |V_{0g}^{\text{theor}}| \right|}{\sum_g |V_{0g}^{\text{exp}}|}, \quad (3)$$

where V_{0g}^{exp} is the experimental values of V_{0g} and V_{0g}^{theor} is the V_{0g} value calculated based on the structure model used.

Minimization of the reliability factor is one of the most important problems of diffraction analysis. Obviously, in accordance with inequality (2), the reliability factor can be minimized either by reducing the object thickness or by increasing the accelerating voltage for each particular specimen. At the same time, the results obtained in a number of experiments [4, 5] are somewhat unusual. Thus, diffraction analysis in [4] was performed at accelerating voltages ranging from 100 to 300 keV. With a decrease in the accelerating voltage, the reliability factor did not decrease, as was expected, but increased. This may only signify that the object was too thick and electron scattering was of a dynamical nature. Nevertheless, diffraction analysis within the framework of the kinematical theory gave a satisfactory value for the reliability factor. In [5], HREM study of the thick part of a thick wedgelike crystal (dynamical scattering) gave an image analogous to the "correct" image observed at the wedge edge in the region of small thicknesses.

These data make the investigation of the conditions and possibilities of diffraction analysis of arbitrarily thick objects within the framework of the kinematical approximation quite important. First and foremost, it is necessary to study the characteristics of the reliability factor and its dependence on the specimen thickness and beam energy within the framework of the dynamical theory of diffraction.

As an example, consider here a ⟨111⟩ Si crystal, E = 100 keV, with the number of diffracted waves taken into account being N = 61, which provides sufficient accuracy of determination of the main parameters of the wave function. The wave function of an electron, $\Psi(r)$, is determined by a set of the Block waves

$$\Psi(r) = \sum_{j=1}^{61} \Psi_0^{j*} \Psi^j(r) = \sum_{j=1}^{61} \Psi_0^{j*} \sum_{g=0}^{60} \Psi_0^{j*} \Psi_g^j \exp\{2\pi i(\mathbf{k}^j + \mathbf{g})\mathbf{r}\}. \quad (4)$$

The intensity of the diffracted beam is determined to be

$$I_g(z) = \left| \sum_{j=1}^{61} \Psi_0^{j*} \Psi_g^j \exp\{2\pi i(k_z^j - K_z)z\} \right|^2, \quad (5)$$

where $\mathbf{k}^j$ is the wave vector of the jth Bloch wave, the zero Fourier component of the wave function, Ψ_0^{j*}, plays the role of the excitation amplitude of the jth wave, and $K_z = \sqrt{K_0^2 + V_0}$.

The reflection intensities thus calculated were considered experimental ones.

Figure 1 shows the reliability factor and the intensities of the primary and diffracted beams as functions of the crystal thickness. The $R(z)$ curve shows the global minimum and two local minima in the thickness range $200 < z < 250$ Å, where the reliability factor decreases by a factor of almost three. The behavior of $R(z)$, as well as the behavior of $I_g(z)$, can be explained based on the degree of excitation of Bloch waves classified according to their transverse energy $E_\perp^j = K_0^2 - (k_z^j)^2$ (see table). High density $\varepsilon^j = |\Psi_0^j|^2$ is possessed only by sub- and near-barrier waves $\Psi^1(r)$ and $\Psi^2(r)$. The density of the first above-barrier wave $\Psi^3(r)$ can be called moderate, because the densities of the remaining waves are negligible.

The intensities of the first two reflections, (000) and $(\bar{2}02)$, depend mainly on the first two Bloch waves, and, therefore, their $I_g(z)$ curves are of a quasi-sinusoidal nature. The same two Bloch waves also modulate the $I_g(z)$ functions of other reflections.

With an increase in the reflection order, the ever-increasing number of Bloch waves influence the reflection intensity, which makes the $I_g(z)$ functions more complicated. Thus, only three waves participate in the formation of the intensity of the third ring, $I_{\bar{4}22}(z)$,

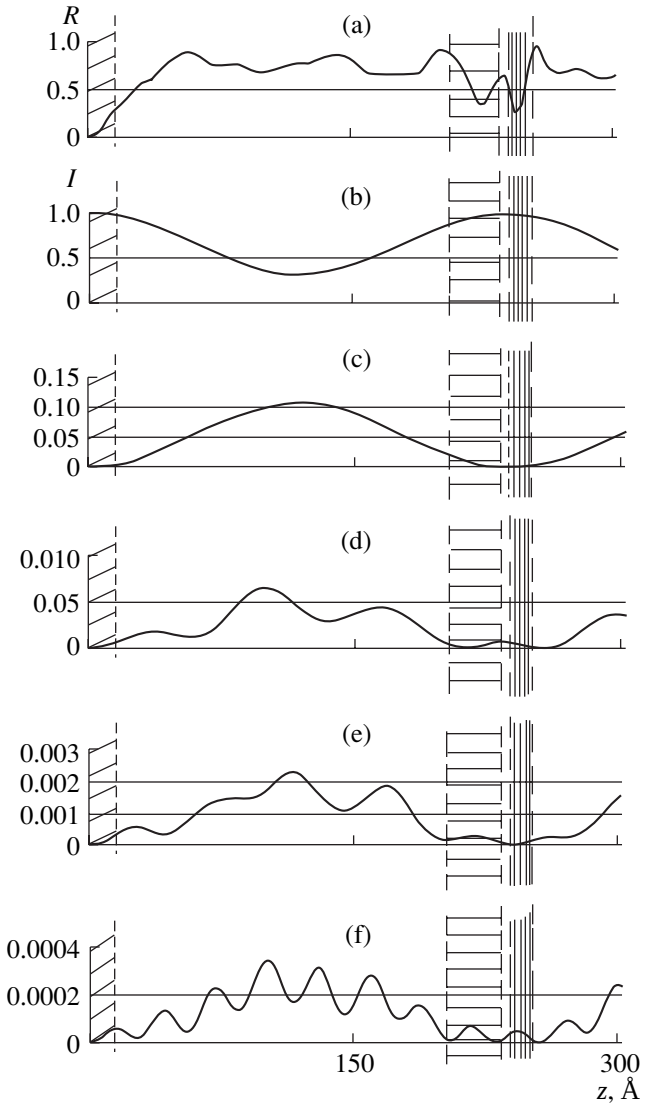

Fig. 1. (a) Reliability factor R and (b) intensities of the transmitted, I_{000}, and diffracted (c) $I_{\bar{2}02}$, (d) $I_{\bar{4}22}$, (e) $I_{0\bar{4}4}$, and (f) $I_{\bar{2}\bar{4}6}$ waves as functions of the thickness of a ⟨111⟩ Si crystal at E = 100 keV.

which explains the local maximum observed at the thickness z = 237 Å, where $I_{\bar{2}02}$ has a minimum. In Fig. 1, the diagonally hatched region is the region of kinematical diffraction.

The quasi-sinusoidal dependences of the intensities of the basic reflections, $I_{000}(z)$ and $I_{\bar{2}02}(z)$, allow one to call the vertically hatched region the region of the direct quasi-kinematical diffraction, and the region hatched horizontally (where, also, $I_{000}(z) \sim z^2$ and $I_{\bar{2}02}(z) \sim z^2$) the region of quasi-kinematical backscattering. It is these regions that determine the position of the global minimum of the $R(z)$ function. Therefore, if the crystal thickness is within the quasi-kinematical region, diffraction analysis of a thick dynamically scattering crystal performed within the framework of the kinematic theory may still yield satisfactory results.

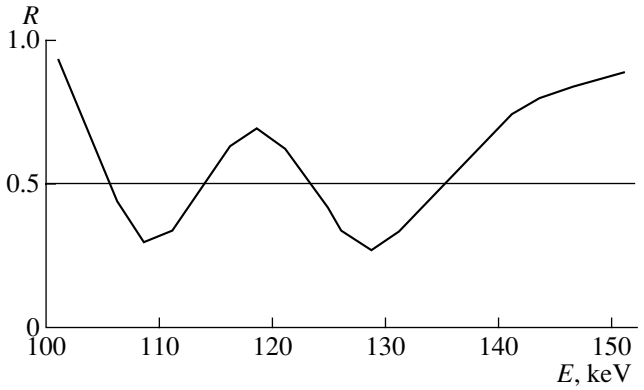

Fig. 2. Reliability factor as a function of electron energy E for a ⟨111⟩ Si crystal with the thickness $z \simeq 254$ Å.

If we have a specimen of an arbitrary thickness, it is possible to bring the quasikinematical region to the exit surface by varying the accelerating voltage of the beam. Thus, Fig. 2 shows the reliability factor as a function of the electron energy, $R(E)$, for a crystal with the thickness ~254 Å (thickness of 27 unit cells). One can readily see that an increase in the accelerating voltage for this crystal of about 10 kV reduces the reliability factor by a factor of three and allows one to perform diffraction analysis of the dynamically scattering specimen within the framework of the kinematical theory.

Whether the quasi-kinematical region is attained or not can be established from the character of the variations in intensities of the main diffracted beams. The region of the global minimum of $R(z)$ corresponds to the maximum of $I_0(z)$ and the minimum of $I_{\bar{2}02}(z)$. The region of the local minimum corresponding to the direct or quasi-kinematical backscattering is determined by the behavior of the intensities of the reflections of the third ring, in our case, $I_{\bar{4}22}(z)$.

We considered here the case of two strongly excited Bloch waves. Their number can vary depending on the atomic number of the element and crystal orientation. Nevertheless, for conventional electron energies, the potential wells of atomic chains are shallow and can include only a small number of Bloch states with high densities. These cases should be considered separately. For multicomponent crystals, one can refine the positions of light atoms in the presence of heavy ones by varying the accelerating voltage.

ACKNOWLEDGMENTS

The authors are grateful to S.A. Krasnikov, K.L. Sorokina, and V.V. Volkov for fruitful cooperation and V.V. Klechkovskaya for her interest in their work. The study was supported by Project NSh.1404.2003.2.

REFERENCES

1. B. K. Vaĭnshteĭn, *Structure Analysis by Electron Diffraction* (Akad. Nauk SSSR, Moscow, 1956; Pergamon Press, Oxford, 1964).
2. J. M. Cowley, *Diffraction Physics* (Elsevier, New York, 1975; Mir, Moscow, 1979).
3. H. S. Fan, S. B. Xiang, F. H. Li, *et al*., Ultramicroscopy **36**, 361 (1991).
4. V. V. Udalova, V. I. Khitrova, Z. G. Pinsker, and A. F. Fedotov, Kristallografiya **17** (4), 750 (1972) [Sov. Phys. Crystallogr. **17**, 657 (1972)].
5. P. L. Fejes, S. Iijima, and J. M. Cowley, Acta Crystallogr., Sect. A: Cryst. Phys., Diffr., Theor. Gen. Crystallogr. **29**, 710 (1973).

Translated by L. Man

Crystallography Reports, Vol. 49, No. 3, 2004, pp. 357–369. From Kristallografiya, Vol. 49, No. 3, 2004, pp. 422–434.

DIFFRACTION AND SCATTERING OF IONIZING RADIATIONS

Indicators of the Magnetic State in the Charge Distributions of MnO, CoO, and NiO. II: Para- and Antiferromagnetism of CoO[1]

J.-P. Vidal*, G. Vidal-Valat*, and K. Kurki-Suonio**

** Laboratoire d'Analyse Multipolaire des Répartitions de Charges Expérimentales, Université Montpellier 2, 34095 Montpellier Cedex 05, France*

e-mail: jpgvidal@univ-montp2.fr

*** Department of Physics, P.O. Box 64, FIN–00014 University of Helsinki, Finland*

Received July 2, 2002

Abstract—X-ray diffraction intensities from CoO were measured above and below the Néel temperature. The data were submitted to a non-parametric multipole analysis aiming at formulation of experimentally valid statements on the nature of the charge distribution. Strong "bonding maxima" are seen between the Co ⟨110⟩O nearest neighbors. In the paramagnetic state they are formed by the Co-ion alone, in the antiferromagnetic state they involve a strong CoO coupling. The outer electrons of oxygen give rise to slight maxima in the ⟨110⟩ directions, making the atom into an O^{2-} ion. In the paramagnetic state, their coupling with the bonding feature forms an octahedral electron cage around each oxygen atom. Broad density maxima between the atoms in ⟨111⟩ directions are present in both states. They connect the "bonding maxima" in the ⟨110⟩ directions, more strongly in the antiferromagnetic state, building up an interatomic three-dimensional network. Such electron network structures seem to be characteristic of metal oxides more generally. *© 2004 MAIK "Nauka/Interperiodica".*

1. INTRODUCTION

This is the second part of an investigation aiming at finding characteristics of the different magnetic states of the first-row transition metal monoxides MnO, CoO, and NiO with the help of a multipole interpretation of their charge densities based on accurate X-ray diffraction data. This paper reports the experiments performed, interpretational procedures used in the case of cobalt oxide, and the conclusions reached on its para- and antiferromagnetic states.

Our principle of interpretation is completely different from the conventional parametric multipole analysis. It does not aim at any sophisticated models that would fit the data, but at the formulation of experimentally valid statements on the nature of the charge distribution that would be as independent as possible of any models. As has been shown repeatedly in earlier papers on direct multipole analysis, a simple reference model is sufficient to achieve this. Results that are expressed in terms of the radial multipole scattering factors and accumulation-of-charge densities of the single atoms do not depend on the reference model, as long as it is "asymptotically valid." It is argued that, in the Fourier representation of the charge density, only such features can be significant as arise from low order multipole components of the ionic distributions. Moreover, comparison of the Fourier representation with the multipole densities of the ions allows one to conclude how the electrons of the different ions contribute to the features found to be significant, as in [1].

The electronic states of transition-metal monoxides have been studied intensively over several decades using many different experimental methods and an abundance of theoretical models with an increasing degree of sophistication. In this respect, there is little to be added to the introductory review of Vidal-Valat, Vidal, K. Kurki-Suonio, and R. Kurki-Suonio in [2].

Bredow and Gerson [3] have made quantum chemical calculations on bulk properties of MgO, NiO, and CoO with various periodic models. They have found that, for NiO and CoO, a combination of the Hartree-Fock exchange functional with the Lee-Young-Parr density functional correlation is the best method in terms of relative stability and geometry and the electronic structure of the valence band.

Recently, Neubeck [4] has made an extensive study of antiferromagnetic MnO, CoO, and NiO by X-ray magnetic scattering. Using nonresonant magnetic scattering, they found nonzero orbital moments in CoO and NiO, which is contrary to what was earlier thought. In comparing their experimental resonance scattering amplitudes with modeled amplitudes based on spin-orbit perturbated crystal field states, they found a good agreement for MnO and NiO, but not for CoO.

Neubeck [4] also presents an excellent review of the development of our understanding of the magnetic structure of these compounds. From this, it is clear that CoO differs from MnO and NiO in some essential

[1] This article was submitted by the authors in English.

respects. For instance, the magnetic moment of CoO is not in the (111) plane, as it is in the case of NiO and MnO, as concluded by Laar [5] and Hermann-Ronzaud, Burlet, and Rossat-Mignot [6] from their neutron studies.

Obviously, the observed properties of CoO have been the most difficult of these three monoxides to interpret, and its electronic structure is not yet understood. Our accurate X-ray diffraction study of its charge distribution may make a new contribution. Preliminary results of this investigation have been available on videotape (Vidal *et al.* [7]) for some time.

2. EXPERIMENTAL PROCEDURES

A single crystal of CoO of full stoichiometry was kindly provided by the Laboratoire de Chimie des Solides, Université d'Orsay (France). It was synthesized by float-zone refining techniques from high-purity powder 5N. By this method, a high degree of mosaicity is produced, minimizing the effect of extinction on the diffracted intensities so that conventional extinction corrections are satisfactory as stated by Vidal, Vidal-Valat, and Zeyen [8]. The full stoichiometry of the crystal was checked and confirmed by optical and crystallographic methods, as reported by Revcolevschi [9].

The crystal was cleaved several times parallel to the (001) crystal faces. It was hard and, when sufficiently thin, optically fully transparent with a light garnet-red color. Cleaving below a certain size reduced the crystal, however, to small pieces. The sample chosen for the X-ray diffraction measurements was a parallelepiped of size $0.134 \times 0.191 \times 0.217$ mm^3. Sometimes, the surface of cleavage was somewhat streaked. The faces of the sample used were, however, seen to be perfectly smooth. The freshly cleaved sample was coated with plastic to avoid oxidization. This protection was seen to be perfectly transparent to the X-ray beam.

The first measurements were made on the grown sample in its freshly cleaved state. It was, however, impossible to obtain acceptable data. A slight random motion of the Bragg peaks around their positions during data registration was observed, this causing random variations in the collected intensities as well. At the same time, background scattering was very high, and reflections beyond $\sin\theta/\lambda = 0.85$ Å^{-1} did not emerge from it. In particular, the *hhh* reflections were suppressed the more strongly the higher *h* was.

These phenomena, which were observed to be similar in both of the magnetic phases, are probably caused by the presence of a high number of vacancies formed in the growth of the crystals and their migration, which is enhanced by the strong magnetostriction in the magnetic phase transition. However, within a year, all these disturbing effects vanished. The *hhh* reflections recovered their intensities. No more motion of the Bragg peaks was observed, and the background scattering attained a normal level, in accordance with the requirements of accurate registration of intensities. Thus, a complete experiment was conducted. The reflections with the most regular profiles were chosen for further analysis.

An accurate X-ray diffraction study of CoO was carried through both above and below the Néel temperature—at 298 K for the paramagnetic phase and 85 K for the antiferromagnetic phase. The temperature was controlled to within ±1 K. Neither a magnetic field nor mechanical stress was applied to the sample in the X-ray diffraction measurements.

Relative integrated intensities of all reflections up to about 1 Å^{-1} in $\sin\theta/\lambda$ in three octants were collected three times in both temperatures on an automated four-circle Enraf-Nonius CAD–4 diffractometer with MoK_α radiation. The data thus obtained consisted of 26 independent reflections. Equivalent reflections differing in integrated intensity by >4% from the average were discarded. The excluded reflections were seen to be randomly distributed. The observed intensity of a reflection was taken to be the mean of the remaining symmetry-related reflections.

The integration was done in the θ-2θ scan mode with programmed scan and aperture at the scanning speed of 2 arcmin s^{-1}. The dead-time correction was automatically taken into account by the analyzer.

The multiple-scattering effect was eliminated by setting the crystallographic and diffractometer axes differently. As a check, all forbidden reflections were measured in a whole octant. No effect was detected.

Background, Lorentz and polarization corrections were made on the intensities, as described by Vidal, Vidal-Valat, Galtier, and Kurki-Suonio [10], as well as the absorption corrections of Busing and Levy [11], using the linear absorption factors 21.696 mm^{-1} and 21.850 mm^{-1} for CoO at 298 and 85 K, respectively.

TDS contaminations were evaluated with the program of Merisalo and Kurittu [12] using the elastic constants of Subhadra and Sirdeshmuk [13]. The effects were small—less than 3% in intensity—owing to the hardness of these compounds.

The data registration was made in terms of the observed triclinic unit cell. The systematic extinctions of the Bragg intensities show, however, that the structure in both phases is very close to the cubic NaCl structure of the symmetry group $Fm\bar{3}m$. Least-squares refinement based on X-ray diffraction patterns yielded the lattice constants 4.260(4) and 4.250(4) Å for the cubic cell at 298 and 85 K, respectively.

The atomic distances corresponding to the ideal cubic structure differ from the real distances by, at most, 0.1%. The analysis was based on the cubic cell.

3. TREATMENT OF DATA

The data were submitted to "direct multipole analysis," as described in the first part of our study on MnO. All that was said about the analysis in that context on the reference model and on the representation of results holds in this case, even in detail, except for data referring specifically to the Co atom and to the numerical values used or obtained, and will not be repeated here.

For the Co^{2+} ion of the reference model, the relativistic Hartree-Fock values of [14] were used with the anomalous scattering factors $f' = 0.299$ and $f'' = 0.973$ by Cromer and Liberman [15] for MoK_α.

Also for CoO, the isotropic mosaic-spread extinction gave lower R factors, 0.010 and 0.013, than particle-size extinctions, which were 0.011 and 0.014 at 298 and 85 K, respectively, and yielded the values $0.035(5) \times 10^4$ rad^{-1} and $0.036(7) \times 10^4$ rad^{-1} for the mosaic spread parameter g and $B_{Co} = 0.366$ (0.035) Å^2, $B_O = 0.516$ (0.052) Å^2 and $B_{Co} = 0.365$ (0.016) Å^2, $B_O = 0.497$ (0.071) Å^2 for the isotropic Debye-Waller factors in 298 and 85 K, respectively. No more significant improvement was obtained by any of the more sophisticated models.

In the successive iterative local Fourier-refinement of the scale and the Debye-Waller factors (cf. Vidal-Valat, Vidal, K. Kurki-Suonio, and R. Kurki-Suonio [16]), the scale factors remained unchanged, while $B_{Co} = 0.348$ Å^2, $B_O = 0.516$ Å^2 and $B_{Co} = 0.348$ Å^2, $B_O = 0.506$ Å^2 were obtained as the final refined values of the Debye-Waller factors of the reference model for 298 and 85 K, respectively.

The results are represented by figures and tables as in the case of MnO.

Table 1 gives the final experimental structure factors, F_0, on an absolute scale, corrected for isotropic mosaic-spread extinction and for anomalous dispersion, together with the extinction factors y and the standard errors of the mean δF_0.

Figure 1 shows the radial accumulation-of-charge densities $s_{i0}(r_i)$ and the radial electron counts $Z_{i0}(R_i)$ around the ionic sites.

Table 2 is related to Fig. 1 and, as spherical characteristics of the ionic charge distributions, gives:

(1) The radii r_0 of best separation at which the radial accumulation-of-charge densities $s_0(r)$ reach their minima, as a measure of the size or the effective "range" of the ionic charge distribution.

(2) The corresponding minimum radial density $s_{0min} = s_0(r_0)$, as a measure of the inseparability of the ion from its surroundings.

(3) The electron count $Z_0 = Z_0(r_0)$ within the radius of best separation as a measure of the charge concentrated in the main bulk of the ionic charge density peak.

Table 1a. Structural factors for CoO at 298 K

h k l	2sinθ/λ, Å^{-1}	F_0	F_c	δF_0	y
0 0 0	0.0000		140.000		
1 1 1	0.4066	60.7835	60.2010	0.3300	0.846
2 0 0	0.4695	97.8882	98.6173	0.5800	0.681
2 2 0	0.6639	79.5798	78.2897	0.5000	0.849
3 1 1	0.7786	45.6229	45.9879	0.2100	0.944
2 2 2	0.8132	63.9447	65.4940	0.3100	0.909
4 0 0	0.9390	57.5381	56.5804	0.3100	0.947
3 3 1	1.0232	35.8417	35.8621	0.2000	0.977
4 2 0	1.0498	50.5362	50.0001	0.2400	0.952
4 2 2	1.1500	45.0762	44.9557	0.2000	0.968
3 3 3	1.2197	25.9159	29.3344	0.1600	0.988
5 1 1	1.2197	28.7003	29.3344	0.1600	0.988
4 4 0	1.3279	37.0973	37.7667	0.2000	0.979
5 3 1	1.3887	25.3801	24.9804	0.1800	0.991
4 4 2	1.4084	34.5427	35.1216	0.2000	0.987
6 0 0	1.4084	34.6821	35.1216	0.1900	0.982
6 2 0	1.5393	32.9947	32.9011	0.2000	0.988
5 3 3	1.5571	22.1988	21.9456	0.1500	0.994
6 2 2	1.6263	30.7432	31.0044	0.1600	0.990
4 4 4	1.6263	26.3238	29.3579	0.1400	0.991
5 5 1	1.6764	20.5625	19.7211	0.1100	0.994
7 1 1	1.6764	19.2766	19.7211	0.1200	0.996
6 4 0	1.6927	28.0562	27.9076	0.1300	0.989
6 4 2	1.7566	27.1865	26.6129	0.1200	0.991
5 5 3	1.8031	18.0288	18.0025	0.1000	0.996
7 3 1	1.8031	17.9282	18.0025	0.1000	0.996
8 0 0	1.8779	24.4096	24.3760	0.1200	0.994

Table 1b. Structural factors for CoO at 85 K

h k l	2sinθ/λ, Å^{-1}	F_0	F_c	δF_0	y
0 0 0	0.0000		140.000		
1 1 1	0.4075	60.2018	60.1711	0.3500	0.840
2 0 0	0.4706	97.1731	98.5045	0.6000	0.672
2 2 0	0.6655	80.0369	78.1600	0.5300	0.843
3 1 1	0.7804	45.8626	45.8925	0.2200	0.942
2 2 2	0.8151	63.2570	65.3664	0.3400	0.906
4 0 0	0.9412	56.8815	56.4612	0.3200	0.945
3 3 1	1.0256	35.1756	35.7553	0.2000	0.976
4 2 0	1.0523	50.7228	49.8912	0.2500	0.950
4 2 2	1.1527	44.5647	44.8567	0.2200	0.966
3 3 3	1.2226	24.5571	29.2315	0.1600	0.988
5 1 1	1.2226	28.5452	29.2315	0.1600	0.988
4 4 0	1.3110	37.2309	37.6875	0.2100	0.978
5 3 1	1.3920	25.4383	24.8850	0.2000	0.990
4 4 2	1.4118	34.2523	35.0508	0.2000	0.986
6 0 0	1.4118	34.4353	35.0508	0.2000	0.981
6 2 0	1.4881	33.3573	32.8376	0.2000	0.988
5 3 3	1.5429	21.7674	21.8572	0.1500	0.994
6 2 2	1.5608	31.6652	30.9471	0.1600	0.984
4 4 4	1.6302	24.7864	29.3059	0.1500	0.990
5 5 1	1.6803	20.3818	19.6381	0.1200	0.994
7 1 1	1.6803	19.5570	19.6381	0.1200	0.995
6 4 0	1.6967	27.7776	27.8599	0.1300	0.988
6 4 2	1.7608	27.0272	26.5688	0.1300	0.991
5 5 3	1.8073	18.0272	17.9231	0.1000	0.996
7 3 1	1.8073	17.9013	17.9231	0.1100	0.996
8 0 0	1.8823	24.3714	24.3373	0.1300	0.994

Table 2. Spherical characteristics of the ionic electron distributions

Co^{2+}	r_0, Å	s_{0min}, *e*/Å	Z_0, *e*	r_{2+}, Å
Experimental				
298 K	1.05	4.419	25.0	1.05
85 K	1.05	2.186	24.88	1.10
Reference model				
298 K	1.10	3.975	25.18	1.05
85 K	1.10	4.012	25.19	1.055
O^{2-}	r_0, Å	s_{0min}, *e*/Å	Z_0, *e*	r_{2-}, Å
Experimental				
298 K	0.92/1.40	4.57/5.36	7.25/9.92	1.42
85 K	0.85/1.37	5.00/5.10	6.93/9.87	1.40
Reference model				
298 K	1.15	4.570	8.69	1.40
85 K	1.15	4.600	8.69	1.39

Note: r_0 is the radius of best separation at which the radial accumulation-of-charge density $s_0(r)$ reaches its minimum, the minimum radial density $s_{0min} = s_0(r_0)$, the electron count $Z_0 = Z_0(r_0)$ within the radius of best separation, and the r_{2+} and r_{2-} are the radii where the electron counts reach the values 25*e* and 10*e* corresponding to the doubly ionized states

(4) The radii r_{2+} and r_{2-}, where the electron counts reach the values 25*e* and 10*e* corresponding to the doubly ionized states.

Figure 2 presents the radial multipole scattering factors $f_{in}(b; R_i)$ as deviations from the reference model. The partitioning radii R_{Co} = 1.15 Å and R_O = 1.30 Å were deduced on the basis of Fig. 1 and were taken to be slightly larger than the radii r_0 of best separation, as in Kurki-Suonio [17]. For oxygen, the same radius has been used in all of our oxide studies. With their error bars, the figures indicate the significance of the components with respect to the errors of mean of the structure factors. All components up to the 10th order were calculated. The components of order 4, 6, and 8 are of about equal significance, while the 10th-order component is insignificant and is not shown. These are the primary results of the multipole analysis from which the significance of the different features of the real space distributions are concluded.

Figure 3 shows, for sake of visualization and easier interpretation, the same components in real space in terms of the multipole accumulation-of-charge densities $s_{in}(r_i)$ around the ionic sites as deviations from the reference model. The areas under the curves $Z_{in}(R_i)$ give the electron counts under the positive lobes of $K_n(\theta, \varphi)$ within the radii R_i. These multipole electron counts serve as non-spherical integral characteristics of the ionic charge distributions as indicated by the numbers given in the figures.

To facilitate understanding of the curves in Figs. 2 and 3, the angular behavior of the relevant harmonics is shown at each of the curves as a reduced map-on-sphere.

In Fig. 4, the results are visualized in terms of difference-density maps representing the multipole expansions at the ionic sites, as composed of the components shown in Figs. 2 and 3. For each ion, maps of the three main lattice planes—(100), (110), and (111)—through the ionic site are shown. For comparison, the conventional Fourier difference-density maps on the same planes are shown. This comparison is important.

Finally, Fig. 5 shows views of the three-dimensional nature of the ionic multipole expansions to support the discussion of results.

Colored versions of Fig. 5 are available at the Internet address www.cines.fr/EWUS.

4. DISCUSSION

Comparison of the radial densities s_0 of the reference model at the two temperatures, shown by dotted lines in Fig. 1 and by the corresponding parameters in Table 2, shows that the effect of the temperature factors on the nature of the ionic charge distributions is negligible. The differences between the experimental curves and parameters at the two temperatures are, thus, of electronic origin and can be attributed to differences of the magnetic states. These are evident in the deviations of the experimental curves from the reference curves in Fig. 1 and in the numerical values of Table 2. They are shown in a larger scale by the Δs_0 curves of Fig. 3.

The radial density $s_0(r)$ of the oxygen has a peculiar feature. Based on earlier observations on oxide peaks (cf. Vidal-Valat, Vidal, and Kurki-Suonio [18] and Vidal-Valat, Vidal, K. Kurki-Suonio, and R. Kurki-Suonio [19]), one would expect a separating minimum to occur in the overlap region, as in the case of MnO. However, there is, similarly in both magnetic states, an intermediate maximum that is stronger than one would expect in the case of simple covalent bonding. In addition, the outer part of the main density peak is strongly compressed as compared with the reference model, while it is slightly expanded in MnO. In Table 2, values corresponding to both minima are given. The maximum makes the separation of oxygen from its surroundings ambiguous. If the maximum is included in the oxygen, the peak electron count comes to about 10*e*, corresponding to O^{2-}, the radii r^{2-} being just slightly larger, while in MnO, as well as in the earlier observations, the oxide peak comes to 9*e*.

In both states of CoO, the separating minimum of the cation is deeper and sharper than in the reference model, while, in the paramagnetic MnO, some flattening was stated. Together with a slight increase of density at smaller *r*, this gives the impression of the cation being compressed. This leads to rather well-defined radii of best separation. The electron counts of the cat-

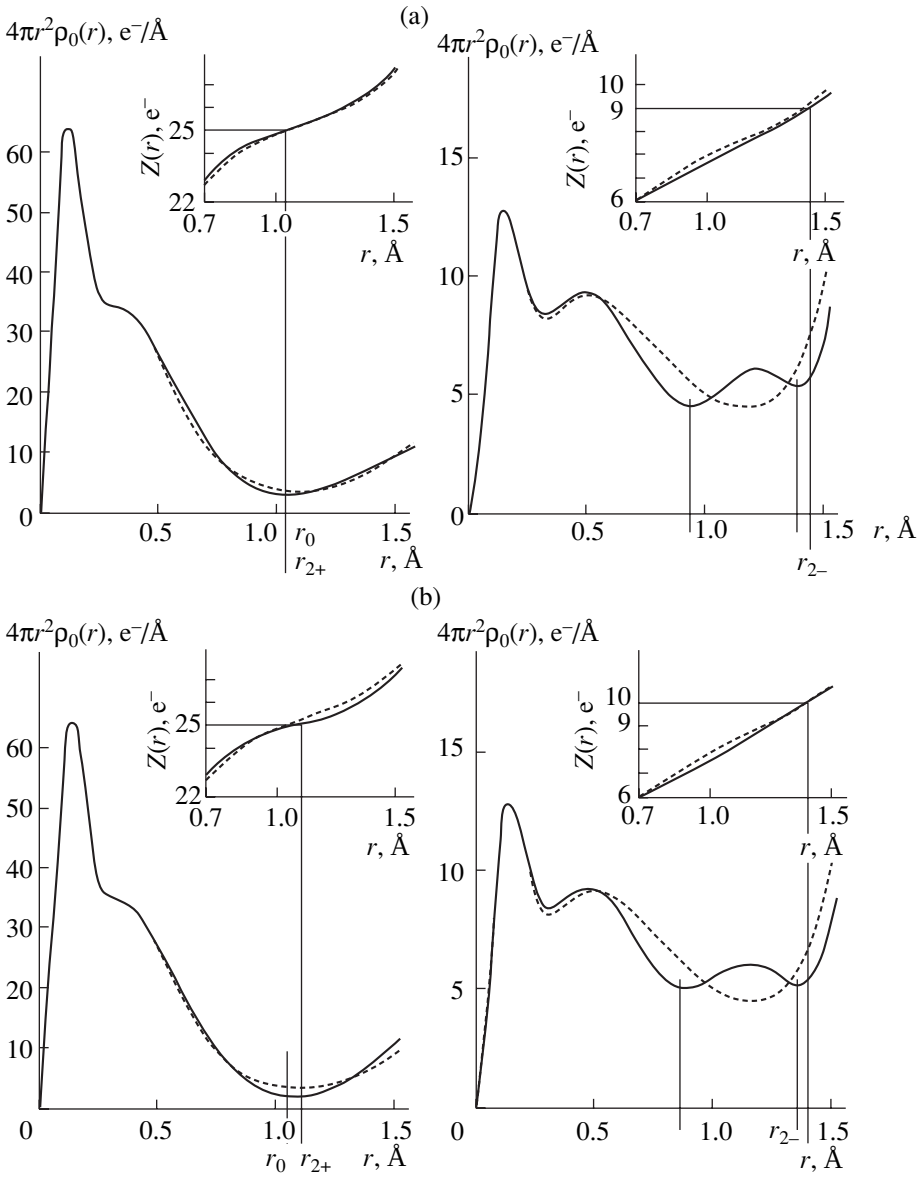

Fig. 1. Radial accumulation-of-charge densities $s_0(r)$ and electron counts $Z_0(r)$ around the ionic sites of Co^{2+} and O^{2-}, experimental (solid lines), reference model (dashed lines). (a) The paramagnetic state (298 K); (b) the antiferromagnetic state (85 K). The radii r_0 of "best separation" or minimum s_0 and the radii r_{2+} and r_{2-}, where the electron counts correspond to double ionization of the ions, are indicated for the experimental curves.

ion peaks correspond very closely to the doubly ionized state Co^{2+} with 25*e* in both states. In the paramagnetic state of CoO, the density $s_0(r_0)$ at the minimum equals that of MnO. Like MnO, it decreases in the phase transformation to the antiferromagnetic state, even getting significantly lower. The values are, however, remarkably higher than one would expect for an ion (cf. Vidal-Valat, Vidal, and Kurki-Suonio [18] and Vidal, Vidal-Valat, Galtier, and Kurki-Suonio [10]).

To understand the origin of these spherical average features, it is necessary to find out how they arise from the three-dimensional ionic distributions built up from low-order multipole components. The radial multipole scattering factors $f_{in}(b; R_i)$ of Fig. 2 and their error bars form the basis for making a judgment about the empirical significance of the components. The radial accumulation-of-charge densities Δs_n of Fig. 3 show, as described in the first part of our study, how the significant multipoles contribute to the three-dimensional ionic electron densities [2].

The density maps of Fig. 4 form the final tool of the analysis. To facilitate the perception of their connections in three dimensions, the representative lines of a number of main crystallographic directions are drawn in one set of maps. In the local map representations, only those features are significant that are significant in

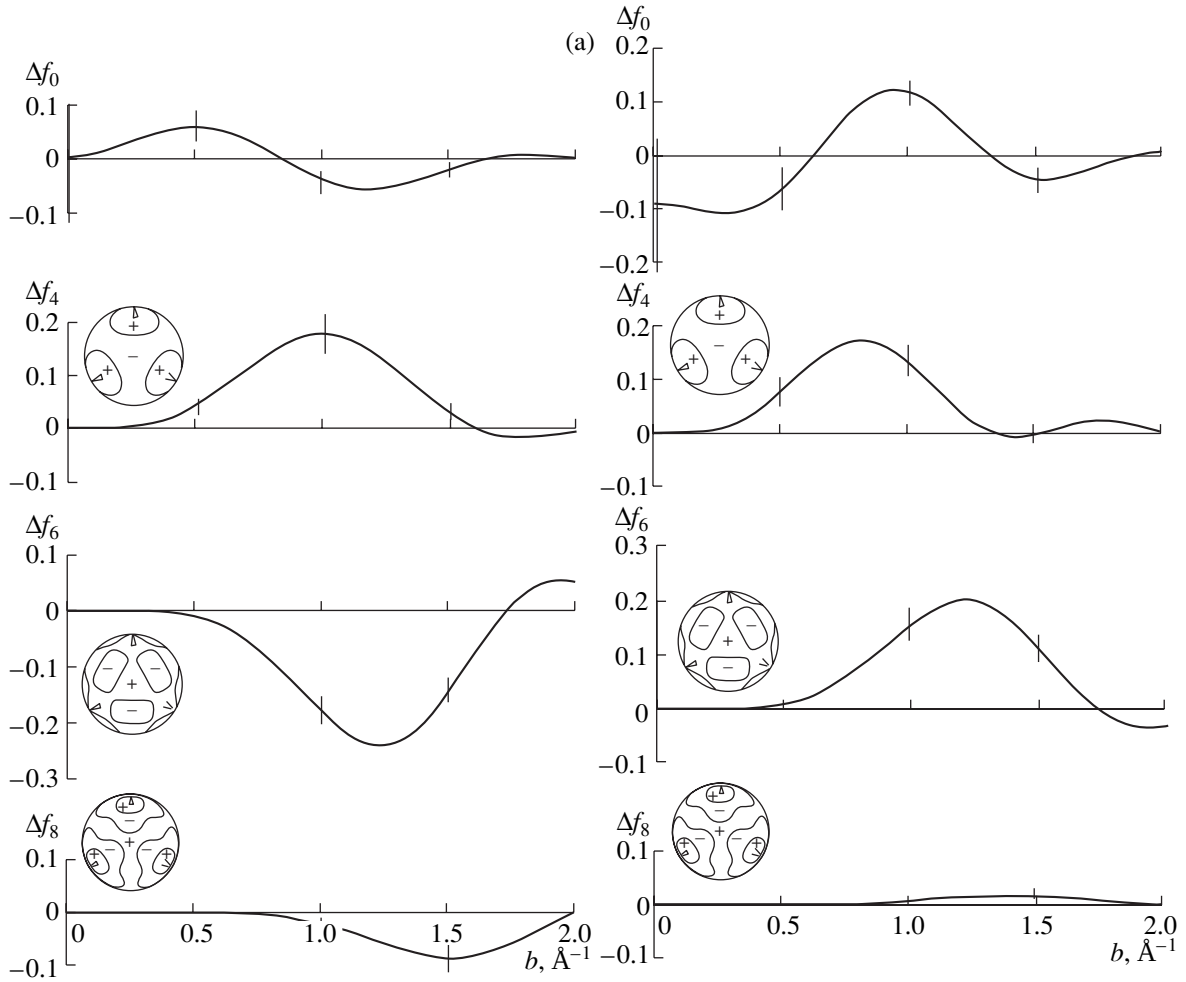

Fig. 2. Radial multipole scattering factors of the ions Co^{2+} and O^{2-} within the partitioning radii R_{Co} = 1.15 Å and R_O = 1.30 Å. The results refer to cubic harmonics normalized to the maximum value $K_n(\theta, \varphi) = 1$, and the curves represent deviations Δf_n from the reference model. (a) The paramagnetic state (298 K); (b) the antiferromagnetic state (85 K).

the angular-integral representation of Fig. 3. Thus, no attention need be paid to the difference densities at the ionic centers in any of the maps. Similarly, local features of the Fourier maps, which do not appear in the multipole maps of Fig. 4, do not arise from the integral systematics of the low-order multipoles and must be regarded as insignificant. Comparison with the multipole maps makes it possible to note how the features seen in the Fourier maps originate from the different atoms (Kurki-Suonio [1]).

The results are discussed in terms of three significant features, which are labeled A, B, and C for their identification in the different maps and in the three-dimensional representation of Fig 5.

A: Feature A looks much like covalent CoO bonding. It consists of density maxima between the nearest neighbors, Co⟨100⟩O, within the radius r_{2+} of Co. However, according to the multipole maps, it has a different electronic origin in the two magnetic states. In the paramagnetic CoO, it is built up almost solely by cation electrons, while in the antiferromagnetic CoO, where it is also clearly stronger, both ions contribute.

B: Feature B has maxima in the ⟨110⟩ directions from the oxygen site. It can be identified in all the maps through the oxygen site. It is a pure oxygen feature, lies within the oxygen radius r_{2-}, and is obviously responsible for the intermediate maxima in the radial density $s_0(r)$ of oxygen in Fig. 1.

C: Feature C consists of broad maxima between the O⟨111⟩Co neighbors. Although it lies outside any reasonable ionic partitioning spheres of the atoms, it definitely belongs to the low-order multipole behavior of both ions at the same time. It is, thus, understood to be significant, contrary to the maxima observed at these sites in MnO, and is interpreted to originate from a Co⟨111⟩O coupling. It dominates the view in Fig. 5, where it resembles triangular "pillows" fixed at the vertices of a cube in which the ion lies in the middle.

All three features A, B, and C, as such, are clearly stronger in the antiferromagnetic than in the paramag-

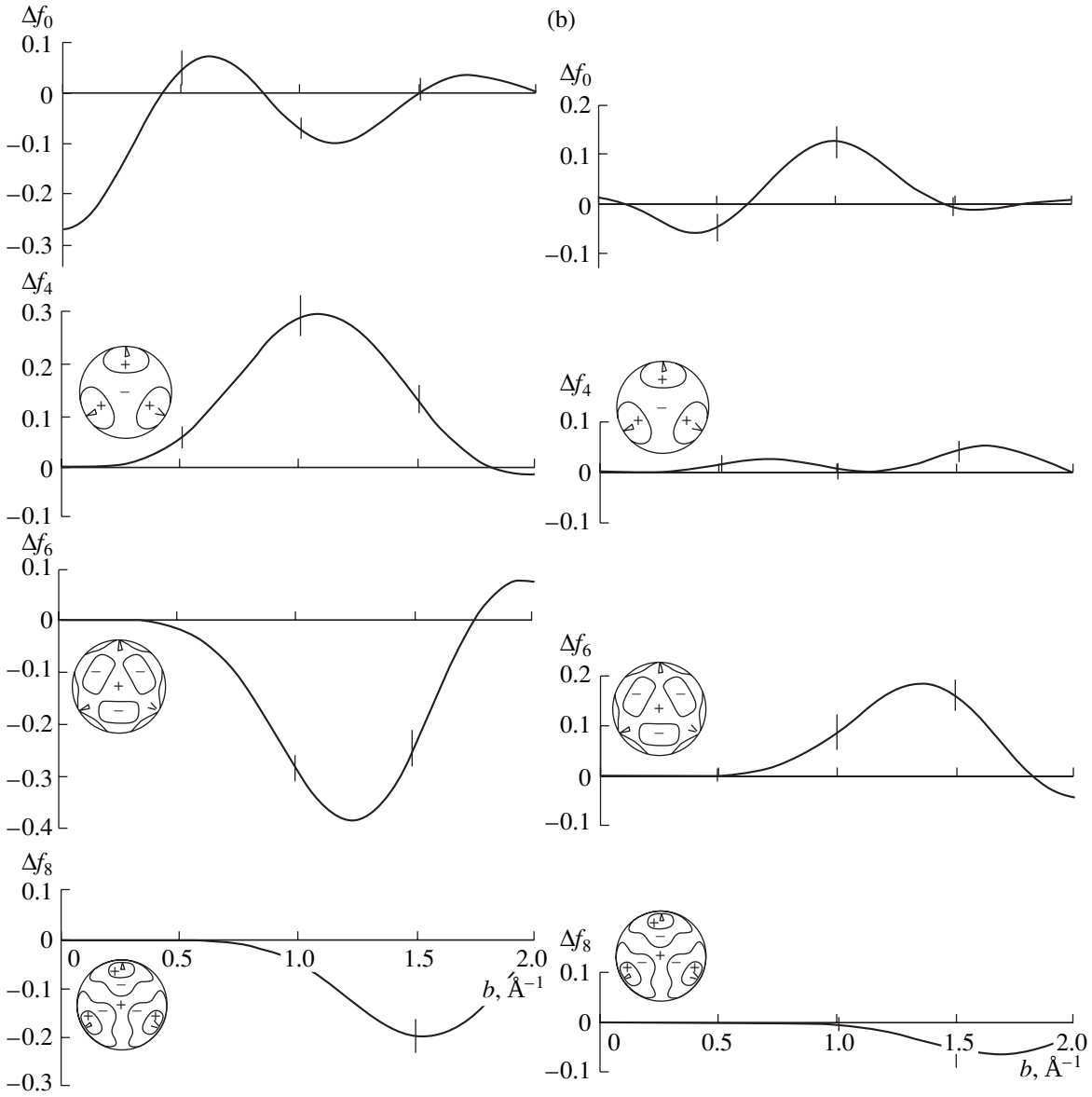

Fig. 2. (Contd.)

netic phase. While the multipole maps indicate how these features originate from the electrons of the different ions, the Fourier maps show how these features are coupled together, building up a complicated three-dimensional electronic network in the space between the atoms. Three types of possible couplings can be noted. The resulting networks seem to be different in the two magnetic states due to different mutual roles of these couplings.

ABA, oxygen cages: A and B build up an octahedral arrangement around each oxygen ion. The maxima of A lie at the vertices and the maxima of B in the middle of the edges of the octahedron, as seen in Fig. 5.

In the paramagnetic state, the oxygen feature B and the bonding feature A are closely coupled. Continuous ABA bridges are formed along the edges of the octahedron. Each oxygen atom becomes, thus, closed into its own electronic cage, which has the shape of an octahedron, and this is clearly visible in Fig. 5.

In the antiferromagnetic state, this coupling has largely vanished. There are no more of the continuous ABA bridges that built up the octahedral cage. On the other hand, the internal coupling of oxygen electrons that is responsible for feature B is stronger. This is shown from its tightness—it is significantly closer to the oxygen center, as can be seen also from the position of the intermediate maximum of the radial density $s_0(r)$ in Fig. 1—and from the slightly more unified ring formation surrounding oxygen in the (111) plane.

ACA: From the (110) Fourier maps, we note that the ⟨111⟩-intercation feature C connects the maxima of the

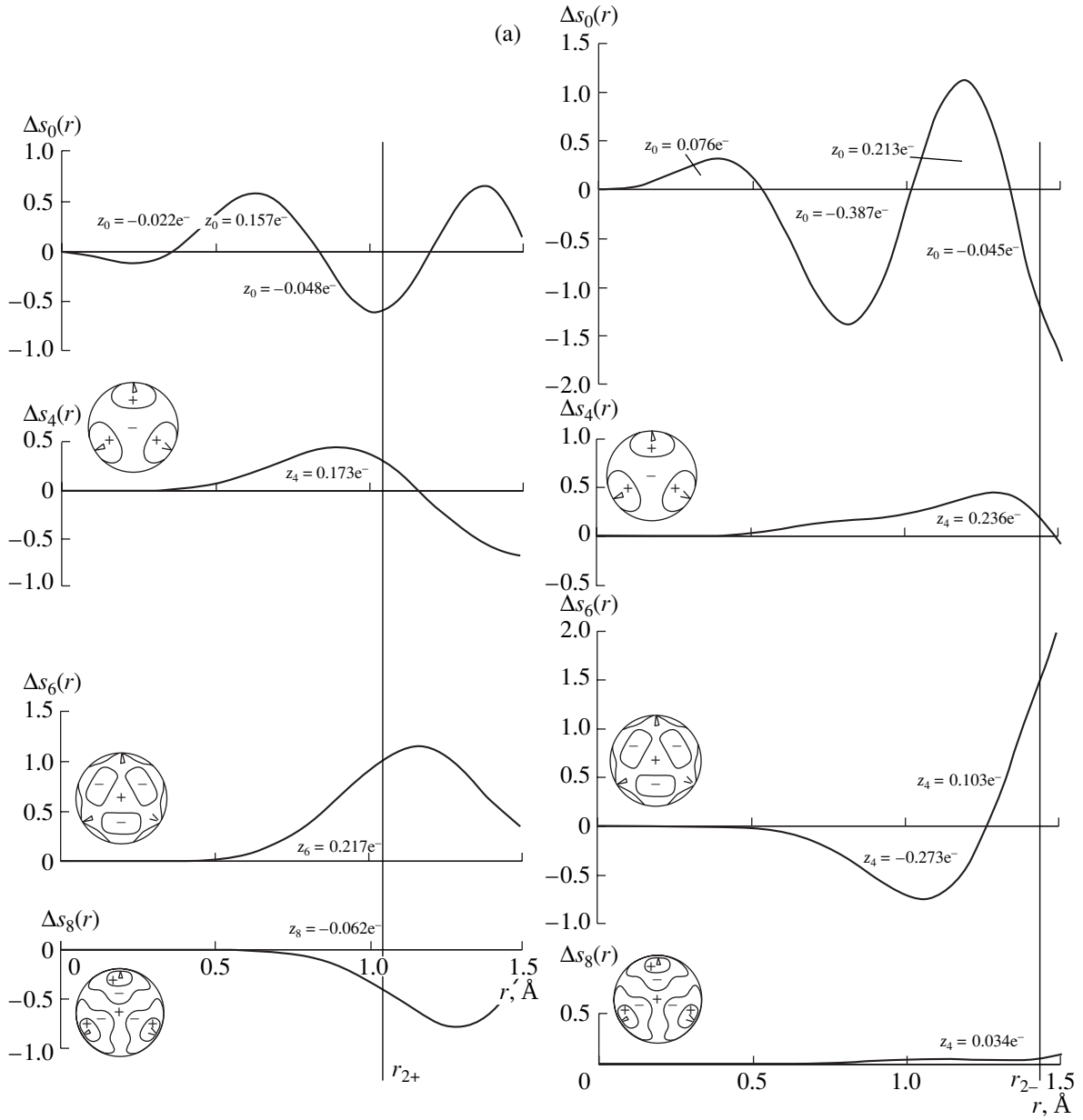

Fig. 3. Multipole accumulation-of-charge densities $s_n(r)$ around the ionic sites of Co^{2+} and O^{2-}. The curves represent deviations Δs_n from the reference model. (a) The paramagnetic state (298 K); (b) the antiferromagnetic state (85 K).

bonding feature A, and, in the paramagnetic state, the vertices of the neighboring octahedral cages, into more or less unified linear chains …CACA… on both sides of the ⟨110⟩ arrays of oxygen ions. These chains, running in the intermediate space between the ions in all symmetry-equivalent directions ⟨110⟩, build up a complicated three-dimensional electronic network. This network structure is clearly stronger and more unified, and, hence, the interactions responsible for this ACA coupling must be stronger in the antiferromagnetic state. Noting that A was found to be an internal phenomenon of Co in the paramagnetic state and a CoO coupling phenomenon in the antiferromagnetic state and that C was interpreted as originating from an O⟨111⟩Co interaction, we realize that the nature of this coupling is different in the two magnetic states and quite sophisticated in both.

BCB: The (111) Fourier maps through the oxygen site also give some indication of a possible BCB coupling of feature B of different oxygen atoms into (111) planar net structures with the aid of feature C. This indication is slightly stronger in the antiferromagnetic state. However, the empirical significance of this coupling remains unclear, since it is not visible in the multipole maps.

Formation of electron net structures in the interatomic space seems to be a general phenomenon in

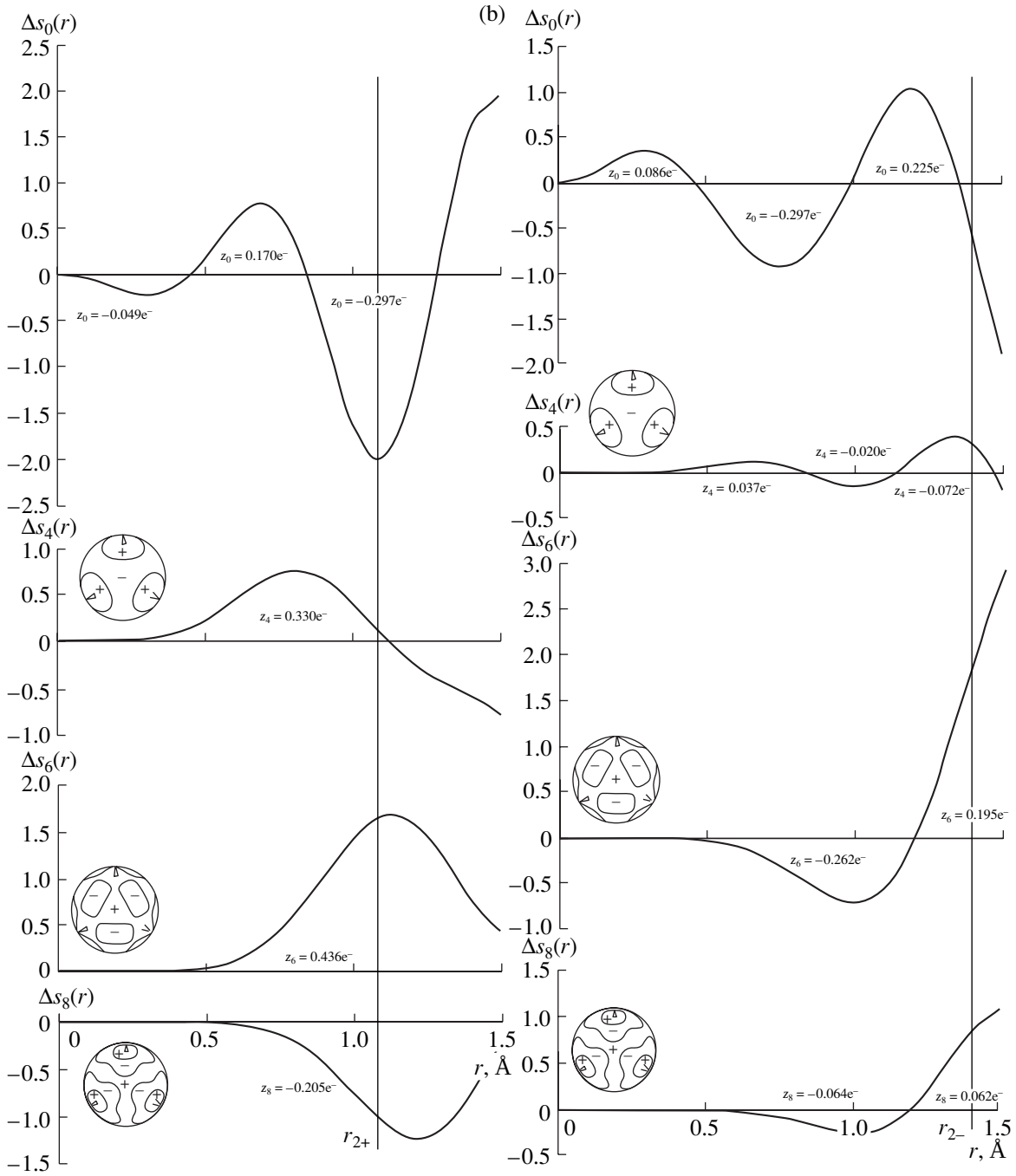

Fig. 3. (Contd.)

metal oxides (cf. the first part of our study). In MnO, this appeared as a three-dimensional network with the oxygen atoms in its cage-like pockets. In CoO, a comparable network is found that, however, is much more complicated. In the paramagnetic CoO, each oxygen has an octahedral cage of its own with its "walls" inside the radius r_{2-}, and the three-dimensional net is formed by connecting the vertices of these octahedra, while, in MnO, the oxygen cages were just pockets of the net outside the radius r_{2-} of double ionization. The couplings responsible for the cage formation and for the net buildup are obviously different in the two magnetic states. In the antiferromagnetic state, the net buildup, and with it the cage formation, were less obvious in MnO, while in CoO the cages have vanished but the net build-up is essentially stronger.

The problem of estimating the significance of such features in real space as revealed by the present method of analysis, in comparison with the accuracies obtained for the model parameters in the traditional fitting meth-

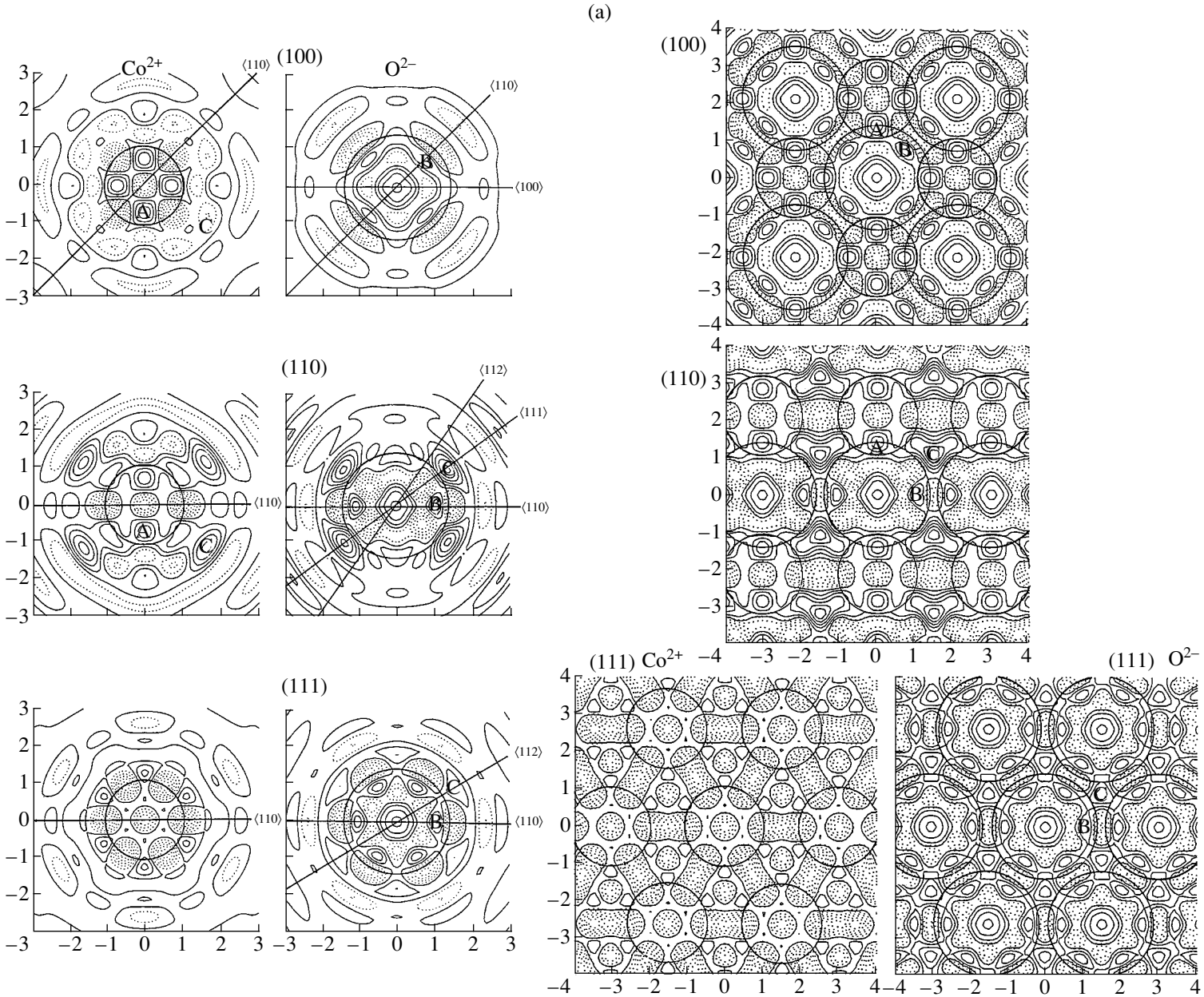

Fig. 4. Difference density maps of the multipole expansions up to $n = 8$ together with the corresponding Fourier difference-density maps on the lattice planes (100), (110), and (111) through the ionic sites. The circles indicate the radii of doubly ionized ions. (a) The paramagnetic state (298 K); (b) the antiferromagnetic state (85 K). Solid line positive, dashed line negative, and dotted line zero.

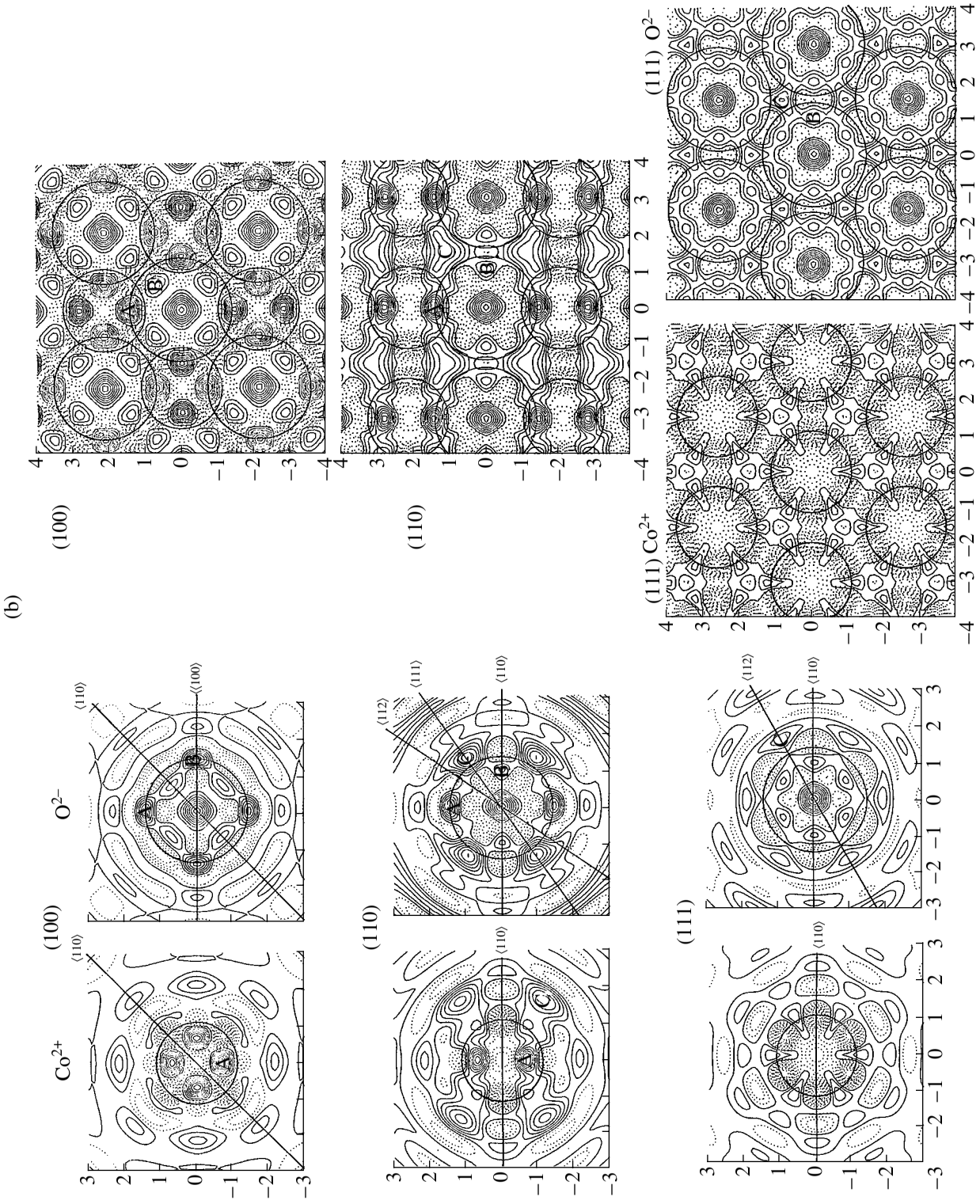

Fig. 4. (Contd.)

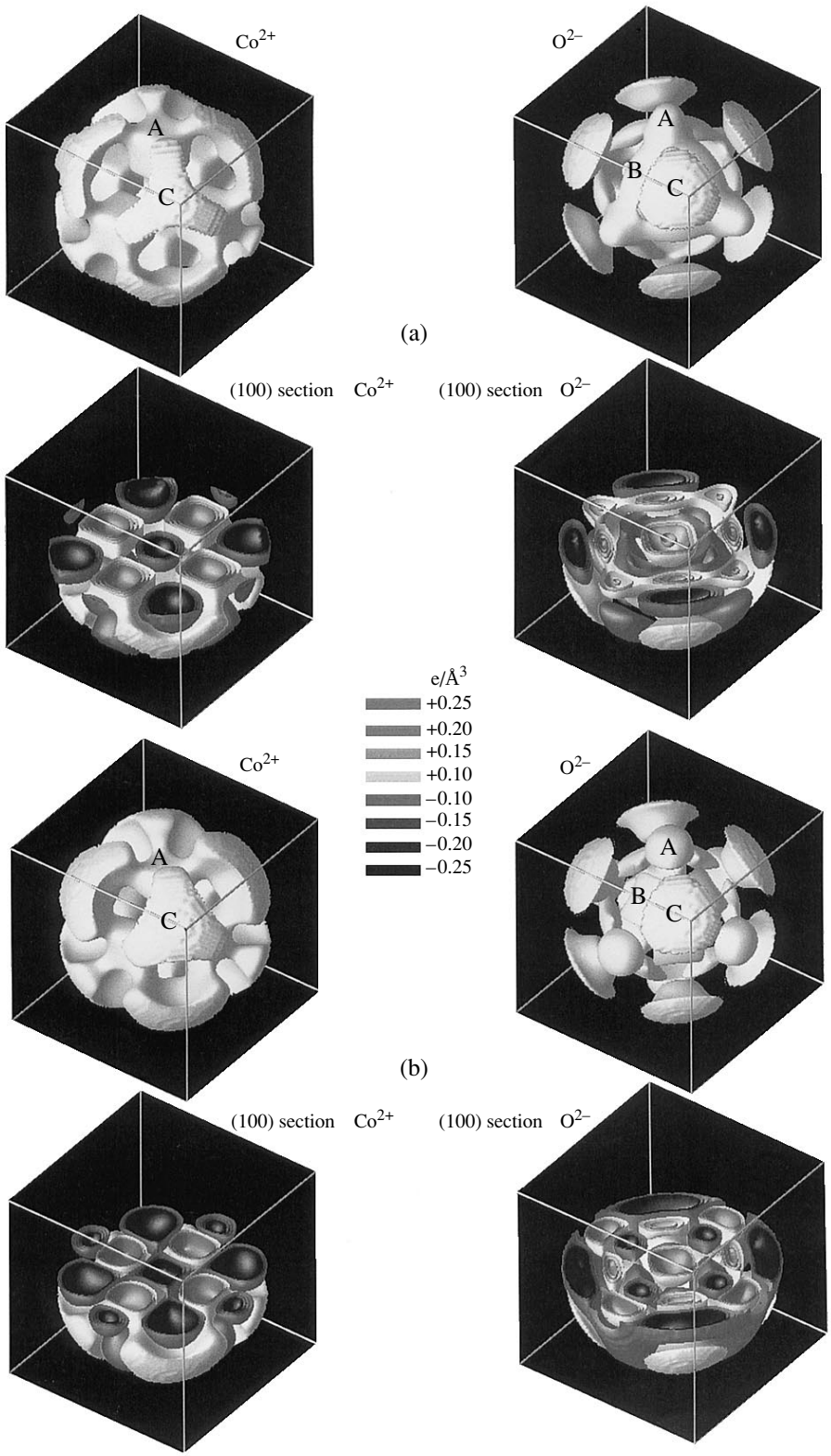

Fig. 5. Three-dimensional view of the equivalue surfaces of the ionic multipole expansions. (a) The paramagnetic state (298 K) within the radii R_{Co} = 1.3 Å, R_O = 1.8 Å; (b) the antiferromagnetic state (85 K) within the radii R_{Co} = 1.5 Å, R_O = 1.8 Å. For colors, see www.cines.fr/EWUS.

ods, has been discussed by Kurki-Suonio [1]. While the significance or insignificance is merely due to the accuracy of the measured data, it is expressed only by the error bars in $\Delta f_n(b)$, reflecting the large-scale integral nature of the information, and cannot be transformed into local accuracy statements. Local features can be regarded as significant to the relative extent expressed by the error bars insofar as they are parts of the integral multipole behavior.

ACKNOWLEDGMENTS

We thank the Centre Informatique National de l'Enseignement Supérieur (Montpellier, France) for financial support and technical assistance.

REFERENCES

1. K. Kurki-Suonio, in *Proceedings of Symposium Franco-Finlandais. Structure de la Matiére, Repartitions Electroniques dans les Cristaux, Paris, 1993*, Ed. by J.-P. Vidal (Montpellier, 1994), p. F1; in *Honour of the 75th Anniversary of Academician Boris Vainshtein*, Ed. by V. Simonov (Nauka, Moscow, 1996), p. 46.
2. J.-P. Vidal, G. Vidal-Valat, K. Kurki-Suonio, and R. Kurki-Suonio, Kristallografiya **47** (3), 391 (2002) [Crystallogr. Rep. **47**, 347 (2002)].
3. T. Bredow and A. R. Gerson, Phys. Rev. B **61** (8), 5196 (2000).
4. W. Neubeck, PhD Thesis (Univ. de Grenoble I, 2000).
5. B. V. Laar, Phys. Rev. **138**, 584 (1965).
6. D. Hermann-Ronzaud, P. Burlet, and J. Rossat-Mignot, J. Phys. C: Solid State Phys. **11**, 2123 (1978).
7. J.-P. Vidal, K. Kurki-Suonio, G. Vidal-Valat, and R. Kurki-Suonio, in video-film *The Wonderful World of the Crystal*, Ed. by J.-P. Vidal (Service du Film de Recherche Scientifique, Ministére de l'Education Nationale, Vanves, France, 1994).
8. J.-P. Vidal, G. Vidal-Valat, and C. M. E. Zeyen, Nucl. Instrum. Methods Phys. Res. A **228**, 569 (1985).
9. A. Revcolevschi, Rev. Int. Hautes Temp. Refract. **7**, 73 (1970).
10. J.-P. Vidal, G. Yidal-Valat, M. Galtier, and K. Kurki-Suonio, Acta Crystallogr., Sect. A: Cryst. Phys., Diffr., Theor. Gen. Crystallogr. **37**, 826 (1981).
11. W. R. Busing and H. A. Levy, Acta Crystallogr. **10**, 180 (1978).
12. M. Merisalo and J. Kurittu, J. Appl. Crystallogr. **11**, 179 (1978).
13. K. G. Subhadra and D. Sirdeshmukh, Indian J. Pure Appl. Phys. **16**, 693 (1978).
14. *International Tables for X-ray Crystallography* (Kluwer Academic, Dordrecht, 1999), Vol. C.
15. D. T. Cromer and D. Liberman, J. Chem. Phys. **53**, 1891 (1970).
16. G. Vidal-Valat, J.-P. Vidal, K. Kurki-Suonio, and R. Kurki-Suonio, Acta Crystallogr., Sect. A: Found. Crystallogr. **48**, 46 (1992).
17. K. Kurki-Suonio, Acta Crystallogr., Sect. A: Cryst. Phys., Diffr., Theor. Gen. Crystallogr. **24**, 379 (1968).
18. G. Vidal-Valat, J.-P. Vidal, and K. Kurki-Suonio, Acta Crystallogr., Sect. A: Cryst. Phys., Diffr., Theor. Gen. Crystallogr. **34**, 594 (1978).
19. G. Vidal-Valat, J.-P. Vidal, K. Kurki-Suonio, and R. Kurki-Suonio, Acta Crystallogr., Sect. A: Found. Crystallogr. **43**, 540 (1987).

Crystallography Reports, Vol. 49, No. 3, 2004, pp. 370–378. Translated from Kristallografiya, Vol. 49, No. 3, 2004, pp. 435–444.

STRUCTURE OF INORGANIC COMPOUNDS

Dedicated to the 80th Birthday of L.A. Shuvalov

3D-Incommensurate Composite Structures in $(Rb_x(NH_4)_{(1-x)})_2SO_4$ Crystals

I. M. Shmyt'ko, N. S. Afonikova, and E. A. Arnautova

Institute of Solid State Physics, Russian Academy of Sciences, Chernogolovka, Moscow oblast, 142432 Russia

e-mail: shim@issp.ac.ru

Received June 27, 2003

Abstract—Detailed structural studies of $(Rb_x(NH_4)_{(1-x)})_2SO_4$ solid solutions have been performed. It is shown that the crystals consist of incommensurate composite phases. The newly discovered composite structures differ from the traditional composite phases—in the general case, the host and guest structures of these crystals are incommensurate along all the three crystallographic axes. © *2004 MAIK "Nauka/Interperiodica".*

INTRODUCTION

In addition to the well known quasicrystals and incommensurately modulated structures, the notion of aperiodic crystals also includes the so-called crystalline composites or incommensurate intergrowth compounds. The first representative of this family of aperiodic crystals, $Hg_{3-\delta}AsF_6$, was discovered by Brown *et al.* in 1974 [1–3]. Its structure consists of two nonequivalent host and guest structures. The host substructure is built by AsF_6 groups forming the basic tetragonal lattice with nonintersecting free channels along the *a* and *b* directions filled with chains of Hg atoms, the period of which differs from the periods of the basic host lattice (the periods of the host structure, $a = b =$ 7.54 Å, differ from three Hg–Hg distances (7.92 Å) of the chain). Thus, the structure of Hg–Hg chains (guest structure) is incommensurate with respect to the host structure of AsF_6 groups. Later, a large number of new composites were discovered (see, e.g., the review by van Smaalen [4]). There are three types of incommensurate composite structures. The first type consists of channel composite structures similar to $Hg_{3-\delta}AsF_6$. The second type can be described as structures with two types of parallel columns with different periodicities inside the columns. The third type is formed by the so-called layer compounds consisting of alternating chemically different atomic layers. The most important characteristic of the above types of composites is that they consist of several chemical compounds and exist under atmospheric pressure at room temperature. Therefore, they are referred to as incommensurate intergrowth compounds.

Recently, elemental composites have been discovered, which are the high-pressure Ba, Sr, and Bi phases [5, 6]. Elemental composites cannot be related to intergrowth compounds and should be referred to as incommensurate composite phases.

Although, today, more than ten composite phases are known, no physical interpretation of their formation has been suggested as yet. One can single out, in all the known one-dimensional composite compounds, a certain geometrical factor such that it would admit the incommensurability of two structures along the channels, planes, or column axes. However, as is shown below, no such channels, planes, or columns can exist along all the three crystallographic axes in three-dimensionally incommensurate structures based on the $(Rb_x(NH_4)_{(1-x)})_2SO_4$ solid solutions. An attempt to explain the formation of composite phases in high-pressure elemental phases proceeding from their band structure was made in [7], but this interpretation is inapplicable to dielectric crystals. Obviously, the physical interpretation of the formation of incommensurate composite structures requires some additional investigation, in particular, the search for new compounds possessing characteristic structural features and the study of structural transformations of incommensurate composite phases over wide temperature ranges and the behavior of their physical properties.

With this aim, we studied the crystals of the solid solutions of the $(Rb_x(NH_4)_{(1-x)})_2SO_4$ family (at $x = 0.0$, 0.1, and 0.7). We discovered a number of anomalous structural effects and interpreted them as the manifestation of the three-dimensional incommensurability of the composite phases characteristic of this family of solid solutions. Rubidium–ammonium sulfate crystals of the composition $(Rb_x(NH_4)_{(1-x)})_2SO_4$ form a continuous series of solid solutions [8]. At 223 K, the crystals of pure ammonium sulfate $(NH_4)_2SO_4$ undergo a first-order ferroelectric phase transition accompanied by a change of the symmetry from *Pnam* to $Pna2_1$. With lowering of the temperature, reversal of spontaneous polarization is observed [9]. It is also known that the

1063-7745/04/4903-0370$26.00

ferroelectric phases in the $(Rb_x(NH_4)_{(1-x)})_2SO_4$ system are preserved up to the composition with $x \simeq 0.6$–0.65. The attempts to interpret the nature of the ferroelectric phase transition observed in this family were made based on the order–disorder model [10] and other approaches based on improper ferroelectrics [11], coupled oscillators [12], coupled oscillators–relaxors [13], and two nonequivalent ferroelectric sublattices [14]. The enumerated approaches show that the mechanism of phase transitions in this family is rather complicated and not clear as yet.

Moreover, the above compounds can also be considered as forming a very peculiar class of orientational glasses in which lowering of the temperature results in a frozen subsystem of multipolar moments. In this case, the compounds show the disorder intermediate between a crystal and a conventional "canonic" glass [15–18].

We undertook the study of $(Rb_x(NH_4)_{(1-x)})_2SO_4$ crystals in order to structurally interpret the formation of a newly discovered three-dimensional (3*D*) incommensurate composite state and its transformation depending on the changes in the composition, temperature, and pressure. We also made an attempt to establish the structural mechanism of formation of the composite phases and determine the energy of interaction between the host and guest structures.

SAMPLES AND EXPERIMENTAL METHODS

We studied crystals of three compositions—those with $x = 0.0$, 0.1, and 0.7. The study of pure ammonium sulfate was dictated by the necessity to prove that the structural states and their transformations in the samples of other compositions are not caused by nonuniform rubidium distributions. The crystals with the composition $x = 0.1$ were studied, on the one hand, because of a low rubidium content in the lattice, and, therefore, possible preservation of the properties of pure $(NH_4)_2SO_4$. On the other hand, they were studied because of the presence of substitutional atoms that could be responsible for the formation of the structural features typical of compositions with x ranging within $0 < x < 0.6$ (the range of low-temperature ferroelectric phases). The crystals with $x = 0.7$ were studied because they underwent no ferroelectric phase transition. The above three compositions determined the change of the structure, depending on the content of substitutional rubidium atoms.

The sample quality was checked by the Laue and precession methods. The unit-cell symmetry and precise lattice parameters were determined on a four-circle AFC6S (Rigaku) diffractometer (MoK_α radiation) at the Laboratory of Applied Analysis (SIDI) of the Autonomic University of Madrid. The spherical samples with a diameter ranging within ~0.25–0.35 mm were used for diffraction analysis. The space groups determined before and after the ferroelectric transformation are consistent with the published data—*Pnam* and $Pna2_1$, respectively. The structural parameters for all the three compositions studied are indicated in the table.

The possible formation of superstructural reflections was checked on a D500 (Siemens) X-ray diffractometer, which was modified at the program level in order to calculate the one- and two-dimensional reciprocal-lattice sections for single-crystal cuts. The samples, $2 \times 3 \times 3$ mm^3 parallelepipeds with faces parallel to the basic unit-cell faces, allowed us to make measurements from various crystallographic cuts of the same sample.

Low-temperature measurements were made in a helium cryostat designed and constructed at the Institute of Solid State Physics of the Russian Academy of Sciences [19, 20], which allowed us to make precision measurements of the unit-cell parameters in the temperature range from 4.2 to 300 K.

The samples for experiments with the oriented deformation were made on $3 \times 3 \times 5$ mm^3 parallelepipeds with the faces parallel to the (001), (010), and (100) basal planes, respectively. The loading direction coincided with the [100] direction. We recorded the diffraction spectra from the {001} planes parallel to the loading axis. A crystal was placed into a specially designed loading device mounted on the diffractometer goniometer in such a way that it allowed us to smoothly vary the mechanical load and record diffraction spectra in the 2θ range from 0° to 120°. The maximum load applied to the dies was 300 kg, which, being recalculated to the sample area, amounted to 3300 kg/cm^2.

RESULTS AND DISCUSSION

Figure 1 shows some typical sections of large regions of the (b^*–a^*) plane of the $(Rb_{0.1}(NH_4)_{0.9})_2SO_4$ reciprocal lattice at room temperature. These sections have a number of superstructural 0k0 and hk0 reflections [21] along the b^* axis. The distances from these reflections to the main reflection depend on the reflection order, in accordance with the coexistence of two lattice parameters, and are equal to 10.5525 Å for the Bragg reflections and 10.2593 Å for satellite ones. Similar sections of the (b^*–c^*) planes were also obtained. It is seen that the superstructural 0kl reflections are located along the b^* direction. In the reciprocal space, the sections obtained correspond to two lattices imbedded into one another so that the projections of all the lattice points onto the (a^*–c^*) plane practically coincide and preserve the motif of the initial structure. Along the b^* axis, the distances between the lattice points increase with an increase of the distance from the origin of the coordinate system.

Similar results were also obtained for $(NH_4)_2SO_4$ crystals containing no rubidium atoms [22]. As in the case of the composition $x = 0.1$, for the composition with $x = 0.0$, we recorded not only the known Bragg reflections from all the basal planes of the basic struc-

Structural characteristics of crystals

Crystal	*T*, K	Sp. gr.	*a*, Å; Δ*a*	*b*, Å; Δ*b*	*c*, Å; Δ*c*	α, deg; Δα	β, deg; Δβ	γ, deg; Δγ
$(NH_4)_2SO_4$	300	*Pnma*	7.7800 0.0017	10.6403 0.0019	5.9950 0.0009	90.0194 0.0148	90.0229 0.0117	89.9920 0.0160
$(Rb_{0.1}(NH_4)_{0.9})_2SO_4$	300	*Pnma*	5.8081 0.0010	10.5525 0.0016	5.9862 0.0008	90.003 0.012	90.038 0.010	89.994 0.011
	203	$Pna2_1$	7.8161 0.0018	10.5206 0.0012	5.9564 0.0012	90.024 0.012	89.985 0.013	89.978 0.018
$(Rb_{0.1}(NH_4)_{0.9})_2SO_4$	300	*Pnma*	7.8261 0.0013	10.4517 0.0015	5.9738 0.0004	90.027 0.008	90.009 0.009	89.957 0.012

ture in the reciprocal space but, also, some additional reflections. The distances to the latter reflection depend on the reflection order, in accordance with the coexistence of two types of crystal lattices with the following parameters:

$$a_{Bragg} = 7.7880,\ a_{sat} \approx 7.790\ Å,\ (a_{Bragg}/a_{sat}) = 0.9997;$$

$$b_{Bragg} = 10.6403,\ b_{sat} \approx 10.674\ Å,\ (b_{Bragg}/b_{sat}) = 0.9968;$$

$$c_{Bragg} = 5.9950,\ c_{sat} = 6.104\ Å,\ (c_{Bragg}/c_{sat}) = 0.9821.$$

Figure 2 shows some typical diffraction spectra of $(Rb_{0.7}(NH_4)_{0.3})_2SO_4$ crystals along the basic directions. It is seen that, in a way similar to the crystals with the compositions $x = 0.0$ and 0.1, the satellite reflections are formed along all the directions, except for the basic ones. The positions of the Bragg and satellite reflections correspond to the coexistence of two sublattices with the parameters related as

$$a_{Bragg} = 7.8261,\ a_{sat} = 7.429\ Å,\ (a_{Bragg}/a_{sat}) = 1.0535;$$

$$b_{Bragg} = 10.4517,\ b_{sat} = 10.711\ Å,\ (b_{Bragg}/b_{sat}) = 0.9758;$$

$$c_{Bragg} = 5.9738,\ c_{sat} = 6.607\ Å,\ (c_{Bragg}/c_{sat}) = 0.9042.$$

A number of additional reflections on the diffraction patterns from single-crystal samples can satisfactorily be explained based on several models. The first one is the model of interlayers of inclusions of the new phase with the lattice parameters different from the parameters of the matrix along the crystallographic directions. It should be noted that these inclusions of the new phase do not correspond to enrichment or depletion of some crystal regions with Rb atoms, because the above reflections are also recorded for pure ammonium sulfate crystals. This model is also invalid for $(Rb_{0.1}(NH_4)_{0.9})_2SO_4$ crystals. Indeed, it follows from Fig. 1 that the b_{sat} parameter of possible phase inclusions is less than the corresponding b_{Bragg} parameter of the matrix b_{Bragg} ($b^*_{sat} > b^*_{Bragg}$). In accordance with the concentration dependence of the *b* parameter, *b*(*x*), obtained in [8], this would have corresponded to enrichment of the phase inclusions with Rb atoms. However, the measured b_{sat} parameter of the inclusions equals 10.2593 Å, whereas, for pure Rb_2SO_4, it should be at least as large as 10.44 Å. Moreover, for the concentration model, variation in the *b* parameter should give rise to variation in the *a* and *c* parameters, which contradicts the experimental data. The *a* and *c* parameters of the inclusions are practically equal to the corresponding parameters of the matrix.

The second model is the structure model with the substitution modulations. The distance from the satellite reflection to the reflection of the basic structure in the reciprocal space may also be dependent on the reflection order, and the satellites may be observed only on one side of the main reflection [23]. In this model, the role of the substitution element can be played, e.g., by the orientation of a NH_4 tetrahedron with respect to an SO_4 tetrahedron, with the Rb atoms being statistically distributed over the NH_4 positions. The choice of a NH_4 tetrahedron as an ordering element corresponds to extremely low intensities of the superstructural reflections (Fig. 2).

The third model is that of a structure described as an incommensurate crystalline composite in which two weakly interacting nonequivalent intergrowth structures (host and guest) coexist. These structures belong to the same crystal system, but their lattice parameters are incommensurate. In this case, it is logical to assume that the guest lattice is formed by NH_4 groups with low reflectivity, which results in the intensities of the satellite reflections being low with respect to the intensities of reflections of the host lattice containing SO_4 groups.

And, finally, we have to reject the assumption that additional reflections are formed because of the degradation of the subsurface layer of the sample. The depth of the diffracting layer is finite, ~5–50 μm, and the intensity ratio of the additional and basic reflections is proportional to 1/500. Therefore, the thickness of the disturbed subsurface layer does not exceed 100–1000 Å. This layer can readily be polished away. However, even thorough mechanical polishing of the sample did not result in disappearance of the additional reflections, which indicated that the above inclusions are dis-

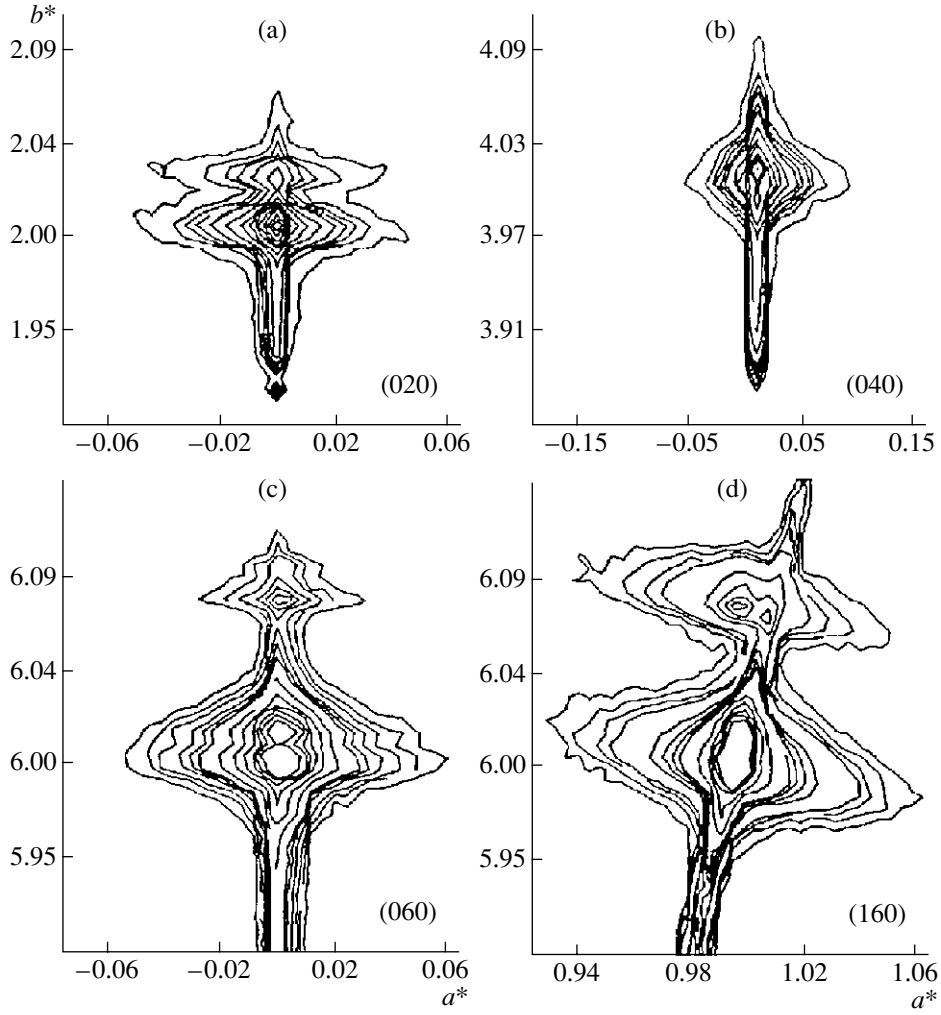

Fig. 1. Reciprocal-lattice sections around the (a) 020, (b) 040, (c) 060, and (d) 160 reciprocal-lattice points for a $(Rb_{0.1}(NH_4)_{0.9})_2SO_4$ crystal.

tributed over the matrix. Moreover, the transmission diffraction experiments on spherical samples with a diameter as small as ~0.3 mm (MoK_α radiation) showed the same results as the reflection experiments (CuK_α radiation).

The above results allow us to select the most appropriate model. Indeed, in the case of the model with substitution modulations, the basic and superstructural lattices should be multiple. For an incommensurate composite, the ratio of its lattice parameters should be an irrational number. It is possible to estimate the multiplicity or irrationality by considering the $d_{sat}/(d_{Bragg} - d_{sat})$ ratio following from the coincidence (or noncoincidence) of the points of both lattices observed after N periods, $d^*_{sat}(N+1) = d^*_{Bragg}N$. This ratio should be integral for the first two models and irrational for incommensurate structures. Using the above parameters for the composition with $x = 0.1$, we find $N_b = 7.369\ldots$. For the compositions with $x = 0.0$ and $x = 0.7$, we have $N_b = 315.736\ldots$ and $N_b = 40.245\ldots$, respectively. Thus, the most probable model of the structure is an incommensurate crystalline composite.

It should be noted that the host and guest structures are described by different space groups. This follows from the absence of the guest-structure reflection and the presence of the host-structure reflection for the composition with $x = 0.1$ (Fig. 1b) and the presence of the guest-structure reflection and the absence of the matrix reflection for the composition with $x = 0$ [22]. For the composition with $x = 0.7$, the host and guest structures have different symmetries, which is seen from the diffraction spectra in Fig. 2. The 300, 050, and 001 reflections of the host structure have finite intensities although these reflections are forbidden by the symmetry of the sp. gr. *Pnma*, whereas the guest structure gives only the 300 and 050 reflections. There is no 001 reflection from the guest structure. It turned out that the ratio of the integrated intensities

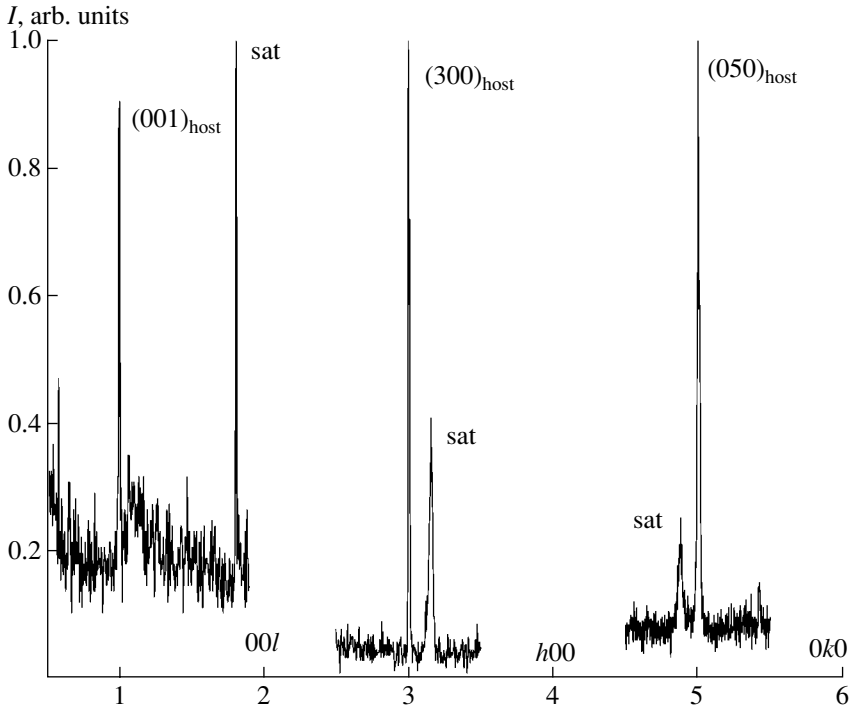

Fig. 2. Example of one-dimensional diffraction spectra of $(Rb_{0.7}(NH_4)_{0.3})_2SO_4$ crystals along the basic directions.

$I(300)_{guest}/I(300)_{host}$ for the forbidden 300 reflection is considerably higher than the ratio of the integrated intensities $I(200)_{guest}/I(200)_{host}$ and $I(400)_{guest}/I(400)_{host}$ for the allowed 200 and 400 reflections, respectively. These characteristics show that the coexisting host and guest substructures have different atomic structures and symmetries and, thus, confirm the term "incommensurate intergrowth compounds" often used for this class of aperiodic structures.

The additional characteristics of the composite structures of single crystals of the $(Rb_x(NH_4)_{(1-x)})_2SO_4$ family were obtained from the consideration of the temperature behavior of the superstructural reflections. These characteristics were studied most thoroughly for crystals of pure ammonium sulfate. Hereafter, the difference between the reciprocal lattice parameters of the guest and host lattices will be referred to as the parameter mismatch along a selected crystallographic axis. Figure 3 illustrates the temperature behavior of the mismatch and the intensity of one of the superstructural reflection along the *c* axis. It is seen that mismatch strongly depends on temperature, which, along with the different symmetries of the host and guest structures, indicates their relative independence from one another. However, they are independent only within certain limits of the parameters of various external factors. Thus, a jumpwise change in the intensity of the $(002)_{sat}$ reflection (Fig. 3b), the anomaly in the mismatch in the vicinity of 223 K, and the temperature behavior of the *c* parameter of the host structure (Fig. 4) show that, in the region of the ferroelectric transformation, both composite structures simultaneously undergo phase transitions; in other words, the change of one structure can give rise to a change of the other structure.

The temperature behavior of the mismatch along the *b* axis calculated from the $(0120)_{host}$ and $(0120)_{guest}$ reflections is shown in Fig. 5. It is seen that the mismatch parameter strongly depends on temperature. Its behavior is consistent with the temperature behavior of the mismatch parameter along the *c* direction and characterizes $(NH_4)_2SO_4$ as, at least, a two-dimensionally incommensurate composite.

The superstructural guest reflections along the *a* direction above the temperature of the ferroelectric phase transition T_C are so close to the host reflections that they are seen only as an anomaly of the angular intensity distribution of the Bragg reflections (Fig. 6a). Their resolution and intensities are so weak that we failed to decompose the spectra into components. Below T_C, the superstructural reflections along the *a* direction appear in new positions far from the Bragg reflections (Fig. 6b). This transformation of the diffraction spectra indicates the dramatic change of the guest structure after the ferroelectric phase transition and, therefore, the composite crystal can be described as a crystal consisting of independent structural formations.

Figure 7 shows the temperature dependence of the mismatch along the *a* direction and the integrated intensity of the superstructural 10.00 reflection below T_C. A jumpwise variation of the mismatch in the $(NH_4)_2SO_4$ crystals indicates the phase transition above 170 K

from the incommensurate composite structure into composite phases commensurate along the *a* direction in the temperature ranges 4.2–50 and 50–170 K. We believe that the existence of these transitions is very important and, to a certain degree, characterizes the nature of incommensurate crystalline composites. Indeed, using the lattice and mismatch (Fig. 7), it is possible to demonstrate that, in the temperature ranges where the mismatch is constant, the host and guest lattices fully coincide. In the temperature range 50–170 K, they coincide at a distance of 238 unit cells, which, on the real scale, is equal to 1864 Å (we wonder whether range forces can act at such distances?). Assuming that, at $T_{inc} \sim 170$ K, the transition to the incommensurate state occurs because of a "break" of long-range interactions between the lattices by thermal fluctuations, we can estimate the energy of these interactions. This energy is determined by the temperature of the transition from the commensurate composite phase to the incommensurate one and is equal, by an order of magnitude, to 1.2×10^{-2} eV.

Finally, consider the temperature behavior of the mismatch parameter in the range 175–223 K. In accordance with Figs. 3, 5, and 7, the parameters in this temperature range continuously vary with the temperature along all the three coordinate axes. This characterizes $(NH_4)_2SO_4$ as a three-dimensionally incommensurate crystalline composite.

The additional data on the characteristics of the real structure of the composite state were obtained by analyzing the basic two-dimensional reciprocal-lattice sections of the $(Rb_{0.7}(NH_4)_{0.3})_2SO_4$ crystals. Figure 8 shows two-dimensional sections of the 050 reciprocal-lattice point at room temperature and at 224 K, corresponding to the one-dimensional diffraction spectrum along the *b* axis (Fig. 2b). One can see two rodlike satellite reflections normal to the reciprocal-lattice vector b^*.[1] The simultaneous existence of two satellite and one Bragg reflections indicates that the composite consists of one host and two guest structures, $guest_1$ and $guest_2$, respectively. In the direct space of the guest structure, the rodlike shape of the satellite reciprocal-lattice points corresponds to disordered periodic chains along the *b* direction with the periods $b_{guest_1} = 10.723$ Å and $b_{guest_1} = 10.46$ Å, respectively. Similar chains for the guest structure were also observed in other composites, namely, in the high-pressure Ba, Bi, and Sr phases mentioned above.

Comparing the spectra in Figs. 8a and 8b, we see that lowering of the sample temperature results in a considerable decrease in the intensity and half-width of the rodlike guest reflections and a considerable increase in the maximum intensity of the host reflection. It is seen that a decrease in the intensities of the $guest_1$ and $guest_2$ reflections is accompanied by their displacement with respect to the host reflection along the b^* direction. Thus, the composite can be considered a really incommensurate one along the b^* direction. It should also be noted that, because of the low intensities, no satellite guest reflections can be recorded on the one-dimensional diffractograms below 5°C, which indi-

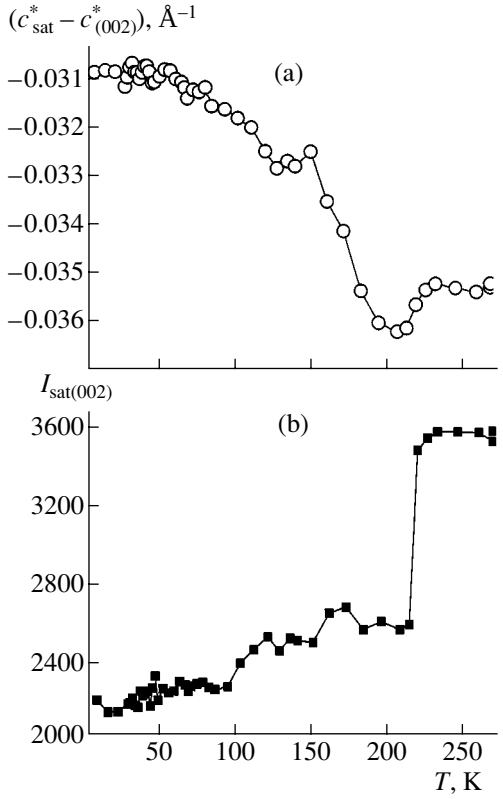

Fig. 3. Temperature behavior of the (a) mismatch parameter and (b) intensity of a superstructural reflection along the *c* direction for an $(NH_4)_2SO_4$ crystal.

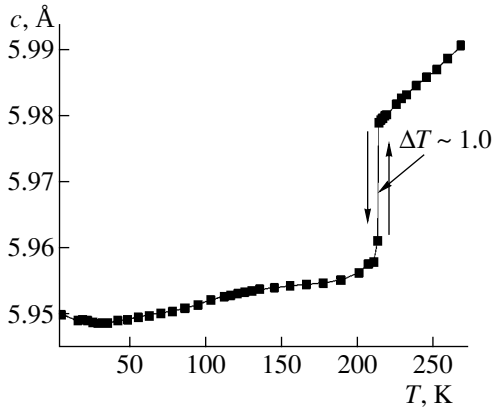

Fig. 4. Temperature behavior of the *c* parameter of the host structure for $(NH_4)_2SO_4$.

[1] The absence of the second satellite in the vicinity of the 050 reflection on the one-dimensional section in Fig. 2 is explained by its low intensity and its practical coincidence with the host reflection along the reciprocal-lattice vector at room temperature.

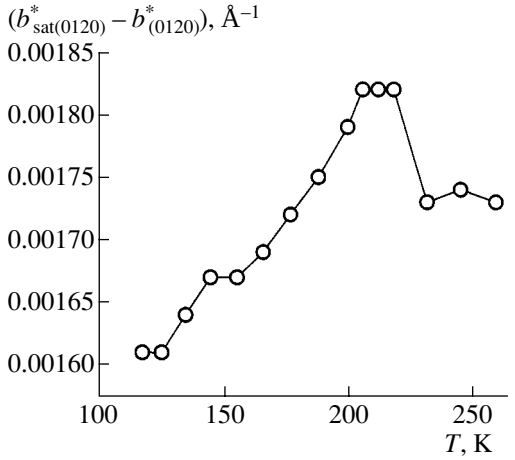

Fig. 5. Temperature behavior of the mismatch parameter along the *b* direction for $(NH_4)_2SO_4$.

cates that it is two-dimensional sections that are most informative. Further lowering of temperature results in the complete disappearance of rodlike satellite reflections also on the two-dimensional reciprocal-lattice sections.

Heating of the sample to room temperature does not lead to diffraction-spectrum reconstruction (at least within several hours of recording the diffraction spectra). Moreover, an increase in the temperature above room temperature (up to ~40°C) did not result in the restoration of the initial state of the crystal. The restoration of the initial intensity distribution of the rodlike guest reflections was observed only during subsequent long keeping (for about 36 h) of the sample at room temperature.

The result obtained allows us to draw some conclusions about the structural mechanism of the formation of composite phases. The process is thermally acti-

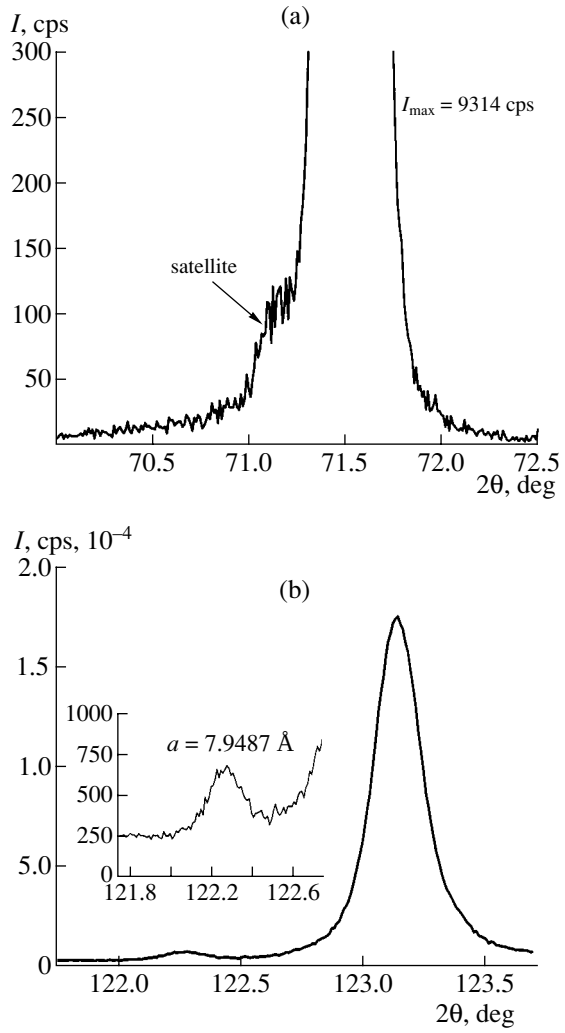

Fig. 6. Angular distribution of the diffracted intensity of the (a) 600 reflection before the phase transition (T = 250 K) and (b) 10.00 reflection after the phase transition (T = 112 K) for a $(NH_4)_2SO_4$ crystal.

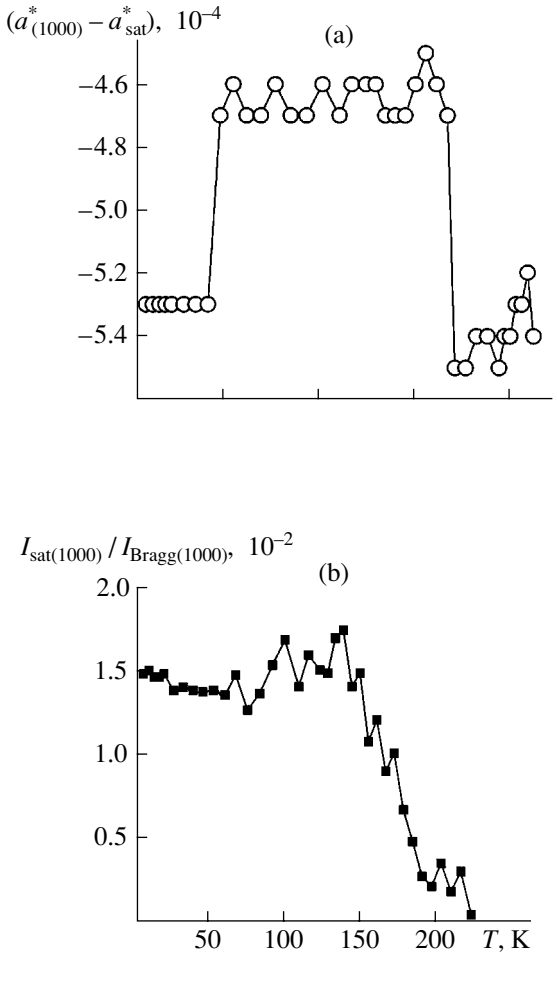

Fig. 7. Temperature behavior of the (a) mismatch parameter along the *a* direction and (b) integrated intensity of the superstructural 10.00 reflection below T_C for $(NH_4)_2SO_4$.

vated; at the initial stages, the periodic chains of atoms are formed. With an increase in the temperature, these chains start ordering, which results in the formation of a three-dimensional guest structure.

The host and guest structures are relatively independent, which is clearly seen under the action of oriented external mechanical stresses. We studied $(NH_4)_2SO_4$ crystals. Figure 9 shows the relative positions of the Bragg and satellite reflections from $(NH_4)_2SO_4$ under variation of the applied load within the range P = 0–1652 kg/cm^2. It is seen that the relative positions of the reflections change with the stress variation. Thus, under the applied mechanical stress, the composite behaves as an incommensurate composite. Moreover, an increase in the load in the above range is accompanied by considerable broadening of the Bragg θ-2θ reflections, which indicates the formation of an inhomogeneously deformed sample state. Upon the attainment of the stress $P \sim 1652$ kg/cm^2, one observes a dramatic increase in deformation accompanied by a decrease in the load (P = 864 kg/cm^2) at the initial moments, disappearance of nonuniformly deformed sample state (which manifests itself in narrowing of the diffraction reflections), and crystal disintegration into several blocks. The intensity of the satellite guest reflection first increases (with respect to the host reflection) and then, after long keeping of the sample under the conditions of the residual stationary loading, drops below the relative intensity of the initial state. The subsequent removal of the mechanical load does not result in the restoration of the initial intensities of the host and guest reflections.

Although the maximum intensity of the guest reflection after the pressure drop noticeably decreases, the new structural state of the sample is not accompanied by a noticeable decrease in the total volume of the guest structure. The structural state formed after the attainment of the critical load is characterized by the decomposition of the initial one-component orientational state of the guest structure into several orientational components. The two-dimensional reciprocal-lattice sections in the vicinity of the 002 point show the existence of three orientational states of the guest structure, $M_{(+)}$, $M_{(-)}$, and O (Fig. 10). It is rather surprising that the host matrix preserves only one orientational state.

The formation of several orientational components of the guest structure inside the single-domain host matrix indicates a structural phase transition in the guest structure after the attainment of a certain critical mechanical load (in our case, 1652 kg/cm^2). The existence of three orientational components can be interpreted as the transformation during the phase transition of the orthorhombic unit cell into a monoclinic or triclinic one. In this interpretation, two end orientational components, $M_{(+)}$ and $M_{(-)}$, characterize the formation of a twin structure, which reflects the equivalence of shear along the [010] and $[0\bar{1}0]$ directions for the ini-

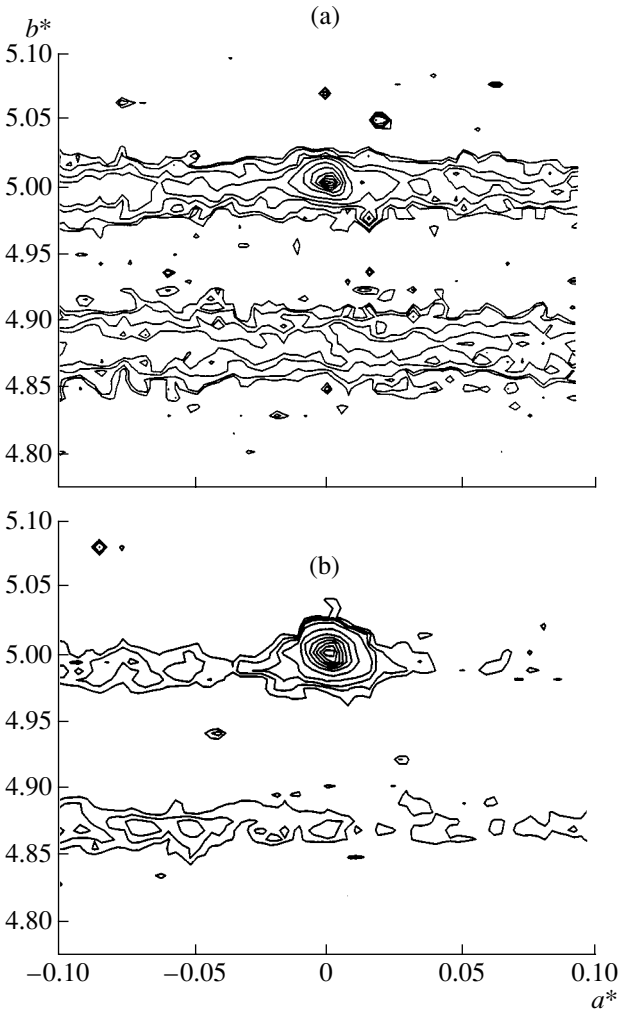

Fig. 8. Reciprocal-lattice section of the 050 reciprocal-lattice point (a) at room temperature and (b) at 224 K for $(Rb_{0.7}(NH_4)_{0.3})_2SO_4$.

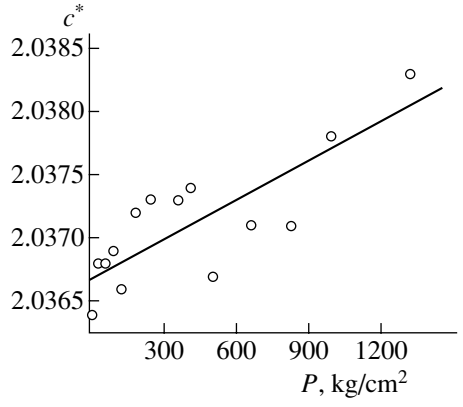

Fig. 9. Relative position of the $(002)_{guest}$ reflection from an $(NH_4)_2SO_4$ crystal as a function of the load in the range P = 0–1652 kg/cm^2.

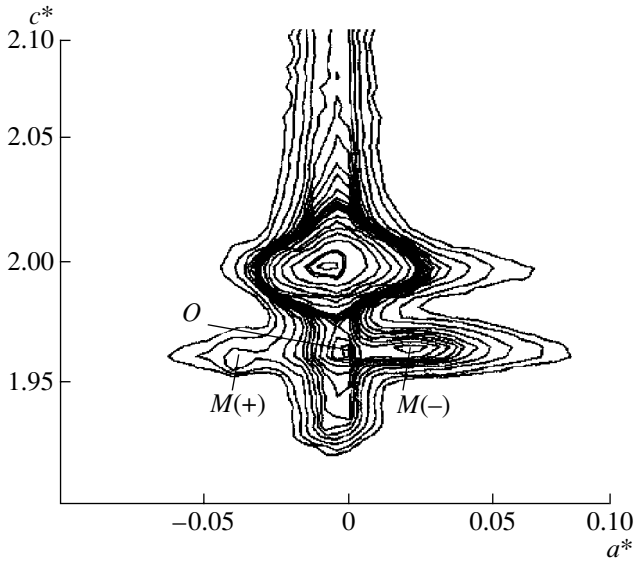

Fig. 10. Two-dimensional reciprocal-lattice section of ammonium sulfate in the vicinity of the 002 reciprocal-lattice point after the attainment of the critical load.

tial orthorhombic unit cell. Different intensities of these components are explained by different volume fractions of (+) and (–) twins. The middle component *O* can be interpreted in two ways. The first interpretation is based on the incompleteness of the phase transition from the orthorhombic to the monoclinic (or triclinic) unit cell. Then the orientational state (*O*) characterizes the residual fraction of the initial orthorhombic phase (analogue of residual austenite). The second interpretation is based on the existence of two nonequivalent twinning planes, (010) and (001). The component *O* corresponds to the (001) twinning plane; the components $M_{(+)}$ and $M_{(-)}$ corresponds to the (010) twinning plane. We believe that the first interpretation is more favorable, because, despite the fact that simultaneous twinning along nonequivalent planes is observed in some compounds [24], it is extremely rare (in the orthorhombic lattices, the (100), (010), and (001) planes are not equivalent).

CONCLUSIONS

Thus, the study of crystals of solid solutions of ammonium sulfate and rubidium, $(Rb_x(NH_4)_{(1-x)})_2SO_4$, revealed, in addition to three well known types of one-dimensional incommensurate composite compounds, also a new, fourth type of composite structures incommensurate along all the three coordinate axes. It is shown that crystals of pure ammonium sulfate undergo a number of temperature-induced transformations from the incommensurate to commensurate composite structures along one of the axial directions. It is also established that the mechanism of formation of composite phases is thermally activated. The latter fact allowed us to estimate the characteristic energy of the interaction between the host and gust structures based on the consideration of the temperature of the phase transition from the commensurate composite into incommensurate phase as ~0.01 eV. The existence of a number of transformations from the incommensurate to commensurate composite structures allows one to consider the known incommensurate composite structures, not as a specific type of intergrowth chemical compounds, but as the phase states of these compounds.

REFERENCES

1. I. D. Brown, B. D. Cutforth, C. G. Davides, *et al.*, Can. J. Chem. **52**, 791 (1974).
2. J. M. Hastling, J. P. Pouget, G. Shirane, *et al.*, Phys. Rev. Lett. **39**, 1484 (1977).
3. A. J. Schultz, J. M. Williams, N. D. Miro, *et al.*, Inorg. Chem. **17**, 646 (1978).
4. S. van Smaalen, Crystallogr. Rev. **4**, 79 (1995).
5. R. J. Nelmes, D. R. Allan, M. I. McMahon, and S. A. Belmonte, Phys. Rev. Lett. **83**, 4081 (1999).
6. M. I. McMahon, T. Bovornratanaraks, D. R. Allan, *et al.*, Phys. Rev. B **61**, 3135 (2000).
7. V. Heine, Nature **403**, 836 (2000).
8. K. Ohi, J. Osaka, and H. Uno, J. Phys. Soc. Jpn. **44**, 529 (1978).
9. N. G. Unruh, Solid State Commun. **8**, 1915 (1970).
10. D. E. O'Reily and T. Tsang, J. Chem. Phys. **46**, 1301 (1967).
11. T. Ikeda, K. Fudjibayashi, T. Nada, and J. Kobayashi, Phys. Status Solidi A **16**, 279 (1973).
12. A. Sawada, Y. Tagagi, and Y. Ishibashi, J. Phys. Soc. Jpn. **34**, 748 (1973).
13. J. Petzelt, J. Grigas, and I. Myerova, Ferroelectrics **6**, 225 (1974).
14. A. Sawada, S. Ohya, Y. Ishibashi, and Y. Takagi, J. Phys. Soc. Jpn. **38**, 1408 (1975).
15. E. Courtens, Ferroelectrics **72**, 229 (1987).
16. U. T. Hochli, K. Knorr, and A. Loidl, Adv. Phys. **39**, 405 (1990).
17. P. Simon, Ferroelectrics **135**, 169 (1992).
18. D. DeSousa Meneses, G. Hauret, and P. Simon, Phys. Rev. B **51**, 2669 (1995).
19. L. S. Kruts, G. S. Med'ko, and I. M. Shmyt'ko, USSR Inventor's Certificate No. 993220 (October 1, 1982).
20. I. M. Shmyt'ko, N. Ya. Donchenko, S. S. Klimyuk, *et al.*, USSR Inventor's Certificate No. 1148452 (December 1, 1984).
21. I. M. Shmyt'ko, N. S. Afonikova, and V. I. Torgashev, Fiz. Tverd. Tela (St. Petersburg) **44** (11), 2069 (2002) [Phys. Solid State **44**, 2165 (2002)].
22. I. M. Shmyt'ko, N. S. Afonikova, and V. I. Torgashev, Fiz. Tverd. Tela (St. Petersburg) **44** (12), 2204 (2002) [Phys. Solid State **44**, 2309 (2002)].
23. A. Guinier, *Théorie et Technique de la Radiocristallographie* (Dunod, Paris, 1956; Fizmatgiz, Moscow, 1961).
24. I. K. Bdikin, I. M. Shmytko, A. M. Balbashov, and A. V. Kazansky, J. Appl. Crystallogr. **26**, 71 (1993).

Translated by L. Man

Crystallography Reports, Vol. 49, No. 3, 2004, pp. 379–389. From Kristallografiya, Vol. 49, No. 3, 2004, pp. 445–455.

STRUCTURE OF INORGANIC COMPOUNDS

The Crystal Structure of Zr_2Se Reinvestigated by Electron Crystallography and X-ray Powder Diffraction[1]

Th. E. Weirich

Gemeinschaftslabor für Elektronenmikroskopie der Rheinisch-Westfälischen Technischen Hochschule Aachen, Ahornstr. 55, D-52074 Aachen, Germany

e-mail: weirich@gfe.rwth-aachen.de

Received August 5, 2003

Abstract—The metal-rich compound Zr_2Se is of particular interest for electron crystallography, since it was one of the first examples that proved that heavy-atom structures can be solved via quasi-automatic direct methods from selected area electron diffraction intensities [1]. For this reason, Zr_2Se has been chosen as a model to discuss the possibilities and the limits of the quasi-kinematical approach that has been successfully used to determine this and related structures from high-resolution electron microscopy (HREM) images and selected area electron diffraction. In order to quantify the achievable accuracy of the electron crystallography techniques used, the corresponding structures are compared with results from structural analysis with X-ray powder data and with a model received from first-principles calculations. The latter structure was chosen in this study as a reference, since the calculations do not depend on experimental parameters. Analysis of the obtained result from electron diffraction structural analysis (EDSA) shows that the structural model is, on average, only off by 0.08 Å, despite the investigated crystal having an effective thickness of 286 Å. The corresponding result from Rietveld refinement with X-ray powder data agrees to within 0.04 Å with the structure from calculation and within 0.03 Å with the result from an earlier single crystal X-ray study [2]. © *2004 MAIK "Nauka/Interperiodica".*

INTRODUCTION

In the preface to the 1949 Russian edition of the book *Difraktsiya Elektronov* (Electron Diffraction) [3], the author, Prof. Z.G. Pinsker, wrote the following lines: "Doubts have been raised in the literature as to whether a definite correlation between the structure of a scattering crystal and the intensities of the maxima in the (electron) diffraction patterns could be established." These lines reflect the beginning of a debate that continued over nearly 50 years over whether results from structural analysis with electron diffraction data are trustworthy or not. Unfortunately, the increasing understanding of the scattering of electrons by crystalline matter during the mid-1950s led many scientists (mostly in Western countries) to believe that the intensities of spots in electron diffraction patterns cannot be used for structural determination in the same way as they are used in X-ray diffraction [4, 5]. Therefore, it took until 1976 for the potential of selected area electron diffraction for structural determination of organic materials to be seriously examined by D. Dorset in the United States [6, 7]. It should be mentioned that the Russian scientists around Pinsker and, later, Vaĭnshteĭn and Zvyagin, had at that time already solved dozens of inorganic and mineral structures by applying their own developed techniques for EDSA [8, 9]. (For a condensed summary of the achievements of the Moscow group, see the review of Klechkovskaya and Imamov [10].) Probably encouraged by the successful work of Dorset on organic materials, EDSA became increasingly popular also outside the former Soviet Union. Over the years, it turned slowly into an accepted method for determining crystal structures that were unexaminable for X-ray crystallography, e.g., small molecular structures [11, 12], precipitates [13], zeolites [14], oxides [15, 16], and several metal-rich structures

[1] This article was submitted by the author in English.

Table 1. Atomic coordinates for Zr_2Se as obtained by crystallographic image processing of a HREM image (Fig. 1a). The coordinates and peak heights have been determined from the pseudo-projected potential map in Fig. 1d. Note that all atoms are located on mirror planes ($z = 0$). The z coordinates of the atoms were derived using chemical criteria (see text)

	x	y	Peak height
Zr1	0.169	0.007	991
Zr2	0.096	0.242	942
Zr3	0.593	0.079	926
Zr4	0.474	0.402	983
Zr5	0.808	0.204	994
Zr6	0.869	0.414	859
Se1	0.442	0.214	791
Se2	0.218	0.398	692
Se3	0.697	0.350	752

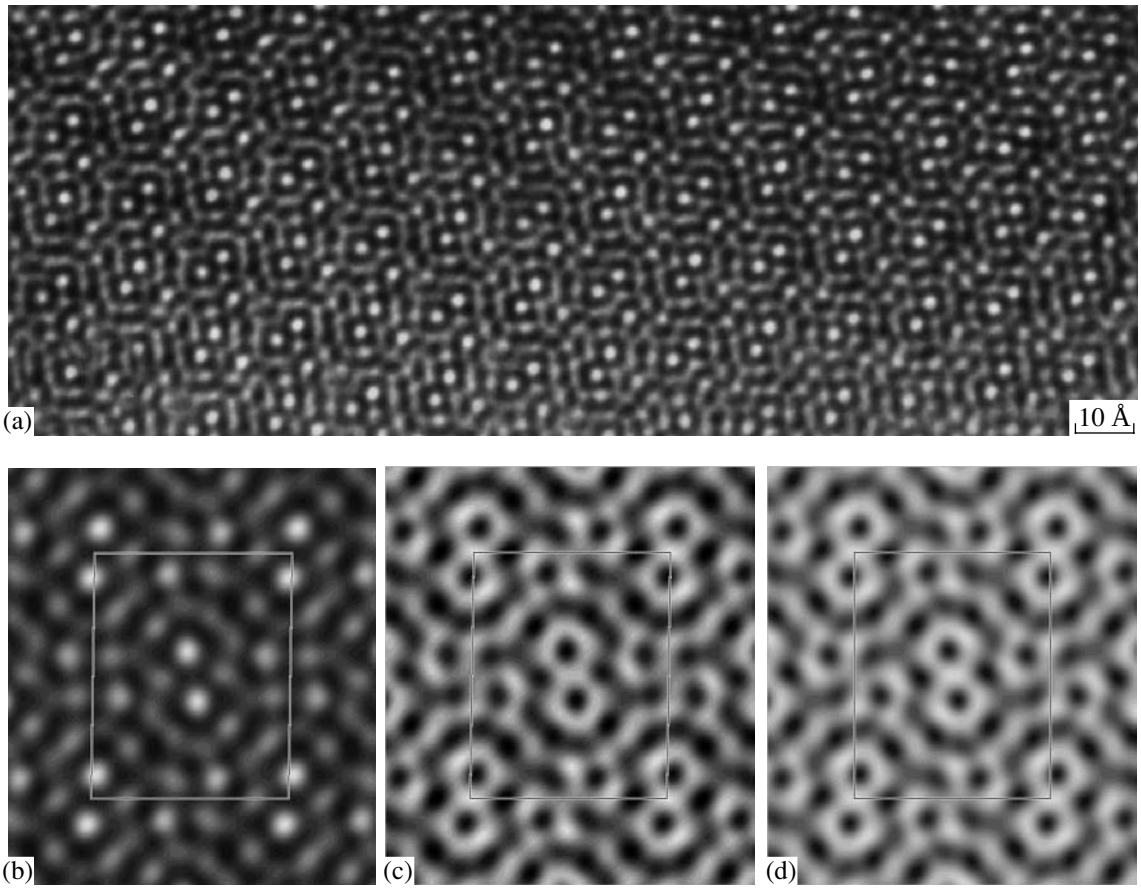

Fig. 1. (a) Experimental high-resolution electron micrograph of a Zr_2Se crystallite aligned along the [001] direction. The images in (b) and (c) show the lattice averaged images with *p*2 symmetry before and after applying corrections for the contrast transfer function and astigmatism on the extracted amplitudes and phases. The image in (d) was obtained after imposing constraints on the amplitudes and phases according to *p*2*gg* symmetry; $|F(hk)| = |F(-h, -k)|$, $|F(-hk)|$; $\phi(hk) = 0$ or π; $\phi(hk) = -\phi(-h - k)$, $\phi(-hk) + (h + k)\pi$. The image can be considered the restored pseudo-potential map, whereas black features in the image represent high potential, i.e., atom columns in projection. The map in (d) was used to obtain the two-dimensional atomic coordinates listed in Table 1. Note that the positions of zirconium have a significantly higher potential than that of selenium, as expected for small crystal thicknesses from the potential ratio curve in Fig. 6. The corresponding structure model derived from the HREM image in (a) is shown in Fig. 3a.

[1, 17–20]. The metal-rich compound mentioned in our title, Zr_2Se, is in this context of particular interest since it was one of the first examples for which it could be shown that even heavy-atom structures can be solved by quasi-automatic direct methods from selected area electron diffraction intensities [1]. For this reason, Zr_2Se has been chosen as a model structure to show the possibilities, and also the limits, of the quasi-kinematical approach that has been so successfully used to determine this and related structures. In order to allow quantitative measurement of accuracy, structures from electron crystallography are compared with results from structural analysis with X-ray powder data and with results from first-principles calculations within the density functional theory.

The structure of Zr_2Se was first determined in 1968 from single crystal X-ray data [2]. In the search for new compounds that contain the structural motif of condensed metal-clusters [21], the metal-rich branch of the zirconium-selenium system was reinvestigated by the present author [22]. The results presented in what follows were obtained by recent reanalysis of images that were recorded during at the Max-Planck Institute for Solid State Research in Stuttgart (Germany; by the group of Prof. Arndt Simon).

EXPERIMENTAL

Sample

Zirconium powder (DEGUSSA, m3N) and selenium pearls (HEK GmbH, m3N) were mixed in a molar ratio of 7 : 2 in a glove box under purified argon gas. The mixture was filled in a one-sided closed tube made from pure tantalum metal (Plansee, m2N8). The open end of the metal tube was squeezed and sealed by arc welding under a purified argon atmosphere. The received metal ampoule was placed in a gas-tight corundum tube, which was then heated to 670 K under

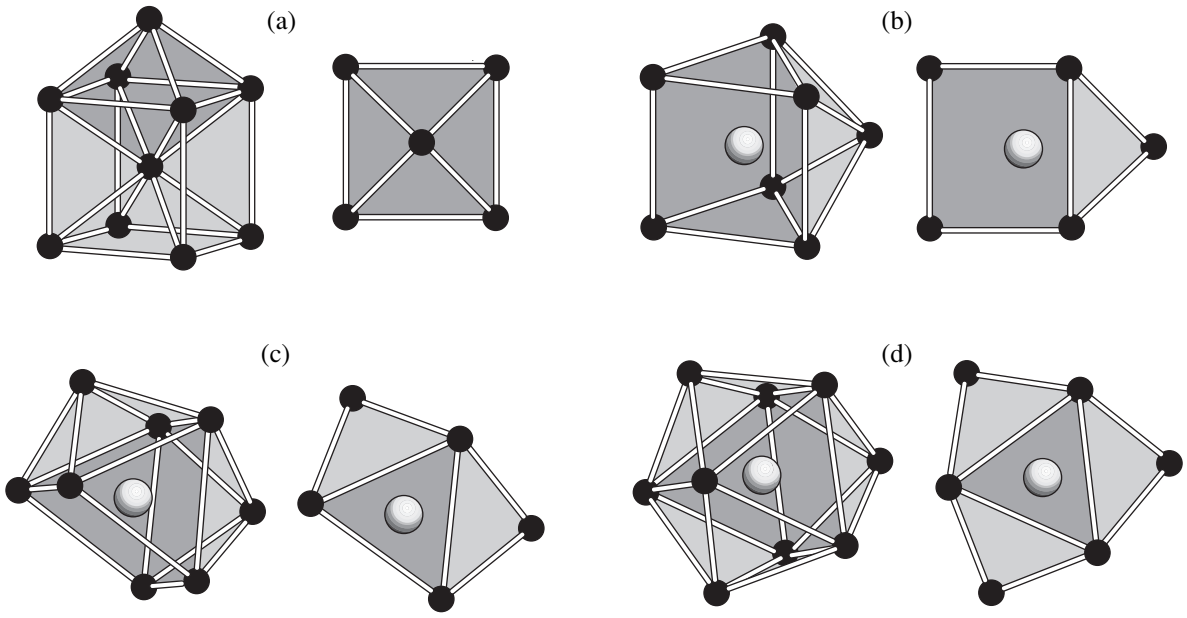

Fig. 2. Different types of polyhedra that have been used to derive a three-dimensional structure model from the potential maps shown in Figs. 1d and 5a. Each polyhedron is shown in clinographic view (left) and as observed when the structure is projected along the short *c* axis (right view). Zirconium atoms are shown in black and selenium atoms in light gray. (a) Cube of body centered β-zirconium respectively as vertex linked (condensed) Zr_6-octahedron [21]; (b) single-capped trigonal prism with selenium at the center; (c) double-capped trigonal prism; (d) triple-capped trigonal prism.

dynamic vacuum (about 10^{-5} Torr). The temperature was increased after annealing the sample for 2 h at 670 K with a gradient of 80° per hour. At 1070 K, the heating rate was increased to 120° per hour until the final temperature of 1670 K was reached. The sample was kept for 3 h under these conditions before the furnace was switched off and the sample was allowed to cool down to room temperature.

Structural Determination from Hrem Images

This section describes the structural determination of Zr_2Se by crystallographic image processing (CIP) of a single high-resolution electron microscopy image. A detailed outline of this technique has been published elsewhere [23–25].

Thin crystallites of the crushed sample were investigated in a Philips CM30/ST microscope at 300 kV. High-resolution electron microscopy (HREM) images from a Zr_2Se crystal aligned along the [001] zone axis were recorded on film (Fig. 1a). The negative was digitized with a video-rate CCD camera and then processed using the CRISP program [26]. An image area close to the crystal edge that contains about 20 unit cells in projection was selected and used to calculate its Fourier transform. Amplitudes and phases were extracted from the refined lattice positions in the Fourier transform (point resolution approximately 1.9 Å), and the lattice averaged image was calculated from the extracted amplitudes and phases (Fig. 1b). The first crossover of the contrast transfer function (CTF) was estimated from the amorphous region at the crystal edge and used to determine the defocus value ($\Delta f = -748$ Å with astigmatism of ±42 Å). The effect of the CTF on the amplitudes and phases was corrected, and a new potential map was obtained (Fig. 1c). Atoms appear now as black features in the map (*pseudo Scherzer image*). The seven possible plane groups for rectangular lattices were tested, and the one that gave the lowest phase residual indicated the correct symmetry (*p*2*gg* in the present case). The corresponding phase relationships, according to *p*2*gg* symmetry, were imposed on the amplitudes and phases, and a new potential map was received (Fig. 1d). Two-dimensional atomic coordinates were extracted from this map (Table 1) and used to construct a three-dimensional structural model, since the basic building blocks in this type of metal-rich compound are well known, i.e., the metal atoms form M_6 octahedral units and trigonal prisms around the non-metal atoms (Fig. 2). Since these type of metal-rich structures require that all the atoms be located on mirror planes at heights of 0.5 or zero along the short axis, it was also possible to derive the missing *z* coordinates for all the atoms. The derived structure model from CIP is shown in Fig. 3a.

Structural Determination from Selected Area Electron Diffraction

Selected area electron diffraction patterns from the thinnest crystal areas of Zr_2Se were recorded on standard photographic EM film (Kodak SO-163 Electron

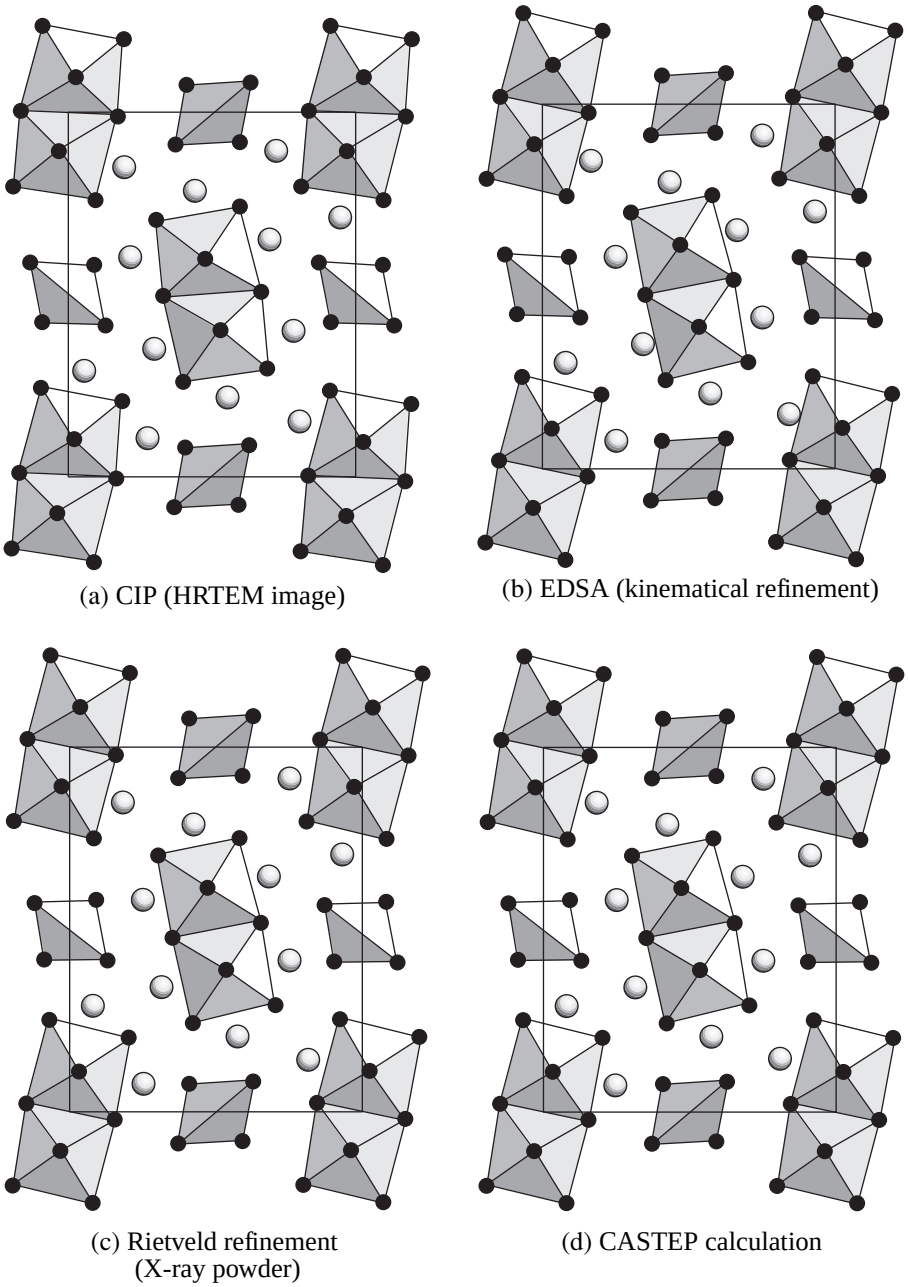

Fig. 3. Structure models for Zr_2Se in projection along the short *c* axis as obtained by different methods (see text). The zirconium atoms (black bullets ●) form M_6 cluster-units, which are linked (condensed) via common atoms along the viewing direction. The selenium atoms (white balls ○) are situated within capped trigonal prisms of zirconium atoms (see polyhedra in Fig. 2). Note that, whereas the structures from Rietveld refinement on X-ray powder data and CASTEP calculation are virtually identical, the structure model from electron diffraction reveals some small misplacements of atoms.

Image Film) in a Philips CM30/ST electron microscope operated at 300 kV. Lattice parameters for the *a* and *b* axes were determined from a calibrated electron diffraction pattern recorded along the [001] direction. The determined lattice parameters are $a = 12.6$ Å and $b = 15.7$ Å. The diffraction pattern shown in Fig. 4a was digitized by using a 1024 × 1280 pixel 16-bit CCD camera (CALIDRIS, model KITE). The image data were corrected for non-linearity in the blackening curve, and reflection intensities I_{hkl} were estimated using the ELD program [27, 28]. Analysis of systematic extinctions in the diffraction pattern shows that $h0$: $h = 2n + 1$ and (less clearly) $0k = 2n + 1$. These extinctions suggest plane group symmetry $p2gg$, which is compatible with the centrosymmetric space groups *Pbam* (55), *Pnnm* (58), and *Pbnm* (62). Merging the intensities according to the $p2gg$ symmetry of the pattern yielded a data set of 219 crystallographically non-equivalent

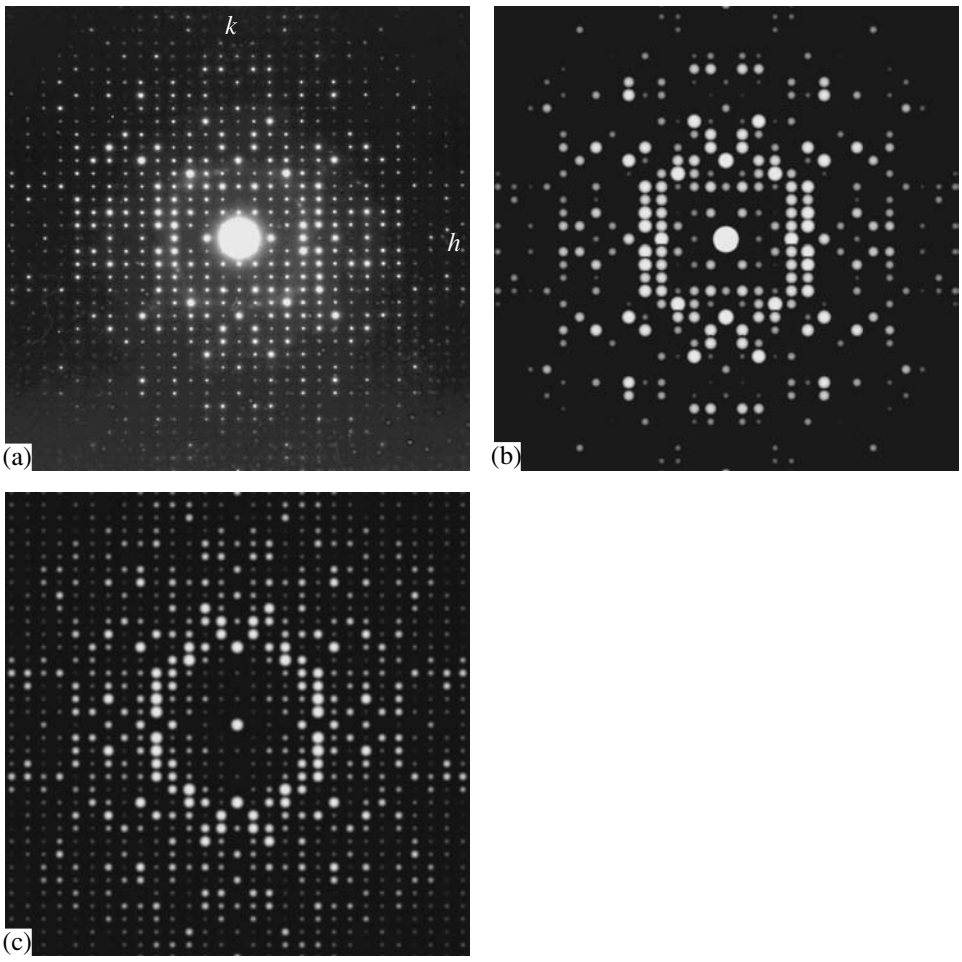

Fig. 4. The row of images shows the experimentally obtained SAED pattern of Zr_2Se recorded along [001] in (a), the calculated dynamical diffraction pattern for a crystal thickness of 286 Å in (b) and the corresponding calculated kinematical pattern in (c) using the atomic coordinates from first principles calculation. Violation of the extinction rules in the experimental diffraction pattern along *k* arises from secondary scattering, which indicates a slight misalignment of the crystal and/or presence of defects (see [19]).

*hk*0 reflections with a resolution of about 0.8 Å. The internal *R*-factor of symmetry-related reflections in the merged data set was 9.5%. In accordance with the earlier result from single crystal X-ray diffraction [2], only space group *Pnnm* was tried for solving the structure by direct methods with the SIR97 program [29]. The program was modified for this purpose with electron scattering factors calculated by Jiang and Li [30]. As in previous studies [1, 18, 19], suspected dynamical diffraction was taken into account by using a phenomenological compensation based on the approximation $I_{hkl} \propto |V_{hkl}|$, which has been derived as the limit for thick crystals under two-beam conditions [31, 32, 3], where V_{hkl} (in volts) designates the structure factor amplitude for electrons. The most probable solution found by SIR97 had an *R*-factor of 24.8%. All 36 atoms in the unit cell are clearly visible in the potential map calculated from the 53 largest *hk*0 E-values (Fig. 5a). A structural model could readily be constructed from the coordinates obtained from the projected potential map using the above outlined topological principles.

A subsequent (kinematical) least-squares structure refinement on $|V_{hkl}|^2$ using the SHELXL97-2 program [33] yielded displacement factors for all atoms of the same order as obtained in previous investigations [1, 17–19, 34]. The overall *R*-factor of the refined structure was 35.8% (28 parameters refined, unit weights). Since the intensities were not corrected for the curvature of the Ewald sphere, the obtained atomic displacement factors from least-squares refinement cover both the intensity decay due to the excitation error and the true thermal displacement. The refined atomic coordinates, together with the displacement factors U_{eq}, are listed in Table 2. The average positional shift of the atoms during the refinement was 0.07 Å (maximum shift 0.22 Å for Se-3). The potential map after least-squares refinement and the complete structural model for Zr_2Se from electron diffraction are shown in Figs. 5b and 3b.

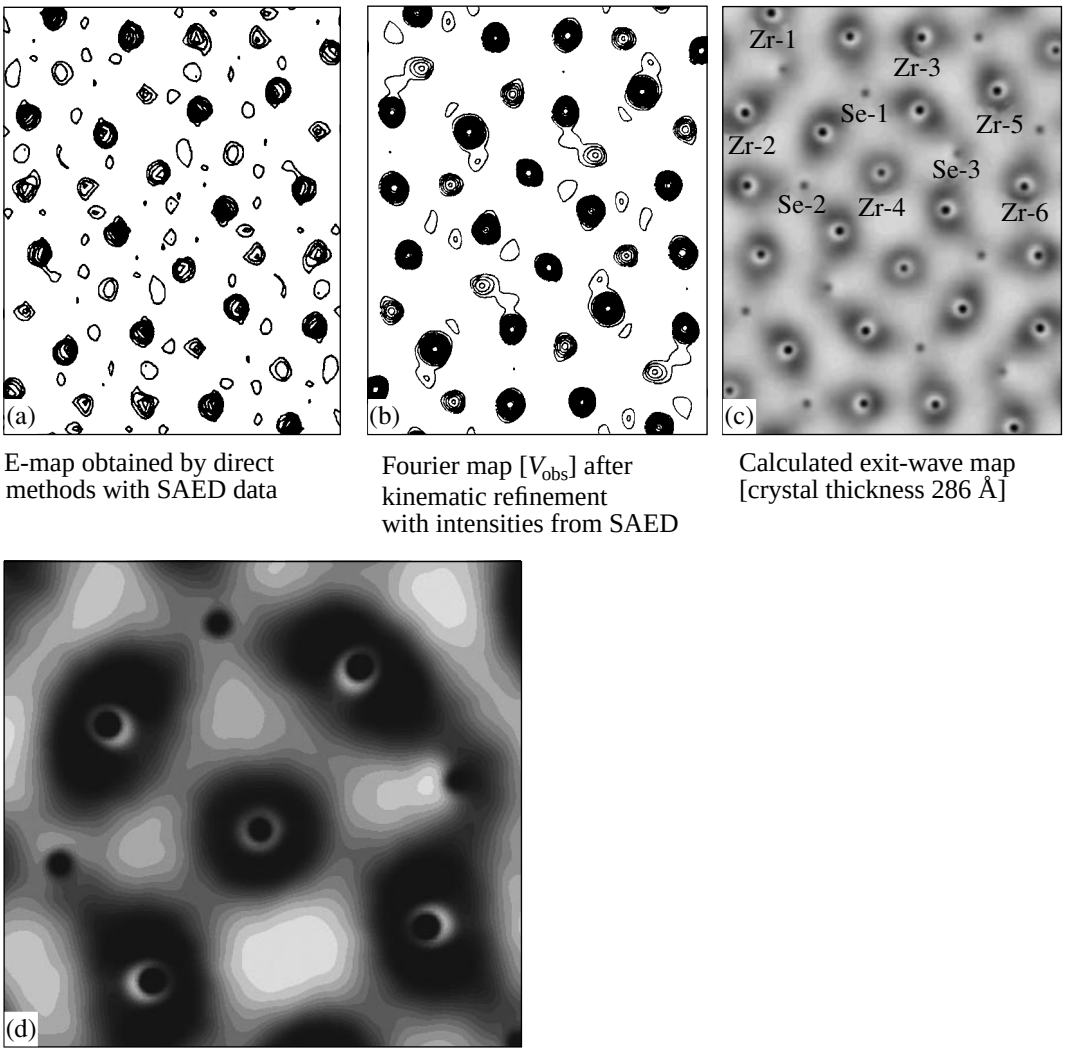

E-map obtained by direct methods with SAED data

Fourier map [V_{obs}] after kinematic refinement with intensities from SAED

Calculated exit-wave map [crystal thickness 286 Å]

Enlarged part of the calculated exit-wave map for a crystal thickness of 286 Å (contrast enhanced image)

Fig. 5. Projected potential maps for Zr_2Se along [001] as obtained from experiment and multislice calculations. Note that the zirconium atoms in the enlarged calculated exit-wave map in (d) have a potential distribution that indicates excitation of higher Bloch states (2*s* and 2*p* respectively), whereas the potential of the selenium atoms has a 1*s* character. Due to excitation of the (less-localized) higher Bloch states, atoms of former similar projected potential become different, i.e., the central zirconium atom (Zr-4) has a lower potential in the map than the surrounding atoms (Zr-1, Zr-2, Zr-5). Also. the three selenium atoms have a significantly different potential according to the distinct number of their next-neighbor atoms. These striking features are also present in the experimental map shown in (b). Moreover, the diffuse potential around Se-3 is possibly the reason for the slight misplacement during (kinematical) LS-refinement (see text).

Estimation of Average Crystal Thickness

Exit-wave maps were calculated with NCEMSS program [35] for estimating the average crystal thickness by the earlier described potential-ratio method [18]. Quantification of the received potential maps for crystal thicknesses between 5 and 400 Å (step width 5 Å) yielded the Zr-Se effective potential ratio curve for Zr-4 and Se-3 that is shown in Fig. 6. The experimental Zr-Se ratio $\varphi_{Zr}/\varphi_{Se}$ for the two atoms, as determined from the potential map after structure refinement (Fig. 5b), is 1.8. This value is in agreement with an average crystal thickness of about 87, 123, 172, 208, 286, and 383 Å (horizontal line in Fig. 6). The influence of secondary scattering, crystal bending, and crystal tilt on the potential ratio was not taken into account in this analysis. Visual comparison of the experimentally (Fig. 4a) and dynamically calculated electron diffraction patterns for the above given values yielded the best agreement for a crystal with a thickness of 286 Å (Fig. 4b). The corresponding exit-wave map for this thickness is shown in Fig. 5c. The kinematical diffrac-

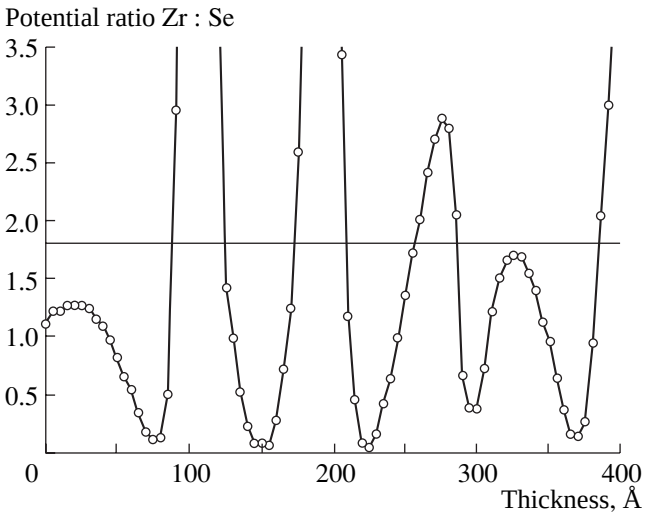

Fig. 6. Trace of the effective Zr-4 : Se-3 potential ratio vs. crystal thickness for Zr_2Se as obtained from calculated exit-wave maps. The calculation was carried out in steps of 5 Å for crystal thicknesses up to 400 Å. The value of zero thickness was determined from the projected potential map. The experimental Zr-4 : Se-3 ratio ($\varphi_{Zr}/\varphi_{Se}$ = 1.8, horizontal line) was determined from the potential map in Fig. 5b after kinematic LS-refinement. The determined value agrees with the crystal thicknesses of 87, 123, 172, 208, 256, 286, and 383 Å (see text). Note that the selenium columns entirely dominate the exit-wave maps with a periodicity of about 75 Å.

tion pattern as calculated with the JEMS program (P. Stadelmanm, Lausanne) is shown in Fig. 4c.

Rietveld Refinement with X-ray Powder Data

X-ray powder data of the crushed sample were collected in transmission on a STADI/P diffractometer (Stoe and Cie., Darmstadt, Germany) using copper Ka radiation. A subsequent Rietveld analysis of the powder data with the program FULLPROF [36] and using structural parameters for Zr_2Se from EDSA as a starting model showed that the sample contained, alongside Zr_2Se, α-zirconium (JCPDS Powder diffraction file no. 5-665) as well. Structural parameters for both phases were successively refined until convergence was reached. The obtained results from Rietveld refinement are compiled in Tables 3 and 4. The calculated and the experimental diffraction profiles, together with the difference curve obtained after refinement, are shown in Fig. 7. The structural model obtained from Rietveld refinement is shown in Fig. 3c.

Structure Validation by First-Principles Calculations

The main goal of EDSA is defined as the determination of crystal structures that cannot be determined by

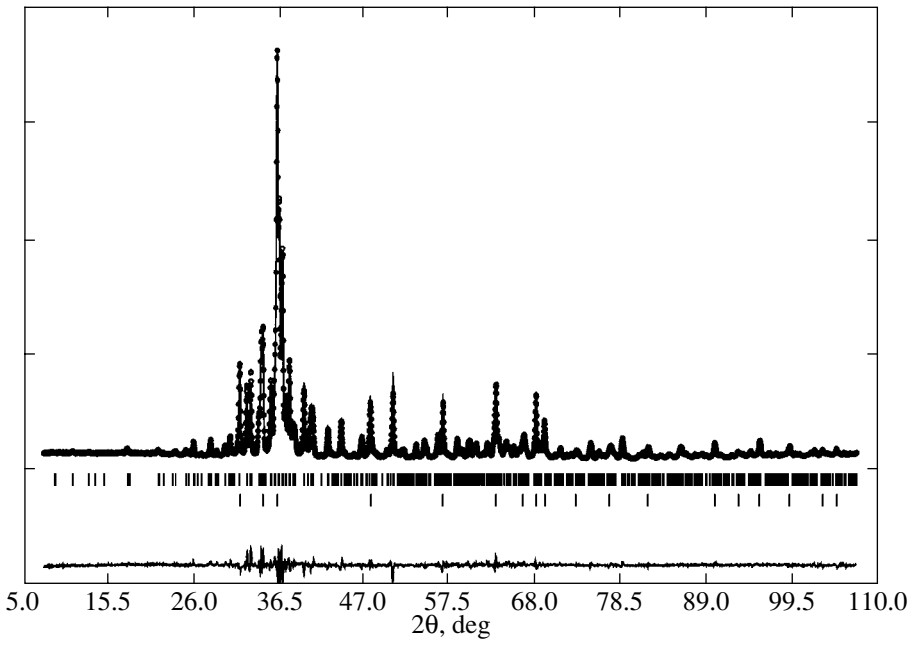

Fig. 7. Graphic representation of the result from Rietveld refinement with X-ray powder data. Vertical bars (|) indicate positions of Bragg reflections for Zr_2Se and hexagonal zirconium (18 reflections). The deviations between the observed and the calculated intensities from the refined models are shown in the difference plot in the lower part of the diagram (dots—observed intensities; solid line—calculated intensities).

Table 2. Atomic coordinates and atomic displacement factors for Zr_2Se from electron diffraction. Standard uncertainties are given in parentheses. The tabulated atomic coordinates labeled DM refer to the peak maxima in the potential map received from SIR97 (Fig. 5a). The corresponding rows labeled LS show the coordinates after least-squares structural refinement with SHELXL-97-2 (Fig. 5c). All atoms for space group *Pnnm* are located on Wyckoff position 4*g* ($z = 0$). The *z* coordinates of the atoms were derived using chemical criteria (see text)

	x(DM)	*y*(DM)	*x*(LS)	*y*(LS)	*U*, Å^2
Zr(1)	0.150	0.021	0.1514(16)	0.0216(11)	0.014(6)
Zr(2)	0.075	0.250	0.0779(17)	0.2529(12)	0.022(7)
Zr(3)	0.574	0.078	0.5843(18)	0.0754(13)	0.028(8)
Zr(4)	0.471	0.390	0.4707(15)	0.3907(11)	0.018(6)
Zr(5)	0.797	0.207	0.7992(17)	0.2035(11)	0.020(7)
Zr(6)	0.872	0.420	0.8755(12)	0.4193(9)	0.005(6)
Se(1)	0.424	0.207	0.4264(35)	0.2107(25)	0.060(13)
Se(2)	0.250	0.418	0.2479(26)	0.4178(17)	0.040(10)
Se(3)	0.678	0.342	0.6610(44)	0.3451(29)	0.074(16)

Table 3. Results of Rietveld refinement with X-ray powder data

Wavelength = 1.54060 Å

2θ range: 2.64–107.73 deg

Number of data points: 3504

Refined parameters: 49

$R_{p(conv)} = 9.61\%$

$R_{wp(conv)} = 10.8\%$

$R_{exp(conv)} = 4.54\%$

GoF = 2.4

Zr_2Se

Space group: *Pnnm* (58)

Number of formula units per unit cell: 12

$a = 12.5985(11)$ Å, $b = 15.7448(14)$ Å, $c = 3.61256(32)$ Å

$V = 716.58(11)$ Å^3

$D_{calcd} = 7.27$ g/cm^3

Bragg positions: 513

Zirconium

Space group: $P6_3/mmc$ (194)

Number of formula units per unit cell: 2

$a = 3.24687(58)$ Å, $c = 5.17671(48)$ Å

$V = 47.26(1)$ Å^3

$B = 4.91(6)$ Å^2

$D_{calcd} = 6.41$ g/cm^3

Bragg positions: 18

$R_{Bragg} = 5.17\%$

$R_F = 4.5\%$

any other method. However, the final step in a structural determination from electron data—the validation of the result—remains often difficult. The low-*R*-factor criterion, which is commonly used in X-ray crystallography to justify the correctness of a structure, can usually not be applied due to the non-kinematic nature of the electron data. To solve this dilemma, geometrical optimization and energy minimization by first-principles calculations within density functional theory have been recently used to check the structures of α- and β-Ti_2Se that have been determined from electron diffraction [37]. In addition to calculation of physical properties and band structure, first-principles calculations also permit *refining* the geometry (lattice parameters and atomic coordinates) of a provided structure model by minimizing the total energy of the system. The present calculations for Zr_2Se were performed using the *Cambridge Serial Total Energy Package*, *CASTEP* [38], with structural parameters obtained from EDSA as input. The calculations were carried out with nonrelativistic ultrasoft pseudopotentials (us-PP) [39] and the general-gradient approximation (GGA) to include exchange and correlation [40]. The structural relaxation was stopped after 27 iterations, when the energy gain per atom was less than 1.3×10^{-5} eV (cut-off energy for plane waves was 270 eV).

The *rms* displacement for the six zirconium and three selenium atoms in the asymmetric unit was less than 0.001 Å, and the *rms* force was below 0.013 eV/Å at this level. The structural result from this *energetic structural refinement* is listed in Table 5. The corresponding model is shown in Fig. 3d.

DISCUSSION

The above example of the heavy atom structure Zr_2Se demonstrates again that standard electron microscopy can provide data of sufficient quality to

Table 4. Atomic coordinates for Zr_2Se as obtained from Rietveld refinement with X-ray powder data. All atoms in space group *Pnnm* are located on Wyckoff position 4*g* (*z* = 0)

	x	*y*	*B*, Å^2
Zr(1)	0.15169(34)	0.02288(28)	4.65(12)
Zr(2)	0.08041(36)	0.25396(31)	5.24(13)
Zr(3)	0.58537(30)	0.07929(32)	4.98(12)
Zr(4)	0.46922(32)	0.38994(27)	4.86(12)
Zr(5)	0.80091(28)	0.20398(28)	4.80(13)
Zr(6)	0.87643(34)	0.42267(34)	5.55(14)
Se(1)	0.42149(39)	0.20845(40)	4.95(14)
Se(2)	0.24568(45)	0.42002(42)	6.46(16)
Se(3)	0.68331(37)	0.34916(33)	4.64(14)

Table 5. Structural parameters for Zr_2Se as obtained from first-principles calculations with the program CASTEP. The lattice parameters after structural relaxation by energy minimization are *a* =12.696 Å, *b* = 15.827 Å, and *c* = 3.630 Å. All atoms are located on Wyckoff position 4*g* (*z* = 0)

	x	*y*
Zr(1)	0.1513	0.0248
Zr(2)	0.0755	0.2516
Zr(3)	0.5839	0.0809
Zr(4)	0.4675	0.3902
Zr(5)	0.7984	0.2023
Zr(6)	0.8761	0.4234
Se(1)	0.4179	0.2080
Se(2)	0.2483	0.4215
Se(3)	0.6828	0.3481

retrieve the atomic structure of extremely small crystallites, often only a few tens of nanometers in size. However, as can be seen from the potential ratio curve shown in Fig. 6, the assumption of kinematics (single scattering) is sometimes a rough approximation of the scattering processes in a crystal, in particular when the material of interest is mainly composed of heavy atoms. In view of these strong effects from dynamical scattering, one could get the impression that *ab initio* structural investigations with SAED data are not possible at all. Luckily, practical work has shown that the thinnest available crystals often yield data that can be treated—at least in the initial stages of a structural analysis, i.e., for solving the structure—as quasi-kinematical. In some cases, even a pure kinematical L.S.-refinement can be applied with success. However, the main question that remains after structural determination with electron data is: *how can I check that the structure is correct?* To give a quantitative answer to this question, the structures determined from the HREM image, from SAED, from Rietveld refinement with X-ray powder data, and from first-principles calculations will be compared with the result from the earlier single crystal X-ray study [2]. Since the result from first-principles calculations does not depend on experimental data, the corresponding model was chosen as a reference in the following analysis.

Because of the limited resolution of the data and a rather steep rise in crystal thickness, the result from CIP was found to be most in error. The average positional deviation between the result from GASTEP (Table 5) and CIP (Table 1) is 0.26 Å (maximum deviation 0.54 Å for Se-2). However, despite this relatively large error, all columns of atoms can be distinguished, as is seen in the final potential map (Fig. 1d). As expected, the model obtained from electron diffraction with subsequent (kinematical) least-squares refinement is much closer to the structure derived from calculation (Table 2). The average deviation is, in this case, only 0.08 Å (maximum deviation 0.28 Å for Se-3). Comparison of the corresponding result obtained from Rietveld refinement with X-ray powder data (Table 4) shows an average agreement in position within 0.04 Å (maximum deviation 0.07 Å for Zr-2). A slightly better result was only found for the model earlier determined from single crystal X-ray diffraction [2], where the average deviation is 0.03 Å (maximum deviation 0.06 Å for Zr-2). The two structures determined from X-rays differ on average by less than 0.03 Å (maximum deviation 0.04 Å for Se-3). Concerning lattice parameters, the agreement between Rietveld refinement with X-ray powder data (Table 3) and first-principles calculation (Table 5) is better than 0.8%. The same agreement is obtained when the published lattice parameters from single crystal X-ray diffraction are compared with the unit cell from calculation. The excellent agreement of the two X-ray structures with the result from first-principles calculation demonstrates again (see also [37]) that quantum-mechanical calculations are a useful complement for structural validation when reliable reference data from other sources are unavailable.

As derived from the analysis of the Zr-Se potential ratio, the investigated crystal had an effective average thickness of about 286 Å. Although this is already a rather large value for a heavy atom structure, the derived model is surprisingly less in error. As can be seen by comparison of the projected structure models in Fig. 3, the largest misplacement (0.28 Å) is found for atom Se-3 (for the labeling of the atoms, see Fig. 5c), whereas the average positional error is only 0.08 Å. Inspection of the calculated exit-wave maps in Figs. 5c and 5d seems to explain why the quasi-kinematical approach yields a partially wrong structure. Excitations of higher (less-localized) Bloch states has the effect of smearing the potential over a larger area (2*s* states) or to generate potential between the atom columns (2*p* states). Moreover, atoms that have a similar potential in the projected potential map have a significant different

potential in the exit-wave map, e.g., the selenium atoms inside the three types of the trigonal prisms (see Fig. 2). On the other hand, a similar analysis carried out for α-Ti_2Se showed a misplacement for one atom of the same magnitude as detected in this study, but without indication of the excitation of higher Bloch states [19]. Thus, other effects, such as mistakes in estimating the intensities or secondary scattering, must also be taken into consideration when discussing these errors.

CONCLUSION

Application of the quasi-kinematical approach in combination with modern direct methods software succeeded in solving several heavy atom structures from two-dimensionally selected area electron diffraction data. This includes the metal-rich structures Ti_2S, Ti_9Se_2, Ti_8Se_3 [1], Ta_2P [17], α-Ti_2Se [37], and Zr_2Se (this study). For all these structures, reference data exist from X-ray crystallography that allowed a critical review of the obtained results from electron diffraction. Moreover, the structures of β-Ti_2Se [1], $Ti_{11}Se_4$ [34], and $Ti_{45}Se_{16}$ [18], which have been intractable for X-ray crystallography, were solved and refined using the same approach. First-principles calculations with density functional theory have been used to validate the results for these three structures [37, 41]. As demonstrated by the example of Zr_2Se, first-principles programs, with their unique capabilities for minimizing total energy and geometrical optimization, are a highly valuable tool for checking structures obtained from electron crystallography for errors.

In addition to being convinced that the proposed method works and that the determined structures are correct, within limits, it is also of importance to understand why the method applied here worked so surprisingly well. If electron-channeling theory is applied to this problem, the incident electrons can be assumed to be fast in the beam direction and relatively slow in the perpendicular direction. If a principal zone axis of a crystal with well-separated rows of atoms is selected, the first excited Bloch states are the 1*s* states. Since the 1*s* states are the most highly localized states around the atom columns, the corresponding exit-wave maps necessarily consist of discrete peaks (1*s* scattering condition). Since the peak heights in the exit-wave map depend strongly on specimen thickness, it follows that the diffracted intensities do not necessarily allow retrieving a true picture in terms of a projected structure with peak intensities proportional to the atomic number (see Fig. 6). Nevertheless, direct methods appear relatively robust in cases of such changes, as can be deduced from Sayre's theorem [42]. Sayre pointed out that a structure consisting of non-overlapping peaks of (nearly) equal weight can be "squared" without changing the geometric part (the phases) of the structure factor. Thus, even if the shape of the atomic scattering factor has become unphysical (by dynamical diffraction), the structure can still be solved (and possibly refined) from such data, since the positions of the atomic peaks themselves are unchanged by squaring the structure factors. Hence, direct methods can solve a structure even from dynamical intensities, provided that the most important strong reflections are still ranked among the highest E-values after normalizing the data. The latter has been quantitatively worked out by Dorset and McCourt for diketopiperazine [43]. From this, it is then possible to derive the following boundary conditions, for which quasi-automatic direct methods have a good chance for solving the structure:

(1) The structure must be (approximately) monoatomic, i.e., all atoms should have an almost identical electrostatic potential.

(2) A projection with non-overlapping atom columns should exist (atomic resolution data).

(3) The most significant part of the unit-cell transform must be covered by the data.

All these conditions are clearly met by the here investigated short-axis compound Zr_2Se and related structures. It is very surprising that the above-stated conditions obviously hold also in a thickness range when Bloch states that are already high are exited, as was shown above.

However, the essence of the present study of Zr_2Se can be expressed in the words of Pinsker, who stated more than 50 years ago [3] that "from the experimental values of intensities of the reflections in electron diffraction patterns, we can obtain accurate values of the atomic coordinates and the potential distribution within the lattice, by using the trial and error method or the Fourier synthesis of structure factors and structure amplitudes."

REFERENCES

1. T. E. Weirich, X. D. Zou, R. Ramlau, *et al.*, Acta Crystallogr., Sect. A: Found. Crystallogr. **56**, 29 (2000).
2. H. F. Franzen and L. J. Norrby, Acta Crystallogr., Sect. B: Struct. Crystallogr. Cryst. Chem. **24**, 601 (1968).
3. Z. G. Pinsker, *Electron Diffraction* (Akad. Nauk SSSR, Moscow, 1949; Butterworths, London, 1953).
4. D. B. Williams and C. B. Carter, *Transmission Electron Microscopy* (Plenum, New York, 1996), p. 203.
5. J. J. Hu, F. N. Chukhovskii, and L. D. Marks, Acta Crystallogr., Sect. A: Found. Crystallogr. **56**, 458 (2000).
6. D. L. Dorset and H. A. Hauptrnan, Ultramicroscopy **1**, 195 (1976).
7. D. L. Dorset, *Structural Electron Crystallography* (Plenum, New York, 1995).
8. B. K. Vaĭnshteĭn, *Structural Analysis by Electron Diffraction* (Akad. Nauk SSSR, Moscow, 1956; Pergamon, Oxford, 1964).
9. B. B. Zvyagin, *Electron Diffraction Analysis of Clay Mineral Structures* (Nauka, Moscow, 1964; Plenum, New York, 1967).

10. V. V. Klechkovskaya and R. M. Imamov, Kristallografiya **46**, 598 (2001) [Crystallogr. Rep. **46**, 534 (2001)].
11. I. G. Voigt-Martin, Microsc. Res. Tech. **46**, 178 (1999).
12. U. Kolb and G. N. Matveeva, Z. Kristallogr. **218**, 259 (2003).
13. J. Gjónnes, V. Hansen, B. S. Berg, *et al.*, Acta Crystallogr., Sect. A: Found. Crystallogr. **54**, 306 (1998).
14. S. Nicolopoulos, J. M. Gonzalez Calbet, M. Vallet-Regi, *et al.*, J. Am. Chem. Soc. **117**, 8947 (1995).
15. M. Gemmi, L. Righi, G. Calestani, *et al.*, Ultramicroscopy **84**, 133 (2000).
16. C. Bougerol-Chaillout, Micron **32**, 473 (2001).
17. Th. E. Weirich, S. Hovmöller, H. Kalpen, *et al.*, Kristallografiya **43**, 1027 (1998) [Crystallogr. Rep. **43**, 956 (1998)].
18. T. E. Weirich, Acta Crystallogr., Sect. A: Found. Crystallogr. **57**, 183 (2001).
19. T. E. Weirich, Z. Kristallogr. **218**, 269 (2003).
20. M. Gemmi, X. D. Zou, S. Hovmöller, *et al.*, Acta Crystallogr., Sect. A: Found. Crystallogr. **59**, 117 (2003).
21. A. Simon, Angew. Chem. Int. Ed. Engl. **20**, 1 (1981).
22. T. E. Weirich, DrS Thesis (Univ. of Osnabrück, Germany, 1996).
23. X. D. Zou, Chem. Commun., No. 5, 38 (1995).
24. X. D. Zou, T. E. Weirich, and S. Hovmöller, in *Progress in Transmission Electron Microscopy*, Vol. 1: *Concepts and Techniques*, Ed. by X. F. Zhang and Z. Zhang (Springer, Berlin, 2001), pp. 191–222.
25. S. Hovmöller, X. D. Zou, and T. E. Weirich, in *Advances in Imaging and Electron Physics*, Ed. by P. W. Hawkes (Academic, Amsterdam, 2002), Vol. 123, p. 257.
26. S. Hovmöller, Ultramicroscopy **41**, 121 (1992).
27. X. Zou, Y. Sukharev, and S. Hovmöller, Ultramicroscopy **49**, 147 (1993).
28. X. Zou, Y. Sukharev, and S. Hovmöller, Ultramicroscopy **52**, 436 (1993).
29. A. Altomare, M. C. Burla, M. Camalli, *et al.*, J. Appl. Crystallogr. **32**, 115 (1999).
30. J. S. Jiang and F. H. Li, Acta Phys. Sin. **33**, 845 (1984).
31. H. Bethe, Ann. Phys. (Leipzig) **87**, 55 (1928).
32. C. H. MacGillavry, Physica (Utrecht) **7**, 329 (1940).
33. G. M. Sheldrick, *SHELXL-97-2. Program for Crystal Structure Refinement* (Univ. of Göttingen, Germany, 1998).
34. T. E. Weirich, R. Ramlau, A. Simon, *et al.*, Nature **382**, 144 (1996).
35. R. Kilaas, *NCEMSS—Program for the Simulation of HRTEM Images* (National Center for Electron Microscopy, Materials Science Division, Lawrence Berkeley Laboratory, Univ. of California, Berkeley, USA, 1997).
36. J. Rodriguez-Carvajal, *FULLPRO, a Program for Rietveld, Profile Matching and Integrated Intensities Refinement of X-ray and/or Neutron Data* (Laboratoire Leon Brillouin, CEA-Saclay, France, 2000).
37. K. Albe and T. E. Weirich, Acta Crystallogr., Sect. A: Found. Crystallogr. **59**, 18 (2003).
38. M. Payne, M. Teter, D. Alien, *et al.*, Rev. Mod. Phys. **64**, 1045 (1992).
39. M. H. Lee, PhD Thesis (Cambridge Univ., England, 1991).
40. J. Perdew and Y. Wang, Phys. Rev. B **45**, 13244 (1992).
41. T. E. Weirich, Z. Kristallogr. (Suppl. 20), S94 (2003).
42. D. Sayre, Acta Crystallogr. **5**, 60 (1952).
43. D. L. Dorset and M. McCourt, Acta Crystallogr., Sect. A: Found. Crystallogr. **50**, 287 (1994).

Crystallography Reports, Vol. 49, No. 3, 2004, pp. 390–395. Translated from Kristallografiya, Vol. 49, No. 3, 2004, pp. 456–461.

STRUCTURE OF INORGANIC COMPOUNDS

Synthesis and Structure of Iron Zirconium Phosphate $Fe_{1/3}[Zr_2(PO_4)_3]$

E. R. Gobechiya*, Yu. K. Kabalov*, A. I. Orlova, I. G. Trubach**, D. M. Bykov**, and V. S. Kurazhkovskaya***

** Moscow State University, Vorob'evy gory, Moscow, 119992 Russia*
e-mail: elgob@mail.ru
*** Nizhni Novgorod State University, pr. Gagarina 23, Nizhni Novgorod, 603950 Russia*
Received December 27, 2002

Abstract—Iron zirconium phosphate $Fe_{1/3}[Zr_2(PO_4)_3]$ is synthesized by heat treatment of gels with the stoichiometric composition of components. The compound prepared is characterized using electron probe microanalysis, X-ray diffraction, and IR spectroscopy. The crystal structure of the $Fe_{1/3}[Zr_2(PO_4)_3]$ phosphate is refined in space group $P2_1/n$ by the Rietveld method in the isotropic approximation for atomic displacements of all elements. © *2004 MAIK "Nauka/Interperiodica".*

INTRODUCTION

Among crystalline zirconium compounds of complex composition, framework orthophosphates of the $M_xZr_2(PO_4)_3$ type ($x = 1/z$, where z is the charge of an M cation) have been studied in sufficient detail to date. The structure of these compounds consists of a mixed $[Zr_2(PO_4)_3]_{3\infty}$ framework formed by discrete zirconium octahedra and phosphate tetrahedra (the discreteness of coordination polyhedra is governed by the cation ratio Zr : P = 2 : 3 [1]). In framework structures of this type, it is possible to distinguish a characteristic fragment (unit) $[Zr_2(PO_4)_3]$, which is formed by two zirconium–oxygen octahedra linked together by three bridging tetrahedra (a "lantern"). The number of structural types in which the $M_xZr_2(PO_4)_3$ phosphates can crystallize depends on the character of the joining of these groupings and is limited under the condition of discreteness of the coordination polyhedra.

It is evident that the structure of compounds with a mixed $[Zr_2(PO_4)_3]_{3\infty}$ anionic framework substantially depends on the type of M cations compensating for the negative charge of this framework. An analysis of the data available in the literature demonstrates that the $M_xZr_2(PO_4)_3$ phosphates crystallize in two modifications, namely, the trigonal (or rhombohedral) modification of sodium zirconium phosphate $NaZr_2(PO_4)_3$ (NZP) with space group $R\bar{3}c$ or $R\bar{3}$ [2–16] and the monoclinic modification of scandium tungstate $Sc_2(WO_4)_2$ [or iron sulfate β-$Fe_2(SO_4)_3$] with space group $P2_1/n$ [17–20]. The difference between the structures of these modifications is associated with the different types of packing of $[Zr_2(PO_4)_3]$ fragments. In the trigonal modification, these fragments are located along the $\bar{3}$ axis and form infinite columns along the c crystallographic axis. In turn, these columns are joined together into a three-dimensional framework through phosphate tetrahedra. In the monoclinic modification, the $[Zr_2(PO_4)_3]$ fragments are arranged in a tiling manner and also form columns; however, in this case, the columns are rotated through an angle of 71° with respect to each other [21].

The packing of fragments in the above modifications determines the number and type of holes in their structures. In the trigonal or rhombohedral structure, there exist holes of the $M1$ and $M2$ types, which correspond to the 6*b* and 18*e* crystallographic positions, respectively. The $M1$ holes are formed by lateral trigonal faces of two adjacent lanterns of the same column and have the shape of a distorted octahedron (the coordination polyhedron is a trigonal antiprism, and the coordination number is 6). Larger sized holes of the $M2$ type are located between the adjacent columns around the $M1$ holes. The quantitative ratio between the $M2$ and $M1$ holes is 3 : 1 in accordance with the chemical formula of compounds with an NZP-type structure: $(M1)(M2)_3L_2(PO_4)_3$, where L is the position occupied by zirconium with a coordination number of 6 in the framework. In the structure of monoclinic phosphates, holes in the framework have the shape of a distorted tetrahedron (the coordination number is 4) [20]. An analysis of the structural features of the known rhombohedral and monoclinic modifications shows that compounds with large-sized cations (r_{kt} = 0.71–1.67 Å) crystallize with the formation of an NZP-type structure in which cations have a more favorable octahedral coordination. Phosphates with singly or doubly charged small-sized compensating cations (r_{kt} = 0.57–0.66 Å) predominantly crystallize with the formation of a monoclinic structure. For these cations, the tetrahedral environment of oxygen atoms is most preferable.

1063-7745/04/4903-0390$26.00 © 2004 MAIK "Nauka/Interperiodica"

At the same time, a number of multiply charged cations, such as magnesium, scandium, lanthanide, zirconium, and other cations (r_{kt} = 0.72–1.03 Å), can fulfill a framework-forming function. As regards multiply charged cations of smaller sizes, they fulfill only a framework-forming function in compounds with the $[Zr_2(PO_4)_3]_{3\infty}$ framework. The question of their possible incorporation into holes remains open.

In the present work, we synthesized iron zirconium phosphate of the composition $Fe_{1/3}Zr_2(PO_4)_3$ and elucidated the role played by iron in the structure formation. Earlier [22, 23], it was established that, in $Na_{1+x}Zr_{2-x}Fe_x(PO_4)_3$ iron phosphates, iron and zirconium play the role of a framework-forming cation.

EXPERIMENTAL

The iron zirconium phosphate $Fe_{1/3}Zr_2(PO_4)_3$ was synthesized by the sol–gel technique [24]. The initial reactants used in the synthesis were 1 M aqueous solutions of iron chloride $FeCl_3$, zirconium oxychloride $ZrOCl_2$, and orthophosphoric acid H_3PO_4. All the reactants were chemically pure. The synthesis was performed in several stages. At the first stage, phosphoric acid (in the amount calculated from the reaction stoichiometry) was slowly added with vigorous continuous stirring to a mixture of aqueous solutions of iron chloride and zirconium oxychloride taken in stoichiometric amounts. The gel formed was dried at a temperature of 85°C for 24 h, ground in an agate mortar, and heat treated at T = 600, 800, and 1000°C (the heat treatment time at each temperature was one or two days). Each annealing stage alternated with dispersion.

The compound synthesized was identified and then studied using a combination of physicochemical methods, such as electron probe microanalysis, IR spectroscopy, and X-ray powder diffraction and X-ray structure analyses. The electron probe microanalysis was carried out on a Camebax microanalyzer equipped with a Link AN-100 energy-dispersive detector. The compositions were calculated by the ZAF correction method (the accuracy in determining the composition was equal to 2.5 mol %). The IR absorption spectrum of the sample prepared in the form of a finely disperse film on a KBr substrate was recorded on a Specord-75 IR spectrophotometer in the frequency range 1800–400 cm^{-1}. The phase composition of the sample in the course of the synthesis was checked using X-ray powder diffraction analysis (DRON-2.0 diffractometer, filtered CoK_α radiation). The structure was refined on an ADP-2 diffractometer (λCuK_α; Ni filter; 2θ scan mode; step width, 0.02°; exposure time, 10 s). The X-ray diffraction patterns were processed according to the WYRIET (version 3.3) software package [25]. The peak profiles were approximated by the Pearson VII function. The peak asymmetry was refined in the range $2\theta < 60°$. The ion scattering curves were used for all elements. The crystal structure was refined by progressively adding refined parameters with continuous graphic simulation of the background until the R factors became equal to a constant value.

Table 1. Unit cell parameters and results of the Rietveld refinement for the crystal structure of the $Fe_{1/3}Zr_2(PO_4)_3$ phosphate

a, Å	12.4164(4)
b, Å	8.9359(3)
c, Å	8.8395(3)
β, deg	90.434(2)
V, Å^3	980.73(3)
Space group	$P2_1/n$
2θ range, deg	10.50–99.98
Number of reflections measured	2125
Number of parameters refined	86
R_{wp}	3.49
R_B	2.34
R_F	1.66
S	1.47
DWD	0.96

Note: $R_{wp} = [\Sigma w|I_e - I_c|^2/\Sigma w I_e^2]^{1/2}$, $R_B = \Sigma|I'_e - I'_c|/\Sigma I'_e$ (where I'_e and I'_c are the experimental and calculated integrated intensities of the Bragg reflections, respectively), $R_F = \Sigma|F_e - F_c|/\Sigma F_e$, and DWD is the Durbin–Watson statistics [26].

The sample prepared had the form of a yellow powder. As follows from the X-ray powder diffraction data, the crystalline product was formed at a temperature of 800°C (after heat treatment at 600°C for 48 h, the sample remained X-ray amorphous).

According to the electron probe microanalysis, the composition of the sample was as follows (wt %): Fe_2O_3, 5.46; ZrO_2, 45.35; and P_2O_5, 44.04 (Σ = 94.85). This composition, when expressed in terms of 12 O^- anions, corresponds to iron zirconium phosphate of the chemical formula $Fe_{0.34}Zr_{1.85}P_3O_{12}$, which is close to the calculated formula $Fe_{1/3}Zr_2P_3O_{12}$.

An analysis of the X-ray diffraction data obtained revealed the similarity of the structure of the iron zirconium phosphate under investigation to the structure of the nickel zirconium phosphate $Ni_{0.5}Zr_2(PO_4)_3$ (structural type of scandium tungstate $Sc_2(WO_4)_3$) [12]. On this basis, the X-ray diffraction pattern of the sample was indexed in space group $P2_1/n$.

For the $Fe_{1/3}Zr_2(PO_4)_3$ samples subjected to either isothermal treatment at 800°C for a day or short-term treatment (for a few hours) at 1000°C, the X-ray diffraction patterns exhibit reflections of the α-$(ZrO)_2P_2O_7$ and ZrP_2O_7 crystalline phases and an unidentified phase. This indicates that the $Fe_{1/3}Zr_2(PO_4)_3$ phosphate undergoes decomposition.

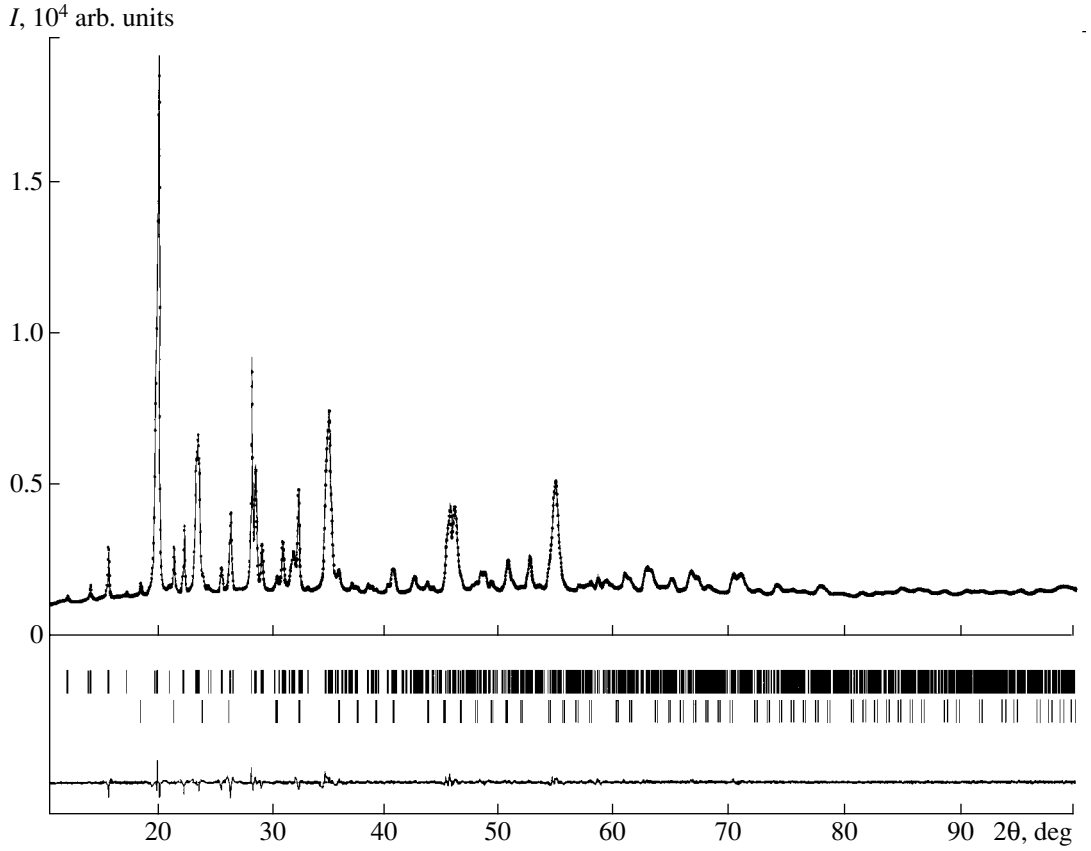

Fig. 1. Experimental (solid line) and theoretical (points) X-ray diffraction patterns of the $Fe_{1/3}Zr_2(PO_4)_3$ compound.

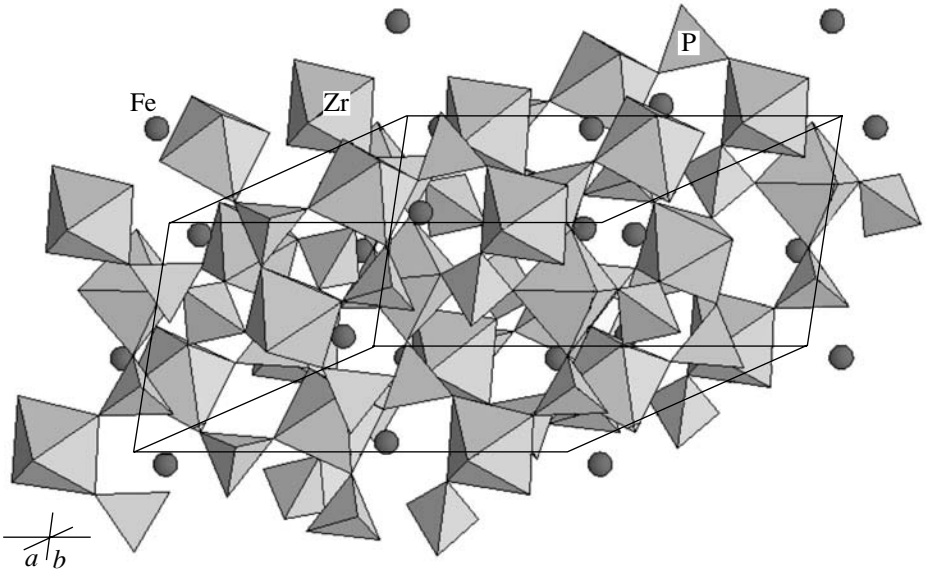

Fig. 2. Structure of the $Fe_{1/3}Zr_2(PO_4)_3$ phosphate.

Table 2. Atomic coordinates, thermal parameters, and site occupancies in the crystal structure of the $Fe_{1/3}Zr_2(PO_4)_3$ phosphate

Atom	*x*	*y*	*z*	B_{iso}	*q*
Fe^{3+}	0.171(2)	0.201(2)	0.713(2)	1.1(6)	0.3333
Zr(1)	0.1194(4)	0.0291(6)	0.2503(8)	0.8(1)	1.0
Zr(2)	0.3902(3)	0.0393(5)	0.7480(7)	1.0(2)	1.0
P(1)	0.504(1)	0.254(2)	0.466(2)	1.0(3)	1.0
P(2)	0.147(1)	0.382(2)	0.395(2)	0.9(4)	1.0
P(3)	0.354(1)	0.398(2)	0.885(2)	1.0(4)	1.0
O(1)	0.582(3)	0.328(3)	0.570(3)	1.3(8)	1.0
O(2)	0.573(2)	0.174(3)	0.351(4)	1.3(8)	1.0
O(3)	0.427(2)	0.355(3)	0.387(3)	1.1(9)	1.0
O(4)	0.433(2)	0.144(3)	0.555(4)	1.1(9)	1.0
O(5)	0.170(2)	0.220(4)	0.374(3)	1.7(8)	1.0
O(6)	0.035(2)	0.424(3)	0.336(4)	1.6(9)	1.0
O(7)	0.161(3)	0.409(3)	0.562(3)	1.4(8)	1.0
O(8)	0.227(2)	0.483(4)	0.316(3)	1.2(9)	1.0
O(9)	0.329(3)	0.243(3)	0.828(3)	1.3(8)	1.0
O(10)	0.360(3)	0.389(3)	0.057(4)	1.2(9)	1.0
O(11)	0.461(3)	0.451(3)	0.817(3)	1.2(8)	1.0
O(12)	0.268(2)	0.519(4)	0.833(4)	1.1(7)	1.0

The structural model of the $Ni_{0.5}Zr_2(PO_4)_3$ compound (taken from [20]) was used as the starting model in the refinement of the atomic parameters of the iron zirconium phosphate synthesized in the present work. The selected parameters and the results of the refinement of the $Fe_{1/3}Zr_2(PO_4)_3$ crystal structure are presented in Table 1. The experimental and calculated diffraction patterns of the $Fe_{1/3}Zr_2(PO_4)_3$ compound are shown in Fig. 1.

RESULTS AND DISCUSSION

The results obtained suggest that the $Fe_{1/3}Zr_2(PO_4)_3$ and $Ni_{0.5}Zr_2(PO_4)_3$ compounds (monoclinic unit cell, space group $P2_1/n$) are isostructural to each other. Both compounds contain a complex radical anion, namely, $[Zr_2(PO_4)_3]$. Consequently, the crystal structure of iron zirconium phosphate, like nickel zirconium phosphate, involves a three-dimensional mixed framework of the $Sc_2(WO_4)_3$ (*S*) type [12]. In the structure of these compounds, the framework is formed by isolated zirconium octahedra and phosphorus tetrahedra joined through their vertices. Each zirconium octahedron is bound to six phosphorus tetrahedra (Fig. 2) [27]. In the framework, holes have the shape of a distorted tetrahedron and are partially occupied by trivalent iron cations (Table 2). It should be noted that phosphate with an *S*-type framework in which holes contain triply charged cations with a radius smaller than the radius of cations in known compounds with a similar structure [18–20] is synthesized for the first time.

In the structure of iron zirconium phosphate, the polyhedra are slightly distorted: the P–O bond lengths fall in the range 1.49–1.58 Å, the Zr–O bond lengths lie in the range 1.98–2.15 Å, and their mean values are close to standard values (Table 3). The interatomic distances in zirconium–oxygen and phosphorus–oxygen

Table 3. Interatomic distances (Å) in the crystal structure of the $Fe_{1/3}Zr_2(PO_4)_3$ phosphate

Zr(1)–O(1)	2.09(3)	Zr(2)–O(2)	2.15(3)
O(3)	2.05(3)	O(4)	2.02(3)
O(5)	2.11(3)	O(6)	1.98(3)
O(8)	2.04(3)	O(7)	2.14(3)
O(10)	2.13(3)	O(9)	2.09(3)
O(11)	2.07(3)	O(12)	2.09(3)
Mean	⟨2.08⟩		⟨2.08⟩
P(1)–O(1)	1.49(3)	P(2)–O(5)	1.49(4)
O(2)	1.51(3)	O(6)	1.52(3)
O(3)	1.48(3)	O(7)	1.51(3)
O(4)	1.54(3)	O(8)	1.52(3)
Mean	⟨1.51⟩		⟨1.51⟩
P(3)–O(9)	1.51(3)	Fe^{3+}–O(2)	2.06(4)
O(10)	1.52(3)	O(7)	2.29(4)
O(11)	1.53(3)	O(9)	2.24(4)
O(12)	1.58(3)	O(12)	1.84(4)
Mean	⟨1.54⟩		⟨2.11⟩

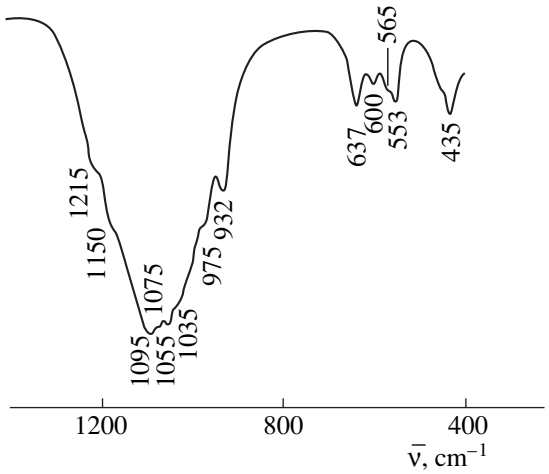

Fig. 3. IR spectrum of the $Fe_{1/3}Zr_2(PO_4)_3$ phosphate.

polyhedra in the iron zirconium phosphate under investigation are close to those in the $Ni_{0.5}Zr_2(PO_4)_3$ compound studied previously: the differences in the interatomic distances are within the limits of experimental error.

Thus, our experimental results demonstrate that polyhedra in the $[Zr_2(PO_4)_3]$ anionic frameworks of the $Fe_{1/3}Zr_2(PO_4)_3$ and $Ni_{0.5}Zr_2(PO_4)_3$ compounds are characterized by similar insignificant distortions. This implies that the difference in the nature (sizes, charges) of cations located in holes of the *S*-type structures virtually do not affect distortions of the *S* framework.

As regards the nearest oxygen environment of these cations (nickel, iron), the refined data indicate that the maximum differences between the *M*–O distances in the iron–oxygen tetrahedra FeO_4 are somewhat larger than those in the nickel–oxygen tetrahedra: $\Delta(Fe–O)_{max}$ = 0.45 Å and $\Delta(Ni–O)_{max}$ = 0.37 Å. It is obvious that the FeO_4 tetrahedra are distorted to a greater extent. Judging from the results of the structure refinement of the phosphate studied and the available data for the $Ni_{0.5}Zr_2(PO_4)_3$ compound, the crystal chemical formula for the iron zirconium phosphate can be represented in the form $Fe_{1/3}[Zr_2(PO_4)_3]$.

Table 4. Determination of the number of vibrational bands for a PO_4 tetrahedron in the structure of the $Fe_{1/3}Zr_2(PO_4)_3$ phosphate (space group $P2_1/n$)

Vibration mode	Symmetry T_d of isolated tetrahedron	Positional symmetry C_1 of tetrahedron	Factor group C_{2h}
ν_1	A_1*	A	$3A_g + 3A_u$
ν_2	E	$2A$	$6A_g + 6A_u$
ν_3, ν_4	F_2	$3A$	$9A_g + 9A_u$

* The band inactive in the spectrum.

From analyzing the IR spectrum of the $Fe_{1/3}[Zr_2(PO_4)_3]$ compound (Fig. 3), we can draw the conclusion that this phosphate belongs to the class of orthophosphates. The bands in the range 1215–930 cm^{-1} are assigned to the stretching vibrations and the bands in the range 640–435 cm^{-1} are attributed to the bending vibrations of the P–O bonds in phosphorus tetrahedra. The positional symmetry of the PO_4 ionic complex in the structure with space group $P2_1/n$ (C_{2h}) lowers from T_d to C_1. The data presented in Table 4 illustrate the changeover from a regular tetrahedron with T_d symmetry to a tetrahedron with C_1 symmetry and then to the factor group C_{2h}. As the symmetry of the PO_4 ionic complex is reduced to C_1, the ν_1 inactive symmetric vibrations become active. The degeneracy of doubly (E) and triply (F_2) degenerate vibrations is removed. Two bands should be attributed to the ν_2 symmetric stretching vibrations, and three bands should correspond to the ν_3 asymmetric stretching vibrations and ν_4 asymmetric bending vibrations. The changeover to the factor group C_{2h} leads to separation of vibrations into symmetric (g) and asymmetric (u) vibrations with respect to the inversion center. For three independent positions of phosphorus in the unit cell, the number of bands is trebled. Since the bands of g vibrations are observed only in the Raman spectra, the IR spectra should involve three bands of the ν_1 vibrations, six bands of the ν_2 vibrations, nine bands of the ν_3 vibrations, and nine bands of the ν_4 vibrations.

In the IR spectrum, six out of the nine bands allowed by the selection rules (1215–1035 cm^{-1}) are attributed to the ν_3 asymmetric stretching vibrations. The high-frequency bands assigned to the P–O vibrations at 1215 and 1150 cm^{-1} are not characteristic of orthophosphates and can be explained by the contribution from the electron density of (small-sized, multiply charged) Zr^{4+} ions to the P–O (Zr) bond, which results in large force constants of this bond. The ν_1 symmetric stretching vibrations are represented by two (out of three allowed) bands at 975 and 932 cm^{-1}. In the range of the ν_4 asymmetric bending vibrations (937–553 cm^{-1}), the IR spectrum contains four bands. The band at 435 cm^{-1} is assigned to the ν_2 symmetric stretching vibrations. The other lower frequency bands of the ν_2 vibrations cannot be recorded on the spectrophotometer used. The IR spectrum described above is similar to the IR spectra of zirconium orthophosphates with bivalent d elements and magnesium, which crystallize in space group $P2_1/n$ [28]. Since Fe^{3+} ions occupy their positions in the structure incompletely and statistically, the IR spectrum of the $Fe_{1/3}[Zr_2(PO_4)_3]$ compound is more diffuse (contains more poorly resolved bands) than the IR spectra of zirconium and bivalent d metal phosphates.

CONCLUSIONS

Thus, the results of the complex investigation of a new phosphate, namely, $Fe_{1/3}Zr_2(PO_4)_3$, and their comparison with the data available in the literature on the structure formation of known framework phosphates of the $M_xZr_2(PO_4)_3$ family allowed us draw the following inferences.

(1) The iron zirconium phosphate $Fe_{1/3}Zr_2(PO_4)_3$, which was synthesized and studied in this work, complemented the class of known double zirconium phosphates of the general formula $M_xZr_2(PO_4)_3$ with a framework structure, including those crystallizing in the structural type of scandium tungstate.

(2) The phosphate with an *S*-type framework in which holes are occupied by triply charged cations was synthesized for the first time.

(3) The minimum radius of *M* compensating cations in $M_xZr_2(PO_4)_3$ phosphates is determined by the radius of Fe^{3+} cations and is equal to 0.49 Å. Previously, the minimum size of *M* cations was thought to correspond to the radius of Mg^{2+} cations and assumed to be equal to 0.57 Å.

ACKNOWLEDGMENTS

This work was supported by the Russian Foundation for Basic Research (project nos. 01-03-33013, 02-03-06007, 03-05-64054) and the Program "Russian Universities" of the Ministry of Education of the Russian Federation.

REFERENCES

1. R. G. Sizova, V. A. Blinov, A. A. Voronkov, *et al.*, Kristallografiya **26** (2), 293 (1981) [Sov. Phys. Crystallogr. **26**, 165 (1981)].
2. M. Sljukič, B. Matkovič, B. Prodič, and S. Scavnicar, Croat. Chem. Acta **39** (2), 145 (1967).
3. H. Y.-P. Hong, Mater. Res. Bull. **11** (2), 173 (1976).
4. A. I. Orlova, V. I. Pet'kov, and O. V. Egor'kova, Radiokhimiya **38** (1), 15 (1996).
5. O. V. Egor'kova, A. I. Orlova, V. I. Pet'kov, and D. V. Kemenov, Radiokhimiya **38** (6), 481 (1996).
6. S. Ikeda, M. Takanashi, and J. Ishikawa, Solid State Ionics **23**, 123 (1987).
7. D. K. Agrawal and V. S. Stubican, Mater. Res. Bull. **20**, 99 (1985).
8. S. Y. Limaye, D. K. Agrawal, and H. A. McKinstry, J. Am. Ceram. Soc. **70**, 232 (1987).
9. R. Alamo and R. Roy, J. Mater. Sci. **21**, 444 (1986).
10. V. I. Pet'kov, A. I. Orlova, and D. A. Kapranov, Zh. Neorg. Khim. **43** (9), 1534 (1998).
11. R. Brochu, M. El-Yacoubi, M. Louer, *et al.*, Mater. Res. Bull. **32**, 15 (1997).
12. S. Tamura, N. Imanaka, and G. Adachi, Solid State Ionics **136–137**, 423 (2000).
13. M. Alami Talbi, R. Brochu, C. Parent, *et al.*, J. Solid State Chem. **110**, 350 (1994).
14. S. Tamura, N. Imanaka, and G. Adachi, J. Mater. Sci. Lett. **20**, 2123 (2001).
15. S. Tamura, N. Imanaka, and G. Adachi, J. Alloys Compd. **323–324**, 540 (2001).
16. J. Alamo and R. Roy, Commun. Am. Ceram. Soc., No. 5, 80 (1984).
17. D. Petit, Ph. Colomban, G. Collin, and J. P. Boilot, Mater. Res. Bull. **21**, 365 (1986).
18. A. Kazacos-Kijowski, S. Komarneni, and D. Agrawal, Mater. Res. Bull. **23**, 1177 (1988).
19. V. I. Pet'kov, A. I. Orlova, G. I. Dorokhova, and Ya. V. Fedotova, Kristallografiya **45** (1), 36 (2000) [Crystallogr. Rep. **45**, 30 (2000)].
20. A. Jouanneaux, A. Verbaere, Y. Piffar, *et al.*, Eur. J. Solid State Inorg. Chem. **28**, 683 (1991).
21. V. B. Kalinin and S. Yu. Stefanovich, Itogi Nauki Tekh., Ser.: Khim. Tverd. Tela **8** (1992).
22. O. V. Egor'kova, A. I. Orlova, and V. I. Pet'kov, Neorg. Mater. **34** (3), 373 (1998).
23. J. M. Winand, A. Rulmont, and P. Tarte, J. Mater. Sci. **25** (9), 4008 (1990).
24. A. I. Orlova, V. I. Pet'kov, and O. V. Egor'kova, Radiokhimiya **38** (1), 15 (1996).
25. J. Schneider, in *Proceedings of International Workshop on the Rietveld Method* (Petten, 1989).
26. G. W. Beall, L. A. Boatner, D. F. Millica, and W. O. Milligan, J. Inorg. Nucl. Chem. **43** (1), 101 (1981).
27. E. Dowty, *Atoms 3.2: A Computer Program for Displaying Atomic Structures* (Kingsport, 1995).
28. V. I. Pet'kov, V. S. Kurazhkovskaya, A. I. Orlova, and M. L. Spiridonova, Kristallografiya **47** (3), 529 (2002) [Crystallogr. Rep. **47**, 736 (2002)].

Translated by O. Borovik-Romanova

Crystallography Reports, Vol. 49, No. 3, 2004, pp. 396–400. Translated from Kristallografiya, Vol. 49, No. 3, 2004, pp. 462–466.

STRUCTURE OF INORGANIC COMPOUNDS

New Phosphate $Fe_{0.5}Nb_{1.5}(PO_4)_3$ with an Electrically Neutral Framework. Synthesis and Crystal Structure

I. G. Trubach*, A. I. Orlova*, A. I. Beskrovnyĭ, A. K. Koryttseva*, M. V. Zharinova*, V. S. Kurazhkovskaya***, and E. V. Lipatova***

** Nizhni Novgorod State University, pr. Gagarina 23, Nizhni Novgorod, 603950 Russia*
e-mail: oai@uic.nnov.ru
*** Joint Institute for Nuclear Research, Dubna, Moscow oblast, 141980 Russia*
**** Moscow State University, Vorob'evy gory, Moscow, 119899 Russia*
Received August 22, 2002

Abstract—A new iron–niobium phosphate, $Fe_{0.5}Nb_{1.5}(PO_4)_3$, has been prepared and studied by X-ray diffraction, electron microprobe analysis, IR spectroscopy, and neutron powder diffraction. On the basis of X-ray powder data, it was found that the synthesized phosphate crystallizes into the sp. gr. $R\bar{3}c$ and corresponds to the structural type of sodium–zirconium phosphate $NaZr_2(PO_4)_3$. The structure was refined by the Rietveld method based on a powder neutron diffraction experiment. The obtained phosphate belongs to complex niobium orthophosphates and has a framework structure with a zero framework charge. © *2004 MAIK "Nauka/Interperiodica".*

INTRODUCTION

Framework phosphates with the framework formula $[T_2(PO_4)_3]^{n-}$ or, in a more detailed form, $[T'_aT''_bT'''_c\ldots(PO_4)_3]^{n-}$ (where T', T'', $T'''\ldots$ are cations with oxidation states from 1+ to 5+ in various combinations, $a + b + c + \ldots = 2$, and n is the framework charge), may have various chemical compositions. For some of them, n equals zero; i.e., the framework is electrically neutral and its composition coincides with the compound composition. As calculations showed, one of the cations T in these phosphates is necessarily an element in the oxidation state 5+. The known and predicted phosphate compositions can be described by the series $M^{IV}C^{V}(PO_4)_3 \longrightarrow R^{III}_{1/2}C^{V}_{3/2}(PO_4)_3 \longrightarrow B^{II}_{1/3}C^{V}_{5/3}(PO_4)_3 \longrightarrow A^{I}_{1/4}C^{V}_{7/4}(PO_4)_3$.

To date, the compounds described by the general formula $T'_aT''_b(PO_4)_3$ (where $T'_aT''_b = M^{IV}C^{V}$ and $R^{III}_{1/2}C^{V}_{3/2}$; M^{IV} = Ti, Ge, Zr, Nb, V; C^{V} = Nb, Ta; R^{III} = Sb, Nd, Eu, Bi; and B^{II} = Co, Ni) have been studied [1–9]. Most of these compounds are assigned to the structure of sodium–zirconium phosphate $NaZr_2(PO_4)_3$ (NZP [10]), sp. gr. $R\bar{3}c$. Structural investigations have been performed for $Nb_2(PO_4)_3$ and $TiNb(PO_4)_3$ phosphates only [1, 8].

The series of known phosphates with the composition $T'_aT''_b(PO_4)_3$ can be expanded by synthesizing new compounds. This problem is of interest, since such compounds serve as a basis for promising materials with good thermal–mechanical characteristics, in particular low and ultralow thermal expansion.

In this paper, we report the results of studying a new representative of the above series: iron–niobium phosphate $Fe_{0.5}Nb_{1.5}(PO_4)_3$. The aim was to synthesize and characterize this compound crystallochemically, as well as refine its structure by neutron powder diffraction analysis.

EXPERIMENTAL

The iron–niobium phosphate was synthesized as follows. Stoichiometric amounts of aqueous solutions of ferric chloride (III) and niobium fluoride complex (V) were merged at room temperature; then, under continuous stirring, phosphoric acid was slowly added in an amount calculated from the reaction stoichiometry; and, after that, the mixture was evaporated at 80°C for 24 h. The powder formed was successively heated at 200°C (12 h), 400°C (12 h), 600°C (24 h), 800°C (1 day), 1000°C (8 h), and 1100°C (8 h), alternating heating with grinding.

The sample obtained was studied by electron microprobe analysis, X-ray diffraction, IR spectroscopy, and neutron powder diffraction. Electron microprobe analysis was performed on a Camebax microprobe with a Link AN-100 energy-dispersive detector, using the ZAF correction method to calculate the sample composition. The X-ray diffraction patterns of a sample were recorded on a DRON-3M diffractometer using CoK_α filtered radiation (λ = 1.78892 Å) in the range of reflec-

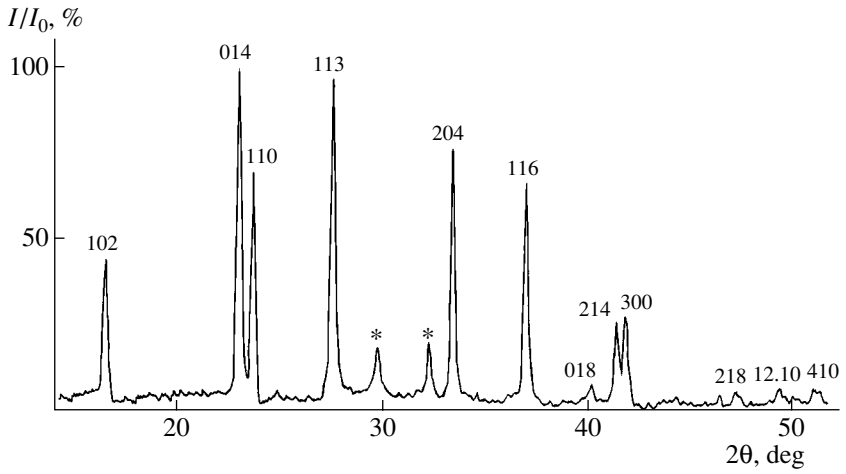

Fig. 1. X-ray diffraction pattern of $Fe_{0.5}Nb_{1.5}(PO_4)_3$.

tion angles $2\theta = 14°–50°$. The IR spectrum was recorded on a SPECORD-75IR spectrophotometer in the frequency range 1200–400 cm^{-1}. A sample in the form of a fine-dispersed suspension in isopropyl alcohol was deposited on a KBr substrate and dried. The neutron diffraction pattern of the powder sample placed in a cylindrical container with diameter $d = 10$ mm was recorded at room temperature on a DN-2 time-of-flight diffractometer (with maximum resolution $\Delta d/d = 0.01$) mounted in an IBR-2 pulsed reactor (Joint Institute for Nuclear Research, Dubna). The compound structure was refined by the Rietveld method using the Mria program [11].

RESULTS AND DISCUSSION

The sample obtained was a light brown powder. The elemental composition of the sample determined by microprobe analysis corresponded to the formula $Fe_{0.58}Nb_{1.54}P_3O_{12}$; i.e., it was similar to the calculated composition.

The X-ray diffraction data indicate that the crystallization occurs at 800°C; a further increase in temperature increases the sample crystallinity. The X-ray diffraction pattern of the sample (Fig. 1) exhibits a set of reflections indexed in the sp. gr. $R\bar{3}c$, which suggests that the obtained phosphate belongs to the NZP structural type. Along with the reflections of the main trigonal phase, the diffraction pattern also contains reflections of niobium oxophosphate $NbOPO_4$ (JCPDF 73-1609) and iron phosphate $FePO_4$ (JCPDF 84-0876) (the maximum intensity of the impurity lines of niobium oxophosphate was 15%). A change in the synthesis conditions and the calcination temperature almost did not affect the contents of the noted impurity phases.

The IR spectrum of the synthesized sample (Fig. 2) is characterized by a set of absorption bands typical of the framework of NZP-type orthophosphates: bands in the range 1200–850 cm^{-1}, which are due to valence oscillations of phosphor tetrahedra, and a set of bands related to bending vibrations in the range 635–400 cm^{-1}. The appearance of the high-frequency strong band at 1185 cm^{-1}, which is not characteristic of phosphates, is explained by the contribution of a small, highly charged Nb^{5+} ion to the P–O bond. The shoulder at 850 cm^{-1} is due to oscillations of the Nb–O bond.

The structure of the iron–niobium phosphate was refined within the sp. gr. $R\bar{3}c$ using the structural characteristics of titanium–niobium phosphate $TiNb(PO_4)_3$ as starting points [8]. The calculation parameters also included the structural data on $NbOPO_4$ [12], which were refined during the calculation.

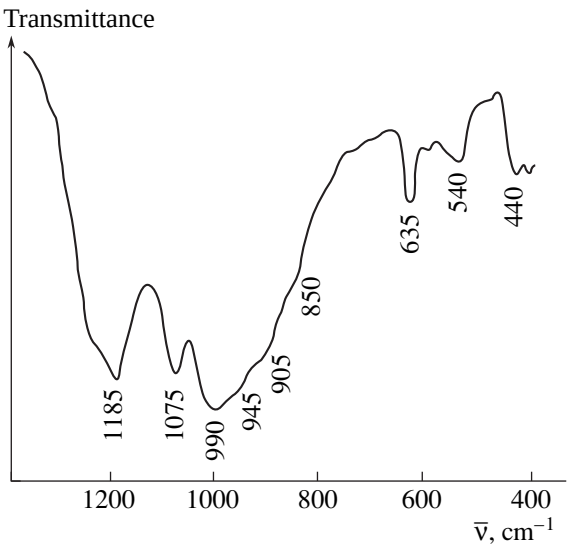

Fig. 2. IR spectrum of $Fe_{0.5}Nb_{1.5}(PO_4)_3$.

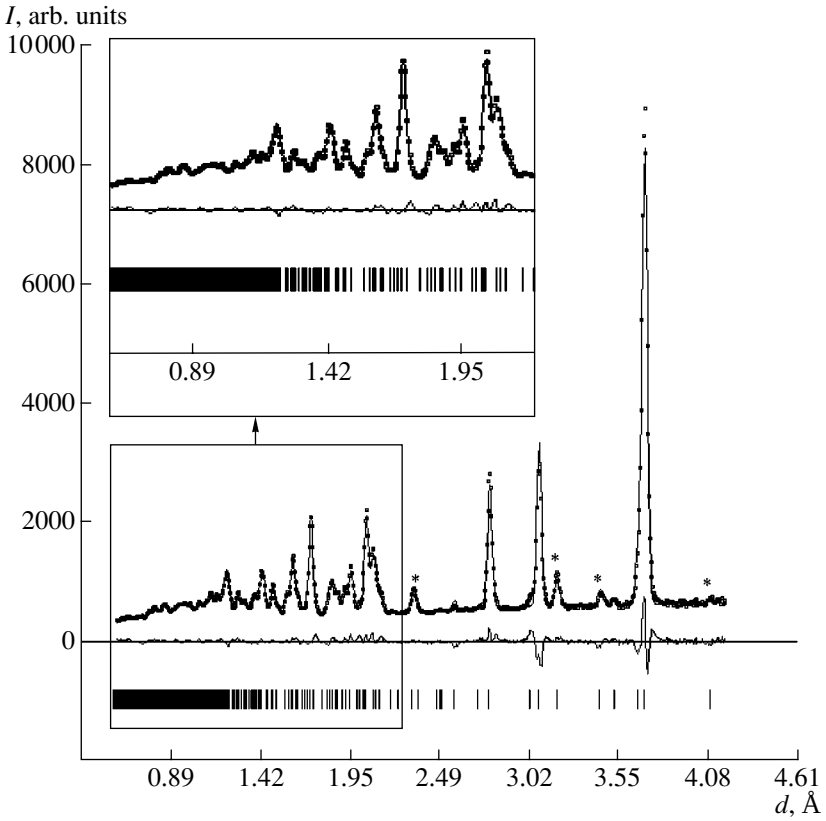

Fig. 3. Experimental (o), theoretical (solid line), and difference (experiment minus calculation) profiles of the neutron diffraction pattern of an $Fe_{0.5}Nb_{1.5}(PO_4)_3$ (*$NbOPO_4$) sample. The difference profile is normalized to the root-mean square deviation at a point.

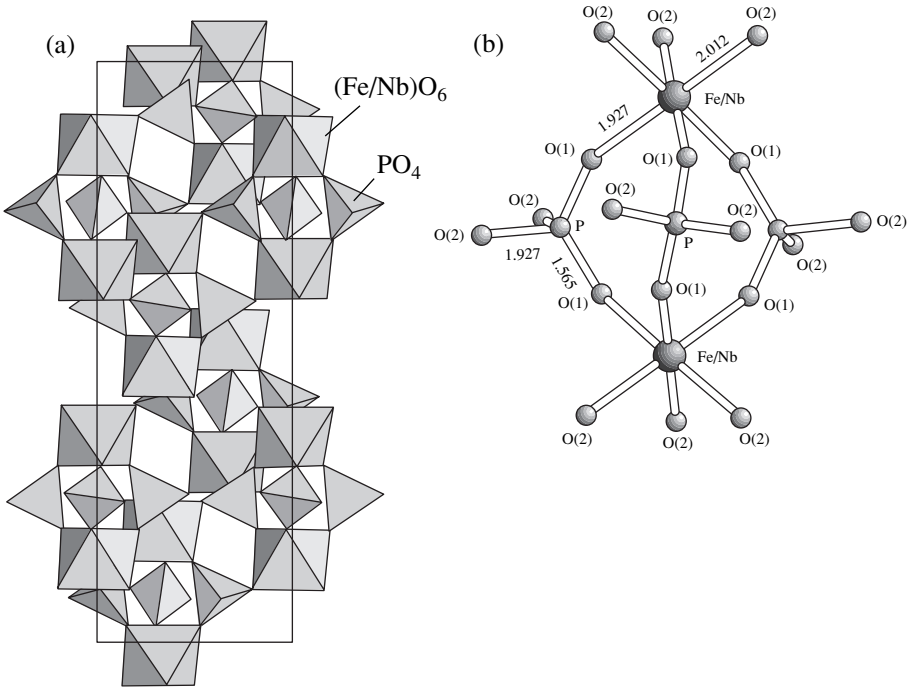

Fig. 4. A fragment of the $Fe_{0.5}Nb_{1.5}(PO_4)_3$ structure: (a) projection onto the [100] plane, (b) bonds in the "dimer" $\{T_2(PO_4)_3\}$.

Table 1. Unit-cell parameters and the results of refinement of the crystal structure of $Fe_{0.5}Nb_{1.5}(PO_4)_3$

Characteristic	
Space group	$R\bar{3}c$
a, Å	8.6317(6)
c, Å	22.125(12)
V, Å^3	1427.63
Z	6
Color	light brown
d range, Å	0.58–4.10
Number of reflections*	1020
R_{exp}	3.30
R_{wp}	4.36
R_p	5.01
χ^2	7.2
Number of refined parameters*	39

* Including the parameters of the impurity phase $NbOPO_4$.

The unit-cell parameters and the results of the refinement of the crystal structure of $Fe_{0.5}Nb_{1.5}(PO_4)_3$ are listed in Table 1. The experimental and theoretical profiles of the neutron diffraction pattern of the sample under study and the difference curve (experiment minus calculation), as normalized to the root-mean square deviation at a point, are shown in Fig. 3. The calculated positional and thermal parameters of $Fe_{0.5}Nb_{1.5}(PO_4)_3$ are listed in Table 2 (for niobium oxophosphate, in Table 3). The corresponding interatomic distances and bond angles for iron–niobium phosphate are listed in Table 4. It is noteworthy that the refined structural parameters of $NbOPO_4$ are in good agreement with the data of [12].

A fragment of the structure of $Fe_{0.5}Nb_{1.5}(PO_4)_3$ phosphate constructed based on the obtained data (Table 2) is shown in Fig. 4. This structure is based on a three-dimensional mixed framework with the general formula $Fe_{0.5}Nb_{1.5}(PO_4)_3$ composed of discrete polyhedra: octahedra TO_6 (in the case under consideration, $(Fe/Nb)O_6$) and phosphate tetrahedra PO_4. The discreteness of two kinds of Pauling polyhedra follows, according to [14], from the ratio T : P = 2 : 3. Iron and niobium cations are located at the $\bar{3}$ axes and are statistically distributed over the 12-fold position (00z), being coordinated by six oxygen atoms.

A dimer group $\{T_2(PO_4)_3\}$, which consists of two octahedra linked by three bridge tetrahedra, is a characteristic fragment of the framework of such a type. The presence of this group is typical of a large number of framework orthophosphates with NASICON-type structure [15, 16]. The aforementioned groups are located at the $\bar{3}$ axis; they form a three-dimensional bond by sharing the terminal oxygen atoms of neighboring dimers. Thus, the formed three-dimensional mixed framework $[Fe_{0.5}Nb_{1.5}(PO_4)_3]$ involves all the cations of the structure.

The bond lengths in the coordination polyhedra of the $Fe_{0.5}Nb_{1.5}(PO_4)_3$ phosphate and its analogue $TiNb(PO_4)_3$ are rather similar. In $Fe_{0.5}Nb_{1.5}(PO_4)_3$, they are equal to 1.93–2.01 Å in $(Fe/Nb)O_6$ octahedra (1.92–1.97 Å in $TiNb(PO_4)_3$) and 1.46–1.57 Å in PO_4 tetrahedra (1.48–1.56 Å in $TiNb(PO_4)_3$). However, it should be noted that distortions of phosphate tetrahedra in the compound under study are much larger in comparison with the analogue. Specifically, we observed larger distortions of the bond angles O–P–O (99.2°–110.4° in comparison with 106.3°–107.4° in $TiNb(PO_4)_3$) and a larger spread in the values of interatomic distances P–O (0.11 and 0.07 Å, respectively). Apparently, the reason

Table 2. Occupations of positions (p), coordinates, and thermal factors of atoms in the structure of $Fe_{0.5}Nb_{1.5}(PO_4)_3$

Atom	Position	p	x	y	z	B_{iso}
Fe	12c	0.25	0.00000	0.00000	0.1435(4)	1.6 (2)
Nb	12c	0.75	0.00000	0.00000	0.1444(4)	1.6 (2)
P	18e	1	0.2674(12)	0.00000	0.25000	2.2 (3)
O(1)	36f	1	0.1652(10)	0.9708(11)	0.1947(3)	2.2 (2)
O(2)	36f	1	0.2033(9)	0.1752(9)	0.0919(3)	1.4 (2)

Table 3. Structural characteristics of $NbOPO_4$ (sp. gr. $P4/n$, a = 6.4048(4) Å, c = 4.1087(2) Å, V = 168.55 Å^3)

Atom	Position	x	y	z	B_{iso}
Nb	2c	1/4	1/4	0.896(10)	1.4
P	2b	1/4	3/4	0.413(9)	0.4
O(1)	2c	1/4	1/4	0.181(15)	0.4
O(2)	8g	0.704(1)	0.479(2)	0.321(2)	1.3

Table 4. Selected interatomic distances (Å) and bond angles (deg) in $Fe_{0.5}Nb_{1.5}(PO_4)_3$

Fe/Nb–O(1)	1.927 × 3
Fe/Nb–O(2)	2.011 × 3
P–O1	1.459 × 2
P–O2	1.565 × 2
O(1)–P–O(1)	118.0
O(1)–P–O(2)	110.4
O(1)–P–O(2)	108.6
O(1)–P–O(2)	108.6
O(1)–P–O(2)	110.4
O(2)–P–O(2)	99.2

	Average	Theoretical*
⟨Fe/Nb–O⟩	1.97	2.02
⟨P–O⟩	1.51	1.57
⟨O–P–O⟩	109.2	109.5

* The interatomic distances were calculated from the values of ionic radii according to Shannon [13].

is that iron and niobium cations, which statistically occupy crystallographic positions of the same type, have a larger difference in size ($\Delta r/r_{min}$ = 16%) and charge than titanium and niobium cations ($\Delta r/r_{min}$ = 5%), which gives rise to larger structural deformations.

In summary, it should be noted that the results of this study verify the possibility of forming new framework compounds $[T'_a T''_b(PO_4)_3]$ with electrically neutral frameworks—in particular, double phosphates entering the formula series $M^{IV}C^{V}(PO_4)_3 \longrightarrow R^{III}_{1/2}C^{V}_{3/2}(PO_4)_3 \longrightarrow B^{II}_{1/3}C^{V}_{5/3}(PO_4)_3 \longrightarrow A^{I}_{1/4}C^{V}_{7/4}(PO_4)_3$. We also verified that a trigonal structural modification with a rhombohedral cell, which is characteristic of the set of structural NZP analogues, can be implemented in such compounds in the case of a small difference in radius (no more than 25%) and charge of framework-forming cations.

The results of the structural analysis show that an increase in the difference in size and charge of framework-forming cations in compounds with electrically neutral frameworks is accompanied by an increase in structural deformations. However, the increase in deformations does not change the lattice symmetry, which is confirmed by the existence of a trigonal structure with the sp. gr. $R\bar{3}c$, implemented and identified for the iron–niobium phosphate $Fe_{0.5}Nb_{1.5}(PO_4)_3$

ACKNOWLEDGMENTS

This study was supported by the Russian Foundation for Basic Research (project nos. 01-03-33013, 02-03-32181, and 02-03-06007), and the Ministry of Industry, Science, and Technology of the Russian Federation (grant in support of the development of unique equipment in Russia).

REFERENCES

1. A. Leclaire, M.-M. Borel, A. Grandin, and B. Raveau, Acta Crystallogr., Sect. C: Cryst. Struct. Commun. **45**, 699 (1989).
2. D. Tereh, Br. Ceram. Trans. J. **90** (2), 64 (1991).
3. P. A. Agaskar, K. K. Grasselli, D. J. Buttrey, and B. White, Stud. Surf. Sci. Catal. **110**, 219 (1997).
4. K. Kasthuri Rangan and J. Gopalakrishnan, Inorg. Chem. **34** (7), 1969 (1995).
5. A. Jouanneaux, A. N. Fitch, S. Oyetola, *et al.*, Eur. J. Solid State Inorg. Chem. **28**, 755 (1991).
6. A. Jouanneaux, A. N. Fitch, S. Oyetola, *et al.*, Eur. J. Solid State Inorg. Chem. **30** (1–2), 125 (1991).
7. S. Oyetola, A. Verbaere, D. Guyomard, and Y. Piffard, J. Solid State Chem. **77**, 102 (1988).
8. F. J. Berry, C. Greaves, and J. F. Marco, J. Solid State Chem. **96**, 408 (1992).
9. A. I. Orlova, V. I. Pet'kov, M. V. Zharinova, *et al.*, Zh. Prikl. Khim. (St. Petersburg) **76** (1), 14 (2003).
10. H. Y.-P. Hong, Mater. Res. Bull. **11** (2), 173 (1976).
11. V. B. Zlokazov and V. V. Chernyshev, J. Appl. Crystallogr. **25**, 447 (1992).
12. J. M. Longo and P. Kierkegaard, Acta Chem. Scand. **20**, 72 (1966).
13. R. D. Shannon, Acta Crystallogr., Sect. A: Cryst. Phys., Diffr., Theor. Gen. Crystallogr. **32**, 751 (1976).
14. A. A. Voronov, V. V. Ilyukhin, and N. V. Belov, Kristallografiya **20**, 556 (1975) [Sov. Phys. Crystallogr. **20**, 340 (1975)].
15. R. G. Sizova, V. A. Blinov, A. A. Voronkov, *et al.*, Kristallografiya **26** (2), 293 (1981) [Sov. Phys. Crystallogr. **26**, 165 (1981)].
16. V. I. Pet'kov, G. I. Dorokhova, and A. I. Orlova, Kristallografiya **46** (1), 76 (2001) [Crystallogr. Rep. **46**, 69 (2001)].

Translated by Yu. Sin'kov

Crystallography Reports, Vol. 49, No. 3, 2004, pp. 401–426. Translated from Kristallografiya, Vol. 49, No. 3, 2004, pp. 467–491.

STRUCTURE OF ORGANIC COMPOUNDS

Structural Chemistry of Oxoperoxo Complexes of Vanadium(V): A Review

V. S. Sergienko

Kurnakov Institute of General and Inorganic Chemistry, Russian Academy of Sciences, Leninskiĭ pr. 31, Moscow, 119991 Russia

e-mail: sokol@igic.ras.ru

Received July 3, 2002

Abstract—This paper presents a review of the structural features of monomeric, dimeric, and polymeric oxoperoxo complexes of vanadium(V). The structural manifestations of the *trans* effect of multiply bonded oxo and peroxo ligands in pseudooctahedral oxo monoperoxo complexes of vanadium(V) are compared. The dependence of the geometric parameters of the structural fragment $V(O_2)_n$ (n = 1, 2) (V–O, O–O bond lengths; OVO angles) on the type of coordination seven-vertex polyhedron (pseudooctahedron, n = 1; pseudotrigonal bipyramid, n = 2) of the metal atom is analyzed. Regular distortions of the coordination polyhedra of vanadium atoms (pseudooctahedron, pseudotrigonal bipyramid, pseudotetragonal pyramid, pseudotetrahedron) are considered.

CONTENTS

1. INTRODUCTION

Vanadium(V) coordination compounds containing O_2^{2-} peroxo ligands possess a high reactivity in the processes of homolytic and heterolytic oxidation of organic substances [1] and disproportionation of hydrogen peroxide [2]. This property is governed by the formation of reactive intermediate products upon inner-sphere transformations of O_2 ligands due to a change in the type of their coordination with the metal atom. The occurrence of these transformations and the stability and reactivity of dioxygen complexes of metals depend on their composition, the coordination number and coordination polyhedron of the metal atom, and the mutual influence of the ligands.

The structural data obtained as of 1986 for peroxo compounds of vanadium(V) are presented in the monograph by Vol'nov [3]. Butler *et al.* [4] summarized the data available in the literature on the V–O(oxo), V–O(O_2), and O–O bond lengths in 26 vanadium(V) oxoperoxo complexes, which were structurally characterized by 1994. However, in their review [4], the

1063-7745/04/4903-0401$26.00

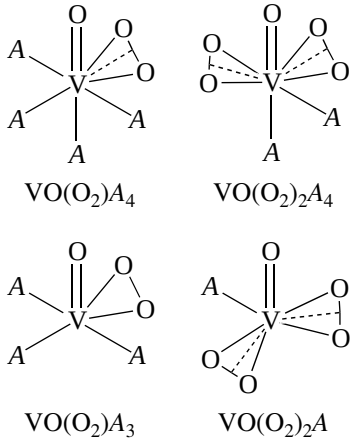

Scheme 1.

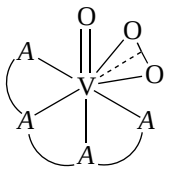

Scheme 2.

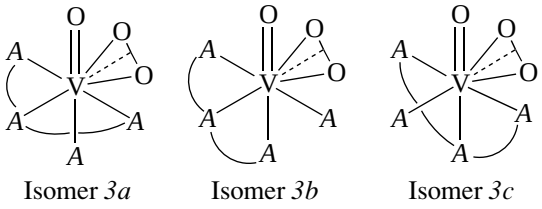

Scheme 3.

authors predominantly considered the chemical properties (in particular, reactivity) of vanadium(V) peroxo complexes, whereas the structural characterization of these compounds takes up only a few lines (a quarter of the page). The structural data accumulated over the last two decades for peroxo complexes of vanadium(V) (specifically for oxoperoxo complexes) have not been analyzed in the literature.

This paper presents a review of the specific features revealed in the structure of vanadium(V) oxoperoxo complexes containing $VO(O_2)_nA_m$ coordination structural units (where *A* is a donor atom of the monodentate or polydentate ligand; $n = 1, 2$; $m = 1–4$).

In the oxoperoxo complexes under consideration, the dioxygen ligand O_2 can be considered either as a bidentate chelating ligand or as a ligand bonded to the metal atom in an η^2 mode and occupying one coordination site. In the former case, the metal atom has a sevenfold pentagonal bipyramidal ($n = 1$, $m = 4$; $n = 2$, $m = 2$) or (more rarely) sixfold pentagonal pyramidal ($n = 1$, $m = 3$; $n = 2$, $m = 1$) coordination. In the latter case, there are four geometric variants of coordination sites, namely, pseudooctahedral ($n = 1$, $m = 4$), pseudotrigonal bipyramidal ($n = 2$, $m = 2$), pseudotetragonal pyramidal ($n = 1$, $m = 3$), and pseudotetrahedral ($n = 2$, $m = 1$) coordination sites (see Scheme 1).

2. STRUCTURE OF PSEUDOOCTAHEDRAL OXO MONOPEROXO COMPLEXES OF VANADIUM(V)

All structurally characterized complexes of this type have one feature in common: in the structure of these compounds, the oxo and peroxo ligands are located in adjacent vertices of the pseudooctahedron (in the *cis* position with respect to each other).

The averaged geometric parameters of monomeric, dimeric, and polymeric pseudooctahedral oxo monoperoxo complexes of vanadium(V) are listed in Table 1.

2.1. Monomeric Pseudooctahedral Oxo Monoperoxo Complexes of Vanadium(V)

There are five types of $VO(O_2)A_4$ monomeric complexes with different combinations of four donor atoms *A*: $VO(O_2)L^{4d}$, $VO(O_2)L^{3d}L^{1d}$, $VO(O_2)(L^{2d})_2$, $VO(O_2)L^{2d}(L^{1d})_2$, and $VO(O_2)(L^{1d})_4$, where L^{4d}, L^{3d}, L^{2d}, and L^{1d} are the tetradentate, tridentate, bidentate, and monodentate ligands, respectively.

To date, the crystal structures have been determined for 12 compounds (**I**–**XII**, Table 1) [5–16] containing an anionic or neutral complex $[VO(O_2)L^{4d}]^{n-}$ ($n = 0–2$) (see Scheme 2).

In the complexes under investigation, the tetradentate chelating ligands L^{4d} with different combinations of four donor atoms of nitrogen (from one to three) and oxygen (from three to one) are predominantly represented by anions of monoamine (*Nta*$^{3-}$, *Heida*H^{2-}, *Cmida*$^{2-}$, *Ceida*$^{2-}$) and diamine (*Edta*H$^{2.5-}$) complexones.

Compounds of the $VO(O_2)L^{3d}L^{1d}$ type, which contain tridentate chelating and monodentate ligands in the coordination sphere of the metal atom, can in principle have three geometric isomers (without regard for the mutual arrangement of three donor atoms *A* in the L^{3d} ligand) (see Scheme 3).

Two of these three isomers are revealed in compounds with a known structure: (i) isomers *3a* are observed in the structure of the $[VO(O_2)(H_2O)(Dipic)]^-$ anionic complex (**XIII**) [17] and the $[VO(O_2)(Py)(Pyanaph)]$ molecule (**XIV**) [18], and (ii) isomers *3b* are found in the structure of the $[VO(O_2)\{HB(Pz)_3\}(PzH)]$ molecular complex (**XV**) [19].

The structure of $[VO(O_2)(L^{2d})_2]$ monomeric compounds is shown in Scheme 4. Seven molecular or

Table 1. Selected bond lengths (Å) in monomeric, dimeric, and polymeric pseudooctahedral oxo monoperoxo complexes of vanadium(V)*

No.	Compound	V–O(oxo)	V–*L*, *trans* to O(oxo) V–*L*, *trans* to O_2	V–L_{cis}	Δ(Δ') (O) Δ(Δ) (O_2)	References
I	$Na_2[VO(O_2)(Nta)] \cdot 5H_2O$	1.610(5)	2.190(4) O(*Nta*) 2.172(4) N(*Nta*)	2.047(4) ± 0.005 O(*Nta*)	0.143 (0.036)	[5]
II	$K_2[VO(O_2)(Nta)]$	1.607(4)	2.170(4) O(*Nta*) 2.196(4) N(*Nta*)	2.037(4) ± 0.007 O(*Nta*)	0.133 (0.060)	[6]
III	$K_2[VO(O_2)(Nta)] \cdot 2H_2O$	1.617(4)	2.121(2) O(*Nta*) 2.199(3) N(*Nta*)	2.038(8) ± 0.053 O(*Nta*)	0.083 (0.063)	[7]
IIIa	$K_2[VO(O_2)(Nta)] \cdot 2H_2O$	1.610(1)	2.113(1) O(*Nta*) 2.202(1) N(*Nta*)	2.041(1) O(*Nta*)	0.073 (0.066)	[8]
IV	$Ba[VO(O_2)(Nta)]$	1.591(8)	2.108(8) O(*Nta*) 2.196(9) N(*Nta*)	2.035(8) ± 0.022 O(*Nta*)	0.073 (0.060)	[9]
V	$K[VO(O_2)(HeidaH)] \cdot H_2O$	1.601(1)	2.236(2) OH(*Heida*) 2.194(2) N(*Heida*)	2.045(1) ± 0.007 O(*Heida*)	0.191 (0.058)	[10, 11]
VI	$K[VO(O_2)(Cmida)] \cdot 4H_2O$	1.611(1)	2.218(1) O(*Cmida*) 2.193(1) N(*Cmida*)	2.044(1) ± 0.012 O(*Cmida*)	0.174 (0.057)	[10]
VIa	$K[VO(O_2)(Cmida)] \cdot 4H_2O$	1.625(2)	2.239(3) O(*Cmida*) 2.219(2) N(*Cmida*)	2.064(2) ± 0.012 O(*Cmida*)	0.175 (0.083)	[12]
VII	$K[VO(O_2)(Ceida)] \cdot 2H_2O$	1.605(2)	2.223(2) O(*Ceida*) 2.192(2) N(*Ceida*)	2.024(2) ± 0.007 O(*Ceida*)	0.199 (0.056)	[13]
VIII	$Cs[VO(O_2)(Ceida)] \cdot H_2O$	1.594	2.231 O(*Ceida*) 2.166 N(*Ceida*)	2.039 ± 0.001 O(*Ceida*)	0.192 (0.030)	[14]
IX	$K_{1.5}[VO(O_2)(EdtaH)] \cdot 0.8H_2O$	1.59(2)	2.24(1), 2.40(1) } N(*Edta*H)	2.06(2) ± 0.05 O(*Edta*H)	(0.104) (0.264)	[15]
X	$(NH_4)_{1.5}[VO(O_2)(EdtaH)]$	1.68(1)	2.31(1), 2.32(1) } N(*Edta*H)	1.97(1) ± 0.02 O(*Edta*H)	(0.174) (0.184)	[15]
XI	$K[VO(O_2)(DL\text{-}Cmhis)] \cdot H_2O$	1.598(1)	2.144(1) O(*Cmhis*) 2.169(2) N(*Cmhis*)	2.045(1) O(*Cmhis*) 2.156(2) N(*Cmhis*)	0.099 0.013	[16]
XII	$[VO(O_2)(Bpg)] \cdot H_2O$	1.615(1)	2.085(2) O(*Bpg*) 2.217(2) N(*Bpg*)	2.143(2) ± 0.005 N(*Bpg*)	(0.058) 0.074	[10]
XIII	$(NH_4)[VO(O_2)(H_2O)(Dipic)] \cdot 1.3H_2O$	1.579(2)	2.211(2) O(H_2O) 2.088(2) N(*Dipic*)	2.059(2) ± 0.006 O(*Dipic*)	0.151 (–0.048)	[17]
XIV	$[VO(O_2)(Py)(Pyanaph)]$	1.708	2.439 N(*Py*) 2.124 N(*Pyanaph*)	2.124 N(*Pyanaph*) 2.001 O(*Pyanaph*)	0.315 0.000	[18]
XV	$[VO(O_2)\{HB(Pz)_3\}(PzH)] \cdot THF$	1.603(4)	2.324(5), 2.203(5) } N(HB(Pz)$_3$)	2.122(5) N(HB(Pz)$_3$) 2.165(5) N(*Pz*H)	0.202 0.081	[19]
XVI	$[VO(O_2)(Bipy)_2]ClO_4$	1.625(3)	2.243(4), 2.247(4) } N(*Bipy*)	2.131(4) ± 0.005 N(*Bipy*)	0.112 0.116	[20]
XVII	$[VO(O_2)(Phen)_2]ClO_4$	1.60(1)	2.24(2), 2.24(2) } N(*Phen*)	2.125(20) ± 0.005 N(*Phen*)	0.115 0.115	[20]
XVIII	$[VO(O_2)(Bipy)(Pic)] \cdot H_2O$	1.604(5)	2.270(6) N(*Bipy*) 2.039(5) O(*Pic*)	2.126(6) N(*Bipy*) 2.128(6) N(*Pic*)	0.144 (0.012)	[21]
XIX	$[VO(O_2)(Phen)(Pic)] \cdot 0.5CH_2Cl_2$	1.595(2)	2.303(2) N(*Phen*) 2.032(2) O(*Pic*)	2.126(2) N(*Phen*) 2.139(2) N(*Pic*)	0.177 (0.005)	[22]
XX**	$(PPh_4)[VO(O_2)(Pic)_2] \cdot 2.5H_2O$	1.632(8)	2.103(7) ± 0.015 O(*Pic*)	2.109(8) ± 0.000 N(*Pic*)	(0.076) (0.076)	[22]
XXI	$(NH_4)[VO(O_2)(Pca)_2] \cdot 2H_2O$	1.598(1)	2.189(1), 2.087(1) } O(*Pca*)	2.127(1) ± 0.013 N(*Pca*)	(0.162) (0.060)	[23]
XXII	$K_3[VO(O_2)(Ox)_2] \cdot 0.5H_2O$	1.625(6)	2.142(3), 2.147(3) } O(*Ox*)	2.021(3) ± 0.003 O(*Ox*)	0.121 0.126	[24]
XXIII	$[VO(O_2)(Phen)(H_2O)_2]Cl \cdot 0.38H_2O$	1.589(2)	2.209(3) O(H_2O) 2.201(2) N(*Phen*)	2.075(2) O(H_2O) 2.157(2) N(*Phen*)	0.134 0.044	[22]

Table 1. (Contd.)

No.	Compound	V–O(oxo)	V–*L*, *trans* to O(oxo) V–*L*, *trans* to O_2	V–L_{cis}	Δ(Δ') (O) Δ(Δ) (O_2)	References
XXIV	$[VO(O_2)(H_2O)_2(Pic)]$	1.583(2)	2.307(2) O(H_2O) 2.016(2) O(*Pic*)	2.046(2) O(H_2O) 2.137(2) N(*Pic*)	0.261 (–0.011)	[25]
XXV	$(NH_4)[VO(O_2)(Bipy)F_2] \cdot 2H_2O$	1.602(9) ± 0.006	2.223(8) ± 0.030 F 2.20(1) ± 0.024 N(*Bipy*)	1.891(9) ± 0.015 F 2.21(1) ± 0.01 N(*Bipy*)	0.332 –0.01	[26]
XXVI	$(NH_4)_2[VO(O_2)(\mu\text{-}MalH)]_2 \cdot 2H_2O$	1.602(1) ± 0.001	2.286(1) ± 0.016 O_{ch}(*Mal*H) 2.000(1) ± 0.009 $O_{ch–br}$(*Mal*H)	2.036(1) ± 0.001 O_{ch}(*Mal*H) 2.030(1) ± 0.000 $O_{ch–br}$(*Mal*H)	0.250 –0.030	[27]
XXVII	$K_2[VO(O_2)(\mu\text{-}CitH_2)]_2 \cdot 2H_2O$	1.601(1)	2.561(1) O_{ch}(*Cit*H_2) 1.991(1) $O_{ch–br}$(*Cit*H_2)	2.013(1) O_{ch}(*Cit*H_2) 2.039(1) $O_{ch–br}$(*Cit*H_2)	0.548 –0.048	[28]
XXVIII	$K_2[\{VO(O_2)(\mu\text{-}TartH_2)\}_2(\mu\text{-}H_2O)] \cdot 5H_2O$	1.586(6) ± 0.002	2.394(6) ± 0.004 O_{br}(H_2O) 2.018(5) ± 0.008 $O_{ch–br}$(*Tart*H_2)	2.002(6) ± 0.005 O_{ch}(*Tart*H_2) 2.009(5) ± 0.006 $O_{ch–br}$(*Tart*H_2)	(0.334) 0.009	[29]
XXIX	$\{(NH_4)[VO(O_2)(\mu\text{-}Ida)]\}_n$	1.587(3)	2.375(3) $O_{ch–br}$(*Ida*) 2.138(4) N_{ch}(*Ida*)	2.015(3) ± 0.008 O_{ch}(*Ida*)	0.360 (0.002)	[30]
XXX***	$(NEt_4)_2[VO(\mu\text{-}O_2)(GlyGly)]_2 \cdot 3.16H_2O$	1.593(4) ± 0.008	2.617(4) ± 0.044 O_{br}(O_2) 2.034(5) ± 0.001 N_{ch}(*GlyGly*)	2.010(5) ± 0.001 O_{ch}(*GlyGly*) 2.114(4) ± 0.003 N_{ch}(*GlyGly*)	(0.607) –0.080	[31]

Note: Acid designations: H_3*Nta*—nitrilotriacetic acid, H_2*Ida*—iminodiacetic acid, H_3*Heida*—*N*-(2-hydroxyethyl)iminodiacetic acid, H_2*Cmida*—*N*-(carbamoylmethyl)iminodiacetic acid, H_2*Ceida*—*N*-(carbamoylethyl)iminodiacetic acid, H_4*Edta*—ethylenediaminetetraacetic acid, H_2*Dipic*—pyridine-2,6-dicarboxylic acid, H*Pic*—pyridine-2-carboxylic acid, H*Pca*—pyrazine-2-carboxylic acid, H_2*Ox*—oxalic acid, H_3*Mal*—malonic acid, H_4*Cit*—citric acid, and H_4*Tart*—tartaric acid. Ligand designations: *DL*-H_2*Cmhis*—*DL*-*N*-carboxymethylhistidine, H*Bpg*—*N*,*N*-bis(2-pyridylmethyl)glycine, H*Pyanaph*—1-(2-pyridyl-2-naphthalene), $H_2B(Pz)_3$—hydrotris(3,5-diisopropyl-1-pyrazolyl)borate, *Pz*H—3,5-diisopropylpyrazole, *Bipy*—2,2'-bipyridyl, *Phen*—1,10-phenanthroline, and H_2*GlyGly*—glycylglycine. In Tables 1–8, a blank means that the relevant data are not available in the original work. In Tables 1–7, the functions of a coordinating atom are denoted as follows: ch—chelating, ch–br—chelating–bridging, br—bridging, and term—terminal.

* Geometric parameters of $V(O_2)$(peroxo) fragments are presented in Table 4.

** For structure **XX**, the bond lengths are given for one of the two orientations of the $VO(O_2)$ fragment in which the occupancies of the O(oxo) and O_2 ligand positions are equal to 0.7.

*** In structure **XXX**, the peroxo group fulfills an (η^2,$\mu^{0.5}$) chelating–bridging function.

anionic complexes (**XVI**–**XXII**) [20–24] each involve two identical or different bidentate chelating ligands L^{2d}.

Monomeric pseudooctahedral complexes $VO(O_2)(L^{2d})(L^{1d})_2$, which contain one bidentate chelating and two monodentate ligands, can in principle have three spatial isomers shown (see Scheme 5).

In all three studied complexes of this type (**XXIII**–**XXV**) [22, 25, 26], there are isomers *5a* with *trans* positions of the L^{1d} monodentate ligand with respect to the O(oxo) atom and the *A* donor atom of the L^{2d} bidentate chelating ligand with respect to the O_2(peroxo) group.

For the fifth type of monomeric pseudooctahedral oxo monoperoxo complexes of vanadium(V) with four monodentate ligands $VO(O_2)(L^{1d})_4$, structurally characterized examples are not available in the literature.

It should be noted that the peroxo ligands in all the monomeric complexes $VO(O_2)_nA_m$ are coordinated to the metal atom in a bidentate chelating η^2 mode,

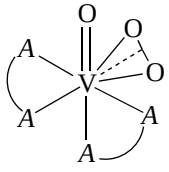

Scheme 4.

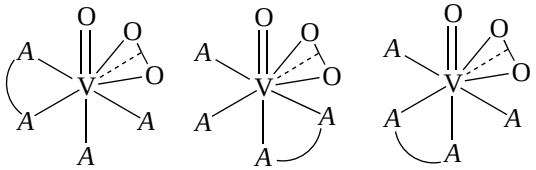

Scheme 5.

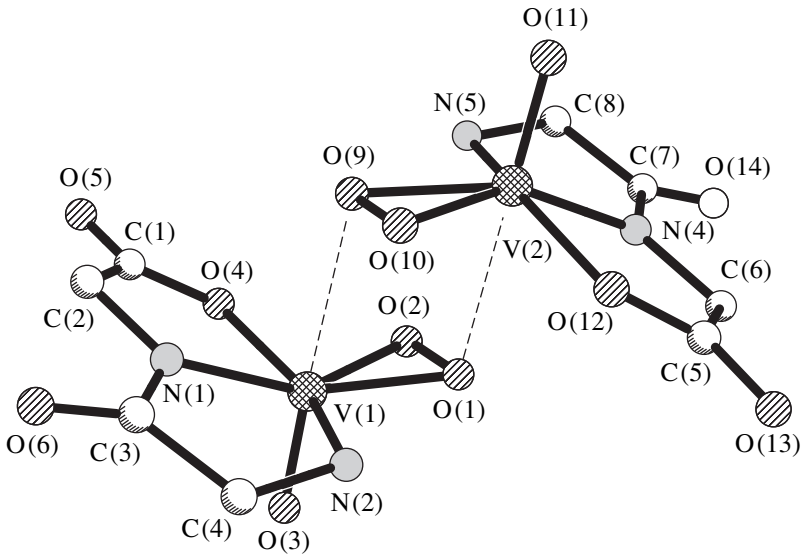

Fig. 1. Structure of the $[VO(O_2)(GlyGly)]_2$ dimeric complex.

whereas the O_2 ligands in binuclear oxoperoxo complexes of vanadium(V), in a number of cases, fulfill a chelating–bridging function (for greater details, see below).

2.2. Pseudooctahedral Oxo Monoperoxo Complexes of Vanadium(V) with Dimeric and Polymeric Structures and η^2 Coordination of O_2 Ligands

In two compounds, the dimeric anionic complexes of the general formula $[VO(O_2)(\mu\text{-}L)]_2$ with $L = Mal H^{2-}$ (**XXVI**) [27] and $L = Cit H_2^{2-}$ (**XXVII**) [28] have a similar structure. The dianions of malonic and citric acids serve as tridentate chelating–bridging ligands.

Unlike dimeric complexes **XXVI** and **XXVII**, in the dimeric anionic complex of the $K_2[\{VO(O_2)(\mu\text{-}Tart H_2)\}_2(\mu\text{-}H_2O)] \cdot 5H_2O$ compound (**XXVIII**) [29], the anion of α-hydroxycarboxylic acid (the $Tart H_2^{2-}$ anion of tartaric acid) fulfills not a tridentate but bidentate chelating–bridging function and is coordinated to the metal atom through the $O_{ch–br}$ hydroxyl and O_{ch} carboxylate deprotonated oxygen atoms. The metal atoms are additionally linked through the bridging aqua ligand [in the *trans* position with respect to the O(oxo) atom].

To the best of my knowledge, only one example of a polymeric structure in the compounds under investigation is available in the literature. This is the structure of $(NH_4)[VO(O_2)(Ida)]$ monoperoxo vanadyl (**XXIX**) [30], in which the anionic complexes are joined together into $[VO(O_2)(\mu\text{-}Ida)]_n$ polymeric chains. The dianion of iminodiacetic acid (H_2Ida) fulfills a tetradentate function, namely, a tridentate chelating (N, $2O_{ch}$) function with respect to one vanadium atom and a bridging (O_{br}) function with respect to the other vanadium atom.

2.3. Dimeric Pseudooctahedral Oxo Monoperoxo Complex of Vanadium(V) with a Chelating–Bridging (η^2,μ) Function of the O_2 Ligand

As was noted above, in all the aforementioned pseudooctahedral oxo monoperoxo complexes of vanadium(V) (**I**–**XXIX**), the dioxygen ligand is coordinated to the metal atom in the η^2 (bidentate chelating) mode. The sole exception is provided by the glycylglycinate complex in the $(NEt_4)[VO(O_2)(GlyGly)] \cdot 1.58H_2O$ compound (**XXX**) [31]. The metal atom in the equatorial plane of the pseudooctahedron is coordinated by the η^2-peroxo ligand and three atoms (2N, O) of the tridentate chelating glycylde-*N*-hydroglycinate ligand ($GlyGly^{2-}$). The vanadium atom deviates from the equatorial plane by ~0.4 Å toward the axial oxo ligand. The second axial position of the pseudooctahedron is occupied by one of the oxygen atoms of the dioxygen ligand of the adjacent anion. Therefore, the $[VO(O_2)(GlyGly)]^-$ anions are bound in pairs into pseudocentrosymmetric dimers (Fig. 1) through two peroxo groups that fulfill a bidentate chelating–bridging (η^2,$\mu^{0.5}$) function.[1] The V–(μ-O) semicoordination bonds in structure **XXX** [2.573(4), 2.660(4) Å] are the longest among those in pseudooctahedral oxo monoperoxo complexes of vanadium(V) (Table 1). Einstein

[1] Hereafter, the superscript *n* on μ^n refines the bridging function of the peroxo ligand: at $n = 0.5$, one $O(O_2)$ atom is involved in the coordination and semicoordination (V···O, 2.35–3.00 Å) bonds; at $n = 1$, one $O(O_2)$ atom participates in two coordination bonds; and, at $n = 2$, two $O(O_2)$ atoms each are involved in two coordination bonds.

et al. [31] carried out the ^{51}V NMR investigation of an aqueous solution of compound **XXX** and, with due regard for other physicochemical data, made the inference that the dimeric complex in the studied solution dissociates into monomeric fragments due to the breaking of the V–O(O_2) bridging bond. In the monomeric complex, the second axial position [*trans* to the O(oxo) atom] is most likely occupied by the oxygen atom of the coordinated water molecule.

2.4. Specific Features of the Structural Manifestation of the trans Effect of Peroxo Ligands in Pseudooctahedral Oxo Monoperoxo Complexes of Vanadium(V)

The presence of a partner in the *trans* position for the dioxygen ligand in VO(O_2)A_4 complexes determines a number of specific features in their structure. Since two multiply bonded ligands, namely, O(oxo) and O_2(peroxo), are located in *cis* positions with respect to each other, we can draw an analogy between the VO(O_2) oxo monoperoxo and VO_2 dioxo complexes. As in the general case of octahedral oxo complexes of Group V–VII d^0 metals, the formation of a specific geometric isomer upon competition of donor atoms in heteroligand complexes is governed by the self-consistency rule [32]. According to this rule, a *trans* position with respect to a multiply bonded ligand is predominantly occupied by an atom (a ligand) whose bond can be weakened more easily (in particular, the neutral donor ligand as compared to the acido ligand). The self-consistency rule holds true virtually without exception for oxo ligands and, in general terms, can be applied to O_2 ligands.

The *trans* effect of the peroxo ligands on the structure is slightly weaker than that of the oxo ligands and depends more strongly on the nature of oppositely located ligands (donor atoms of ligands). Specifically, the structural manifestation of the *trans* effect either is weakly pronounced or is absent [$\Delta(O_2)$ or $(\Delta')(O_2)$ = –0.08…+0.08 (see Table 1)][2] in complexes containing asymmetric chelating ligands (*Pic*, *Pca*, *Dipic*, *Pyanaph*, monoamine complexones, anions of carboxylic acids) with nitrogen and oxygen donor atoms in the *trans* position with respect to the O_2 ligands.

The analysis of the structural data available in the literature allows the assumption that the dioxygen ligand does not exhibit a *trans* effect in the case where the concomitant chelating ligand contains inequivalent potentially donor atoms (N, O).

The dependences of the geometric parameters of the $V(O_2)_n$ structural fragment (V–O_{peroxo}, O–O bond lengths) on the parameter n = 1 and 2 (i.e., in the presence or in the absence of the partner in the *trans* position for the dioxygen ligand) and, correspondingly, on the coordination number and the type of coordination polyhedron of the metal atom will be thoroughly analyzed in Sections 6 and 7.

The complete description of structures **I**–**XXIX** and detailed analysis of the factors responsible for the structural features of pseudooctahedral oxo monoperoxo complexes of vanadium(V) (in particular, the specific features of the structural manifestation of the *trans* effect of dioxygen ligands) are presented in my recent review [33].

3. STRUCTURE OF PSEUDOTRIGONAL BIPYRAMIDAL OXO DIPEROXO COMPLEXES OF VANADIUM(V)

Except for the bond lengths in VO(O_2)$_2$ structural fragments, the selected bond lengths for 17 pseudotrigonal bipyramidal oxo diperoxo complexes of vanadium(V) (**XXXI**–**XLVII**) [34–49] are given in Table 2.

3.1. Monomeric Pseudotrigonal Bipyramidal Oxo Diperoxo Complexes of Vanadium(V)

In the vast majority of anionic complexes of the general formula $[VO(O_2)_2(L^2)]^{m-}$ (m = 1–3) (**XXXI**–**XL**, **XLII**) [33–41, 43], the coordination polyhedron of the metal atom, apart from the oxygen atoms of the oxo and peroxo ligands, contains two donor atoms (2O, 2N, or O and N) of the bidentate chelating ligand (CO_3, *Ox*, *Pic*, *Pic*OH, *Acpic*, *Dipic*', *Phen*NO_2, or *Bipy*).

In the structures of all these compounds, the multiply bonded oxo ligand occupies the apical position. The second apical position [*trans* to O(oxo)] is occupied by the donor atom (O, N) of the bidentate chelating ligand L^2. Two peroxo ligands and the second donor atom (O, N) of the L^2 ligand are located in the equatorial plane of the pseudotrigonal bipyramid.

In structure **XXXI** (Fig. 2a) [34], the $[VO(O_2)_2(CO_3)]^{3-}$ anionic complex has crystallographic symmetry C_s: the V and O(oxo) atoms and the carbonate ligand lie in the m plane. In the CO_3 planar ligand, three C–O bonds differ in length. The C–O_{term} terminal bond is the shortest bond [1.254(4) Å]. The C–O_{axial} bond [1.297(4) Å] with the oxygen atom in the axial position of the coordination polyhedron is shorter than the C–O_{equat} equatorial bond [1.317(4) Å]. The C–O_{axial} and C–O_{equat} bond lengths are antibatic with

[2] The parameter Δ serves as a quantitative measure of the structural manifestation of the *trans* effect: Δ is determined as the difference between the lengths of the V–L_{trans} and V–L_{cis} bonds with like donor atoms of the L ligands. The quantity Δ' is the difference between the V–L_{trans} bond length and the mean (standard) length of the V–L_{stand} bond with the participation of a like atom [in the absence of identical ligands in the *trans* and *cis* positions with respect to O(oxo) and (or) O_2 ligands]. The V–L_{stand} bond lengths are taken equal to the following V–L_{cis} bond lengths: V–N(neutral), 2.136 Å (2.100–2.165 Å for 10 structures in Table 1); V–O(acido), 2.027 Å (1.970–2.064 Å for 17 structures); and V–O(H_2O), 2.060 Å (the mean value of bond lengths in two structures: 2.075 Å in **XXIII** and 2.046 Å in **XXIV**).

Table 2. Selected bond lengths (Å) in monomeric, dimeric, and polymeric pseudotrigonal bipyramidal oxo diperoxo complexes of vanadium(V)

No.	Compound	V–O(oxo)	V–*L*, *trans* to O(oxo)	V–L_{cis}	Δ(Δ') (O)	References
XXXI	$K_3[VO(O_2)_2(CO_3)]$	1.617(3)	2.301(3) O(CO_3)	2.039(3) O(CO_3)	0.262	[34]
XXXII	$K_3[VO(O_2)_2(Ox)] \cdot H_2O$	1.622(4)	2.251(4) O(O_{ch})	2.060(4) O(O_{ch})	0.191	[35]
XXXIII	$K_3[VO(O_2)_2(Ox)] \cdot H_2O_2$	1.620(3)	2.249(3) O(O_{ch})	2.062(3) O(O_{ch})	0.187	[36]
XXXIV	$K_2[VO(O_2)_2(Pic)] \cdot 2H_2O$	1.599(4)	2.290(4) O(*Pic*)	2.123(5) N(*Pic*)	(0.263)	[37]
XXXV	$K_2[VO(O_2)_2(PicOH)] \cdot 3H_2O$	1.606(2)	2.314(2) O(*Pic*OH)	2.137(2) N(*Pic*OH)	(0.287)	[37]
XXXVI	$K_3[VO(O_2)_2(Acpic)] \cdot 2H_2O$	1.620	2.190 O(*Acpic*)	2.179 N(*Acpic*)	(0.163)	[38]
XXXVII	$K_3[VO(O_2)_2(Dipic')] \cdot 3.25H_2O$	1.622 ± 0.029	2.300 ± 0.012 O(*Dipic*')	2.144 ± 0.026 N(*Dipic*')	(0.273)	[38]
XXXVIII	$K[VO(O_2)_2(PhenNO_2)] \cdot 2H_2O$	1.613	2.347 N($PhenNO_2$)	2.143 N($PhenNO_2$)	0.204	[39]
XXXIX	$(NH_4)[VO(O_2)_2(Bipy)] \cdot 4H_2O$ (–100°C)	1.619(3)	2.288(3) N(*Bipy*)	2.149(4) N(*Bipy*)	0.139	[40]
XXXIXa	$(NH_4)[VO(O_2)_2(Bipy)] \cdot 4H_2O$ (18°C)	1.612(2)	2.295(2) N(*Bipy*)	2.151(2) N(*Bipy*)	0.144	[36]
XL	$(HBipy)[VO(O_2)_2(Bipy)] \cdot 3.4H_2O_2 \cdot 1.6H_2O$	1.619(3)	2.284(4) N(*Bipy*)	2.137(4) N(*Bipy*)	0.147	[41]
XLI	$(NH_4)_3[VO(O_2)_2F_2]$	1.609(2)	2.306(1) F	1.958(1) F	0.348	[42]
XLII	$(HBipy)[\{VO(O_2)_2(Bipy)\}_2(\mu\text{-}H)] \cdot 0.5H_2O \cdot 5.5H_2O_2$	1.612(2)	2.290(3) N(*Bipy*)	2.154(3) N(*Bipy*)	0.136	[43]
XLIII	$(NH_4)_3[\{VO(O_2)\}_2(\mu\text{-}OH)(\mu\text{-}O_2)_2] \cdot H_2O$	1.597(4) ± 0.000	2.499(3) ± 0.021 $O_{ch–br}(O_2)$	1.993(3) ± 0.010 O_{br}(OH)	(0.472)	[44]
XLIIIa	$(NH_4)_3[\{VO(O_2)\}_2(\mu\text{-}OH)(\mu\text{-}O_2)_2] \cdot H_2O$	1.602(2) ± 0.004	2.502(2) ± 0.024 $O_{ch–br}(O_2)$	2.002(2) ± 0.007 O_{br}(OH)	(0.475)	[45]
XLIV	$(NH_4)_4[\{VO(O_2)\}_2(\mu\text{-}O)(\mu\text{-}O_2)_2]$	1.607(3) ± 0.006	2.501(3) ± 0.021 $O_{ch–br}(O_2)$	2.004(2) ± 0.010 $O_{br}(O_{oxo})$	(0.474)	[46]
XLV	$(NH_4)_5[\{VO(O_2)\}_2(\mu\text{-}PO_4)(\mu\text{-}O_2)_2] \cdot H_2O$	1.587(4) ± 0.002	2.381(4) ± 0.030 $O_{ch–br}(O_2)$	1.973(4) ± 0.004 $O_{ch–br}(PO_4)$	(0.354)	[47]
XLVI	$K_3[\{VO(O_2)F\}_2(\mu\text{-}F)(\mu\text{-}O_2)] \cdot HF \cdot 2H_2O$	1.599(4) ± 0.001	2.122(3) ± 0.003 F_{br}	1.888(4) ± 0.009 F_{term}	0.234	[48]
XLVII	$\{(NH_4)_2[V(\mu\text{-}O)(O_2)_2F]\}_n$	1.613(1)	2.505(1) $O_{br}(O_{oxo})$	1.929(1) F_{term}	(0.478)	[49]

Note: Acid designations: H*Pic*OH–3-hydroxypyridine-2-carboxylic acid, H_2*Acpic*–3-acetoxypyridine-2-carboxylic acid, and H_2*Dipic*'– pyridine-2,4-dicarboxylic acid. Ligand designation: *Phen*NO_2–5-nitro-1,10-phenanthroline. The other designations are given in Table 1.

respect to the adjacent vanadium–oxygen bond lengths: the V–O_{equat} bond [2.039(3) Å] is considerably shorter than the V–O_{axial} bond [2.301(3) Å].

In two compounds of the general formula $K_3[VO(O_2)_2(Ox)] \cdot Solv$, where *Solv* = H_2O (**XXXII**) [35] and *Solv* = H_2O_2 (**XXXIII**) [36], the structure involves the $[VO(O_2)_2(Ox)]^{3-}$ anionic complex (Fig. 2b) with two O_2 groups and the oxygen atom of the bidentate chelating oxalate ion in the equatorial plane. The V–O_{axial} bonds (for two structures, the mean bond length is equal to 2.250 ± 0.001 Å), on average, are 0.189 Å longer than the V–O_{equat} bonds (2.061 ± 0.001 Å). As was assumed earlier in [36, 40], compounds **XXXIII** and $(NH_4)[VO(O_2)(Bipy)] \cdot 4H_2O$ (**XXXIX**) contain the $K_3[V(O_2)_3(Ox)] \cdot H_2O$ and $(NH_4)[V(O_2)_3(Bipy)] \cdot 3H_2O$ triperoxo complexes, respectively. According to Campbell *et al.* [36], the concentration of H_2O_2 used in the synthesis of peroxo complexes is a factor controlling the precipitation of hydrates (at a low H_2O_2 concentration), perhydrates (with an excess of H_2O_2), or a mixture of both compounds.

In four compounds of the general formula $K_n[VO(O_2)_2(L^2)^{-n+1}] \cdot mH_2O$, the L^2 ligands are monoanions and dianions of different pyridinecarboxylic acids: pyridine-2-carboxylic acid (*Pic*, *n* = 2, *m* = 2) (**XXIV**) [37], 3-hydroxypyridine-2-carboxylic acid (*Pic*OH, *n* = 2, *m* = 3) (**XXV**) [37] (Fig. 2c), 3-acetoxypyridine-2-carboxylic acid (*Acpic*, *n* = 3, *m* = 2) (**XXVI**) [38] (Fig. 2d), and pyridine-2,4-dicarboxylic acid (*Dipic*', *n* = 3, *m* = 3.25) (**XXVII**) [38] (Fig. 2e). In all these four compounds, the bidentate chelating ligand L^2 is coordinated to the metal atom so that the axial position of the pseudotrigonal bipyramid is occupied by the deprotonated (acido) oxygen atom of the

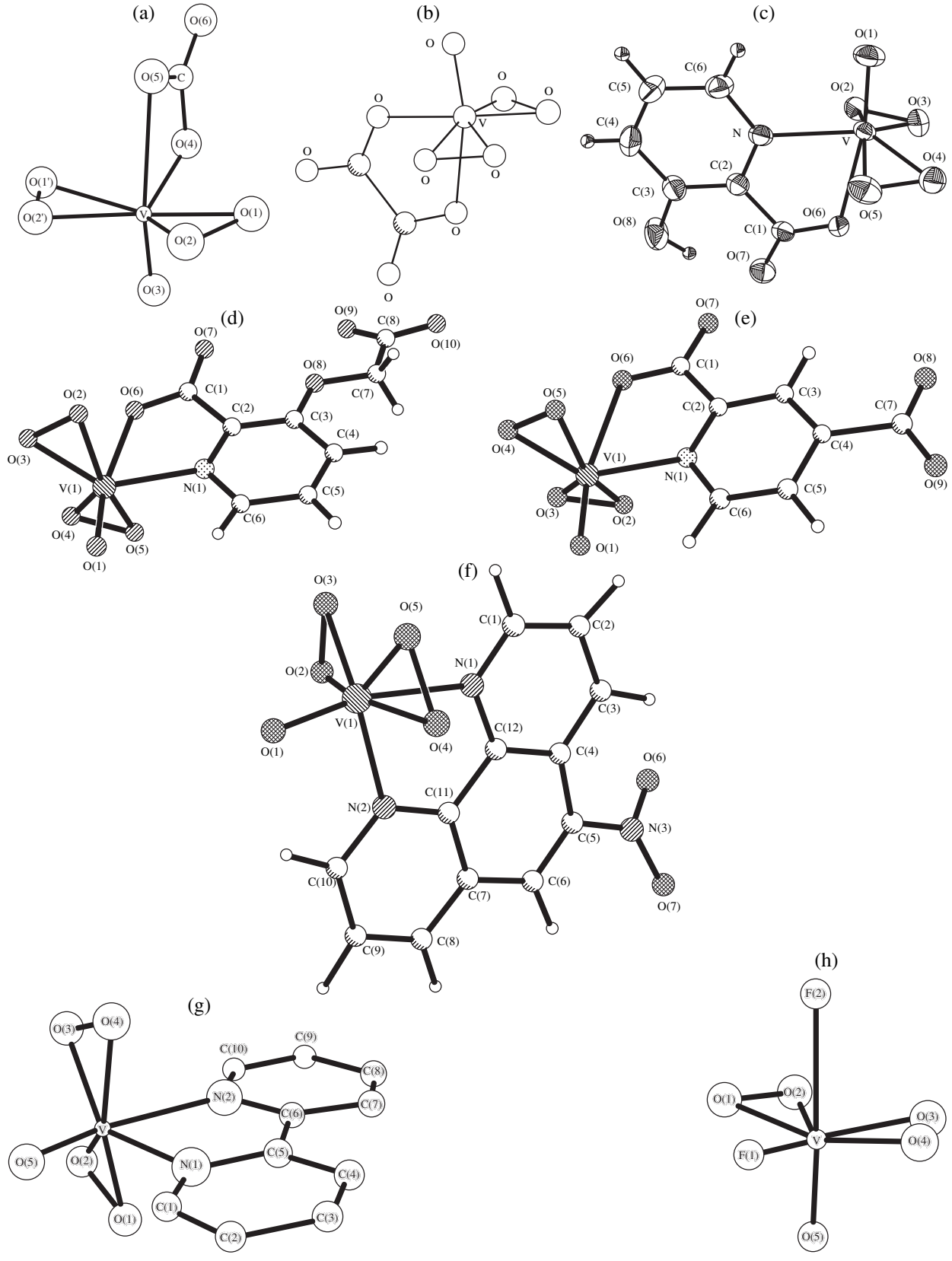

Fig. 2. Structures of monomeric pseudotrigonal bipyramidal oxo diperoxo complexes of vanadium(V): (a) $[VO(O_2)_2(CO_3)]^{3-}$, (b) $[VO(O_2)_2(Ox)]^{3-}$, (c) $[VO(O_2)_2(PicOH)]^{2-}$, (d) $[VO(O_2)_2(Acpic)]^{3-}$, (e) $[VO(O_2)_2(Dipic')]^{3-}$, (f) $[VO(O_2)_2(PhenNO_2)]^{-}$, (g) $[VO(O_2)_2(Bipy)]^{-}$, and (h) $[VO(O_2)_2F_2]^{3-}$.

carboxylate group and the equatorial position is occupied by the nitrogen neutral donor atom of the pyridine ring. This coordination mode is not typical of oxo complexes of Group V–VII d^0 transition metals [particularly of vanadium(V)] and violates the self-consistency rule (see Section 2.4). A similar inverted coordination mode of the asymmetric bidentate chelating (O, N) ligand is also observed in two pseudooctahedral oxo monoperoxo complexes of vanadium(V) (Table 1): $[VO(O_2)(Pic)_2]^-$ (**XX**) [22] and $[VO(O_2)(Pca)_2]^-$ (**XXI**) [23]. In these structures, the *trans* positions with respect to the oxo ligand are also occupied by the O acido atoms rather than by the nitrogen neutral donor atoms of the *Pic* (*Pca*) ligands. The factors responsible for this anomalous coordination mode are discussed in greater detail in [22, 23, 50].

In structures **XXXIV** and **XXXV**, the $[VO(O_2)_2(Pic)]^{2-}$ and $[VO(O_2)_2(PicOH)]^{2-}$ anionic complexes possess similar geometric parameters with the sole difference: the C(1)=O(7) terminal bond in **XXXV** [1.268(2) Å] is longer than that in **XXXIV** [1.23(1) Å] and is substantially longer than the C(1)=O(7) bond in free H*Pic* (1.214 Å) [51]. In structure **XXXV**, the terminal 3-hydroxy group, which is not coordinated to the metal atom, participates in the formation of the strong intraionic hydrogen bond O(8)–H···O(7) [O(8)–H, 0.86(3) Å; H···O(7), 1.69(4) Å; O(8)HO(7) angle, 158(3)°]. The O(8)–C(3) bond length in structure **XXXV** is equal to 1.347(3) Å. Complexes **XXXIV** and **XXXV**, which rapidly oxidize cysteine to cystine, can serve as model compounds for use in analyzing the insulin-mimetic activity of vanadium peroxo compounds in aqueous solutions.

In three compounds of the general formula $A[VO(O_2)_2(L^2)] \cdot Solv$ {where L^2 = 5-nitro-1,10-phenanthroline (*Phen*NO_2), A = K^+, and $Solv$ = $2H_2O$ (**XXXVIII**) [39] (Fig. 2f); L^2 = *Bipy*, A = NH_4^+, and $Solv = 4H_2O$ (**XXXIX**) [36, 40] (Fig. 2g); and L^2 = *Bipy*, A = H*Bipy*$^+$, and $Solv = 3.4H_2O_2 \cdot 1.6H_2O$ (**XL**) [41]}, the neutral bidentate chelating ligand L^2 in the $[VO(O_2)_2(L^2)]^-$ anionic complex is coordinated to the metal atom through two nitrogen atoms (in the axial and equatorial positions of the coordination polyhedron). In compounds **XXXIX** and **XL**, structural units in the crystals are joined together by an extended network of hydrogen bonds with the participation of NH_4^+ (H*Bipy*$^+$) cations, anionic complexes, and H_2O (H_2O_2) molecules of crystallization. In structure **XXXIX**, all four oxygen atoms of the peroxo groups are involved in the hydrogen bonds with the ammonium cations [N···O, 2.797(5) and 2.813(5) Å] and water molecules [O···O, 2.774(5)–2.806(5) Å] and all the four V–O(O_2) bonds are close in length [1.880(3)–1.911(3) Å]. In structure **XL**, only three of the four O(O_2) atoms participate in strong hydrogen bonds with hydroperoxide molecules [O··O, 2.624(5)–2.655(5) Å] and the V–O bonds with these oxygen atoms [1.914(3), 1.938(3), and 1.942(3) Å], on average, are 0.07 Å shorter than the V–O(O_2) bond with the oxygen atom not involved in the formation of hydrogen bonds. In structure **XL**, the *Bipy* ligand and the unusual monoprotonated H*Bipy*$^+$ cation are substantially nonplanar: the dihedral angles between the planes of two *Py* rings are equal to 5.4° and 7.1°, respectively. It is worth noting that, in structure **XXXIX**, the dihedral angle in the *Bipy* ligand is considerably smaller (only 1.4°). The bipyridinium cation in structure **XL** adopts a fairly rare *cis* configuration.[3] The proton is strongly localized at one of the nitrogen atoms. However, the HN–C [1.351(7) ± 0.006 Å] and N–C [1.352(7) ± 0.009 Å] bonds in the cation and the N–C bond [1.351(5) ± 0.012 Å] in the *Bipy* ligand are comparable in length.

Among vanadium(V) monomeric pseudotrigonal bipyramidal complexes of the $[VO(O_2)_2(L^1)_2]$ type, only one structure is known, namely, ammonium difluorooxo diperoxovanadate(V) $(NH_4)_3[VO(O_2)_2F_2]$ (**XLI**) [42]. In the $[VO(O_2)_2F_2]^-$ anion (Fig. 2h), the V–F axial bond, as usual, is considerably longer (by 0.348 Å) than the equatorial bond. In the crystal, the structural units are linked together by an extended network of N–H···F and N–H···O interionic hydrogen bonds with the participation of all fluorine and oxygen atoms [N···F ≥ 2.731(3) Å, N···O≥ 2.803(3) Å]. Stomberg [42] considered the difference between similar potassium and ammonium fluorooxoperoxovanadates. Crystals of $A_2[VO(O_2)_2F]$ (A = K, NH_4) are not isomorphic. In contact with the growth solution, the potassium salt remains unchanged for several months, whereas the ammonium salt transforms into difluorooxo diperoxovanadate **XLI** for several days. Possibly, it is this extended network of hydrogen bonds in compound **XLI** that plays the important stabilizing role.

3.2. Dimeric Pseudotrigonal Bipyramidal Oxo Diperoxo Complexes of Vanadium(V)

In five oxo diperoxovanadium(V) compounds **XLII**–**XLVI** (see Table 2) [43–48] with a pseudotrigonal bipyramidal coordination of the metal atom, the anionic complex has a dimeric structure.

According to analytical, spectroscopic, and X-ray powder diffraction data, the formula $(H_2Bipy)[\{VO(O_2)_2(Bipy)\}_2] \cdot 6H_2O$ or $(H_2Bipy)H_2[\{VO(O_2)_2(Bipy)\}_2(\mu\text{-}O)] \cdot 5H_2O$ was initially assigned to compound **XLII** [43]. The X-ray structural analysis revealed that this compound is actually described by the formula

[3] According to the NMR data, the free molecule of 2,2'-bipyridyl in different solutions has a planar *trans* configuration [52]. In strongly acidic solutions, the H*Bipy*$^+$ and H_2Bipy^{2+} cations exhibit a skewed transoid conformation in which the dihedral angles between the planes of two *Py* rings are equal to 30° and 60°, respectively [53].

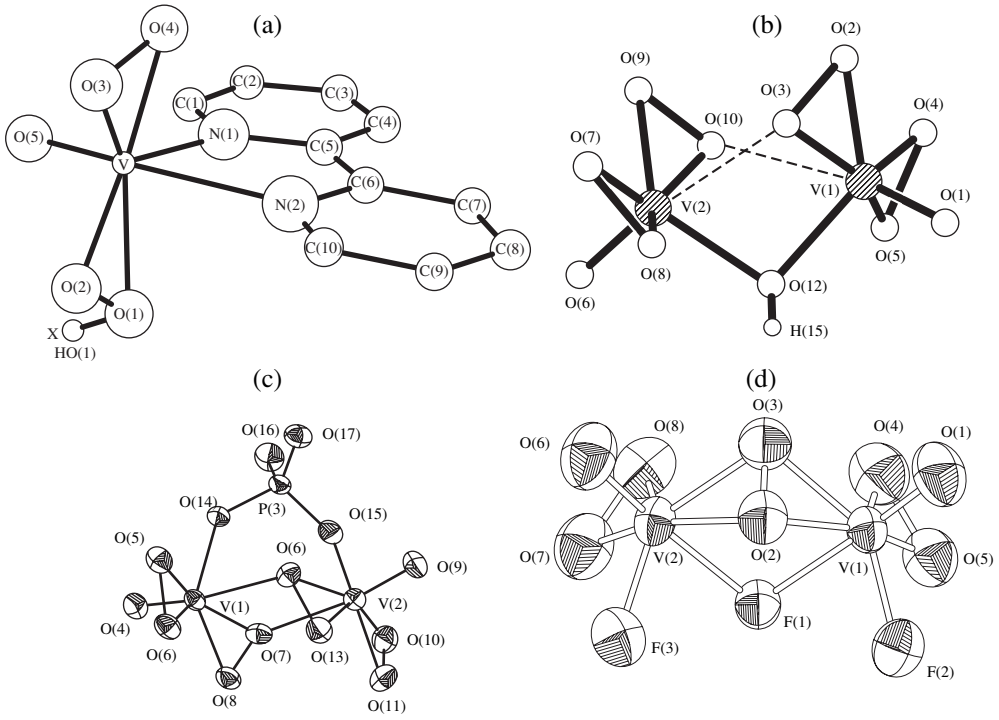

Fig. 3. Structures of dimeric pseudotrigonal bipyramidal oxo diperoxo complexes of vanadium(V): (a) $[\{VO(O_2)_2(Bipy)\}(\mu\text{-}H)]^-$ (asymmetric part of the dimer), (b) $[\{VO(O_2)_2\}_2(\mu\text{-}OH)(\mu\text{-}O_2)_2]^{3-}$, (c) $[\{VO(O_2)\}_2(\mu\text{-}PO_4)(\mu\text{-}O_2)_2]^{5-}$, and (d) $[\{VO(O_2)F\}_2(\mu\text{-}F)(\mu\text{-}O_2)]^{3-}$.

$(HBipy)[\{VO(O_2)_2(Bipy)\}_2(\mu\text{-}H)] \cdot 0.5H_2O_2 \cdot 5.5H_2O$. In the centrosymmetric anionic complex, two halves of the $VO(O_2)_2(Bipy)H_{0.5}$ dimer (Fig. 3a) are linked by the strong asymmetric hydrogen bond O–H···O [O–H, 0.93(11) Å; O···O, 2.456(4) Å; OHO angle, 176(11)°]. The bridging hydrogen atom is statistically disordered over two equally probable positions about the inversion center. All atoms of the bipyridinium cation are also disordered over two equally probable positions, which are related by the inversion center and are spaced 0.6 Å apart. One of the three crystallographically nonequivalent water molecules is statistically "mixed" with the hydroperoxide molecule in the ratio 0.75 : 0.25. In crystal **XLII**, the structural units are joined together through an extended network of hydrogen bonds [O···O≥ 2.60(1) Å, N···O ≥ 2.928(6) Å]. Three V–$O(O_2)$ distances [1.869(2), 1.892(2), 1.903(2) Å] have standard values and, on average, are 0.107 Å shorter than the V–OH bond [1.995(2) Å] with the peroxo oxygen atom involved in the formation of the strong hydrogen bond.

Compound **XLII** crystallizes from a solution of V_2O_5 and 2,2'-*Bipy* in 25% H_2O_2 at a temperature of 5°C and pH 3.5. The holding of the reaction mixture for a long time under the same conditions (5°C, pH 3.5) leads to the formation of one more crystalline phase, $(HBipy)[VO(O_2)_2(Bipy)] \cdot 3.4H_2O_2 \cdot 1.6H_2O$ (**XL**, Table 2), which contains a mononuclear anionic complex. Szentivanyi and Stomberg [43] believed that compound **XLII** can be an isolobal intermediate product of the reaction used to synthesize complex **XL**.

Compounds $(NH_4)_3[V_2O_{11}H] \cdot H_2O$ (**XLIII**) [44, 45] and $(NH_4)_4[V_2O_{11}]$ (**XLIV**) [46] contain structurally similar anionic complexes $[\{VO(O_2)_2\}_2(\mu\text{-}OH)(\mu\text{-}O_2)_2]^{3-}$ (Fig. 3b) and $[\{VO(O_2)_2\}_2(\mu\text{-}O)\ (\mu\text{-}O_2)_2]^{4-}$, respectively.[4] Crystals **XLIII** and **XLIV** are isostructural (the oxygen atom of the H_2O molecule in compound **XLIII** occupies a position identical to the position of the nitrogen atom in one of the NH_4^+ ions in compound **XLIV**). In dimeric anionic complexes, the metal atoms are linked through three bridging oxygen atoms of two peroxo and one hydroxo (in **XLIII**) or oxo (in **XLIV**) ligands. Consequently, two peroxo groups fulfill an η^2 chelating function and the two other groups serve as $\eta^2,\mu^{0.5}$ chelating–bridging ligands. In the pseudotrigonal bipyramid, the *trans* positions with respect to the oxo ligands are occupied by the bridging $O(O_2)$ atoms at large V···O distances (2.478–2.522 Å). In each structure, two $V\text{–}O(O_2)_{ch\text{–}br}$ bonds with the chelating–bridging oxygen atoms of the peroxo groups, on average, are 0.025 (in **XLIII**) and 0.028 Å (in **XLIV**) longer than four $V\text{–}O(O_2)_{ch}$ bonds (1.908 and

[4] Structure **XLIV** was determined earlier by the photo method with the use of a twinned crystal [54].

1.883 Å according to more accurate data for **XLIIIa** and 1.913 and 1.885 Å for **XLIV**, respectively). In structure **XLIII**, the bridging hydroxo ligand participates as a donor and an acceptor in the formation of two bonds O–H···O (O···O, 2.69 Å) and O···H–O (O···O, 2.73 Å) with water molecules; as a result, the ligand environment is completed to the tetrahedral configuration. The protonation of the bridging oxygen atom in structure **XLIII** is confirmed by the IR spectroscopic data, according to which the absorption band observed at a frequency of 1034 cm^{-1} corresponds to vibrations of the V–OH bond [55].

The structure of the dimeric anionic complex in the $(NH_4)_5[\{VO(O_2)\}_2(\mu\text{-}PO_4)(\mu\text{-}O_2)_2] \cdot H_2O$ compound (**XLV**) [47] (Fig. 3c) is similar to that of the anionic complexes in compounds **XLIII** and **XLIV**. The only difference is that the bridging hydroxo (in **XLIII**) or oxo (in **XLIV**) ligand is replaced by the bridging phosphate ligand, which is coordinated to two vanadium atoms through two oxygen atoms (for each oxygen atom, there is one vanadium atom). As in structures **XLIII** and **XLIV**, in structure **XLV**, the V–O(O_2) bonds with the chelating–bridging ($\eta_2,\mu^{0.5}$) peroxo oxygen atoms in the apical positions of the pseudotrigonal bipyramids [*trans* to the O(oxo) atoms] are substantially weakened [V–O, 2.351(4) and 2.411(4) Å], whereas the V–O(O_2) bonds with the $\eta^2,\mu^{0.5}$-oxygen atoms, on average, are 0.042 Å longer than the V–O(O_2) bonds with η^2 chelating oxygen atoms [1.916(4) and 1.874(4) Å, respectively]. The anionic complexes, ammonium cations, and water molecules of crystallization are joined together through an extended network of hydrogen bonds [the shortest N···O(PO_4) contact is equal to 2.681 Å].

In the $K_3[V_2F_3O_8] \cdot HF \cdot 2H_2O$ crystal (**XLVI**) [48], the structural units represent dimeric anionic complexes, K^+ ions, and water and hydrogen fluoride molecules of crystallization, which are joined by electrostatic and weak hydrogen bonds. In the $[\{VO(O_2)F\}_2(\mu\text{-}F)(\mu\text{-}O_2)]^{3-}$ anion (Fig. 3d), the vanadium atoms are linked by the bridging peroxo and fluorine ligands. Two halves of the dimer are related by the *m* pseudoplane passing through the F(1), O(2), and O(3) bridging atoms. The O(2, 3) peroxo ligand fulfills a bischelating–bridging ($2\eta^2,\mu^2$) function. Unlike structures **XLII**–**XLV** (in which either of the two $\eta^2,\mu^{0.5}$-peroxo ligands contains only one bridging oxygen atom), in structure **XLVI**, either of the two oxygen atoms of the relevant O_2 peroxo ligand fulfills a symmetric bridging function. In this case, the V–O(2) bonds [2.047(4) ± 0.009 Å], on average, are 0.072 Å longer than the V–O(3) bonds [1.975(4) ± 0.001 Å]. Such an asymmetric coordination of the peroxo ligands irrespective of their function in the structure is characteristic of oxo diperoxo complexes of metals (for greater details, see below). In general, the chelating–bridging bonds V–O(O_2) (the mean bond length is 2.011 Å) are substantially longer than the chelating bonds (the mean bond length is 1.868 Å). The bridging F(1) atoms are located at the apical positions in the vanadium coordination polyhedra [the *trans* position with respect to the O(1) and O(6) atoms]. The V–F(1) bonds with the bridging fluorine atom [2.122(3) ± 0.003 Å], on average, are 0.234 Å longer than the V–F(2) and V–F(3) terminal bonds [1.888(4) ± 0.009 Å]. The dihedral angle between the planes of the equatorial ligands of two metal atoms is equal to 84.9(3)°. The position of the F(4) atom of the hydrogen fluoride molecule is not completely occupied: the occupancy factor is equal to 0.78(2). Lapshin *et al.* [48] believed that isothermal decomposition of compound **XLVI** is accompanied by the release of H_2O and HF molecules; i.e., the release of hydrogen fluoride molecules does not result from the transformation of the anionic complex, as was assumed earlier by Schwendt and Joniakova [56].

3.3. Pseudotrigonal Bipyramidal Oxo Diperoxo Complex of Vanadium(V) with a Polymeric Chain Structure

In the NH_4^+–V_2O_5–F^-–H_2O_2 system, the $(NH_4)[VO(O_2)_2F]$ compound (**XLVII**) [49] was synthesized in addition to the $(NH_4)_3[VO(O_2)_2F_2]$ compound (**XLI**) described earlier [42]. Upon prolonged contact with a growth solution, orange-yellow crystals **XLVII** often transform into yellow polycrystalline compound **XLI**. In a similar potassium system, it was possible to obtain crystals of only one very stable compound, namely, $K_2[VO(O_2)_2F]$. Although crystals of compound **XLVII** and its potassium analogue have a similar composition and very close lattice parameters, they are not isomorphic; furthermore, the $[VO(O_2)_2F]^{2-}$ anionic complexes in these compounds have radically different structures (see below).

In the anionic complex of structure **XLVII**, the pentagonal pyramidal (pseudotetrahedral) fragments $VO(O_2)_2F$ are joined with two similar fragments through the V···O(oxo) weakened contacts with the formation of zigzag chains [the O=V···O angle is 174.8(1)°, the V=O···V angle is 157.10(8)°, and the dihedral angle between the pentagonal planes of the adjacent $VO(O_2)F$ fragments is equal to 21.7°]. Therefore, the oxo ligands fulfill a bridging function, thus linking the vanadium polyhedra at common vertices and forming infinite chains =O··V=O··V=O··· with alternating metal–oxygen bonds [V=O, 1.613(1) Å; V··O, 2.505 Å]. A fragment of the $\{[V(\mu\text{-}O)(O_2)_2F]^{2-}\}_n$ anionic complex and the packing of structural units in crystal **XLVII** are shown in Figs. 4a and 4b, respectively. In crystal **XLVII**, the structural units are linked through an extended system of N–H··O and N–H··O hydrogen bonds [N··F ≥ 2.765(2) Å, N··O ≥ 2.840(3) Å].

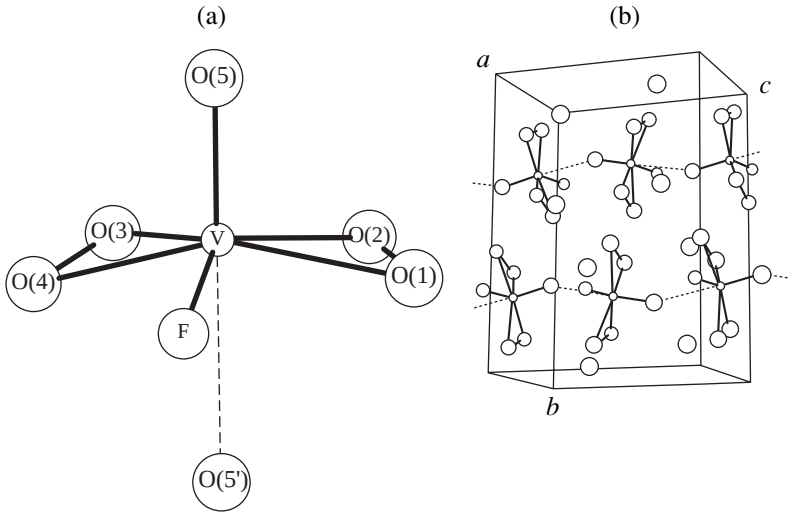

Fig. 4. Polymeric chain structure of the $\{[V(\mu\text{-}O)(O_2)_2F]^{2-}\}_n$ pseudotrigonal bipyramidal oxo diperoxo complex of vanadium(V): (a) a fragment of the anionic complex and (b) packing of structural units in the crystal.

4. STRUCTURE OF DIMERIC OXOPEROXO COMPLEXES OF VANADIUM(V) $[V_2O_2(O_2)_2(L^2)_2]^{2-}$

Table 3 presents the main geometric parameters of four compounds with dimeric anionic complexes of the general formula $[\{VO(O_2)\}_2(\mu\text{-}L^2)_2]^{2-}$, where L^2 are dianions of α-hydroxycarboxylic acids: $C_2H_4O_3$ glycolic acid H_2*Gly* (**XLVIII**) [57] (Fig. 5a), $C_3H_5O_3$ lactic acid H_2*Lact* (**XLIX**, **L**) [58, 59] (Fig. 5b), and $C_8H_8O_3$ phenylhydroxyacetic (mandelic) acid H_2*Mand* (**LI**) [60] (Fig. 5c). In all four compounds, the L^2 ligands fulfill a bidentate chelating–bridging function and are

Table 3. Selected bond lengths (Å) in dimeric pseudotetragonal pyramidal oxo monoperoxo complexes and monomeric and dimeric pseudotetrahedral oxo diperoxo complexes of vanadium(V)

No.	Compound	V–O(oxo)	V–L_{cis}	References
XLVIII	$(NBu_4)_2[\{VO(O_2)\}_2(\mu\text{-}Gly)_2] \cdot H_2O$	1.541(8)*	1.991(6) O_{ch}(*Gly*) 1.967(4) ± 0.044 $O_{ch–br}$(*Gly*)	[57]
XLIX	$K_2[\{VO(O_2)\}_2(\mu\text{-}Lact)_2]$	1.591(3)	2.005(3) O_{ch}(*Lact*) 1.979(3) ± 0.022 $O_{ch–br}$(*Lact*)	[58]
L	$(\dot{I}\text{-}Bu_4N)_2[\{VO(O_2)\}_2(\mu\text{-}Lact)_2] \cdot 2H_2O$	1.605 ± 0.004	1.956 ± 0.006 O_{ch}(*Lact*) 1.984 ± 0.066 $O_{ch–br}$(*Lact*)	[59]
LI	$(\dot{I}\text{-}Bu_4N)_2[\{VO(O_2)\}_2(\mu\text{-}Mand)_2] \cdot H_2Mand$	1.579(2)	1.991(2) O_{ch}(*Mand*) 1.990(2) ± 0.011 $O_{ch–br}$(*Mand*)	[60]
LII	$(NH_4)_2[VO(O_2)_2(NH_3)]$	1.606(3)	2.110(4) N(NH_3)	[63]
LIII	$(Im\text{H})[VO(O_2)_2(Im)] \cdot H_2O$	1.603(2)	2.092(2) N(*Im*)	[64, 65]
LIV	$K_2[VO(O_2)_2F]$	1.603(6)	1.903(4) ± 0.003 F	[66]
LV	$Cs_2[VO(O_2)_2F]$	1.62(3) ± 0.00	$1.87_5(1_5)$ ± 0.00_5 F	[67]
LVI	$K_2[\{VO(O_2)_2\}(\mu\text{-}O_2)\{VO(O_2)(H_2O)\}] \cdot 3H_2O$	1.595(4) ± 0.009	1.998(4) O(H_2O) 2.032(3) $O_{ch–br}$(O_2)	[68]
LVII	$(NMe_4)_2[\{VO(O_2)_2\}(\mu\text{-}O_2)\{VO(O_2)(H_2O)\}] \cdot 2H_2O$	1.596(4) ± 0.005	2.030(4) O(H_2O) 2.045(3) $O_{ch–br}$(O_2)	[69]
LVIII	$(Cym\text{H}_2)[\{VO(O_2)_2\}(\mu\text{-}O_2)\{VO(O_2)(H_2O)\}] \cdot 2H_2O$	1.596(5) ± 0.000	2.005(5) O(H_2O) 2.035(5) $O_{ch–br}$(O_2)	[70]

Note: Acid designations: H_2*Gly*–glycolic acid, H_2*Lact*–lactic acid, and H_2*Mand*–mandelic acid. Ligand designations: *Im*–imidazole and *Cym*–5,5,7,12,12,14-hexamethyl-1,4,8,11-tetraazacyclotetradecane.
* The V–O(oxo) bond length for one (main) of the two orientations of the disordered complex (the occupancy factor is 0.66).

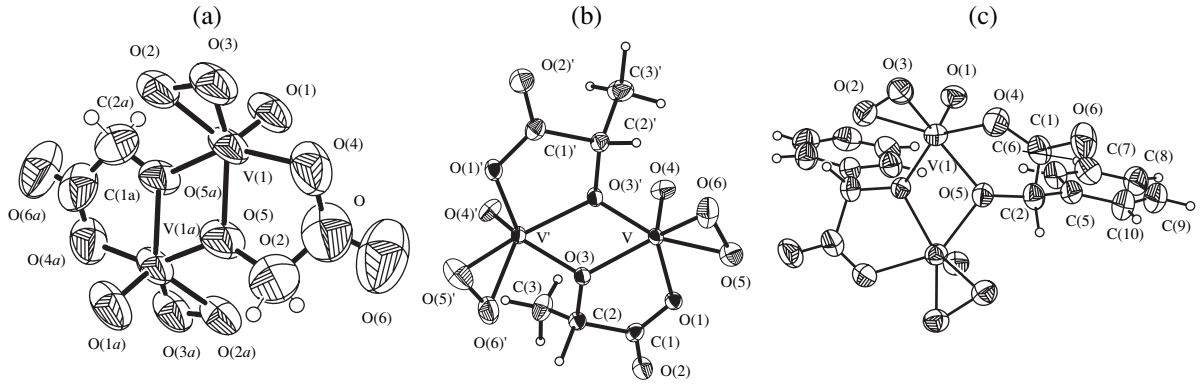

Fig. 5. Structures of $[V_2O_2(O_2)_2(\mu\text{-}L^2)_2]^{2-}$ dimeric oxoperoxo complexes of vanadium(V): (a) $L^2 = Gly^{2-}$, (b) $L^2 = Lact^{2-}$, and (c) $L^2 = Mand^{2-}$.

coordinated to the metal atom through two deprotonated oxygen atoms, namely, the O_{ch-br} hydroxyl and O_{ch} carboxylate atoms. A similar function is fulfilled by the dianion of tartaric acid (H_4Tart) in the dimeric anionic complex $[\{VO(O_2)\}_2(\mu\text{-}TartH_2)_2(\mu\text{-}H_2O)]^{2-}$ of the oxo monoperoxo compound of vanadium(V) with a pseudooctahedral coordination of the metal atom (**XXVIII**, Table 1) [29].

Orange-red or red complexes of the general formula $A_2[\{VO(O_2)\}_2(\mu\text{-}Gly)_2] \cdot nH_2O$ (A^+ = K, Cs, NH_4, NBu_4, NPr_4; n = 0, 1) were prepared by crystallization in the AVO_3–glicolic acid–H_2O_2–H_2O–(*Et*OH) system. In structurally characterized compound **XLVIII** (A^+ = NBu_4, n = 1), the centrosymmetric anionic complex is statistically disordered: two orientations of oxygen atoms of the peroxo and oxo ligands with respect to the central atoms are characterized by occupancy factors of 0.66 and 0.34 for the O(1–3) and O(1*a*–3*a*) atoms, respectively. This variant of disordering, which is typical of metal oxoperoxo complexes, was thoroughly described by Stomberg [61].

In two compounds of the general formula $A_2[\{VO(O_2)\}_2(\mu\text{-}Lact)_2] \cdot nH_2O$, the anionic complexes have a similar structure but differ in symmetry. The anion is located at the crystallographic axis 2 in structure **XLIX** (A = K^+, n = 0) and occupies the general position in structure **L** ($A = n\text{-}Bu_4N^+$, n = 2). Demartin *et al.* [58] compared the structures of compounds **XLIX** and $K_2[(VO_2)_2(\mu\text{-}Cit)_2] \cdot 6H_2O$ [62] and established that the replacement of the peroxo ligand by the oxo ligand (the changeover from the oxo monoperoxo complex to the dioxo complex) and the change in the bridging ligand (the dianion of α-hydroxycarboxylic acid) does not lead to a change in the structural type of the anionic complex.

In the structure of the $(n\text{-}Bu_4N)_2[\{VO(O_2)\}_2(\mu\text{-}Mand)_2] \cdot H_2Mand$ compound (**LI**), the anionic complex and the H_2Mand molecule of crystallization are located along the crystallographic axis 2. In the anionic complex, the central bimetallic ring V_2O_2 is nonplanar [the dihedral angle between the VO_2 planes is equal to 151.79(8)°], as is the case in compounds **XLIX** and **L**. Note that the V_2O_2 ring in centrosymmetric complex **XLVIII** is strictly planar. The H_2Mand solvate molecule in structure **LI** is disordered over two positions with respect to the crystallographic axis 2. One carboxylate oxygen atom (on the axis 2) is in contact with both vanadium atoms [V···O, 2.550(3) Å] in the axial position opposite to the oxo ligand and completes the coordination polyhedron of each vanadium atom to the pseudooctahedron. The vanadium–vanadium distances [3.238(1) Å in **XLIX**)] in the dimers exceed the length of the metal–metal single bond. The VOV angles are larger than 90° [109.9(1)° in **XLIX**; 105.6(1)° in **LI**).

The coordination polyhedron of vanadium atoms in structures **XLVIII–LI** can be represented as a strongly distorted pseudotetragonal pyramid with the oxo ligand in the apical position [or as a six-vertex polyhedron (pentagonal bipyramid) with the axial O(oxo) atom, provided that the peroxo ligand occupies two equatorial positions]. However, there exists an alternative description. For structure **XLIX**, Demartin *et al.* [58] described the metal coordination polyhedron as a strongly distorted pseudotrigonal bipyramid in which the O_{ch} and O'_{ch-br} atoms occupy the axial positions and the O(oxo) atom, the O_{ch-br} atom, and the $\mu\text{-}O_2$ ligand are located in the equatorial positions. As was noted above, the vanadium coordination polyhedron in structure **LI** can be represented as a (5 + 1) asymmetric pseudooctahedron similar to the pseudooctahedron in the structure of the dimeric complex $[VO(\mu^{0.5}\text{-}O_2)(GlyGly)]_2$ (**XXX**) [31].[5]

[5] The distortion of metal coordination polyhedra in different oxoperoxo complexes will be considered in greater detail in Section 8.

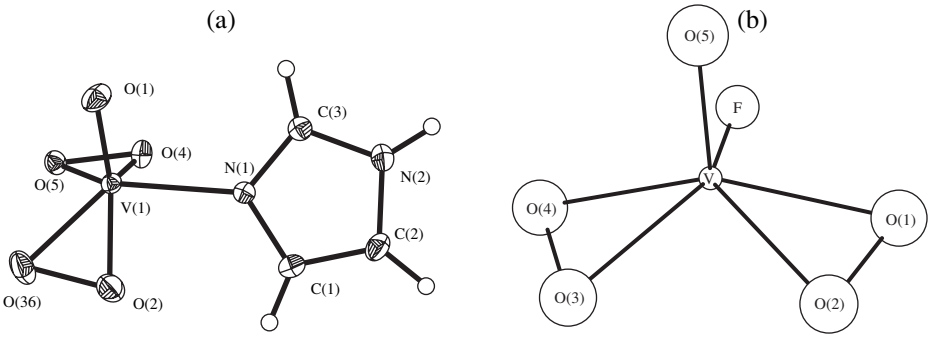

Fig. 6. Structures of monomeric pseudotetrahedral oxo diperoxo complexes of vanadium(V): (a) $[VO(O_2)_2(Im)]^-$ and (b) $[VO(O_2)_2F]^{2-}$.

5. STRUCTURE OF PSEUDOTETRAHEDRAL OXO DIPEROXO COMPLEXES OF VANADIUM(V)

The selected bond lengths in monomeric and dimeric pseudotetrahedral oxo diperoxo complexes of vanadium(V) **LII**–**LVIII** [63–70] are listed in Table 3.[6]

5.1. Monomeric Pseudotetrahedral Oxo Diperoxo Complexes of Vanadium(V)

In four compounds **LII**–**LV** [63–67] (Table 3), the metal atoms in the monomeric anionic complexes of the general formula $[VO(O_2)L^1]^{n-}$ (n = 1, 2) have a pseudotetrahedral coordination that is provided by the O(oxo) atom, two η^2-coordinated peroxo ligands, and the donor atom of the L_1 monodentate ligand.

In structure **LII** [63], both the ammonium cation and the $[VO(O_2)(NH_3)]^-$ anionic complex lie in the *m* crystallographic plane passing through the V, O(oxo), N(NH_3), and N(NH_4) atoms. The anionic complexes are joined by the V···O(oxo) interionic contacts [2.926(3) Å] into polymeric chains similar to those in the structure of the $(NH_4)[VO(O_2)_2F]$ compound (**XLVII**) [49]. In structure **XLVII**, the V···O(oxo) contact [2.505(1) Å] corresponds to a bond weakened through the *trans* effect of the multiply bonded oxo ligand. By contrast, according to [63], the V···O(oxo) contact in structure **LII** is due to the electrostatic interaction; as a result, the coordination polyhedron of the metal atom tends to be completed to a strongly distorted pseudotrigonal bipyramid [O(oxo)VO(oxo)' angle, 178.8(1)°; VO(oxo)V' angle, 135.0(2)°]. The structural units in crystal **LII** are linked by the weak hydrogen bonds N–H···O(oxo) and N–H···O(peroxo) (N···O, 2.872–2.955 Å; O···H, 2.22–2.37 Å; NHO angles, 130°–151°).

According to [63], the vanadium atom in structure **LII** has a distorted tetrahedral coordination under the assumption that the peroxo ligands form three-center bonds involving vacant sd^3 hybrid orbitals. In the pseudotetrahedron, the MVM angle [128.5(1)°] (where M is the midpoint of the O–O bond) is maximum in magnitude due to the repulsion of two O_2 groups, the O(oxo)–V–N(NH_3) angle [97.5(1)°] is minimum, and the angles O(oxo)–V–M [107.2(1)°] and N(NH_3)–V–M [106.1(1)°] are intermediate in magnitude.

The structural units in the $(Im\text{H})[VO(O_2)_2(Im)] \cdot H_2O$ crystal (**LIII**) [64, 65] are the anionic complexes (Fig. 6a), the $N_2C_3H_5$ imidazolium cations (*Im*H), and water molecules of crystallization. The V–N(*Im*) bonds [2.110(4) Å] in structure **LIII** and the V–N(NH_3) bonds [2.092(2) Å] in structure **LII** are comparable in length, even though the N(sp^3) and N(sp^2) coordinated atoms of the ammonia and imidazole molecules are characterized by different hybridizations. Crans *et al.* [64] and Keramidas *et al.* [65] noted that the vanadium atoms in compounds **LII** and **LIII** have an unusual sixfold pentagonal pyramidal (pseudotetrahedral) coordination rather than a sevenfold pentagonal bipyramidal (pseudotrigonal bipyramidal) coordination, which is characteristic of oxo diperoxo complexes. In particular, the latter coordination is observed in the structure of the $[VO(NH_2O)_2(Im)_2]Cl$ oxo dihydroxylamide complex [65] with a composition similar to that of oxo diperoxo complex **LIII**. In the former structure, both *Im* molecules are incorporated in the coordination environment of the vanadium atom, whereas the coordination environment in compound **LIII** involves one coordinated *Im* molecule and the $Im\text{H}^+$ cation. In the $[VO(NH_2O)_2(Im)_2]^+$ cationic complex, the equatorial V–N bond [2.079(4) Å] is only 0.013 Å shorter than the V–N(*Im*) bond in the anionic complex of structure **LIII**, whereas the axial V–N(*Im*) bond is considerably elongated [to 2.333(4) Å] due to the *trans* effect of the oxo ligand. From analyzing the multinuclear NMR data, Keramidas *et al.* [65] made the assumption that complex **LIII** remains monomeric in solutions. Investigation into the dynamic processes occurring in solutions (aqueous, CD_3CN–*DMSO-d*[6]) [65] demonstrated

[6] If the O2(peroxo) ligands are treated as bidentate chelating ligands, the vanadium coordination polyhedron represents a pentagonal pyramid with the oxo ligand in the apical position.

that the rate of exchange between free imidazole and complex **LIII** is comparable to the exchange rate for a similar hydroxylamide complex. In [65], the higher lability of complex **LIII** (as compared to diperoxo complexes that, as a rule, are more inert to exchange reactions [71, 72]) was explained by the presence of the free coordination site *trans* to the O(oxo) atom in the $[VO(O_2)_2(Im)]^-$ complex under consideration.

Isomorphic crystals of two $A_2[VO(O_2)_2F]$ compounds with $A = K^+$ (**LIV**) [66] and Cs^+ (**LV**) [67] are formed by the $[VO(O_2)_2F]^{2-}$ anionic complexes (Fig. 6b) and alkali metal cations.[7] In similar crystals, namely, **LIV** and **LV**, the anionic complex is disordered over two orientations (*A* and *B*) [the occupancy factors for compound **LIV** are equal to 0.60(2) and 0.40(2), respectively]. Within the limits of experimental error, the vanadium atoms in two orientations occupy identical positions. The positions of the oxo O(*A*) and O(*B*) atoms in structure **LIV** differ by only 0.26 Å. The equatorial planes of the fluorine atoms and four O(peroxo) atoms in orientations *A* and *B* form a dihedral angle of 5.6° in **LIV** (8.2° in **LV**) and are rotated with respect to each other about the averaged V–O(oxo) axis through an angle of 126° (125°).

As was noted above (Section 3.3), the crystals of ammonium salt **XLVII** [49], which have a similar composition and close lattice parameters but are not isomorphic to crystals **LIV** and **LV**, are characterized by a substantially differing polymeric chain structure of the $\{[V(\mu\text{-}O)(O_2)F]^{2-}\}_n$ anion owing to the asymmetric bridging function of the oxo ligand (see Table 2).

5.2. Dimeric Pseudotetrahedral Oxo Diperoxo Complexes of Vanadium(V)

Three compounds of the general formula $A_2[V_2O_{11}H_2] \cdot mH_2O$ ($A = K^+$, $m = 3$, **LVI** [68]; $A = NMe_4^+$, $m = 2$, **LVII** [69]; $A_2 = Cym H_2^{2+}$, $m = 2$, **LVIII** [70])[8] contain the $[\{VO(O_2)\}_2(\mu\text{-}O_2)\{VO(O_2)(H_2O)\}]^{2-}$ binuclear anionic complexes (Fig. 7). In the structure, the peroxo ligands fulfill different functions. Three O_2 groups are bidentate chelating (η^2) ligands. The fourth O_2 group [O(6), O(7)] is the bidentate chelating–bridging (η^2,μ^1) ligand [the bidentate chelating ligand for the V(2) atoms and the bridging ligand for the V(1) atom]. Therefore, two chemically nonequivalent vanadium atoms have different pseudotetrahedral coordination environments. The V(1) atom coordinates the O(5) oxo ligand, two O_2 (η^2) ligands, and the bridging O(6) atom of the η^2,μ^1-peroxo ligand. The V(2) atom coordinates the oxo ligand, two peroxo [bridging O(6, 7) and chelating O(8, 9)] (η^2) ligands, and the O(21) atom of the coordinated water molecule. In structures **LVI**–**LVIII**, the coordination polyhedron of the vanadium atoms is completed to an asymmetric elongated pentagonal bipyramid (pseudotrigonal bipyramid) owing to the V···O(peroxo) contacts [V(1)···O(9) = 2.597(4), 2.707(4), and 2.980(4) Å and V(2)···O(4) = 2.606(3), 2.697(3), and 2.764(3) Å in structures **LVI**, **LVII**, and **LVIII**, respectively]. The O(5)V(1)O(4) [O(10)V(2)O(9)] angles in structures **LVI** and **LVII** are equal to 167.5(2)° [172.7(2)°] and 167.6(2)° [169.6(2)°], respectively.[9] The differences between the V···O(peroxo) distances in three structures (in compounds **LVI**, **LVII**, and **LVIII**, the mean distances are equal to 2.602 ± 0.005, 2.702 ± 0.005, and 2.872 ± 0.108 Å, respectively) correlate with the dihedral angles between the equatorial planes of the V(1) and V(2) atoms [O(1–4, 6)/O(6–9, 21)] and the V(1)O(6)V(2) angles at the bridging oxo oxygen atom [**LVI**, 57.1°, 100.2(1)°; **LVII**, 60.8°, 103.8(2)°; **LVIII**, 64.9°, 109.0(2)°].

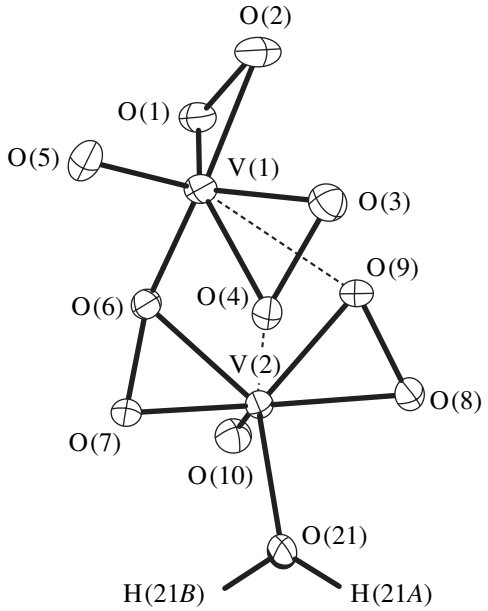

Fig. 7. Structure of the $[\{VO(O_2)\}_2(\mu\text{-}O_2)\{VO(O_2)(H_2O)\}]^{2-}$ dimeric pseudotetrahedral oxo diperoxo complex of vanadium(V).

Sucha *et al.* [70] noted that the nature of cations (especially, organic cations) is an important factor governing the thermal stability of solid peroxo complexes. In particular, unlike compounds **LVI** and **LVII** crystallizing at –25°C and decomposing at 0–5°C, compound **LVIII** is thermally stable up to 60°C. The decomposi-

[7] The unit cell volume of crystal **LIV** [$V = 687.5(2)$ Å^3] is approximately 25% greater than that of crystal **LV** [$V = 546.2(2)$ Å^3], which accounts for the difference between the ionic radii of potassium and cesium cations.

[8] *Cym* is 5,5,7,12,12,14-hexamethyl-1,4,8,11-tetraazacyclotetradecane $C_{16}H_{38}N_4$.

[9] Making allowance for the weak (semicoordination) V···O contacts, the peroxo groups in structures **LVI**–**LVIII** can be coordinated in three modes: η^2 [O(1), O(2)], η^2,μ^1 [O(6), O(7)], and $\eta^2,\mu^{0.5}$ [O(3), O(4); O(8), O(9)].

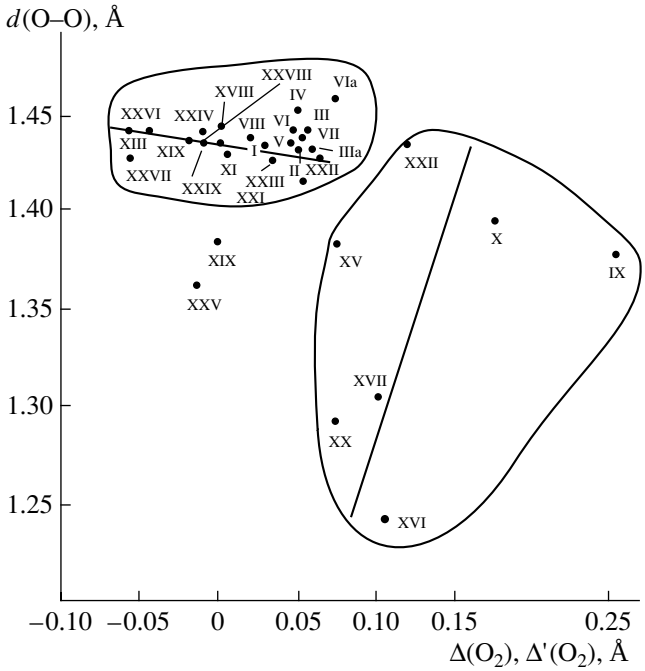

Fig. 8. Dependence of the O–O bond length on the parameter $\Delta(O_2)$ or $\Delta'(O_2)$ for structures of the $VO(O_2)$ pseudooctahedral complexes.

tion begins at 85°C and is accompanied by the simultaneous removal of active oxygen and three water molecules (the weight loss is equal to 30.75%). The final product is identified as the anhydrous metavanadate $(CymH_2)(VO_3)_2$ (according to the IR spectra measured at 95 and 150°C). The high thermal stability of solid compound **LVIII** as compared to complexes **LVI** and **LVII** can be associated with the interionic interaction of the $CymH_2^{2+}$ cation with the peroxovanadate anion.

6. OXYGEN–OXYGEN DISTANCES IN COORDINATED PEROXO GROUPS OF OXOPEROXO COMPLEXES OF VANADIUM(V)

The geometric parameters of $V(O_2)_{peroxo}$ fragments in monomeric, dimeric, and polymeric oxo monoperoxo complexes of vanadium(V) (**I**–**XXX**, **XLVIII**–**LI**) are listed in Table 4. Similar parameters of $V(O_2)_2$ fragments in oxo diperoxo complexes of vanadium(V) (**XXXI**–**XLII**, **XLVII**, **LII**–**LV**) are given in Table 5. In all the compounds in Tables 4 and 5, the peroxo ligands fulfill a pseudochelating η^2 function. The bond lengths and bond angles of $V(O_2)_2$ fragments in dimeric oxo diperoxo complexes of vanadium(V) (**XLIII**–**XLVI**, **LVI**–**LVIII**) with η^2- and η^2,μ^n-coordinated peroxo ligands (n = 0.5, 1, 2) are presented in Table 6.

The O–O distances in coordinated bidentate peroxo groups in different compounds of Group IV–VI transition metals fall in a rather wide range (from 1.36 to 1.54 Å [73]). In vanadyl complexes, these distances do not exceed 1.49 Å. In pseudotrigonal bipyramidal and pseudotetrahedral oxo diperoxovanadate(V) complexes, the O–O distances vary over a relatively narrow range (from 1.440 to 1.487 Å for 23 structures presented in Tables 5 and 6). The changeover to oxo monoperoxovanadate(V) complexes leads to a decrease in the O–O bond lengths. In the majority of the compounds presented in Table 4 (31 out of 34), the O–O distances lie in a wide range (from 1.347 to 1.457 Å). The anomalously short O–O distances falling outside the above range are found in structures **XVI** [1.236(8) Å] [20], **XVII** [1.30(3) Å] [20], and **XX** [1.29(2) Å] [22].[10]

Very short O–O bonds in η^2-coordinated dioxygen ligands are also found in the structures of the complexes $[Re(O_2)Cl(PPh_3)_2(NNCO_2Me)]$ [1.26(3) Å] [74] and $[Co(O_2)L]$ [1.262(8) Å] [75], where L is the anion of hydrotris(3-*tert*-butyl-5-methypyrazolylborate).[11] However, it should be noted that these two complexes were prepared by adding molecular oxygen. Very short $O–O(O_2)$ bonds were also revealed in the structures of porphyrin complexes of iron (1.23–1.25 Å) and cobalt (1.25–1.30 Å) compounds with coordinated monodentate dioxygen ligands [77].

The O–O bond lengths (<1.30 Å) are also characteristic of singly charged superoxide anions O_2^- (for example, the α-KO_2 ionic superoxide [1.28(2) Å] [78] and the $R_4H_4[Cu(IO_6)_2]O_2 \cdot 6H_2O$ compound [1.214(8) Å] [79]), and molecular oxygen O_2 [1.207(8) Å] [80].

Therefore, the O–O bond lengths in pseudooctahedral $VO(O_2)$ complexes **I**–**XXX** (Table 4) fall in the wide range 1.236–1.457 Å. This range lies virtually below the lower limit of the narrow range of the O–O bond lengths (1.456–1.474 Å) observed in 14 formally seven-coordinate $VO(O_2)_2$ complexes **XXXI**–**XLIV**, which, however, have a radically different pseudotrigonal bipyramidal geometry (Tables 5, 6).

It is of interest to elucidate whether the O–O bond length correlates with the parameter $\Delta(O_2)$ [or $\Delta'(O_2)$], which is a quantitative measure of the structural manifestation of the *trans* effect of peroxo ligands (see Section 2.4). As can be seen from Fig. 8, such a correlation, even if not well pronounced, is observed for pseudooctahedral oxo monoperoxo complexes of vanadium. Judging from the dependence of the O–O bond length on the parameter $\Delta(O_2)$ or $\Delta'(O_2)$ (Fig. 8), the weak *trans* effect of the peroxo group or the lack of this effect [$\Delta(O_2)$ or $\Delta'(O_2)$ = –0.05…+0.08 Å] is typical of com-

[10]Possibly, the shortening of the O–O bond in structure **XX** is a consequence of statistical mixing of the positions of the oxo and peroxo ligands in the crystal.

[11]In the latter case, the bond between the metal atom and the dioxygen ligand can be represented either as the Co(II)–O_2^{2-} bond or as the Co(III)–O_2^- bond [76].

Table 4. Geometric parameters of the $V(O_2)$ fragment in oxo monoperoxo complexes of vanadium(V)

No.	Bond lengths, Å		Bond angles, deg	
	$V–O(O_2)$	O–O	$O(O_2)–V–O(O_2)$	$V–O(O_2)–O(O_2)$
I	1.864(4) ± 0.001	1.432(6)	45.2(2)	67.5
II	1.877(4) ± 0.003	1.431(6)		67.4
III	1.861(8) ± 0.070	1.438(4)	45.3(2)	67.4(6) ± 5.2
IIIa	1.862(1)	1.428(1)	45.07(4)	67.5
IV	1.841(9) ± 0.007	1.45(1)	46.4	67.3
V	1.865(1) ± 0.001	1.432(2)	45.17(7)	67.3(1) ± 0.3
VI	1.870(1) ± 0.003	1.438(2)	45.24(5)	
VIa	1.889(2) ± 0.003	1.457(3)	45.4(1)	
VII	1.870(2) ± 0.003	1.436(3)	45.18(8)	67.4(1) ± 0.2
VIII	1.876(2) ± 0.006	1.438	45.1	67.0
IX	1.87(2) ± 0.03	1.37(4)	43(1)	
X	1.805(10) ± 0.070	1.39(2)	45.5(4)	
XI	1.878(1) ± 0.004	1.429(2)	44.72(6)	
XII	1.867(2) ± 0.003	1.424(2)	44.84(7)	
XIII	1.871(2) ± 0.001	1.441(3)	45.3(1)	67.4(1) ± 0.1
XIV	1.853 ± 0.006	1.440	45.7	66.8
XV	1.875(5) ± 0.013	1.379(6)	43.2(2)	69.4
XVI	1.840(5) ± 0.028	1.236(8)	39.2(2)	70.4(4) ± 2.4
XVII	1.845(20) ± 0.015	1.30(3)	41.1(9)	69.5(1.0) ± 1.5
XVIII	1.874(5) ± 0.013	1.424(7)	44.7(2)	67.7(3) ± 0.9
XIX	1.881(2) ± 0.010	1.383(3)	43.13(8)	68.5(1) ± 0.8
XX	1.836(9) ± 0.064	1.29(2)	40.8(5)	69.6(7) ± 5.3
XXI	1.877(1) ± 0.014	1.412(2)	44.18(6)	
XXII	1.876(6) ± 0.006	1.43(1)	44.8(3)	67.6(4) ± 0.4
XXIII	1.876(2) ± 0.011	1.424(3)	44.6(1)	67.7(1) ± 0.7
XXIV	1.873(2) ± 0.006	1.435(3)	45.06(8)	67.47(9) ± 0.43
XXV	1.88(2) ± 0.03	1.36(3) ± 0.09	42.2(8) ± 2.9	
XXVI	1.878(1) ± 0.007	1.442(2) ± 0.001	45.13(6) ± 0.001	67.44(7) ± 0.50
XXVII	1.880(1) ± 0.008	1.427(2)	44.61(6)	67.70(8) ± 0.55
XXVIII	1.882(5) ± 0.021	1.434(7) ± 0.011	44.8(2) ± 0.3	67.6(3) ± 1.4
XXIX	1.881(3) ± 0.005	1.435(5)	44.9(2)	67.6(2) ± 0.4
XXX	1.893(4) ± 0.016	1.440(5) ± 0.006	44.7(1) ± 0.4	67.7(2) ± 0.8
XLVIII*	1.856(6) ± 0.008	1.44(1)	45.5(4)	67.2(4) ± 0.6
XLIX	1.837(4) ± 0.005	1.347(5)	43.0(2)	
L	1.857 ± 0.029	1.380 ± 0.051	43.6 ± 1.5	68.2 ± 2.3
LI	1.880 ± 0.001	1.432(3)	44.8(1)	67.6(1) ± 0.1

* The geometric parameters for one of the two orientations of the disordered ligand O_2 (the occupancy factor is 0.66).

Table 5. Geometric parameters of the $V(O_2)_2$ fragment in oxo diperoxo complexes of vanadium(V) with η^2-coordinated peroxo ligands

No.	Bond lengths, Å		Bond angles, deg	
	$V–O(O_2)_{cis}$ $V–O(O_2)_{trans}$	O–O	$O(O_2)–V–O(O_2)$	$V–O_{cis}–O_{trans}$ $V–O_{trans}–O_{cis}$
XXXI	1.945(2) 1.873(2)	1.467(3)	45.2(1)	
XXXII	1.923(4) ± 0.012 1.861(4) ± 0.005	1.456(6) ± 0.005	45.3(2) ± 0.1	65.2(2) ± 0.2 69.7(2) ± 0.3
XXXIII	1.923(3) 1.876(3)	1.466(4)		
XXXIV	1.908(4) ± 0.009 1.888(4) ± 0.007	1.461(6) ± 0.003	45.3(2) ± 0.3	66.7(2) ± 0.1 68.1(2) ± 0.2
XXXV	1.916(2) ± 0.008 1.890(2) ± 0.013	1.462(2) ± 0.001	45.18(7) ± 0.23	66.44(9) ± 0.27 68.39(9) ± 0.04
XXXVI	1.929 ± 0.012 1.872 ± 0.006	1.470 ± 0.009	45.45 ± 0.05	? 69.3 ± 0.2
XXXVII	1.911 ± 0.019 1.868 ± 0.029	1.456 ± 0.027	45.3 ± 0.7	65.9 ± 0.7 69.0 ± 1.0
XXXVIII	1.893 ± 0.013 1.877 ± 0.002	1.457 ± 0.004	45.5 ± 0.1	66.3 67.5
XXXIX	1.910(3) ± 0.001 1.882(3) ± 0.002	1.468(4) ± 0.003	45.6(1) ± 0.2	66.2(2) ± 0.1 68.2(2) ± 0.0
XXXIXa	1.912(2) 1.875(2)	1.467(3)		
XL	1.940(3) ± 0.002 1.889(3) ± 0.027	1.474(4) ± 0.001 1.468(5) ± 0.010*	45.3(1) ± 0.3	65.5(2) ± 1.1 69.3(2) ± 0.9
XLI	1.924(2) ± 0.003 1.889(2) ± 0.002	1.464(2) ± 0.002	45.1(1) ± 0.1	
XLII	1.903(2); 1.995(2)** 1.881(2) ± 0.012	1.461(3); 1.471(3)**	44.1(1)	66.0(1); 64.1(1)** 68.4(1); 72.1(1)**
XLVII	1.904(1) ± 0.001 1.877(2) ± 0.003	1.461(2) ± 0.001	45.47(7) ± 0.01	66.30(9) ± 0.13 68.24(9) ± 0.13
LII	1.872(3) 1.871(3)	1.463(4)	46.0(1)	
LIII	1.866(2) ± 0.001 1.903(2) ± 0.019	1.471(3) ± 0.04	45.93(8)	68.4(1) ± 0.7 65.7(1) ± 0.6
LIV***	1.904(5) ± 0.003 1.881(5) ± 0.001	1.487(7) ± 0.019	46.0(2) ± 0.4	
LV***	1.90(2) ± 0.00 $1.87_5(2) \pm 0.02_5$	1.45(3) ± 0.01		

* The O–O bond length in the H_2O_2 molecule of structure **XL**.
** Geometric parameters for the fragment involving the O(1) protonated atom.
*** Geometric parameters for one of the two orientations of the disordered peroxo group (the occupancy factor is 0.6).

plexes with relatively long O–O bond lengths (1.41–1.46 Å). The points corresponding to these complexes lie close to each other. By contrast, for complexes in which the O_2 groups have a strong effect on the oppositely lying bonds [$\Delta(O_2)$ or $\Delta'(O_2)$ = 0.08–0.26 Å], the O–O distances (1.24–1.43 Å), on average, are considerably shorter than those in compounds of the first group. Note that the O–O bond lengths in compounds of the second group vary over a wide range.[12] The mean val-

[12]The parameters of two compounds **XIX** and **XXV** are inconsistent with those of the aforementioned two groups of complexes. Although the O–O bonds are relatively short [1.383(3) and 1.36(3) Å, respectively], these complexes do not exhibit a *trans* effect: $\Delta'(O_2)$ = 0.005 Å for **XIX** and $\Delta(O_2)$ = –0.01 Å for **XXV**.

Table 6. Geometric parameters of the $V(O_2)_2$ fragment in dimeric oxo diperoxo complexes of vanadium(V) with η^2- and η^2,μ^n-coordinated peroxo ligands*

No.	Bond lengths, Å			Bond angles, deg	
	$V–O(O_2)_{cis}(\eta^2)$ $V–O(O_2)_{cis}(\eta^2, \mu^n)$	$V–O(O_2)_{trans}(\eta^2)$ $V–O(O_2)_{trans}(\eta^2, \mu^n)$	O–O	$O(O_2)–V–O(O_2)$	$V–O_{cis}–O_{trans}$ $V–O_{trans}–O_{cis}$
XLIII	1.887(4) ± 0.006 1.914(3) ± 0.002 ($\mu^{0.5}$)	1.875(4) ± 0.010			
XLIIIa	1.893(2) ± 0.003 1.908(2) ± 0.003 ($\mu^{0.5}$)	1.878(2) ± 0.005	1.464(2) ± 0.009	45.59(7) ± 0.33	66.4(1) ± 0.5 68.0(1) ± 0.5
XLIV	1.896(3) ± 0.001 1.913(3) ± 0.001 ($\mu^{0.5}$)	1.880(3) ± 0.005	1.468(4) ± 0.006	44.5(2) ± 0.6	66.3(2) ± 0.6 68.2(2) ± 0.9
XLV	1.894(4) ± 0.010 1.916(4) ± 0.000 ($\mu^{0.5}$)	1.863(4) ± 0.004	1.444(5) ± 0.009	45.1(2) ± 0.6	65.9(2) ± 0.3 69.1(2) ± 1.0
XLVI	1.872(5) ± 0.001 2.046 ± 0.009 (μ^2)	1.864(5) ± 0.008 1.975(4) ± 0.001 (μ^2)	1.444(5) ± 0.003 (μ^2) 1.467(5) (η^2, μ^2)	45.5(2) ± 0.0 (μ^2) 42.6(2) (η^2, μ^2)	
LVI	1.896(4) ± 0.018 1.869(4) ($\mu^{0.5}$)	1.880(4) ± 0.011 1.878(4) ($\mu^{0.5}$); 1.947(4) (μ^1)	1.465(4) ± 0.008	45.5(2) ± 0.6	
LVII	1.869(4) ± 0.011 1.878(3) ($\mu^{0.5}$)	1.876(4) ± 0.008 1.868(3) ($\mu^{0.5}$); 1.919(4) (μ^1)	1.463(5) ± 0.005	45.8(2) ± 0.5	
LVIII	1.873(4) ± 0.004 1.885(4) ($\mu^{0.5}$)	1.883(5) ± 0.004 1.868(4) ($\mu^{0.5}$); 1.943(4) (μ^1)	1.471(6) ± 0.009	45.9(2) ± 0.4	66.6(2) ± 0.2; 64.8(2) (μ^1) 67.3(2) ± 0.3; 69.7(2) (μ^1)

* n = 0.5, 1, or 2 (for details, see Section 2.3).

ues of the parameters $\Delta(O_2)$ [$\Delta'(O_2)$] and the O–O bond lengths for compounds of the first (second) group are equal to +0.028 (+0.137) and 1.434 (1.342) Å, respectively.

Although the second group (involving only seven compounds) is insufficiently representative, the inference can be made that there is a tendency toward antibatic and symbatic correlations between the O–O distances and the parameters $\Delta(O_2)$ [$\Delta'(O_2)$] for the first and second groups, respectively. The first correlation can be treated as "normal" (expected), because the shortening of the O–O bond should be considered an indication of transfer of the electron density from the upper completed (antibonding) π^* orbital of the peroxo group to the metal atom, which leads to a weakening of the bond with the *trans* partner. In particular, it should be noted that the O–O bonds are substantially shortened in structures with π-acceptor chelating ligands (*Bipy*, *Phen*) lying in the equatorial plane, which most likely enhances the π-donation from O_2 groups to metal atoms [81]. For example, this is true in regard to structures **XVI**, **XVII**, and **XXV**. The correlation in the second group of compounds (if ever exists) is sufficiently unexpected, because it is not consistent with the model concepts. Most probably, the scatter of points corresponding to compounds of this group indicates that, in complexes with symmetric chelating partners in *trans* positions with respect to both multiply bonded ligands, the *trans* extension is specific to the oxo and peroxo groups. The origin of this behavior remains unclear.

The shortening of O–O bonds in $VO(O_2)$ complexes should be attended by a decrease in the OVO angles in dioxygen ligands (Table 4). Indeed, the dependence of the O–O bond length on the OVO angle in η^2-coordinated peroxo groups in pseudooctahedral oxoperoxo complexes of vanadium(V) exhibits an almost linear behavior (Fig. 9). The sole obvious "outlier" is provided by structure **X**.

7. DISTANCES V–(O_2) AND LENGTHS OF V–O(PEROXO) MULTIPLE BONDS

The shortening of the O–O bond in the η^2-dioxygen ligand implies an enhancement of the transfer of the electron density from this ligand to the central atom and, in principle, should be accompanied by the shortening of the three-center O_2–V multiple bond [82]. Such a correlation (the general tendency) can actually be observed in Fig. 10. The O–O bond lengths in the range 1.360–1.457 Å for 27 oxo monoperoxo complexes presented in Table 4 correspond to the V–O(peroxo) distances in the range 1.853–1.889 Å. The shortest O–O bonds in structures **XVI** (1.236 Å), **XVII** (1.30 Å), **XX** (1.29 Å), and **XLIX** (1.347 Å) correspond to the short V–O(peroxo) bonds (1.840, 1.845, 1.836, and 1.837 Å, respectively).[13] This tendency is violated in two compounds; namely, (i) in complex **IV**,

[13] In structure **XX**, the statistical superposition of the O(oxo) atom and one of the O(peroxo) atoms leads to an underestimation of one of the V–O(O_2) bond lengths.

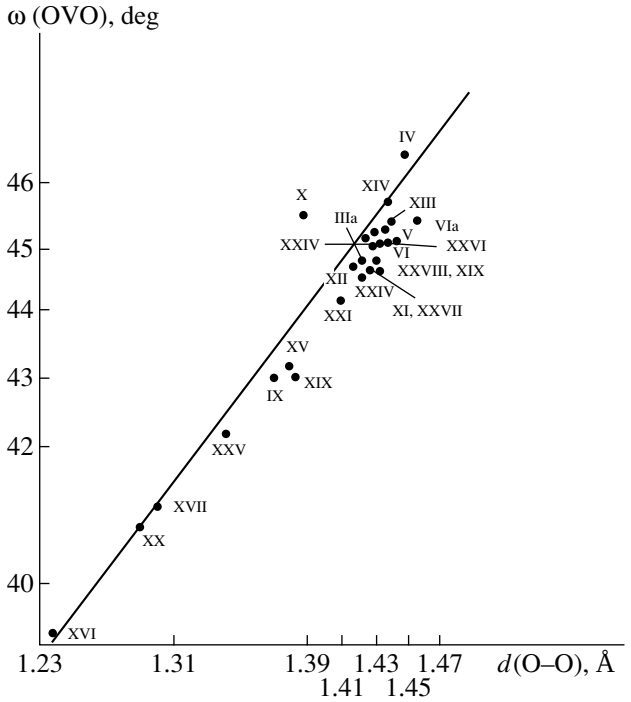

Fig. 9. Dependence of the ω(OVO) angle on the O–O bond length in peroxo groups of the $VO(O_2)$ pseudooctahedral complexes.

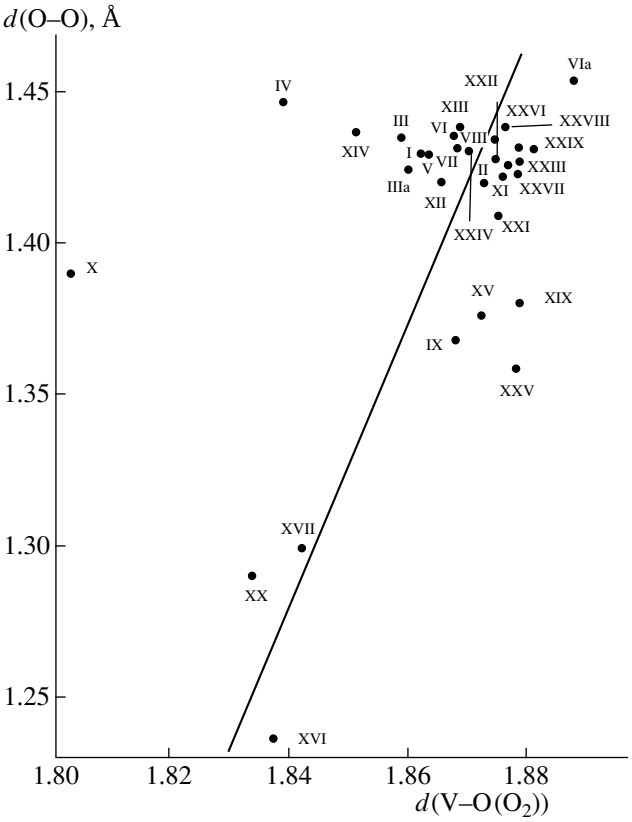

Fig. 10. Dependence of the O–O bond length on the $V–O(O_2)$ bond length in structures of the $VO(O_2)$ pseudooctahedral complexes.

the standard O–O bond length [1.45(1) Å] corresponds to short $V–O(O_2)$ distances [1.841(9) ± 0.007 Å], and, especially, (ii) in the complex $(NH_4)_{1.5}[VO(O_2)(Edta H)]$ (**X**) [15], the O–O bond [not the shortest bond, 1.39(2) Å] corresponds to the shortest mean $V–O(O_2)$ distance [1.805(10) ± 0.070 Å]. In this complex, the peroxo group is drastically asymmetric with respect to the vanadium atom: the V–O distance to one of the oxygen atoms is 0.14 Å shorter than that to the second atom.[14] Possibly, this asymmetry (if it actually exists, rather than stemming from the low quality of the crystal) decreases the transfer of the electron density to the metal atom. In the other compounds presented in Table 4, the difference between the $V–O(O_2)$ distances is considerably less and, for the most part, does not exceed 0.015 Å.

A comparison of the pseudooctahedral oxo monoperoxo complexes and the oxo diperoxo complexes with the pseudotrigonal bipyramidal and pseudotetrahedral coordination of the metal atoms revealed a clear symbatic correlation of the variations in the $V–O(O_2)$ and O–O bond lengths. As was noted above, the O–O distances in the last complexes are longer than similar distances in pseudooctahedral complexes. Correspondingly, the mean lengths of the $V–O(O_2)$ bonds in these complexes are also the largest (1.872–1.915 Å for 17 compounds in Table 5). Most likely, one of the factors responsible for the weakening of transfer of the electron density in these complexes lies in the increase in the number of multiply bonded ligands. This implies that, first, two peroxo groups compete with each other for the donation of electrons to the metal atom and, second, the peroxo groups are necessarily oriented with a substantial asymmetry due to steric hindrances between equatorial ligands. Up to this point, we have considered the mean values of two $V–O(O_2)$ bond lengths. However, closer examination demonstrates that these bonds, as a rule, are nonequivalent in the η^2 coordination of dioxygen ligands. In this case, the degree of their asymmetry is determined by the geometry of coordination polyhedra of metal atoms. In diperoxo complexes of transition metals [in particular, vanadium(V)] with coordination polyhedra in the form of a pseudotrigonal bipyramid (a pentagonal bipyramid) or a pseudotetrahedron (a pentagonal pyramid), the lengths of two $M–O(O_2)$ bonds in both equatorial peroxo ligands differ significantly. Note that the $M–O(O_2)_{cis}$ bonds, which are located closer to the equatorial donor atom of the *L* heteroligand, are longer than the $M–O(O_2)_{trans}$ bonds, which occupy adjacent positions and are far from this atom. It can be seen from Table 5 that, for 15 compounds, the mean lengths of the $V–O(O_2)_{cis}$ bonds fall in the range 1.893–1.945 Å and the mean lengths of the

[14] A similar asymmetry of the $V–O(O_2)$ bonds (1.790 and 1.929 Å), which is revealed in structure **III** [7], most likely, can be associated with the erroneous choice of the noncentrosymmetric space group $Pna2_1$ instead of the true centrosymmetric space group *Pnam* (**IIIa** [8]).

Table 7. Geometric characteristics of the distortion of the coordination polyhedra of the metal atoms in oxoperoxo complexes of vanadium(V)

No.	Coordination polyhedron	Distance, Å			
		Δ_V	$(\Delta_{eq})_{max}$	$(\Delta_{eq})_{mean}$	V–L_{axial}
IV	PO	0.211	0.037		2.108 O(*Nta*)
VIa	PO	0.260	0.070		2.239 O(*Cmida*)
VII	PO	0.239	0.017		2.223 O(*Ceida*)
X	PO	0.24	0.13		2.32 N(*Edta*H)
XIII	PO	0.250	0.005	0.003	2.211 O(H_2O)
XVIII	PO	0.27			2.270 N(*Bipy*)
XXII	PO	0.247	0.064	0.049	2.142 O(*Ox*)
XXVI	PO	~0.30			2.286 O(*Mal*H)
XXVII	PO	0.24			2.561 O(*Cit*H)
XXIX	PO	0.28			2.375 O(*Ida*)
XXXI	PTBP	0.359	0.062	0.051	2.301 O(CO_3)
XXXII	PTBP	0.276	0.046	0.031	2.251 O(*Ox*)
XXXIX	PTBP	0.318	0.011	0.008	2.288 N(*Bipy*)
XL	PTBP	0.284	0.036	0.020	2.284 N(*Bipy*)
XLI	PTBP	0.309	0.032	0.024	2.306 F_{term}
XLII	PTBP	0.308			2.290 N(*Bipy*)
XLIIIa	PTBP	0.451; 0.442	0.065; 0.050	0.042; 0.030	2.525; 2.478 O(O_2)
XLIV	PTBP	0.453; 0.444	0.068; 0.042		2.520; 2.488 O(O_2)
XLV	PTBP	0.316; 0.371			2.351; 2.411 O(O_2)
XLVI	PTBP	0.287; 0.301	0.045; 0.042		2.119 F_{br}
XLVII	PTBP	0.364		0.040	2.505 O_{oxo}
LI	PTP (PO?)	0.32	0.10		2.550 O(H_2*Mand*)
XXX	PO (PTP?)	~0.4			2.660; 2.573 O(O_2)
LII	PT	0.461	0.071	0.065	2.926 O_{oxo}
LIII	PT	~0.5			>3.1
LIV	PT	0.457; 0.471	0.039; 0.051	0.027; 0.034	>3.1
LV	PT	0.47; 0.53		0.04; 0.06	>3.1
LVI	PT	0.485; 0.502	0.014; 0.075		2.597; 2.606 O(O_2)
LVII	PT	0.509; 0.479	0.026; 0.114		2.707; 2.697 O(O_2)
LVIII	PT	0.522; 0.469	0.051; 0.069		2.980; 2.764 O(O_2)

Note: PO is a pseudooctahedron, PTBP is a pseudotetragonal bipyramid, PTP is a pseudotetragonal pyramid, PT is a pseudotetrahedron, Δ_V is the deviation of the vanadium atom from the root-mean-square equatorial plane, and $(\Delta_{eq})_{max}$ and $(\Delta_{eq})_{mean}$ are the maximum and mean deviations of the equatorial donor atoms from the root-mean-square equatorial plane, respectively. The designations of axial ligands L_{axial} are given in Tables 1–3.

V–$O(O_2)_{trans}$ bonds lie in the range 1.861–1.890 Å (their difference $\Delta_{cis–trans}$ varies from 0.016 to 0.072 Å).[15] Moreover, the $L_{equat}VO_{cis}$ angles (84.8°–90.0°) are substantially smaller than the $L_{equat}VO_{trans}$ angles (128.6°–134.3°), and the $VO_{cis}O_{trans}$ angles (65.2°–66.7°) are smaller than the $VO_{trans}O_{cis}$ angles (67.5°–69.7°).[16]

In pseudooctahedral oxo monoperoxo complexes of vanadium(V), both oxygen atoms of the O_2 ligand are equivalent with respect to the adjacent equatorial *cis* ligands. In these compounds, the asymmetry in the

[15]The sole exception is provided by compound **LII** with a symmetric coordination of the O_2 ligand [V–$O(O_2)_{cis}$, 1.872 Å; V–$O(O_2)_{trans}$, 1.871 Å] and, especially, complex **LIII**, in which the V–$O(O_2)_{cis}$ bond (1.866 Å) is 0.037 Å shorter (rather than longer) than the V–$O(O_2)_{trans}$ bond (1.903 Å).

[16]The asymmetry of the V–O(peroxo) bonds in oxoperoxo complexes of transition metals is thoroughly considered in [41, 82].

Table 8. Selected bond angles (deg) in oxo monoperoxo complexes of vanadium(V)

No.	O(oxo)–V–O(O_2)	O(O_2)–V–L_{trans}	O(oxo)–V–L_{trans}	L_{trans}–V–L_{cis}
I	104.8(2) ± 0.04	152.2(2) ± 1.2	166.9(2)	149.2(1)
II	105.2 ± 1.1	152.4 ± 0.3	167.3	150.4
III			165.8(2)	
IIIa	103.74(4)	153.6(1)	165.87(3)	150.83(2)
IV	104.8 ± 1.5	151.3 ± 0.5	166.7	149.5
V	105.32(7) ± 0.13		167.72(7)	150.28(6)
VI	104.83(5) ± 1.18		166.94(5)	150.39(4)
VIa	104.8(1) ± 1.3	151.5(1) ± 0.9	166.9(1)	150.4(1)
VII	104.11(9) ± 1.00	153.42(8) ± 1.16	172.84(8)	150.07(8)
VIII	102.5 ± 0.00	154.2 ± 0.3	173.4	149.7
IX	100(2) ± 2	154.5(1.0) ± 1.5	167(2)	150(2)
X	101.7(8) ± 1.4	155.6(4) ± 1.2	161.6(7)	149.3(6)
XI	103.15(7) ± 1.03			
XII	104.33(9) ± 0.38		164.35(8)	149.70(7)
XIII	102.1(1) ± 0.2	152.9(1) ± 0.1	172.1(1)	147.2(1)
XIV	98.6 ± 1.2	152.0 ± 1.6	173.3	145.6
XV	102.8 ± 1.0	154.9 ± 0.4	170.6	156.1
XVI	105.1(2) ± 0.7	154.7(2) ± 5.0	162.8(2)	157.8(2)
XVII	104.4(8) ± 0.5	154.5(8) ± 4.4	163.6(6)	157.8(7)
XVIII			166.4(2)	
XIX	102.75(9) ± 0.57	151.63(8) ± 0.18	168.43(8)	150.28(8)
XX	102.2(5) ± 1.6	155.1(4) ± 3.4	168.1(4)	152.8(4)
XXI	103.12(6) ± 1.09	153.16(5) ± 0.97	163.65(6)	152.30(5)
XXII	102.9(3) ± 0.2	154.4(2) ± 2.0	166.0(2)	153.0(1)
XXIII	103.1(1) ± 1.1	152.5(1) ± 3.8	168.3(1)	155.6(1)
XXIV	102.22(8) ± 1.23			
XXV	99.7(6) ± 3.7	156.0(5) ± 11.7	168.9(4) ± 1.1	151.4(4) ± 2.0
XXVI	101.18(6) ± 1.01	149.91(6) ± 1.78	173.52(6) ± 0.05	149.06(5) ± 0.09
XXVII	101.80(7) ± 1.23	145.55(6) ± 0.35	175.54(6)	149.72(5)
XXVIII	102.4(3) ± 0.4	148.7(2) ± 1.1	167.9(2) ± 0.3	145.9(2) ± 0.5
XXIX			175.4(2)	
XXX	104.2(2) ± 3.4	144.8(2) ± 4.6	176.4(2) ± 0.2	150.5(2) ± 0.3

coordination of the dioxygen ligand, as a rule, is considerably less pronounced. In the vast majority of complexes, the differences $\Delta_{cis-trans}$ fall in the range 0.002–0.030 Å. In structure **IIIa**, both V–O(O_2) bonds are crystallographically equivalent and, correspondingly, are equal in length. It should be noted that, in these complexes, the somewhat shorter V–O$(O_2)_{trans}$ bond is more linear with respect to the oppositely located donor atom than the longer V–O$(O_2)_{cis}$ bond. For example, in the complexes $[VO(O_2)(Bipy)_2]^+$ (**XVI**) and $[VO(O_2)(Phen)_2]^+$ (**XVII**), the $O_{trans}VN$ angles are equal to 159.7° and 158.9° and the $O_{cis}VN$ angles are 149.7° and 150.2°, respectively [20].

Let us now consider in greater detail the dimeric oxo diperoxo complexes of vanadium(V), which contain both the η^2-coordinated O_2 ligands and the peroxo ligands with a chelating–bridging (η^2,μ^n) function (Table 6).

In three compounds with dimeric anionic complexes of the general formula $[\{VO(O_2)\}_2(\mu\text{-}L)^{-m}(\mu^{0.5}\text{-}O_2)_2]^{-m-2}$ [L = OH^- (**XLIII**), O^{2-} (**XLIV**), PO_4^{3-} (**XLV**)], the vanadium atoms are linked not only by the bridging L ligands but also by two chelating–bridging (η^2,$\mu^{0.5}$) peroxo ligands due to weak (semicoordination) V⋯O$(O_2)_{cis}$ bonds. The V–O$(O_2)_{cis}$ bonds with the

chelating–bridging oxygen atoms (1.908–1.916 Å), on average, are 0.015–0.027 Å longer than the V–$O(O_2)_{cis}$ bonds with the chelating oxygen atoms of the $\eta^2,\mu^{0.5}$- and η^2-peroxo ligands (1.887–1.896 Å) and are naturally longer than the V–$O(O_2)_{trans}$ (η^2) bonds (1.863–1.880 Å).

In the dimeric anionic complex $[\{VO(O_2)F\}_2(\mu\text{-}F)(\mu^2\text{-}O_2)_2]^{3-}$ of structure **XLVI** (Table 6), one of three peroxo groups fulfills an unusual chelating–bridging (η^2,μ^2) function: either of the two oxygen atoms $O(O_2)_{cis}$ and $O(O_2)_{trans}$ forms coordination bonds with two metal atoms. Note that the geometric parameters of the η^2- and η^2,μ^2-peroxo ligands differ significantly. Apart from the elongation of the V–$O(O_2)$ bridging bonds as compared to the chelating bonds, the mean difference $\Delta_{cis-trans}$ between the V–$O(O_2)_{cis}$ (1.872 Å) and V–$O(O_2)_{trans}$ (1.864 Å) bond lengths in the η^2-peroxo ligands is equal to only 0.008 Å. At the same time, the difference $\Delta_{cis-trans}$ between the corresponding bonds (2.046 and 1.975 Å) in the η^2,μ^2-peroxo ligands is considerably larger (0.071 Å). Furthermore, in the η^2-peroxo ligands, the O–O bonds (1.444 Å), on average, are 0.023 Å shorter and the $O(O_2)$–V–$O(O_2)$ angles (45.5°) are 2.9° larger than those in the η^2,μ^2-peroxo ligands (1.467 Å and 42.6°, respectively).

In the dimeric anionic complexes $[\{VO(O_2)\}(\mu^1\text{-}O_2)(\mu^{0.5}\text{-}O_2)_2\ \{VO(H_2O)\}]^{2-}$ of structures **LVI**–**LVIII** (Table 6), four peroxo ligands are coordinated to the vanadium atoms in three modes, namely, as two chelating–bridging η^1,μ^1-peroxo ligands, one chelating–bridging $\eta^2,\mu^{0.5}$-peroxo ligand, and one chelating η^2-peroxo ligand. The semibridging function is fulfilled by the $O(O_2)_{cis}$ atom in one of the two $\eta^2,\mu^{0.5}$ ligands and by the $O(O_2)_{trans}$ atom in the other ligand (recall that, in structures **XLIII**–**XLV**, only the $O(O_2)_{cis}$ atoms fulfill a $\mu^{0.5}$ function). In the η^2,μ^1-peroxo ligand, $O(O_2)_{trans}$ is the bridging atom. Note that the V–$O(O_2)_{cis}$ and V–$O(O_2)_{trans}$ bonds lengths in the η^2- and $\eta^2,\mu^{0.5}$-peroxo ligands, regardless of their function (chelating, semibridging), are close to each other: the mean lengths of the V–$O(O_2)_{cis}$ (η^2), V–$O(O_2)_{cis}$ ($\eta^2,\mu^{0.5}$), V–$O(O_2)_{trans}$ (η^2), and V–$O(O_2)_{trans}$ ($\eta^2,\mu^{0.5}$) bonds for three compounds are equal to 1.879 ± 0.017, 1.877 ± 0.008, 1.880 ± 0.004, and 1.871 ± 0.007 Å, respectively. The V(2)–O(6) bridging bond (Fig. 7) with the $O(O_2)_{trans}$ atom in the chelating–bridging η^2,μ^1-peroxo ligand is substantially longer (the mean bond length is 1.936 ± 0.017 Å). The μ^1-peroxo bridge in structures **LVI**–**LVIII** is asymmetric: the V(1)–O(6) bond (the mean bond length is 2.037 ± 0.008 Å) with the peroxo ligand coordinated to the vanadium atom in a monodentate mode, on average, is 0.101 Å longer than the V(2)–O(6) bond. The coordination environment of the V(1) and V(2) atoms in these three structures is also asymmetric: in addition to the coordination of the oxo ligand, the bridging $\mu^{0.5}$-$O(O_2)$ atom of the $\eta^2,\mu^{0.5}$-peroxo ligand [*trans* to O(oxo)], and two η^2-$O(O_2)$ atoms of the second $\eta^2,\mu^{0.5}$-peroxo ligand, the V(1) atom coordinates two O(1, 2) atoms of the η^2-peroxo ligand and the O(6) atom of the η^2,μ^1-peroxo ligand (in a monodentate mode) and the V(2) atom coordinates the O(21) atom of the water molecule and the O(6, 7) atoms of the η^2,μ^1-peroxo ligand (in a bidentate mode) (Fig. 7).

8. DISTORTIONS OF COORDINATION POLYHEDRA OF VANADIUM(V)

In mononuclear oxoperoxo complexes of vanadium(V), there are five types of metal–ligand distances. These are short distances to multiply bonded oxo ligands, longer distances to oxygen atoms of multiply bonded peroxo ligands, the longest distances to ligands (atoms) in *trans* positions with respect to oxo ligands, the second longest distances to ligands (atoms) in *trans* positions with respect to peroxo ligands, and intermediate (standard) distances to ligands (atoms) in *cis* positions with respect to peroxo and oxo ligands. The corresponding lengths of the vanadium–oxygen bonds lie in the following ranges: 1.58–1.71 Å (O_{oxo}), 1.80–1.94 Å (O_{peroxo}), 2.09–2.31 Å (O_{axial}, *trans* to O_{oxo}), 2.02–2.15 Å (O_{equat}, *trans* to O_{peroxo}), and 1.97–2.07 Å (O_{equat}, *cis* to O_{oxo}, O_{peroxo}). This nonequivalence of the metal–ligand distances leads to regular distortions of the coordination polyhedra of vanadium atoms.

Specifically, the presence of the multiply bonded oxo ligand at a very short distance from the metal atom brings about the repulsion of the electron clouds of the V=O_{oxo} π bond and V–L_{equat} σ bonds and the displacement of equatorial donor atoms downward (or toward the oppositely located axial ligand in pseudooctahedral and pseudotrigonal bipyramidal complexes). As a consequence, the vanadium atom is substantially displaced from the equatorial plane formed by five approximately coplanar donor atoms (namely, two or four peroxo oxygen atoms and three or one donor atoms of the concomitant ligands) toward the axial oxo ligand. Table 7 presents the geometric characteristics of these displacements Δ_V in 30 compounds, for which the corresponding data were obtained in original works.

As can be seen from Table 7, the quantities Δ_V vary over a wide range (0.2–0.5 Å). Moreover, there is a clear correlation between the coordination number (or polyhedron type) of the metal atom and the quantity Δ_V, which increases with a decrease in the coordination number. Actually, the values of Δ_V are equal to 0.21–0.30 Å (mean value, 0.254 Å) for 10 pseudooctahedral (pentagonal bipyramidal) complexes [the coordination number is six (seven)], 0.28–0.45 Å (mean value, 0.343 Å) for 11 pseudotrigonal bipyramidal (pentagonal bipyramidal) complexes [the coordination number is five (seven)], 0.32 and 0.40 Å (mean value, 0.36 Å)

for 2 pseudotrigonal pyramidal (pentagonal pyramidal) complexes [the coordination number is five (six)], and 0.46–0.53 Å (mean value, 0.488 Å) for 7 pseudotetrahedral (pentagonal pyramidal) complexes [the coordination number is four (six)].

The lengths of the axial V–L_{axial} bonds with the oxygen, nitrogen, or fluorine donor atoms in the *trans* position with respect to the oxo ligand are given in the last column of Table 7. The lengths of these bonds (elongated as a result of the *trans* effect of the multiply bonded oxo ligand) fall in a very wide range. In a number of cases, this complicates the unique identification of the coordination polyhedron of the metal atom. As was noted above, additional contacts (2.35–3.00 Å) between the vanadium atom and the chelating–bridging peroxo ligands, bridging oxo ligands, or oxygen atoms of H_2*Mand* solvate molecules (in structure **LI**) are treated as semicoordination bonds (with a conditional multiplicity of 0.5). The V–L_{axial} contacts whose length exceeds 3.1 Å indicate the lack of bonding. Within this approach, the anionic complexes of compounds **LVI**–**LVIII** can be represented as both pseudotetrahedral and pseudotrigonal bipyramidal polyhedra. Similarly, the V$\cdot\cdot$O(H_2*Mand*) contact (2.550 Å) in structure **LI** completes the coordination polyhedron of the metal atom (pseudotrigonal pyramid) to the pseudooctahedron. The structure of compound **LI** is described in Section 4 (not in Section 2.3) together with the structures of compounds **XLVIII**–**L**, because all four compounds contain similar dimeric anionic complexes $[\{VO(O_2)\}_2(\mu\text{-}L^2)_2]^{2-}$, which involve dianions of α-hydroxycarboxylic acids as chelating–bridging ligands L^2.

The angular distortions of vanadium polyhedra are conveniently considered by using the example of pseudooctahedral oxo monoperoxo complexes **I**–**XXX** (Table 8). In particular, the angle between the V–O_{oxo} bonds and the plane of the V(O_2) triangle regularly increases to 98.6°–105.3°. The bonds with the three remaining atoms of the *L* ligands that occupy the *cis* positions with respect to the oxo ligand also deviate from the equatorial plane ($O_{oxo}VL_{cis}$ angles > 90°). As a result, the angles between two *trans* V–*L* bonds ($L_{cis}VL_{cis}$ angles in Table 8) are decreased to 147.2°–157.8°. The deviation of the coordination polyhedron from orthogonality due to ligand–ligand nonbonded interactions leads to a nonlinear arrangement of the V–O_{oxo} and V–L_{trans} bonds: the angle between these bonds in structures **I**–**XXX** is decreased to 161.6°–175.5°. It can be seen from Table 8 that the nonlinearity of the O(O_2)–V–L_{trans} fragments is even more pronounced than that of the O_{oxo}–V–L_{trans} fragments: the corresponding angles fall in the range 145.6°–156.0°. This situation is quite predictable, because the ligands in the *trans* positions with respect to the O_2 and O_{oxo} ligands are simultaneously the *cis* ligands with respect to the O_{oxo} and O_2 ligands and the repulsion of the *cis* ligands from the V–O_{oxo} bond should be stronger than that from the V–O_{peroxo} bond.

9. CONCLUSIONS

Thus, the main structural features of oxoperoxo complexes of vanadium(V) can be summarized as follows.

(i) The oxo and peroxo ligands occupy *cis* positions.

(ii) The geometric parameters of the peroxo ligand [V–O(O_2), O–O bond lengths; OVO(peroxo) angles] depend on the type of coordination seven-vertex polyhedron of the metal atom (pseudooctahedron or pseudotrigonal bipyramid).

(iii) The coordination polyhedra of vanadium atoms are characterized by regular distortions.

(iv) The structural manifestation of the *trans* effect of the peroxo ligand is slightly less than or comparable in magnitude to that of the oxo ligand in pseudooctahedral oxo monoperoxo complexes of vanadium(V).

ACKNOWLEDGMENTS

The author would like to thank A.V. Churakov for his assistance in using the Cambridge Structural Database (version 5.2.2, October 2001) [83] and acknowledges the support of the Russian Foundation for Basic Research in the payment of the license for using the Cambridge Structural Database (project no. 02-07-90322).

REFERENCES

1. H. Mimoun, Isr. J. Chem. **23**, 451 (1983).
2. A. P. Makarov, A. E. Gekhman, V. M. Nekipelov, *et al.*, Izv. Akad. Nauk SSSR, Ser. Khim., No. 8, 1914 (1985).
3. I. I. Vol'nov, *Peroxocomplexes of Vanadium, Niobium, and Tantalum* (Nauka, Moscow, 1987).
4. A. Butler, M. J. Clague, and G. E. Meister, Chem. Rev. **94** (3), 625 (1994).
5. D.-X. Wu, X.-J. Lei, R. Cao, and M.-C. Hong, Jiegou Huaxue **11** (1), 65 (1992).
6. J.-G. Wei, S.-W. Zhang, C.-Q. Huang, and M.-C. Shao, Polyhedron **13** (10), 1587 (1994).
7. C. Djordjevic, P. L. Wilkins, E. Sinn, and R. J. Bucher, Inorg. Chim. Acta **230** (2), 241 (1995).
8. A. E. Lapshin, Y. I. Smolin, Y. F. Shepelev, *et al.*, Acta Crystallogr., Sect. C: Cryst. Struct. Commun. **49** (5), 867 (1993).
9. L. Kuchta, M. Sivák, and K. F. Ravelčik, J. Chem. Res., Synop. **393** (1993); J. Chem. Res., Miniprint, 2801 (1993).
10. G. J. Copas, B. J. Hamstra, J. W. Kampf, and V. L. Recoraro, J. Am. Chem. Soc. **118** (14), 3469 (1996).
11. G. J. Copas, B. J. Hamstra, J. W. Kampf, and V. L. Recoraro, J. Am. Chem. Soc. **116** (8), 3627 (1994).
12. M. Sivák, J. Turselová, and F. Povelčik, Polyhedron **15** (7), 1057 (1996).

13. M. Sivák, V. Suchá, L. Kuchta, and J. Marek, Polyhedron **18** (1–2), 93 (1999).
14. L. Kuchta, M. Sivák, J. Marek, *et al.*, New J. Chem. **23** (1), 43 (1999).
15. A. E. Lapshin, Yu. I. Smolin, Yu. F. Shepelev, *et al.*, Kristallografiya **37** (6), 1415 (1992) [Sov. Phys. Crystallogr. **37**, 764 (1992)].
16. K. Kanamori, K. Nashida, N. Miyata, and K. Okamoto, Chem. Lett., 1267 (1998).
17. R. E. Drew and W. B. Einstein, Inorg. Chem. **12** (4), 829 (1973).
18. M. Shao, X. Dong, and J. Tang, Sci. Sin. Ser. B **31**, 789 (1988).
19. M. Kosugi, S. Hikichi, M. Acita, and Y. Morooka, J. Chem. Soc. Dalton Trans., No. 9, 1369 (1999).
20. V. S. Sergienko, V. K. Borzunov, and M. A. Poraĭ-Koshits, Zh. Neorg. Khim. **37** (5), 1062 (1992).
21. H. Szentivanyi and R. Stomberg, Acta Chem. Scand. A **37** (7), 709 (1983).
22. V. S. Sergienko, M. A. Poraĭ-Koshits, B. K. Borzunov, and A. B. Ilyukhin, Koord. Khim. **19** (10), 767 (1993).
23. G. Suss-Fink, A. Stanislas, G. B. Shul'pin, *et al.*, J. Chem. Soc. Dalton Trans., No. 18, 3169 (1999).
24. R. Stomberg, Acta Chem. Scand. A **40** (2), 168 (1986).
25. H. Mimoun, L. Saussine, E. Daire, *et al.*, J. Am. Chem. Soc. **105** (10), 3101 (1983).
26. V. S. Sergienko, V. K. Borzunov, and M. A. Poraĭ-Koshits, Dokl. Akad. Nauk SSSR **301** (5), 1141 (1988).
27. C. Djordjevic, M. Lee-Renslo, and E. Sinn, Inorg. Chim. Acta **233** (1), 97 (1995).
28. C. Djordjevic, M. Lee, and E. Sinn, Inorg. Chem. **28** (4), 719 (1989).
29. P. Shwendt, P. Svancarek, L. Kuchta, and L. Marek, Polyhedron **17** (13–14), 2166 (1998).
30. C. Djordjevic, S. A. Craig, and E. Sinn, Inorg. Chem. **24** (9), 1281 (1985).
31. F. W. Einstein, R. J. Batcheloz, S. J. Angus-Dunne, and A. S. Tracey, Inorg. Chem. **35** (6), 1680 (1996).
32. M. A. Poraĭ-Koshits and L. O. Atovmyan, Koord. Khim. **1** (9), 1271 (1975).
33. V. S. Sergienko, Russ. J. Inorg. Chem. **48 (**Suppl. 1) (2003) (in press).
34. R. Stomberg, Acta Chem. Scand. A **39** (10), 725 (1985).
35. D. Begin, F. W. B. Einstein, and J. Field, Inorg. Chem. **14** (8), 1785 (1975).
36. N. J. Campbell, M. V. Capparelli, W. P. Griffith, and A. C. Skapski, Inorg. Chim. Acta **77** (2), L215 (1983).
37. A. Shaver, J. B. Ng, D. A. Hall, *et al.*, Inorg. Chem. **32** (14), 3109 (1993).
38. A. Shaver, D. A. Hall, J. B. Ng, *et al.*, Inorg. Chim. Acta **229** (2), 253 (1995).
39. A. Shaver, J. B. Ng, R. C. Hynes, and B. I. Posner, Acta Crystallogr., Sect. C: Cryst. Struct. Commun. **50** (7), 1044 (1994).
40. H. Szentivanyi and R. Stomberg, Acta Chem. Scand. A **37** (7), 553 (1983).
41. R. Stomberg and H. Szentivanyi, Acta Chem. Scand. A **38** (2), 121 (1984).
42. R. Stomberg, Acta Chem. Scand. A **38** (7), 541 (1984).
43. H. Szentivanyi and R. Stomberg, Acta Chem. Scand. A **38** (2), 101 (1984).
44. N. J. Campbell, J. Flanagan, W. P. Griffith, and A. C. Skapski, Transition Met. Chem. (London) **10** (2), 353 (1985).
45. V. K. Borzunov, L. Kh. Minacheva, and V. S. Sergienko, Zh. Neorg. Khim. **48** (12), 2015 (2002).
46. R. Stomberg, S. Olson, and I.-B. Svensson, Acta Chem. Scand. A **38** (8), 653 (1984).
47. P. Schwendt, J. Tyrselova, and F. Pavelcik, Inorg. Chem. **34** (7), 1964 (1995).
48. A. E. Lapshin, Y. I. Smolin, Y. F. Shepelev, *et al.*, Acta Crystallogr., Sect. C: Cryst. Struct. Commun. **46** (11), 1753 (1990).
49. R. Stomberg and S. Olson, Acta Chem. Scand. A **38** (10), 801 (1984).
50. V. S. Sergienko, V. K. Borzunov, and A. B. Ilyukhin, Koord. Khim. **21** (2), 108 (1995).
51. F. Takusagawa and A. Shimada, Chem. Lett., No. 10, 1089 (1973).
52. T. M. Spotswood and C. I. Tanzer, Aust. J. Chem. **20** (14), 1227 (1967).
53. S. Castallano, H. Gunther, and S. Ebersole, J. Phys. Chem. **69**, 4166 (1965).
54. I.-B. Svensson and R. Stomberg, Acta Chem. Scand. **25** (3), 898 (1971).
55. K. Weighardt and N. Quilitzsch, Z. Naturforsch. B **34** (2), 242 (1979).
56. P. Schwendt and D. Joniakova, Thermochim. Acta **68** (3), 297 (1983).
57. P. Svancarek, P. Schwendt, J. Tatiersky, *et al.*, Monatsch. Chem. **131** (1), 145 (2000).
58. F. Demartin, M. Biagioli, L. Strinna-Erre, *et al.*, Inorg. Chim. Acta **299** (1), 123 (2000).
59. P. Schwendt, P. Svancarek, I. K. Smatanova, and J. Marek, J. Inorg. Biochem. **80** (1–2), 59 (2000).
60. I. K. Smatanova, J. Marek, P. Svancarek, and P. Schwendt, Acta Crystallogr., Sect. C: Cryst. Struct. Commun. **56** (2), 154 (2000).
61. R. Stomberg, Acta Chem. Scand. A **40** (1), 168 (1986).
62. D. W. Wright, R. T. Chang, S. K. Mandal, *et al.*, J. Biol. Inorg. Chem. **1** (1), 143 (1996).
63. R. E. Drew and F. W. B. Einstein, Inorg. Chem. **11** (5), 1079 (1972).
64. D. C. Crans, A. D. Keramidas, H. Hoover-Litty, *et al.*, J. Am. Chem. Soc. **119** (23), 5447 (1997).
65. A. D. Keramidas, S. M. Miller, O. P. Anderson, and D. C. Crans, J. Am. Chem. Soc. **119** (38), 8901 (1997).
66. R. Stomberg, Acta Chem. Scand. A **38** (3), 223 (1984).
67. R. Stomberg and S. Olson, Acta Chem. Scand. A **38** (10), 821 (1984).
68. A. E. Lapshin, Y. I. Smolin, Y. F. Shepelev, *et al.*, Acta Crystallogr., Sect. C: Cryst. Struct. Commun. **46** (5), 738 (1990).
69. A. E. Lapshin, Y. I. Smolin, Y. F. Shepelev, *et al.*, Acta Crystallogr., Sect. C: Cryst. Struct. Commun. **45** (10), 1477 (1989).
70. V. Sucha, M. Sivak, J. Tyrselova, and J. Marek, Polyhedron **16** (16), 2837 (1997).

71. A. F. Ghiron and R. C. Thompson, Inorg. Chem. **29** (22), 4457 (1990).
72. A. Butler, M. J. Clague, and G. Meister, Chem. Rev. **94**, 625 (1994).
73. R. Stomberg, Acta Chem. Scand. **24** (6), 2024 (1970).
74. T. Nicholson and J. Zubieta, Inorg. Chim. Acta **134** (2), 191 (1987).
75. J. W. Egan, B. S. Haggerty, A. L. Rheingold, *et al.*, J. Am. Chem. Soc. **112** (6), 2446 (1990).
76. L. Vaska, Acc. Chem. Res. **9** (2), 175 (1976).
77. J. E. Newton and M. B. Hall, Inorg. Chem. **23** (26), 4627 (1984).
78. S. C. Abrahams and J. Kalnajs, Acta Crystallogr. **8** (3), 503 (1955).
79. R. Masse and A. Durif, J. Solid State Chem. **73** (2), 206 (1988).
80. H. D. Barcock and L. Herzberg, Astrophys. J. **108** (2), 167 (1948).
81. V. K. Borzunov, V. S. Sergienko, and M. A. Poraĭ-Koshits, Koord. Khim. **19** (10), 782 (1993).
82. P. Schwendt, K. Volka, and M. Suchanek, Spectrochim. Acta A **44** (5), 839 (1998).
83. F. H. Allen and O. Kennard, Chem. Design Autom. News **8** (1), 31 (1993).

Translated by O. Borovik-Romanova

Crystallography Reports, Vol. 49, No. 3, 2004, pp. 427–429. From Kristallografiya, Vol. 49, No. 3, 2004, pp. 492–494.

STRUCTURE OF ORGANIC COMPOUNDS

Crystallographic Investigations of 1,4-Benzothiazin-2(1H)one and 3-Methyl-1,4-Benzothiazin-2(1H)one[1]

Rajnikant*, V. K. Gupta*, Dinesh*, A. Kumar*, M. B. Deshmukh, D. K. Salunke**, A. R. Mulik**, and B. Varghese*****

** Crystallography Laboratory, Post-Graduate Department of Physics, University of Jammu, Jammu Tawi-180 006, India*

e-mail: rajni_kant_verma@hotmail.com

*** Department of Chemistry, Shivaji University, Kolhapur-416 004, Maharashtra, India*

**** Regional Sophisticated Instrumentation Centre, Indian Institute of Technology, Chennai-600 036, India*

Received April 2, 2001

Abstract—The crystal structures of 1,4-benzothiazin-2(1H)one (C_8H_7SNO) (**I**) and 3-methyl-1,4-benzothiazin-2(1H)one (C_9H_9SNO) (**II**) have been determined by X-ray diffraction methods. **I** crystallizes in the monoclinic system with space group $P2_1/n$, while **II** crystallizes in triclinic with space group $P\bar{1}$. The molecular features in both the structures are almost similar; however, there exists an intermolecular interaction in (**II**) that could be due to the methyl group. *© 2004 MAIK "Nauka/Interperiodica".*

INTRODUCTION

The reaction mechanism [1] for the synthesis of both the compounds is shown in Fig. 1.

EXPERIMENTAL

Three-dimensional intensity data of **I** (m.p. 448 K) and **II** (m.p. 398 K) were collected on an Enraf-Nonius CAD-4 diffractometer using MoK_α radiation with a ω/2θ-scan mode. The cell parameters were obtained from a least-squares fit of the setting angle of 25 reflections in the range of $11.96° < \theta < 14.21°$ for **I** and $10.73° < \theta < 14.11°$ for **II**. For both compounds, two standard reflections showed no significant variation in the intensity data. The reflection data were corrected for Lorentz and polarization effects. Absorption and extinction corrections were not applied.

Both the crystal structures have been solved by using the SHELXS97 program [2], and all non-hydrogen atoms were located using the E-map. Full-matrix

[1] This article was submitted by the authors in English.

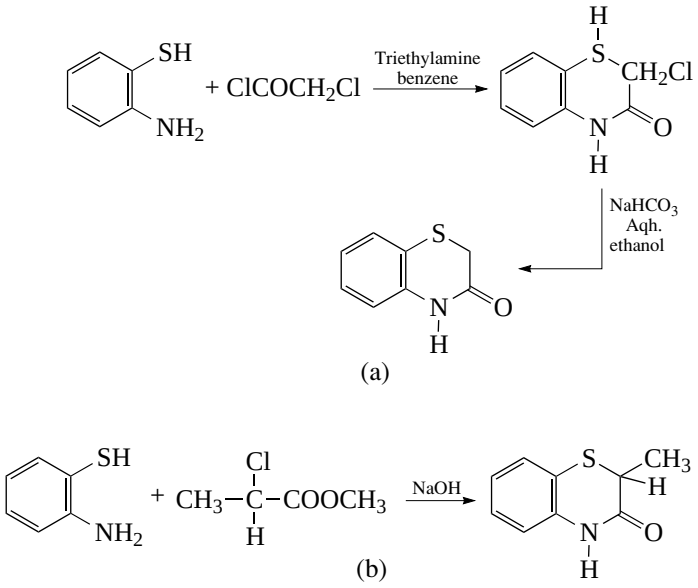

Fig. 1. Reaction mechanism for (**I**) (a), reaction mechanism for (**II**) (b).

1063-7745/04/4903-0427$26.00 © 2004 MAIK "Nauka/Interperiodica"

Table 1. Crystal data and details of the X-ray diffraction experiment for structures **I** and **II**

Empirical formula	C_8H_7NOS (**I**)	C_9H_9NOS (**II**)
Formula weight	165.21	179.23
Crystal system	Monoclinic	Triclinic
Space group	$P2_1/n$	$P\bar{1}$
a, Å	8.031(5)	4.700(3)
b, Å	4.502(2)	8.651(4)
c, Å	20.860(8)	11.496(3)
α, deg	90.0	112.01(3)
β, deg	98.77(4)	91.63(4)
γ, deg	90	94.01(4)
V, Å^3	745.4(7)	431.6(3)
Z	4	2
ρ_{calcd}, g/cm^3	1.472	1.379
Crystal size, mm	$0.1 \times 0.1 \times 0.2$	$0.3 \times 0.1 \times 0.1$
θ range for data collection, deg	$2.61 < \theta < 24.93$	$2.54 < \theta < 24.98$
Reflections collected/unique	1442/1250	1723/1522
Data/parameters	1250/129	1522/146
GooF	1.042	1.159
R_1/wR_2	0.0536/0.1272	0.0383/0.0994
$\Delta\rho_{max}/\Delta\rho_{min}$, eÅ^{-3}	0.509/–0.278	0.310/–0.216

least-squares refinement of the structures has been carried out by using the SHELXL97 program [3]. The positional and thermal parameters of non-hydrogen atoms were refined isotropically. All the hydrogen atoms were located from a difference Fourier map, and their positional and isotropic temperature factors were refined. Few cycles of refinement with anisotropic thermal parameters for non-hydrogen atoms resulted in a final value of *R*-factor 0.053 for **I** and 0.038 for **II**, respectively. Atomic scattering factors were taken from [4]. The crystallographic data for both structures are listed in Table 1.

RESULTS AND DISCUSSION

The final crystallographic information is deposited in the Cambridge Crystallographic Data Center (deposit CCDC nos. 213 596 and 213 597). Some selected bond lengths, bond angles, and torsion angles are depicted in Tables 2, 3, and 4, respectively. A general view of the molecule, indicating the atomic numbering scheme (thermal ellipsoids drawn at 50% probability), is shown in Fig. 2 for both structures [5]. Geometrical calculations were performed using the PARST program [6].

The bond distances and angles agree well with the values reported in the literature for some analogous structures [7–12]. The bond length C(2) = O(1) (1.231(3) Å) in **II** is slightly less than that of 1.243(5) Å, as observed in **I**. The C–H···O intermolecular interaction in molecule **II** (C(3)···O(1) 3.406, H(31)···O(1) 2.490 Å, angle C(3)2H(31)···O(1) 152.9°; symmetry code: *x* + 1, *y*, *z*) is weak and can hardly account for the slight variation observed in the bond length C(2)=O(1). The bond shortening, however, could be due to the electron effect of the methyl group located C(3). In both the molecules (**I** and **II**), an intermolecular N–H···O hydrogen bond (N(1)···O(1) 2.885, H(1)···O(1) 2.040 Å,

Table 2. Selected bond distances *d* (Å) for structures **I** and **II**

Bond	*d* (I)	*d* (II)
O(1)–C(2)	1.243(5)	1.231(3)
N(1)–C(2)	1.321(5)	1.338(4)
N(1)–C(9)	1.416(5)	1.407(3)
C(2)–C(3)	1.515(6)	1.516(4)
C(3)–S(4)	1.797(4)	1.812(2)
S(4)–C(10)	1.757(3)	1.750(3)
C(3)–C(11)		1.510(5)

Table 3. Selected bond angles ω (deg) for structures **I** and **II**

Angle	ω (I)	ω (II)
C(2)–N(1)–C(9)	127.4(3)	127.8(2)
O(1)–C(2)–N(1)	122.4(4)	121.5(2)
N(1)–C(2)–C(3)	117.7(4)	117.4(2)
O(1)–C(2)–C(3)	119.8(3)	120.9(2)
C(2)–C(3)–S(4)	112.1(3)	110.8(1)
C(3)–S(4)–C(10)	98.3(2)	99.2(1)
N(1)–C(9)–C(8)	118.5(3)	119.0(2)
N(1)–C(9)–C(10)	120.8(3)	121.3(2)
S(4)–C(10)–C(9)	120.5(3)	120.2(2)
S(4)–C(10)–C(5)	120.3(3)	120.4(2)
C(6)–C(5)–C(10)	119.8(4)	120.6(2)
C(5)–C(6)–C(7)	121.3(4)	120.3(2)
C(2)–C(3)–C(11)		112.1(2)
S(4)–C(3)–C(11)		109.0(2)

Table 4. Selected torsion angles φ (deg) for structures **I** and **II**

Angle	φ (I)	φ (II)
C(2)–N(1)–C(9)–C(10)	19.9(6)	–17.8(4)
C(9)–N(1)–C(2)–C(3)	4.2(6)	–7.2(3)
N(1)–C(2)–C(3)–S(4)	–42.7(5)	43.9(3)
C(2)–C(3)–S(4)–C(10)	50.8(3)	–51.0(2)
C(3)–S(4)–C(10)–C(9)	–31.8(3)	31.8(2)
N(1)–C(9)–C(10)–S(4)	0.5(5)	–1.0(3)

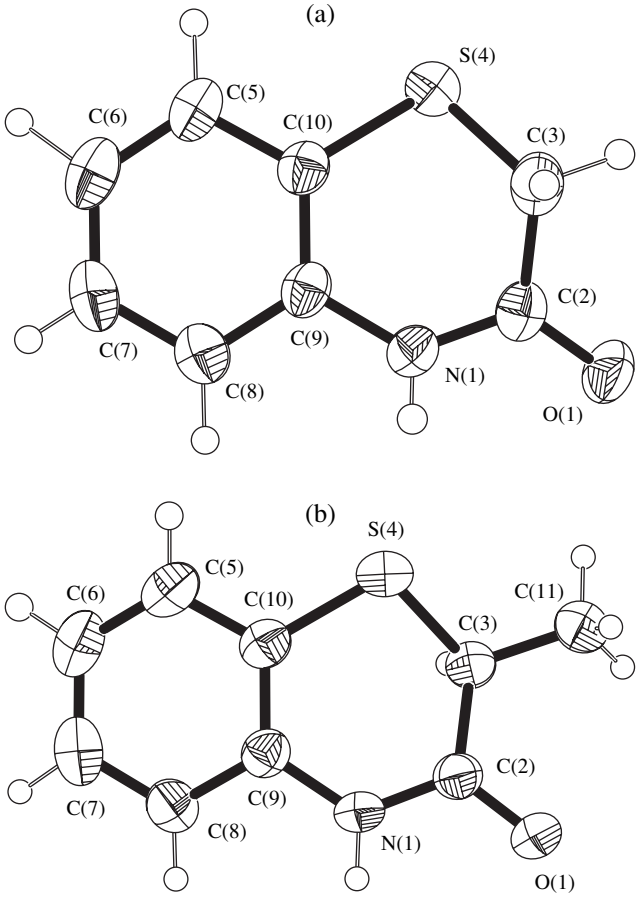

Fig. 2. Structures of molecules (a) **I** and (b) **II**.

angle N(1)–H(1)···O(1) 172.2°; symmetry code: $-x$, $2-y$, $2-z$ and N(1)···O(1) 2.934, H(1)···O(1) 2.153 Å, angle N(1)–H(1)···O(1) 169.4°; symmetry code: $2-x$, $1-y$, $2-z$) exists. The ring *B*–N(1)C(2)C(3)S(4)C(10)C(9) of both the structures adopts a 2,3-*half-chair*-conformation, while the ring *A*–C(5)C(6)C(7)C(8)C(9)C(10) shows almost planar conformation. The dihedral angle between the two rings of both structures is 9.2(1)° and 10.3(6)° respectively.

The atom C(11) in molecule **II** has been found below the plane of atoms N(1)C(2)C(3)S(4)C(9)C(10) (deviation for C(11) being –0.304(3) Å. The atom O(1) in both the molecules has been found above the plane of C(5)···C(10) atoms (deviations for O(1) being 0.372(3) and 0.456(1) Å for **I** and **II** respectively).

ACKNOWLEDGMENTS

One of the authors (Dinesh) is grateful to the University of Jammu, Govt. of India, for research funding under a University Scholarship.

REFERENCES

1. M. B. Deshmukh, private communication (Shivaji Univ., Kolhapur, India, 2000).
2. G. M. Sheldrick, *SHELXS97. Program for the Solution of Crystal Structures* (Univ. of Göttingen, Germany, 1997).
3. G. M. Sheldrick, *SHELXL97. Program for the Refinement of Crystal Structures* (Univ. of Göttingen, Germany, 1997).
4. *International Tables for Crystallography* (1992), Vol. C, Tables 4.2.6.8 and 6.1.1.4.
5. L. J. Farrugia, J. Appl. Crystallogr. **30**, 565 (1997).
6. M. Nardelli, Comput. Chem. **7**, 95 (1993).
7. B. E. Rivero, M. A. Bianchet, and R. D. Bravo, Acta Crystallogr., Sect. C: Cryst. Struct. Commun. **49**, 544 (1993).
8. P. N. Rodier, Y. Mettey, and J.-M. Vierfond, Acta Crystallogr., Sect. C: Cryst. Struct. Commun. **47**, 1058 (1991).
9. K. Kozawa and T. Uchida, Acta Crystallogr., Sect. C: Cryst. Struct. Commun. **46**, 1006 (1990).
10. P. C. Follet-Houttemane, J. C. Boivin, J. P. Bonte, and D. Lesieur, Acta Crystallogr., Sect. C: Cryst. Struct. Commun. **47**, 882 (1991).
11. N. Davidovic, D. Matkovic-Calogovic, Z. Popovic, and L. Fiser-Jakic, Acta Crystallogr., Sect. C: Cryst. Struct. Commun. **55**, 119 (1999).
12. W. L. Duax, G. M. Weeks, and D. C. Rohrer, *Topics of Stereochemistry*, Ed. by E. L. Eliel and N. Allinger (Wiley, New York, 1976), Vol. 9, p. 271.

Crystallography Reports, Vol. 49, No. 3, 2004, pp. 430–436. Translated from Kristallografiya, Vol. 49, No. 3, 2004, pp. 495–501.

STRUCTURE OF ORGANIC COMPOUNDS

X-ray Mapping in Heterocyclic Design: XIII. Structure of Substituted Tetrahydroquinolines

D. V. Albov, V. B. Rybakov, E. V. Babaev, and L. A. Aslanov

Faculty of Chemistry, Moscow State University, Leninskie gory, Moscow, 119899 Russia

e-mail: albov@biocryst.phys.msu.su

Received July 3, 2003

Abstract—The structures of 4-methyl-2-chloro-5,6,7,8-tetrahydroquinoline [a = 8.138(2) Å, b = 11.127(4) Å, c = 11.234(2) Å, β = 111.30(2)°, Z = 4, space group $P2_1/c$, 4-methyl-2-methoxy-5,6,7,8- tetrahydroquinoline [a = 5.765$\underline{1}$(16) Å, b = 8.530(2) Å, c = 10.455(3) Å, α = 73.76(2)°, β = 86.95(2)°, γ = 83.97(2)°, Z = 2, space group $P\bar{1}$, 4-methyl-2-(4-chlorophenacyl)-5,6,7,8-tetrahydro-1*H*-quinolin-2-one [a = 8.873(2) Å, b = 17.137(2) Å, c = 24.515(4) Å, Z = 8, space group $Pbn2_1$], and 2-(4-chlorophenyl)-5-methyl-6,7,8,9-tetrahydrooxazolo[3.2-*a*]quinolin-10-ylium perchlorate [a = 8.110(6) Å, b = 17.818(7) Å, c = 17.721(5) Å, β = 100.46(4)°, Z = 4, space group $P2_1/c$] are studied by single-crystal X-ray diffraction. The structures are solved by direct methods and refined by the full-matrix least-squares procedures in the anisotropic approximation to R = 0.0581, 0.0667, 0.0830, and 0.0607, respectively. © *2004 MAIK "Nauka/Interperiodica".*

INTRODUCTION

This study continues our structural investigation of heterocyclic compounds that are able to undergo various rearrangements, in particular, to enter into cyclization reactions [1–13]. As was done in our previous works, we perform X-ray diffraction analysis of all the intermediates and final products of multistage cyclization reactions and rearrangements. 2-Pyridone derivatives are structural precursors in many of the systems studied earlier.

In this work, we studied a series of transformations from 4-methyl-5,6,7,8-tetrahydro-1*H*-quinolin-2-one (**I**) into 2-(4-chlorophenyl)-5-methyl-6,7,8,9-tetrahydrooxazolo[3.2-*a*]quinolin-10-ylium perchlorate (**V**) (Scheme 1).

The data on the molecular structures of compounds **II**–**V** discussed in this paper are not available in the Cambridge Structural Database (version 11.02) [14].

EXPERIMENTAL

Compound **I** was synthesized and characterized in our earlier work [11]. This paper reports the synthesis and structures of compounds **II**–**V**.

4-Methyl-2-chloro-5,6,7,8-tetrahydroquinoline (II). Our attempt to convert pyridone **I** into chloropyridine **II**

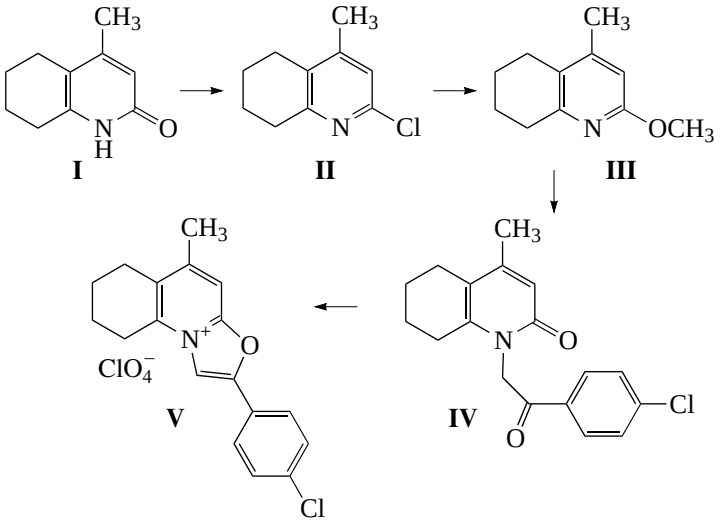

Scheme 1.

Table 1. Crystal data, data collection, and refinement parameters for the crystal structures of compounds **II–V**

Empirical formula	$C_{10}H_{12}NCl$ (**II**)	$C_{11}H_{15}NO$ (**III**)	$C_{20}H_{21}N_2O_2Cl$ (**IV**)	$C_{18}H_{17}NO_5Cl_2$ (**V**)
Molecular weight	181.66	177.24	356.84	398.23
Crystal system	Monoclinic	Triclinic	Orthorhombic	Monoclinic
Space group	$P2_1/c$	$P\bar{1}$	$Pbn2_1$	$P2_1/c$
a, Å	8.138(2)	5.7651(16)	8.873(2)	8.110(6)
b, Å	11.127(4)	8.530(2)	17.137(2)	17.818(7)
c, Å	11.234(2)	10.455(3)	24.515(4)	17.721(5)
α, deg	90	73.76(2)	90	90
β, deg	111.30(2)	86.95(2)	90	100.46(4)
γ, deg	90	83.79(2)	90	90
V, Å^3	947.8(4)	490.6(2)	3727.7(13)	1807.7(17)
Z	4	2	8	4
ρ_{calcd}, g/cm^3	1.273	1.200	1.272	1.463
$\mu(K_\alpha)$, cm^{-1}	3.46	0.77	19.33	34.97
θ range, deg	2.67–25.97	2.03–25.95	3.60–69.78	5.54–69.77
Index ranges	$-10 \le h \le 9$	$-7 \le h \le 1$	$0 \le h \le 10$	$-7 \le h \le 7$
	$0 \le k \le 13$	$-10 \le k \le 10$	$0 \le k \le 20$	$0 \le k \le 18$
	$0 \le l \le 13$	$0 \le l \le 12$	$0 \le l \le 29$	$0 \le l \le 17$
Crystal size, mm	$0.26 \times 0.29 \times 0.30$	$0.31 \times 0.32 \times 0.35$	$0.22 \times 0.24 \times 0.29$	$0.27 \times 0.29 \times 0.30$
Number of reflections measured	1892	1158	3342	3271
Number of unique reflections	1799	1140	3342	3271
Number of reflections used in the least-squares refinement/number of parameters refined	1799/114	1140/121	3342/456	3271/237
GooF	1.020	1.026	0.914	0.998
R_1/wR_2 [$I \ge 2\sigma(I)$]	0.0581/0.1474	0.0667/0.1793	0.0830/0.1991	0.0607/0.1604
$\Delta\rho_{max}/\Delta\rho_{min}$, eÅ^{-3}	0.284/–0.232	0.172/–0.151	0.592/–0.208	0.303/–0.325

Table 2. Bond lengths d (Å) in structure **II**

Bond	d	Bond	d
N(1)–C(2)	1.301(4)	C(5)–C(10)	1.384(4)
N(1)–C(10)	1.344(4)	C(5)–C(6)	1.516(4)
C(2)–C(3)	1.357(4)	C(6)–C(7)	1.468(7)
C(2)–Cl(2)	1.754(3)	C(7)–C(8)	1.350(8)
C(3)–C(4)	1.377(4)	C(8)–C(9)	1.496(8)
C(4)–C(5)	1.388(4)	C(9)–C(10)	1.510(5)
C(4)–C(11)	1.502(4)		

Table 3. Bond angles ω (deg) in structure **II**

Angle	ω	Angle	ω
C(2)–N(1)–C(10)	116.1(2)	C(10)–C(5)–C(6)	120.9(3)
N(1)–C(2)–C(3)	126.5(3)	C(4)–C(5)–C(6)	120.5(3)
N(1)–C(2)–Cl(2)	115.4(2)	C(7)–C(6)–C(5)	114.3(4)
C(3)–C(2)–Cl(2)	118.1(2)	C(8)–C(7)–C(6)	119.9(5)
C(2)–C(3)–C(4)	117.8(3)	C(7)–C(8)–C(9)	120.5(5)
C(3)–C(4)–C(5)	118.2(3)	C(8)–C(9)–C(10)	111.9(4)
C(3)–C(4)–C(11)	119.9(3)	N(1)–C(10)–C(5)	122.8(3)
C(5)–C(4)–C(11)	121.9(3)	N(1)–C(10)–C(9)	114.7(3)
C(10)–C(5)–C(4)	118.5(2)	C(5)–C(10)–C(9)	122.5(3)

simply through boiling in $POCl_3$ failed. The procedure described in [15] requires heating to 180°C in a sealed ampule, which is impracticable. Therefore, we worked out an original path of synthesis of compound **II**. Weighed portions of **I** (10 g) and benzyltrimethylammonium chloride (11 g) were refluxed in $POCl_3$ (33 ml) until the formation of HCl ceased (within about 5 h). A hot homogeneous dark solution was poured in a glass with ice. Activated carbon was added, and the solution was stirred and filtered off. The light solution thus prepared was neutralized with solid sodium hydrogen carbonate to pH = 7, and the precipitate was filtered off. A

Table 4. Bond lengths *d* (Å) in structure **III**

Bond	*d*	Bond	*d*
N(1)–C(2)	1.328(5)	C(5)–C(10)	1.337(5)
N(1)–C(10)	1.368(4)	C(5)–C(6)	1.537(4)
C(2)–O(1)	1.363(4)	C(6)–C(7)	1.531(6)
C(2)–C(3)	1.381(6)	C(7)–C(8)	1.444(7)
C(3)–C(4)	1.369(4)	C(8)–C(9)	1.501(5)
C(4)–C(5)	1.422(5)	C(9)–C(10)	1.514(5)
C(4)–C(11)	1.492(6)	O(1)–C(1)	1.402(6)

Table 5. Bond angles ω (deg) in structure **III**

Angle	ω	Angle	ω
C(2)–N(1)–C(10)	115.3(3)	C(4)–C(5)–C(6)	118.5(3)
N(1)–C(2)–O(1)	118.7(4)	C(7)–C(6)–C(5)	111.2(3)
N(1)–C(2)–C(3)	124.8(3)	C(8)–C(7)–C(6)	115.1(3)
O(1)–C(2)–C(3)	116.5(3)	C(7)–C(8)–C(9)	113.2(4)
C(4)–C(3)–C(2)	118.7(3)	C(8)–C(9)–C(10)	112.4(3)
C(3)–C(4)–C(5)	117.9(4)	C(5)–C(10)–N(1)	124.5(3)
C(3)–C(4)–C(11)	120.7(3)	C(5)–C(10)–C(9)	122.8(3)
C(5)–C(4)–C(11)	121.4(3)	N(1)–C(10)–C(9)	112.6(3)
C(10)–C(5)–C(4)	118.7(3)	C(2)–O(1)–C(1)	118.1(3)
C(10)–C(5)–C(6)	122.8(3)		

Table 6. Bond lengths *d* (Å) in structure **IV**

Bond	*d*	Bond	*d*
Cl(1)–C(17)	1.728(9)	C(7)–C(8)	1.438(15)
N(1)–C(2)	1.361(10)	C(8)–C(9)	1.471(13)
N(1)–C(10)	1.422(10)	C(9)–C(10)	1.513(11)
N(1)–C(12)	1.456(10)	C(12)–C(13)	1.509(11)
C(2)–O(2)	1.232(11)	C(13)–O(13)	1.215(9)
C(2)–C(3)	1.417(12)	C(13)–C(14)	1.495(10)
C(3)–C(4)	1.355(11)	C(14)–C(19)	1.390(10)
C(4)–C(5)	1.459(12)	C(14)–C(15)	1.402(10)
C(4)–C(11)	1.591(14)	C(15)–C(16)	1.375(10)
C(5)–C(10)	1.376(12)	C(16)–C(17)	1.376(10)
C(5)–C(6)	1.498(11)	C(17)–C(18)	1.377(11)
C(6)–C(7)	1.552(15)	C(18)–C(19)	1.389(11)

white powder obtained was recrystallized from chloroform. The yield was 8.6 g (78%). The melting point was equal to 35–40°C. ^{1}H NMR (DMSO-d_6, δ, ppm): 1.82 (m, 4H, 6-CH_2 + 7-CH_2), 2.19 (s, 3H, 4-CH_3), 2.60 (t, 2H, 5-CH_2), 2.78 (t, 2H, 8-CH_2), 6.95 (s, 1H, 3-CH).

4-Methyl-2-methoxy-5,6,7,8-tetrahydroquinoline (III). No indications of the reaction (precipitation of sodium chloride) were observed in our attempt to prepare methoxy pyridine **III** from chloropyridine **II** according to the procedure described in [16]. An analysis of the reaction mixture showed that the product was not formed and the starting substance remained without changes. We proposed an original procedure with the use of a high-boiling inert solvent that dissolves both the initial substance and sodium methylate and is water-mixable for the facilitation of the product isolation. Diglym satisfies these conditions. Metallic sodium (2.8 g) was dissolved in absolute methanol (20 ml), the excess methanol was distilled off, and a solution of compound **II** (7.8 g) in absolute diglyme (40 ml) was added. The mixture was heated at 120°C for 3 h. This process was accompanied by a thickening of the mixture because of the copious precipitate formation. The reaction mixture was poured into water and stirred. The precipitate was filtered off and washed with water. The white powder obtained was recrystallized from chloroform. The yield was 6.1 g (80%). The melting point was equal to 35–40°C. ^{1}H NMR (DMSO-d_6, δ, ppm): 1.80 (m, 4H, 6-CH_3 + 7-CH_2), 2.15 (s, 3H, 4-CH_3), 2.54 (t, 2H, 5-CH_2), 2.70 (t, 2H, 8-CH_2), 3.78 (s, 3H, OCH_3), 6.35 (s, 1H, 3-CH).

4-Methyl-2-(4-chlorophenacyl)-5,6,7,8-tetrahydro-1*H*-quinolin-2-one (IV). Compound **IV** was synthesized according to a modified procedure described in [16]. Weighed portions of compound **III** (3 g) and 4-chlorophenacyl bromide (4 g) were refluxed in CH_3CN (20 ml) for 5 h. As a result, a poorly soluble compound, namely, 4-chlorophenacyl bromide, dissolved. The degree of conversion was controlled by thin-layer chromatography (hexane : ethyl acetate = 1 : 1). For both initial substances, we obtained R_f = 0.72, and, for the product, R_f = 0.1. Upon cooling of the solution, colorless crystals of the product containing solvate CH_3CN molecules precipitated. Only minor amounts of the product remained in the mother liquor. The yield was 2 g (40%). The melting point was equal to 163–165°C. ^{1}H NMR (DMSO-d_6, δ, ppm): 1.75 (m, 4H, 6-CH_2 + 7-CH_2), 2.13 (s, 3H, 4-CH_3), 2.50 (m, 4H, 5-CH_2 + 8-CH_2), 5.45 (s, 2H, NCH_2CO), 6.15 (s, 1H, 3-CH), 7.55, 8.10 (dd, 4H, *Ar*).

2-(4-Chlorophenyl)-5-methyl-6,7,8,9-tetrahydrooxazolo[3.2-*a*]quinolin-10-ylium perchlorate (V). The synthesis of compound **V** was also performed according to the procedure worked out earlier in [16]. Compound **IV** (1.2 g) was dissolved in concentrated H_2SO_4 (12 ml) and allowed to stand for a night. The solution was poured into a 3% $HClO_4$ solution (100 ml). The precipitate was left in the solution for a night and then filtered off and washed with water. The white powder obtained was recrystallized from CH_3CN. The yield was 1.5 g (98%). The melting point was 300°C (with explosion). ^{1}H NMR (DMSO-d_6, δ,

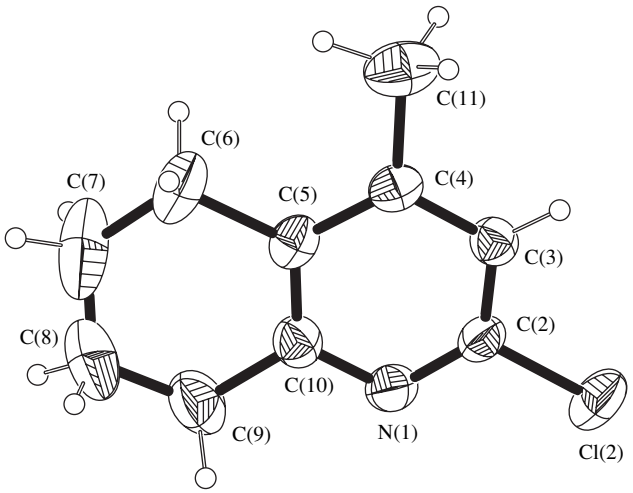

Fig. 1. Molecular structure and atomic numbering for compound **II**. Hereafter, the ellipsoids of thermal vibrations are shown at the 50% probability level.

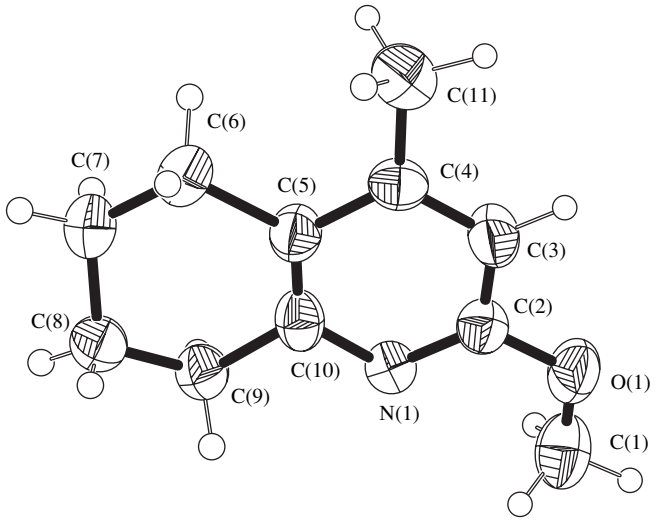

Fig. 2. Molecular structure and atomic numbering for compound **III**.

ppm): 1.95 (m, 2H, 7-CH_2), 2.05 (m, 2H, 8-CH_2), 2.58 (s, 3H, 5-CH_3), 2.85 (t, 2H, 6-CH_2), 3.15 (t, 2H, 9-CH_2), 7.63–7.66, 8.03–8.06 (dd, 4H, *Ar*), 8.11 (s, 1H, 4-CH), 9.37 (s, 1H, 1-CH).

X-ray Diffraction Experiment

For single crystals of compounds **II** and **III**, the experimental intensities were measured on a CAD4 diffractometer [17] (λMoK_α, graphite monochromator) at room temperature. The unit cell parameters were determined and refined using 25 reflections in the θ range 12°–15°. For compounds **IV** and **V**, the experiment was performed on a CAD4 diffractometer (λCuK_α, graphite monochromator). The unit cell parameters were determined and refined using 25 reflections in the θ range 25°–30°.

Since the crystals of the compounds studied were small in size and had small linear absorption coefficients ($\mu R \le 0.4$), the experimental data were not corrected for absorption. The primary processing of the sets of diffraction data was performed with the WinGX program package [18]. All the subsequent calculations were performed with the SHELX97 program package [19]. The crystal structures were determined by direct methods. All the non-hydrogen atoms were refined in the anisotropic approximation of thermal parameters.

The main parameters of the X-ray diffraction experiments and crystal data for the compounds studied are summarized in Table 1. The interatomic distances and bond angles are listed in Tables 2–9. The molecular structures with atomic numberings are shown in Figs. 1–4. The drawings were obtained with the ORTEP-3 program [20, 21].

Crystal data for the compounds studied are deposited in the Cambridge Structural Database (deposit nos. 231747–231750).

RESULTS AND DISCUSSION

In molecule **II** (Fig. 1), the N(1)···C(10) six-membered ring is planar within 0.011 Å. The Cl(2), C(6), C(9), and C(11) atoms lie in the plane of this ring. The C(7) and C(8) atoms deviate from this plane by 0.124 and –0.290 Å, respectively. The thermal ellipsoids of

Table 7. Bond angles ω (deg) in structure **IV**

Angle	ω	Angle	ω
C(2)–N(1)–C(10)	124.7(8)	C(5)–C(10)–N(1)	117.0(7)
C(2)–N(1)–C(12)	115.1(7)	C(5)–C(10)–C(9)	125.1(8)
C(10)–N(1)–C(12)	120.1(7)	N(1)–C(10)–C(9)	117.9(8)
O(2)–C(2)–N(1)	120.7(8)	N(1)–C(12)–C(13)	112.3(7)
O(2)–C(2)–C(3)	123.9(9)	O(13)–C(13)–C(14)	122.8(7)
N(1)–C(2)–C(3)	115.1(8)	O(13)–C(13)–C(12)	120.7(8)
C(4)–C(3)–C(2)	125.5(10)	C(14)–C(13)–C(12)	116.4(7)
C(3)–C(4)–C(5)	116.0(9)	C(19)–C(14)–C(15)	119.7(8)
C(3)–C(4)–C(11)	125.8(10)	C(19)–C(14)–C(13)	123.3(7)
C(5)–C(4)–C(11)	118.0(9)	C(15)–C(14)–C(13)	117.0(7)
C(10)–C(5)–C(4)	121.6(8)	C(16)–C(15)–C(14)	122.1(9)
C(10)–C(5)–C(6)	118.5(9)	C(15)–C(16)–C(17)	118.3(9)
C(4)–C(5)–C(6)	119.8(9)	C(16)–C(17)–C(18)	119.6(9)
C(5)–C(6)–C(7)	112.3(9)	C(16)–C(17)–Cl(1)	123.1(8)
C(8)–C(7)–C(6)	119.4(13)	C(18)–C(17)–Cl(1)	117.2(8)
C(7)–C(8)–C(9)	109.4(12)	C(17)–C(18)–C(19)	123.4(10)
C(8)–C(9)–C(10)	114.6(10)	C(18)–C(19)–C(14)	116.7(9)

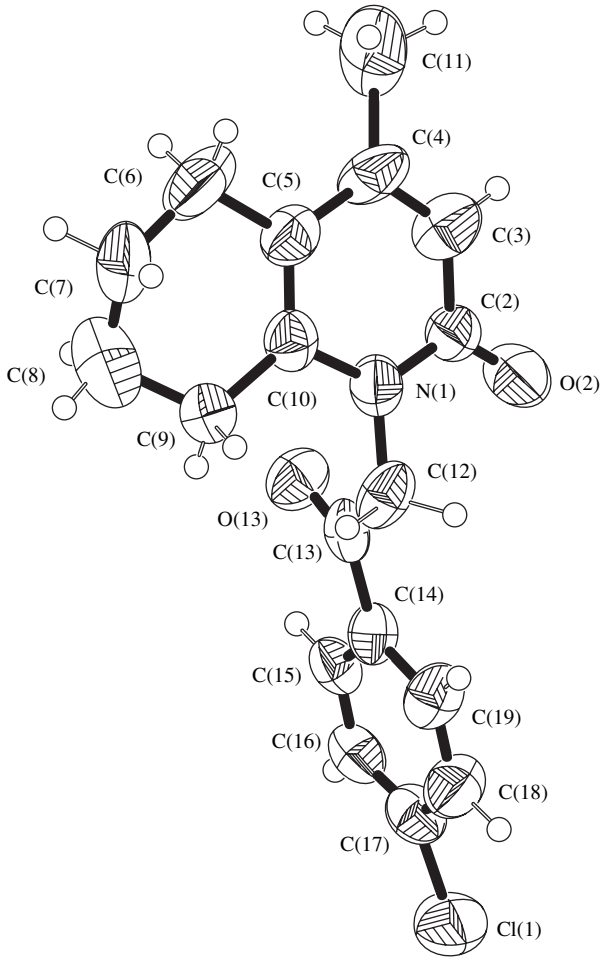

Fig. 3. Molecular structure and atomic numbering for compound **IV**. Acetonitrile solvate molecules are omitted.

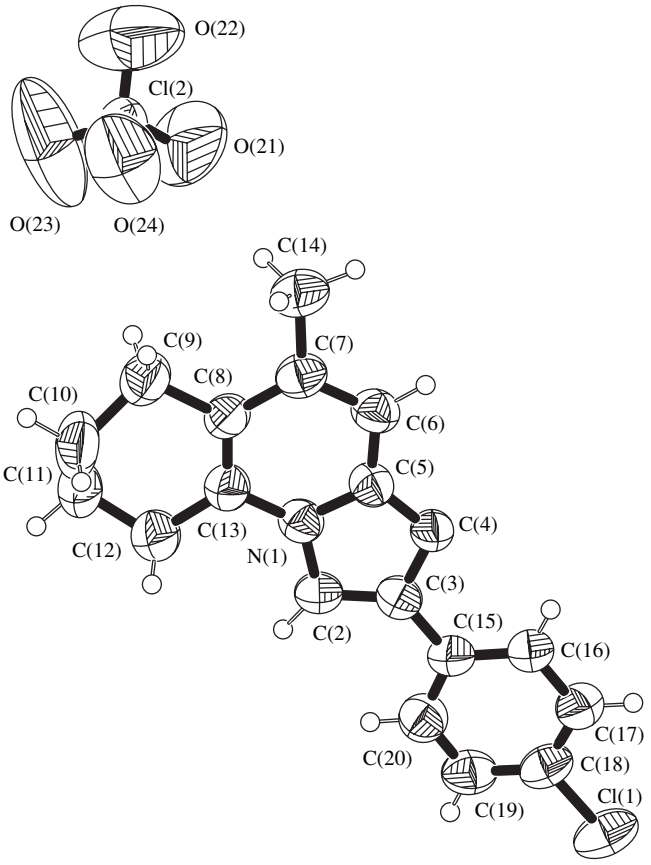

Fig. 4. Molecular structure and atomic numbering for compound **V**.

the C(7) and C(8) atoms are characterized by strong anisotropy, which results in a significant shortening of the distance between these atoms (1.35 Å) with respect to the C(5)–C(6), C(6)–C(7), C(8)–C(9), and C(9)–C(10) distances (Table 2). However, with due regard for the anisotropy of thermal parameters [22], this distance is 1.58 Å, which corresponds to the C(sp^3)–C(sp^3) bond length. In the heterocyclic bicycle of **II**, the single bonds shortened and the double bonds slightly elongated compared to the initial compound **I** [11], which is in accord with the expected aromatic structure of the pyridine fragment (Scheme 1).

In molecule **III** (Fig. 2), the N(1)···C(10) six-membered ring is planar within 0.01 Å. The O(1), C(1), C(6), C(9), and C(11) atoms lie in the plane of this ring. The C(7) and C(8) atoms deviate from this plane by –0.237 and 0.405 Å, respectively. As in molecule **II**, the ellipsoids of thermal vibrations of the C(7) and C(8) atoms exhibit strong anisotropy and, as a consequence, the distance between these atoms (1.44 Å) is shorter than the C(5)–C(6), C(6)–C(7), C(8)–C(9), and C(9)–

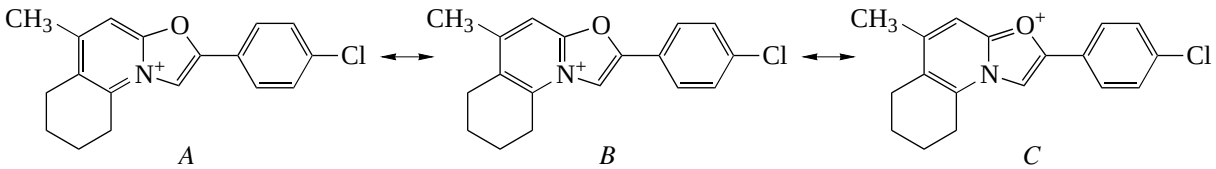

Scheme 2.

C(10) distances (Table 4). However, with due regard for the anisotropy of thermal parameters [22], the C(7)–C(8) distance is 1.57 Å, which corresponds to the C(sp^3)–C(sp^3) bond length. As in the previous case, the structure of the pyridine fragment of the bicycle agrees with the expected aromatic structure (Scheme 1).

In crystals **IV** (Fig. 3), the incomplete occupancy of the positions of the CH_3CN solvate molecules led to problems in the course of structure refinement. For their solution, the lengths of the corresponding pairs of bonds in two crystallographically independent molecules were averaged. The N(1)···C(10) six-membered ring is planar within 0.02 Å. The O(1), C(1), C(6), C(9), and C(12) atoms lie in the plane of this ring. The C(7), C(8), and C(11) atoms deviate from this plane by –0.256, 0.340, and –0.204 Å, respectively. The alternation of single and double bonds in the heterocycle corresponds to a nonaromatic pyridone structure (Scheme 1). As in structures **I**–**III**, the distance between the C(7) and C(8) atoms is short (1.44 Å, Table 6). However, after the correction for anisotropy of thermal vibrations was introduced [22], this distance was found to be 1.54 Å. The C(14)···C(19) phenyl ring is planar within 0.013 Å. The Cl(1), C(13), and C(12) atoms lie in the plane of this ring. The O(13) and N(1) atoms deviate from this plane by –0.116 and –0.373 Å, respectively. The dihedral angle between the planes of the pyridone fragment and the aryl group is 86.45°. The structure of two CH_3CN solvent molecules is standard and needs no comments.

In cation **V** (Fig. 4), the N(1)···C(13) nine-membered oxazolopyridinium bicycle is planar within 0.03 Å. The C(12), C(14), C(15), C(19), and C(20) atoms lie in the plane of this ring. The C(9), C(10), C(11), C(16), C(17), and C(18) atoms deviate from this plane by 0.119, 0.562, –0.225, 0.275, 0.348, and 0.226 Å, respectively. The C(15)···C(20) phenyl ring is planar within 0.01 Å. The Cl(1) and C(3) atoms lie in the plane of this ring. The structure of the phenyl ring corresponds to the expected aromatic structure. The dihedral angle between the planes of the heterocycle and the phenyl ring is only 7.37°, which indicates the conjugation of the aromatic rings.

The structure of the oxazolopyridinium cation can be represented by three resonance forms; in two of them, the positive charge is localized at the nitrogen atom, and, in the third form, the positive charge is localized at the oxygen atom (see Scheme 2).

The question arises as to which of these formulas represents the structure of the cation more adequately. The C(6)–C(7), C(7)–C(8), and C(8)–C(13) bond lengths (Fig. 5) are equal to 1.378(5), 1.423(5), and 1.359(5) Å, respectively (Table 8). This location of double bonds in the pyridine fragment of the molecule suggests that structure *A* makes a minor contribution. For the final decision between structures *B* and *C*, we searched in the Cambridge Structural Database (Version 11.02) [14] for compounds that contain an amide group protonated at the oxygen or nitrogen atom (or alkylated at the oxygen atom). As a result, we found that the C=O bond length in these fragments falls in the range 1.25–1.30 Å. Sixty formulas are drawn with a positive charge at the oxygen atom, and more than 200 formulas have a charge at the nitrogen atom. In

Table 8. Bond lengths *d* (Å) in structure **V**

Bond	*d*	Bond	*d*
Cl(1)–C(18)	1.727(4)	C(7)–C(8)	1.423(5)
Cl(2)–O(23)	1.334(4)	C(7)–C(14)	1.506(5)
Cl(2)–O(21)	1.357(4)	C(8)–C(13)	1.359(5)
Cl(2)–O(24)	1.367(4)	C(8)–C(9)	1.515(5)
Cl(2)–O(22)	1.392(5)	C(9)–C(10)	1.555(6)
N(1)–C(5)	1.339(4)	C(10)–C(11)	1.467(7)
N(1)–C(13)	1.381(4)	C(11)–C(12)	1.520(6)
N(1)–C(2)	1.398(4)	C(12)–C(13)	1.501(5)
C(2)–C(3)	1.335(5)	C(15)–C(20)	1.382(5)
C(3)–O(4)	1.394(4)	C(15)–C(16)	1.388(5)
C(3)–C(15)	1.450(5)	C(16)–C(17)	1.376(5)
O(4)–C(5)	1.339(4)	C(17)–C(18)	1.387(6)
C(5)–C(6)	1.374(5)	C(18)–C(19)	1.380(6)
C(6)–C(7)	1.378(5)	C(19)–C(20)	1.370(5)

Table 9. Bond angles ω (deg) in structure **V**

Angle	ω	Angle	ω
O(23)–Cl(2)–O(21)	112.7(5)	C(13)–C(8)–C(7)	120.6(3)
O(23)–Cl(2)–O(24)	108.3(3)	C(13)–C(8)–C(9)	119.0(3)
O(21)–Cl(2)–O(24)	120.1(4)	C(7)–C(8)–C(9)	120.3(3)
O(23)–Cl(2)–O(22)	107.1(6)	C(8)–C(9)–C(10)	110.5(3)
O(21)–Cl(2)–O(22)	100.0(4)	C(11)–C(10)–C(9)	112.9(4)
O(24)–Cl(2)–O(22)	107.5(4)	C(10)–C(11)–C(12)	109.8(4)
C(5)–N(1)–C(13)	121.2(3)	C(13)–C(12)–C(11)	111.8(4)
C(5)–N(1)–C(2)	108.2(3)	C(8)–C(13)–N(1)	118.0(3)
C(13)–N(1)–C(2)	130.5(3)	C(8)–C(13)–C(12)	126.6(3)
C(3)–C(2)–N(1)	106.5(3)	N(1)–C(13)–C(12)	115.4(3)
C(2)–C(3)–O(4)	109.0(3)	C(20)–C(15)–C(16)	118.7(3)
C(2)–C(3)–C(15)	133.5(3)	C(20)–C(15)–C(3)	119.8(3)
O(4)–C(3)–C(15)	117.5(3)	C(16)–C(15)–C(3)	121.6(3)
C(5)–O(4)–C(3)	106.9(2)	C(17)–C(16)–C(15)	121.5(3)
N(1)–C(5)–O(4)	109.4(3)	C(16)–C(17)–C(18)	118.3(4)
N(1)–C(5)–C(6)	123.1(3)	C(19)–C(18)–C(17)	121.1(3)
O(4)–C(5)–C(6)	127.4(3)	C(19)–C(18)–Cl(1)	119.7(3)
C(5)–C(6)–C(7)	116.9(3)	C(17)–C(18)–Cl(1)	119.1(3)
C(6)–C(7)–C(8)	120.1(3)	C(20)–C(19)–C(18)	119.3(4)
C(6)–C(7)–C(14)	120.2(3)	C(19)–C(20)–C(15)	121.0(4)
C(8)–C(7)–C(14)	119.8(3)		

pyridones, the C=O bond lengths fall in the range between 1.21 and 1.25 Å, which indicates that protonation (or alkylation) of the oxygen heteroatom results in an elongation of the double carbon–oxygen bond. In structure **V**, the C(5)–O(4) bond length is 1.339(4) Å. This value is intermediate between the single and double C–O bond lengths in the positively charged amide group. The N(1)–C(5) bond length is also 1.339(4) Å. This bond is shorter than the two other C–N bonds at the same nitrogen atom [1.381(4) and 1.398(4) Å]. Based on these arguments, we concluded that the structure of the oxazolopyridinium cation can be described by a superposition of the *B* and *C* formulas (with a slightly larger contribution of the *B* structure). Probably, the structure of the cation is most adequately represented by the following charge delocalization:

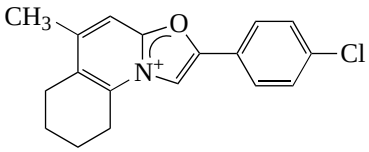

Scheme 3.

The thermal ellipsoids of the oxygen atoms in the perchlorate anion exhibit strong anisotropy in the plane perpendicular to the Cl–O bond (Fig. 4). This suggests some degree of rotational freedom of the perchlorate ion about the chlorine atom.

ACKNOWLEDGMENTS

This work was supported by the International Association of Assistance for the promotion of cooperation with scientists from the New Independent States of the Former Soviet Union (project INTAS no. 00-0711). We also acknowledge the support of the Russian Foundation for Basic Research in the payment of the license for using the Cambridge Structural Database, project no. 02-07-90322.

REFERENCES

1. V. B. Rybakov, S. G. Zhukov, E. V. Babaev, *et al.*, Kristallografiya **44** (6), 1067 (1999) [Crystallogr. Rep. **44**, 997 (1999)].
2. V. B. Rybakov, S. G. Zhukov, E. V. Babaev, *et al.*, Kristallografiya **45** (1), 108 (2000) [Crystallogr. Rep. **45**, 103 (2000)].
3. V. B. Rybakov, S. G. Zhukov, E. V. Babaev, *et al.*, Kristallografiya **45** (2), 292 (2000) [Crystallogr. Rep. **45**, 261 (2000)].
4. V. B. Rybakov, S. G. Zhukov, K. Yu. Pasichnichenko, and E. V. Babaev, Koord. Khim. **26** (9), 714 (2000).
5. V. B. Rybakov, S. G. Zhukov, E. V. Babaev, and E. J. Sonneveld, Kristallografiya **46** (3), 435 (2001) [Crystallogr. Rep. **46**, 385 (2001)].
6. V. B. Rybakov, S. I. Troyanov, E. V. Babaev, *et al.*, Kristallografiya **46** (6), 1069 (2001) [Crystallogr. Rep. **46**, 986 (2001)].
7. V. B. Rybakov, E. V. Babaev, K. Yu. Pasichnichenko, and E. J. Sonneveld, Kristallografiya **47** (1), 76 (2002) [Crystallogr. Rep. **47**, 69 (2002)].
8. V. B. Rybakov, E. V. Babaev, and V. V. Chernyshev, Kristallografiya **47** (3), 473 (2002) [Crystallogr. Rep. **47**, 428 (2002)].
9. V. B. Rybakov, E. V. Babaev, and K. Yu. Pasichnichenko, Kristallografiya **47** (4), 678 (2002) [Crystallogr. Rep. **47**, 622 (2002)].
10. V. B. Rybakov, E. V. Babaev, A. A. Tsisevich, *et al.*, Kristallografiya **47** (6), 1042 (2002) [Crystallogr. Rep. **47**, 973 (2002)].
11. D. V. Al'bov, V. B. Rybakov, E. V. Babaev, and L. A. Aslanov, Kristallografiya **48** (2), 277 (2003) [Crystallogr. Rep. **48**, 280 (2003)].
12. V. B. Rybakov, L. G. Boboshko, N. I. Burakov, *et al.*, Kristallografiya **48** (4), 627 (2003) [Crystallogr. Rep. **48**, 576 (2003)].
13. D. V. Al'bov, O. S. Mazina, V. B. Rybakov, *et al.*, Kristallografiya **49** (2), 208 (2004) [Crystallogr. Rep. **49**, 158 (2004)].
14. F. H. Allen, Acta Crystallogr., Sect. B: Struct. Sci. **58**, 380 (2002).
15. H. E. Mertel, *Pyridine and Derivatives*, Ed. by E. Klingsberg (Interscience, New York, 1962), Part 3, p. 525.
16. E. V. Babaev, A. V. Efimov, D. A. Maiboroda, and K. Jug, Eur. J. Org. Chem., 193 (1998).
17. *Enraf–Nonius CAD4 Software, Version 5.0* (Enraf–Nonius, Delft, Netherlands, 1989).
18. L. J. Farrugia, J. Appl. Crystallogr. **32**, 837 (1999).
19. G. M. Sheldrick, *SHELX97: Program for the Solution and Refinement of Crystal Structures* (Univ. of Göttingen, Germany, 1997).
20. M. N. Burnett and C. K. Johnson, ORTEP. Report ORNL 6895 (Oak Ridge National Laboratory, Tennessee, USA, 1996).
21. L. J. Farrugia, J. Appl. Crystallogr. **30**, 565 (1997).
22. W. R. Busing and H. A. Levy, Acta Crystallogr. **17**, 142 (1964).

Translated by I. Polyakova

Crystallography Reports, Vol. 49, No. 3, 2004, pp. 437–442. Translated from Kristallografiya, Vol. 49, No. 3, 2004, pp. 502–507.

STRUCTURE OF ORGANIC COMPOUNDS

Molecular Structures of 17*a*β-Acetoxy-3-Methoxy-6-Oxa-*D*-Homo-8-Isoestra-1,3,5(10)-Triene and Its 4-Methyl Derivative

G. L. Starova, S. S. Selivanov, M. S. Egorov, S. I. Selivanov, and A. G. Shavva

Department of Chemistry, St. Petersburg State University, Universitetskiĭ pr. 26, Petrodvorets, St. Petersburg, 198504 Russia

e-mail: starova@vk4829.spb.edu

Received May 28, 2002

Abstract—The molecular structures of 17*a*β-acetoxy-3-methoxy-6-oxa-*D*-homo-8-isoestra-1,3,5(10)-triene (**I**) and 17*a*β-acetoxy-3-methoxy-4-methyl-6-oxa-*D*-homo-8-isoestra-1,3,5(10)-triene (**II**) have been established by X-ray diffraction analysis. The presence of the methyl group at the C(4) atom in compound **II** leads to slight changes in the conformation of the carbon skeleton of this molecule and the orientation of the methoxy group with respect to the C(2)–C(3) bond. © *2004 MAIK "Nauka/Interperiodica".*

In the last two decades, a search for enzyme inhibitors responsible for the metabolism of steroid hormones has been underway. An important requirement for new potential inhibitors is that they should not exhibit hormonal activity (in some cases, antihormonal properties are required). As examples, we should mention the design of inhibitors of 5α-reductase [1], 17β-hydroxysteroid dehydrogenase [2], and estrone sulfatase [3, 4]. To solve these problems, it is important to know which modifications in the structures of steroid hormones and their analogues lead to a drop in hormonal activity or its complete disappearance.

We chose model compounds for the synthesis and investigation of hormonal action based on X-ray diffraction data for the complex of the natural hormone estradiol with an α receptor [5] and the results of analysis of the relationship between the structure and biological properties of modified estrogens [6]. We also took into account that the introduction of the methyl group at position 4 of 8-iso analogues of steroid estrogens [7] leads to a decrease in the affinity for estradiol receptors in rat uterus and inhibition of uterotropic activity.

We found that, when injected into ovariectomized rats in doses of 5 mg per kg of body weight per day (*per os*), 17*a*β-acetoxy-3-methoxy-4-methyl-6-oxa-*D*-homo-8-isoestra-1,3,5(10)-triene (**II**) does not exhibit uterotropic activity and has no effect on body weight. In addition, compound **II** has no hypocholesterolemic and hypertriglyceridemic activities. Steroidal compounds possessing such properties hold promise for the design of enzyme inhibitors responsible for metabolism of steroid hormones. When injected in the same dose, analogous compound **I** devoid of the methyl group at the C(4) atom exhibits pronounced uterotropic activity (the uterus weight of ovariectomized rats increases by a factor of

Table 1. Crystallographic characteristics and structure refinement parameters for compounds **I** and **II**

Compound	**I**	**II**
Formula	$C_{21}H_{28}O_4$	$C_{22}H_{30}O_4$
Molecular weight	328.43	358.46
Space group	$P2_1/b$	$P2_1/n$
a, Å	15.065(5)	16.397(4)
b, Å	12.602(5)	13.571(3)
c, Å	10.402(5)	18.628(5)
α, deg	90	90
β, deg	90	115.20
γ, deg	110.43	90
V, Å^3	1850.6(13)	3750.7(16)
Z	4	8
ρ_{calcd}, g/cm^3	1.236	1.270
μ, mm^{-1}	0.084	0.086
Crystal dimensions, mm	0.3 × 0.2 × 0.15	0.3 × 0.2 × 0.2
Θ-angle range, deg	2.43–32.13	2.03–22.00
Ranges of indices	$0 \le h \le 20$	$-17 \le h \le 9$
	$-18 \le k \le 15$	$-14 \le k \le 14$
	$0 \le l \le 8$	$-16 \le l \le 19$
Number of reflections with $I > 4\sigma(I)$	1052	4557
GooF	1.075	0.801
R_1	0.042	0.076
wR_2	0.1006	0.1741
Residual electron density, *e*Å^{-3}	0.154	0.529

Table 2. Bond lengths *d* (Å) in compound **I**

Bond	*d*	Bond	*d*
O(1)–C(3)	1.373(6)	C(8)–C(9)	1.532(6)
O(1)–C(3*a*)	1.416(6)	C(8)–C(14)	1.538(6)
O(2)–C(20)	1.335(6)	C(9)–C(10)	1.512(6)
O(2)–C(17*a*)	1.465(6)	C(9)–C(11)	1.527(7)
O(3)–C(20)	1.201(7)	C(11)–C(12)	1.528(7)
O(6)–C(5)	1.378(5)	C(12)–C(13)	1.531(6)
O(6)–C(7)	1.447(5)	C(13)–C(18)	1.530(6)
C(1)–C(2)	1.377(7)	C(13)–C(17*a*)	1.530(6)
C(1)–C(10)	1.392(7)	C(13)–C(14)	1.554(7)
C(2)–C(3)	1.385(7)	C(14)–C(15)	1.530(7)
C(3)–C(4)	1.368(6)	C(15)–C(16)	1.537(7)
C(4)–C(5)	1.400(6)	C(16)–C(17)	1.526(7)
C(5)–C(10)	1.383(6)	C(17)–C(17*a*)	1.515(7)
C(7)–C(8)	1.519(6)	C(20)–C(21)	1.490(9)

Table 3. Bond angles ω (deg) in compound **I**

Angle	ω	Angle	ω
C(3)O(1)C(3*a*)	117.0(4)	C(1)C(10)C(9)	122.1(5)
C(20)O(2)C(17*a*)	116.7(5)	C(9)C(11)C(12)	112.6(4)
C(5)O(6)C(7)	114.6(4)	C(11)C(12)C(13)	112.9(4)
C(2)C(1)C(10)	122.6(5)	C(18)C(13)C(17*a*)	110.2(4)
C(1)C(2)C(3)	119.6(5)	C(18)C(13)C(12)	110.0(4)
C(4)C(3)O(1)	125.0(5)	C(17*a*)C(13)C(12)	109.7(4)
C(4)C(3)C(2)	119.5(5)	C(18)C(13)C(14)	113.5(4)
O(1)C(3)C(2)	115.5(5)	C(17*a*)C(13)C(14)	104.6(4)
C(3)C(4)C(5)	120.0(5)	C(12)C(13)C(14)	108.7(4)
O(6)C(5)C(10)	123.5(4)	C(15)C(14)C(8)	113.8(4)
O(6)C(5)C(4)	114.8(4)	C(15)C(14)C(13)	112.7(4)
C(10)C(5)C(4)	121.6(5)	C(8)C(14)C(13)	115.6(4)
O(6)C(7)C(8)	110.5(4)	C(14)C(15)C(16)	110.5(4)
C(7)C(8)C(9)	108.8(4)	C(17)C(16)C(15)	111.8(5)
C(7)C(8)C(14)	116.0(4)	C(17*a*)C(17)C(16)	110.0(5)
C(9)C(8)C(14)	112.7(4)	O(2)C(17*a*)C(17)	108.8(4)
C(10)C(9)C(11)	113.4(4)	O(2)C(17*a*)C(13)	108.8(4)
C(10)C(9)C(8)	110.2(4)	C(17)C(17*a*)C(13)	113.3(4)
C(11)C(9)C(8)	111.4(4)	O(3)C(20)O(2)	123.9(6)
C(5)C(10)C(1)	116.6(5)	O(3)C(20)C(21)	124.4(6)
C(5)C(10)C(9)	121.3(5)	O(2)C(20)C(21)	111.7(6)

four to five). In addition, compound **I** exhibits hypertriglyceridemic activity. Hence, it was of interest to perform a comparative analysis of compounds **I** and **II**.

Colorless plate-like crystals of both compounds suitable for single-crystal X-ray diffraction study were grown from hexane. The crystallographic characteris-

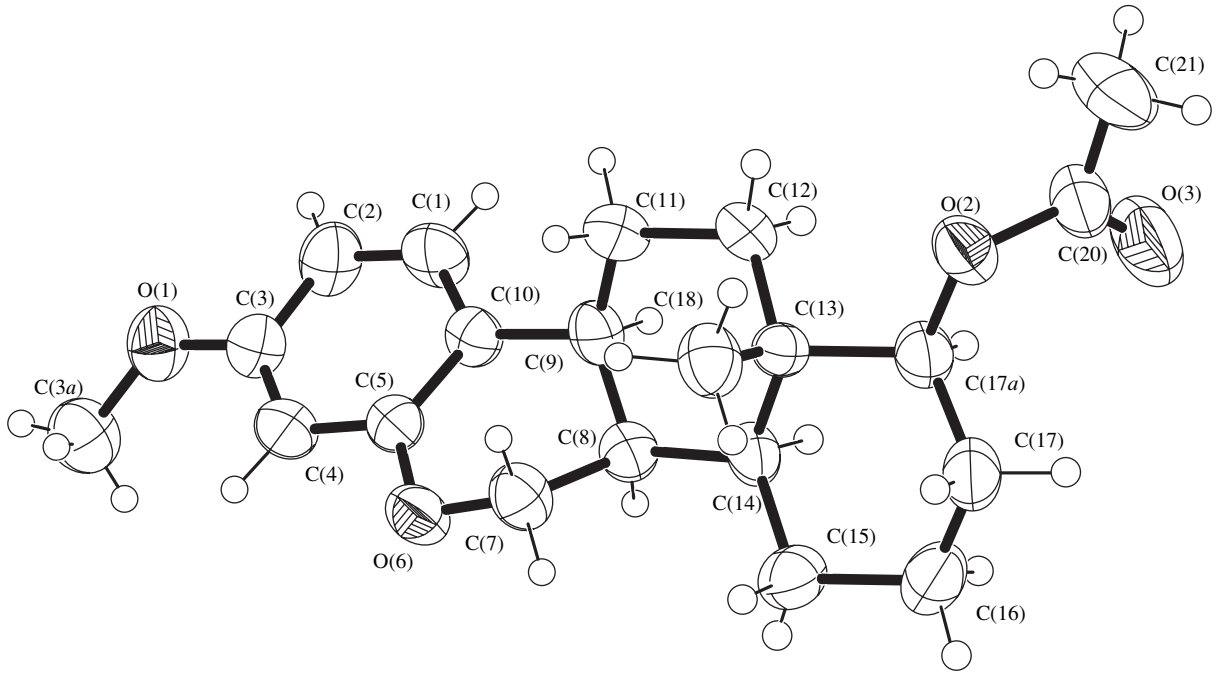

Fig. 1. Atomic numbering scheme and the molecular structure of compound **I**.

Table 4. Bond lengths *d* (Å) in compound **II**

Bond	*d*	Bond	*d*
O(1)–C(3)	1.375(6)	O(1')–C(3')	1.402(6)
O(1)–C(3*a*)	1.439(6)	O(1')–C(3*a*')	1.417(6)
O(2)–C(20)	1.350(6)	O(2')–C(20')	1.346(6)
O(2)–C(17*a*)	1.462(6)	O(2')–C(17*a*')	1.461(6)
O(3)–C(20)	1.193(6)	O(3')–C(20')	1.207(6)
O(6)–C(5)	1.371(6)	O(6')–C(5')	1.401(6)
O(6)–C(7)	1.464(5)	O(6')–C(7')	1.440(5)
C(1)–C(2)	1.375(7)	C(1')–C(10')	1.373(6)
C(1)–C(10)	1.382(7)	C(1')–C(2')	1.394(7)
C(2)–C(3)	1.388(7)	C(2')–C(3')	1.376(7)
C(3)–C(4)	1.391(7)	C(3')–C(4')	1.385(7)
C(4)–C(5)	1.394(7)	C(4')–C(5')	1.392(7)
C(4)–C(4*a*)	1.507(7)	C(4')–C(4*a*')	1.499(7)
C(5)–C(10)	1.402(7)	C(5')–C(10')	1.393(7)
C(7)–C(8)	1.529(7)	C(7')–C(8')	1.530(7)
C(8)–C(14)	1.501(7)	C(8')–C(9')	1.534(6)
C(8)–C(9)	1.531(6)	C(8')–C(14')	1.547(6)
C(9)–C(10)	1.515(7)	C(9')–C(10')	1.503(7)
C(9)–C(11)	1.531(7)	C(9')–C(11')	1.533(7)
C(11)–C(12)	1.502(7)	C(11')–C(12')	1.525(6)
C(12)–C(13)	1.531(6)	C(12')–C(13')	1.539(6)
C(13)–C(18)	1.529(7)	C(13')–C(18')	1.525(7)
C(13)–C(17*a*)	1.539(7)	C(13')–C(17*a*')	1.543(7)
C(13)–C(14)	1.562(7)	C(13')–C(14')	1.549(7)
C(14)–C(15)	1.528(6)	C(14')–C(15')	1.538(7)
C(15)–C(16)	1.532(6)	C(15')–C(16')	1.531(7)
C(16)–C(17)	1.521(7)	C(16')–C(17')	1.519(7)
C(17)–C(17*a*)	1.515(7)	C(17')–C(17*a*)	1.507(7)
C(20)–C(21)	1.499(7)	C(20')–C(21')	1.484(7)

tics, selected parameters of the X-ray diffraction study, and details of structure refinement are listed in Table 1. The structures of both compounds were solved by direct methods and refined against structure factors with anisotropic thermal parameters for non-hydrogen atoms. The hydrogen atoms were placed in calculated positions. Absorption was ignored. Calculations were carried out using the CSD [8] and SHELX97 [9] program packages. The crystallographic data for compounds **I** and **II** were deposited at the Cambridge Structural Database (refcodes 164 257 and 164 249, respectively). The bond lengths and bond angles of compound **I** are listed in Tables 2 and 3, respectively, and the corresponding characteristics of compound **II** are listed in Tables 4 and 5, respectively.

The molecules of both steroids adopt similar conformations (Figs. 1, 2; Table 6). The ring *A* is planar, the ring *B* adopts a distorted half-chair conformation, and the *trans*-fused rings *C* and *D* have virtually regular chair conformations. The deviation of the carbon atom of the methoxy group at the C(3) atom from the plane of ring *A* in molecule **I** is somewhat larger than that in two molecules of compound **II**. In molecule **I**, this carbon atom is in the *trans* position with respect to the C(2)–C(3) bond, whereas these atoms, in both independent molecules of compound **II**, are in the *cis* position (Figs. 1, 2). In addition, the mutual orientation of the rings in compound **I** is somewhat different from that in both independent molecules of steroid **II**, which manifests itself in the distances between the oxygen atoms at

Table 5. Bond angles ω (deg) in compound **II**

Angle	ω	Angle	ω
C(3)–O(1)–C(3A)	117.6(4)	C(3')–O(1')–C(3A')	117.0(4)
C(20)–O(2)–C(17A)	117.1(4)	C(20')–O(2')–C(17A')	118.1(4)
C(5)–O(6)–C(7)	117.2(4)	C(5')–O(6')–C(7')	116.5(4)
C(2)–C(1)–C(10)	112.5(5)	C(10')–C(1')–C(2')	122.3(5)
C(1)–C(2)–C(3)	119.4(5)	C(3')–C(2')–C(1')	118.2(5)
O(1)–C(3)–C(2)	123.6(5)	C(2')–C(3')–C(4')	122.6(5)
O(1)–C(3)–C(4)	115.6(4)	C(2')–C(3')–O(1')	112.8(4)
C(2)–C(3)–C(4)	120.7(5)	C(4')–C(3')–O(1')	114.6(4)
C(3)–C(4)–C(5)	118.1(5)	C(3')–C(4')–C(5')	116.6(5)
C(3)–C(4)–C(4A)	120.7(4)	C(3')–C(4')–C(4A')	121.4(5)
C(5)–C(4)–C(4A)	121.2(5)	C(5')–C(4')–C(4A')	122.0(5)
O(6)–C(5)–C(4)	115.6(4)	C(4')–C(5')–C(10')	123.2(5)
O(6)–C(5)–C(10)	122.1(4)	C(4')–C(5')–O(6')	115.2(4)
C(4)–C(5)–C(10)	122.3(5)	C(10')–C(5')–O(6')	121.5(4)
O(6)–C(7)–C(8)	109.7(4)	O(6')–C(7')–C(8')	110.0(4)
C(14)–C(8)–C(7)	117.4(4)	C(7')–C(8')–C(9')	108.3(4)
C(14)–C(8)–C(9)	111.5(4)	C(7')–C(8')–C(14')	118.2(4)
C(7)–C(8)–C(9)	109.0(4)	C(9')–C(8')–C(14')	110.7(4)
C(10)–C(9)–C(8)	110.5(4)	C(10')–C(9')–C(11')	112.1(4)
C(10)–C(9)–C(11)	113.0(4)	C(10')–C(9')–C(8')	110.7(4)
C(8)–C(9)–C(11)	111.5(4)	C(11')–C(9')–C(8')	111.2(4)
C(1)–C(10)–C(5)	116.9(4)	C(1')–C(10')–C(5')	117.0(4)
C(1)–C(10)–C(9)	121.7(4)	C(1')–C(10')–C(9')	121.3(4)
C(5)–C(10)–C(9)	121.3(4)	C(5')–C(10')–C(9')	121.7(4)
C(12)–C(11)–C(9)	111.3(4)	C(12')–C(11')–C(9')	111.4(4)
C(11)–C(12)–C(13)	113.4(4)	C(11')–C(12')–C(13')	112.9(4)
C(18)–C(13)–C(12)	110.6(4)	C(18')–C(13')–C(12')	110.2(4)
C(18)–C(13)–C(17A)	108.8(4)	C(18')–C(13')–C(17A')	109.2(4)
C(12)–C(13)–C(17A)	109.8(4)	C(12')–C(13')–C(17A')	108.9(4)
C(18)–C(13)–C(14)	114.6(4)	C(18')–C(13')–C(14')	114.8(4)
C(12)–C(13)–C(14)	108.2(4)	C(12')–C(13')–C(14')	109.0(4)
C(17A)–C(13)–C(14)	104.6(4)	C(17A')–C(13')–C(14')	104.4(4)
C(8)–C(14)–C(15)	114.8(4)	C(15')–C(14')–C(8')	113.9(4)
C(8)–C(14)–C(13)	115.3(4)	C(15')–C(14')–C(13')	111.9(4)
C(15)–C(14)–C(13)	112.0(4)	C(8')–C(14')–C(13')	115.0(4)
C(14)–C(15)–C(16)	112.1(4)	C(16')–C(15')–C(14')	110.4(4)
C(17)–C(16)–C(15)	111.2(4)	C(17')–C(16')–C(15')	112.0(4)
C(17A)–C(17)–C(16)	110.4(4)	C(17A')–C(17')–C(16')	111.2(4)
O(2)–C(17A)–C(17)	108.5(4)	O(2')–C(17A')–C(17')	110.3(4)
O(2)–C(17A)–C(13)	108.5(4)	O(2')–C(17A')–C(13')	108.4(4)
C(17A)–C(17A)–C(13)	114.3(4)	C(17')–C(17A')–C(13')	113.5(4)

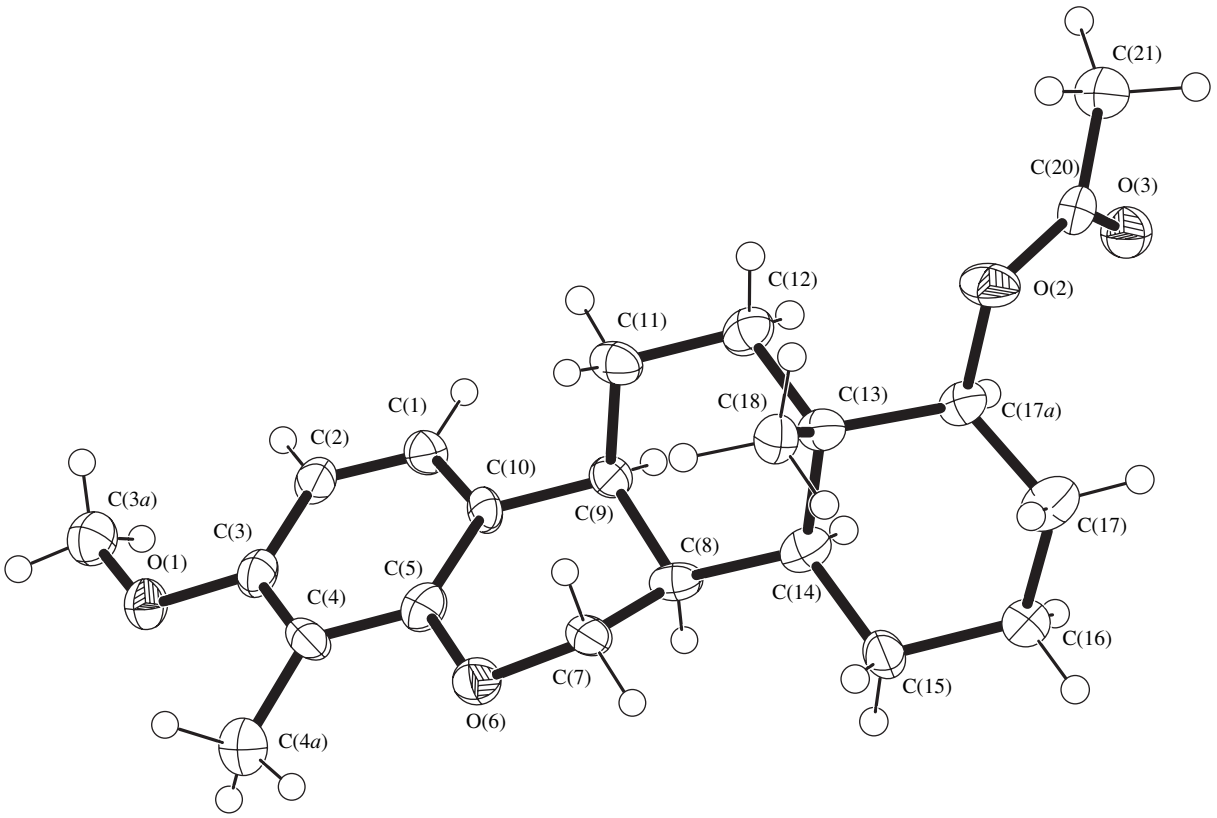

Fig. 2. Atomic numbering scheme and the molecular structure of compound **II**.

the rings *A* and *D* (this distance is of importance for binding with estrogen receptors). In compound **I**, this distance is 10.764(5) Å. The corresponding distances in two independent molecules of 8-iso analogue **II** are 10.718(8) and 10.704(8) Å. In both compounds, these distances are noticeably shorter than in the natural hormone estradiol (10.93 Å) [10].

Since certain differences in the conformations of steroids **I** and **II** may be caused by the molecular packing in the crystals, we examined the ^{1}H NMR spectra of these compounds in chloroform. A strong nuclear Overhauser effect between the protons of the methoxy group and the H(2) and H(4) protons observed for steroid **I** is indicative of a relatively free rotation of the CH_3O group.

Table 6. Conformational characteristics of molecules **I** and **II**

Compound		Angle between the ring planes, deg		
		A and *C*	*A* and *D*	*C* and *D*
II	Molecule 1	39.6	41.1	11.2
	Molecule 2	45.4	47.7	10.6
I		45.9	46.7	12.6

For compound **II**, the nuclear Overhauser effect between the protons of the methyl group at the C(4) atom and the methoxy group was almost unobservable. Hence, these groups are separated by a distance no less than 3 Å. In other words, rotation of the methoxy group with respect to the C(3)–O(1) bond is inhibited, and the conformation of steroid **II** about the ring *A* in the crystal is close to that in a solution.

It is known that a replacement of the methylene group at position 6 of 8-iso analogues of steroid estrogens by an oxygen atom causes a decrease in hormonal activity [11, 12]. The results of our study demonstrate that the simultaneous presence of the O(6) atom and the methyl group at the C(4) atom is a crucial factor responsible for the complete loss of estrogen activity in compound **II**. It appears that the methyl group near the C(4) atom is of most importance in this regard, because its introduction into the steroid leads not only to a change in molecular conformation but also to a hindrance to rotation of the methoxy group relative to the C(3)–O(1) bond.

REFERENCES

1. D. A. Holt, M. A. Levy, D. L. Ladd, *et al.*, J. Med. Chem. **33**, 937 (1990).

2. K.-M. Sam, F. Labrie, and D. Poirier, Eur. J. Med. Chem. **35** (2), 217 (2000).
3. L. W. L. Woo, N. M. Hawarth, A. Purohit, *et al.*, J. Med. Chem. **41** (7), 1068 (1998).
4. A. Purohit, L. W. L. Woo, B. V. L. Potter, and M. J. Reed, Cancer Res. **60**, 3394 (2000).
5. A. M. Brzozowski, C. Ashley, A. C. Pike, *et al.*, Nature **389**, 753 (1997).
6. H. Gao, J. A. Katzenellenbogen, R. Garg, and C. Hansch, Chem. Rev. **99**, 723 (1999).
7. V. V. Korkhov, V. P. Makusheva, G. E. Lupanova, *et al.*, Khim.–Farm. Zh., No. 5, 574 (1986).
8. L. G. Acselrud, Yu. N. Griun, P. Zavalii, *et al.*, in *Collected Abstracts of XII European Crystallographic Meeting* (Nauka, Moscow, 1989), Vol. 3, p. 155.
9. G. M. Sheldric, *SHELXL97. Program for the Solution and Refinement of Crystal Structures* (Univ. of Göttingen, Germany, 1997).
10. B. Busetta and M. Hospital, Acta Crystallogr., Sect. B: Struct. Crystallogr. Cryst. Chem. **28**, 560 (1972).
11. R. M. Tomarelli, T. M. Dougherty, and F. W. Bernhart, J. Pharm. Sci. **55** (12), 1392 (1966).
12. I. Yu. Kameneva, A. G. Shavva, V. T. Lozovskiĭ, and V. E. Ryzhenkov, Byull. Éksp. Biol. Med., No. 3, 262 (1994).

Translated by T. Safonova

Crystallography Reports, Vol. 49, No. 3, 2004, pp. 443–449. Translated from Kristallografiya, Vol. 49, No. 3, 2004, pp. 508–514.

LATTICE DYNAMICS AND PHASE TRANSITIONS

Dedicated to the 80th Birthday of L.A. Shuvalov

Dielectric Properties of Triglycine Sulfate Crystals with Defects at Low and Infralow Frequencies

A. V. Shil'nikov*, V. A. Fedorikhin*, B. A. Strukov, and N. V. Ratina***

** Volgograd State Architectural and Civil Engineering Academy, Akademicheskaya ul. 1, Volgograd, 400074 Russia*
e-mail: postmaster@vgasa.ru
*** Faculty of Physics, Moscow State University, Vorob'evy gory, Moscow, 119992 Russia*
Received June 5, 2003

Abstract—Dielectric responses of several crystals in ultraweak measuring fields at low and infralow frequencies are compared, namely, of nominally pure, Cr- and Lα-alanine-doped triglycine sulfate (TGS) crystals and TGS + Cr^{3+} crystals irradiated with X-rays. It is shown that dopant-induced bias fields give rise to crystal unipolarity, suppress the domain contribution to their dielectric response, and diffuse the phase transition. It is established that X-ray irradiation of the crystals results in "radiation annealing" of TGS + Cr^{3+} crystals, which increases their permittivity and diminishes diffusion of the phase transition. © *2004 MAIK "Nauka/Interperiodica".*

INTRODUCTION

In recent decades, the influence of structural defects on macroscopic physical properties (including dielectric) of ferroelectric crystals remains important for both fundamental and applied studies. Experimenters are focussing their efforts on studies of model triglycine sulfate (TGS) crystals, which undergo a second-order phase transition and possess a labile, comparatively simple 180° domain structure. The structure of Cr^{3+}-doped TGS crystals was studied in [1–3], their dielectric and pyroelectric properties, in [4–12], and their thermal and elastic properties, in [13]. The dielectric and pyroelectric properties of *L*α-alanine-doped TGS single crystals were investigated in [12, 14–16], and their thermal and elastic properties, in [13]. Low doses of X-ray radiation influence the processes of pulsed switching in Cr^{3+}-doped TGS crystals, which was studied at various Cr^{3+} concentrations in [17]. It was established that the specific features of the phase transition [13] and crystal response determined by the domain structure of the crystal [5] are rather sensitive to defects and, in particular, to the incorporation of Cr^{3+} [1–13], replacement of *L*α-alanine [9, 14–16], and defects induced by X-ray irradiation, e.g., in (TGS + Cr^{3+})*R* [17]. The present study was undertaken with the aim of establishing the influence of the lattice defects formed by domain and phase boundaries on the dielectric parameters characterizing the phase transitions, the influence of lattice defects formed by Cr and *L*α-alanine dopants on these parameters, and the influence of the defects induced by X-ray irradiation of TGS + Cr^{3+} single crystals, as well as to clarify the role played by crystal history (direction of the temperature change, annealing above the phase-transition temperature, duration of keeping crystal at constant temperature, etc.).

Moreover, we also considered it to be necessary to study the nature of some switching characteristics, because the bias fields induced by impurities such as Cr [1–13] considerably influence the dielectric response in TGS crystals.

MEASURING METHODS AND SAMPLES

A nominally pure sample was cut out from a TGS single crystal grown at $T = 295$ K at the Institute of Crystallography of the Russian Academy of Sciences. The sample history included prolonged aging without action of any external factors at room temperature, subsequent sample heating from 293 to 393 K, 36-h annealing of the sample at 393 K, and its cooling to 293 K.

A Cr^{3+}-doped sample was cut out from a TGS + Cr^{3+} crystal grown from the TGS solution with addition of the $Cr_2(SO_4)_3 \cdot 6H_2O$ salt at 317 K at the Institute of Radioelectronics of the Czechoslovakian Academy of Sciences. According to the photocolorimetric data, the chromium concentration in the crystal did not exceed 0.02 wt %.

This sample was cleaved into smaller plates. One of these plates was supplied with silver-leaf electrodes (the same was also made for a TGS sample).

The sample history included prolonged aging at room temperature without action of any external factors, the first heating cycle in the temperature interval from 293 to 373 K, 15-h annealing at 373 K, subse-

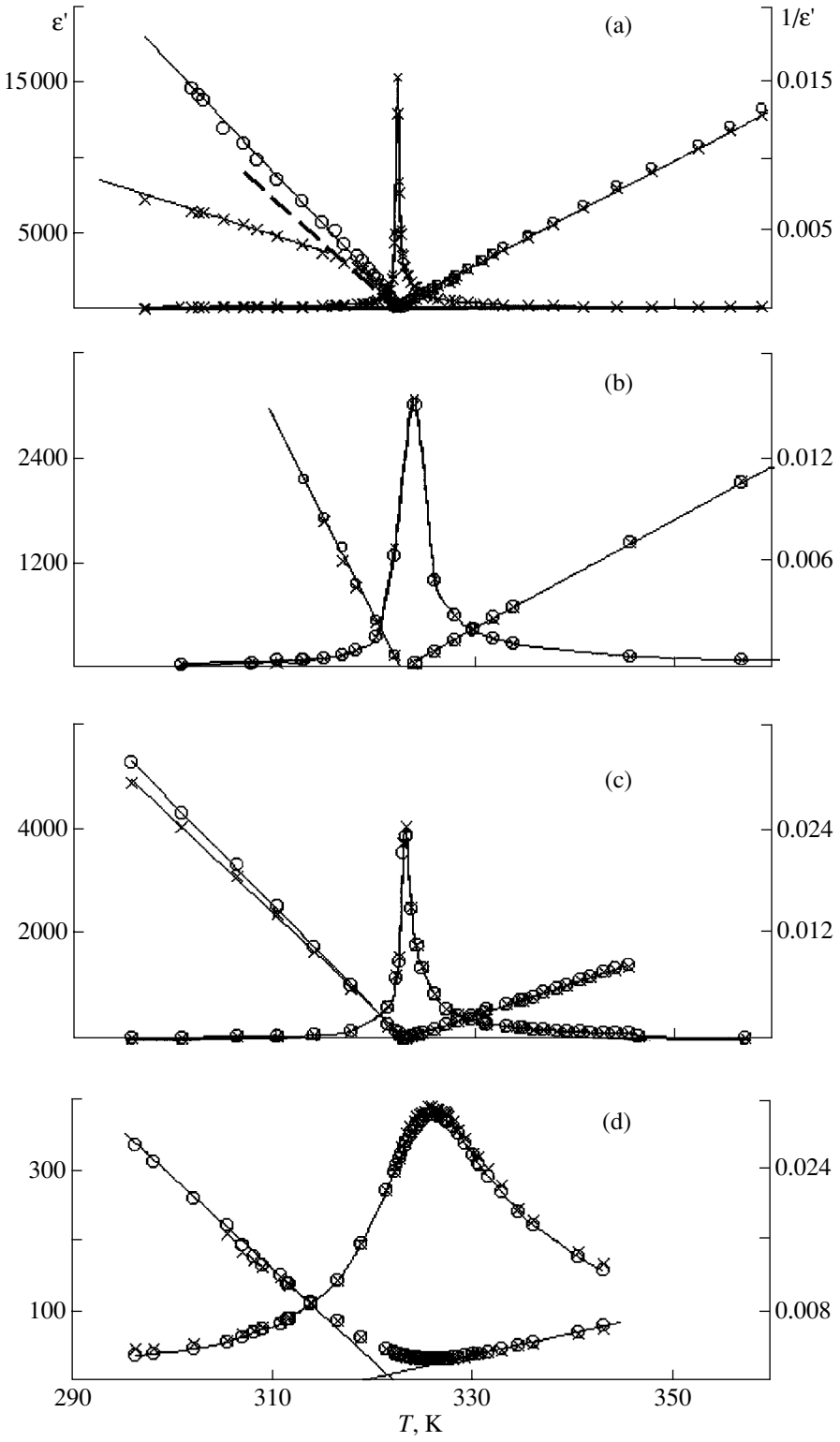

Fig. 1. Temperature dependences of the real part (ε_0') of the initial complex permittivity (ε_0^*) obtained in the heating mode in the fields $E_0 \le 0.4$ V cm^{-1} and its reciprocal value $(1/(\varepsilon_0'))$ for (a) nominally pure TGS, (b) TGS + Cr^{3+}, (c) (TGS + Cr^{3+})*R*, and (d) (TGS + *L*α-alanine) crystals at (○) 1 kHz and (×) 1 Hz. Dashed line shows the initial (in the vicinity of the phase transition) slope of the $1/(\varepsilon_0')(T)$ curve.

quent cooling to 293 K, the second heating cycle in a narrow temperature interval (317–324 K), and, finally, cooling to 308 K.

The *L*α-alanine-doped sample was cut out from a LATGS crystal grown at 305 K at the *Polyus* Research Institute. The *L*α-alanine concentration in the solution was 10% and, in the crystal, ~0.01%.[1] Sample history included prolonged aging at room temperature without action of any external factors, 20-h-heating from 293 to 243 K, and subsequent cooling to 306 K. One of the TGS + Cr^{3+} samples described above was irradiated with the characteristic CuK_α radiation along the polar axis with the energy 30 eV (at a dose of ~80 kR and a dose rate N_D ~ 240 kR/h) at the temperature ~303 K. After prolonged aging at room temperature, the samples were heated from 293 to 373 K, annealed at 373 K, and cooled to 293 K. We also annealed an irradiated (TGS + Cr^{+3})*R* sample to check the stability of its ferroelectric properties and the influence of X-ray irradiation.

The amplitude–frequency characteristics of complex permittivity ε* of all the samples at room temperature were measured on a bridge-type setup [18] in the frequency range from 10^{-1} to 10^4 Hz and with the measuring-field amplitude E_0 not exceeding 0.4 V/cm, with the real (ε') and imaginary (ε") components of complex permittivity ε* being measured separately with an error of about 1% in ε' and 2–5% in ε". The temperature was maintained with an accuracy not worse than ±0.05 K, the measurement accuracy was ± 0.001 K.

The low- and infralow frequency spectra of ε* were studied during sample cooling and heating at 15–20 frequencies ranging from 10 kHz to 0.1 Hz. The mean rates of the first heating and cooling cycles did not exceed 4 mK/s, and the mean rates of the second heating and cooling cycles did not exceed 0.2 mK/s. The time necessary for recording each ε* spectrum at 15–20 measuring frequencies ranged from 700 to 900 s.

It should be noted that the early history of all the samples was the same (prolonged aging at room temperature). We believe that, in this case, growth defects in a nominally pure crystal, intentionally induced defects (Cr^{3+}, *L*α-alanine), radiation-induced (*R*) defects, and defects formed by domain and phase boundaries should be in the most stable state and, giving rise to frozen fluctuations [13], should influence the dielectric parameters characterizing the phase transitions.

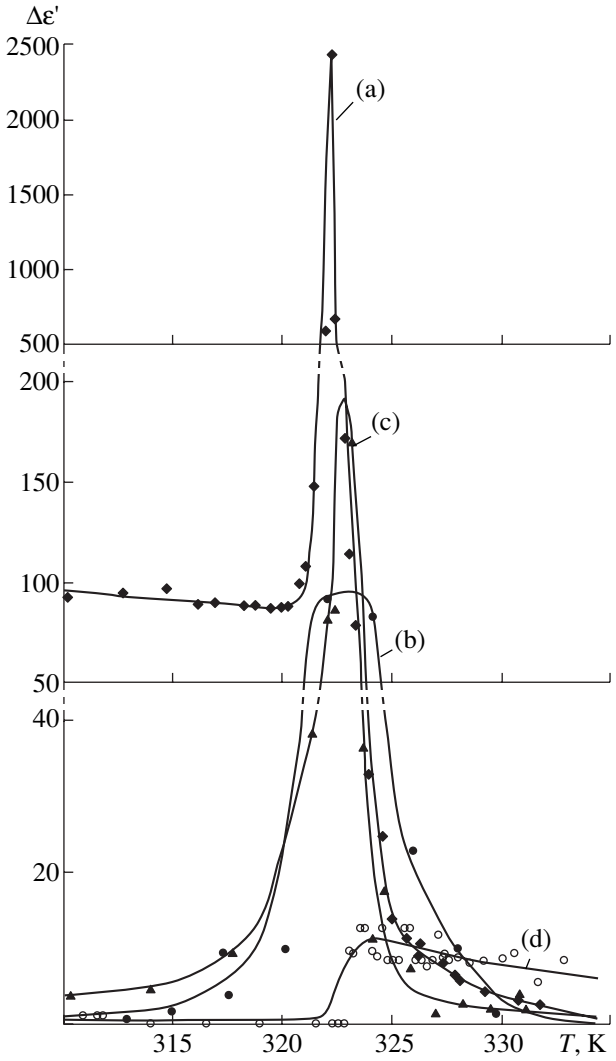

Fig. 2. Temperature dependences of the effective depth of dispersion ($\Delta\varepsilon' = \varepsilon'_{\text{eff 1 Hz}} - \varepsilon'_{\text{eff 1 kHz}}$) for (♦) (a) TGS, (●) (b) (TGS + Cr^{3+}), (▲) (c) (TGS + Cr^{3+})*R*, and (○) (d) (TGS + *L*α-alanine) crystals.

RESULTS AND DISCUSSION

Figure 1 shows the temperature dependence of the real part of the initial complex permittivity $\varepsilon'_0(T)$ and the quantity $1/\varepsilon'_0(T)$ for a nominally pure TGS crystal (Fig. 1a), a (TGS + Cr^{3+}) crystal (Fig. 1b), (TGS + Cr^{3+})*R* crystal (Fig. 1c), and (TGS + *L*α-alanine) crystal (Fig. 1d) measured in the heating mode at (≤0.4 V cm^{-1}) low and infralow frequencies (1 Hz and 1 kHz, respectively). It is clearly seen that the Curie–Weiss law characterizing the phase transition is obeyed in all the crystals in both paraelectric and polar phases. However, like the character of the dielectric response observed in

[1] Heat conductivity C_p^E and permittivity ε_{22} (ν = 1 kHz, E_0 = 0.1 V/cm) were measured by the method of absolute adiabatic vacuum calorimetry; the velocities of longitudinal ultrasonic waves V_z at the frequency 10 MHz were measured by the Raman–Nutt method on a sample cut out from such a single crystal [13].

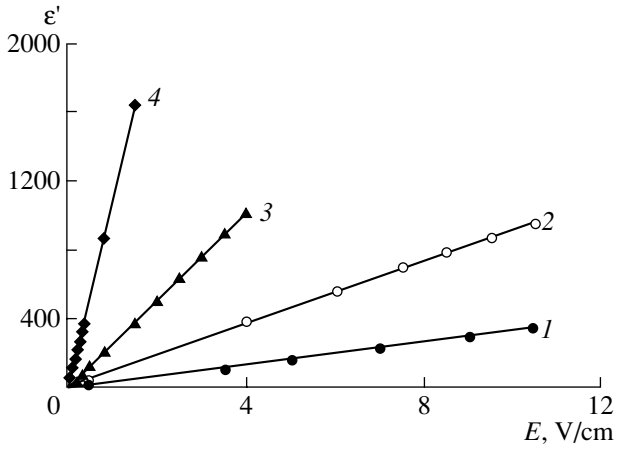

Fig. 3. Amplitude dependences of ε'_{eff} for (*1*) (TGS + Cr^{3+}) at t = 23.5°C, (*2*) (TGS + *L*α-alanine) at t = 23.5°C, (*3*) (TGS + Cr^{3+})*R* at t = 27°C, and (*4*) TGS crystals at t = 26.1°C obtained at the frequency 1 Hz and provided by the irreversible domain-boundary motion by the hysteresis mechanism.

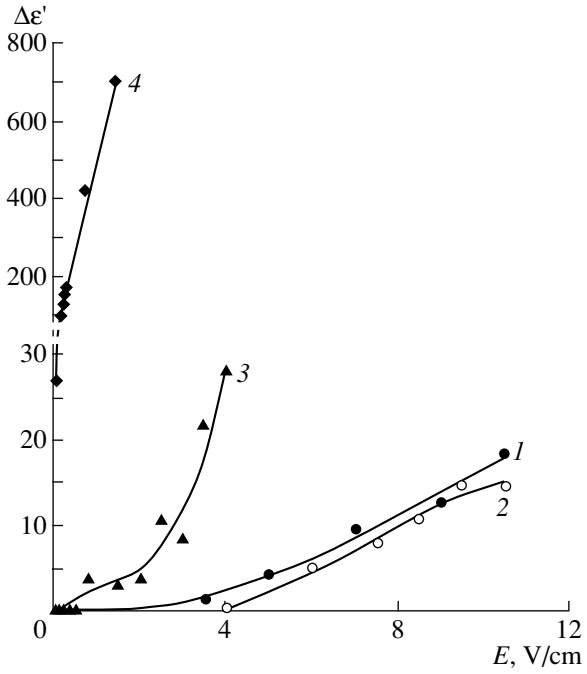

Fig. 4. Amplitude dependences of the effective depth of dispersion ($\Delta\varepsilon' = \varepsilon'_{eff\ 1Hz} - \varepsilon'_{eff\ 1kHz}$) of (*1*) (TGS + Cr^{3+}), (*2*) (TGS + *L*α-alanine), (*3*) (TGS + Cr^{3+})*R*, and (*4*) TGS crystals.

Rochelle salt crystals [19], a nominally pure TGS crystal (Fig. 1a) shows the dispersion of the Curie–Weiss "constant" associated with the contribution to ε'_0 of domain boundaries whose vibrations relax in ultraweak LF and ILF electric fields. Moreover, at a frequency of 1 Hz, the straight line, which describes the Curie–Weiss law, acquires a kink (two values of the Curie–Weiss constant—one value in the direct vicinity of the phase-transition point and another value in the bulk of the polar phase).

It should be noted that, in this case, cooling of a pure TGS crystal below T_c, makes the ε_0^* (ε'_0 and ε''_0) values essentially nonequilibrium because of a considerable time-dependent domain contribution. This leads, in particular, to extremely low C_p/C_f values (table).

The Cr^{3+} and *L*α-alanine impurities give rise to the formation of internal bias fields polarizing the TGS crystals in the polar phase (leading to practical absence of domain boundaries). Therefore, contrary to nominally pure crystals (Figs. 1a and 2), the (TGS + Cr^{3+}) (Fig. 1b) and (TGS + *L*α-alanine) (Fig. 1d) crystals show practically no dispersion of ε'_0 in the polar phase, and, as a consequence, no dispersion of the Curie–Weiss constant (Figs. 1b and 1d). The (TGS + Cr^{3+})*R* crystal shows weak (~6.7%) dispersion of C_f.

It is worth noting that the Cr^{3+} and *L*α-alanine impurities somewhat diffuse the phase transition in TGS crystals containing them (Figs. 1b and 1d), whereas in nominally pure TGS and (TGS + Cr^{3+})*R* crystals, phase transitions take place practically at a point (Figs. 1a and 1c). The Cr^{3+} and *L*α-alanine impurities lead to different degrees of phase-transition diffusion (Figs. 1b and 1d). The most pronounced dispersion of ε'_0 in these crystals is observed in the region of the diffused phase transition (Fig. 2).

Comparing the dependences in Figs. 1b and 1c with those in Figs. 2b and 2c, we see that X-ray irradiation of (TGS + Cr^{3+}) crystals results in the so-called radiation annealing of the sample—its permittivity increases, and the phase transition becomes less diffuse. However, it should be emphasized that the region of pronounced dispersion of ε* in this crystal, as well as in (TGS + Cr^{3+}) and (TGS + *L*α-alanine) crystals, is observed mainly in the temperature range near the phase transition. Therefore, one can assume that radiation annealing only partly reduces unipolarity of the (TGS + Cr^{3+}) crystal. One may also assume that the consequences of radiation annealing indicated above are caused (at a low irradiation dose) [20] by the destruction of a certain number of chelate complexes of chromium biglycine sulfate responsible for the formation of the unipolar state in a (TGS + Cr^{3+}) crystal [1–3].

The table indicates the dielectric characteristics of crystals having different histories depending on the measuring-field frequency. It should be noted that a possible dependence of the maximum ε/ value at the phase-transition point on the crystal thickness was not taken into account in our measurements.

It is seen that, in most of the cases, the so-called "law of two" is not fulfilled. There is not much sense in referring to the adiabatic dielectric response in this case, because, at infralow frequencies (i.e., under the

Main dielectric characteristics of samples having different histories

Parameters	ε'_{max}	ε'_{max}	C_p, K (paraelectric phase)		C_f, K (ferroelectric phase)		T_c, K obtained from $1/\varepsilon' = f'(T)$		C_p / C_f	
	Experiment									
Mode	1 kHz	1 Hz	1 kHz	1 Hz	1 kHz	1 Hz	1 kHz	1 Hz	1 kHz	1 Hz
TGS heating	12 899 ± 129	15 331 ± 153	2667 ± 46	2688 ± 46	969 ± 31	1112 ± 63	322.25 ± 0.02	322.55 ± 0.02	2.75 ± 0.12	2.42 ± 0.11
(TGS + Cr^{3+}) heating	3002 ± 30	3084 ± 31	3173 ± 3	3288 ± 4	919 ± 4	928 ± 4	323.10 ± 0.02	322.85 ± 0.02	3.45 ± 0.03	3.54 ± 0.03
(LA TGS) heating	376 ± 4	389 ± 4	4156 ± 46	4604 ± 51	1160 ± 7	1226 ± 8	323.00 ± 0.02	323.20 ± 0.02	3.58 ± 0.07	3.76 ± 0.08
TGS + Cr^{3+} + *R* heating	3905 ± 39	4076 ± 41	2584 ± 26	2695 ± 25	851 ± 3	912 ± 5	322.92 ± 0.02	322.89 ± 0.02	3.04 ± 0.07	2.95 ± 0.05
TGS cooling	30277 ± 303	32 368 ± 324	2890 ± 51	2933 ± 52	3546 ± 186	5348 ± 304	322.00 ± 0.02	322.00 ± 0.02	0.82 ± 0.03	0.55 ± 0.02
(TGS + Cr^{3+}) cooling	3084 ± 31	3084 ± 31	3176 ± 2	3338 ± 2	1559 ± 8	1787 ± 7	322.70 ± 0.02	322.40 ± 0.02	2.04 ± 0.04	1.87 ± 0.04
(LA TGS) cooling	376 ± 4	391 ± 4	4063 ± 41	4474 ± 48	1233 ± 9	1129 ± 9	323.70 ± 0.02	322.80 ± 0.02	3.30 ± 0.03	1.96 ± 0.03
TGS + Cr^{3+} + *R* cooling	3084 ± 31	3084 ± 31	3176 ± 2	3338 ± 2	1559 ± 8	1787 ± 7	322.70 ± 0.02	322.40 ± 0.02	2.04 ± 0.04	1.87 ± 0.04

Note: C_p and C_f are the Curie–Weiss constants determined for the para- and ferroelectric phases, respectively.

conditions close to isothermal) this law is not fulfilled either. Moreover, as follows from the table and [19], the inequality $C_p/C_f < 2$ becomes stronger with a decrease in the measuring-field frequency and after annealing of the crystal in the nonpolar phase.

The problem seems to be associated, first of all, with defects in crystals, which is confirmed by the presence or absence of domain boundaries (Fig. 1), crystal history (e.g., the above note on essentially nonequilibrium ε values after crystal annealing), etc. Only by making appropriate allowance for the total polarization of the crystal caused not only by the "lattice factors" but also by the contribution of various defects to polarizability can give the true value of the C_p/C_f ratio.

Figure 3 shows the amplitude dependences $\varepsilon'_{\text{eff}}(E_0)$ for (TGS + Cr^{3+}), (TGS + Cr^{3+})*R*, and (TGS + *L*α-alanine) crystals and a nominally pure TGS crystal obtained at a frequency of 1 Hz. It is clearly seen that the Rayleigh law (first established for ferromagnetics [21]) is fulfilled for all the crystals and, for ferroelectrics, can be written as

$$\varepsilon'_{\text{eff}} = \varepsilon'_0 + bE,$$

where ε'_0 is the initial value of permittivity and *b* is the Rayleigh constant characterizing the slope of the $\varepsilon'_{\text{eff}}(E_0)$ line in Fig. 3 or the distribution function over coercive and internal fields in the Preizach model [22]. Since the Rayleigh law corresponds to the hysteresis switching mechanism, one can draw the conclusion that, within the ranges of a weak field ($E_0 \approx 0.1$–10.5 V/cm) and frequencies (ν = 1 Hz–1 kHz), TGS crystals are switched by the hysteresis mechanism of domain-boundary motion [32] earlier observed for nominally pure TGS crystals in weak fields at a frequency of 50 Hz [24]. However, it should be emphasized that, depending on the unipolarity degree of the crystal, the hysteresis switching mechanism may manifests itself in different ranges of the field.

Figure 4 illustrates the amplitude dependence of the effective dispersion depth ($\Delta\varepsilon' = \varepsilon'_{\text{eff 1 Hz}} - \varepsilon'_{\text{eff 1 kHz}}$) obtained in switching of TGS crystals in the above ranges of the fields and frequencies. It is seen that, with an increase of the field (increase in the number of domain boundaries participating in hysteresis switching and the amplitudes of their vibrations), the $\Delta\varepsilon'$ value also increases. Thus, in a way similar to a nominally pure crystal (Fig. 1a), the (TGS + Cr^{3+}), (TGS + Cr^{3+})*R*, and (TGS + *L*α-alanine) crystals also show dispersion of $\varepsilon^*_{\text{eff}}$ at low and infralow frequencies caused by the contribution of domain-boundary vibrations into $\varepsilon^*_{\text{eff}}$.

CONCLUSIONS

Lattice defects in TGS crystals, such as domain and interphase boundaries, Cr^{3+} and *L*α-alanine impurities, defects induced by X-ray irradiation in (TGS + Cr^{3+}) crystals, and crystal history, play the key part in the character of the dielectric response of these crystals at low and infralow frequencies. The low and infralow dispersion of complex permittivity ε* of the crystals studied is explained by the contribution that comes to ε* from domain boundaries and other defects. In switching of nominally pure, Cr^{3+} and *L*α-alanine-doped TGS crystals and X-ray irradiated (TGS + Cr^{3+}) crystals in weak fields at low and infralow frequencies, the hysteresis mechanism of domain-boundary motion is observed, and the character of switching is described by the Rayleigh law.

ACKNOWLEDGMENTS

The authors are grateful to A.P. Pozdnyakov for his participation in measurements of ε*(*T*) in nominally pure TGS crystals. The study was supported by the Russian Foundation for Basic Research (project no. 02-02-16232), the Competition Center of the Ministry of Education of the Russian Federation (project no. E02-3.4-424), and the Program "Scientific Research of Higher Schools along the Priority Directions of Science and Technology" (project no. 202.03.02.04), and The Leading Scientific School (project NSh-15.14.2003.2).

REFERENCES

1. W. Windsch, Izv. Akad. Nauk SSSR, Ser. Fiz. **39** (5), 914 (1975).
2. W. Windsch and G. Völkel, Ferroelectrics **9**, 187 (1975).
3. V. A. Yurin, S. Waplak, J. Stankowski, *et al.*, Kristallografiya **21** (2), 327 (1976) [Sov. Phys. Crystallogr. **21**, 177 (1976)].
4. S. D. Milovidova, I. V. Vavresyuk, I. I. Evseev, and O. V. Poluchina, Izv. Akad. Nauk, Ser. Fiz. **57** (3), 184 (1993).
5. I. S. Zheludev and Ts. Zh. Ludupov, Izv. Akad. Nauk SSSR, Ser. Fiz. **31** (7), 1184 (1967).
6. L. N. Kamysheva, L. A. Godovannaya, S. D. Milovidova, and V. P. Konstantinova, Izv. Akad. Nauk SSSR, Ser. Fiz. **39** (4), 857 (1975).
7. S. D. Milovidova, N. D. Gavrilova, B. V. Selyuk, *et al.*, Izv. Akad. Nauk SSSR, Ser. Fiz. **39** (5), 1020 (1975).
8. B. V. Selyuk, N. D. Gavrilova, and V. K. Novik, Izv. Akad. Nauk SSSR, Ser. Fiz. **39** (5), 1052 (1975).
9. J. Stankowska, Acta Phys. Pol. A **64**, 115 (1983).
10. H. Schlemmbach and W. Windsch, Wiss. Beitr. M. Luther–Univ. Halle–Wittenberg O. **16**, 120 (1985).
11. A. S. Sidorkin, S. D. Milovidova, N. Yu. Ponomareva, and O. V. Rogazinskaua, Ferroelectrics **219**, 23 (1998).
12. V. K. Novik and N. D. Gavrilova, Fiz. Tverd. Tela (St. Petersburg) **42** (6), 961 (2000) [Phys. Solid State **42**, 991 (2000)].
13. B. A. Strukov, T. P. Spiridonov, K. A. Minaeva, *et al.*, Kristallografiya **27** (2), 313 (1982) [Sov. Phys. Crystallogr. **27**, 190 (1982)].

14. K. L. Bye, P. W. Wipps, and E. T. Keve, Ferroelectrics **4** (4), 253 (1972).

15. A. Hadni and R. Thomas, Appl. Phys. **10** (1), 91 (1976).

16. V. E. Mudryĭ and V. A. Yurin, *Ferroelectrics and Piezoelectrics* (Kalinin, 1977), p. 49.

17. L. N. Kamysheva, S. N. Drozhdin, and O. M. Golitsyna, Fiz. Tverd. Tela (St. Petersburg) **44** (2), 347 (2002) [Phys. Solid State **44**, 361 (2002)].

18. A. V. Shil'nikov, E. G. Nadolinskaya, V. A. Fedorikhin, and S. V. Rodin, Kristallografiya **39** (1), 84 (1994) [Crystallogr. Rep. **39**, 74 (1994)].

19. A. V. Shil'nikov, N. M. Galiyarova, E. G. Nadolinskaya, *et al.*, Kristallografiya **31** (2), 326 (1986) [Sov. Phys. Crystallogr. **31**, 192 (1986)].

20. A. P. Dem'yanchuk, Candidate's Dissertation in Physics and Mathematics (Kiev, 1976).

21. R. S. Lord Rayleigh, Philos. Mag. **23**, 225 (1887).

22. F. Preisach, Z. Phys. **94**, 277 (1935).

23. A. V. Shil'nikov, N. M. Galiyarova, S. V. Gorin, *et al.*, Izv. Akad. Nauk SSSR, Ser. Fiz. **55** (3), 578 (1991).

24. A. V. Shil'nikov, *Physics of Dielectrics and Semiconductors* (VPI, Volgograd, 1970), Vol. 29, p. 95.

Translated by L. Man

Crystallography Reports, Vol. 49, No. 3, 2004, pp. 450–458. Translated from Kristallografiya, Vol. 49, No. 3, 2004, pp. 515–523.

LATTICE DYNAMICS AND PHASE TRANSITIONS

Theory of Phase Transitions of Proper-Decomposition Type in Binary Solid Solutions

A. Yu. Gufan

Research Institute of Physics, Rostov State University, pr. Stachki 8, Rostov-on-Don, 344090 Russia

e-mail: gufan_gufan@mail.ru

Received January 15, 2003

Abstract—A theory of "proper decomposition" of solid solutions has been constructed. The theory differs from earlier theories in that it phenomenologically takes into account three- and four-particle interactions. It is shown that this theory allows one to describe four essentially different types of phase diagrams. Within the framework of the theory developed, the structure and composition of the native Au_cAg_{1-c} solid solutions are discussed. The decomposition of these solid solutions observed at $0.02 < c < 0.12$ results from the competition of the proper and improper decompositions. The improper decomposition is associated with the formation of küstelite. © *2004 MAIK "Nauka/Interperiodica".*

INTRODUCTION

The *T–c* phase diagrams of binary (or quasi-binary) solid solutions and alloys [1] show two essentially different types of decomposition: stratification [2] and dissociation [3]. The first type corresponds to the dissociation of a solid solution with the average concentration *c* of one of the components (*A*) into the mechanical mixture of two solid solutions (*1*) and (*2*) with different concentrations of the component *A*, c_1 and c_2 ($c_1 > c > c_2$).[1] The characteristic feature of the first-type decomposition is that the compositions of phases *1* and *2* can vary depending on the external conditions, such as temperature, pressure, etc. Then, the solid-solution decomposition is dependent on the characteristics of the interaction between the atomic components. As a result, the energy of isotropic (efficient pairwise) and anisotropic (multiparticle) interactions between the constituent atoms of the solid solution at low temperatures ($T < T_D$) makes the mechanical mixture of the homogeneous phases with the concentrations c_1 and c_2 thermodynamically stable. By analogy to the proper ferroelectric and ferroelastic phase transitions, this type of solid-solution decomposition may be called a proper decomposition. Proper decompositions are observed, e.g., in relaxor quasi-binary systems such as $PbMg_{1/3}Nb_{2/3}O_3$ [4]. This statement is based on the fact that the concentration stratification of the subsystem of ions in the positions of the perovskite structure, i.e., Mg–Nb ions, breaks the ferroelectric order in solid solutions [5]. The second type of solid-solution decomposition is caused by the ordering-type phase transitions in the solid solution and the formation of ordered phases with simple nonstoichiometric compositions similar to the Kurnakov phases in ordering alloys. In this case, the interatomic interactions at low temperatures stabilize the formation of ordered stoichiometric phases. The equilibrium thermodynamic potential of the ordered phases (G_K) in the vicinity of the stoichiometric composition ($c = c_0$) (corresponding to ordering in the atomic distribution over the lattice sites) turns out to be lower than the thermodynamic potential of the disordered mother G_0 solid solution ($G_K(c - c_0)$). The $G_K(c - c_0)$ dependence differs from the $G_0(c - c_0)$ dependence, so that at a certain *c* value such that $c = \tilde{c}$ we have $G_K(\tilde{c}) = G_0(\tilde{c})$. In this case, there exists a region of *c* values where the mechanical mixture of the ordered phase and the mother solid solution has the free energy lower than the free energy of any of the mixture components. In accordance with the classical concepts of the physical–chemical analysis [3], the existence of two different equilibrium states of a solid solution (dissociated into two phases and homogeneous) at the same concentrations of the component and at $G_{dec} < G_K$ and $G_{dec} < G_0$ always results in the decompositions of the solid solution in this concentration range (Rosebom diagrams [2, 3]). In the second type of solid-solution decomposition, at least one of the components has a constant composition and structure irrespectively of the external conditions. The second type of solid-solution decomposition not directly dependent on the component interactions is called improper decomposition. Improper decompositions have been repeatedly described based on various models [2, 6–9].

Below, we describe our study of proper decomposition of solid solutions. For the first time, we studied the proper decompositions within the framework of the phenomenological theory and illustrated possible

[1] If the products of the decomposition include a pure component, then the compositions of the particle forming the mechanical mixture are independent of the external conditions. Therefore, the feature indicated above is only one sign indicating the occurrence of the proper decomposition.

applications of this theory to the description of decomposition of the low-quality native gold $Ag_{1-c}Au_c$ [10] at $0.02 < c < 0.12$. Following Frenkel's ideas [11], the proper decomposition of a solid solution is considered as a specific type of ordering with a nonequilibrium coordinate (order parameter) that is the concentration of one of the components. However, unlike in the phenomenological Landau theory of phase transitions [12], the generalized nonequilibrium coordinate in the solid-solution decomposition is determined from the condition of the minimum equilibrium free energy G (or, depending on the conditions fixed at the thermostat, of any other thermodynamic potential). This minimum does not correspond to the extremum nonequilibrium Landau potential, because, when searching for this potential, one has to compare the values of the equilibrium thermodynamic potentials of different stable phases (states of the substance), whereas the equilibrium conditions are determined by the equality of the chemical potentials of the components in two thermodynamically stable phases.

We assume that the decomposition of a binary solid solution occurs without changes of the symmetry: the mother solid solution A_cB_{1-c} has the same structure and symmetry as the solid solutions formed as a result of the decomposition, $(A_{c_1}B_{1-c_1})$ and $(A_{c_2}B_{1-c_2})$. It is this simplest case that is considered in all the studies on the effect (see review articles [6–9, 11]). In particular, it is also the case with respect to the $Ag_{1-c}Au_c$ solid solutions, where both pure components and all the intermediate phases have the fcc structure ($A1$) with the symmetry O_h^5.

CONDITIONS OF SOLID SOLUTION DECOMPOSITION. THE COMPOSITION AND FREE ENERGY OF THE MIXTURE OF THE DECOMPOSITION PRODUCTS

The equilibrium free energy of the solid solution, which is the function of the average concentration (playing a part analogous to that of the order parameter in the Landau theory), can be approximated by a fourth-order polynomials

$$G = G_0 - \mu_1 c + \mu_2 c^2 + \mu_3 c^3 + \mu_4 c^4. \quad (1)$$

The approximation made in Eq. (1) is justified by the following. Assuming that we should like to answer the question whether the decomposition of the solid solution with the set composition and structure can be considered as proper or improper (i.e., induced) ordering, we consider the simplest type of inducing ordering described by one single-component order parameter η. Then, to answer this question within the framework of the phenomenological theory, we have to consider all the crystal-lattice points as belonging to two mutually penetrating sublattices *1* and *2* and, as usual, to assume that the probabilities of filling the sites of these sublattices with A atoms can spontaneously change. The states of each crystal-lattice point in the ordered and disordered states are characterized by the probability of filling of the point with the coordinates ijk by A atoms, $P_{ijk}(A)$. As usual in the theory of ordering phase transitions, we assume that these characteristics have constant values at all the sites j of each sublattice. Thus, now, the theory has two different characteristics of the sites. Using a linear transformation, one can express these characteristics in terms of symmetrically collective characteristics of the states

$$P_1(A) = c + \eta, \quad P_2(A) = c - \eta, \quad (2)$$

where η is the Landau order parameter and c is the average concentration of A atoms. The nonequilibrum Landau potential, which describes the ordering phase transition, can be represented by the function of the probabilities of filling of the crystal-lattice sites, $P_1(A)$ and $P_2(A)$ or, as is used in the Landau theory [12] and the theory of the static concentration waves [7], by the function of generalized collective coordinates of the system, c and η. In order to be able to describe the ordering phase transition, the minimum degree of the Landau potential, a function of η, should not be less than four. Because of the linear relation between $P_i(A)$ and η, Eq. (2), the Landau potential, being a function of the individual characteristics of filling the lattice sites $P_i(A)$, should also be of degree four with respect to $P_i(A)$. Therefore, in the transition from $P_i(A)$ to c and η, the concentration c, in accordance with Eq. (2), should enter the potential as a polynomial of degree four. Since the sublattices are equivalent, the Landau potential dependent on the nonequilibrium parameter η and one of the "conditions at the thermostat" (concentration c) takes the form

$$\Phi_L = a_1\eta^2 + a_2\eta^4 + \gamma_1\eta^2 c + \gamma_2\eta^2 c^2 - \mu_1' c + \mu_2' c^2 + \mu_3' c^3 + \mu_4' c^4. \quad (3)$$

Other conditions at the thermostat implicitly determine the phenomenological parameters a_i, γ_j, and μ_k in Eq. (3).

The equilibrium value corresponding to Eq. (3) is

$$\eta_0^2 = -(a_1 + \gamma_1 c + \gamma_2 c^2)/2a_2 \quad (4)$$

or

$$\eta = 0,$$

and, thus, the value of the potential $\Phi(\eta_0)$, i.e., the equilibrium free energy [9], acquires the form of Eq. (1) or the form given by Eq. (1) with the renormalized coefficients

$$G_0 = -a_1^2/4a_2;\ \mu_1 = \mu_1' - a_1\gamma_1/2a_2;$$

$$\mu_2 = \mu_2' - \gamma_1^2/4a_2 - a_1\gamma_2/2a_2; \quad (5)$$

$$\mu_3 = \mu_3' - \gamma_1\gamma_3/2a_2 \text{ and } \mu_4 = \mu_4' - \gamma_2^2/4a_2.$$

Obviously, one can readily extend the above considerations based on the linear relation between the individual characteristics of site filling, P_i^α, and the set of their symmetric combinations (c, η_1, η_2, …) to more complex types of ordering. Thus, the polynomial approximating the equilibrium free energy of a decomposing binary solid solution, being the function of concentration c, should be at least of degree four.

The model thermodynamic potential of form (1) describes the decomposition of the solid solution into the mechanical mixture of the products of decomposition, whose compositions differ from the average composition of the solution only if $(G - G_0)$ has negative curvature at a certain formally determined portion of the c curve determined from the form of Eq. (1). Using Eq. (1), one can readily see that, at $\mu_4 > 0$, the dependence $G(c)$ has a negative curvature if

$$c_2^* < c < c_1^*, \tag{6}$$

where

$$c_{1,2}^* = \left|-\mu_3 \pm \sqrt{\mu_3^2 - 8/3\mu_2\mu_4}\right|/4\mu_4.$$

If $\mu_4 < 0$, the ranges of c variation, where the curvature of $G(c)$ is negative, are located at $c_1^* < c < c_2^*$. Further consideration is made for the case where $\mu_4 > 0$.

If the concentration range corresponding to the negative curvature of $G(c)$ is in the range of the real values of the formal parameter c, i.e., if c_1^* and $c_2^* \in [0, 1]$, then two variants of the proper decomposition of a binary solid solution are possible.

The first variant of the decomposition corresponds to the case in which the boundary points of the conode

$$c_{1,2} = \left|-\mu_3 \pm \sqrt{3\mu_3^2 - 8\mu_2\mu_4}\right|/4\mu_4 \tag{7}$$

also belong to the range of the real c values, $c \in [0.1]$. Then, the free energy of the mechanical mixture of two solid solutions with concentrations of component A equal to c_1 and c_2, respectively, Eq. (6), linearly depends on the average concentration c

$$G_{mix} = -\left|\mu_1 + \mu_3\Delta/8\mu_4^2\right|c - \Delta^2/64\mu_4^3, \tag{8}$$

where $\Delta \equiv 4\mu_2\mu_4 - \mu_3^2$. Since both c_1 and $c_2 \in [0, 1]$ belong to the same interval [0, 1], then $\Delta > 0$.

The chemical potentials of pure A and B components, $\chi_1(A)$ and $\chi_1(B)$, in the newly formed concentration interval $[c_2c_1]$ of the mechanical mixture of the solid solutions with the concentrations of the A component c_1 and c_2 are

$$\begin{aligned}\chi_1(A) &= -\Delta/64\mu_4^3,\\ \chi_1(B) &= -\mu_1 - \Delta(8\mu_3\mu_4 + \Delta)/64\mu_4^3.\end{aligned} \tag{9}$$

The fractions of the solid solutions with the concentrations of the A component c_1 and c_2 in the mechanical mixture (ν_1 and ν_2) are determined using the lever rule as

$$\nu_1 = (c - c_2)/(c_1 - c_2); \quad \nu_2 = (c_1 - c)/(c_1 - c_2). \tag{10}$$

The second variant of the decomposition corresponds to the situation in which one of the boundary concentrations c_1 or c_2, Eq. (7), formally obtained as the coordinates of the tangential points of conode (8) and free energy (1), is beyond the limits of the values of the interval [0, 1]. For definiteness, assume that $c_1 > 1$. This is possible if $(\mu_3 - \mu_4)^2 < 3\mu_4(\mu_4 + \mu_2)$ and $\mu_3 + \mu_2 + \mu_4 > 0$. If these inequalities are valid, the mother solid solution decomposes into the mechanical mixture of the pure component B and the solid solution with the concentration of the A component

$$\begin{aligned}x_1 &= \left|-(\mu_3 + \mu_4) - \sqrt{\mu_3^2 - \mu_3\mu_4 - 2\mu_4^2 - 3\mu_2\mu_4}\right|/3\mu_4.\end{aligned} \tag{11}$$

If c_2 formally determined from (7) is less than zero, $c_2 < 0$, then the mother solid solution decomposes into the mechanical mixture of the pure A component and the solid solution with the concentration of the component A

$$x_2 = \left|-\mu_3 + \sqrt{\mu_3^2 - 3\mu_2\mu_4}\right|/3\mu_4. \tag{12}$$

In this case, the free energy per particle of the component A (chemical potential) in the mixture of the solid solutions with the concentration x_2 is $\chi_2(A) = 0$. Correspondingly, the chemical potential of the B component in this mixture is

$$\begin{aligned}\chi_2(B) &= -\mu_1\\ &+ \{(2\mu_3^2 - 9\mu_2\mu_4)\mu_3 - 2(\mu_3^2 - 3\mu_2\mu_4)^{3/2}\}/27\mu_4^2.\end{aligned} \tag{13}$$

Thus, in order to establish the phase diagram, the equilibrium compositions of the mixtures, dependence of the temperature of the proper decomposition on the average concentration of one of the components $T_D(c)$, and other characteristics of the solid- solution decomposition, one must know the ranges of the varying phenomenological parameters of the theory in which the qualitatively different $G(c)$ dependences can be formed.

PHASE DIAGRAM IN THE SPACE OF PHENOMENOLOGICAL PARAMETERS OF THE THEORY

The characteristic determining the solid-solution decomposition is the curvature of $G(c)$ in Eq. (1) independent of μ_1 and, therefore, the space of the phenomenological parameters that should be classified with respect to different forms of the $G(c)$ dependence, is the plane (μ_3^*, μ_2^*), where $\mu_3^* = \mu_3/\mu_4$ and $\mu_2^* = \mu_2/\mu_4$. The condition for existence of real (c_1^*, c_2^*) and (c_1, c_2) and their belonging to the interval of real values $c \in [0, 1]$ determine all the possible differences between the $G(c)$ dependences and various forms of the phase diagrams. The results of the formal analysis of these conditions with no allowance made for possible experimental separation of various types of decomposition are shown in Fig. 1a. Various forms of the $G(c)$ dependence are shown in Fig. 2, where the positions of the c_1^*, c_2^*, c_1, c_2, x_1, and x_2 points are indicated for each $G(c)$ dependence if these points are in the interval [0, 1], $c \in [0, 1]$. Figure 2 also shows the regions of solid-solution decomposition for such an arrangement of the characteristic points of $G(c)$. The regions on the $(\mu_3^*\mu_2^*)$ plane with different arrangements of c_1^*, c_2^*, c_1, and c_2 with respect to the interval [0, 1] are numbered as *1–13*, as well as the forms of the potentials $G(c)$ characteristic of each of these regions shown in Fig. 2. In region *1* (where $\mu_2^* \geq 3\mu_3^{*2}/8$), no decomposition is observed at all and the potential G has a positive curvature within the whole variation range of the solid-solution concentration, $c \in [0, 1]$. In region *2*, the thermodynamic potential has two minima (c_1, c_2, c_1^*, and c_2^* are within the interval [0, 1]). This is the only region considered in all the "molecular–kinetic" [6, 8] or statistical [7, 9, 10] theories of solid-solution decomposition. Statistical theories state that it is the only possible form of the Gibbs thermodynamic potential in a decomposing solid solution. It is clear from the phenomenological theory that this proper decomposition of a solid solution can take place only under rather rigid restrictions on the relationship between μ_3^* and μ_2^*. Four inequalities should necessarily be satisfied:

$$\mu_2^* \leq 3\mu_3^{*2}/8, \quad \mu_2^* \geq \mu_3^{*2}/4,$$
$$\mu_2^* > (\mu_3^* - 2)^2/4 - 3, \quad \mu_3 < 0. \tag{14}$$

This seeming contradiction between the unambiguous predictions of the statistical theories and a relatively low *a priori* probability of such a "classical decomposition" of a solid solution of the phenomenological theory can be explained as follows. In all the statistical theories of decomposition [6–9, 11], the expression for the energy of a binary solid solution takes into account only the effective atomic-pair interactions of the compo-

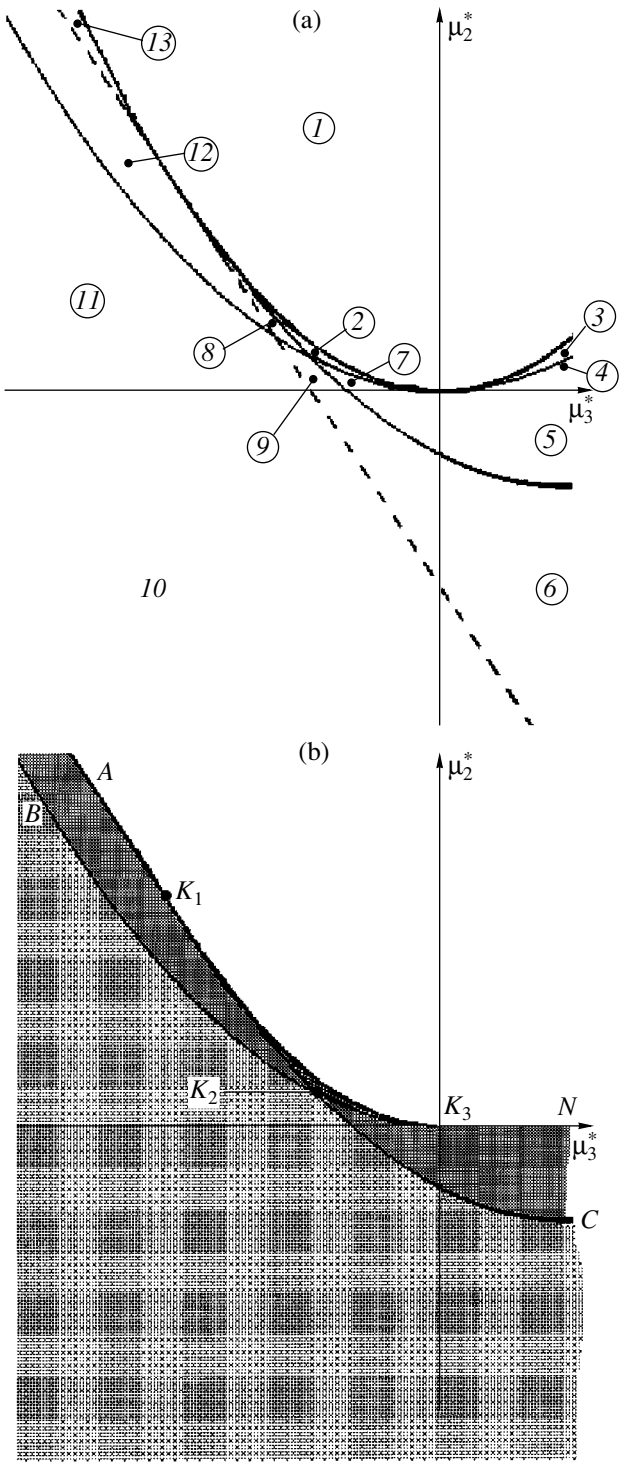

Fig. 1. Phase diagram in the space of the phenomenological parameters of the equilibrium thermodynamic potential, which corresponds to the proper solid-solution decomposition considered within the framework of the theory based on thermodynamic potential described by Eq. (1). (a) Boundaries between formally different types of $G(c)$; (b) regions of the phenomenological parameters, where $G(c)$ has essentially different forms. The points K_1, K_2, and K_3 correspond to the intersections and tangential points of the lines whose equations are given in the text. The letters *A*, *B*, *C*, and *N* are introduced for the description of the lines in the text.

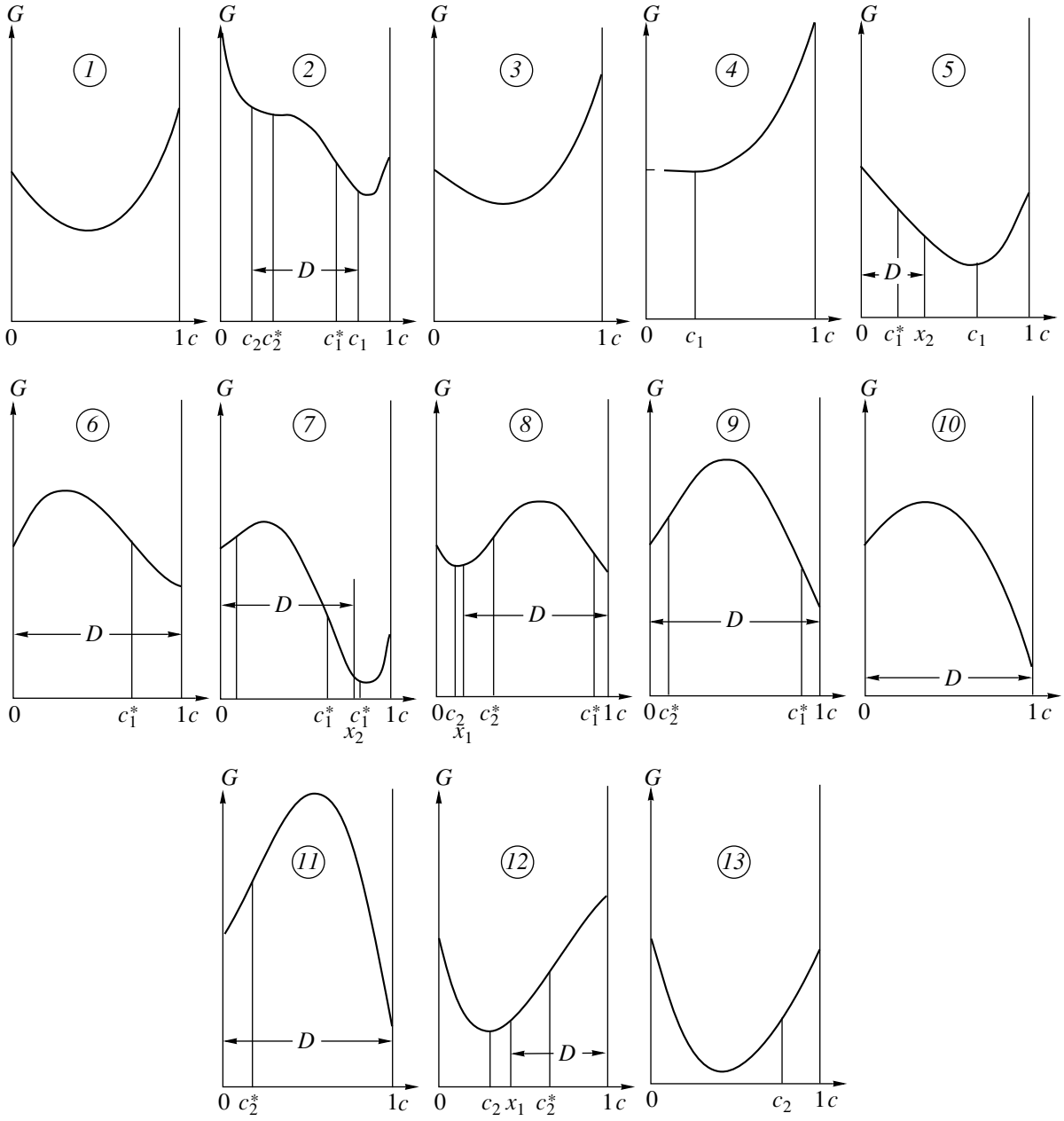

Fig. 2. Various forms of the $G(c)$ dependence given by the phenomenological theory based on thermodynamic potential described by Eq. (1). The numbers on the $G(c)$ plot correspond to the numbers in Fig. 1a (see text). For notation of the concentrations and decomposition regions, see text.

nents and only the configurational entropy (usually in the Gorsky–Bragg–Williams (GBW) approximation not taking into account any correlations). As is shown in [12–15], this approximation is "topologically equivalent," i.e., can give only the results equivalent to those obtained from the phenomenological theory based on the thermodynamic potential of degree four with respect to c, i.e., the potential of form (1). However, the phenomenological parameters determining the form of the potential G in Eq. (1), which is topologically equivalent to the transcendental potentials discussed in the approximation of the static concentration waves or the GBW theory, are not independent. Thus, proceeding from the form of the thermodynamic potential in the statistical theory [13, 15]

$$G^* = -m_1 c + m_2 c^2 + T[c\ln c + (1-c)\ln(1-c)], \quad (15)$$

we arrive at a potential of the phenomenological theory topologically equivalent to form (1), which is determined by the least squares method from Eq. (14) and is

characterized by the following parameters:

$$\mu_1 = m_1 - 39T/10, \quad \mu_2 = m_2 + 42T/5, \quad \mu_3 = -133T/15, \quad \mu_4 = 217T/50. \tag{16}$$

Considering the proof given in [13–15], we see that the equivalence of potentials (14) and (1) determined by parameters in Eq. (15) takes place only in the vicinity of the temperature of the solid- solution decomposition, $T_D \sim -m_2/2$, at which the equilibrium thermodynamic potential of form *1* (Fig. 2) is transformed into the thermodynamic potential of form *2* (Fig. 2). Making allowance for three- and four-particle interactions within the statistical theory with the configurational entropy of the GBW type (calculated without taking correlations into account) results in one-to-one correspondence of the predictions of the statistical and phenomenological theories.

Figure 2 shows various forms of the potentials characteristic of the regions shown in Fig. 1a. This figure allows one to determine the formal causes that give rise to stratification of the $(\mu_3^*\mu_2^*)$ plane shown in Fig. 1a. Thus, in region *3*, where $\mu_3^* > 0$ and $\mu_3^*/4 < \mu_2^* < 3\mu_3^{*2}/\gamma_1$, the formally determined c_1, c_2, c_1^*, and c_2^* values are real numbers, but even the maximum one is less than zero, $c_1 < 0$. Therefore, within the interval $0 < c < 1$, the potential G is a concave function of c, and, therefore, the formal separation of regions *1* and *3* cannot be detected on the experimentally studied phase diagram. Within the interval $0 \le c \le 1$, the function G remains concave also in region *4* ($0 < \mu_2^* < \mu_3^{*2}/4$, $\mu_3^* > 0$), where $c_1 > 0 > c_1^*$. However, in region *5* ($\mu_3^* \ge 0, 0 \ge \mu_2^* \ge [(\mu_3^* - 2)^2/4 - 3], 1 \ge c_1^* > c_1 > 0, c_2 < c_2^* < 0$), the decomposition of the solid solution into the pure *A* component and the solid solution containing x_2 at % *A* should be observed at the average concentration of the *A* component in the range $0 < c < x_2$ [see Eq. (12)]. The gain in free energy in the decomposition is relatively low. In region *6*, determined by inequalities $0 > \mu_2^* > -3\mu_3^* - 6$ and $\mu_2^* \le [(\mu_3^* - 2)^2/4 - 3]$, $c_1 > 0$, $0 < c_1^* < 1$, c_2, $c_2^* < 0$, the decomposition into two pure components, *A* and *B*, accompanied by a considerable gain in energy, proceeds within the whole interval of the average concentrations of the component *A*, $0 < c < 1$. Region *7* is separated from region *5* by the boundary $\mu_2^* = 0$ (Fig. 1), above which $c_2 < 0$ at $\mu_3^{*2}/4 > \mu_2^* > [(\mu_3^* - 2)^2/4 - 3]$ (as in region *5*), but $0 < c_2^* < c_1^* < c_1 < 1$. In this region, the energy characteristics of the solid-solution decomposition approach those of the decomposition along the conode. Nevertheless, the form of the phase diagram and the compositions of the components of the mechanical mixture formed after the decomposition are the same as in region *5*. Region *8*, which frames the region of the classical decomposition along the conode (region *2*), has a phase diagram similar to that of region *7*, with the only stipulation being that all the characteristics of component *A* in region *7* should be related to component *B* in region *8* and the boundary concentration of decomposition x_2 given by Eq. (12) should be substituted by x_1 given by Eq. (11). The asymmetries of Eqs. (12) and (11), as well as the differences in the interactions of the components, *A–A* and *B–B*, manifest themselves in a number of the physical characteristics of the mechanical mixture. However, regions *6* and *8* on the phase diagram can be distinguished only if, varying the external conditions, one can "translate" the same set of compositions (rather densely distributed along the *c* axis) from region *6* to region *8* of the (μ_3^*, μ_2^*) plane.

Despite the obvious differences in the arrangements of the points $c_2^* \le c_1^*$ with respect to the real interval of possible concentrations of the component *A* in the solution in Fig. 2, regions *9*, *10*, and *11* of the plane $(\mu_3^* - \mu_2^*)$ cannot be distinguished on the phase diagram: the decomposition of the solid solution below the stratification temperature ($T_D(c)$) in all three regions is observed at all the concentrations of the component *A*. Similar to regions *7* and *8*, region *12* in Fig. 1a and region *5* cannot be distinguished on the phase diagram. In this sense, region *13* is similar to region *3*. Proceeding from Fig. 1a and the above equations for the boundaries of regions *2–8*, it is also possible to write the boundaries of regions *9–13*.

The results of the analysis of the phase diagrams for various relationships between μ_2^* and μ_3^* are shown in Fig. 1b, where four regions with considerably different phase diagrams are hatched in different ways. Since the range of the concentration variations in the solid solutions is limited by definition ($c \in [0, 1]$), then, contrary to the Landau theory of second-order phase transitions, the requirement of the positive coefficient before the nonequilibrium variable in the highest degree, i.e., μ_4 in Eq. (1), cannot be the natural restriction of the phenomenological theory. Possibly, the μ_4 value calculated based on the microscopic theory for some concrete compositions and types of the solid-solution components can be negative. In this case, all the analytical results considered above remain valid. The form of the phase diagram on the (μ_2^*, μ_3^*) plane is the same as in Fig. 1, but the directions of an increase in μ_2^* and μ_3^* change to the opposite ones.

MUTUAL INFLUENCE OF ORDERING AND DECOMPOSITION OF BINARY SOLID SOLUTIONS. PHASE DIAGRAMS IN THE *T–c* SPACE

As was indicated in the premises, when choosing the form of the thermodynamic potential of a solid solution, one has remember that the proper decompositions, being of microscopic nature, are very closely related to ordering and, therefore, to improper decompositions. This follows from the form of potential (3) and the relationship between μ_i and $\tilde{\mu}_i$. Therefore, it is not accidental that almost all the *T–c* phase diagrams [1, 9] of the decomposition regions also have the regions of stability of ordered (stoichiometric) phases. Thus, in the natural $Ag_{1-x}Au_x$ solid solution studied here, one observes, along with the decomposition region (at room temperature, decomposition is observed in the range of gold concentrations $0.02 < c < 12$), also the region of the stoichiometric compound with $c = 0.25$ (küstelite, Ag_3Au [10, 16]). According to the above definition, the existence of küstelite leads to improper decomposition. The existence of the regions of improper decomposition was confirmed by direct calculations based on the GBW model [17–19] with due regard for only the efficient pair interactions. The studies of the native gold also confirm the existence of the regions of improper decomposition with the formation of küstelite on the *T–c* phase diagram of $Ag_{1-x}Au_x$ [10, 16]. However, the theory of improper decomposition [17–19] fails to describe consistently the whole phase diagram. Thus, in the calculations [17–19], only the efficient pair interactions were taken into account. The incompleteness of such a theory follows, e.g., from the absence of the ordered Au_3Ag phases in the known native gold samples. In terms of the theory taking into account only the effective pair interactions, the temperatures of ordering and stability of the Ag_3Au and Au_3Ag phases should coincide. Then, the theory taking into account only the effective pair interactions leads to conclusions inconsistent with the well known sonic-velocity measurements even in pure components of the solid solution [20]. Thus, according to the theory taking into account only the effective pair interactions, the following relationships between the elasticity moduli should be fulfilled in cubic gold and silver crystals (the Cauchy relationships) $c_{1122} = c_{1212}$. However, in actual fact, it was obtained at $T = 0$ K [20]:

$$c_{1122}(\mathrm{Au}) = 1697 \text{ kbar}, \quad c_{1212}(\mathrm{Au}) = 454 \text{ kbar},$$

$$c_{1122}(\mathrm{Ag}) = 973 \text{ kbar}, \quad c_{1212}(\mathrm{Ag}) = 511 \text{ kbar}.$$

It is clear from what has been stated above that the phenomenological theory based on the Landau potential described by Eq. (3) and leading to the Gibbs potential described by Eq. (1) is more adequate for the data obtained for natural $Ag_{1-x}Au_x$ solid solutions [10, 16–19] than the approach based on the GBW model [6–9].

Putting, as usual, $a = \alpha(T - T_C^0)$ in the Landau theory of second-order phase transitions, we obtain the "ordering dome" in a disordered solid solution

$$T_C = T_C^0 - (\gamma_2/\alpha)\{(c - \gamma_1/2\gamma_2)^2 - (\gamma_1/2\gamma_2)^2\}. \quad (17)$$

The construction of the "decomposition dome" for a solid solution also requires some preliminary assumptions on the $\mu_2(T)$ and $\mu_3(T)$ dependences. It is seen from Eqs. (5) and (14) that, proceeding from the GBW model and under the assumption of renormalization of μ_2 and μ_3 caused by ordering, one can assume the linear dependence of μ_2 on *T*, i.e.,

$$\mu_2 = \delta(T_D^0 - T). \quad (18)$$

In this case, the decomposition dome for the solid solution is

$$T_D(c) = T_D^0 - [(4\mu_4 c + \mu_3)^2 - 3\mu_3^2]/8\delta\mu_4. \quad (19)$$

To discuss the concrete path of the evolution of the equilibrium composition of the solid solution, one must invoke experimental data. Thus, it is known that the top of the decomposition dome for the $Ag_{1-x}Au_x$ solid solution at $T = 300$ K lies at $c_{\max} = 0.07$ ($c_{\max} = (0.02 + 0.12)/2 = 0.07$), whereas that of the ordering dome is at $c_K = 0.25$. Then, it follows that

$$\mu_3^* = 0.28; \quad \gamma_1 = 0.5\gamma_2. \quad (20)$$

The maximum temperatures of ordering and decomposition (17, 19) are less reliable. It is known that cooling of artificial gold–silver alloys does not lead to the formation of küstelite-type compounds. Therefore, one can only assume that $\max T_C$ is lower than the crystallization temperature of the $Ag_{1-x}Au_x$ alloys (1300 K) and higher than the deposition temperature of solid solutions from hydrothermal salt solutions (600 K). The data on the maximum temperature of decomposition are even more scarse. A direct experiment using gold deposition from the solutions of gold–silver salts [10] showed that this temperature is close to 600 K. Assuming that $\max T_C = 1200$ K and $\max T_D = 600$ K, we see that all the theoretical parameters turn out to be limiting and that the phase *T–c* diagram takes the form shown in Fig. 3. The qualitative picture of the equilibrium evolution of the solid-solution state with the gold concentration $0.05 < c < 0.25$ depending on a decreases in temperature is shown in Fig. 3 by arrows indicating the direction of this evolution. The evolution predicted by the phenomenological theory qualitatively differs from all the five types of evolution in the Rosebom classification [3]. The fact that the type of the evolution considered in the present study is inconsistent with any of the known physical–chemical schemes is explained by the fact that, within the framework of the physical–chemical analysis [3, 19], the form of the thermodynamic potential of each component of the solid solution is assumed to be constant. In the phenomenological

theory used in our study, the equilibrium thermodynamic potential of one of the components qualitatively changes with change in the temperature. Within the assumptions made, the evolution of the structure of the solid solution with the composition $0.05 < c < 0.25$ during cooling is as follows. At a certain temperature $T_2 < T_1 < T_C$, the thermodynamic path brings the representative point of the system to the improper-decomposition dome. With a further lowering of the temperature, the equilibrium solid solution should have two coexisting phases—one with a composition close to $AuAg_3$ and only weakly dependent on T and the other with a composition determined by the lever rule and having the average (initial) concentration c. At $T = \max T_D$, the dependence of the thermodynamic potential of the gold-depleted phase on c acquires two bending points (region *2* in Fig. 1a). At $T = T_3$ (~550 K) and $c \sim 0.05$, one observes solution bifurcation of the equations of state. The evolution of the system consisting of three solid solutions (which are in equilibrium at this noninvariant point) can proceed along one of three possible paths in Fig. 3. At low temperatures, the phase with a composition exponentially close to $AuAg_3$ can be in equilibrium with one of the two phases into which the gold-depleted solid solution decomposes at $T < T_3$. The $AuAg_3$ phase turns out to be metastable and may be dissolved by the peritectic reaction in more gold-depleted phases of variable compositions determined by the decomposition dome. Thus, the equilibrium temperature evolution of the solid solution at low temperatures is dependent on one additional phenomenological parameter, μ_1, which cannot be determined from the decomposition character at high temperatures.

Some conclusions on μ_1 can be made based on the microprobe and electron microscopy data on poor-quality native gold at room temperatures [10, 17–19]. The quality and chemical composition of the sample surface show that the poor-quality native gold consists mainly of a matrix with a composition intermediate between $c = 0.02$ and $c = 0.25$. The regions of the matrix composition are separated by narrow strips of almost pure silver clearly seen on etched samples [17–19]. Küstelite grains occupy an even smaller volume [10, 16–18]. Since the ternary system cannot be in equilibrium under varying temperature conditions [12], one can assume that the real equilibrium low-temperature evolution of the Au_xAg_{1-x} solid solution proceeds according to variant 3, but that, at moderate c values ($c < 0.25$) küstelite had not enough time to be dissolved in more stable compounds. To a large extent, the dissolution (nucleation time) τ is determined by the surface energy and the diffusion coefficients of atoms at the given temperature. In this case, the dependence of τ on the surface energy σ ($\tau \sim \exp(\sigma^3)$) is so pronounced that the 50%-change in σ results in the change in τ lying within 10^{-15} to 10^{24} s (the lifetime of the universe) [21]. At the same time, σ also depends on T and c, and the diffusion at $T \sim 300$ K is almost frozen. Thus, it is still unclear to what extent the equilibrium state is attained in real native solid solutions, and the low-temperature evolution of the Au_xAg_{1-x} solid solution suggested above can be determined from the known data only with a certain probability. Nevertheless, it seems to be of interest to give here the general relationships determining the energy gain obtained upon decomposition of solid solutions. Formally, the maximum distance of $G(c)$ from the connode at fixed c attains a value of $\mu_3^2[4\Delta - \mu_3^2]/4\mu_4^3$. However, the potential barrier that should be overcome by a particle of the solid solution in order to move from a *B*-depleted compound to a more *B*-rich one is determined by the relationship

$$\Delta G = (-\mu_1 - \mu_3\Delta/8\mu_4^2)c_2^*$$

and, thus, linearly depends on μ_1.

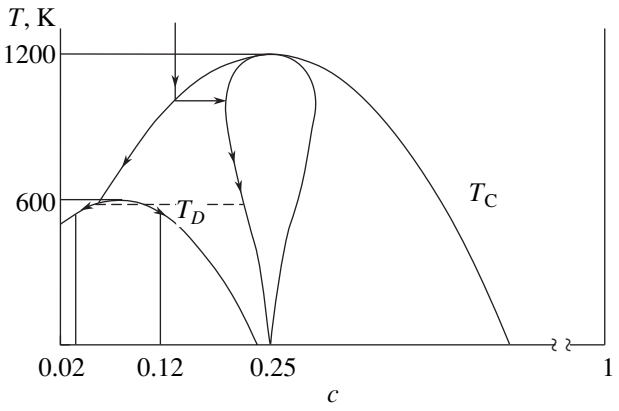

Fig. 3. Phase *T*–*c* diagram obtained in accordance with Eqs. (1), (17), (19), and (20) for the Au_cAg_{1-c} solid solutions.

ACKNOWLEDGMENTS

The author is grateful to M.I. Novgorodova for formulation of the problem and K.Yu. Gufan for his help in preparation of the publication. The study was supported by the Russian Foundation for Basic Research (projects nos. 02-05-06441a and 02-02-17921a). The author is also grateful to the Dinastiya Foundation of Noncommercial Programs for the scholarship.

REFERENCES

1. N. P. Lyakishev, O. A. Bannykh, and L. L. Rokhlin, *Handbook of Phase Diagrams of Binary Metal Systems* (Mashinostroenie, Moscow, 1986), Vol. 1.
2. A. G. Morachevskiĭ, *Textbook on Thermodynamics of Phase Equilibria* (Min. VSS Obr. RSFSR, LPI, Leningrad, 1983).
3. V. Ya. Anosov, M. I. Ozerova, and Yu. Ya. Fialkov, *Fundamentals of Physical–Chemical Analysis* (Nauka, Moscow, 1976).

4. B. Noheda, D. E. Cox, G. Shirane, *et al.*, Phys. Rev. Lett. **86**, 3891 (2001).
5. D. La-Orauttapong, B. Noheda, Z.-G. Ye, *et al.*, cond-mat/0108264,V.2,1 (2001).
6. M. A. Krivoglaz and A. A. Smirnov, *The Theory of Order–Disorder in Alloys* (Fizmatgiz, Moscow, 1958; Macdonald, London, 1964).
7. A. G. Khachaturyan, *Theory of Phase Transformations and Structure of Solid Solutions* (Nauka, Moscow, 1974).
8. A. A. Smirnov, *Molecular-Kinetic Theory of Metals* (Nauka, Moscow, 1966), pp. 275–314.
9. A. I. Gusev and A. A. Rempel', *Nonstoichiometry, Disorder, and Order in Solids* (Ural. Otd. Ross. Akad. Nauk, Yekaterinburg, 2001).
10. M. I. Novgorodova, Itogi Nauki Tekh., Ser.: Kristallokhim. **29** (1994).
11. Ya. I. Frenkel, *Introduction to the Theory of Metals* (Nauka, Leningrad, 1972).
12. L. D. Landau and L. M. Lifshitz, *Course of Theoretical Physics*, Vol. 5: *Statistical Physics*, 5th ed. (Fizmatlit, Moscow, 2001; Pergamon Press, Oxford, 1980).
13. Yu. M. Gufan, G. G. Urushadze, and V. B. Shirokov, Dokl. Akad. Nauk SSSR **277** (6), 1365 (1984) [Sov. Phys. Dokl. **29**, 654 (1984)].
14. A. M. Prokhorov, Yu. M. Gufan, E. S. Larin, *et al.*, Dokl. Akad. Nauk SSSR **277** (6), 1369 (1984) [Sov. Phys. Dokl. **29**, 656 (1984)].
15. Yu. M. Gufan, G. G. Urushadze, and V. B. Shirokov, Fiz. Tverd. Tela (Leningrad) **27** (5), 1442 (1985) [Sov. Phys. Solid State **27**, 869 (1985)].
16. V. M. Malyshev and D. V. Rumyantsev, *Gold* (Metallurgiya, Moscow, 1979).
17. Yu. M. Gufan, M. I. Novgorodova, E. N. Klimova, *et al.*, Izv. Ross. Akad. Nauk, Ser. Fiz. **65** (6), 795 (2001).
18. Yu. M. Gufan, M. B. Stryukov, M. I. Novgorodova, *et al.*, Izv. Ross. Akad. Nauk, Ser. Fiz. **65** (6), 799 (2001).
19. Yu. M. Gufan, M. I. Novgorodova, and A. N. Sadkov, in *Proceedings of All-Russian Scientific Conference on Geology, Geochemistry, and Geophysics at the Boundary between 20th and 21st Centuries* (Moscow, 2002), p. 257.
20. O. Anderson, in *Physical Acoustics*, Ed. by W. P. Mason (Academic, New York, 1965; Mir, Moscow, 1968), Vol. 3, Part B.
21. D. McLean, in *Controls of Metamorphism*, Ed. by W. S. Pitcher and G. W. Flinn (Oliver and Boyd, Edinburgh, 1965; Mir, Moscow, 1967).

Translated by L. Man

Crystallography Reports, Vol. 49, No. 3, 2004, pp. 459–462. Translated from Kristallografiya, Vol. 49, No. 3, 2004, pp. 524–527.

PHYSICAL PROPERTIES OF CRYSTALS

Optics and Spectroscopy of a $Pb_3Ga_2Ge_4O_{14}$:Nd^{3+} Crystal, a New Representative of the Langasite Family

A. V. Butashin*, L. E. Li*, A. F. Konstantinova*, and I. A. Gudim**

** Shubnikov Institute of Crystallography, Russian Academy of Sciences, Leninskiĭ pr. 59, Moscow, 119333 Russia*

e-mail: afkonst@ns.crys.ras.ru

*** Institute of Physics, Siberian Division, Russian Academy of Sciences, Akademgorodok, Krasnoyarsk, 660036 Russia*

Received December 22, 2003

Abstract—Absorption and luminescent properties of a $Pb_3Ga_2Ge_4O_{14}$:Nd^{3+} crystal have been studied. The refractive indices are measured in the range from 0.405 to 1.064 μm, and the molecular refraction is calculated.

INTRODUCTION

Today, more than 100 acentric trigonal compounds with the langasite structure type, $La_3Ga_5SiO_{14}$, have been synthesized [1–4]. However, only some of these crystals have attracted the attention of researchers and engineers. These are the single crystals possessing valuable piezoelectric, laser, and nonlinear optical properties that can be grown by the Czochralski method from melt [5–8]. These are the crystals of langasite $La_3Ga_5SiO_{14}$ and isostructural compounds such as $Ca_3Ga_2Ge_4O_{14}$, $Sr_3Ga_2Ge_4O_{14}$, $La_3Ga_{5.5}Nb_{0.5}O_{14}$, $La_3Ga_{5.5}Ta_{0.5}O_{14}$, $La_3Ga_5GeO_{14}$, and $Nd_3Ga_5SiO_{14}$. In particular, it was established that these crystals possess rather pronounced optical nonlinearity [7] comparable with the optical nonlinearity of the well known nonlinear crystals β-BaB_2O_4 and $KTiOPO_4$. However, their insufficiently good fundamental optical properties do not allow one to use the above crystals with the langasite structure for synchronous conversion of the frequencies of the laser generation in the visible and near IR spectrum ranges. The analysis of data [5–8] shows that the piezoelectric, spectral generation, and nonlinear optical properties of these crystals are essentially dependent on their composition. Therefore, it is important to synthesize and study new compounds of this class in order to find the crystals with the optimum lasing properties appropriate for transformation of lasing frequencies.

One of the promising materials is the compound of the composition $Pb_3Ga_2Ge_4O_{14}$; the solid-phase synthesis of which was first described in [1]. Since $Pb_3Ga_2Ge_4O_{14}$ melts incongruently, it cannot be grown by the Czochralski method. Therefore, $Pb_3Ga_2Ge_4O_{14}$ crystals were grown by a specially developed, more universal method based on crystallization on a seed from flux [9].

Below, we describe our experiments on growth of Nd-doped $Pb_3Ga_2Ge_4O_{14}$ crystals and their absorption, luminescent, and optical properties, undertaken with the aim of determining their possibilities for creating minilasers, including with self-transformation of the lasing frequencies.

GROWTH OF $Pb_3Ga_2Ge_4O_{14}$:Nd^{3+} CRYSTALS

The $Pb_3Ga_2Ge_4O_{14}$:Nd^{3+} single crystals were grown on a seed from the flux of the composition 40 wt % (PbF_2 + 1.42 GeO_2) + 60 wt % $Pb_{2.87}Nd_{0.13}Ga_{1.93}Si_{0.07}Ge_4O_{14}$. The flux with the weight $P_{l\text{-}m}$ = 100 g was prepared in a cylindrical platinum crucible with a diameter of 40 mm at the temperature t = 1000°C. The saturation temperature of the flux (950°C) was lower by 50°C than the temperature of the $Pb_3Ga_2Ge_4O_{14}$ decomposition (~1000°C). In order to attain a more homogeneous Nd^{3+} distribution between the crystal and the flux, we added some amount of amorphous SiO_2 powder to the flux.

The vertical component of the temperature gradient at the stages of homogenization and growth did not exceed 1°C/cm. For the flux of the above composition dt_{sat}/dn = 1.4°C wt % and, that is, at the initial flux weight of 100 g, the use of the mode of a temperature decrease in the range $\Delta t = t_{sat} - t_0$ = 50°C should allow one to grow a crystal with a weight of 21 g. It was shown experimentally that the most stable faceted growth was observed with the horizontal surface of the seed being normal to the three-fold axis. In this case, the crystal grows as a hexagonal prism.

As a result of the growth experiment, $Pb_3Ga_2Ge_4O_{14}$: Nd^{3+} crystals up to 2 cm^3 in volume of satisfactory optical quality were grown. According to

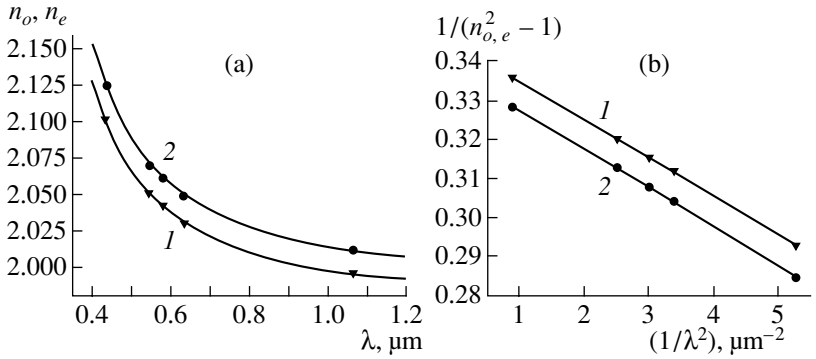

Fig. 1. (a) Refractive indices of $Pb_3Ga_2Ge_4O_{14}:Nd^{3+}$ crystals and (b) approximation of the refractive indices by Selmeyer formula (1) for (*1*) ordinary and (*2*) extraordinary rays.

the microanalysis data (EAGLE II X-ray fluorescent microanalyzer, μ probe, Rh tube, U = 40 kV, I = 200 μA), the concentration of Nd^{3+} ions in the crystals grown amounts to $C \sim 5 \times 10^{20}$ cm^{-3}. Proceeding from the structural data [2, 6], we assumed that Nd^{3+} ions substitute Pb^{2+} in the 3*e* positions (with the point symmetry C_2) of the $Pb_3Ga_2Ge_4O_{14}$ structure and are coordinated with eight oxygen atoms.

OPTICAL PROPERTIES OF $Pb_3Ga_2Ge_4O_{14}$ CRYSTALS

The refractive indices of $Pb_3Ga_2Ge_4O_{14}$ crystals were measured by the method of minimum beam deflection on a prism with the refractive angle α = 40.00746° on a GS-5 goniometer [10] in the wavelength range 0.405–1.064 μm (Fig. 1a). The refractive indices $n_{o,e}$ were measured in the range 0.436–0.633 μm at λ = 0.405 within an accuracy of ±0.001 and at λ = 1.064 μm within an accuracy of ±0.002. In the spectrum range studied, the refractive indices of the $Pb_3Ga_2Ge_4O_{14}$ crystal were approximated by the Selmeyer one-term dispersion formula

$$n^2_{o,e} - 1 = K_{o,e}\lambda^2/(\lambda^2 - \lambda^2_{o,e}), \quad (1)$$

where K_o = 2.904022 and λ_o = 0.1680089 μm and K_e = 2.9638411 and λ_e = 0.1716406 μm are the coefficients and the corresponding characteristic wavelengths and λ is the wavelength of the incident light in micrometers. The $1/(n^2_{o,e} - 1) = f(1/\lambda^2)$ dependences are of a linear nature and, therefore, are well approximated by a straight line in this spectrum range (Fig. 1b).

Since there exist numerous crystals with similar structures, it is possible to evaluate their refractive indices proceeding only from the crystal composition, as was done in [8] for crystals of a rather large langasite family. One can also invoke the achievements of structural refractometry, where a substance is characterized by the molecular refraction R [11]:

$$R = [(n^2 - 1)/(n^2 + 2)](M/\rho). \quad (2)$$

Here, M is the molecular weight of the material, and ρ is its density.

A method for calculating molecular refractions proceeding from the material composition with due regard for the bonding nature was suggested in [11]. It is based on the additivity principle, according to which the molecular refraction of the material equals the sum of the refractions of the individual structural components. As was shown in [8], the additivity principle is valid for the crystals considered here and, therefore, following [8], we divided the crystal into the following structural fragments:

$$Pb_3Ga_2Ge_4O_{14} = (3PbO)(Ga_2O_3)(4GeO_2). \quad (3)$$

The tables of covalent and ionic refractions for all the elements of the Periodic Table can be found in [11]. Using these tables, one can calculate the covalent (R_c) and ionic (R_i) refractions of various materials. We calculated the R_c and R_i refractions and also the experimental refraction R_{obs} based on the experimentally determined refractive indices at λ = 0.589 μm. We also calculated the molecular refraction R_{calcd} using the calculated molecular refractions of the structural fragments and the refractive indices and densities of these fragments experimentally measured in [12]. For comparison, we tabulated all the calculated data for the crystals with the closest compositions, $Ca_3Ga_2Ge_4O_{14}$ and $Sr_3Ga_2Ge_4O_{14}$. It is seen from the table that, in these crystals, bonding is mainly ionic, since the data for R_i are rather close to the experimental values R_{obs}. More-

Molecular refraction of $Pb_3Ga_2Ge_4O_{14}$, $Ca_3Ga_2Ge_4O_{14}$, and $Sr_3Ga_2Ge_4O_{14}$

Crystal	n_{av}	ρ, g/cm^3	R_c	R_i	R_{obs}	R_{calcd}
$Pb_3Ga_2Ge_4O_{14}$	2.049	6.877	157.4	94.8	95.73	96.21
$Ca_3Ga_2Ge_4O_{14}$	1.812	4.589	175.4	69.3	72.92	72.01
$Sr_3Ga_2Ge_4O_{14}$	1.807	5.087	208.4	73.8	77.56	75.85

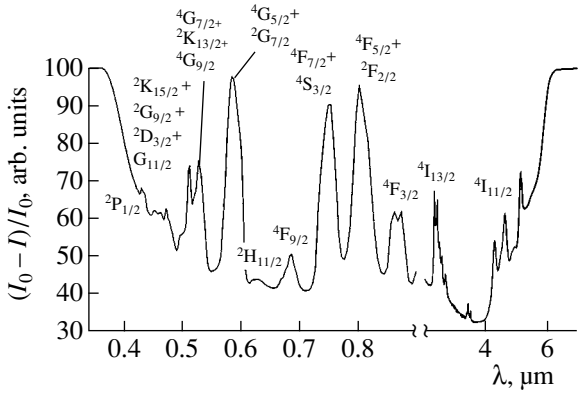

Fig. 2. Absorption spectrum of a $Pb_3Ga_2Ge_4O_{14}$: Nd^{3+} crystal obtained along the crystallographic *c*-axis at 300 K.

over, it is seen that the R_r and R_{obs} values agree quite well, which confirms the validity of our division of the crystal into structural fragments in the calculations of the molecular refractions using the additivity scheme.

Thus, the principle of additivity can be used when calculating molecular refractions for the crystals of this class. Using the calculated molecular refractions, one can evaluate the refractive indices of new crystals of this type. Moreover, knowing the molecular refractions of individual structural fragments at various wavelengths, one can also evaluate the dispersion in the refractive indices of complex crystals in the transparency range and the average refractive indices of new crystals having similar compositions.

SPECTROSCOPY OF $Pb_3Ga_2Ge_4O_{14}$:Nd^{3+} CRYSTALS

Figure 2 shows the absorption spectrum of a $Pb_3Ga_2Ge_4O_{14}$:Nd^{3+} crystal obtained along the crystallographic *c* axis at room temperature. The transparency range of the crystal lies in the spectral range 0.4–6.0 μm. The spectrum shows the main multiplet transitions of Nd^{3+} ions in the spectral range studied (0.35–7.00 μm).

Luminescence was studied at 300 and 77 K. The luminescence spectra were recorded on a setup consisting of an MDR-23 monochromator (26 A/mm dispersion), a PEM, an amplifier, and a block for recording signals. Luminescence was excited by the radiation of a tunable dye laser. The optimum wavelength of the exciting radiation was selected based on the maximum luminescence signal and was λ_{ex} = 0.57 μm at 300 K and λ_{ex} = 0.56 μm at 77 K. Figure 3 shows the luminescence spectra due to $^4F_{3/2} \longrightarrow {}^4I_{9/2}$ and $^4I_{11/2}$ transitions of a Nd^{3+} ion taken along the crystallographic *c* axis at 300 and 77 K. It is seen that lowering of the temperature from 300 to 77 K results in a slight narrowing of the lines, which is explained by nonuniform line broadening due to a considerable variety of structurally nonequivalent positions of neodymium ions in the disordered $Pb_3Ga_2Ge_4O_{14}$ matrix.

The analysis of the luminescence spectra allowed us to construct the scheme of Stark splitting of the multiplets of Nd^{3+} ions—$^4F_{3/2}$, $^4I_{9/2}$, and $^4I_{11/2}$ (the data obtained will be further refined by detailed spectroscopic studies of the concentration series of the crystals). The crystalline splitting of the $^4F_{3/2}$ level of Nd^{3+} ions in a $Pb_3Ga_2Ge_4O_{14}$ crystal is equal to ~250 cm^{-1}. The curves of luminescence decay at 300 and 77 K is practically of the exponential nature. The measured lifetime of the $^4F_{3/2}$ state at 300 and 77 K is $\tau \approx 100$ μs. The low value of this parameter can partly be explained by the effects of concentration quenching of luminescence in the sample studied, where, according to our measurements, the activator concentration is comparatively high, $C_{Nd} \approx 5 \times 10^{20}$ cm^{-3}.

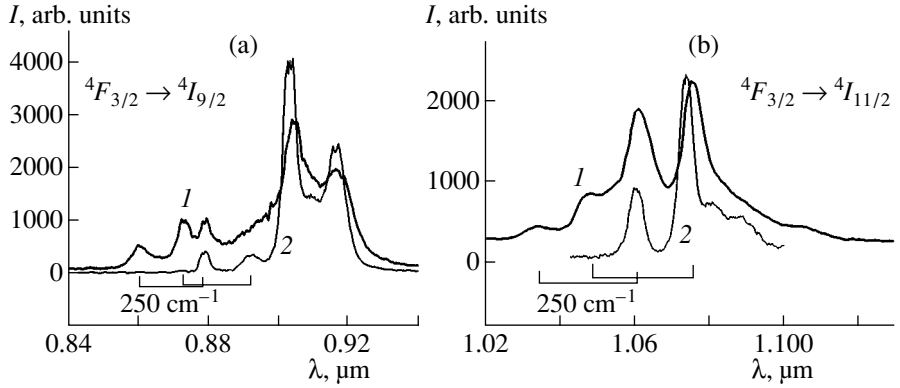

Fig. 3. Luminescence spectra of a $Pb_3Ga_2Ge_4O_{14}$: Nd^{3+} crystal due to the multiplet (a) $^4F_{3/2} \longrightarrow {}^4I_{9/2}$ and (b) $^4F_{3/2} \longrightarrow {}^4I_{11/2}$ transitions obtained at 300 (curve *1*) and 77 K (curve *2*). Brackets indicate splitting of the $^4F_{3/2}$ multiplet.

CONCLUSION

Thus, our optical and spectroscopic studies showed that a new disordered representative of the langasite family—a $Pb_3Ga_2Ge_4O_{14}:Nd^{3+}$ crystal—is rather interesting as a new lasing material that can be used for creating lasers with selective (diode) pumping. The spectral and luminescent characteristics obtained allow one to assume that this crystal can, possibly, be used as an active element in laser chips.

The analysis of the dispersion in refractive indices and birefringence of a uniaxial $Pb_3Ga_2Ge_4O_{14}$ crystal shows that the *ee–o*-type condition of phase matching in the second-harmonic generation with the wavelength 1.06 μm is not fulfilled.

We also plan to perform a further studies of spectra and generation on the concentration series of $Pb_3Ga_2Ge_4O_{14}:Nd^{3+}$ crystals. The analysis of the intensity characteristics of a new material from the langasite family should also include the calculation of the intensity parameters within the Judd–Offelt approximation [13, 14] and the evaluation of the spectroscopic quality of this crystal [15].

ACKNOWLEDGMENTS

We are grateful to V.M. Markushev and V.P. Orekhova for their help in performing the luminescence and optical measurements.

The study was supported by the Integration Project of the Siberian Division of the Russian Academy of Sciences no. 88, the Russian Foundation for Basic Research (project no. 01-02-16074), and also the Program “Laser Systems” of the Department of Physical Sciences of the Russian Academy of Sciences (project no. 2-30).

REFERENCES

1. B. V. Mill’, A. V. Butashin, and A. M. Éllern, Izv. Akad. Nauk SSSR, Neorg. Mater. **19** (10), 1715 (1983).
2. B. V. Mill’, A. V. Butashin, G. G. Khodzhabagyan, *et al.*, Dokl. Akad. Nauk SSSR **264** (6), 1385 (1982) [Sov. Phys. Dokl. **27**, 434 (1982)].
3. B. V. Mill’, E. L. Belokoneva, and T. Fukuda, Zh. Neorg. Khim. **43** (8), 1270 (1998).
4. B. V. Mill’, Zh. Neorg. Khim. **47** (3), 384 (2002).
5. D. V. Mill and Yu. V. Pisarevsky, in *Proceedings of 2000 IEEE/EIA International Frequency Control Symposium* (Kansas City, Missouri, USA, 2000), p. 133.
6. A. A. Kaminskiĭ, B. V. Mill’, and S. É. Sarkisov, in *Physics and Spectroscopy of Laser Crystals*, Ed. by A. A. Kaminskiĭ (Nauka, Moscow, 1986), p. 197.
7. A. A. Kaminskiĭ, A. V. Butashin, I. A. Maslyanitsin, and V. D. Shigorin, Phys. Status Solidi A **112**, K49 (1989).
8. O. N. Baturina, B. N. Grechushnikov, A. A. Kaminskiĭ, *et al.*, Kristallografiya **32** (2), 406 (1987) [Sov. Phys. Crystallogr. **32**, 236 (1987)].
9. L. N. Bezmaternykh, A. D. Vasil’ev, I. A. Gudim, and V. L. Temerov, Kristallografiya **49** (2), 325 (2004).
10. N. M. Melankholin, *Methods for Studying Optical Properties of Crystals* (Nauka, Moscow, 1970).
11. S. S. Batsanov, *Structural Refractometry* (Vysshaya Shkola, Moscow, 1976).
12. A. N. Winchell and H. Winchell, *The Microscopical Characters of Artificial Inorganic Solid Substances: Optical Properties of Artificial Minerals*, 3rd ed. (Academic, New York, 1964; Mir, Moscow, 1967).
13. B. R. Judd, Phys. Rev. **127**, 750 (1962).
14. G. S. Offelt, J. Chem. Phys. **37**, 511 (1962).
15. L. Li, Candidate’s Dissertation in Physics and Mathematics (Moscow, 1975).

Translated by L. Man

Crystallography Reports, Vol. 49, No. 3, 2004, pp. 463–468. Translated from Kristallografiya, Vol. 49, No. 3, 2004, pp. 528–533.

PHYSICAL PROPERTIES OF CRYSTALS

Dedicated to the 80th Birthday of L.A. Shuvalov

The Nature of Spontaneous Twisting of $(NH_4)_2SO_4$ Crystals at the Curie Point

S. A. Gridnev, O. N. Ivanov, and A. T. Kosilov

Voronezh State Technical University, Moskovskiĭ pr. 14, Voronezh, 394026 Russia

e-mail: gridnev@nsl.vstu.ac.ru

Received June 27, 2003

Abstract—Spontaneous twisting of $(NH_4)_2SO_4$ crystals at the phase transition from the paraelectric phase *Pnam* to the ferroelectric phase *Pna*2 (T_C = 223 K) was studied using the method of low-frequency torsion pendulum. It is shown that the macroscopic twisting of samples is caused by the rearrangement of ferroelastic twins with the {011} and {031} twinning planes existing in both the paraelectric and ferroelectric phases. A model interpreting the effect of the spontaneous twisting below the ferroelectric Curie point is proposed. © *2004 MAIK "Nauka/Interperiodica"*.

INTRODUCTION

Ammonium sulfate $(NH_4)_2SO_4$ belongs to the family of α-K_2SO_4 compounds with the general formula A_2BX_4 [1]. A number of specific features make this type of crystal rather attractive for basic research. Among these, we should note the following:

(1) The ferroelectric phase transition (symmetry transformation from *Pnam* to *Pna*2, the Curie point at T_C = 223 K) is characterized by very small values of the spontaneous polarization and the Curie–Weiss constant (C_{cw} = 15 K), which are typical of weak ferroelectrics [2].

(2) The sign of spontaneous polarization changes at about 85 K, which indicates a complex mechanism of the ferroelectric phase transition. The latter may be related, for example, to the occurrence of ferroelectricity in two different sublattices which are characterized by different temperature dependences of the spontaneous polarization [3].

(3) There exists a system of ferroelastic twins with the {011} and {031} twinning planes in both the paraelectric and ferroelectric phases [4, 5]. It is believed that the formation of elastic twins occurs as a result of the high-temperature phase transition from the hypothetic hexagonal phase $P6_3/mmc$ to the orthorhombic phase *Pnam*. This transition does not manifest itself in actual experiments due to the chemical instability of ammonium sulfate at high temperatures (above 420 K).

It is important that the ferroelectric phase transition in $(NH_4)_2SO_4$ occurs within the range of existence of the ferroelastic phase containing elastic twins. In this case, one would expect that the ferroelastic twin structure existing in the course of the ferroelectric phase transition should affect the behavior of some characteristics of ammonium sulfate (first of the all, its elastic and anelastic properties) in the vicinity of the Curie point. In fact, the anomalous variation in the internal friction and the shear modulus near T_C was observed in ammonium sulfate at infralow frequencies [6].

In this paper, we show that the anomalous effect of spontaneous twisting of $(NH_4)_2SO_4$ single crystals at the transition from the paraelectric to ferroelectric phase (revealed previously by the method of inverted torsion pendulum [7]) is related to the rearrangement of ferroelastic twins at T_C.

EXPERIMENTAL

$(NH_4)_2SO_4$ single crystals used in our experiments were grown from a saturated aqueous solution with pH 4 by evaporation at 303 K. The aqueous solution was prepared from twice recrystallized ammonium sulfate.

The temperature dependence of the spontaneous-twist angle of a sample was measured using a setup (Fig. 1) involving an inverted torsion pendulum (see [8] for more details). Long twisting rod *1* with rigidly fixed spider and inertial weights is connected by a collet chuck with sample *2*, whose lower end is gripped in a fixed collet. When an external stress (alternating or constant) is applied to a sample through the twisting rod, the sample is rotated by a certain angle with the use of a differential electromagnetic system. The system consists of two coils *3*, through which an electric current is passed. The coils, located diametrically opposite to the pendulum axis, interact with two permanent magnets *4* with pole pieces made of soft iron. When measuring the

1063-7745/04/4903-0463$26.00 © 2004 MAIK "Nauka/Interperiodica"

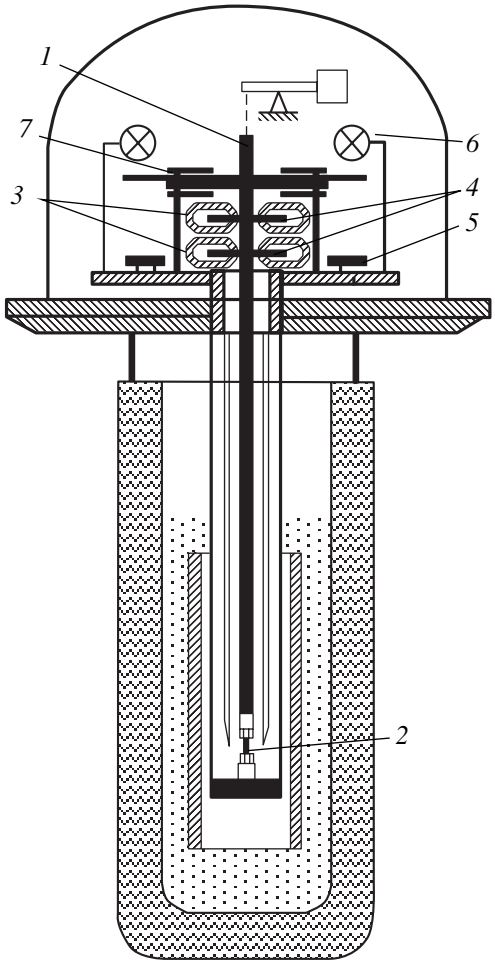

Fig. 1. Schematic diagram of the torsion pendulum: (*1*) twisting rod; (*2*) sample; (*3*) coils of an electromagnet, generating the torque; (*4*) permanent magnets; (*5*) photoelectric sensors for measuring small strains; (*6*) electric lamps; (*7*) capacitance sensors for measuring large strains.

spontaneous twisting of samples, the electromagnetic system was switched off. To measure small torsional strains (10^{-5}–10^{-3}), we used photoelectric sensors *5* with lamps *6*. Large strains (>10^{-3}) were measured by capacitive sensors *7*.

The samples for studying the torsion strains had the shape of rectangular bars $2 \times 2 \times 18$ mm^3 in size, with the long side oriented along the crystal axes *a*, *b*, and *c* (the *X*-, *Y*-, and *Z*-oriented samples, respectively). The spontaneous twisting of a sample made the pendulum rotate by angle φ. In experiments, the temperature dependence of the rotation angle φ for the samples of each crystallographic orientation was automatically plotted by an XY-recorder. The dependence φ(*T*) was measured upon continuous cooling at a rate of about 0.2 K/min in the temperature range 270–150 K. The shear strain at the sample surface was determined by the formula

$$\varepsilon = \varphi\frac{d}{2l}, \quad (1)$$

where *d* and *l* are the cross-sectional size and the length of a sample, respectively. As a result, we found the temperature dependences of the strains ε^X, ε^Y, and ε^Z (which correspond to the twisting of *X*-, *Y*-, and *Z*-oriented samples about the *a*, *b*, and *c* axes, respectively).

We should note here that, upon twisting, both strains and stresses vanish at the center of a sample and attain their maximum values at the sample surface. Thus, the shear stresses in the sample turn out to be inhomogeneous along the radius of the sample; hence, the strain estimated by formula (1) is maximum at the sample surface.

EXPERIMENTAL RESULTS

The temperature dependences of the torsional strains ε^X, ε^Y, and ε^Z are shown in Fig. 2. We can see that the spontaneous twisting is absent in the paraelectric phase at $T > T_C = 223$ K for each of the three orientations under study. However, the samples of all three orientations undergo spontaneous twisting after the transition to the ferroelectric phase. All the measured strains, ε^X, ε^Y, and ε^Z, arise abruptly at $T = T_C$ and then gradually increase upon cooling a sample in the ferroelectric phase. The largest and smallest torsional strains are observed for *Z*- and *X*-oriented samples, respectively. For *Z*- and *Y*-oriented samples, the jumps in the torsion strains $\Delta\varepsilon$ at $T = T_C$ turned out to be equal to 3×10^{-3} and 1.2×10^{-3}, respectively.

DISCUSSION

Spontaneous twisting of crystals in a torsion-pendulum system at a structural phase transition was observed previously in a number of ferroelectric crystals: $KH_3(SeO_3)_2$ and $KD_3(SeO_3)_2$ [9], K_2ZnCl_4 [10], $KLiSO_4$ [11], $SrTiO_3$ [12], single crystals of the KH_2PO_4 family [13], and so on. All these compounds are ferroelastics, and the ferroelastic phase transition, which gives rise to the spontaneous twisting, is accompanied by the formation of new shear-strain components in the low-symmetry ferroelastic phase, which were absent in the high-symmetry paraelastic phase (the shear-type phase transition). For example, at the phase transition $mmm \longrightarrow m/2$ in $KH_3(SeO_3)_2$ crystals, the shear-strain component ε_{13} arises in the ferroelastic phase ($m/2$), whereas, in KH_2PO_4 crystals, the shear strain ε_{12} arises as the result of the phase transition with the symmetry transformation $\bar{4}2m \longrightarrow mm2$, and so on. It was shown in [14] that it is the formation of new shear-strain components at the phase transition under the condition of existence of noncompensated spontaneous strain in the twinning structure which may cause

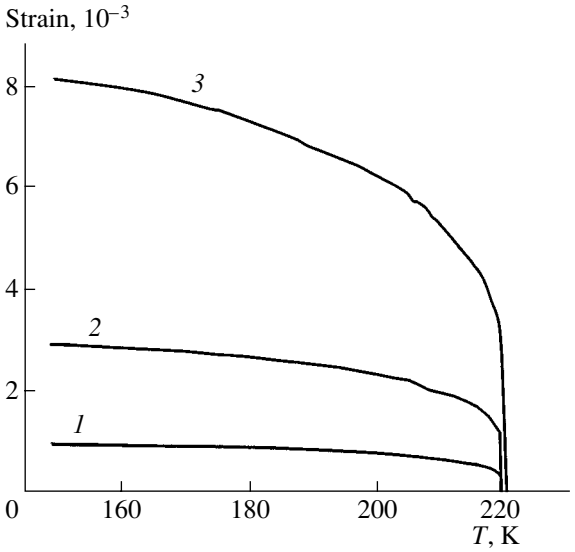

Fig. 2. Temperature dependence of the spontaneous-twisting strains for $(NH_4)_2SO_4$ crystals with different orientations: (*1*) *X*, (*2*) *Y*, and (*3*) *Z*.

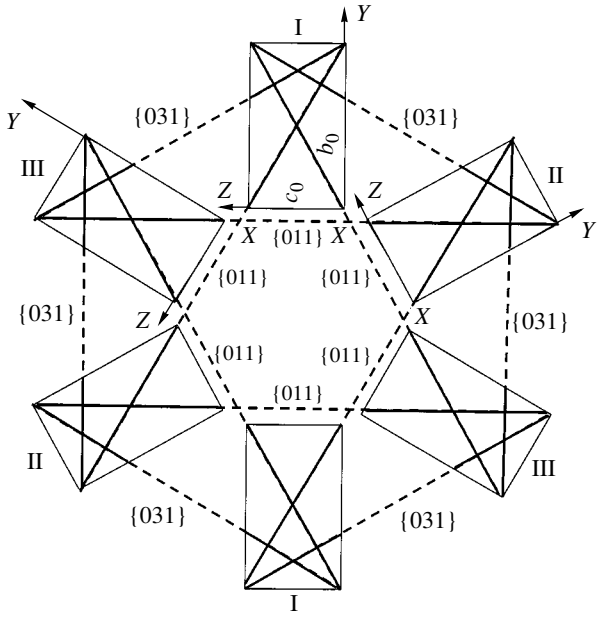

Fig. 3. Arrangement of unit cells for the three orientations of ferroelastic twins.

the macroscopic effect—the spontaneous twisting of a sample.

The situation is drastically different in the case of spontaneous twisting at the ferroelectric phase transition in $(NH_4)_2SO_4$ crystals near 223 K. This phase transition occurs from the paraelectric orthorhombic phase *Pnam* to the ferroelectric orthorhombic phase *Pna*2 and is accompanied by a change in the lattice parameters; i.e., a spontaneous strain arises [15]. Since the crystal system does not change (remains orthorhombic) at this transition, the principal axes on the spontaneous-strain tensor coincide with the *X*, *Y*, and *Z* axes. Hence, the spontaneous twisting of samples should be absent for any of the orientations under study (*X*, *Y*, or *Z*). However, Fig. 2 shows pronounced twisting of the samples with all three orientations below T_C. To get insight into the nature of the observed twisting, let us consider the behavior of each of the three types of ferroelastic twins in $(NH_4)_2SO_4$ single crystals [4] which are present in both the paraelectric and ferroelectric phases.

According to [4], the symmetry of twins, observed experimentally in the paraelectric phase, stems from the symmetry of the hypothetic high-temperature hexagonal phase $P6_3/mmc$. The symmetry of twins manifests itself in the fact that the unit cells for the three twin orientations are arranged in such a way that their *X* axes (the lattice parameter a_0) coincide with each other, whereas their *Y* axes (the parameter b_0), as well as the *Z* axes (the parameter c_0), form an angle of 60° with each other (Fig. 3). Figure 3 shows the twinning planes {011} and {031} (solid lines within the unit cells). Possible variants of matching between the twins of different types (I, II, and III) are shown by dashed lines.

The spontaneous twisting of samples may be caused by two reasons. First, if we suggest that the change in the lattice parameters at the phase transition and upon subsequent cooling of samples at temperatures below T_C is not accompanied by displacement of twin boundaries, then the sample twisting may be caused only by the absence of balance between the macroscopic strains due to the difference in the types of twins. The second reason for the spontaneous twisting of a crystal is its detwinning. If a sample is twisted in the initial state due to the twinning strain, the change in the unit-cell parameters of matched twins, caused by the phase transition, results in the rotation of the corresponding lattices relative to each other. This circumstance leads to the violation of the matching conditions for the different types of twins and to the formation of internal stress fields. Due to the detwinning, the internal stress fields are relieved. As a result, the crystal shape changes (among other reasons, due to the torsional strain).

Let us consider the model of twin-boundary pinning. We assume that the sample axis coincides with the *Y* axis of twin I. In this case, the spontaneous-strain tensor for twin I has the following form in the system of axes related to twin I:

$$\varepsilon_{ik}^{I(I)} = \begin{bmatrix} \varepsilon_1 & 0 & 0 \\ 0 & \varepsilon_2 & 0 \\ 0 & 0 & \varepsilon_3 \end{bmatrix}. \quad (2)$$

In the axes related to twins II and III, the spontaneous-

strain tensor can be written as

$$\varepsilon_{ik}^{\mathrm{II,\,III(I)}} = \begin{bmatrix} \varepsilon_1 & 0 & 0 \\ 0 & \left(\frac{1}{4}\varepsilon_2 + \frac{3}{4}\varepsilon_3\right) & \pm\frac{\sqrt{3}}{4}(\varepsilon_3 - \varepsilon_2) \\ 0 & \pm\frac{\sqrt{3}}{4}(\varepsilon_3 - \varepsilon_2) & \left(\frac{3}{4}\varepsilon_2 + \frac{1}{4}\varepsilon_3\right) \end{bmatrix}, \qquad (3)$$

where the plus and minus signs before the component ε_{yz} correspond to twins II and III, respectively. In expressions (2) and (3), $\varepsilon_{ik}^{N(M)}$ denotes the strain tensor for twin *N* in the crystallographic axes related to twin *M*.

The form of tensors (2) and (3) suggests the following:

(1) For the *X*-oriented samples, the components ε_{XY}^s and ε_{XZ}^s, which could give rise to twisting, are zero for all three types of domains. Hence, the *X*-oriented samples should not undergo twisting at the ferroelectric phase transition.

(2) For the *Y*-oriented samples, the components ε_{YX}^s and ε_{YZ}^s are responsible for the torsional strain. However, for all three types of twins, we have $\varepsilon_{YX}^s = 0$. The only nonzero components are $\varepsilon_{YZ}^{\mathrm{II(I)}} = \frac{\sqrt{3}}{4}(\varepsilon_3 - \varepsilon_2)$ and $\varepsilon_{YZ}^{\mathrm{III(I)}} = \frac{\sqrt{3}}{4}(\varepsilon_3 - \varepsilon_2)$. As can be seen, the strain components for twins of types II and III ($\varepsilon_{YZ}^{\mathrm{II(I)}}$) and ($\varepsilon_{YZ}^{\mathrm{III(I)}}$), respectively) have the same magnitudes and opposite signs. Therefore, the torsional strains caused by the spontaneous strains in the type-II and type-III domains have opposite signs (opposite twisting directions).

(3) For the *Z*-oriented samples, the spontaneous-strain components responsible for the torsional strain are the same as in the case of *Y*-oriented samples ($\varepsilon_{YZ}^{\mathrm{II(I)}}$) and ($\varepsilon_{YZ}^{\mathrm{III(I)}}$).

Thus, the twisting occurs when the following conditions are met. First, the principal components of the spontaneous-strain tensor $\varepsilon_2^s(T)$ and $\varepsilon_3^s(T)$ should not be equal to each other: $\varepsilon_2^s(T) \neq \varepsilon_3^s(T)$. Second, the magnitudes of the macroscopic torsional strains in the entire sample, caused by the type-II and type-III twins, should be different.

It is easy to show that the first condition is satisfied. Indeed, the behavior of the unit-cell parameters *a*, *b*, and *c* at the phase transition and upon subsequent cooling [16] indicates that the parameter ($\varepsilon_2^s - \varepsilon_3^s$) monotonically decreases with decreasing temperature.

The second condition is virtually always satisfied since the twinning structure is irregular and the structural states with equal macroscopic torsional strains due to the type-II and type-III twins can hardly be realized. Note that the condition of equality of these macroscopic strains does not imply the equality of the volumes of type-II and type-III twins since the effect of twisting of a twin depends not only on its volume but also on the distance between the twin and the twist axis and an azimuthal angle [14].

Let us find the relationship between the spontaneous-twisting direction in a crystal and the type of rearrangement of its twinning structure. First of all, we will consider the changes in the twinning structure of a *Y*-oriented sample due to an external torque applied along the *Y* axis (see Fig. 4). It can be seen from Fig. 4 that the only component of the stress tensor σ_{YZ} (in the crystallographic axes corresponding to the type-I twin; see Fig. 3) that determines the force acting on the twin boundaries has different signs at the different sides of the *YZ* plane.

Figure 5 shows all possible types of matching between the twins located in the region of the crystal defined by $x > 0$, as well as the shear stresses σ acting at the twin boundaries (antiparallel arrows) and the directions $\bar{v}$ for the motion of twin boundaries, which were determined on the basis of the models of twinning for this system [4, 5]. The system of arrows describes the elements of the medium (Fig. 4) for which the condition $x > 0$ is satisfied (the elementary volume is shown by solid lines in Fig. 4). On going to the region where $x < 0$ (the corresponding elementary volume is shown by dashed lines in Fig. 4), the signs of the shear stresses σ and the directions of the boundary motion change to the opposite. Figure 5 shows that stresses applied to a sample increase the volume of type-II and type-III twins in the regions $x > 0$ and $x < 0$, respectively. At the same time, these stresses decrease the volume of type-III and type-II twins in the regions $x > 0$ and $x < 0$, respectively. As a result of such a preliminary retwinning strain, type-II twins in the region at $x > 0$ and type-III twins in the region at $x < 0$ become dominant in the further shape changes accompanying the ferroelectric transition. Let us find the spontaneous-twisting direction for such a preliminary twisted sample upon cooling at $T < T_C$. If it turns out that $\varepsilon_{YZ}^{\mathrm{II(I)}} > 0$ and $\varepsilon_{YZ}^{\mathrm{III(I)}} < 0$ at $x > 0$ and $\varepsilon_{YZ}^{\mathrm{II(I)}} < 0$ and $\varepsilon_{YZ}^{\mathrm{III(I)}} > 0$ at $x < 0$, untwisting of the sample should be observed.

Let us compare the conclusions of the above model with the experimental results. Figure 6 shows the temperature dependence of the quantity ($\varepsilon_3^s - \varepsilon_2^s$) plotted using the data of [16]. It is worth noting that the quantity ($\varepsilon_3^s - \varepsilon_2^s$) has rather small negative values in a narrow temperature range (about 20 K) in the vicinity of the phase transition. Upon further cooling, this parameter changes its sign and monotonically increases with

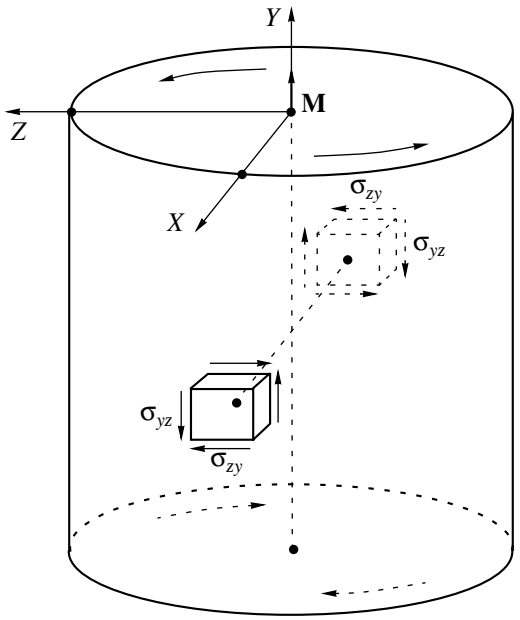

Fig. 4. Effect of the external torque **M** on the twinning structure of a [010]-oriented sample.

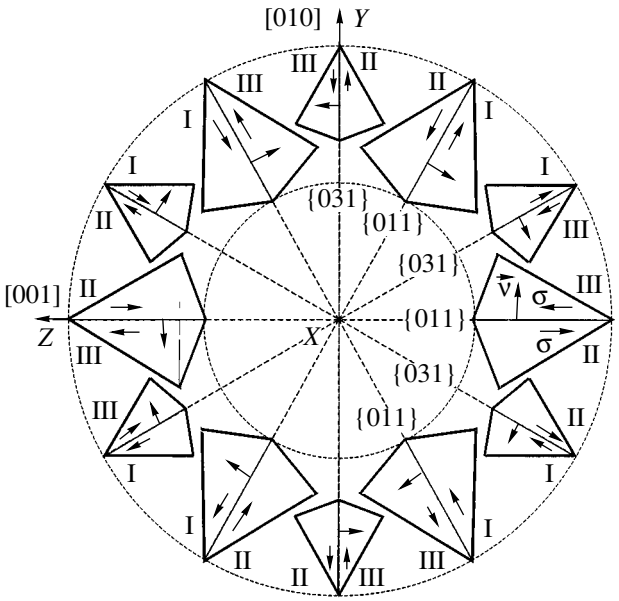

Fig. 5. Schematic diagram of possible configurations of twins with {011} and {031} twinning planes for each pair of domain combinations: I–II, II–III, and III–I.

decreasing temperature. Therefore, the spontaneous-twisting strain should also change its sign near T_C. Upon cooling below 200 K, the twisting direction should be opposite to the direction of preliminary twisting in the paraelectric phase. The larger the preliminary strain is, the more pronounced the effect should be. Nevertheless, the experimental curves (Fig. 2) do not show any change in the spontaneous-twisting direction in the vicinity of T_C upon sample cooling. The sample is twisted in the same direction both at $T = T_C$ and upon subsequent cooling below 200 K. Therefore, it is unlikely that the first mechanism, related to changes in the shape of ferroelastic domains due to the pinning of domain boundaries, is dominant.

The model taking into account the detwinning of a crystal at the ferroelectric phase transition, i.e., the absorption of ferroelectric twins of one type by twins of another type, seems to be more likely. The X-ray-diffraction data of [16] clearly indicate detwinning processes (but not the domain merging) in $(NH_4)_2SO_4$ at $T = T_C$. In particular, at the phase-transition temperature and upon subsequent cooling of a sample, the redistribution of the relative intensities of reflections from twins of different orientations was observed. This redistribution is related to the changes in the volume fractions of these twins, which accompany the partial detwinning.

According to the above model, the spontaneous twisting should be absent in *X*-oriented samples. However, a slight twisting was observed experimentally even in a sample with this orientation (Fig. 2). This fact may be related to some disorientation of the twist axis of the sample with respect to the [100] crystallographic direction, which arises during sample preparation.

The model also implies that *Y*- and *Z*-oriented samples should undergo spontaneous twisting below the ferroelectric Curie point, and the torsional strains in these samples should have the same magnitude. Slightly different strains in the samples with these orientations, observed in practice in the ferroelastic phase (Fig. 2), may be related to the different realizations of the arising twin structures. Note that, upon varying the temperature of a sample in the paraelectric phase, the

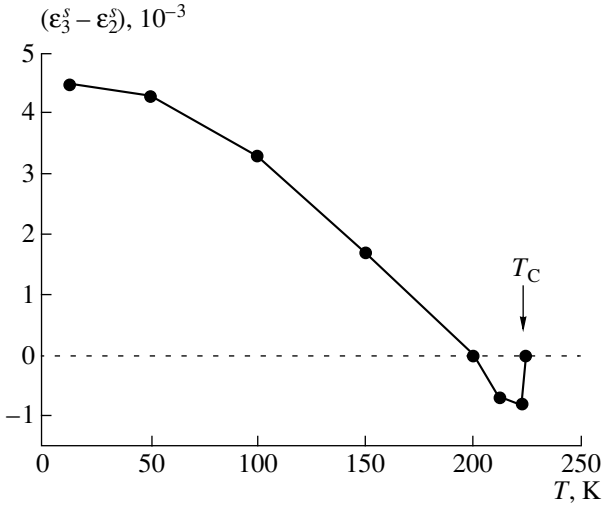

Fig. 6. Temperature dependence of the parameter $(\varepsilon_3^s - \varepsilon_2^s)$ plotted using the data of [16].

sample undergoes no steady twisting due to the difference in the thermal expansion coefficients of twins in the X and Z directions. According to [15, 16], these coefficients are comparable to those for the ferroelectric phase. Such a temperature behavior is an additional argument in favor of the detwinning mechanism at $T < T_C$. Only the jumplike volume rearrangement of the structure at the phase-transition point ensures the depinning of twin boundaries and their subsequent shift, which leads to spontaneous twisting.

ACKNOWLEDGMENTS

This work was supported by the Russian Foundation for Basic Research, project no. 01-02-16097, and by the Ministry of Education of the Russian Federation, project no. UR.01.01.016.

REFERENCES

1. K. S. Aleksandrov and B. V. Beznosikov, *Structural Phase Transitions in Crystals (Potassium Sulfate Family)* (Nauka, Novosibirsk, 1993).
2. A. K. Tagantsev, I. G. Siniĭ, and S. D. Prokhorova, Izv. Akad. Nauk SSSR, Ser. Fiz. **49**, 2082 (1985).
3. V. Dvorak and Y. Ishibashi, J. Phys. Soc. Jpn. **41**, 548 (1976).
4. A. Sawada, Y. Makita, and Y. Takagi, J. Phys. Soc. Jpn. **41**, 174 (1976).
5. Y. Makita, A. Sawada, and Y. Takagi, J. Phys. Soc. Jpn. **41**, 167 (1976).
6. S. A. Gridnev, O. N. Ivanov, L. P. Mikhaĭlova, and T. N. Davydova, Fiz. Tverd. Tela (St. Petersburg) **40** (12), 2202 (1998) [Phys. Solid State **40**, 1998 (1998)].
7. S. A. Gridnev, O. N. Ivanov, L. P. Mikhaĭlova, and T. N. Davydova, Fiz. Tverd. Tela (St. Petersburg) **43** (4), 693 (2001) [Phys. Solid State **43**, 722 (2001)].
8. S. A. Gridnev, V. I. Kudryash, and L. A. Shuvalov, Izv. Akad. Nauk SSSR, Ser. Fiz. **43** (8), 1718 (1979).
9. S. A. Gridnev, V. I. Kudrjash, B. N. Prasolov, and L. A. Shuvalov, Ferroelectrics **26**, 669 (1980).
10. L. A. Shuvalov, S. A. Gridnev, B. N. Prasolov, and V. G. Sannikov, Ferroelectr. Lett. Sect. **1**, 85 (1983).
11. S. A. Gridnev and A. A. Khodorov, Ferroelectrics **199**, 279 (1997).
12. V. V. Lemanov, S. A. Gridnev, and E. V. Ukhin, Fiz. Tverd. Tela (St. Petersburg) **44**, 1106 (2002) [Phys. Solid State **44**, 1156 (2002)].
13. S. A. Gridnev and S. A. Kravchenko, Ferroelectrics **186**, 313 (1996).
14. S. A. Gridnev and A. T. Kosilov, J. Phys. D: Appl. Phys. **35**, 1538 (2002).
15. N. A. Romanyuk, V. M. Gaba, and Z. M. Ursul, Ukr. Fiz. Zh. **33**, 1381 (1988).
16. I. M. Shmyt'ko, N. S. Afonikova, and V. I. Torgashev, Fiz. Tverd. Tela (St. Petersburg) **44**, 2204 (2002) [Phys. Solid State **44**, 2309 (2002)].

Translated by K. Kugel

Crystallography Reports, Vol. 49, No. 3, 2004, pp. 469–475. Translated from Kristallografiya, Vol. 49, No. 3, 2004, pp. 534–540.

PHYSICAL PROPERTIES OF CRYSTALS

Dedicated to the 80th Birthday of L.A. Shuvalov

Temperature Dependence of the Dielectric Parameters of Nonstoichiometric $SrTiO_3$ Single Crystals

Ya. Doĭchilovich*, N. Kulagin, D. Popovich*, and S. Spasovich***

** Unjversity of Belgrade, Belgrade, 11000 Serbia and Montenegro*

*** Kharkov National University for Radioelectronics, Kharkov, ul. Shakespeare 6-48, 61045 Ukraine*

e-mail: kulagin@univer.kharkov.ua

Received March 13, 2003

Abstract—The results of experimental studies of the temperature dependence of the low-frequency permittivity ε_0 and the loss tangent $\tan\delta$ of nominally undoped and doped single crystals of strontium titanate at $T = 10$–300 K are given. The samples were doped with ions of iron-group metals (V, Mn, Fe, Co) and/or ions of rare earth metals (Pr, Nd, Sm, Tm) with concentrations of 10^{-3}–5×10^{-1} at %. Anomalous temperature dependences $\varepsilon_0(T)$ and $\tan\delta(T)$ were found for a number of samples. The anomalies found were attributed to the violation of stoichiometry of the single crystals under study and the transition of some fraction of Ti^{4+} ions to the Ti^{3+} state. © *2004 MAIK "Nauka/Interperiodica".*

INTRODUCTION

Constant interest has been shown in strontium titanate $SrTiO_3$ for more than 30 years [1–6]. Great interest in perovskites ABO_3 (in particular, in strontium titanate) is caused by a number of unique properties of these crystals and the perspectives of their wide application in micro- and optoelectronics. The discussion of the formation of the ferroelectric phase in strontium titanate is still topical [5, 6].

According to different data, a number of phase transitions were revealed in $SrTiO_3$ crystals at 10, 30, 65, and 105 K [7]. Experiments have not given evidence of these transitions, except the one at 105 ± 2 K. The latter, being a structural displacive transition with participation of a soft mode, is accompanied by a change in the crystal symmetry from cubic to tetragonal with decreasing temperature [1, 2]. Investigation of solid solutions formed on the basis of $SrTiO_3$ and $CaTiO_3$, $SrTiO_3$ and $BaTiO_3$, and $Sr_{1-x}[Pb(Ba)]_xTiO_3$ compounds revealed the linear dependence of the phase-transition temperature on x at critical concentrations $x = 0.0015$–0.002. In this case, the Curie temperature $T_C = 40$ K [5].

It should be noted that nominally undoped $SrTiO_3$ crystals are neither ferroelectrics nor antiferroelectrics [1, 2]. Our investigations of the dielectric constants of $SrTiO_3$ crystals also did not reveal any ferroelectric or antiferroelectric anomalies in the temperature range from 50 to 300 K in samples of high structural quality and in crystals doped with iron-group ions with concentrations $C_{dop} < 10^{-1}$ at % [8, 9]. At the same time, the Curie–Weiss law [1, 2]

$$\varepsilon_0(T) = C/(T - T_C) \quad (1)$$

(here C is the Curie constant) is generally used to describe the temperature dependence of the permittivity $\varepsilon_0(T)$ for these crystals.

The presence of the soft mode and the fact that its frequency becomes zero at $T \longrightarrow 105$ K seem to confirm the validity of the Curie–Weiss law. Nevertheless, the values of T_C and C obtained in different experiments differ significantly [3, 8–10]. The spread in the values of T_C and C is probably due to distortions of the crystalline structure of perovskite at temperatures above and below the phase-transition temperature [11, 12].

In our opinion, the difference in the points of view on the existence and temperatures of phase transitions, as well as the values and temperature dependences of the dielectric parameters of $SrTiO_3$, is due to the difference in the impurity and stoichiometric compositions of the crystals studied. Previous investigations [13–16] showed the presence of Ti^{3+} ions in Ti^{4+} sites in most nominally undoped and in almost all impurity $SrTiO_3$ single crystals, which significantly affects the dielectric, electric, and spectral characteristics of $SrTiO_3$ [4, 9, 13, 14]. The transition of up to 20% of Ti^{4+} ions to the Ti^{3+} state with the $3d^1$ configuration, which was observed for a number of $SrTiO_3$ single crystals, is caused by the violation of stoichiometry of these samples with respect to titanium, strontium, and first of all, oxygen during crystal growth [3, 13, 14].

An increase in the concentration of point defects, both oxygen vacancies and Ti^{3+} ions, as well as the formation of macrodefects (blue color and notching [13]), leads to changes in the dielectric and spectral characteristics of strontium titanium in a wide temperature range. Due to the changes in the ratios Sr : Ti and Sr : Ti : O (the violation of stoichiometry) caused by an increase in the concentration of Ti ions with decreasing concentrations of strontium and oxygen ions and the corresponding changes in the valence of some fraction of Ti ions, the lattice constant decreases and the sample density increases. Such radical changes in the crystal structure lead to a decrease in the refractive index and the appearance of birefringence in $SrTiO_3$ crystals (which have the cubic structure [16–18]). For example, for ultrapure crystals, the density $\rho = 4.97$ g/cm^3 and the refractive index $n = 2.409$ (at $\lambda = 589$ nm), whereas, for blue-colored $SrTiO_3$ crystals, $\rho = 5.16$ g/cm^3 and $n = 2.389$ (at the same wavelength) [17, 18]. On going from the ultrapure to blue-colored crystals, the lattice constant a decreases from 3.9051 to 3. 9002 Å, which also indicates significant changes in the crystal lattice of $SrTiO_3$.

Unstable color centers and violation of stoichiometry also play an important role when the crystal structure differs significantly from cubic. For example, the permittivity ε_0 may vary from sample to sample from a few to 360 ± 5 at $T = 300$ K [3, 8, 9].

The anomaly in the high-frequency dielectric properties and ESR spectra of impurity crystals at $T = 100$–120 K and the birefringence revealed in both impurity and a number of nominally undoped $SrTiO_3$ single crystals [8, 19, 20] confirm the significant effect of the structural quality of crystals on their dielectric parameters. We should also note the change in the intensity of the absorption and luminescence bands of impurity $SrTiO_3$ single crystals due to the low-temperature exposure (at $T = 77$ K for 600–1200 s) [8, 19, 20], which indicates nonconventional mechanisms of energy and charge transfer in $SrTiO_3$. At the same time, no particular changes have been revealed in the Raman spectra of these crystals in a wide temperature range [20].

The temperature dependences $\varepsilon_0(T)$ and $\tan\delta(T)$ were measured for some $SrTiO_3$ crystals, both nominally undoped and doped with iron-group ions (about 10^{-2} at %), at frequencies of 800 Hz and 1 MHz [8, 9]. The data obtained showed an anomaly in the high- and low-frequency dielectric properties of the dependences $\varepsilon_0(T)$ and $\tan\delta(T)$ for $SrTiO_3$ crystals.

In this study, along with analysis of the dependences $\varepsilon_0(T)$ and $\tan\delta(T)$ at $T < 300$ K for $SrTiO_3$ single crystals doped with iron-group impurities (V, Mn, Fe, Co), we also investigated the effect of impurity rare earth ions (REIs), which occupy A (Sr^{2+}) sites in ABO_3, on the dielectric parameters of $SrTiO_3$ single crystals.

OPTICAL-ABSORPTION SPECTRA OF IMPURITY $SrTiO_3$ SINGLE CRYSTALS

The $SrTiO_3$ single crystals studied by us previously were grown by the Verneuil method. They are described in detail in [3, 8–10, 13]. The pure (reference) samples were grown from high-purity mixture and the total concentration of paramagnetic impurities in these samples did not exceed 10^{-5} at %. Nominally pure samples grown from standard-quality mixture, which, in accordance with the ESR data, contained Cr, Mn, and Fe ions with the total concentration $C_{imp} \sim 10^{-2}$ at %, were also analyzed in these studies. As the spectral analysis showed, the content of other impurities (Ca, Mg, and so on) also did not exceed 10^{-2} at %. The presence of Ti^{3+} ions was detected in all the doped samples by the method of valence shifts of X-ray lines [10, 11].

The samples doped with iron-group ions (V, Mn, Fe, Co) with concentrations from 1.2×10^{-2} to 5×10^{-1} at %, along with the activator, contained unintentional impurity ions of Cr, Ca, and Mg with a total concentration of about 10^{-2} at %.

According to the data of spectral analysis, the impurity concentration in $SrTiO_3$ samples doped with Pr, Nd, Sm, and Tm ions did not exceed $(2–5) \times 10^{-3}$ at %, although the initial mixture contained up to 1 at % of rare earth oxides. Both the ESR measurements and spectral analysis showed the presence of iron-group ions (Cr, Fe, Mn) with a concentration of about 10^{-3} at % in $SrTiO_3$: REI crystals.

The samples for optical and dielectric measurements, as well as for X-ray spectroscopic analysis of stoichiometry and determination of the valence of regular ions, were shaped as plates about 10 mm in diameter and 0.8–1 mm thick.

The optical spectra of $SrTiO_3$ crystals, nominally undoped and doped with iron-group ions, were studied in [13, 21]. The edge of fundamental optical absorption near 395 nm (Fig. 1) is determined by indirect optical transitions, in which phonons with the energy $E_{ph} = 5.1 \times 10^{-2}$ eV are involved. Direct optical transitions begin with the energy $E = 4.11$ eV [22].

High-purity crystals are transparent to light with wavelengths up to 7500 nm. Generally, the absorption spectra of undoped $SrTiO_3$ contain wide bands peaked at 430 and 520 nm and, in many cases, a band at 620 nm (Fig. 1) [18–20].

Both the ESR data for Cr, Mn, Fe, and other iron-group impurities [23, 24] and the results of optical measurements indicate nonisovalent substitution typical of impurity (*Me*) ions: $Me^{3+} \longrightarrow Ti^{4+}$ in $SrTiO_3$ crystals. At the same time, the ESR spectrum of Cr^{5+} ions in tetrahedral sites of $SrTiO_3$ was studied in [24].

The introduction of 3*d* ions even with relatively low concentrations ($C < 10^{-1}$ at %) leads to a shift of the optical-absorption edge, which is caused by the charge

transfer ($Me^{3+} \longrightarrow O^{2-}$). As an example, the optical absorption spectrum of $SrTiO_3$: Co samples with different dopant concentrations is shown in Fig. 2. According to the spectral analysis, the samples under study contained (1.2, 2.5, 6.0) $\times 10^{-2}$ at % Co ions (Fig. 2, curves *1*, *2*, *3*, respectively). With an increase in C_{Co}, the strong-absorption edge shifts to longer waves.

Cobalt ions, as well as other iron-group ions, occupy mainly *B* sites in crystals with perovskite structure. Analysis of the optical absorption spectra revealed lines corresponding to Co^{3+} ions. No characteristic absorption bands of Co^{4+} were found. The optical bands of Co^{3+} ions were detected at 4.2 K (see inset in Fig. 2). The positions of these bands correspond to the spectrum of trivalent Co ions in the octahedral environment, which confirms the fact of occupation of *B* sites by 3*d* ions in $SrTiO_3$. Note that the optical spectrum of doped $SrTiO_3$ crystals also contains absorption bands of different intensities peaked at 430 and 520 nm (and, for some samples, a band peaked at 620 nm).

Samples of $SrTiO_3$: Mn contained 0.05–0.1 at % Mn ions with the background of Fe^{3+} ($C_{Fe} \sim 10^{-3}$ at %) and Cr^{3+} ($C_{Cr} \sim 10^{-4}$ at %) ions. The total concentration of other impurities did not exceed 10^{-2} at %. The method of valence shifts of X-ray lines showed the presence of Ti^{3+} ions in these samples [13, 14]. The absorption spectrum of $SrTiO_3$: Mn crystals contains characteristic bands of Mn^{3+} ions in octahedral sites [25]. In accordance with the ESR data, these samples contained Mn^{4+} and Mn^{2+} ions with relatively small and unequal concentrations. As in the case of Co-doped crystals, absorption bands peaked at 430 and 520 nm were also detected.

$SrTiO_3$: Fe : V crystals were grown under somewhat varied conditions. According to the ESR data, they contained from 8×10^{-2} to 10^{-1} at % Fe^{3+} ions and, according to the results of chemical analysis, 10^{-1} at % V ions. Note that anomalous ESR spectra and nonlinear optical properties were observed for these crystals at temperatures below 105 K [18–20]. $SrTiO_3$: Fe : V crystals contained Fe^{3+} ions in octahedral and tetrahedral sites [19].

$SrTiO_3$ samples doped with Fe ions differed from those containing iron as an associated impurity by the ratio of the intensities of ESR signals from Fe^{3+} ions with the tetragonal and cubic environmental symmetry. The parameter $x = Fe^{3+}_{tetra}/Fe^{3+}_{octo}$, introduced previously [19], contains information on the sample stoichiometry. The values of x for the crystals under investigation ranged from 0.001 to 0.22. The largest value, $x = 0.22$, was obtained for $SrTiO_3$: Fe : V samples. The smallest value, $x = 0.001$, was observed for nominally undoped samples after oxidation annealing. The increase in x indicates that the concentration of oxygen vacancies increases, which can be used to evaluate the sample stoichiometry.

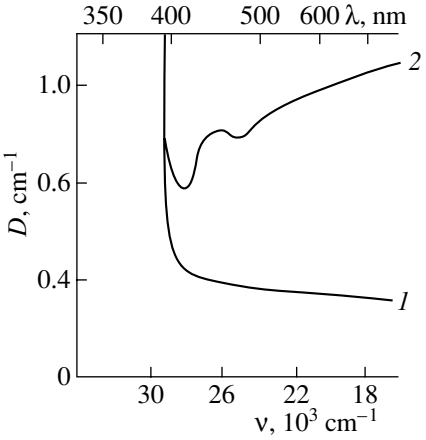

Fig. 1. Optical-absorption spectra of $SrTiO_3$ single crystals: (*1*) a reference sample and (*2*) a sample with violated stoichiometry [18].

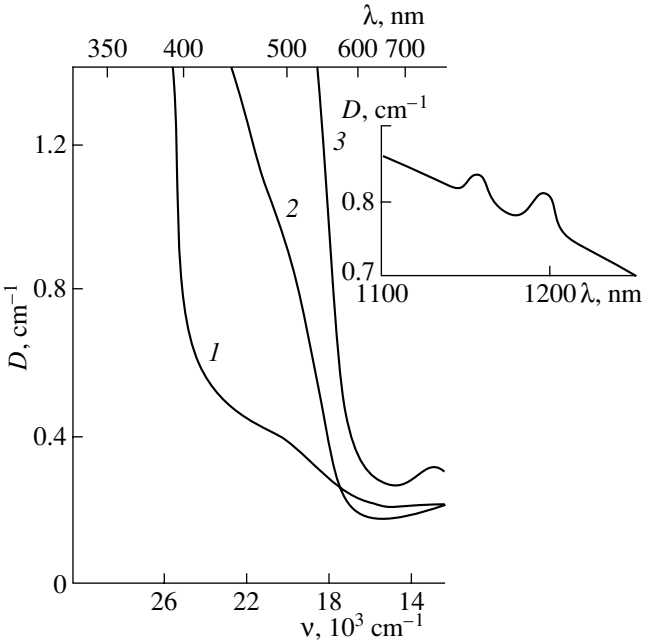

Fig. 2. Optical-absorption spectra of $SrTiO_3$: Co single crystals with the dopant concentration C_{Co} = (*1*) 1.2×10^{-3}, (*2*) 2.5×10^{-2}, and (*3*) 6×10^{-2} at %. The inset shows the spectrum of sample *3* at T = 4.2 K.

Rare earth ions in ABO_3 crystals generally occupy *A* positions and, most often, form the electronic states REI^{2+} and REI^{3+} (the state REI^{4+} is much more rare). In accordance with the data of [26], the ionic radii of ions in the state REI^{2+}, in particular, Sm^{2+} and Tm^{2+} ions, are fairly close to that of Sr^{2+}. The optical-absorption spectra of $SrTiO_3$: REI crystals are shown in Fig. 3. These spectra contain mainly strong bands peaked at 430 and 520 nm, which are observed for nominally undoped samples and for crystals doped with iron-group ions and are related to the violation of stoichiometry.

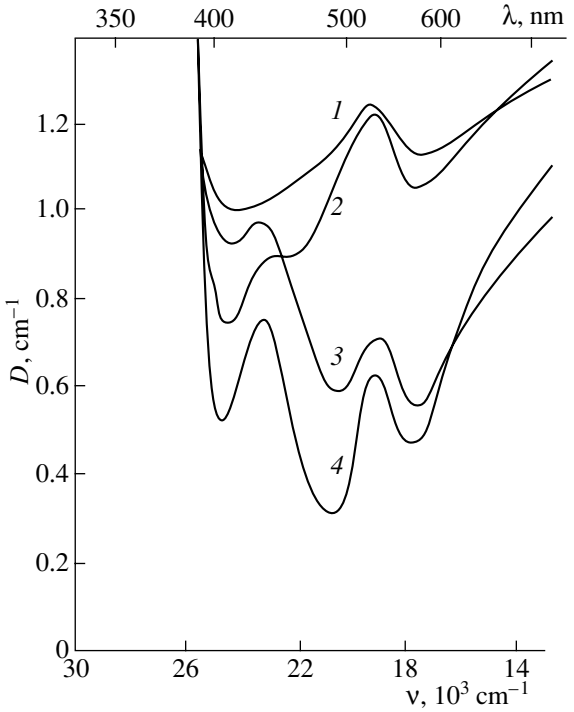

Fig. 3. Optical-absorption spectra of $SrTiO_3$ single crystals doped with (*1*) Sm, (*2*) Pr, (*3*) Nd, and (*4*) Tm.

The data on the parameters of undoped and doped crystals are summarized in the table. It is noteworthy that the REI-doped samples had high conductivity, which hindered their study by the ESR method.

TEMPERATURE DEPENDENCE OF THE DIELECTRIC PARAMETERS OF $SrTiO_3$ SINGLE CRYSTALS

The temperature dependences of the dielectric parameters $\varepsilon_0(T)$ and $\tan\delta(T)$ were measured in vacuum with a residual pressure of 10^{-5} Torr at a frequency of 1 MHz in the temperature range 10–300 K. We used an RLC meter Type HP4271B with a 75D bridge (Boonton Electronics Model). Samples were cooled to 10 K; the temperature and scan parameters were monitored by a 22c-Kriodin instrument (Lake Shore Cryotronics, Inc.). The relative error in determining the dielectric parameters was 1–5%; the error in determining T ranged from 0.2 to 0.5 K.

The dependences $\varepsilon_0(T)$ and $\tan\delta(T)$ were measured upon cooling and heating samples. Temperature was varied with a step of 0.1–1.0 K (depending on the temperature interval) from 300 to 10 K with subsequent heating from 10 to 300 K. The experimental technique is described in detail in [19]. The temperature dependence of the low-frequency permittivity of $SrTiO_3$ at temperatures far from T_C is described with good accuracy by formula (1). At the same time, it is well known that the dependence $\varepsilon_0(T)$ does not change in steplike manner at $T \longrightarrow T_C$. Some anomaly in the dependence $\varepsilon_0(T)$ is observed at temperatures below 50 K, which is quite consistent with the data obtained for $Sr_{1-x}Pb(Ba)_xTiO_3$ solid solutions [5, 6].

The temperature dependence $\varepsilon_0^{-1}(T)$ of the samples under study at a frequency of 1 MHz (Fig. 4) confirms the above considerations. The dependences $\varepsilon_0^{-1}(T)$ for an undoped crystal and for $SrTiO_3$: Mn (a similar dependence was also obtained for $SrTiO_3$: Co) have an inflection in the vicinity of the structural phase transition at T = 107–112 K (Fig. 4, curves *1*, *2*). Note that the values of T_C and C for the samples under study are somewhat different. For pure and Ni-doped samples, $T_C = 108 \pm 1$ and 111 ± 2 K, respectively. The constant C is minimum for pure samples in the tetragonal phase ($C = 0.99 \times 10^5$ K). The values of C are large for Mn- and Fe-doped $SrTiO_3$ crystals ($C = 3.3 \times 10^5$ and 3.56×10^5 K, respectively). Crystals in the high-temperature phase are also characterized by different values of C; the largest value is observed for $SrTiO_3$: V : Fe samples ($C = 4.56 \times 10^5$ K). For undoped and Mn-doped sam-

Main properties of $SrTiO_3$ single crystals

Crystal \ Properties	C_{imp}, at %	ε	Positions of the maxima of absorption bands, nm	C, 10^4 K	Sr/Ti, arb. units	$C_{Ti^{3+}}$, %
$SrTiO_3$ (reference)	10^{-5}	360	–	9.9	1.00	–
$SrTiO_3$ (nominally undoped)	10^{-3}	280	430, 520	15.0	0.98	5 ± 2
$SrTiO_3$ (blue-colored)	10^{-3}	120	430, 520	–	0.80	25 ± 6
$SrTiO_3$: Co	10^{-2}	220	430, 520	37.0	0.85	12 ± 5
$SrTiO_3$: Fe : V	10^{-2}	220	430, 520, 620	45.6	0.82	20 ± 6
$SrTiO_3$: Mn	10^{-2}	220	430, 520	33.0	0.86	15 ± 5
$SrTiO_3$: Sm	10^{-2}	200	430, 520, 620	41.0	0.82	20 ± 6
$SrTiO_3$: Nd	10^{-2}	200	430, 520, 620	40.0	0.80	18 ± 6
$SrTiO_3$: Tm	10^{-2}	200	430, 520, 620	43.0	0.86	15 ± 6

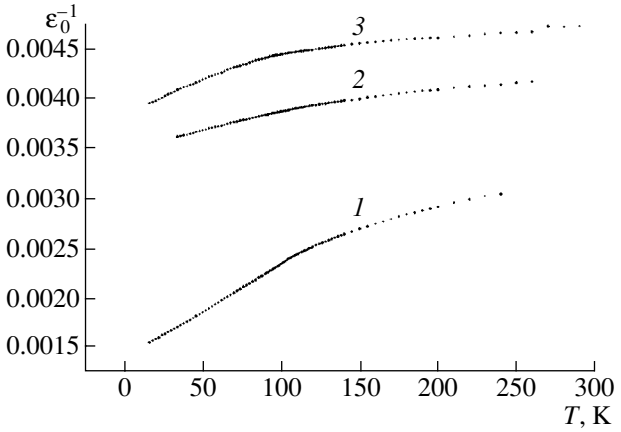

Fig. 4. Temperature dependences ε_0^{-1} for $SrTiO_3$ single crystals: (*1*) nominally undoped $SrTiO_3$, (*2*) $SrTiO_3$: Mn, and (*3*) $SrTiO_3$: Fe : V.

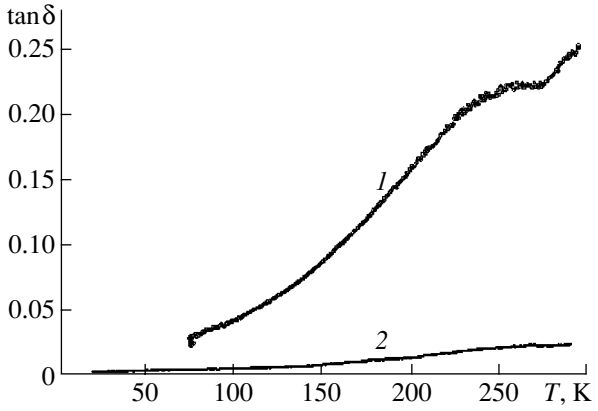

Fig. 5. Temperature dependence $\tan\delta$ for $SrTiO_3$: Fe : V samples (*1*) before and (*2*) after low-temperature treatment.

ples, $C = 1.33 \times 10^5$ and 3.49×10^5 K, respectively. The corresponding data for the constant C are listed in the table.

At the same time, it is obvious that a change in the behavior of the dependence $\varepsilon_0(T)$, which is related to the structural phase transition, is observed at $T_C = 109 \pm 3$ K for pure $SrTiO_3$ crystals and crystals doped with iron-group ions. This fact is in complete agreement with the data in the literature. The dependence $\varepsilon_0^{-1}(T)$ for $SrTiO_3$: Fe : V shows several inflection points at 190, 145, 90, 75, 60, and 35 K. The presence of inflections in this dependence is partially confirmed by the temperature dependence $\tan\delta(T)$ (Fig. 5). The change in the behavior of the dependence $\tan\delta(T)$ can be clearly seen at $T = 108 \pm 3$ K. At the same time, singular points can also be observed in Fig. 4 at 90 and 60 K.

For Mn-doped samples, the phase transition is somehow extended, without a pronounced inflection point. This point can be determined only by mathematical processing of the curve, which yields a somewhat higher value of the phase-transition temperature.

The introduction of iron-group ions, which generally have the electronic state Me^{3+}, may result in smoothing the function $\varepsilon_0(T)$ and the phase-transition parameters, as in the case of $SrTiO_3$: Co or $SrTiO_3$: Mn samples. However, in the samples grown under certain conditions, for example, in $SrTiO_3$: Fe : V crystals, anomaly of dielectric properties with kinks in the temperature dependence may exist. These kinks may be due to multiple microphase transitions. The exponential dependence $\varepsilon_0(T)$ at low T may be related to the ferroelectric phase transition in impurity crystals at $T \sim 10$ K. We should also note the anomalous dependence $\varepsilon_0(T)$ for $SrTiO_3$: Fe : V crystals in the paraelectric phase at a frequency of 800 Hz: with a decrease in temperature up to $T \longrightarrow 150$ K, the value of $\varepsilon_0(T)$ decreases, whereas, in accordance with the classical approach, $\varepsilon_0(T)$ should increase in this temperature range. In a repeated experiment, this anomaly vanished ($\varepsilon_0(T)$ increases at $T \longrightarrow 150$ K). After annealing in air at $T = 600$ K for ~3 h, the crystal undergoes a transition into the initial state. The anomaly of the temperature dependences $\varepsilon_0(T)$ and $\tan\delta(T)$ found by us is in complete agreement with the results of optical experiments [17–20].

As an example of temperature dependence $\varepsilon_0(T)$ for crystals doped with rare earth ions, Fig. 6 shows the corresponding curve for Tu-doped $SrTiO_3$, which corresponds to a large extent to the data for strontium titanate doped with iron-group ions. A similar dependence was obtained for $SrTiO_3$: Sm. Note that an anomalous dependence $\varepsilon_0(T)$ was observed for Pr- and Nd-doped $SrTiO_3$. This fact requires performing another (independent) check.

RESULTS AND DISCUSSION

One of the reasons for the inflections in the dependences $\varepsilon_0(T)$ and $\tan\delta(T)$ can be the mosaicity of crystals and the presence of blocks of different stoichiometric composition. This suggestion is confirmed by the aforementioned data on different concentrations of Fe^{3+} ions in tetrahedral sites, as well as the data on different concentrations of Ti^{3+} ions in the samples under study. The noted distinctions lead to the difference in the concentrations of oxygen vacancies and the unit-cell sizes.

Some microphase transitions responsible for the anomalous temperature behavior of the dielectric parameters may be caused by the reorientation of the dipole moments upon metastable ordering of defects of the strontium titanate structure, which was studied in [13, 17, 23]. This suggestion is confirmed by the disappearance of the anomalous dependence $\varepsilon_0(T)$ in the

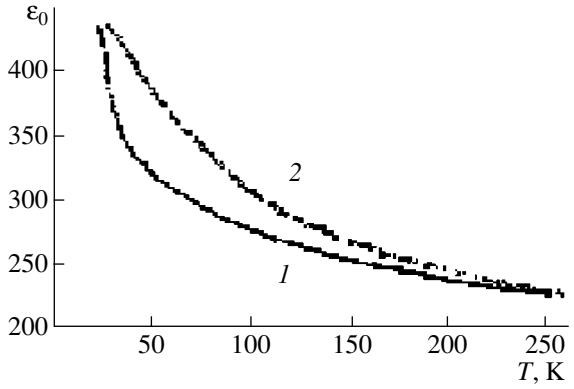

Fig. 6. Temperature dependences $\varepsilon_0(T)$ for $SrTiO_3$: Tm samples, obtained upon (*1*) heating and (*2*) cooling.

paraelectric phase at a frequency of 800 Hz, which occurs when the cycle of measurements is repeated [8]. We suggest that another reason for the existence of multiple microphase transitions or the extended phase transition is the local distortions of the structure. The presence of structural defects of the Ti^{3+} type, oxygen vacancies V_O^{2-}, complexes and clusters of the types Ti^{3+}–V_O^{2-} and Ti^{3+}–Ti^{3+}/Sr^{2+}–V_O^{2-} (clusters with Ti^{3+} ions in Sr^{2+} sites) leads to significant differences in the conditions under which the phase transition occurs.

The anomalous increase in the values of $\varepsilon_0(T)$ at $T <$ 100 K for $SrTiO_3$: Fe:V crystals may account for the existence of the ferroelectric phase transition at temperatures below 10 K and confirms the existence of an efficient mechanism of changing the dielectric characteristics of single crystals upon changing the crystal-growth conditions.

As was shown in [13, 14, 16, 17], a shortage of oxygen ions is observed in most $SrTiO_3$ crystals. The color of crystals with a shortage of oxygen varies from light yellow to dark blue, and, in all the samples studied, Ti^{3+} ions were detected, which give rise to the absorption bands at 430 and 520 nm. It is noteworthy that the samples of the high-temperature modification of rutile TiO_2, in which titanium ions can also be in the Ti^{4+} state, acquire a blue color under certain conditions. This phenomenon is related to the violation of stoichiometry of the samples. We studied colorless and blue-colored samples, whose optical-absorption spectra contained strong bands peaked at 500 and 660 nm with the ratios K(500 nm)/K(660 nm) equal to 0.8/0.95 [14].

CONCLUSIONS

Complex analysis of the results of studying the ESR, Raman, absorption, and luminescence spectra and the dielectric parameters of $SrTiO_3$ crystals allows us to conclude that, in the range of studied concentrations ($C < 10^{-1}$ at %) of iron-group ions, which occupy *B* sites (Ti^{4+}) in the lattice of the ABO_3 type, the anomalies observed are determined mainly by the formation of impurity defects and *d* subbands (Ti^{3+}) in the band gap of strontium titanate and are related to the corresponding changes in the electronic structure of the host rather than to the changes in the polarization properties of $SrTiO_3$. Apparently, the introduction of rare earth ions into *A* sites of $SrTiO_3$ (in our case, Sm and Tm ions) does not significantly affect the polarization properties of crystals, but, changing the conditions of crystallization, it leads to the violation of stoichiometry to a larger extent than in the case of the introduction of iron-group ions. Obviously, the violation of stoichiometry should result in significant changes in the polarization properties of strontium titanate.

ACKNOWLEDGMENTS

This study was supported in part by the Serbian Foundation (MNTC, grant no. 1996) and by the Ukraine Research Program (SB 171).

REFERENCES

1. G. A. Smolenskiĭ, V. A. Bokov, V. A. Isupov, N. N. Kraĭnik, R. E. Pasynkov, A. I. Sokolov, and N. K. Yushin, *The Physics of Ferroelectric Phenomena* (Nauka, Leningrad, 1985).
2. R. Blinc and B. Zeks, *Soft Modes in Ferroelectrics and Antiferroelectrics* (North-Holland, Amsterdam, 1974; Mir, Moscow, 1975).
3. N. A. Kulagin and D. T. Sviridov, *Introduction to Physics of Doped Crystals* (Vysshaya Shkola, Kharkov, 1990).
4. V. V. Lemanov, E. P. Smirnova, P. P. Syrnikov, and E. A. Tarakanov, Phys. Rev. B **54** (5), 3151 (1996).
5. B. B. Lemanov, Fiz. Tverd. Tela (St. Petersburg) **39** (3), 1645 (1997) [Phys. Solid State **39**, 1468 (1997)].
6. B. B. Lemanov, A. V. Sotnikov, E. P. Smirnova, *et al.*, Fiz. Tverd. Tela (St. Petersburg) **41** (4), 1091 (1999) [Phys. Solid State **41**, 994 (1999)].
7. V. V. Bogatko, V. I. Muromtsev, L. A. Litvinov, and Yu. N. Venevtsev, Izv. Akad. Nauk SSSR, Neorg. Mater. **17** (10), 2229 (1981).
8. Ya. Doĭchilovich and N. A. Kulagin, Fiz. Tverd. Tela (St. Petersburg) **38** (10), 2941 (1996) [Phys. Solid State **38**, 1109 (1996)].
9. N. Kulagin and J. Doicilovic, Physica B (Amsterdam) **269** (10), 1645 (1999).
10. N. Kulagin, J. Doicilovic, and D. Popovic, Cryogenics **41** (10), 745 (2001).
11. F. W. Little, J. Appl. Phys. **35** (7), 2212 (1964).
12. M. Fischer, A. Lahmar, M. Maglione, *et al.*, Phys. Rev. B **49** (18), 451 (1994).
13. N. A. Kulagin, Fiz. Tverd. Tela (Leningrad) **25**, 3392 (1983) [Sov. Phys. Solid State **25**, 1952 (1983)].
14. N. A. Kulagin and M. F. Ozerov, Fiz. Tverd. Tela (St. Petersburg) **35** (9), 2471 (1993) [Phys. Solid State **35**, 1225 (1993)].

15. M. Fischer, B. Bonello, J. Itie, *et al.*, Phys. Rev. B **43** (13), 8494 (1990).

16. A. F. Konstantinova, L. A. Korostel', and N. A. Kulagin, Kristallografiya **40** (4), 692 (1995) [Crystallogr. Rep. **40**, 640 (1995)].

17. A. F. Konstantinova, L. A. Korostel', and S. N. Sul'-yanov, Kristallografiya **43** (5), 903 (1998) [Crystallogr. Rep. **43**, 849 (1998)].

18. A. F. Konstantinova, A. N. Stepanov, L. A. Korostel', *et al.*, Kristallografiya **38** (6), 194 (1993) [Crystallogr. Rep. **38**, 813 (1993)].

19. N. A. Kulagin, V. A. Sandulenko, and L. A. Korostel, in *Abstracts of VIII International Meeting on Ferroelectricity, IMF8, Maryland* (1993), p. 428.

20. N. A. Kulagin, L. A. Korostel', V. A. Sandulenko, and A. F. Konstantinova, Izv. Ross. Akad. Nauk, Ser. Fiz. **58** (1), 21 (1994).

21. R. W. Faughan, Phys. Rev. B **4** (10), 3623 (1971).

22. Yu. I. Ukhanov, *Optical Properties of Semiconductors* (Nauka, Moscow, 1977).

23. K. A. Muller, J. Phys. (Paris) **42** (3), 551 (1981).

24. K. A. Muller, K. W. Blazey, and T. W. Kool, Solid State Commun. **85** (1), 381 (1993).

25. D. T. Sviridov, R. K. Sviridova, and Yu. F. Smirnov, *Optical Spectra of Transition-Metal Ions in Crystals* (Nauka, Moscow, 1976).

26. G. H. Dieke, *Spectra and Energy Levels of Rare Earth Ions in Crystals* (Wiley, New York, 1968).

Translated by Yu. Sin'kov

Crystallography Reports, Vol. 49, No. 3, 2004, pp. 476–499. Translated from Kristallografiya, Vol. 49, No. 3, 2004, pp. 541–565.

SURFACE. THIN FILMS

Atomic Force Microscopy Modified for Studying Electric Properties of Thin Films and Crystals. Review

K. L. Sorokina and A. L. Tolstikhina

Shubnikov Institute of Crystallography, Russian Academy of Sciences, Leninskiĭ pr. 59, Moscow, 119333 Russia

e-mail: sorokina@ns.crys.ras.ru

Received June 19, 2003

Abstract—Probe force microscopy continues growing in popularity as a method for studying surfaces of solids and control over crystals and thin films that are grown on various scientific and industrial setups. New modifications of the method increase the possibilities for recording various characteristics of the objects studied. An important role here is played by "electrical" force microscopy, the various modifications and practical applications of which are considered below, as well as the results obtained by this method. © *2004 MAIK "Nauka/Interperiodica".*

CONTENTS

INTRODUCTION

Since the construction of the first atomic force microscope [1], this new method of imaging surfaces has actively been used in various fields of research. The method itself is also rapidly developing and forms the basis for the development of a number of new scanning force techniques.

A microscope probe (elastic cantilever with a fine tip end), moving close to the sample surface, is under the action of various forces. Depending on the material of the probe (conducting or nonconducting, magnetic or nonmagnetic) and the tip–surface distance, these forces influence the probe motion to different extents. This fact is promising for point-to-point recording of the changes in the acting forces, with each of them containing some specific information on the properties of the object. The possibility of extracting the necessary information at each point of the object is provided by the unique system of probe motion with respect to a sample (a piezoelectric ceramic manipulator originally designed for a scanning tunneling microscope ensures the motion on a scale of thousandths of nanometer), the use of superminiaturized probes (100–400-μm-long cantilevers with about 3×30-μm-cross sections and 15–20-μm-long tips with an apex diameter of about several nanometers) and the system of optical detection of cantilever deflection (sensitivity of the laser interferometers is of the order of 10^{-5} nm $Hz^{-1/2}$).

1. FROM IMAGING SURFACES TO PRECISION MEASUREMENTS

The first similar images were obtained with the aid of "magnetic forces"—using a tip prepared from a magnetic material, Martin and Wickramasinghe [2] and Saénz *et al*. [3] managed to visualize the domain structure of surfaces [2, 3]. This gave an impetus to theoreticians for developing the theory of the new method [4–7]. Electrostatic forces also attracted the attention of researchers and, first and foremost, of experimenters [8–12]. This brings up the question whether it is possible to use various physical effects and measure locally defined parameters by scanning objects and, finally, obtain the distribution of thus measured physical quantities over the surface. Earlier, microscopists tried to extract information on surface relief from the data on the variation of a certain physical quantity along the surface (as in the first modification of a scanning capacitance microscope [13]). Now, it has become possible to measure a certain quantity and, at the same time, to study the surface topography. As a result, the precision methods for local determination of various physical parameters were developed on the basis of atomic force microscopy (AFM). These methods allowed one to compare the surface distributions of physical parameters with the observed morphological characteristics.

1063-7745/04/4903-0476$26.00 © 2004 MAIK "Nauka/Interperiodica"

Today, the "magnetic images" mentioned above are studied by magnetic force microscopy [14]. We concentrate our attention on the study of only electric characteristics. We would like to stipulate that the quantities measured can have different degrees of locality, in other words, they can relate to surface regions having different areas. As will be shown later, the "locality" of the electrostatic potential set at each point of the space is determined by certain basic methodological restrictions. The contributions to the capacitance, a characteristic of the whole probe–sample system, come from all the regions of the surface, but these contributions decrease approximately inversely proportionally to the distance of the region from the point of the probe location [15]. The information contained in the differential capacitance (the change in the capacitance with the change in the probe–surface distance) is even more local [16]. Therefore, the local capacitance of the sample (understood here as the capacitance measured when the probe is located at a given point) can closely characterize the surface region closest to the probe.

The knowledge of the surface electric-potential distribution is important for studying different objects—from semiconductors to biological samples. It is the potential value that is the bridge that allows one to relate various observable properties to the local composition and structure of the samples. The widespread method of measuring a local potential with the aid of an electron beam has a rather low spatial resolution (~100 nm) and a poor voltage resolution (hundreds of millivolts) [17]; moreover, the method is destructive. A nanometer resolution is attained by using potentiometry based on scanning tunneling microscopy [18, 19]. However, it is required that the tunneling current flow through the sample, which limits the objects that can be studied by this method only to conducting samples. The AFM modification that allows one to measure electrostatic potentials removes the limits associated with the sample resistance and allows one to study nonconducting samples, which is very important, in particular, for microcircuits with dielectric layers and conducting elements whose surfaces are often strongly oxidized.

In the AFM modifications oriented to studies of electric properties, scanning is usually performed in the noncontact mode (although there is also a dynamic contact modification of the method) with the use of conducting cantilevers and probe tips and a low voltage applied between the tip and the sample. This voltage can be applied to the sample if the tip is grounded or, vice versa, to the tip if the sample is grounded. These two configurations require the use of different schemes of the tip–bimorph separation but yield equivalent results [20]. In the vicinity of the sample surface, the tip is subjected to the action of various forces—electrostatic, van der Waals, and capillary forces (if the surface is coated with a mobile adsorption layer) and also to the counteracting elasticity force from the cantilever.

We do not consider here the particular situations of capillary forces associated with the presence of a liquid (the interactions in the presence of a liquid on a neutral surface are discussed in [21] and those on a charged surface in [22]). Van der Waals forces and electrostatic interactions are observed in all the cases. It is possible to state that a "visiting card" of any force should indicate not only its absolute value but also the dependence of this value on the distance between the objects. In the theoretical analysis of electrostatic interactions, the tip–surface system was first modeled by a sphere of radius R spaced by a distance d from a planar conducting surface (or even by a conventional plane-parallel capacitor) [8, 9, 11, 23]. The first model predicts that the attraction force will be proportional to R/d for distances $d \ll R$ and proportional to $(R/d)^2$ for larger distances. Taking into account the elongated shape of the tip represented as a cone of a length L with the rounded "apex" of a radius R (Fig. 1), we arrive at a weaker law of force decrease: at $L \gg d \gg R$, this decrease is proportional to $\ln(L/4d)$, which reflects the contribution of the macroscopic part of the tip to the tip–surface interaction [24]. At small distances $d \leq R$, the main interaction is that between the tip apex and the surface, and we arrive again at a dependence inversely proportional with respect to d [24, 25]. It should be emphasized that a similar theoretical consideration was first made for the tip interaction with the conducting surface of the sample [24, 26–28], and, only recently, the influence of the geometric parameters of the tip on the forces acting between the tip and the dielectric sample taken into account [25, 29]. Numerical computations by the generalized image-charge method and the analytical expressions obtained for the limiting cases allowed one to establish the differences. For conducting samples, the main part is played by the absolute value of the apex radius, whereas, for dielectric samples, the force is affected by the tip shape and the height of the tip apex above the surface but not by the tip size (in the limit, $d \longrightarrow 0$).

The allowance made for the electrostatic cantilever–sample interaction under the conditions of an AFM experiment shows that the contribution to the force is practically independent of the distance d [27, 30]. However, as the computations for the system "macroscopic cantilever–mesoscopic tip (truncated cone)–tip apex (of the nanometer dimension)" [30] show, it is this interaction that dominates at $d \geq 5$ nm. Therefore, the efficient sample area participating in the interaction considerably increases. To reduce the influence of the cantilever, one must thoroughly select the geometric parameters and use a nonconducting cantilever with a deposited narrow contact strip. It is much easier to suppress the cantilever contribution by measuring not the force but its gradients, because the latter are determined practically by the interaction with the tip apex alone [30].

The tip geometry also influences the van der Waals force, but to a lesser degree, so that under the conditions

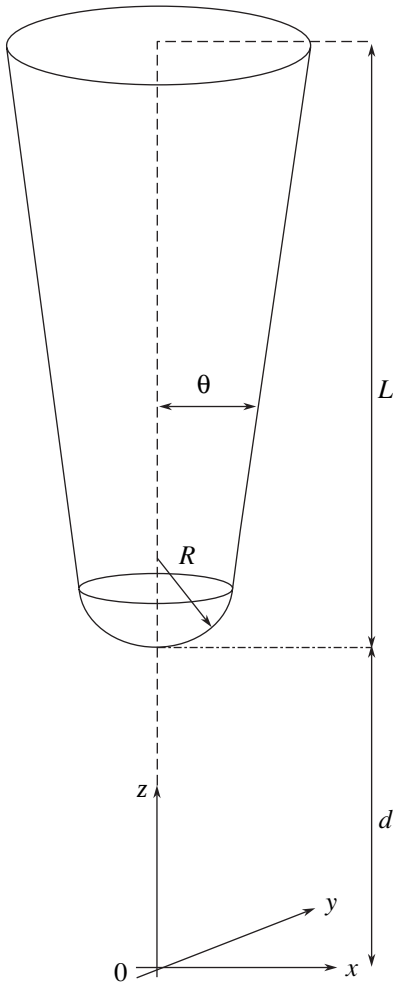

Fig. 1. Model of a cantilever tip and its geometric characteristics *R*, *L*, and θ used in calculations.

of the AFM experiment, the corrections are negligible [24]. At distances of an order of nanometers conventional for measurements of electric characteristics, the electrostatic attraction force exceeds the van der Waals force [8, 24]. This is clearly seen from measurements on graphite samples under various applied voltages, including the zero voltage [24]. Moreover, selective recording is also facilitated by the use of modulation methods. Nevertheless, because of the parallel topographic and electric measurements, the separation of the contributions due to these forces is still rather important [31–34]. Experimental data [24] also show that the interaction decreases with the distance from the surface rather slowly, in other words, the contribution of the macroscopic effects becomes rather important. A very important parameter in this case is tip-apex radius. The value of *R* directly affects the spatial resolution when studying electrostatic forces: as is shown in [35], at $d \ll R$, the spatial resolution is proportional to $\sqrt{dR}$. The methodological errors associated with the tip shape will be discussed somewhat later. Here, we consider the principle underlying the method.

2. THE PRINCIPLE UNDERLYING MEASUREMENTS OF ELECTRIC PARAMETERS

Electrostatic force can directly be determined after singling out its contribution to the cantilever deflection measured by an interferometer and with the use of the experimental dependence of the cantilever deflection on the tip height above the surface [36]. However, it is more efficient to determine the force gradient from a decrease in the amplitude of cantilever oscillations in the tapping mode with its approach to the surface, which is related to the resonance-frequency shift under the action of electrostatic forces [8].[1] It is this method that allows one to attain the atomic resolution [38, 39]. Another variant of force determination proceeds from the amplitude of cantilever oscillations under the applied periodic voltage between the cantilever and the sample [8]. If the applied-voltage frequency coincides with the resonance frequency of free oscillations of the cantilever, the amplitude is proportional to the electrostatic-force spectral component at the given frequency [40]. The formulas relating the amplitude of cantilever oscillations to the electrostatic force (or its gradient) and the system parameters for various types of probe and sample motion with respect to one another can be found in Chapter 11 [40]. In terms of capacitance, the most important of these parameters, the probe–sample system, is modeled by a flat capacitor or a sphere above the plane. The formulas are derived for the voltage applied between a conducting sample and a cantilever whose components are a constant bias and a harmonic component. A possible surface charge (if a sample is coated with a dielectric film) is also taken into account. The oscillations are considered not only at the resonance frequency but also at the frequency corresponding to the maximum steepness of the resonance curve. In principle, this allows one to determine the surface potential (the corresponding formula in [40] is given only in relative units), but the corresponding procedure is far from simple. It is not accidental that, although this possibility was considered in [8], no quantitative interpretation of the images in the potential units was made. Happily, as will be seen later, there exists a method for direct measuring the potential.

The general expression for the electrostatic force of interaction between the tip and the sample can be derived using the method of virtual work. One has to consider the work done by the given force at infinitesimal displacement δz of the tip along the *z* axis normal to the sample surface and, then, to differentiate the expression thus obtained with respect to this coordinate. If both sample and probe are connected to an external voltage source, the derivation should be performed at a constant potential. Then, the force *F* acting between the conducting probe and the sample is:

$$F = -1/2V^2\partial C/\partial z, \quad (1)$$

[1] The detailed consideration of dynamic noncontact AFM modes is made elsewhere [37].

where C is the capacitance of the probe–sample system and V is the potential difference between the probe and the sample, the contribution to which comes not only from the applied voltage V_{app} but also from the contact potential difference V_{CPD}, $V = V_{app} + V_{CPD}$.

It should be remembered that the latter difference arises when two solids with different work functions are brought into electrical contact. In turn, the work function is the work spent on the transfer of an electron from the Fermi level of a solid into a vacuum. In the case of a contact, some electrons pass from the body with the lower work function Φ_s into the body with the higher work function Φ_m. Then, the first body acquires a positive charge, whereas the second acquires a negative one, and a field hindering further transitions arises. The thermodynamic equilibrium is attained when the electrochemical potentials of both bodies become equal, i.e., when $eV_{CPD}^{sm} = \Phi_m - \Phi_s$. The attraction force between such bodies also exists without external voltage because of different potential energies at a vacuum level at both surfaces, $F = -\partial\Phi_{vac}/\partial z$. In other words, within an accuracy of the coefficient equal to the electron charge and with due correction for the origin, the work function is the measure of the surface potential sought.

The work function, being determined, to a large degree, by a double electric layer at the solid boundary, is very sensitive to the state of the surface. It depends not only on the material but also on the crystallographic orientation of the surface and is considerably changed in the presence of either an oxide layer or adsorbed atoms. The work function is sensitive even to the states of adsorbed atoms. Therefore, the work function varies from one portion of a clean polycrystal surface to another (the regions possessing constant work functions are called patches), so that, in the vicinity of the surface, a certain field of patches is formed. Thus, the real situation is rather complicated. However, one also encounters considerable difficulties when modeling even rather simple situations.

Band diagrams in Fig. 2 illustrate the formation of the contact potential difference between metal and semiconductor samples with the front surfaces located at different distances, whereas their back surfaces are electrically connected. It is clearly seen that the situations for these materials are quite different: because of a high metal conductivity, the whole charge may be considered concentrated at the surface. In semiconductors having considerably lower carrier concentrations, the charged region extends into the bulk. With a decrease in the distance between the front surfaces, the thickness of the charged layer increases, and an ever-increasing fraction of V_{CPD} would correspond to the region of the bulk charge, and an ever-decreasing fraction, to the vacuum gap (Fig. 2). The same is true for the distribution of the external voltage applied between the tip and the sample—at the given V_{app} value, the potential of the semiconductor surface depends on the sample–tip distance. Therefore, strictly speaking, Eq. (1) describing the force is valid only for conducting probes and samples. If a probe or a sample is a semiconductor (in studies of semiconductor materials or the use of silicon cantilevers), one must take into account the fact that the probe–sample capacitance stops being passive and starts depending on voltage. The problem becomes even more complicated if one takes into account the surface states, which can considerably influence band bending at the surface of a semiconductor.

This fact has not passed unnoticed. Electrostatic interactions with the participation of semiconductor objects were analyzed theoretically with the invocation of method of images. The corresponding electrostatic problems were considered for a point charge above a semiconductor surface [41] and also for the simplest model of two flat metal and semiconductor plates [42]. If the distance between the objects is on the order of the thickness of the bulk-charge layer, some specific features are observed. The force depends on the distance differently than in the case of two interacting conductors. It was established [42] that this effect manifests itself differently for different states of the subsurface region (in this region, depending on the voltage applied, either the enrichment, depletion, or inversion mode can be observed). At distances less than several depleted-layer thicknesses, the force depends on distance and voltage differently than in the case of two metal objects. The deviation from a quadratic increase in force with an applied voltage (characteristic of interaction of conductors) was also observed in [43]. The interaction force was calculated for the system "metal probe–*n*-type semiconductor (Si) coated with an oxide layer of the given thickness" also in the plane-parallel geometry. At the positive polarity of the applied constant voltage corresponding to an increase in the majority-carrier concentration close to the surface, the force remains proportional to V_{app}^2. At a considerable negative bias, the inflow of minority carriers results in the inversion of the conductivity type in the subsurface region and the $F(V_{app})$ dependence asymptotically tends to a parabola. However, at low negative values, $V_{app} \sim (-1)$–(-2), in the depletion mode, the force increases with an increase in bias more slowly because of the effect of the positive charge of impurity atoms that remained uncompensated after the pushing-away of majority carriers from the subsurface region. This tendency is the more pronounced the closer the probe to the surface and the lower the donor concentration. Therefore, for moderately doped semiconductors, the influence of the space charge should be taken into account. However, as shown in [42, 44], heavily doped Si cantilevers can be regarded as metal ones.

Nevertheless, in practical studies, the above effects have not been not taken into account as yet, and the calculations are still based on Eq. (1), even for semiconductor samples [45]. Only when studying dielectrics

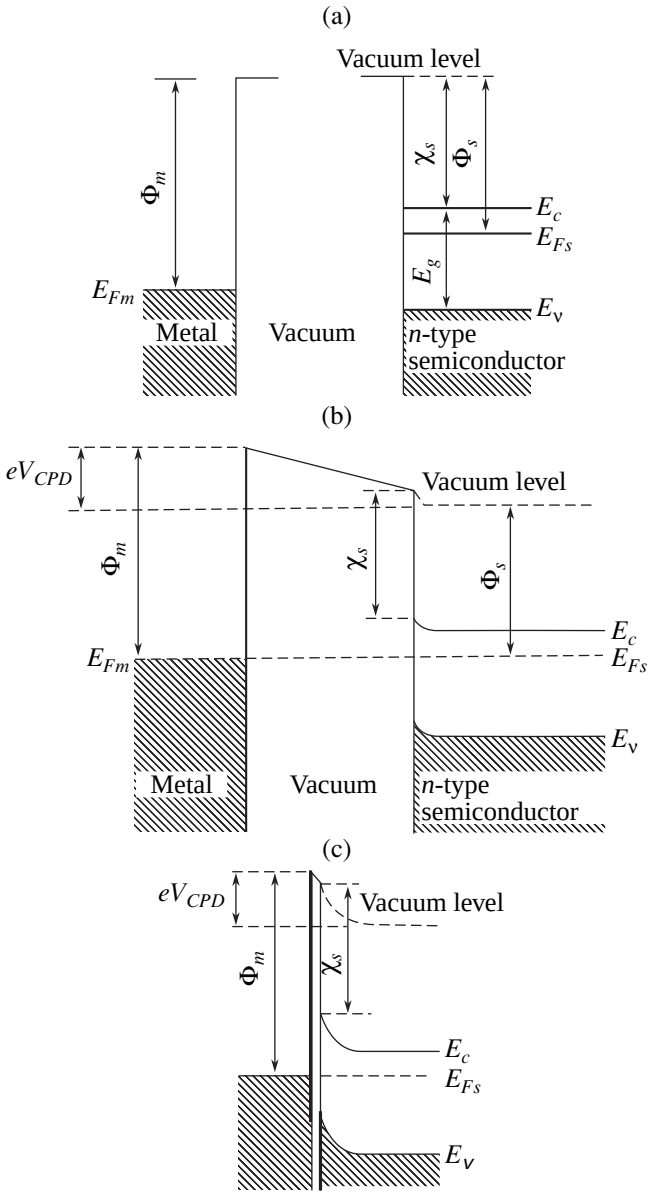

Fig. 2. Illustrating the formation of a contact potential difference V_{CPD} in the system metal–*n*-type semiconductor (the work function of the metal is higher than that of the semiconductor, $\Phi_m > \Phi_s$). Notation of band diagrams: E_{Fm} is the Fermi level in the metal, E_{Fs} is the Fermi level in the semiconductor, E_c is the conduction-band bottom, E_v is the valence-band top, E_g is the band gap, and χ_s is the electron affinity of the semiconductor. (a) No contact between the metal and semiconductor, (b) electric contact between the metal and semiconductor spaced by a considerable distance, and (c) the objects are almost in contact with one another.

does one usually take into account an additional electrical field induced by surface charges and introduce into the force the corresponding contribution expressed in terms of σ (surface charge density) [12, 33, 36, 45, 46]. An alternative approach is the use of the Born approximation of the perturbation theory for the allowance for the force in the case where the field is distorted by a surface charge [47]. In fact, in this case σ itself becomes the main object of the study. However, we return back to initial Eq. (1).

Modulating the applied voltage $V_{app} = V_{DC} + V_{AC}\sin\omega t$, one can represent force (1) as a sum of three components:

the constant force,

$$F_{DC} = -1/2\partial C/\partial z\{(V_{CPD} + V_{DC})^2 + 1/2V_{AC}^2\}, \quad (2)$$

the force varying with the fundamental frequency ω (the first harmonic),

$$F_\omega = -\partial C/\partial z(V_{CPD} + V_{DC})V_{AC}\sin\omega t = F_1\sin\omega t, \quad (3)$$

and one more harmonic force varying with a double frequency (the second harmonic),

$$F_{2\omega} = 1/4\partial C/\partial z V_{AC}^2\cos 2\omega t = F_2\cos 2\omega t. \quad (4)$$

It is seen that the last component depends only on the probe–sample capacitance $\partial C/\partial z$, whereas the force F_ω also contains the information on the contact potential difference. These quantities can be determined by measuring the oscillation characteristics of the cantilever under the action of these periodic forces. If the cantilever moves in the oscillation mode for the topographic measurements, then the third spectral component is observed at the frequency ω_r. In principle, the heterodyne interferometer allows one to record the cantilever deflections at several frequencies simultaneously [20] if the frequencies of the corresponding signals are sufficiently separated, as in Fig. 3. Figure 3 shows the frequency spectrum of cantilever oscillations [48]: similar to the tapping mode in AFM, the signal at the free-motion resonance frequency ω is used to perform the topography measurements, whereas the frequency ω of the modulating electric signal is selected in such a way that both this frequency and the second harmonic are outside the resonance frequency band. Strictly speaking, because of the nonlinear nature of the cantilever–surface interaction, the free oscillations of the cantilever are anharmonic [49, 50], whereas the contribution of higher harmonics is negligible [51] and, in this case, can be ignored. The block-diagram of a modern multifunctional-type setup [48], which enables one to use the possibilities of the so-called electrostatic force microscopy, is shown in Fig. 4. However, researchers often use more specialized apparatus for measuring a potential or a capacitance. In the first case, it is scanning Kelvin probe microscopy; in the second scanning capacitance microscopy. After making some preliminary remarks, we consider the characteristics of both methods.

Since the methods discussed are rather new, both the terminology and the technical characteristics of the setups used are somewhat inconsistent. Thus, the parameters of the oscillating probe systems can considerably differ. As a rule, the cantilevers used are rather rigid and have the spring constant *k* ranging from several new-

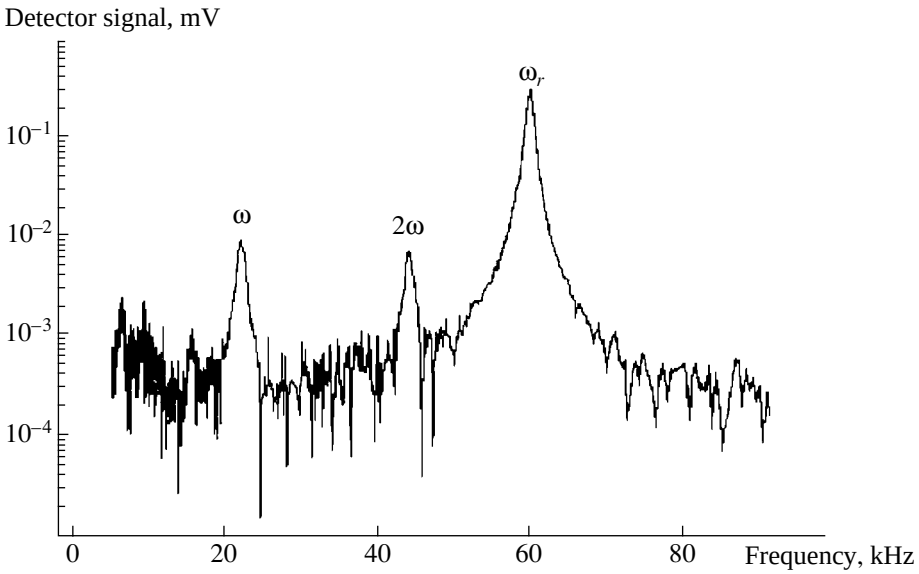

Fig. 3. Cantilever frequency spectrum with a resonance frequency of 60 kHz measured with the aid of a lock-in amplifier at a constant bias voltage of 0.5 V and a.c. frequency of 21 kHz (in the absence of feedback compensating the contact potential difference) [48].

tons to several tens of newtons per meter (most often, 20–30 N/m) and are prepared from heavily doped silicon or, sometimes, also from Si_3N_4 (with a conducting coating) or tungsten. For attaining a higher conductivity, silicon cantilevers may be coated with Au, Co, Cr, or PtIr layers. Unfortunately, these layers are rapidly worn out in air [52]; pure silicon is rapidly oxidized. Comparing the stability of potential images obtained with the aid of silicon cantilevers coated and not coated with a metal favors uncoated cantilevers [53]. It seems that it is better to increase the cantilever conductivity by depositing onto it (chemical vapor deposition) boron-doped thin diamond films. Such coatings may also be used for measuring currents in the contact mode [54]. Similar cantilevers were also used in studies by scanning Kelvin microscopy [55]. The apex radius R usually lies within 5–40 nm, whereas the conventional oscillation amplitude lies within 10–20 nm. The requirements for tips set by the problems of "electric" AFM and the comparative analysis of the tip quality, including the quality of diamond tips, can be found in [56]. The Q values of cantilevers as oscillating systems do not exceed 100–200 in air, but, in vacuum, they increase up to 1000–2000 [57] and even higher (in [31], the Q factor attains a value of 38 000). A better design could have increased the Q values further, but it is not justified because of narrowing of the bandwidth of the system and an increase in the response time [58]. The free-motion resonance frequencies f_0 of the cantilevers range from tens to hundreds of kilohertz. Proceeding from various considerations, the frequency ω of the modulating voltage can be chosen to be the first and the second resonance frequencies or a lower frequency (2–3 kHz or even 300 Hz). The amplitude of a.c. voltage V_{AC} usually varies from tenths of a volt up to several volts.

Thus, the optimum parameters of the system have not been established as yet, so that all the experimenters continue indicating the technical data of their experiments. As to the spatial resolution, some authors indicate the atomic resolution for GaAs(110) [31], Ag/Si(111) [38, 59], Au/Si(111) [39], and Sb/Si(111) [60].

3. SCANNING KELVIN PROBE MICROSCOPY

Scanning Kelvin Probe Force Microscopy, abbreviated in the literature as KPM, SKPM, KPFM, KFM, and SKFM, inherited its name from the method of measuring a contact potential difference suggested by Lord Kelvin as far back as 1898. In this method (also called the method of dynamic capacitor), two samples form a flat capacitor. The electrically connected plates oscillate relative to one another, and the potential difference between the plates is measured. If the plates are not charged, the voltage equals zero and remains zero during plate oscillations. But if the plates have different work functions, a charge arises and the capacitance varying with the distance gives rise to the corresponding change in the voltage. In series switching into the circuit of a d.c. source, one may select its voltage V_{app} in such a way that it is equal to V_{CPD} but has the opposite sign. Then, the charges at the plates become fully compensated, and the oscillations of the voltage measured at the vibrating plates cease, which indicates that, now, $V_{app} = V_{CPD}$. Thus, determining V_{CPD} in such a way and knowing the work function of one of the plates (test plate), one can determine the work function of the sec-

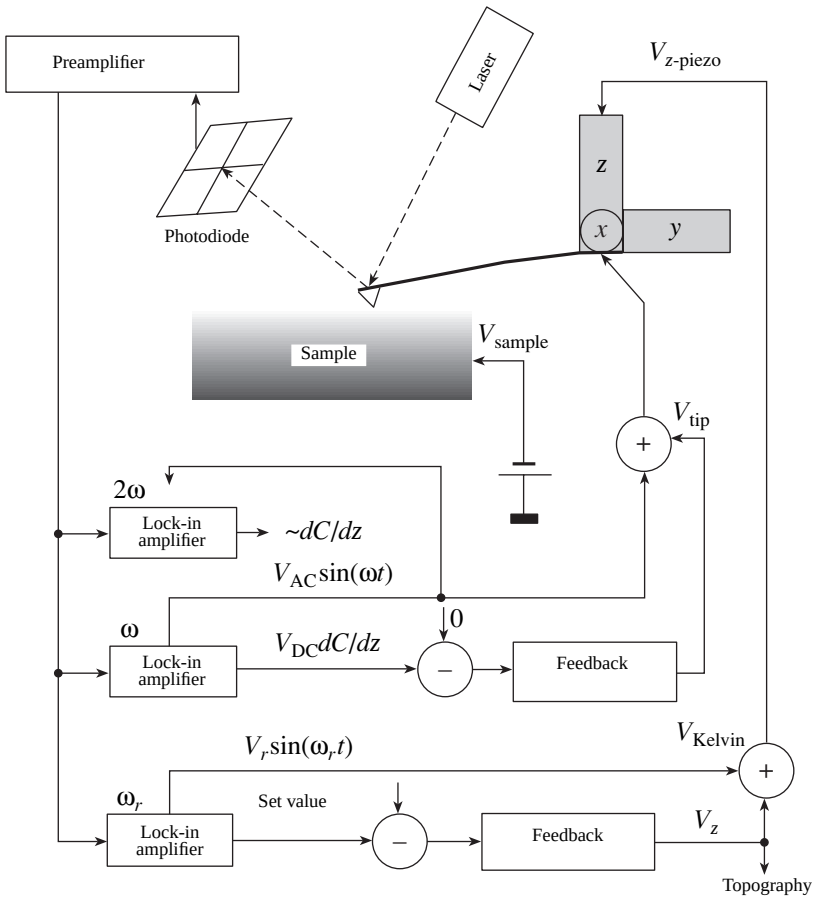

Fig. 4. Schematic of the experimental setup of a scanning electrostatic force microscope based on a noncontact atomic force microscope with a laser deflection system [48].

ond plate. Of course, the value thus obtained is averaged over the whole surface (as in the traditional method of determining the work function—the diode or thermionic method). All attempts to create a microprobe based on the Kelvin method gave a spatial resolution much lower than 1 μm because of the problems associated with measuring the current and existence of a stray capacitance [61]. Nevertheless, efforts in this direction are being continued—attempts are being made to combine the Kelvin method with other techniques, such as measurements of surface photovoltage and deep-level transient spectroscopy (DLTS) [62, 63]. The accuracy of the determination of the work function with a microprobe attains a value of 0.1 mV, but the spatial resolution does not exceed fractions of a millimeter. A high spatial resolution can be attained using photoelectron emission spectroscopy, but the latter is less sensitive to the work function [64]. And only the use of the basic system of an atomic force microscope allows one to obtain high resolution with respect to both geometric and potentiometric parameters.

Figure 5 illustrates the "compensation idea" for a probe–sample system [65]. Here, mechanical excitation is changed to electric excitation—applying an alternating voltage $V_{AC}\sin\omega t$, one records the signal excited by mechanical oscillations of the cantilever under the action of an electric force. As is seen from Eq. (3), the selection of the constant voltage component in such a way that $V_{DC} = -V_{CPD}$, results in a zero value of F_ω and, therefore, the absence of a signal at the frequency of the first harmonic.

A similar scheme for measuring potentials in AFM was first used by Weaver and Abraham [66]. Thus, it became possible to visualize the voltage drop at the microcircuit (amplifier) resistor with a spatial resolution of ~50 nm. Weaver and Abraham called their method atomic force potentiometry [66]. Then, Nonnenmacher *et al.* [67] coined the term Kelvin Probe Force Microscopy. They directly measured the local work function for deposited Au, Pt, and Pd films with an accuracy of about 0.1 mV. In both the above works, it is emphasized that it is possible to perform simultaneous "potential" and topographic imaging. The electric signal was applied at the resonance frequency of the cantilever, and the topographic images were obtained at a somewhat higher frequency.

In modern Kelvin probe microscopes, the topographic images are recorded at frequencies close to res-

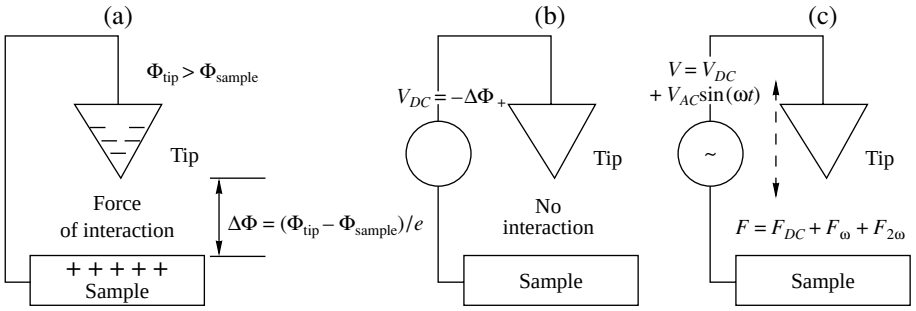

Fig. 5. Illustrating the compensation principle in Kelvin microscopy [65]. (a) Because of a contact potential difference between the tip and the sample, the electrostatic interaction takes place without application of any voltage (for definiteness, it is assumed that the tip work function φ_{tip} exceeds the sample work function φ_{sample}); (b) an appropriately chosen applied constant voltage decreases the interaction force to zero; (c) the application of an alternating voltage gives rise to tip oscillations.

onance and the voltage is modulated at the frequency of the first or second resonance or at a considerably lower frequency. During the first pass along the given scan line, the profile is recorded in the tapping mode (the cantilever oscillations are excited close to the surface by a bimorph). In this case, the feedback in the control system of vertical motion maintains a constant amplitude of cantilever oscillations (amplitude modulation) or a constant shift of its resonance frequency (frequency modulation). Thus, one determines points equidistant from the surface (the force gradients at these points are the same) [58]. Then, the feedback is switched off, the mechanical excitation of oscillations is ceased, and the cantilever rises from the sample to a distance from several to several tens of nanometers (the so-called lift-mode) and second scanning is performed at a constant distance (the tip goes along the trajectory, repeating the profile recorded earlier) but under an applied voltage $V_{DC} + V_{AC}\sin\omega t$. The new feedback establishes the bias V_{DC} in such a way that there is no signal at the frequency ω. The details of the optimum feedback tuning can be found in [53]. The corresponding V_{DC} values after the sign reversal are the V_{CPD} values at each point of the line (it should be indicated that, in a number of studies, another sign convention is used).

The minimum potential thus measured depends on the level at which the alternating-voltage-induced oscillations can be separated. It seems that the thermal and optical noise should contribute to the error of the measured amplitude of cantilever oscillations. In this case, the optical noise is negligible [23], and, therefore, the minimum potential is recorded when the amplitude of induced cantilever oscillations attains a value on the order of random thermal fluctuations [67]

$$V_{\min} = \sqrt{(2k_B TkB/\pi^3 Q f_0)}d/(\varepsilon_0 V_{AC} R), \qquad (5)$$

where k_B is the Boltzmann constant, T is the temperature, ε_0 is the dielectric constant in vacuum, and B is the bandwidth. At the parameter values used in [68], the resolution attains a value of 0.1 mV, i.e., is at the level of earlier studies [67]. However, it seems that it can be improved by two orders of magnitude by performing measurements in a sufficiently high vacuum at low temperatures.

In practice, not only the instrumental errors influence the potential, but also some additional factors associated with the physics of the phenomenon. It turns out that the recorded potential φ_{meas} depends on such factors as the tip used, the height of the tip location above the surface, and the amplitude of the applied alternating voltage, and the recorded changes may exceed the expected error. Then, the question arises why such a situation is possible, how reliable the results obtained are, and whether they may be compared with one another and with the data obtained by other independent methods.

The simplest factor is the effect of a tip, because one measures a contact potential difference that strongly depends on the tip state and the presence there of defects, oxide layers, contaminations, etc. Thus, in [69], after the change of the tip, the measured surface potential of a silicon sample changed by 30–50% (in some cases, even by 100%) (Fig. 6). Therefore, the reproducible results can be obtained only in high vacuum in order to avoid, at least, adsorption from air. Such ultra-high vacuum setups (with the residual pressure $\leq 10^{-10}$ mbar) have already been constructed [59, 70], but, in fact, most studies are still performed in air or, at best, in an atmosphere of dehydrated gas. However, even high-vacuum experiments cannot guarantee tip homogeneity: it is most probable that the tip surface consists of patches—regions having different work functions (because of steps, nonuniform coating, etc.). Burnham *et al.* [71] believe that it is the patches on the tip and sample that are responsible for the long-range component of the interaction force acting between the tip and sample in the case of no applied voltage.

The fields of the sample patches always existing above the inhomogeneous (with respect to the work function) surface play an important role in method accuracy. The mechanism of contrast formation in SKPM and the method resolution were analyzed theo-

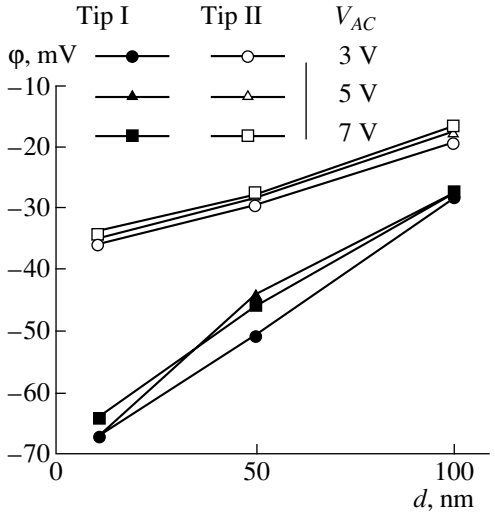

Fig. 6. Measured surface potential of φ Si(100) surface for two different tips as a function of the scanning parameter (the height *d* of the tip location above the surface) at three different alternating-voltage amplitudes [69].

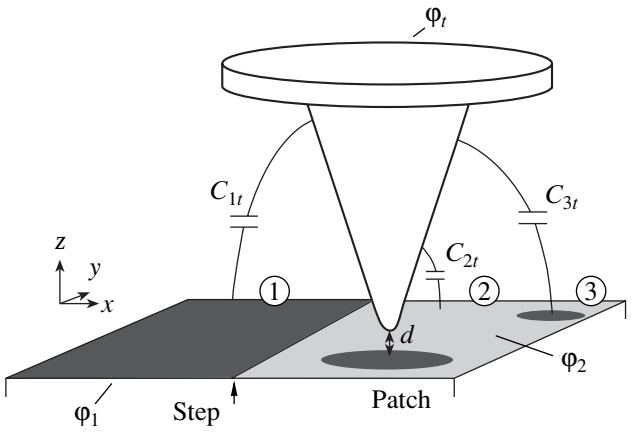

Fig. 7. Model of a surface consisting of ideal conductors with different potentials, which interact with the tip via the mutual capacitance C_{ij} [72].

retically on a sample consisting of a set of *n* ideal conductors with different constant potentials φ_i [72]. The energy of electrostatic interaction in the tip–surface system was calculated with due regard for the capacitance coupling between the tip and various patches (shown in Fig. 7 by capacitance C_{it}) and the capacitance coupling between the patches themselves, C_{ij}; then, the force acting on the tip was determined. Under the conditions of SKPM, the potential φ_{DC} equals not the exact value of φ_i for the patch located directly under the tip—it equals the weighted value averaged over the surface, where the role of the coefficients is played by the $\partial C_{it}/\partial z$ derivatives:

$$\varphi_{DC} = \left(\sum_{i=1}^{n} \partial C_{it}/\partial z \varphi_i\right) \Big/ \left(\sum_{i=1}^{n} \partial C_{it}/\partial z\right). \qquad (6)$$

In the limit of infinitely small regions, Eq. (6) is transformed into a two-dimensional convolution of the real potential with a certain transfer function. Comparing the results of the numerical simulation of two typical situations—the potential distributions in the form of a patch and a step—with the experimental data obtained on specially prepared test structures showed good agreement between the calculated and experimental data. It is important for the method efficiency that both real and simulated measurements in the vicinity of the boundary characterized by a dramatic change of the potential give a smoothened pattern with a continuously varying φ in the transient region. The calculations performed for different tip geometries showed that this smoothening is feebly marked for thin long tips with a blunt apex (high *R* values). It is this configuration that ensures the prevalence of the local electrostatic interaction over the nonlocal interaction, so that the information thus obtained relates mainly to the surface region lying directly under the tip.

Capacitance in Eq. (6) depends on the tip shape (of course, with a certain scatter for different tips) and the height of its location above the surface. Therefore, the variations in the measured potential φ_{meas} caused by the tip change and its locations at different heights above the surface observed in the studies of inhomogeneous samples with the traces of wear in air [69] can be associated with the methodical limitations considered above. The influence of the tip height on the resolution was studied experimentally (on the *p*–*n*-junction in GaP and the steps on GaAs and HOPG samples in high vacuum) and theoretically (a tip was modeled by a "staircase" of flat capacitors switched in parallel, with the semiconductor effect being ignored). The "diffusion" of the work function in the region of its dramatic change and its decrease observed during measurements become more pronounced with an increase of the height, which can be satisfactorily described within the framework of the approximate model considered above. (The possibility of working at smaller heights can also increase the resolution in high-vacuum setups [73].) It should be emphasized that, as earlier, the key role in the above calculations is played by surface inhomogeneity with respect to the work function.

However, the potential measured in high vacuum at heights less than 50 nm on a test atomically smooth HOPG sample also varied [44]. This effect was different for different cantilevers. Thus, for new cantilevers, the effect was on the order of several millivolts, but it dramatically increased up to hundreds of millivolts after the tip contact with the sample. It seems that, here, the key part is played by the tip state—with a decrease of the distance, the tip apex starts playing the most important role and its metal coating gradually wears out. In any case, the assumption that the measured potential depends on the distance because of the incomplete compensation of V_{CPD} [74] is not confirmed here. (Since the amplitude of the recorded signal can be

reduced to zero only within the experimental error, then, in virtue of Eq. (3), the φ_{meas} value depends on the quantity reciprocal to $\partial C/\partial z$.) In [74], the $\partial C(z)/\partial z$ dependence was calculated theoretically by summing up the contributions that come to the capacitance from the individual parts of a tip of the given shape which lie at different distances from the surface. The plot of the reciprocal quantity repeats the shape of the $\varphi_{meas}(z)$ curve. On the contrary, a $\partial C(z)/\partial z$ dependence for HOPG samples at the same heights as φ_{meas} was recorded experimentally [44] in accordance with Eq. (4). It turned out that this curve cannot be used to explain the experimental changes in φ_{meas}. Sommerhalter *et al.* [44] believe that, using the appropriately selected feedback parameters, it is possible to reduce the deflection caused by the incomplete compensation of V_{CPD} to the noise level of the system. Nevertheless, Efimov and Cohen [55] suggested a special algorithm for improving the potential image by separating from it the component associated with "undercompensation" of V_{CPD} for tips having certain geometries. Gil *et al.* [30] explain the sensitivity of the SKPM method to the height of the tip location by the contribution of the interaction of all the parts of the cantilever–tip system. As a result, one measures, in fact, the weighted potential value (similar to Eq. (6)). However, as was indicated above, this interpretation of the $\varphi_{meas}(d)$ dependence is valid only for inhomogeneous surfaces.

The effect of V_{AC} on the measured φ_{meas} value (less pronounced in Fig. 6 than the influence of the height variation or tip change) is of a pure semiconductor nature. Leng *et al.* [75] observed the changes in φ_{meas} up to 1 V in air with an increase in V_{AC} from 1 to 7 V for a disordered GaInP sample and indicated that no such dependence is observed for clean metal samples and tips. Neither was it observed for HOPG samples [44]. However, the dependence was quite pronounced for a *p*-WSe_2 sample [44]. As was to be expected, the dependence was more pronounced at smaller tip–surface distances because, at such distances, the electric field penetrates more deeply into a semiconductor and the band bending becomes more pronounced (Fig. 2). The $\varphi_{meas}(V_{AC})$ dependence is caused by different charging of the surface in the sequence of half-periods of positive and negative polarities (in the depleted state, the potential varies much more pronouncedly than in the enriched state). It should be noted that the nonsymmetric tip–semiconductor surface interaction with the change of the voltage polarity was predicted theoretically as far back as 1992 [43] for all the three force components, F_{DC}, F_ω, and $F_{2\omega}$. The necessity of taking this into account was also indicated in [76].

Therefore, to reduce the influence of V_{AC} on the measured potential, one has to study semiconductor materials at the minimum V_{AC} values (on the order of 100 mV). However, it is seen from Eqs. (3) and (5) that, to increase the method sensitivity, one has to increase the V_{AC} value at least by an order of magnitude, i.e., to increase it up to several volts (this would increase the amplitude of oscillations induced by the force F_ω). These requirements set to V_{AC} become contradictory for the scheme of amplitude modulation described above, in which the complete compensation of the contact potential difference V_{CPD} (attained by the application of the voltage V_{DC}) can be seen from the zero oscillation amplitude at the frequency ω (force measurement [57, 66, 70]). It is expedient to use the second resonance frequency of the cantilever as an alternating-voltage frequency [57]. This allows one to attain a resolution of 5 mV at the small amplitude V_{AC} [44]. The alternative is the use of the frequency-modulation method (force-gradient measurement): the signal circuit should also have a frequency demodulator to control the variation of the oscillation frequency caused by the electrostatic interaction (the frequency shift oscillates with the frequency of the alternating voltage [38, 59]). In this case, the bias equal to the contact potential difference is determined from the absence of frequency oscillations. However, it turned out that, to attain an energy resolution similar to that in the method of the amplitude modulation, one has to use higher V_{AC} values ($\geq$2 V) [44]. On the other hand, the spatial resolution at the frequency modulation is higher (as was indicated above, in terms of the force gradient, the main part in the interaction is played by the tip apex). In the determination of the force, which is less dependent on the distance than its gradient, an important role is played by the averaging effect of the tip and cantilever. The latter effect increases the region around the probe that participates in the interaction. At the same time, at the amplitude modulation, the dependence of the potential measured for inhomogeneous surface on the tip height above the surface is weaker [77]. The influence of the tip geometry on the spatial resolution of SKPM has been studied experimentally [77] and it was shown that, in accordance with the prediction made in [72], the highest resolution is observed for long tips.

The accuracy of the determination of the surface potential can be increased by invoking some additional information on the signal phase [78]. Analysis shows that, unless the absolute V_{DC} value is lower than the contact potential difference, the phase of the component of the electrostatic force at the frequency ω is shifted by $\pm 180°$ with respect to the applied alternating signal. If $|V_{DC}|$ exceeds $|V_{CPD}|$, this phase difference goes to zero, i.e., at $V_{DC} = -V_{CPD}$, the signal phase dramatically changes, which can readily be detected experimentally. In turn, this allows one to fix the moment of the complete compensation of the contact potential difference.

New possibilities for studying semiconductors are provided by the use of near-field optical waveguides with metal coatings as cantilevers. This allows one to illuminate the sample locally and, thus, to complement the Kelvin microscopy with photovoltage measure-

ments (surface photovoltage method, SPV) [79]. Photon absorption gives rise to the formation of electron–hole pairs that are separated in the field of the volume charge in the vicinity of the surface (appearance of photovoltage). In the subsurface region, the carrier concentration increases and band bending (surface potential) is changed. If the incident light is sufficiently intense, flat bands may arise (the photovoltage attains the saturation that allows one to determine the potential barrier height). Varying the wavelength of the monochromatic radiation, it is possible to initiate transitions of electrons from various initial states (from the valence band or the levels in the forbidden band). Then, the change in the work function allows one to obtain information on the distribution of the surface states, recombination centers, etc. Experiments show [79] that new cantilevers ensure potential measurements with an accuracy not less than the accuracy attained by the traditional methods and allow one to record the changes of the potential under illumination. An interesting technical solution for SKPM is suggested in [80]—to use the carbon nanotubes as probes, which should increase the spatial resolution of the method.

Finally, let us answer the question whether it is possible to use SKPM for extracting the absolute quantitative information on the work function. Brushan and Goldade [69], who work in an air atmosphere, have a rather pessimistic opinion. They believe that one can obtain only the qualitative information about the potential variation along the surface. The measurements performed in the N_2 atmosphere [78] are quite consistent with the known data. It is recommended to anneal both samples and tips prior to measurements in order to remove the adsorbed layers, in particular, water [81]. It was shown [70] that, under the conditions of high vacuum, the absolute measurements are rather reliable if each concrete cantilever is preliminarily calibrated against the test surface with the known work function.

The number of problems solved by SKPM is rather large. For crystals, the method allows one to reveal and characterize even feebly marked inhomogeneities. The first SKPM studies allowed one to visualize Pd microparticles on a gold substrate, grains of polycrystalline gold, and their grain boundaries, and observe the changes in the dipole layer at the steps of an as-cleaved HOPG sample [67, 82]. Considering the cross section of a GaInP film on the GaAs substrate, Leng *et al.* [75] managed to distinguish atomically ordered and disordered (with respect to alternation of Ga and In atoms in the (111) planes) submicron regions. Kitamura and Iwatsuki [59], performing experiments under high vacuum, attained the atomic resolution and identified the phases with the 5×2 and 7×7 surface structures in the Au/Si(111) system (the work function for the former regions was higher by 0.5 eV than for the latter ones) with dimensions of tens of nanometers. Sputtering Ag onto the *n*-Si(111) 7×7 surface, Kitamura *et al.* [38] and Kitamura and Iwasaki [59] managed to separate polycrystalline Ag clusters and hexagonal Ag(111) islands (the difference in their work functions attained 20 meV; the contrast against the silicon background attained 10 meV). Kitamura *et al.* [39] studied in detail the Au clusters on the *n*- and *p*-types Si(111) 7×7 surfaces and revealed no differences in the image contrast. Therefore, they suggested that, at an atomic resolution, the contrast is determined mainly by the surface electron density, whereas the calculation of the "true" work function requires the use of the average potential difference between the cluster and substrate. However, Kitamura *et al.* [39] consider the notion of the true work function in association with the position of the Fermi level in the crystal bulk, whereas, on the surface of a semiconductor, the bands are often bent because of the surface states. Close values of the surface potential for the *p*- and *n*-type GaAlSbAs samples were also observed in [83] and were explained by the presence of charged traps on the surface. The shift of the Fermi level with respect to the bulk (different for different sample thicknesses) was clearly observed on InAs(110) by the SKPM method [81]. A jump of the Fermi level in the vicinity of steps on as-cleaved *n*- and *p*-type GaAs(110) surfaces observed in [70] was attributed to the action of the localized states of atoms with a distorted coordination. The work function of the monolayer of TiO_2 islands of nanometer sizes also increases with respect to the work function of the remaining atomically smooth TiO_2(110) surface, but, in this case, continuously—it attains the maximum in the island centers [84]. This was explained by the dipole-type polarization in the vicinity of the island boundaries. Sommerhalter *et al.* [70] indicate that SKPM may also be used to detect impurity centers and determine the sign of their charges (they considered the *p*-type WSe_2(0001) surface cleaved in vacuum). Measurements at an atomic resolution allowed one to identify single species, i.e., to separate the Si and Sb atoms (the surface potential of the latter atoms was higher by 0.2 eV) on the Si(111) $5\sqrt{3} \times 5\sqrt{3}$-Sb (it should be remembered that the topographic image at an atomic resolution fails to distinguish between these atoms) [60]. However, the above value is not consistent with the difference between the work functions of bulk samples or with the difference in the ionization energy of the isolated atoms. Thus, the interpretation of the results obtained requires the detailed theoretical analysis of the energy band of the atoms adsorbed on concrete surfaces. Without such an analysis, it is impossible to reliably establish the mechanism of formation of potential images on the atomic scale [39, 60].

SKPM also turned out to be very a convenient method for studying the wear of materials due to friction [69], analysis of galvanic effects in corrosion of aluminum-based alloys [85], and detection of intermetallic inclusions in alloys (Al_2Cu in the Al–Cu system) [68]. The transition from the qualitative to quantitative interpretation of the experimental data opened new vistas for control for electric processes in various devices

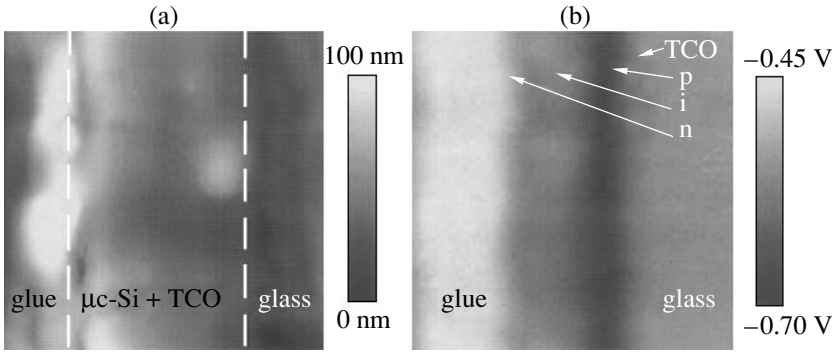

Fig. 8. Topographic image (left) and the corresponding surface potential scan (right) of cross-sectioned *pin*-diode prepared from microcrystalline silicon. Scan size is 3.5×3.5 μm [88].

in microelectronics—from thin-film InGaAs resistors [74] and *p*–*n* junctions on Si [57, 86] to complex heterostructures [86–88].[2] Thus, it is possible to record a built-in potential. Its comparison with the calculated profile revealed the incomplete donor ionization in laser-based n^+-InP/InGaAsP/p^+-InP diodes [87] and explained insufficiently efficient collection of carriers associated with defect and impurity distributions in solar elements based on microcrystalline silicon (Fig. 8) [88]. Studying the potential distribution in the cross section of a multilayer $Al_{0.3}Ga_{0.7}As$/GaAs structure, Tanimoto and Vatel [86] proved, using secondary-ion mass spectroscopy (SIMS), that the SKPM method is sensitive to the Al content in each layer. The measurements performed on illuminated samples allowed one to determine the change in the depleted-layer width, to study the transition to flat bands, and to draw conclusions on the band structure of the cleavage. Applying the bias voltage to laser GaAlSbAs/GaSb(100) diodes cleaved along the (110) surface, one can directly determine the voltage drop at the heterojunction and the active region of the device [83]. It was revealed that, in junction-based GaP diodes, the potential distribution (whose change turned out to be much more pronounced than the applied bias) depends on the electron transitions from shallow localized levels to the conduction band occurring under the action of emitted light [89]. Koley and Spencer [90] recorded the potential distribution around a single dislocation in *n*-GaAs films and $Al_{0.35}Ga_{0.65}N$/GaN heterostructures (Fig. 9), determined the position of the Fermi level in both film and heterostructure, and suggested a band diagram with acceptor dislocation levels.

4. ELECTROSTATIC FORCE MICROSCOPY

As was indicated above, electrostatic force microscopy (EFM) is a combined method that allows one to measure the electrostatic force—usually both its harmonics, F_ω and $F_{2\omega}$. In 1988, when Martin *et al.* [8] first measured the electrostatic force using an atomic force microscope in the range of distances from several to 170 nm and determined the minimum recordable force 10^{-10} N by this method, the term *EFM* had not been coined. Schönwenberger and Alvarado [11] recorded a value of 14×10^{-9} N. Today, when we have instruments that can operate in vacuum and also at low (including helium) temperatures, it is also possible to measure forces less than 10^{-12} N [91]. Among the pioneers of the method are, also, Stern [10] and Terris [12], with coauthors, who tried to use electrostatic forces to visualize the charge distributions on the surfaces of dielectric samples. First, they manage to record the appearance of such a charge by analyzing the contours of constant force gradient measured in the conventional tapping mode of AFM. Because of the Coulomb attraction between the charge on the surface and the corresponding charge induced at the tip, the contour shows sharp peaks. It is possible to single out the charge peaks against the background of topographic images and determine the charge sign by applying a constant bias V_{DC} of different signs and values to the metal electrode under the film [10, 92]. The application of the bias would change the charge induced at the tip and, thus, also the force of interaction, which, in turn, could change the image contrast up to its reversal (Fig. 10). However, the necessity of multiple scanning at various V_{DC} values led the authors to the idea of modifying the method. Working, as usual, in the tapping mode, they applied a.c. voltage $V_{AC}\sin\omega t$ between the cantilever and the metal electrode under the dielectric sample with a frequency much lower than the oscillation frequency in the vicinity of the resonance. Then, the existence of the surface charge can be established from the presence or absence of an additional modulation of the force gradient at the frequency ω [12, 92]. The component with the frequency ω is responsible for the charge imaging, with the charge sign being determined by the signal phase. Thus, Terris *et al.* [92] recorded simultaneously within one scan the signals at different frequencies (as

[2] In this case, when using Eq. (1), one has to take into account in the expression for voltage V also the voltage V_{ind} induced on the surface and associated with the device operation. In other words, the image contrast is determined by the sum $V_{CPD} + V_{ind}$.

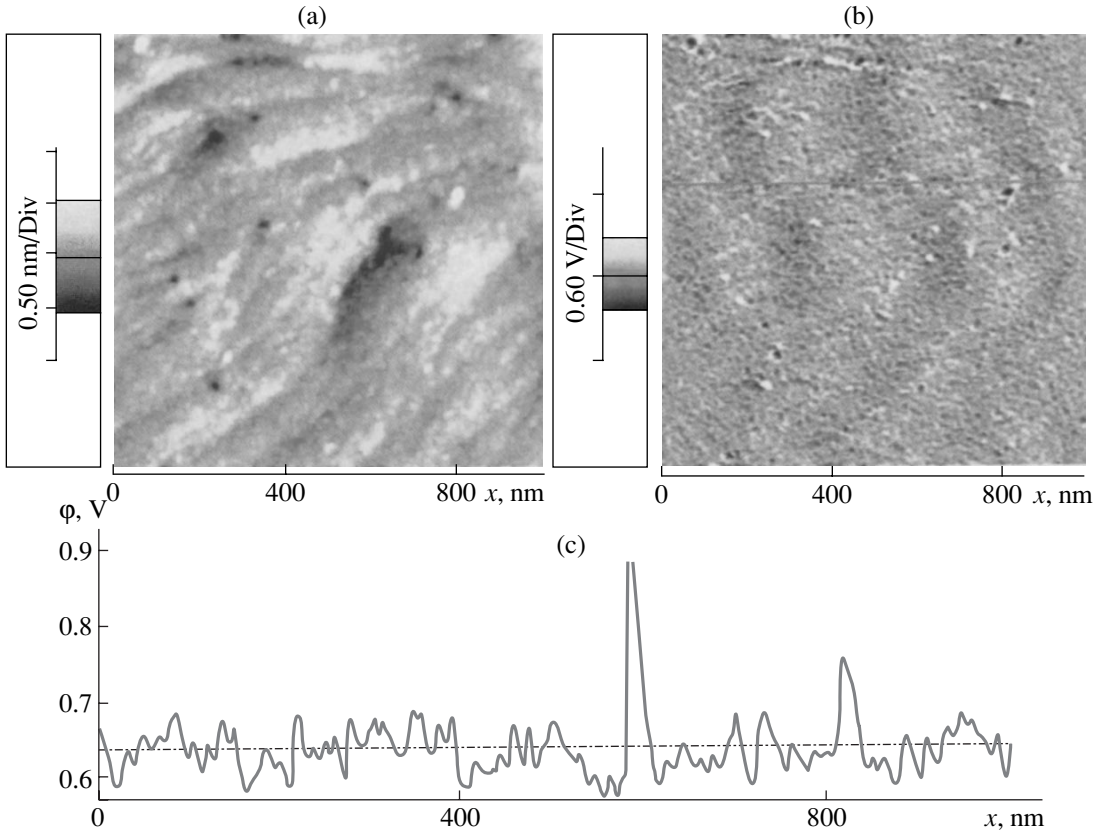

Fig. 9. (a) Topography of an *n*-GaN surface, (b) surface potential image (1×1 μm) taken simultaneously on unintentionally doped *n*-GaN sample, and (c) a cross-sectional line diagram showing typical variation in the surface potential around a dislocation [90].

is made today in modern EFM, although they used the term *force microscopy of localized charges*). The term *EFM* was coined later, e.g., the study by Sugawara *et al.* [31], who studied the charges localized on the surface in a high vacuum (but, as earlier, they determined the charge sign from the change of the contrast at different V_{DC} values).

As a matter of fact, it is difficult to rigorously divide the application spheres of the methods—some modern SKPM instruments also provide control for $\partial C/\partial z$ variation. Thus, the heterodyne system allows one to follow cantilever deflection simultaneously at various frequencies [20, 48, 75] (the cantilever response shows several peaks because the probe behaves as a lumped mass system). If an instrument records only one basic harmonic, one can also measure the capacitance component by tuning the frequency of the applied alternating voltage to ω/2 [44]. However, the authors of the studies cited above prefer to call their approach Kelvin microscopy. Reciprically, EFM still allows one to compensate the contact potential difference by the Kelvin method, see, e.g., [48], where the potential and capacitance images are compared. However, most often, it is the electrostatic force that is the quantity whose spatial distribution forms an image, as is the case in [31], where the images are obtained based on the force gradient distribution, in [93], where the images are considered in terms of the amplitudes of the F_ω component, or in [94], where the images are obtained using the F_ω and $F_{2\omega}$ amplitudes separately.

Leaving aside the two-pass method [36, 95] and recording the signals simultaneously at several frequencies [48, 94] (Figs. 3 and 4), one has to take into account that the electrostatic force can influence the topographic images. Indeed, the application of the modulating voltage $V_{AC}\sin\omega t$ makes the constant force component active even at the compensated contact potential difference ($V_{DC} + V_{CPD} = 0$) in accordance with Eq. (2). Although the van der Waals force varies with distance faster than the electrostatic force and it is its gradient F'_{vdW} that plays the key part in imaging of the constant gradient, the electrostatic-force gradient can also give a contribution. Figure 11 [96] compares the topographic images of the Au sample obtained without application of V_{AC} and with the application of V_{AC} = 10 V and illustrates how this deteriorates the spatial resolution. It follows from Eqs. (2) and (4) that, in the case where $V_{CPD} = -V_{DC}$, the gradient of the constant component of the electrostatic force $F'_{DC} = 1/4(\partial^2 C/\partial z^2)V_{AC}^2$ coincides (by an absolute value) with

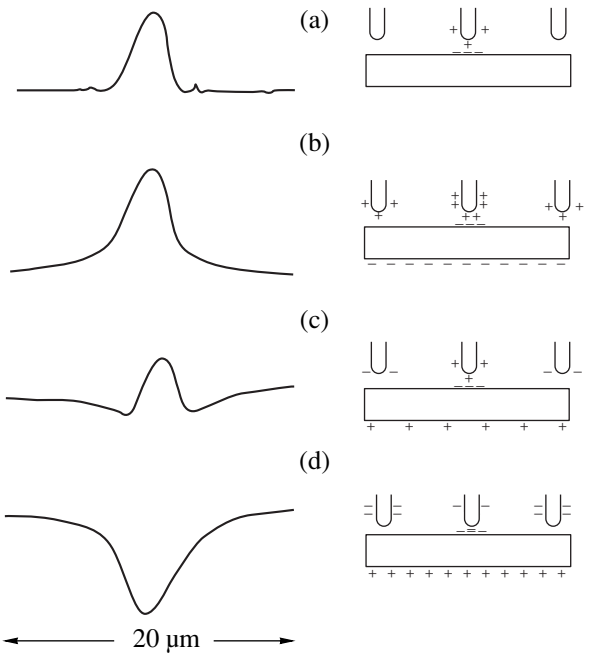

Fig. 10. Contours of constant force gradient acting on the tip above the dielectric polymethyl methacrylate surface and the schematic charge distribution at four different applied constant bias voltages: (a) 0, (b) –6, (c) +6, and (d) +24 V [10].

the gradient of the amplitude of the second harmonic of the force $F_2' = -1/4(\partial^2 C/\partial z^2)V_{AC}^2$. Therefore, it was suggested [34, 93] to avoid possible distortions introduced by F_{DC}' into the topographic images by subtracting the measured amplitude $F_{2\omega}'$ from the gradient of the total constant force $F' = F_{vdW}' + F_{DC}'$. The dependences of the shift of the frequency of cantilever oscillations (measure of the force gradient) on the height of the tip location above the surface (Fig. 12) [93] demonstrate the practical coincidence of the curve constructed in the absence of the a.c. voltage (filled circles) and the curve constructed for the applied a.c. voltage and then corrected by the above method (open circles).

The authenticity of the topographic image in [31] is ensured in a somewhat different way. It is suggested to apply to a sample square-wave voltage trains with the frequency ω. In this case, topographic images are formed in the conventional way at the zero bias (measured from the compensation level of the contact potential difference), whereas the electrostatic characteristics are recorded during the half-period of the bias application.

In turn, Hong *et al.* [46] state that it is possible to overcome the difficulties associated with the separation of the force gradients by using EFM in the dynamic contact mode (dynamic contact mode of EFM, DC–EFM) [97]. It was established that, even in the case of a contact with the solid surface, the cantilever performs continuous oscillations with a finite amplitude. Therefore, the surface profile is measured in the mode analogous to the conventional contact mode in AFM, whereas the electric characteristics are determined from Eqs. (2)–(4) using the oscillation amplitudes at the applied-voltage frequency. In this case, the repulsive van der Waals force is maintained constant with the aid of the feedback in the circuit for the motion control along the vertical coordinate. The above formulas

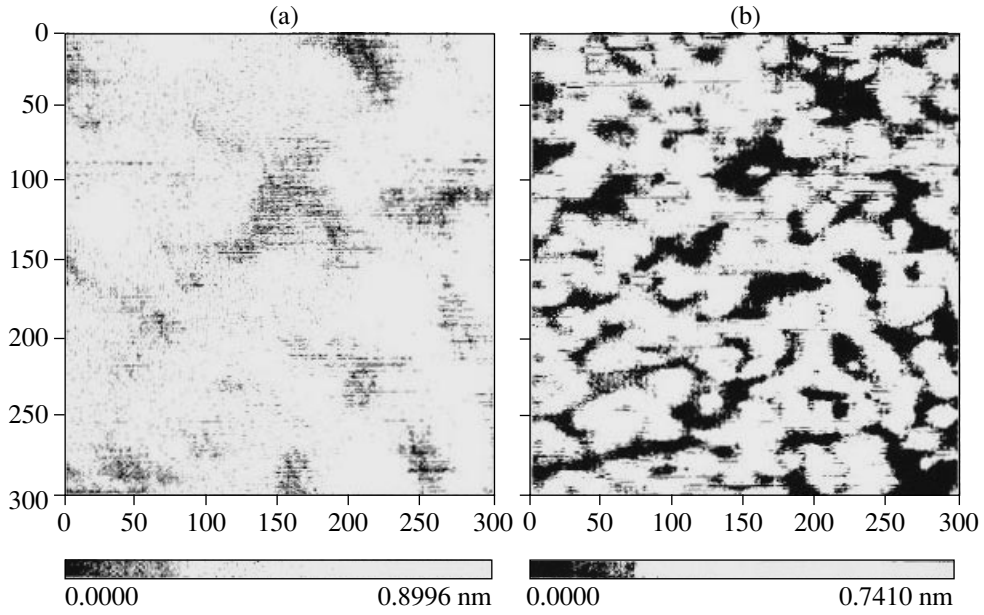

Fig. 11. Topography of the surfaces of arachidic acid and partly fluorinated carboxylic acid-based Langmuir–Blodgett films obtained under (a) 10 V and (b) zero a.c. voltage [96].

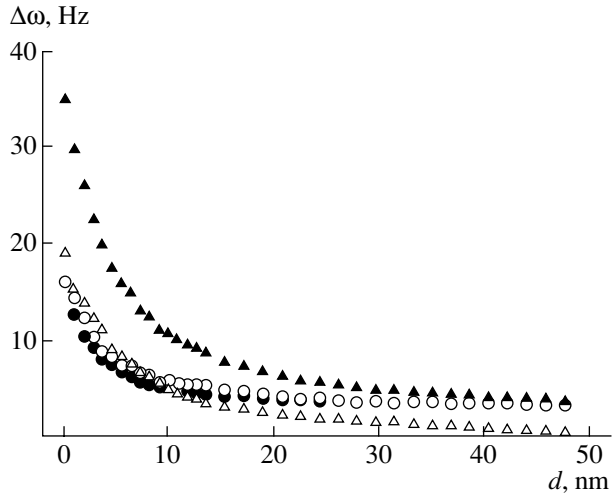

Fig. 12. Frequency shift Δω as a function of tip height d above the Si(111) surface under various experimental conditions [93]. ● with no applied voltage; ▲ with an applied 1 V a.c. voltage at frequency $\omega/2\pi = 300$ Hz; ○ with applied a.c. voltage after the subtraction from the signal of the component corresponding to the frequency 2ω; and △ the signal amplitude at the frequency 2ω.

remain valid, since, despite, the cantilever contact, no current can flow between the sample and cantilever because of the insulating (oxide) layer on the silicon tip. It is true that, if the samples are insufficiently hard, an additional indeterminate factor arises, which is associated with possible variations in the hardness along the surface changing, in turn, the amplitude of cantilever oscillations (on the other hand, this fact can be used for obtaining some information on the mechanical hardness of the sample) [33].

As to the measurable electric quantities, the directly determined F_1 and F_2 values are insufficiently informative for surface characterization. It is more important to determine the surface potential. In EFM, it is sometimes determined using a Kelvin compensation scheme [48]. It is also possible to determine the surface potential directly from the F_1 and F_2 values using Eqs. (3) and (4),

$$|V_{CPD} + V_{DC}| = V_{AC}/4\,|F_1/F_2|. \quad (7)$$

Xu and Hsu proved [94] that the latter method of determining V_{CPD} is equivalent to the SKPM method even if one takes into account the influence of the stray cantilever–sample capacitance C_{cant}. Taking into account this capacitance in both methods equally decreases the measured contact potential difference in comparison with its true value because of the coefficient $\partial C/\partial z/(\partial C/\partial z + \partial C_{\text{cant}}/\partial z)$, amounting in practice to about 85%. Although the determination of V_{CPD} from F_1 and F_2 requires an additional treatment of the experimental data, it also has an advantage—one can obtain potential images at different bias values V_{DC}. As is indicated in [94], varying V_{DC}, it is possible to inverse the contrast for patches having different work functions. Indeed, consider two patches on the surface with the contact potential difference of the first one, V_{CPD1}, being higher than for the second one, V_{CPD2}. Applying a bias V_{DC} exceeding $-V_{CPD2}$, we can make the first patch on the image brighter than the second one (the $|V_{CPD} + V_{DC}|$ value of this patch is higher). And, vice versa, applying $V_{DC} < -V_{CPD1}$, we can make the first patch darker than the second one. Xu and Hsu believe [94] that this can help one to distinguish the true signal of electrostatic origin from the topographic artefacts (the signals at different frequencies were recorded simultaneously). Moreover, analyzing the bias influence (and, first of all, of the bias sign) on the contrast of EFM image with an atomic resolution, Sugawara *et al.* [31] drew conclusions about the sign of a point-defect charge.

The F_1/F_2 ratio is also very useful for studying the character of the electrostatic tip–surface interaction. If the tip and the surface interact as two conductors, then Eq. (7) is valid, with the F_1/F_2 ratio being independent of the tip height above the surface. If semiconductor effects become important, the ratio depends on the tip height [42]. This method suggested in this theoretical study [42] was first used in practice by Sommerhalter *et al.* [44], who verified the validity of the model of conductor interaction for silicon cantilevers.

If a sample is coated with an oxide layer or is an insulator (then, it can be considered as a dielectric interlayer between the lower electrode and the tip), localized charges are formed on the surface. In this case, the force acting on the tip consists not only of the "capacitance component" described by Eq. (1), but one has also to take into account the effect of the field E_s of surface charges (dependent on the surface charge density σ) on the induced charge at the tip, q_t. Information on this density may also be obtained, but in a way more complicated than information about the surface potential [45]. In the dynamic contact EFM [33, 46], the tip is very close to the surface, so that the field of surface charges can be considered to be uniform with the intensity $\sigma/2\varepsilon_0$ (it is assumed that the dimension of the surface-charge region exceeds the apex radius). Introducing an additional contribution $q_tE_s = CV\sigma/2\varepsilon_0$ into Eq. (1), we add the term $C\sigma V_{DC}/2\varepsilon_0$ to the Eq. (2) for the constant force, while the first harmonic in Eq. (3) is then represented as $F_\omega = (\partial C/\partial z(V_{CPD} + V_{DC}) + C\sigma/2\varepsilon_0)V_{AC}\sin\omega t$. Measuring the first harmonic of the electrostatic force at a constant capacitance, one can determine V_{CPD} or σ depending on the experimental conditions used. In order to determine σ (e.g., in ferroelectrics), Hong *et al.* [46] suggested using the compensation method as in the case of V_{CPD}. Using V_{DC} value such that no signal was recorded at the frequency ω, one obtains $\sigma \sim -2\varepsilon_0V_{DC}(\partial C/\partial z)/C$. Taking into account that the sample–surface distance is rather small (~1 nm), the system can be considered as a flat capacitor for which

$(\partial C/\partial z)/C = 1/d$. This allows one to avoid the necessity of knowing the exact value of the capacitance. The uniform field distribution was used in [98] to take into account the influence of a homogeneous charged contaminated layer on the conducting-sample surface. Saint Jean *et al.* [98] drew the conclusion that the contact potential difference determined by the SKPM method for a surface coated with a contaminated layer of the thickness d with the dielectric constant ε and the surface-charge density σ_s is, in fact, the contact potential difference of a clean surface in vacuum with due regard for the additive correction $\sigma_s d/\varepsilon\varepsilon_0$.

However, in the noncontact mode, the problem of determination of the distribution of the surface charges localized in rather small regions cannot be solved correctly under the assumption that the field of charges is uniform. It is more adequate for representing the effect of this field on the tip as an interaction of two point charges spaced by a distance z—a surface charge q_s and an induced charge q_t [12, 36, 40, 93]. Then, the term $q_s q_t/4\pi\varepsilon\varepsilon_0 z^2$ (which appears in addition to the capacitance component of the electrostatic force in Eq. (1)) gives the contributions $q_s^2/4\pi\varepsilon\varepsilon_0 z^2 + q_s V_{DC} C/4\pi\varepsilon\varepsilon_0 z^2$ to the constant force component in Eq. (2) and the contribution $q_s V_{AC} C/4\pi\varepsilon\varepsilon_0 z^2$ to the first harmonic in Eq. (3) [40]. This results in the modulation of the force gradient at the frequency of the first harmonic used in [12, 92] for obtaining a charge image. Terris *et al.* [12] emphasize a very high sensitivity of the method with respect to the electric charge—the minimum detected value equals three elementary charges. The possible recording of the single-electron processes by this method is confirmed by Schönenberger and Alvarado [99], who studied the relaxation of a charge applied to the surface of a Si_3N_4 dielectric. The change in the charge was established from the temporal curve of the first harmonic of the force F_ω (with the tip–surface distance and the $F_{2\omega}$ value being constant), which demonstrated the pronounced signs of quantization. (By the way, the SKPM method also allows one to obtain the screened Coulomb potential of a single charge [70].) According to the estimate made in [29], this charge can be recorded at the tip height of about 15 nm and the dipole moment of 1 D at a distance of 1.5 nm. However, similar studies are still of a qualitative nature [31]. It is important that, in this case, the microscope probe may play not only the passive role (providing the signal forming an image), but also the active one— supplying bias of various values between the cantilever and the substrate, and one may apply to a dielectric film the various charges of different signs. Such recordings can also be made in the noncontact mode (if the voltage pulse is applied with the aid of a crown discharge in the air gap) [92, 99] and also by the contact method [12, 92]. This fact seems to be rather promising for creating memory devices based on ferroelectric materials, whereas the use of EFM allows one both to record and read the information [100, 101].

Ferroelectric crystals are the first "candidates" for studying their properties by EFM because the method allows one both to visualize domains and to study their dynamics and also give the direct information about their signs, e.g., from the contrast variations at different applied bias voltages [36]. The gradient of the interaction force depends on the magnitude of polarization but not on its sign [102]. Nevertheless, interpretation of the results is not easy, because the contributions to the contrast come not only from the electrostatic but also from the piezoelectric effect, which gives rise to surface vibrations and, finally, to modulations of cantilever oscillations, especially for the first harmonic (electrostriction may also take place, but it gives contributions to higher-order harmonics [103]). Happily, the signal associated with piezoelectricity does not depend on the string constant of the cantilever, whereas the electrostatic response is inversely proportional to k. The latter fact allows one to vary the relative contributions of these effects [104]. In turn, the piezoelectric effect may also be studied by EFM, but here one has to take into account the electrostatic interaction. Thus, Durkan *et al.* [105] made it analytically determining the piezoelectric parameters of lead zirconate–titanate. Ni *et al.* [106] studied by EFM the surface polarization of Li-doped ZnO films and revealed the charge of defects induced by the piezoelectric effect.

The possibility of obtaining the images of ferroelectric domains and domain walls by the EFM method at a spatial resolution of 50 nm was demonstrated on $Gd_2(MO_4)_3$ [102]. The nature of the contrast of images of oppositely charged domains and the methodical aspects of their visualization (including the determination of the domain-wall thickness) were analyzed in detail for both noncontact and contact dynamic EFM for triglycine sulfate [104]. Under the conditions of noncontact EFM, the contributions of the electrostatic and piezoelectric effects have the same phases [103], whereas for the contact EFM these effects are in counterphase [100], which simplifies the separation of their contributions. The authors of the contact method [33] state that the contrast of domain images in their experiments is higher than in the noncontact EFM. For a cleaved triglycine sulfate crystal, they manage not only to determine the sign of polarization, but also to calculate the surface-charge density (2.7 $\mu K/cm^2$ at room temperature) by the method described above and to study its change during heating [46]. The polarization switching of domains under pulsed voltage and their further relaxation were also studied in the contact mode [100, 101]. It was established that triglycine sulfate is not an appropriate material for recording information because of its fast return to the initial state (the relaxation time equals 5 min). It is more appropriate to record the information on $BaTiO_3$ crystals—the lines are sharper and remain stable for more than five days

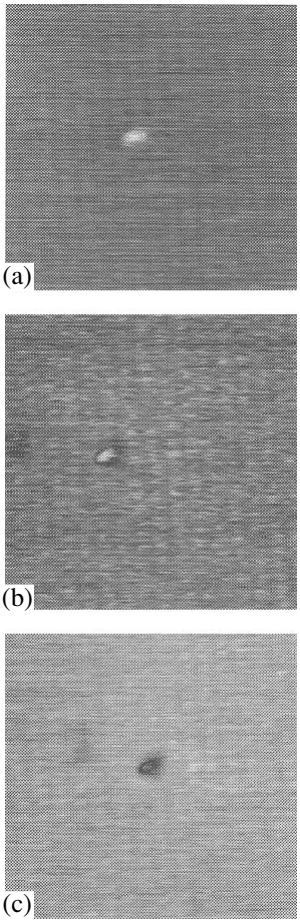

Fig. 13. EFM images of the GaAs(110) surface in the vicinity of a point defect at three different bias voltages: (a) +0.5, (b) –0.22, and (c) –0.43 V. Scan size is 85 × 85 Å [31].

[100]. Using EFM, it is possible to control the spatial–periodic polarization on the surface of $KTiOPO_4$ crystals on the nanoscale ("organized" by selective diffusion of rubidium ions) in fields with an intensity exceeding 750 V/cm [101].

Using the noncontact mode to guanidinium aluminum sulfate hexahydrate samples, Bluhm *et al*. [36] established that the static EFM variant is preferable for studying the domain structure. The topography of the surface was obtained in the contact mode during the first scanning, whereas during the second scanning, the tip moved at a constant height above the surface and the measure of the electrostatic interaction was the cantilever deflection. This method was also successfully used for studying the domain structure of $LiNbO_3$ crystals with polarization-inverted gratings obtained by diffusion of Ti atoms introduced into the structure [107].

The EFM method is also successfully used for solving various problems of microelectronics and, first of all, for defect characterization, e.g., for studying antiphase boundaries on the GaAs/Ge surface [94], point defects on the GaAs surfaces [31] (Fig. 13), and the relaxation of charges trapped by the SiO_2 layer on Si substrates [108], with the charge sign being determined by applying various bias voltages. The possibility of using EFM for studying specific defects on the surface was shown in [95]: inversion domains of the N and Ga polarity (the regions with opposite polarizations formed during crystal growth). The quality of the ohmic Au/Ti contacts and the surface conductivity of the epitaxial layer under these contacts in the n^+-GaInAs/n^+-InP/InP heterostructure, which simulated a transmission line, were determined in [109]. Using EFM, Girard *et al.* [110] observed self-organization of InAs islands on the GaAs(001) surface. Ankudinov *et al.* [111] compared the electric parameters of the laser *pin*-diode based on the AlGaAs/GaAs heterostructure obtained by the noncontact and contact dynamic EFM methods and revealed no considerable differences. They only state that the contact mode allows one to attain a slightly higher spatial sensitivity at the atomic level, whereas the noncontact mode allows one to attain the admissible signal/noise ratio at a lower V_{AC} value.

Considering various EFM applications, one must mention the studies of organic objects examined by this method from the very beginning. Thus, Terris *et al.* [12] visualized the distribution of charges localized on the polymethyl methacrylate (PMMA) surface. The recent studies along this direction are based on the direct measurement of the potential by the SKM method. For organic and biological objects whose properties are determined by polar functional groups (–OH, –COOH, $–NH_2$, etc.), the surface potential is closely related to their functions. Knowing the distribution of the surface potential at the molecular resolution, it is possible to extract detailed information on various complicated chemical processes. Thus, today, it is possible to recognize the regions containing the thiol molecules with chemically different terminal head groups [112], determine the local distribution of the doping (oxidation) level of polymer films (polybithiophene [113, 114]), and analyze the polarization distribution in polymer films (polymethyl methacrylate with 10% chromophore [115]. Thus, one can obtain the necessary information on the homogeneity and domain structure of Langmuir–Blodgett films of various compositions (e.g., experiments on films based on the behenic and perfluorotetradecanoic acids with calcium cations [116], orientation of amphiphilic molecules in multilayer films (experiments with cadmium arachidate [117]), the site of localization of contamination on the surface or under the film on the substrate (experiment with films based on the arachidic and partially fluorinated carboxylic acids [96]), etc. The EFM data allow one to draw some conclusions on the particle boundaries in the poly(styrene-butyl acrylate-acrylic acid) latex films [118], on the electric conductivity of DNA molecules [119] and complexes of these molecules with metal ions [120] and the interaction of DNA molecules with substrates [121]. Similar data should also

be very useful in the study of the electron structure of porphyrines [122] and photoprocesses occurring with their participation on the surface [123] and also in the search for physiologically active substances in cells in immunohistochemical reactions [124].

5. SCANNING CAPACITANCE MICROSCOPY

It is seen from what has been stated above that the relation between the electrostatic force and capacitance allows one to determine the latter. This can be realized by the EFM on the basis of Eq. (4). This was done first by Martin *et al.* [8], who measured the minimum detectable capacitance as 4×10^{-20} F using a constant bias voltage (the capacitance was calculated for a model of flat capacitor or a sphere above the plane with the measured force gradient) and as 8×10^{-22} F using the modulation method (with the separation of the signal at the second harmonic for the same cantilever–sample models). Geometric modeling of the system is dictated here by the fact that, in this case, one controls experimentally not the capacitance itself but its derivative $\partial C/\partial z$ described by Eq. (4). The direct measurement of capacitance can be made by the method of scanning capacitance microscopy (SCM) developed independently of the force methods of recording.

The first scanning capacitance microscope [13] was constructed earlier than the atomic force microscope and used another scanning system based on the scanning RCA videodisk system. The measuring probe was a thin-film vertical electrode with the cross section 0.1×2.0 μm deposited onto a diamond tip and ending 20 nm from its base. The tip, brought into mechanical contact with the sample surface, moved along the spiral, and the capacitance of the electrode–sample system was recorded during this motion by an RCA capacitance sensor. The signal was digitally processed and formed the surface image. It is interesting that the first problem solved by the SCM method was visualization of topography. Considering the changes in the capacitance value, one can extract the information on the probe height above the surface. The next scanning capacitance microscope was designed with the same goal [16]. The probe was a thin metal wire, the spiral scanning was changed to linear scanning performed due to motion of the sample with respect to the probe in the surface plane along two mutually perpendicular directions. The capacitance was controlled by an *LCR* resonance circuit-based sensor, which included the capacitance to be determined. The probe–surface distance was controlled using feedback in such a way that the signal would remain constant. The heights thus obtained formed the image, i.e., allowed one to obtain the contours of constant capacitance (or, more exactly, differential capacitance, because the piezoelectric holder provided sinusoidal modulation of the probe–sample distance, which ensured a high degree of locality of the information obtained). It was assumed that the images thus obtained are directly related to the topography of the surface, although it was also indicated that the images were also dependent on the inhomogeneities of the electric characteristics of the sample. The possibility of obtaining information on the electric properties of the sample in such a way (dielectric constant or the shape of ferroelectric domains) was still indicated in [13].

It was only later that the capacitance value started playing the important role. This happened when an RCA-sensor-based capacitance microscope began using the scanning system and the feedback of a scanning tunneling microscope [125]. This allowed one to independently control also the surface relief (in this study it was reconstructed from the values of the tunneling current) and the capacitance, which could serve as a source of additional information [126]. Williams *et al.* [125] evaluated the minimum recordable capacitance value as 2×10^{-22} F, with the best signal/noise ratio being obtained for the differential capacitance measured by modulating the probe–sample distance. However, in the new modification of the instrument, capacitance first played the auxiliary role, being a component of an electrical oscillating contour and the control system of cantilever deflection [127]. In other words, it was used to determine the force acting on the cantilever, e.g., the magnetic force [128]. Sarid [40] discussed the possible use of capacitance created not by the probe–sample system, but by the probe–special reference plate one. However, the capacitance related to the given sample region can be very informative. This new function (measurement of the capacitance with the aid of an RCA-sensor-based circuit with the sensitivity 10^{-19} F) was used to increase the possibilities of the atomic force microscope with a metallized probe [129]. Thus, the $C(V)$ curves for the metal–dielectric–semiconductor structure were obtained at high frequencies (>1 kHz). If the dielectric layer is charged, then the field of its charges acts as an additional bias at the capacitor and the $C(V)$ curve shifts along the abscissa. This phenomenon can readily be recorded using the $dC(V)/dV$ curves. At the same time, the microscope was used not only for observations but also for recording the information [129, 130]. Applying the pulses of pronounced bias, it was possible to inject charges into the insulating layer locally, where they remained trapped for quite a long time. The record could be erased by applying a voltage pulse of opposite polarity.

Today, a scanning capacitance microscope is an atomic-force microscope equipped with a highly sensitive capacitance sensor usually operating at a frequency of 915 MHz. Its signal is recorded in parallel with the topographic signal [131]. Thus, one can obtain the topographic image of the surface (as usual, measuring cantilever deflections) and, simultaneously, also the distribution of the capacitance over the surface. The sensor is an oscillatory circuit including the capacitance of the sample–electrode system and is excited by a UHF source (Fig. 14). The changes in this capacitance

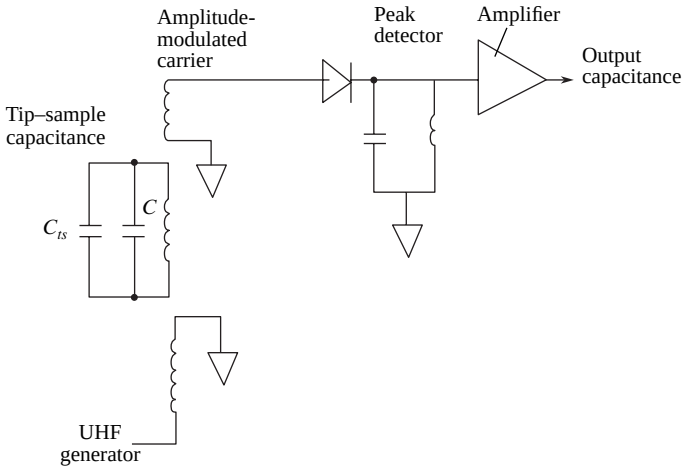

Fig. 14. Schematic of an RCA capacitance sensor.

lead to the shift of the resonance frequency of the circuit; then, the oscillation amplitude varies, which is recorded by a peak detector. At present, designers are attempting to increase the sensitivity of the capacitance part of the circuit. Thus, the sensitivity of a modified instrument demonstrated at the 11th International conference on scanning tunneling microscopy in Vancouver, Canada, in July, 2001 [132], was 30 times higher than the sensitivity of a standard RCA attachment. This was attained by thorough screening of the active components from stray fields in the probe region by using special technical innovations. It was also suggested to use the microscope in the mode of "shear forces," when the probe oscillations are excited electromechanically in the surface plane along the scanning direction [133]. In this case, it is possible to record simultaneously the topographic image and the distribution of the *dC*/*dV* and *dC*/*dx* quantities (where *x* is the coordinate along the surface). Also, the probe technique is developed, which allows one to make measurements at different temperatures [134], including temperatures as low as 1.5 K [135]. The theoretical methods for calculating capacitance of the surfaces with arbitrary profiles have also been developed [136].

Following the classical macroscopic method of determining the doping level of a semiconductor based on the *C*(*V*) dependence, scanning capacitance microscopy also became the standard method for control of two-dimensional dopant distributions in microelectronic devices [137]. In fact, the accuracy of the information thus obtained considerably depends on the adequacy of the models used in data interpretation. The possibility of establishing the distribution of impurity along the surface from the measured *F*(*V*) dependences was predicted theoretically in [43] for the simplest plane-parallel geometry of the tip–vacuum gap–oxide–semiconductor system. It was shown that it is better to use the $F_\omega(V)$ and $F_{2\omega}(V)$ dependences than the $F_{DC}(V)$ dependence. Soon, the use of SCM made it possible to the directly measure the capacitance as a function of voltage for *n*-Si wafers homogeneously doped to different levels. The doping level was evaluated for each wafer (with the tip being in contact with the oxide layer) [138]. Then, detailed theoretical computations were made for the tips of some configurations by both analytical [139, 140] and numerical [141, 142] methods based on the solution of the Poisson equation for a semiconductor. This allowed one to relate the capacitance value *C*(*V*) or *dC*/*dV* to the concentration of electrically active impurity atoms at the given point. These computations were complemented with the comparison of the experimental SCM data for the test structure (e.g., cross sections of silicon p^+/p structure, *p*–*n*-junctions [143] and n^+/n structures [144, 145], and also the Si/Ge system [146]) with the results obtained by secondary ion-mass spectroscopy (SIMS). It became possible to increase the method sensitivity by preparing the samples for the studies in different ways, e.g., by surface bevelling [147–149]. At present, the theoretical basis of the method is being developed for various experimental situations. In particular, analysis showed [150] that the capacitance value is controlled by the macroscopic geometry of the tip, rather than by the sample parameters, and therefore these parameters should be determined using *dC*/*dV*.

Methodically, it is simpler to measure the *dC*/*dV* derivative than the absolute capacitance value (in this case, the effect of a considerable stray capacitance is excluded and the signal/noise ratio increases). However, Tomiye and Yao [151] believe that this may give rise to an additional problem associated with the effect of the V_{AC} value. On the contrary, Stephenson *et al.* [152] believe that a V_{AC} value not exceeding 0.2–0.4 V does not influence the results, whereas the latter can be dependent, to some extent, on the bias voltage. In order to record the *dC*/*dV* curve using a capacitance sensor of

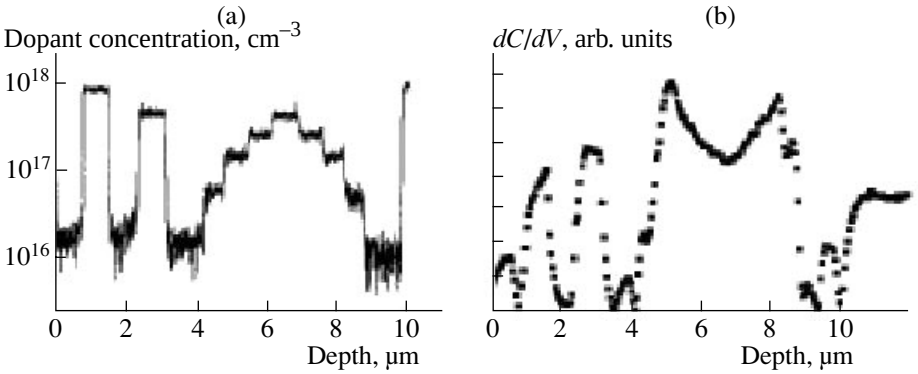

Fig. 15. (a) SIMS profile of nitrogen concentration in the epitaxial *n*-type structure and (b) the differential-capacitance profile of the same sample (V_{AC} = 1 V and V_{DC} = – 4 V) [155].

a microscope, in addition to the bias voltage varying within –10–+10 V, one has also to supply a modulating voltage with the amplitude ≤1 V and the frequency 5–20 kHz and to record the corresponding capacitance change. Another variant of the method is based on the feedback with respect to the variable voltage: the V_{AC} value is chosen in such a way that the variation in the capacitance dC during the whole scanning cycle remains constant and one records the dV/dC values [143, 153]. The results obtained can readily be recalculated into the value of the doping level using the database containing calibration curves calculated by the finite-element method for various doping levels and thicknesses of the oxide layer and the specially designed software [141]. The algorithm suggested here is valid in the case in which the gradient of the doping level is not too high. The limitations associated with this condition are analyzed in detail elsewhere [154] (the rate of the variation of the impurity concentration along the surface should be related in a certain way with the tip diameter).

However, leaving aside the requirements set by the quantitative interpretation of the results, the SCM method allows one to obtain the contrast from doped regions of nanometer sizes as in the case of silicon plates subjected to ion implantation through a mask [153]. In fact, the dC/dV values themselves turn out to be rather informative (Fig. 15, where the curve constructed for the cross section of the epitaxial structure consisting of alternating *n*-(nitrogen-doped) and *p*-(trimethylaluminum-doped) SiC layers neighbors the concentration profile found by SIMS [155]). An example of the quantitative treatment of the dC/dV dependences is illustrated by Fig. 16 [156], which presents the concentration profiles of the majority carriers in the cross section of the N^+-implanted 6H-SiC sample obtained by such a method.

In addition to characterization of the *p–n* junctions [151, 157–161], scanning capacitance microscopy is also used for studying the charging effect in $Al_xGa_{1-x}N$/GaN heterostructures [162, 163] and SiO_2 layers on Si substrates [164, 165], compensation of shallow donor levels in Fe-doped InP [166], ordering in the GaInP sample [167, 168], dislocations in GaN [169], surface depletion at quantum InAs dots on GaAs [170], and comparison of SiO_2 layers obtained by various methods of oxidation [171].

One often invokes as additional information the data on the spatial capacitance distribution in EFM and SKPM studies (in this case, the dC/dz value is recorded). This allows one to determine the dopant profiles [20, 172], analyze the defects in GaAs/Ge [94], etc. Kimura *et al.* [173] suggested taking into account the $C(V)$ dependence arising in semiconductors by using an approximate method under the assumption

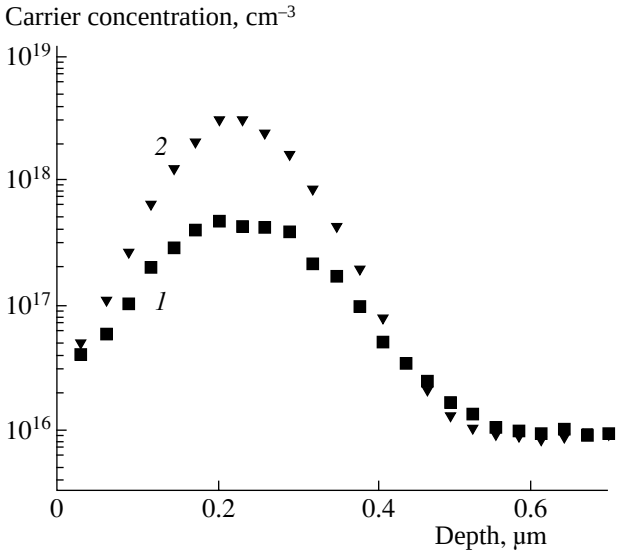

Fig. 16. Carrier concentration profiles measured at room temperature by the SCM method on 200-keV N^+-implanted 6H-SiC samples at two different fluences: (*1*) 1×10^{14} and (*2*) 5×10^{14} cm^{-2} [156].

that we have, in Eq. (1),

$$\partial C/\partial z \approx \partial C(V_{DC}, z)/\partial z + \partial^2 C(V_{DC}, z)/\partial z \partial V\, V_{AC} \sin \omega t.$$

Then, the signal acquires a periodic component corresponding to the third harmonic at 3ω proportional to $\partial^2 C/\partial z \partial V$, which yields the information on $\partial C/\partial V$. Experiments with the test doped *n*- and *p*-type Si samples confirmed that this method can be used for determining two-dimensional doping profiles, with the contrast in the vicinity of the *p*-*n* junction being dependent on the V_{DC} value [173].

Scanning probe microscopy is a rapidly developing method of studying processes on the molecular scale. The theoretical foundations of the method are constantly being refined and the experimental methods are becoming more elaborate. Although the number of papers using this method is increasing in a flood, there still are fields for its new application. There is no doubt that we shall witness numerous interesting discoveries in this field.

ACKNOWLEDGMENTS

This study was supported by the Vainshtein Scientific School on Dynamical and Kinematical Scattering of X-rays and Electrons (Theory, Experimental Methods, and Applications), project NSh-1404.2003.2.

REFERENCES

1. G. Binnig, C. F. Quate, and Ch. Gerber, Phys. Rev. Lett. **56**, 930 (1986).
2. Y. Martin and H. K. Wickramasinghe, Appl. Phys. Lett. **50**, 1455 (1987).
3. J. J. Sáenz, N. Garcia, P. Grütter, *et al.*, J. Appl. Phys. **62**, 4293 (1987).
4. A. Wadas, J. Magn. Magn. Mater. **71**, 147 (1988).
5. U. Hartmann, J. Appl. Phys. **64**, 1561 (1988).
6. J. Sáenz, N. Garcia, and J. C. Slonczewski, Appl. Phys. Lett. **53**, 1449 (1988).
7. M. Mansuripur, IEEE Trans. Magn. **25**, 3467 (1989).
8. Y. Martin, D. W. Abraham, and H. K. Wickramasinghe, Appl. Phys. Lett. **52**, 1103 (1988).
9. R. Erlandsson, G. M. McClelland, C. M. Mate, and S. Chiang, J. Vac. Sci. Technol. A **6**, 266 (1988).
10. J. E. Stern, B. D. Terris, H. J. Mamin, and D. Rugar, Appl. Phys. Lett. **53**, 2717 (1988).
11. C. Schönenberger and S. F. Alvarado, Rev. Sci. Instrum. **60**, 3131 (1989).
12. B. D. Terris, J. E. Stern, D. Rugar, and H. J. Mamin, Phys. Rev. B **63**, 2669 (1989).
13. J. R. Matey and J. Blanc, J. Appl. Phys. **57**, 1437 (1985).
14. I. V. Yaminskiĭ and A. M. Tishin, Usp. Khim. **68** (3), 187 (1999).
15. S. Lányi, J. Török, and P. Řehůřek, Rev. Sci. Instrum. **65**, 2258 (1994).
16. C. D. Bugg and P. J. King, J. Phys. E: Sci. Instrum. **21**, 147 (1988).
17. J. L. de Jong and J. D. Reimer, Scan. Electron Microsc. **3**, 933 (1986).
18. P. Muralt and D. W. Pohl, Appl. Phys. Lett. **48**, 514 (1986).
19. J. P. Pelz and R. H. Koch, Rev. Sci. Instrum. **60**, 301 (1989).
20. A. K. Henning, T. Hochwitz, J. Slinkman, *et al.*, J. Appl. Phys. **77**, 1888 (1995).
21. U. Hartmann, Ultramicroscopy **42–44**, 59 (1992).
22. O. Teschke and E. F. de Souza, Appl. Phys. Lett. **74**, 1755 (1999).
23. Y. Martin, C. C. Williams, and H. K. Wickramasinghe, J. Appl. Phys. **61**, 4723 (1987).
24. H. W. Hao, A. M. Baró, and J. J. Sáenz, J. Vac. Sci. Technol. B **9**, 1323 (1991).
25. S. Gómez-Moñivas, L. S. Froufe-Pérez, A. J. Caamaño, and J. J. Sáenz, Appl. Phys. Lett. **79**, 4048 (2001).
26. S. Belaidi, F. Lebon, P. Girard, *et al.*, Appl. Phys. A **66**, S239 (1998).
27. S. Belaidi, P. Girard, and G. Lévéque, J. Appl. Phys. **81**, 1023 (1997).
28. S. Belaidi, P. Girard, and G. Lévéque, Microelectron. Reliab. **37**, 1627 (1997).
29. D. M. Taylor, Thin Solid Films **331**, 1 (1998).
30. A. Gil, J. Colchero, J. Gómez-Herrero, and A. M. Baró, Nanotechnology **14**, 332 (2003).
31. Y. Sugawara, T. Uchihashi, M. Abe, and S. Morita, Appl. Surf. Sci. **140**, 371 (1999).
32. S. Sounilhac, E. Barthel, and F. Creuzet, Appl. Surf. Sci. **140**, 411 (1999).
33. J. W. Hong, S.-I. Park, and Z. G. Khim, Rev. Sci. Instrum. **70**, 1735 (1999).
34. K. Okamoto, Y. Sugawara, and S. Morita, Appl. Surf. Sci. **188**, 381 (2002).
35. S. Gómez-Moñivas, L. S. Froufe, R. Carminati, *et al.*, Nanotechnology **12**, 496 (2001).
36. H. Bluhm, A. Wadas, R. Wiesendanger, *et al.*, Phys. Rev. B **55**, 4 (1997).
37. A. San Paulo and R. Garcia, Phys. Rev. B **66**, 041406(R) (2002).
38. S. Kitamura, K. Suzuki, and M. Iwatsuki, Appl. Surf. Sci. **140**, 265 (1999).
39. S. Kitamura, K. Suzuki, M. Iwatsuki, and C. B. Mooney, Appl. Surf. Sci. **157**, 222 (2000).
40. D. Sarid, *Scanning Force Microscopy with Applications to Electric, Magnetic, and Atomic Forces* (Oxford Univ. Press, New York, 1994).
41. C. Donolato, J. Appl. Phys. **78**, 684 (1995).
42. S. Hudlet, M. Saint Jean, B. Roulet, *et al.*, J. Appl. Phys. **77**, 3308 (1995).
43. Y. J. Huang, J. Slinkman, and C. C. Williams, Ultramicroscopy **42–44**, 298 (1992).
44. Ch. Sommerhalter, Th. Glatzel, Th. W. Matthes, *et al.*, Appl. Surf. Sci. **157**, 263 (2000).
45. P. Girard, Nanotechnology **12**, 485 (2001).
46. J. W. Hong, D. S. Kahng, J. C. Shin, *et al.*, J. Vac. Sci. Technol. B **16**, 2942 (1998).
47. S. Gómez-Moñivas, J. J. Sáenz, R. Carminati, and J. J. Greffet, Appl. Phys. Lett. **76**, 2955 (2000).

48. F. Muller, A. D. Muller, M. Hietschold, and S. Kammer, Meas. Sci. Technol. **9**, 734 (1998).
49. S. J. T. Van Noort, K. O. Van der Werf, B. G. de Grooth, *et al.*, Ultramicroscopy **69**, 117 (1997).
50. J. P. Spatz, S. Sheiko, M. Moller, *et al.*, Langmuir **13**, 4699 (1997).
51. R. Hillenbrand, M. Stark, and R. Guckenberger, Appl. Phys. Lett. **76**, 3478 (2000).
52. S. J. O'Shea, R. M. Atta, and M. E. Welland, Rev. Sci. Instrum. **66**, 2508 (1995).
53. H. O. Jacobs, H. F. Knapp, and A. Stemmer, Rev. Sci. Instrum. **70**, 1756 (1999).
54. M. C. Hersam, A. C. F. Hoole, S. J. O'Shea, and M. E. Welland, Appl. Phys. Lett. **72**, 915 (1998).
55. A. Efimov and S. R. Cohen, J. Vac. Sci. Technol. A **18**, 1051 (2000).
56. T. Trenkler, T. Hantschel, R. Stephenson, *et al.*, J. Vac. Sci. Technol. B **18**, 418 (2000).
57. A. Kikukawa, S. Hosaka, and R. Imura, Appl. Phys. Lett. **66**, 3510 (1995).
58. T. R. Albrecht, P. Grütter, D. Horne, and D. Rugar, J. Appl. Phys. **69**, 668 (1991).
59. S. Kitamura and H. Iwatsuki, Appl. Phys. Lett. **72**, 3154 (1998).
60. K. Okamoto, K. Yoshimoto, Y. Sugawara, and S. Morita, Appl. Surf. Sci. **210**, 128 (2003).
61. S. Yee, M. Stratmann, and R. A. Oriani, J. Electrochem. Soc. **138**, 55 (1991).
62. I. Baikie, U. Peterman, and B. Lagel, Surf. Sci. **433–435**, 249 (1999).
63. B. Lagel, I. Baikie, and U. Petermann, Surf. Sci. **433–435**, 622 (1999).
64. W. Telieps and E. Bauer, Ultramicroscopy **17**, 57 (1985).
65. B. Bhushan and A. V. Goldade, Appl. Surf. Sci. **157**, 373 (2000).
66. J. M. R. Weaver and D. W. Abraham, J. Vac. Sci. Technol. B **9**, 1559 (1991).
67. M. Nonnenmacher, M. P. O'Boyle, and H. K. Wickramasinghe, Appl. Phys. Lett. **58**, 2921 (1991).
68. M. P. O'Boyle, T. T. Hwang, and H. K. Wickramasinghe, Appl. Phys. Lett. **74**, 2641 (1999).
69. B. Bhushan and A. V. Goldade, Wear **244**, 107 (2000).
70. Ch. Sommerhalter, Th. W. Matthes, Th. Glatzel, *et al.*, Appl. Phys. Lett. **75**, 286 (1999).
71. N. A. Burnham, R. J. Colton, and H. M. Pollock, Phys. Rev. Lett. **69**, 144 (1992).
72. H. O. Jacobs, P. Leuchtmann, O. J. Homan, and A. Stemmer, J. Appl. Phys. **84**, 1168 (1998).
73. S. Sadewasser, Th. Glatzel, R. Shikler, *et al.*, Appl. Surf. Sci. **210**, 32 (2003).
74. O. Vatel and M. Tanimoto, J. Appl. Phys. **77**, 2358 (1995).
75. Y. Leng, C. C. Williams, L. C. Su, and G. B. Stringfellow, Appl. Phys. Lett. **66**, 1264 (1995).
76. A. K. Henning and T. Hochwitz, Mater. Sci. Eng. B **42**, 88 (1996).
77. Th. Glatzel, S. Sadewasser, and M. Ch. Lux-Steiner, Appl. Surf. Sci. **210**, 84 (2003).
78. T. Takahashi and T. Kawamukai, Ultramicroscopy **82**, 63 (2000).
79. R. Shikler and Y. Rosenwaks, Appl. Surf. Sci. **157**, 256 (2000).
80. S. Akita, S. Takahashi, and Y. Nakayama, in *Abstracts of 11th International Conference of Scanning Tunneling Microscopy, Spectroscopy, and Related Techniques* (Vancouver, Canada, 2001), p. 251.
81. S. Ono, M. Takeuchi, and T. Takahashi, Appl. Phys. Lett. **78**, 1086 (2001).
82. M. Nonnenmacher, M. O. O'Boyle, and H. K. Wickramasinghe, Ultramicroscopy **42–44**, 268 (1992).
83. S. Lévéque, P. Girard, E. Skouri, and D. Yarekha, Appl. Surf. Sci. **157**, 251 (2000).
84. A. Sasahara, H. Uetsuka, and H. Onishi, Surf. Sci. **529**, L245 (2003).
85. P. Campestrini, E. P. M. van Westing, H. W. van Rooijen, and J. H. W. de Wit, Corros. Sci. **42**, 1853 (2000).
86. M. Tanimoto and O. Vatel, J. Vac. Sci. Technol. B **14**, 1547 (1996).
87. F. Robin, H. Jakobs, O. Homan, *et al.*, Appl. Phys. Lett. **76**, 2907 (2000).
88. A. Breymesser, V. Schlosser, D. Pieró, *et al.*, Sol. Energy Mater. Sol. Cells **66**, 171 (2001).
89. R. Shikler, T. Meoded, N. Fried, and Y. Rosenwaks, Appl. Phys. Lett. **74**, 2972 (1999).
90. G. Koley and M. G. Spencer, Appl. Phys. Lett. **78**, 2873 (2001).
91. M. Vogel, B. Stein, H. Pettersson, and K. Karrai, Appl. Phys. Lett. **78**, 2592 (2001).
92. B. D. Terris, J. E. Stern, D. Rugar, and H. J. Mamin, J. Vac. Sci. Technol. A **8**, 374 (1990).
93. T. Ishihashi, M. Ohta, Y. Sugawara, *et al.*, J. Vac. Sci. Technol. B **15**, 1543 (1997).
94. Q. Xu and J. W. P. Hsu, J. Appl. Phys. **85**, 2465 (1999).
95. K. M. Jones, P. Visconti, F. Yun, *et al.*, Appl. Phys. Lett. **78**, 2497 (2001).
96. M. Yasutake, D. Aoki, and M. Fujihira, Thin Solid Films **273**, 279 (1996).
97. J. W. Hong, G. H. Noh, S. I. Park, *et al.*, Phys. Rev. B **58**, 5078 (1998).
98. M. Saint Jean, S. Hudlet, C. Güthmann, and J. Berger, Phys. Rev. B **56**, 15391 (1997).
99. C. Schönenberger and S. F. Alvarado, Phys. Rev. Lett. **65**, 3162 (1990).
100. L. M. Eng, M. Abplanalp, and P. Günter, Appl. Phys. A **66**, S679 (1998).
101. L. M. Eng, J.-H. Güntherodt, G. Rosenman, *et al.*, J. Appl. Phys. **83**, 5973 (1998).
102. F. Saurenbach and B. D. Terris, Appl. Phys. Lett. **56**, 1703 (1990).
103. K. Franke, Ferroelectr. Lett. Sect. **19**, 25 (1995).
104. M. Labardi, V. Likodimos, and M. Allegrini, Phys. Rev. B **61**, 14390 (2000).
105. C. Durkan, D. P. Chu, P. Migliorato, and M. E. Welland, Appl. Phys. Lett. **76**, 366 (2000).
106. H. Q. Ni, Y. F. Lu, Z. Y. Liu, *et al.*, Appl. Phys. Lett. **79**, 812 (2001).

107. H. Bluhm, A. Wadas, R. Wiesendanger, *et al.*, Appl. Phys. Lett. **71**, 146 (1997).
108. G. H. Buh, H. J. Chung, and Y. Kuk, Appl. Phys. Lett. **79**, 2010 (2001).
109. J. F. Bresse and S. Blayac, Solid-State Electron. **45**, 1071 (2001).
110. P. Girard, A. N. Titkov, M. Ramonda, *et al.*, Appl. Surf. Sci. **201**, 1 (2002).
111. A. Ankudinov, V. Marushchak, A. Titkov, *et al.*, Phys. Low-Dimens. Semicond. Struct. **3–4**, 9 (2001).
112. J. Lu, E. Delamarche, R. Bennewitz, *et al.*, in *Proceedings of 10th International Conference on STM/PPM* (Seoul, 1999), p. 525.
113. O. A. Semenikhin, L. Jiang, T. Iyoda, *et al.*, Phys. Chem. **100**, 18603 (1996).
114. O. A. Semenikhin, L. Jiang, T. Iyoda, *et al.*, Electrochim. Acta **42**, 3321 (1997).
115. R. Blum, A. Ivankov, S. Schwantes, and M. Eich, Appl. Phys. Lett. **76**, 604 (2000).
116. K. Yagi and M. Fujihira, Appl. Surf. Sci. **157**, 405 (2000).
117. M. Fujihira and H. Kawate, J. Vac. Sci. Technol. B **12**, 1604 (1994).
118. A. J. Keslarek, K. A. R. Costa, and F. Galembeck, Langmuir **17**, 7886 (2001).
119. A. Gil, P. J. de Pablo, J. Colchero, *et al.*, Nanotechnology **13**, 309 (2002).
120. F. Moreno-Herrero, P. Herrero, F. Moreno, *et al.*, Nanotechnology **14**, 128 (2003).
121. K. J. Kwak, S. Yoda, and M. Fujihira, Appl. Surf. Sci. **210**, 73 (2003).
122. C. Di Natale, C. Goletti, R. Paolesse, *et al.*, Sens. Actuators B **57**, 183 (1999).
123. E. Moons, A. Goossens, and T. Savenije, J. Phys. Chem. B **101**, 8492 (1997).
124. S. Yamashina and M. Shigeno, J. Electron Microsc. **44**, 462 (1995).
125. C. C. Williams, W. P. Hough, and S. A. Rishton, Appl. Phys. Lett. **55**, 203 (1989).
126. Š. Lányi, J. Török, and P. Řehůřek, J. Vac. Sci. Technol. **14**, 892 (1996).
127. G. Neubauer, S. R. Cohen, G. M. McClelland, *et al.*, Rev. Sci. Instrum. **61**, 1884 (1990).
128. T. Goddenhenrich, H. Lemke, U. Hartmann, and C. Heiden, J. Vac. Sci. Technol. A **8**, 383 (1990).
129. R. C. Barret and C. F. Quate, J. Appl. Phys. **70**, 2725 (1991).
130. R. C. Barret and C. F. Quate, Ultramicroscopy **42–44**, 262 (1992).
131. N. Nakagiri, T. Yamamoto, H. Sugimura, and Y. Suzuki, J. Vac. Sci. Technol. B **14**, 887 (1996).
132. P. Stopford, T. Lodhi, R. Elgaid, *et al.*, in *Abstracts of 11th International Conference of Scanning Tunneling Microscopy, Spectroscopy, and Related Techniques* (Vancouver, Canada, 2001), p. 354.
133. Y. Naitou and N. Ookubo, Appl. Phys. Lett. **78**, 2955 (2001).
134. C. K. Kim, I. T. Yoon, Y. Kuk, and H. Lim, Appl. Phys. Lett. **78**, 613 (2001).
135. X. Yu, F. D. Callaghan, P. J. Moriarti, *et al.*, in *Abstracts of 11th International Conference of Scanning Tunneling Microscopy, Spectroscopy, and Related Techniques* (Vancouver, Canada, 2001), p. 40.
136. A. Garcia-Valenzuela, N. C. Bruce, and D. Kouznetsov, Appl. Phys. Lett. **77**, 2066 (2000).
137. A. Born and R. Wiesendanger, Appl. Phys. A **66**, 421 (1998).
138. Y. Huang and C. C. Williams, J. Vac. Sci. Technol. B **12**, 369 (1994).
139. Y. Huang, C. C. Williams, and J. Slinkman, Appl. Phys. Lett. **66**, 344 (1995).
140. C. Donolato, Mater. Sci. Eng. B **42**, 99 (1996).
141. J. F. Marchiando, J. J. Kopanski, and J. R. Lowney, J. Vac. Sci. Technol. B **16**, 463 (1998).
142. C. C. Williams, Annu. Rev. Mater. Sci. **29**, 471 (1999).
143. J. J. Kopanski, J. F. Marchiando, D. W. Benning, *et al.*, J. Vac. Sci. Technol. B **16**, 339 (1998).
144. J. S. McMurray, J. Kim, C. C. Williams, and J. Slinkman, J. Vac. Sci. Technol. B **16**, 344 (1998).
145. J. Kim, J. S. McMurray, C. C. Williams, and J. Slinkman, J. Appl. Phys. **84**, 1305 (1998).
146. Y. Huang, C. C. Williams, and M. A. Wendman, J. Vac. Sci. Technol. A **14**, 1168 (1996).
147. F. Giannazzo, F. Priolo, V. Raineri, and V. Privitera, Appl. Phys. Lett. **76**, 2565 (2000).
148. F. Giannazzo, V. Raineri, V. Privitera, and F. Priolo, Mater. Sci. Semicond. Process. **4**, 77 (2001).
149. L. Ciampolini, F. Gainnazzo, M. Ciappa, *et al.*, Mater. Sci. Semicond. Process. **4**, 85 (2001).
150. A. Shik and H. E. Ruda, Surf. Sci. **532–535**, 1132 (2003).
151. H. Tomiye and T. Yao, Appl. Surf. Sci. **159–160**, 210 (2000).
152. R. Stephenson, A. Verhulst, P. de Wolf, *et al.*, J. Vac. Sci. Technol. B **18**, 405 (2000).
153. T. Winzell, S. Anand, I. Maximov, *et al.*, Nucl. Instrum. Methods Phys. Res. B **173**, 447 (2001).
154. J. F. Marchiando, J. J. Kopanski, and J. Albers, J. Vac. Sci. Technol. B **18**, 414 (2000).
155. O. Bowallius, A. Anand, N. Nordell, *et al.*, Mater. Sci. Semicond. Process. **4**, 209 (2001).
156. F. Giannazzo, L. Calcagno, F. Roccaforte, *et al.*, Appl. Surf. Sci. **184**, 183 (2001).
157. H. Edwards, R. McGlothlin, R. San Martin, *et al.*, Appl. Phys. Lett. **72**, 698 (1998).
158. M. L. O'Malley, G. L. Timp, S. V. Moccio, *et al.*, Appl. Phys. Lett. **74**, 272 (1999).
159. J. J. Kopanski, J. F. Marchiando, and B. G. Rennex, J. Vac. Sci. Technol. B **18**, 409 (2000).
160. R. N. Kleiman, M. L. O'Malley, F. N. Baumann, *et al.*, J. Vac. Sci. Technol. B **18**, 2034 (2000).
161. G. H. Buh, H. J. Chung, C. K. Kim, *et al.*, Appl. Phys. Lett. **77**, 106 (2000).
162. D. M. Schaadt, E. J. Miller, E. T. Yu, and J. M. Redwing, Appl. Phys. Lett. **78**, 88 (2001).
163. K. V. Smith, X. Z. Dang, E. T. Yu, and J. M. Redwing, J. Vac. Sci. Technol. B **18**, 2304 (2000).

164. T. Yamamoto, Y. Suzuki, H. Sugimura, and N. Nakagiri, Jpn. J. Appl. Phys. **35**, 3793 (1996).

165. C. J. Kang, G. H. Buh, S. Lee, *et al.*, Appl. Phys. Lett. **74**, 1815 (1999).

166. M. Hammar, E. Rodriguez Messmer, M. Luzuy, *et al.*, Appl. Phys. Lett. **72**, 815 (1998).

167. J.-K. Leong, J. McMurray, C. C. Williams, and G. B. Stringfellow, J. Vac. Sci. Technol. B **14**, 3113 (1996).

168. J.-K. Leong, C. C. Williams, J. M. Olson, and S. Froyen, Appl. Phys. Lett. **69**, 4081 (1996).

169. P. J. Hansen, Y. E. Strausser, A. N. Erickson, *et al.*, Appl. Phys. Lett. **72**, 2247 (1998).

170. H. Yamamoto, T. Takahashi, and I. Kamiya, Appl. Phys. Lett. **77**, 1994 (2000).

171. O. Bowallius and S. Anand, Mater. Sci. Semicond. Process. **4**, 81 (2001).

172. T. Hochwitz, A. K. Henning, Ch. Levey, *et al.*, J. Vac. Sci. Technol. B **14**, 440 (1996).

173. K. Kimura, K. Kobayashi, H. Yamada, and K. Matsushige, Appl. Surf. Sci. **210**, 93 (2003).

Translated by L. Man

Crystallography Reports, Vol. 49, No. 3, 2004, pp. 500–508. Translated from Kristallografiya, Vol. 49, No. 3, 2004, pp. 566–574.

CRYSTAL GROWTH

Growth and Defect Structure of CdF_2 and Nonstoichiometric $Cd_{1-x}R_xF_{2+x}$ Phases (R = Rare Earth Elements and In). I. Growth of $Cd_{1-x}R_xF_{2+x}$ Single Crystals (R = La–Lu, Y)

I. I. Buchinskaya*, E. A. Ryzhova*, M. O. Marychev, and B. P. Sobolev***

** Shubnikov Institute of Crystallography, Russian Academy of Sciences, Leninskiĭ pr. 59, Moscow, 119333 Russia*

e-mail: rahelen@ns.crys.ras.ru

*** Nizhni Novgorod State University, pr. Gagarina 23, Nizhni Novgorod, 603600 Russia*

Received December 24, 2003

Abstract—This article begins a series of publications on growth of single crystals of nonstoichiometric $Cd_{1-x}R_xF_{2+x}$ phases (R = La–Lu, Y, In) with the defect CaF_2-type structure, their crystal structures, and some properties. The present article is dedicated to the phase diagrams of the CdF_2–RF_3 systems in the region of $Cd_{1-x}R_xF_{2+x}$ formation. Their analysis shows that it is possible to synthesize homogeneous $Cd_{0.9}R_{0.1}F_{2.1}$ crystals. The dependence of the defect structure of the crystals on the type and concentration of rare earth elements is studied on specially grown $Cd_{0.9}R_{0.1}F_{2.1}$ (R = La–Lu) and $Cd_{1-x}Y_xF_{2+x}$ (x = 0.1, 0.15, 0.20) crystals. It is shown that, despite the fact that all the $Cd_{0.9}R_{0.1}F_{2.1}$ crystals melted congruently, irrespectively of the rare earth elements used, they were rather homogeneous. The chemical compositions of the $Cd_{1-x}R_xF_{2+x}$ phases (R = Sm, Gd, Tb, Ho, and Lu) determined by the method of inductively coupled plasma atomic emission spectroscopy (ICP–AES) turned out to be close to $Cd_{0.9}R_{0.1}F_{2.1}$. © *2004 MAIK "Nauka/Interperiodica".*

INTRODUCTION

The nonstoichiometric $M_{1-x}R_xF_{2+x}$ phases with the fluorite-type defect structure are the main products of high-temperature chemical interactions occurring in the MF_2–RF_3 systems (M = Ca, Sr, Ba, Cd, Pb; R are rare earth elements (RE) [1]. The interest in the structures of the $Ca_{1-x}R_xF_{2+x}$ phases is historically explained by the fact that Goldschmidt used these phases as an example of isomorphism with filling of the space in his isomorphism classification in 1926 [2]. For quite a long time, this scheme had been confirmed only by density measurements.

The first direct X-ray diffraction studies of the defect (atomic) $Ca_{0.61}Ce_{0.39}F_{2.39}$ structure were performed only in 1969 [3]. In 1970, $Ca_{1-x}Y_xF_{2+x}$ crystals were also studied [4]. Both structural determinations revealed the deviations from the Goldschmidt model. The following structural determinations were also accompanied by the study of some structure-sensitive physical properties of these compounds. The corresponding studies performed up to the year 2000 are reviewed elsewhere [5].

The $Ca_{0.61}Ce_{0.39}F_{2.39}$ crystals were studied in a period of intense search for new fluoride materials for lasers [3]. The study of their defect structures was preceded by the discovery of inhomogeneous broadening of the absorption spectra of RE ions in the crystalline CaF_2 matrices [6, 7]. This fact indicated the formation of an unusual (partly disordered) crystal structure of these nonstoichiometric phases. The characteristic spectra of the RE-doped natural and synthesized fluorite phases were first indicated in [8], but were not interpreted as having inhomogeneous broadening. In the pioneering studies of the corresponding defect structures [3, 4], fluoride ions were revealed in partly occupied interstitial positions.

Later, it was shown [5] that $Ca_{1-x}R_xF_{2+x}$ crystals possess a number of other useful physical properties controlled (often over a rather wide range) by isomorphous substitution in the fluorite structure of various RF_3 amounts (up to 50 mol % under normal pressure). The variation of the physical properties is determined by the concentration of the structural defects in the crystals. Therefore, the study of the defect structures is directly related to synthesis of new multicomponent fluoride materials.

Of the five known MF_2 compounds with the fluorite structure, only CaF_2 and BaF_2 are widespread optical fluoride materials, which are produced on the industrial scale. This explains the interest in producing not only the $Ca_{1-x}R_xF_{2+x}$, but also $Ba_{1-x}R_xF_{2+x}$, single crystals and studying their defect structures. As a result, a wide variety of new multicomponent fluoride materials with improved properties (in comparison with those of MF_2) and characteristics that are not inherent in single-component fluorides were synthesized (see Ch. 10 in [5]).

The defect structure of the $Cd_{1-x}R_xF_{2+x}$ phases has not been studied until recently. The structure of CdF_2

has not been studied in detail either. A fluorite structure was suggested for CdF_2 based only on its X-ray powder diffraction pattern [9]. The structure determinations of SrF_2- and PbF_2-based $M_{1-x}R_xF_{2+x}$ fluorite phases are also rather scarce.

The investigations considered here include the synthesis and the structural study of CdF_2 and $Cd_{1-x}R_xF_{2+x}$ single crystals with R = RE and In and fill the gap in the studies of the defect structure of nonstoichiometric CdF_2-based fluorite phases. These investigations are necessary for the reconstruction of the formation and evolution of the defect structure of nonstoichiometric phases for a series of M^{2+} cations (Ca, Sr, Ba, Cd, and Pb) and 17 rare earth (Sc, Y, La–Lu) and In ions. The defect clusters characteristic of these structures concentrate highly charged R^{3+} cations, interstitial fluoride ions, and anion vacancies and are developed differently in different crystalline MF_2 matrices.

CdF_2, with essentially covalent chemical bonding, occupies an individual place in the family of MF_2 phases with a fluorite structure. This allows one to assume that the defect structure of $Cd_{1-x}R_xF_{2+x}$ crystals should differ from that of all the other "more ionic" $M_{1-x}R_xF_{2+x}$ crystals.

The specific defect structure of CdF_2 and $Cd_{1-x}R_xF_{2+x}$ crystals is also reflected in some of their physical properties. For CdF_2, it is the transition to the semiconductor state after annealing in the reducing atmosphere (e.g., in Cd vapors). The crystals thus obtained belong to high energy-gap semiconductors (7.8 eV) and can have a number of practical applications.

The most specific property of the $Cd_{1-x}R_xF_{2+x}$ phases is their gigantic photorefractive effect, recently discovered in Ga^{3+}- or In^{3+}-activated CdF_2 crystals. The isomorphous introduction of Y^{3+} into such crystals considerably improves the spectroscopic characteristics of these new photorefractive materials [10–12], which are promising optical media for 3D holography and other applications [13]. The knowledge of the defect structure is also a necessary condition for synthesis of materials with the preset properties.

The present study is dedicated to the analysis of the phase diagrams in the CdF_2–RF_3 systems in the range of formation of the $Cd_{1-x}R_xF_{2+x}$ fluorite phases in order to evaluate the growth conditions of the respective crystals by the Bridgman method (directional crystallization with the temperature gradient). The practical goal of this study was growth of a series of crystals from the $Cd_{0.9}R_{0.1}F_{2.1}$ charge (R = La–Lu) and $Cd_{1-x}Y_xF_{2+x}$ (x = 0.1, 0.15, 0.2) charge and the refinement of their chemical composition and optical homogeneity.

EXPERIMENTAL

Selection of crystals for structural investigations. In order to localize interstitial fluoride ions (the main structural defect of the anionic motif) more precisely, it is desirable to study the crystals with the maximum possible concentration of these defects. This corresponds to the maximum RE concentration. The solubility of RF_3 in CdF_2 at eutectic temperatures varies along the RE series from 13 mol % for LaF_3 up to 31 mol % for LuF_3, with the maximum solubility being observed for Tb and Dy (34 mol %).

On the other hand, in studying the evolution of the defect structure along the RE series, one must study crystals with the same RE concentrations. As is seen from the phase diagrams (see below), this maximum concentration can be 13 mol %. This concentration can be attained in the CdF_2–LaF_3 system. However, it is not expedient to use the Bridgman method for growing the crystals from the charge with the limiting RE concentration, because the incongruent melting at the concluding growth stage of crystallization, the crystalline boule, includes the second phase (LaF_3-based solid solution).

We decided to study the structure of the $Cd_{1-x}R_xF_{2+x}$ phases with 10 mol % RF_3 (in the charge). The choice of the $Cd_{0.9}R_{0.1}F_{2.1}$ composition was dictated by our goal—the study of the evolution of the defect structure along the whole RE series. As will be shown later, the compounds with such compositions melt incongruently irrespective of the RE and are not the optimum materials for growth of single crystals with homogeneous distributions of the impurity component (RF_3). The possibility of growing homogeneous $Cd_{0.9}R_{0.1}F_{2.1}$ crystals can be estimated by considering the phase diagrams of the CdF_2–RF_3 systems from [14–16].

To study the variations in the defect structure of the $Cd_{1-x}R_xF_{2+x}$ crystals as functions of the RE content, we considered a series of $Cd_{1-x}Y_xF_{2+x}$ solid solutions (x = 0.1, 0.15, 0.2). The fluorite phases with yttrium also served as model objects in many earlier structural investigations.

Analysis of phase diagrams in the CdF_2–RF_3 systems in the range of $Cd_{1-x}R_xF_{2+x}$ formation with the aim of growing homogeneous $Cd_{0.9}R_{0.1}F_{2.1}$ crystals. Figure 1 shows the regions of the diagrams of the condensed state of the CdF_2–RF_3 systems according to [14–16]. The CdF_2-based solid solutions with the fluorite structure are formed over the wide range of concentrations and have flat liquidus curves. In the systems with R = Sm–Er, the liquidus curves have their maxima [15], where the solution of the binary composition melts congruently (without the change of the composition). It is these compositions that are most favorable for growing homogeneous single crystals.

Mildly sloping liquidus curves (melting) at short temperature intervals between the liquidus and solidus

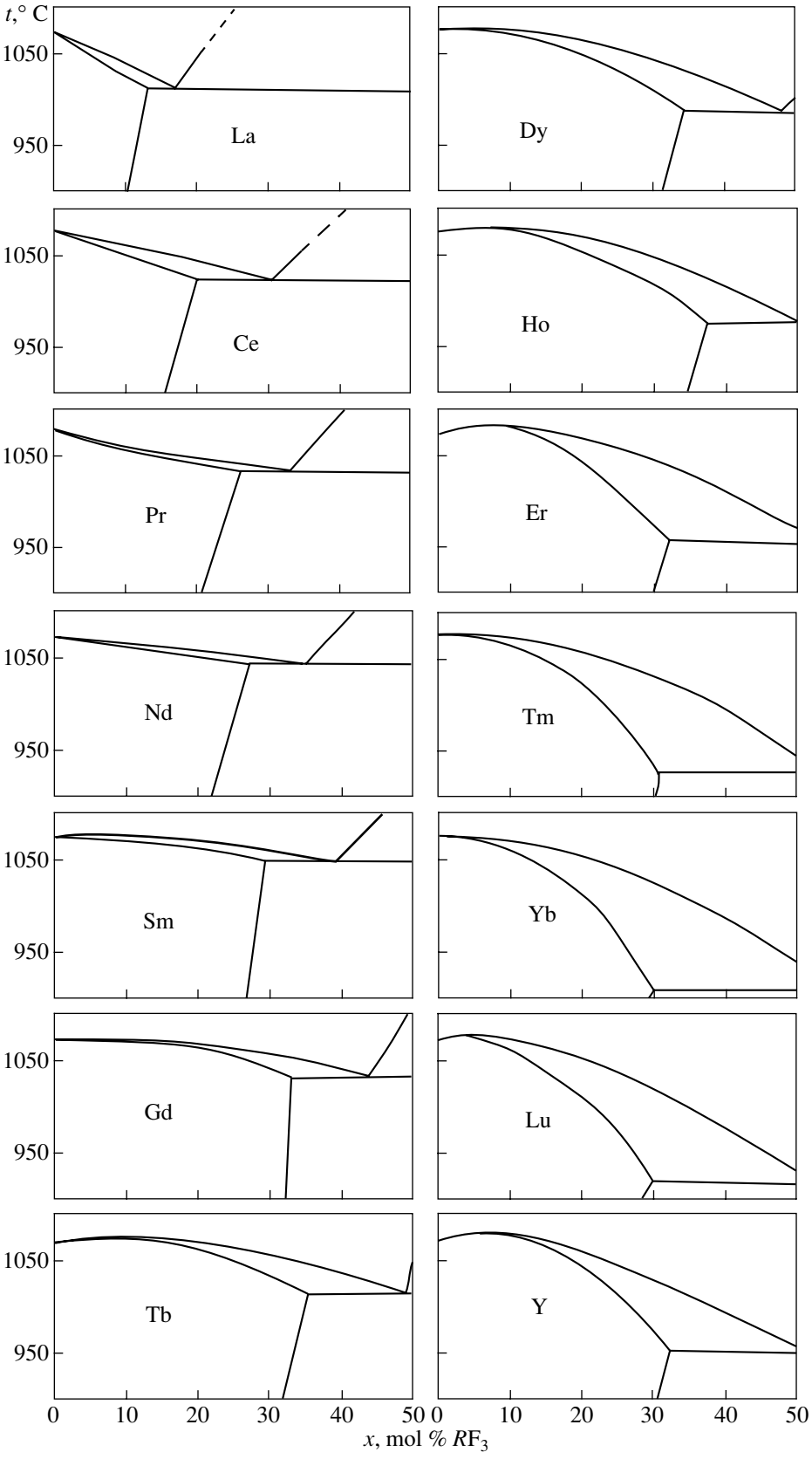

Fig. 1. Fragments of the phase diagrams of the $Cd_{1-x}R_xF_{2+x}$ (R = La–Lu, Y) systems [14–16].

Table 1. Coefficients of the A_1, A_2, and A_3 polynomials, which describe the liquidus temperature and the distribution coefficients k_0 at infinite dilution, and the coordinates C_L and T of the maxima on the liquidus and solidus curves of the $Cd_{1-x}R_xF_{2+x}$ fluorite phases

R	$T_L = 1075 + A_1C_L + A_2C_L^2 + A_3C_L^3$			k_0	Calculated coordinates of the maxima on the liquidus and solidus curves of $Cd_{1-x}R_xF_{2+x}$		k_0 [22]	Coordinates of the maxima on the liquidus and solidus curves of $Cd_{1-x}R_xF_{2+x}$ [16]	
	A_1	A_2	A_3		C_L, mol %	t, °C		C_L, mol %	t, °C
La	−3.2687	−0.015		0.23			0.28		
Ce	−0.8725	−0.1059	0.0028	0.79			0.79		
Pr	−1.6809	0.0188		0.60			0.74		
Nd	−1.4617	0.0173		0.66			0.77		
Sm	0.1395	−0.0167		1.03	4.2	1075.3	0.91	4	1076
Gd	0.2405	−0.0256		1.06	4.7	1075.6	0.95	4	1076
Tb	0.3428	−0.0326		1.08	5.3	1075.9	1.05	6.5	1077
Dy	0.4931	−0.0451		1.12	5.5	1076.3	1.24	6.5	1078
Ho	1.0193	−0.0721	0.0003	1.24	7.4	1078.7	1.21	7.5	1080
Er	1.0132	−0.0731		1.24	6.9	1078.5	1.31	7.5	1081
Tm	0.4778	−0.0543		1.11	4.4	1076.1	1.24		
Yb	0.7963	−0.0948	0.0005	1.19	4.3	1076.6	1.17		
Lu	1.0505	−0.1266	0.0010	1.25	4.4	1077.3	1.22		
Y	1.9634	−0.1520	0.0014	1.46	7.1	1081.8	1.38	5	1077

lines (solidification) allow one to select crystallization parameters that allow growth of almost homogeneous binary crystals. This can be attained if the shape of the crystallization front is either flat or close to flat.

Consider the morphological stability for a flat crystallization front of a binary solid solution under the conditions of the concentration supercooling in the CdF_2–RF_3 systems. The concentration supercooling is considered to be the main cause of concentration fluctuations of the impurity component in a growing crystal and the formation of a cellular substructure.

To characterize the stability of the flat front of a binary melt under the conditions of supercooling [15, 17, 18], one must use the stability function of the flat crystallization front $F(x)$,

$$F(x) = m\Delta x < GD/V, \quad (1)$$

where $\Delta x = x_S - x_L$ is the change in the concentration at the crystallization front, m is the tangent of the slope angle on the liquidus line (dT_L/dx), G is the temperature gradient in the crystallization zone, D is the diffusion coefficient, and V is the growth rate of the crystal. The applicability conditions and the form of the stability function are considered in detail elsewhere [15, 17–19].

The physical sense of the $F(x)$ function is as follows. If the combination of the parameters of the growth process GD/V at the given concentration x has the value exceeding that of $F(x)$, then the flat crystallization front is stable. Obviously, if $F(x) = 0$, the flat crystallization front is stable at any growth parameters.

To calculate $F(x)$, we used the DTA data for the CdF_2–RF_3 system obtained in [14] (Fig. 1). The technical difficulties of the experimental determination of the solidus curves resulted in the fact that, for most of the systems, these curves were not determined at all or were determined with a low accuracy. This results in considerable errors in the calculated distribution coefficients and stability functions.

The liquidus curves in all the systems were approximated by the second- and third-degree polynomials. The polynomials were selected in such a way that they described quite well the regions of the low and moderate concentrations of an RE-fluoride (up to 15 mol %). This allowed us to find analytically the tangent of the slope angle of the liquidus curve, m. Table 1 lists the coefficients of the polynomials, the distribution coefficients k_0 for infinitesimal amounts of impurities (infinite dilution) determined from the initial slope of the liquidus curve, and the coordinates of the maxima on

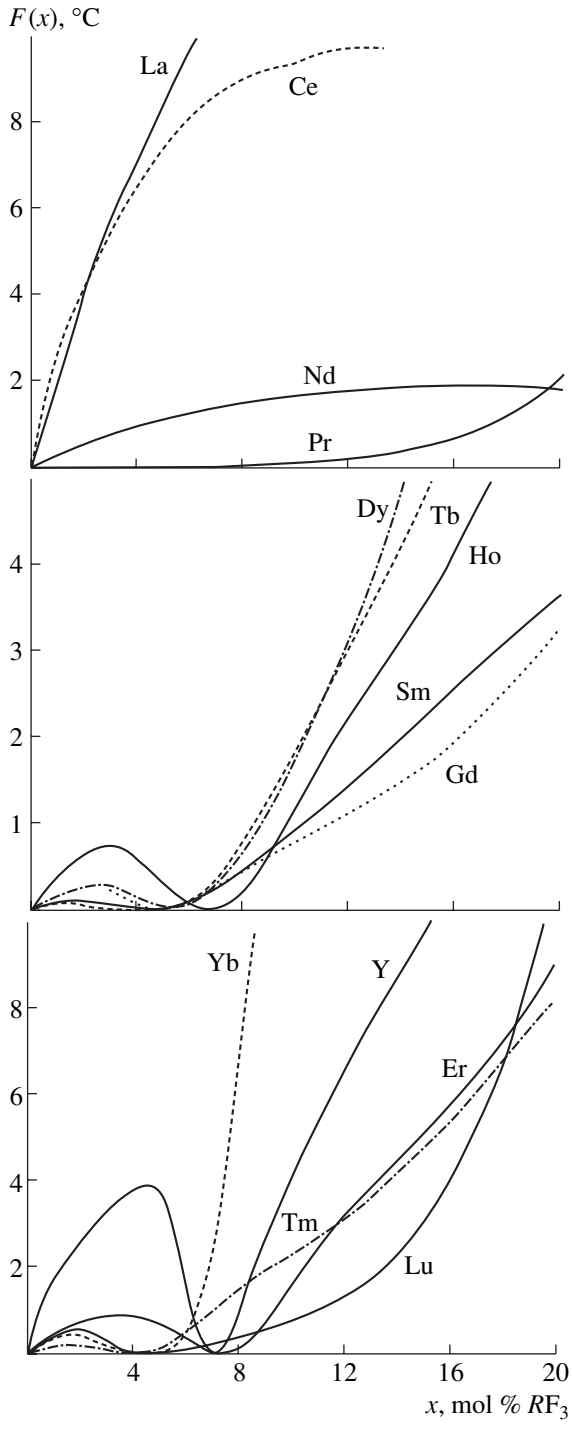

Fig. 2. Stability functions $F(x)$ of a flat crystallization front of the $Cd_{1-x}R_xF_{2+x}$ solid solutions (R = La–Lu, Y).

the liquidus curves determined from the calculated polynomials.

The calculations allow one to assume the existence of the maxima on the solidus and liquidus lines of solid solutions not only in the systems where R = Sm–Er, but also further, up to Lu. This assumption should be verified experimentally, because the coordinates of the maxima exceed the melting point of CdF_2 by only a few degrees, which is within the accuracy of the determination of the phase-transition temperatures by the DTA method.

In addition, Table 1 also lists the k_0 values calculated from the slopes of the polynomials of degree 3 [20] based on the same experimental data [14–16] and also the coordinates of the maxima on the liquidus curves based on data [15]. The difference between the k_0 values from [20] and our data is explained by the fact that the liquidus temperatures in [20] were approximated by the polynomials over wider concentration ranges. The calculated temperatures differ from the experimental ones by not more than 5°C. This corresponds to the accuracy of the DTA experiment. However, one has to take into account that, at this experimental accuracy and such a flatness of the liquidus curve, the error in the determination of the initial slope of the liquidus curve can be rather pronounced. To decrease the error due to approximation, we limited our consideration to the concentration range 0–15 mol %. The composition region we are interested in (about 10 mol %) lies within this interval. At the same time, such a consideration ensures the closeness of our calculations of the liquidus temperature in the range of low and moderate concentrations to the true values, because, in all the systems, the liquidus curve is not approximated with a sufficient accuracy by a polynomial of degrees 2 or 3 in the whole range of phase homogeneity.

The solidus curves for some systems having no maxima on the solidus and liquidus curves were also approximated by polynomials of degree 2. The Δx values were determined from the phase diagrams. The dependences of the stability function on the composition thus obtained are shown in Fig. 2.

In [21], the liquidus and solidus curves and the stability function for the $Cd_{1-x}Ho_xF_{2+x}$ solid solution were processed more accurately. The coordinates of the maxima and the stability functions obtained in [21] practically coincide with our estimations.

Change of the stability function along the RE series depending on their concentrations. Of the three parameters G, D, and V determining the stability function, only the growth rate can be controlled under the experimental conditions. The temperature gradient is constant irrespectively of combination of a heater, a crucible with the substance, and thermal screens. In the first approximation, the diffusion coefficient of the impurity component was constant and had different values for different RE. One could only vary the velocity of the crucible motion through the hot zone. In the first approximation, it was assumed that this rate was equal to the crystallization rate, at least at the initial and middle parts of the crucible.

Thus, the problem of growth of homogeneous (without cells) $Cd_{0.9}R_{0.1}F_{2.1}$ crystals incongruently melting irrespectively of the RE element reduced to the appropriate selection of the growth rate to satisfy the inequal-

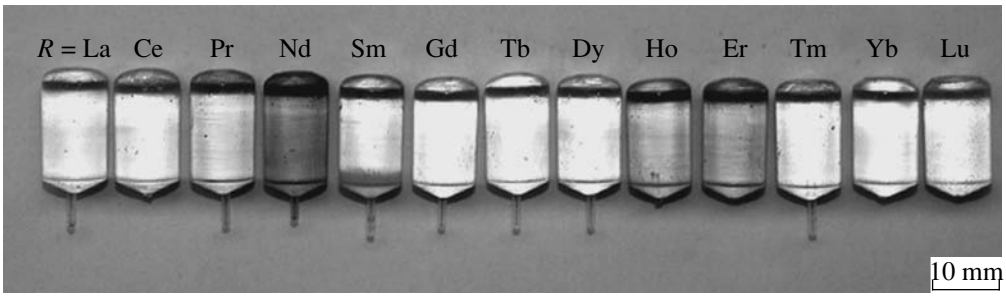

Fig. 3. Crystals of nonstoichiometric $Cd_{1-x}R_xF_{2+x}$ phases (R = La–Lu) grown from melt.

ity $F(x) < GD/V$. This is usually attained by selecting the minimum velocity of the crucible descending at the reasonable duration of the growth cycle. The present study aimed at growing a series of $Cd_{1-x}R_xF_{2+x}$ crystals sufficiently homogeneous for further structural studies.

It is seen from Fig. 2 that the stability function for the $Cd_{0.9}R_{0.1}F_{2.1}$ composition has a higher value for the systems with R = La and Ce. Using this function, it is possible to evaluate the growth rate necessary for growing homogeneous single crystals, $V < GD/F(x)$. Since no diffusion coefficients R^{3+} for the CdF_2 matrix can be found in the literature, we used for the approximate estimation the diffusion coefficients R^{3+} known for the SrF_2 matrix [18]. Thus, we discovered that the growth rate of $Cd_{0.9}La_{0.1}F_{2.1}$ crystals should not exceed 1.7 mm/h.

A considerable decrease in the crystallization rate is limited by the fact that an increase of the time of melt existence leads to losses of the substance for evaporation. The probability of incongruent evaporation of the $Cd_{1-x}R_xF_{2+x}$ melt is rather high. Therefore, long existence of the melt can result in considerable deviations of its composition from the composition of the initial charge. At high pressure of the CdF_2 vapors, the crystals would be enriched with rare earth elements.

The stability functions for the $Cd_{0.9}R_{0.1}F_{2.1}$ crystals with R = Nd–Lu are lower, and, therefore, it is easier to attain a flat crystallization front. A similar estimate of the growth rate made for homogeneous single crystals yields less than 11.6 mm/h for Gd and less than 11 mm/h for Ho. As a result, for the experiment we selected a rate of crucible descent equal to 9.5 mm/h. This rate is sufficient for growth of most of $Cd_{0.9}R_{0.1}F_{2.1}$ crystals without cellular substructure and, at the same time, gives rise to no considerable substance losses for evaporation.

Crystal growth. Traditionally, single crystals of fluorides of divalent metals and solid solutions on their basis are grown from melts by the Bridgman method. Earlier, we managed to grow CdF_2, $Cd_{1-x}R_xF_{2+x}$ single crystals with low (up to 1 mol %) RF_3 concentrations (R = La, Ce, Nd, Sm, Eu, Tb, Tm, In, Bi) and with 3–5 mol % RF_3 concentrations (R = Ce, Nd, Sm, Eu, Tb, Tm) at an R concentration exceeding 10 mol % (R = Ce, Nd, Gd, Dy, Ho, Er, Tm, Yb, and In). The physical properties of these crystals were considered in papers the references to which may be found in [5]. However, these crystals form no isoconcentration series at all the RE elements.

The single crystals forming the isoconcentration series $Cd_{0.9}R_{0.1}F_{2.1}$ (R = La–Lu) were grown from melt by the Bridgman method in the atmosphere of helium and the products of tetrafluoroethylene pyrolysis. The initial materials were extra pure grade CdF_2 and spectroscopic grade RF_3. The reagents were preliminarily dried in a graphite crucible at ~100°C in vacuum (~1 Pa) in the growth setup and, then, were melted and kept for 6 h at a low overheating in the fluorinating atmosphere. Then, the melts were rapidly cooled and formed polycrystalline ingots.

The growth from thus fluorinated reagents was performed in an opened graphite crucible with 13 cells descended at a rate of 9.5 ± 0.5 mm/h at a temperature gradient of about 50 deg/cm. The cooling rate was ~250 K/h. The substance loss during growth amounted to 0.5–1.5 wt %. The crystals grown were 12 mm in diameter and ~30 mm in length (Fig. 3).

The series of $Cd_{1-x}Y_xF_{2+x}$ crystals (x = 0.1, 0.15, 0.2) were grown in a separate experiment under analogous conditions with the following process parameters: the rate of crucible descending was 10 mm/h, the tem-

Table 2. Chemical composition of the crystals

R	The determined R concentration, wt % (ICP-AES)	Refined solid-solution formula
Sm	9.5 ± 0.5	$Cd_{0.984}Sm_{0.096}F_{2.096}$
Ho	9.9 ± 0.5	$Cd_{0.895}Ho_{0.105}F_{2.105}$
Tb	9.9 ± 0.5	$Cd_{0.898}Tb_{0.102}F_{2.102}$
Gd	10.0 ± 0.5	$Cd_{0.900}Gd_{0.100}F_{2.100}$
Lu	10.2 ± 0.5	$Cd_{0.889}Lu_{0.111}F_{2.111}$

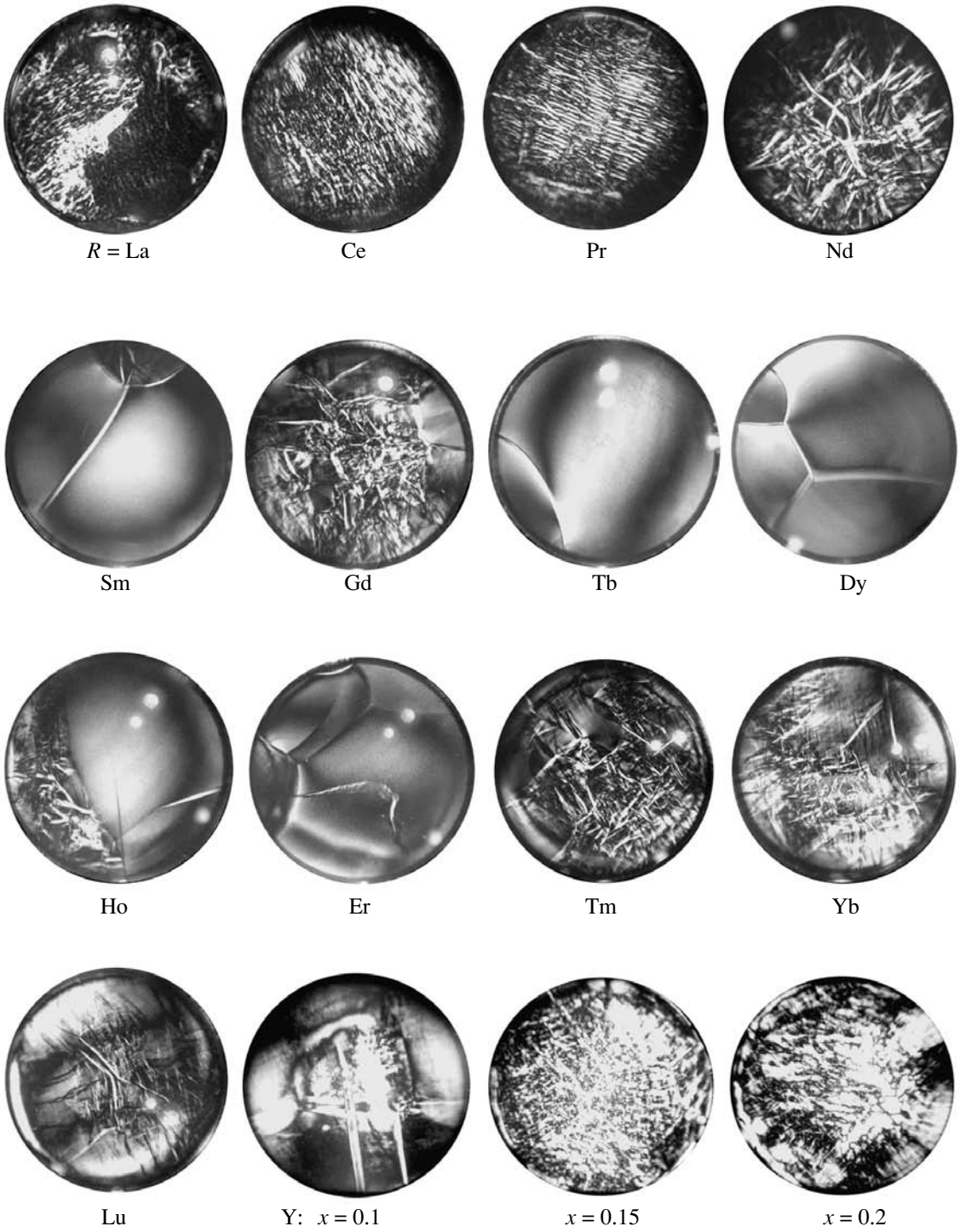

Fig. 4. Photographs of polished $Cd_{0.9}R_{0.1}F_{2.1}$ plates (R = La–Lu) and $Cd_{1-x}Y_xF_{2+x}$ (x = 0.1, 0.15, 0.2) plates in the polarized light.

perature gradient was ~30 K/cm, and the cooling rate varied according to the special program from ~150 to 300 deg/h. The material loss during growth was ~0.5 wt %.

Determination of chemical compositions of crystals. The RF_3 content in some $Cd_{1-x}R_xF_{2+x}$ crystals was determined in the Laboratory of Chemical Analysis of the Russian Research Center Kurchatov Institute by the method of inductively coupled plasma atomic emission spectrometry (ICP-AES) (Table 2).

In the middle parts of the crystal boules selected for chemical analysis, the crystal compositions determined

Table 3. Diffusion coefficients of impurities in $Cd_{1-x}R_xF_{2+x}$ crystals

R	x, mol fraction	$D \times 10^6$, cm^2/s	R	x, mol fraction	$D \times 10^6$, cm^2/s
Nd	0.10*	9	Er	0.10*	9.5
Sm	0.096	5	Tm	0.10*	11.6
Gd	0.100	4.2	Yb	0.10*	84.4
Ho	0.105	7.9	Lu	0.111	5

* RE concentration in the charge.

turned out to be close to the charge composition (10 mol % RF_3), from which follow two conclusions. First, the selected growth rate was sufficient for suppression of the RE differentiation along the crystal length and formation of a cellular substructure (RE differentiation along the crystal diameter) for most RE elements of the yttrium subgroup. Second, under the conditions of growth experiments, it became possible to avoid considerable changes in the crystal composition because of evaporation of incongruent melting.

Estimation of crystal homogeneity. We cut 3-mm-thick plates from the middle parts of crystalline boules gown. The polished plates were photographed in polarized light in crossed Nicol prisms in a MIN-8 polarization microscope (Fig. 4).

The blocks with the nucleated cellular substructure were observed in the $Cd_{0.9}R_{0.1}F_{2.1}$ plates with R = Sm, Ho, and Er to a lesser extent and, to a larger extent, with R = Nd, Gd, Tm, Yb, and Lu. The photographs clearly show that, in some crystal blocks, cells are formed. Only the crystals with R = La, Ce, and Pr had a well developed cellular substructure. The crystals with R = Tb and Dy were almost free of cells. The plates cut out from the $Cd_{1-x}Y_xF_{2+x}$ crystals (x = 0.1, 0.15, 0.2) demonstrated gradual quality deterioration with an increase of the yttrium concentration. At x = 0.1, cells are formed only in some blocks; at x = 0.15, they are formed over the whole plate volume of the plate; and, at x = 0.2, a well developed cellular structure was accompanied by a pronounced block structure.

Estimation of diffusion coefficients of some RE ions in the melt. The presence in $Cd_{0.9}R_{0.1}F_{2.1}$ crystals with R = Nd, Sm, Gd, and Ho–Lu of regions with a nucleated cellular substructure allowed us to assume that these regions had a concentration close to the critical concentration of the formation of a cellular substructure. If this assumption is correct, then it is possible to estimate the diffusion coefficient in the melt of the impurity component, an RE ion. At G = 50 K/cm, V = 9.5 mm/h, and the corresponding values of the stability function, we arrive at the results indicated in Table 3.

The obtained diffusion coefficients of R^{3+} ions coincide, by an order of magnitude, with the values obtained earlier for these ions in the fluorite matrix [18].

CONCLUSIONS

The $Cd_{1-x}R_xF_{2+x}$ (R = La–Lu) single crystals for studying the evolution of the defect structure along the RE series are synthesized from the charge containing 10 mol % RF_3.

The $Cd_{1-x}Y_xF_{2+x}$ crystals with 10, 15, and 20 mol % YF_3 for the study of the concentration variations of the defect structure are also synthesized. The phase diagrams of the CdF_2–RF_3 systems are analyzed in the range of the formation of the $Cd_{1-x}R_xF_{2+x}$ phases. It is shown that, despite the incongruent melting of the $Cd_{0.9}R_{0.1}F_{2.1}$ compounds irrespective of the RE present, it is possible to grow rather homogeneous crystals. The chemical analysis of the $Cd_{1-x}R_xF_{2+x}$ crystals grown with R = Sm, Gd, Tb, Ho, and Lu showed that they have compositions close to the composition of the concentration series $Cd_{0.9}R_{0.1}F_{2.1}$ selected for the X-ray diffraction analysis. The optical homogeneity of the middle regions of crystalline $Cd_{1-x}R_xF_{2+x}$ boules is studied. It is shown that the homogeneity of the samples allows their X-ray diffraction analysis.

ACKNOWLEDGMENTS

The study is supported by the ISTC (project no. 2136) and the Grant of the President of the Russian Federation for support of the Scientific Schools of the Russian Federation (NSh-1954.2003).

REFERENCES

1. B. P. Sobolev, *The Rare Earth Trifluorides*, Part 1: *The High Temperature Chemistry of Rare Earth Trifluorides* (Inst. d'Estudis Catalans, Barcelona, 2000).
2. V. M. Goldschmidt, T. Barth, G. Lunde, and W. Zachariasen, Skr. Nor. Vidensk.-Akad. [Kl.] 1: Mat.-Naturvidensk. Kl. **1** (2), 1 (1926).
3. V. B. Aleksandrov and L. S. Garashina, Dokl. Akad. Nauk SSSR **189** (2), 307 (1969) [Sov. Phys. Dokl. **14**, 1040 (1969)].
4. A. K. Cheetham, B. E. F. Fender, D. Steele, *et al.*, Solid State Commun. **8** (3), 171 (1970).
5. B. P. Sobolev, *The Rare Earth Trifluorides*, Part 2: *Introduction to Materials Science of Multicomponent Metal Fluoride Crystals* (Inst. d'Estudis Catalans, Barcelona, 2001).
6. Kh. S. Bagdasarov, Yu. K. Voronko, A. A. Kaminskii, and V. V. Osiko, Phys. Status Solidi **12** (2), 905 (1965).
7. Kh. S. Bagdasarov, Yu. K. Voron'ko, A. A. Kaminskiĭ, *et al.*, Kristallografiya **10** (5), 746 (1965) [Sov. Phys. Crystallogr. **10**, 626 (1965/1966)].
8. N. Chatterjee, Z. Kristallogr. **102** (4), 245 (1940).

9. H. M. Heandler and W. J. Bernard, J. Am. Chem. Soc., 5218 (1951).
10. A. I. Ryskin, A. S. Shcheulin, B. Koziarska, *et al.*, Appl. Phys. Lett. **67** (1), 31 (1995).
11. A. I. Ryskin, A. S. Shcheulin, E. V. Miloglyadov, *et al.*, Appl. Phys. **83**, 2215 (1998).
12. R. A. Linke, A. S. Sheulin, A. L. Ryskin, *et al.*, Appl. Phys. B **72**, 677 (2001).
13. B. P. Sobolev, P. P. Fedorov, I. I. Buchinskaya, *et al.*, RF Patent No. 2161337 (27 December 2000).
14. M. A. Sattarova, Candidate's Dissertation in Chemistry (Dushanbe, 1987).
15. P. P. Fedorov, Doctoral Dissertation in Chemistry (Moscow Inst. of Fine Chemical Technology, Moscow, 1991).
16. P. P. Fedorov, Z. I. Zhmurova, and B. P. Sobolev, Zh. Neorg. Khim. **29** (9), 2346 (1984).
17. T. M. Turkina, P. P. Fedorov, and B. P. Sobolev, Kristallografiya **31** (1), 146 (1986) [Sov. Phys. Crystallogr. **31**, 83 (1986)].
18. P. P. Fedorov, T. M. Turkina, V. A. Meleshina, and B. P. Sobolev, in *Crystal Growth* (Nauka, Moscow, 1988), Vol. 17, p. 198.
19. B. P. Sobolev, Z. I. Zhmurova, V. V. Karelin, *et al.*, in *Crystal Growth*, Ed. by Kh. S. Bagdasarov and É. L. Lube (Nauka, Moscow, 1988), Vol. 16, p. 58.
20. P. P. Fedorov, T. M. Turkina, O. I. Lyamina, *et al.*, Vysokochist. Veshchestva, No. 6, 67 (1990).
21. P. P. Fedorov, Neorg. Mater. **37** (1), 95 (2001).

Translated by L. Man

Crystallography Reports, Vol. 49, No. 3, 2004, pp. 509–510. Translated from Kristallografiya, Vol. 49, No. 3, 2004, pp. 575–576.

JUBILEES

Vladimir Aleksandrovich Koptsik (On the Occasion of His 80th Birthday)

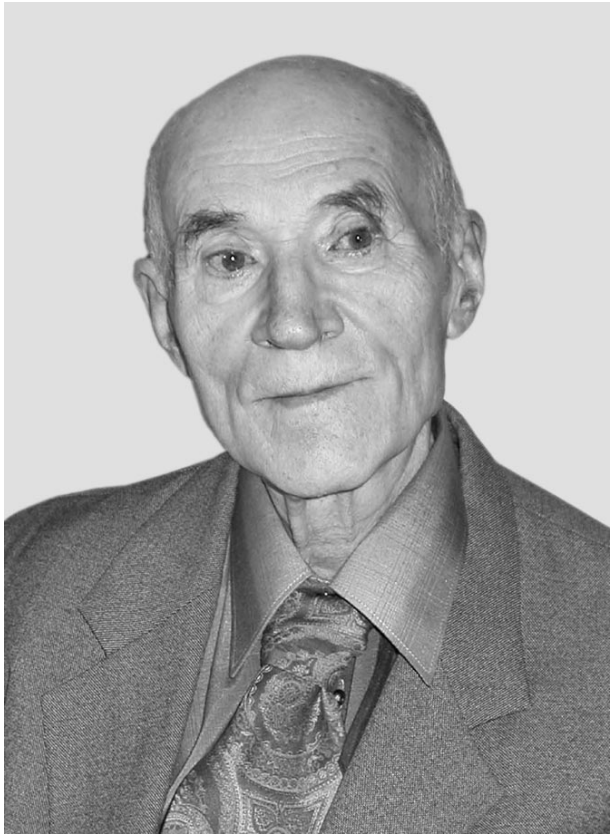

Vladimir Aleksandrovich Koptsik, a doctor of physics and mathematics, an honored professor of Moscow State University, an honored scientist of the Russian Federation, and one of the leading scientists in the field of theoretical crystal physics, in particular the theory of generalized symmetry of real crystals and crystal-like structures and its practical application, turned 80 on February 26, 2004.

Koptsik graduated from the Faculty of Geology of Moscow State University (the Chair of Crystallography and Crystal Chemistry) in 1949. In 1953, he defended his candidate's dissertation under the supervision of A.V. Shubnikov. In 1963, Koptsik defended his doctoral dissertation. Being the closest student and assistant of Academician Shubnikov, Koptsik made great efforts to organize the new Chair of Crystallography and Crystal Physics at the Faculty of Physics of Moscow State University in 1953, where he has been working continually ever since. From 1968–1974, he was the head of the Chair after Shubnikov, where he has been working continuously since 1953. In 1993, the Chair of Crystallography and Crystal Physics was reorganized into the Chair of Physics of Polymers and Crystals, which was headed by Prof. A.R. Khokhlov.

Koptsik is the author of more than 300 publications and several well-known monographs and textbooks. The works of Koptsik and his students have made a significant contribution to the physics of electrically and magnetically ordered crystals, the method of tensor representation of physical properties of anisotropic media, the theory of generalized symmetry of real crystals and quasicrystals, and the development of symmetry and applied aspects of the theory of structural phase transitions.

In the 1950s–1960s, Koptsik performed extended research on the basis of structural symmetry criteria, which made it possible to double the number of piezoelectric crystals (up to several hundreds) and pyroelectrics (to several tens) that were known at the time.

Since the 1960s, the scientific interests of Koptsik have been focused on the theory of the generalized symmetry of crystals and its physical applications. Koptsik's monograph *Shubnikov groups* (1966) became for many researchers a handbook on the symmetry and physical properties of crystal structures, in which crystallographic groups are described with the same completeness as in the well-known *International Crystallographic Tables*. In the monograph *Symmetry in Science and Art*, published together with Shubnikov in 1972 (translated into English and published by Plenum Press (New York, London) in 1974), Koptsik summarized the results of derivation of polychromatic spatial and infinitely colored point symmetry groups performed by he and his students and developed the magnetic interpretation of these groups. He was awarded the Fedorov prize of the Russian Academy of Sciences for this cycle of studies in 1973.

In 1974, Koptsik proposed a new effective approach to theoretical simulation of the structure and physical properties of real crystals, based on tangling of internal-symmetry groups of structural moduli (describing their possible physical states) with external-symmetry groups, which describes the short- and long-range order in crystals on the whole.

In 2004, the second, extended, edition of the monograph *Symmetry in Science and Art* is to be published by the Institute of Computer Science in Izhevsk together with the Regular and Chaotic Dynamics Pub-

1063-7745/04/4903-0509$26.00 © 2004 MAIK "Nauka/Interperiodica"

lishing House. The long period of time (more than 30 years) that has passed since the first edition called for the addition of new material to the book.

The well-known Curie principle, which relates the symmetry of crystals to their physical properties, has been extended to the Curie–Shubnikov–Koptsik principle for composite physical systems.

In accordance with the Curie principle, which is a symmetry aspect of the causality principle, the symmetry of physical properties of crystals cannot be lower than the symmetry of the crystal structure. However, the symmetry of solid condensed media composed of identical (or symmetrically equal) subsystems is not reduced to the intersection of the symmetry groups of these subsystems; according to the Curie–Shubnikov–Koptsik principle, it is generally higher. Hence, the symmetry of a system of physical consequences turns out to be no lower than the symmetry of the system of reasons responsible for these consequences, whereas individual properties of crystals may have any (equal, higher, or lower) symmetry as compared with the symmetry of the system of reasons.

As Curie formulated, "dissymmetry creates the phenomenon." This is true. At the same time, dissymmetry symmetrizes self-organizing (cyberonic) systems composed of identical (structural) parts of subsystems.

Symmetry in Science and Art considers both the pentagonal and cosahedric types of symmetry of quasicrystals that allow for long-range orientational order. In a special appendix to this book, A.L. Talis considers the non-Euclidean symmetry of tetracoordinated structures in terms of projective geometry and algebraic groups. In another appendix, S.V. Petukhov describes the projective symmetry in the world of biomorphology and the structure of the genetic code of such an extremely complex synergetic system as the human brain. As an example of a manifestation of laws of symmetry in art, the compositional symmetry in Pushkin's poetry is considered.

As was shown by Koptsik and his students in the 1980s, a positional approach that they developed, covering all the generalizations of spatial symmetry groups, can be used for modular description (on the basis of lattice models) of all the forms of ordering of condensed media—from amorphous media to incommensurately modulated phases, polymers, and quasicrystals. This approach makes it possible to predict possible physical properties of composite material systems on the basis of a generalized deterministic principle (called by Koptsik the "Shubnikov–Curie principle").

Koptsik is deeply engaged in administrative and pedagogical work. He has supervised 25 candidate's and 7 doctoral dissertations. He organized has the original special courses "Foundations of Crystal Physics," "Principles of Solid-State Physics," "Theoretical Group and Tensor Methods in Solid-State Physics," and "Physics of Crystals with Defects" for students of the Division of Solid-State Physics. Koptsik is a member of several Scientific and Qualification Councils. He is also a member of the editorial boards of the scientific journal *Kristallografiya* (Crystallography Reports) and the international journal *Symmetry: Science and Culture*.

Prominent among Koptsik's studies is a unique cycle of investigations (started in 1972) devoted to the development of synergetic–informational structural–semiotic theories of art. These studies make an original contribution to the problem of bringing together two cultures—natural-science and humanities education—and develop and adapt exact methods of natural sciences as applied to complex systematic investigations of art and its evolution. A good example is the theory of generalized compositional symmetry of creative works of art that was developed by Koptsik.

Russian specialists in crystallography, as well as the editorial board and staff of *Kristallografiya* congratulate Vladimir Aleksandrovich Koptsik on his 80th birthday and wish him good health and success in his scientific work.

Translated by Yu. Sin'kov

Crystallography Reports, Vol. 49, No. 3, 2004, pp. 511–515. Translated from Kristallografiya, Vol. 49, No. 3, 2004, pp. 577–581.

MEMORIAL DATA

On the Occasion of the 100th Birthday of Marina Viktorovna Klassen–Neklyudova (1904–2004)

On January 7, 2004, 100 years had passed since Honored Scientist and Engineer of the Russian Federation and Doctor of Physics and Mathematics Prof. Marina Viktorovna Klassen–Neklyudova was born. Klassen–Neklyudova founded the Laboratory of Mechanical Properties of Crystals of the Institute of Crystallography of the Russian Academy of Sciences and headed this laboratory continuously for many years. Her name is inseparable from the development of the physics of durability and plasticity of materials.

The life of Klassen–Neklyudova (1904–1995), which was full of creative achievements, deep feelings, and gifts and blows of fortune, was, on the whole, successful. But her life, closely connected as it was with that of the 20th century, reflected all the joys, great achievements, and tragedies of that time. Moreover, it was a human fate, in light of which time revealed itself completely as something given to us for creative freedom, pure intentions, benevolence, and happiness. Let us highlight some of the landmarks and follow the naturally outlined stages of this life. Chronologically, three such stages can be selected.

Early years. St. Petersburg. Marina Klassen was born into a family closely connected to science and engineering (her father, Viktor Émil'evich, a Dutchman by birth, was a professor at the Polytechnical Institute). Moreover, she was brought up in a scientific and engineering environment—in a cottage settlement of the Academy of Sciences in a suburb of St. Petersburg. One of the Klassens' neighbors was A.F. Ioffe; thus, the friendship between Marina and Abram Fedorovich began long before their joint work. Another frequent guest of the Klassens was the academician A.N. Krylov (the builder of the first Russian battleships), who used to play with Marina, using a top to enchant her. In summer, the family would go to the Black Sea, and the best pages of Klassen–Neklyudova's "Memoirs" (unpublished) are devoted to their life in Gagry in 1914—the last months of serene life before the beginning of the First World War. She wrote about the sea, the park where she saw Egyptian cranes, the mountain trips and sea voyages, the arrival of the tsar (with whom she did not want to be photographed), and the two bunches of roses that were brought to the carriage, where she sat with her mother, by Prince Ol'denburgskiĭ, who happened to see them at the gate.

Obviously, the imperial motto "autocracy, orthodoxy, and nationality" was not popular in Klassens' environment (although her mother, Valentina Vladimirovna Milovidova, came from a clerical background). The people close to the Klassens were clearly mainly freethinking, partly atheistic; they strove for liberal changes, and the February Revolution was the revolution they had waited for. Nevertheless, after the October Revolution, when a great part of the intelligentsia preferred to emigrate rather than collaborate with the new authorities or was evicted from the country on the "philosophers' ships," Klassens stayed in Russia. In our opinion, along with patriotic feelings, this decision was to some extent because Viktor Émil'evich was personally acquainted with Lenin and enjoyed the confidence of the leader of the October Revolution. Being the deputy of the head of GLAVTOP, he had a mandate for authority from the Council of Workers' and Peas-

1063-7745/04/4903-0511$26.00 © 2004 MAIK "Nauka/Interperiodica"

ants' Defense signed personally by Lenin. No doubt, this circumstance provided safe conduct for the family and saved their lives not only in the 1920s—the years of trouble—but also in the period of the Great Terror.

Both the Klassens' daughters (Marina and Tat'yana) received a higher education, and the father decided to send Marina to the Netherlands to work on probation under the supervision of Burgers, the professor of hydrodynamics. However, the daughter, who had been brought up without parental tyranny, made her own choice. She became a postgraduate student at the Physicotechnical Institute under the supervision of the elder friend of her childhood— Ioffe.

Thus, the early period of Marina Klassen's life ended. The period of St. Petersburg had ended even earlier: the institute where she worked and studied was already called the Leningrad Physicotechnical Institute.

Coming into being. Leningrad. As a dissertation subject, Ioffe suggested that his postgraduate student study the nature of plastic deformation in rock salt crystals experimentally. The important results of this investigation were the step character of deformation (which was revealed for the first time) and the phenomenon of sound emission, which accompanies the process of deformation under certain conditions.

Even before Marina Viktorovna graduated from the postgraduate course, I.V. Obreimov suggested that she and L.V. Shubnikov (a relative of A.V. Shubnikov, he was a talented physicist who perished later in Stalin's concentration camps) develop a polarization-optical method for studying NaCl crystals. She discovered that, even at low temperatures, the formation and propagation of slip traces can be observed in crystals. This meant that, even at –180°C, crystals have plasticity; i.e., a completely brittle fracture is absent. The results of these investigations were included in her candidate's dissertation (1930) and were also published in the monograph *Plasticity and Durability of Crystals* (1933), which became one of the first in the world in this branch of science.

The next stage (1930–1938) of the scientific career of Marina Viktorovna was related to the study of the effect of the surface state on the durability and plasticity of solids. In essence, the case in point was to check the correctness of an observation of Ioffe according to which the durability of rock salt crystals increases upon their stretching in water and, in principle, may attain the calculated values. Some experts were skeptical of this statement. For example, the German physicist Smekal ironically called the discovered phenomenon the "Ioffe effect." According to Smekal, it was nothing but a usual effect that had been placed in quotation marks. However, Marina Viktorovna showed that the low durability of crystals observed in practice is due to the presence of a damaged layer on their surface that includes microcracks, scratches, and other defects. Dissolution of this layer radically increases the durability of samples, making it as high as theoretically possible. This is a general truth, and its validity was confirmed by an example of metals (zinc, bismuth, brass). Thus, the quotation marks were removed from the name of the Ioffe effect and it became a part of physical knowledge, and the researcher who had studied this effect became the first woman in the Soviet Union to hold the title of Doctor of Physics and Mathematics (1936).

This was the end of the first stage of the scientific career of Marina Viktorovna, which coincided with her departure from Leningrad. Another period of her life was ahead.

Achievements. Moscow. Marina Viktorovna wrote in her recollections about A. Shubnikov that "in 1937, I was obliged to leave Leningrad, the climate of which was not appropriate for my health, and go to Moscow. I have learned that Alekseĭ Vasil'evich Shubnikov is going to expand his laboratory at the Division of Geology and Mineralogy and is looking for an expert on the mechanical properties of crystals. On the May holidays, I came to Moscow and went to see Alekseĭ Vasil'evich with a list of my publications and a small monograph, published in 1933. Alekseĭ Vasil'evich received me in a comfortable sunlit study, where an ideal order reigned." He "…did not look through the list of my publications and the monograph: he knew them well. He also remembered me because he had worked in Leningrad at the Physicotechnical Institute, where he organized a laboratory for studying the growth of the large ferroelectric crystals that were required for the developments carried out by I.V. Kurchatov. Shubnikov suggested: "Put in an application." I began to work in Shubnikov's laboratory and have never regretted it, although I had to leave the best physics institute that existed at that time."

The lines of the unpublished *Autobiography* give an idea of the first impressions of the work in Moscow. It is worth noting that Marina Viktorovna left not only for another city and institute, but also for another department: instead of the People's Commissariat of Heavy Industry, which had a relatively high budget and to which the Physicotechnical Institute belonged, it was now the Academy of Sciences, which was low-budget at the time.

"Frankly speaking, I could not even imagine under what wretched conditions intense and valuable research work can proceed in the Academy of Sciences. There were neither workshops, nor laboratory assistants, nor supply department, nor materials store there. Shubnikov and his colleagues did everything with their own hands. I had to start working alone, without anything to begin with. Nevertheless, I was not depressed. I believed in the broad potentials of this laboratory, which was small at that time, and I saw later with my own eyes how this laboratory turned into the Institute of Crystallography, the first in the world, and to the development of which I have contributed."

The laboratory where Marina Viktorovna began to work had, alongside Shubnikov, eight more employees:

(a) (b)

Fig. 1. Watercolor portraits of Klassen–Neklyudova: (a) in a transparent green cloak and (b) with a mantle of golden Chinese brocade. Drawn by A.V. Fonvizin, 1940s.

N.V. Belov, V.P. Butuzov, B.V. Vitovskiĭ, G.F. Dobrzhanskiĭ, G.B. Lemmleĭn, E.E. Flint, E.V. Tsinzerling, and N.N. Sheftal'. The new researcher continued the line of investigation she had begun in Leningrad—the study of the nature of the plasticity and destruction of crystals—in the 20-m^2 area she was allotted. But, now, her scientific interests were focused on synthetic ruby crystals. In 1939–1941, she learned that ruby, which had traditionally been considered a brittle material, can be plastically deformed by prismatic sliding and rhombohedral twinning at high temperatures. Ruby exhibits anisotropy of mechanical properties, and its optical anomalies are caused by traces of plastic deformation and residual stresses arising under synthesis; thus, the conditions of annealing aimed at removing these stresses can be predicted.

The new practical achievement of Marina Viktorovna was the development of high-strength anisotropic materials—glass fibers, which were used to reinforce beams made of high-strength gypsum. The pathos of this work lay in the fact that, at the height of the Great Patriotic War, when the country lay in ruins and the fate of victory was uncertain, Marina Viktorovna, under the supervision of Academician A.E. Fersman, organized a group at the Committee for Assistance to the Red Army with the purpose of obtaining new materials for the needs of reconstruction civil engineering; i.e., the development of wartime was aimed at postwar peaceful life. Based on the investigations performed, this group developed and implemented, at a pilot plant in Moscow, technology for the fabrication of glass cords and glass plywood with a specific durability that exceeded that of steel.

In 1943, it was decided to organize the Institute of Crystallography of the Academy of Sciences. The new institute consisted of five laboratories and included, along with Laboratories 1 and 2, headed by Shubnikov and Belov, respectively, Laboratory 3, headed by Klassen–Neklyudova. It was called the Laboratory of Mechanical Properties of Crystals and Textures. The task of the new laboratory was to analyze the mechanical properties of crystals and glass-fiber materials and study the physical nature of durability.

Marina Viktorovna's last name was changed due to her marriage with Grigoriĭ Ivanovich Neklyudov, who later became a prominent engineer, the developer of a line of machines for the clock industry (the first in the Soviet Union), and a winner of the Lenin and State

Prizes. The marriage turned out to be happy and long for both wife and husband.

In the end of the war, they became friends with the artist Artur Vladimirovich Fonvizin. Fonvizin had returned not long before from Karaganda, where he had been in exile. The cold communal flat on Myasnitskaya ul. became the studio where the artist made two watercolor portraits of Marina Viktorovna. In one, Klassen–Neklyudova is dressed in a transparent green cloak (Fig. 1a); in the other, she is wearing a magnificent mantle of golden Chinese brocade (Fig. 1b). Fonvizin seems to have been enchanted by the beauty of his model, who combined a bright mind and irresistible femininity, a strong will, and anxious tenderness, realism and spirituality. People who had any sense of beauty felt it in personal contact with Marina Viktorovna. She herself possessed this sense in full measure and deeply felt the nature of the artist's creative work. In contrast to those critics who blamed Fonvizin for formalism and trying to escape from reality, Marina Viktorovna asked him to avoid naturalism in order not to make the portraits ponderous: she did not value impeccably drawn pictures "like photographs. At our place, we wanted to have a picture drawn in the inimitable conventional Fonvizin style." The point here was the loyalty of the master to the nature of his gift, rather than adhering to directives imposed from above, the effect of which often happens to be fateful. The Klassen–Neklyudovs proved to be real friends who helped Fonvizin stay at the height of his talent. Marina Viktorovna wrote in the article "Three Portraits" that "it was a real enjoyment for me to follow the creative process of this amazing artist. However, fate had an unpleasant surprise in store me. In 1947, I fell ill with influenzal encephalitis and could only lie on my back, without turning my head. Knowing that I had to lie motionless, Artur Vladimirovich sent me one of his still lives and advised me to hang it at the foot at the bed so that I could look at it. The still life showed a transparent, round glass vase with several twigs of some plant. The picture was done in soft light colors. I lay and looked at it for many months, often all day long."

And, when the illness passed, Marina Viktorovna returned to her active scientific work. She formulated two main lines of investigation for herself: the study of the mechanical properties and real structure of Rochelle salt crystals and the mechanical properties of ruby and leucosapphire crystals. Let us follow how these plans were realized.

Having known from a report of V.L. Ginzburg that macroscopically misoriented regions—domains—may exist in Rochelle salt crystals, Marina Viktorovna suggested to M.A. Chernyshova to try to visualize twins (regions in a crystal that have reoriented due to stresses) and domains with the use of polarized light. When the crystal cuts were prepared, it was learned from a random talk with A.A. Shternberg that he had already seen polysynthetic twins in Rochelle salt crystals in a microscope, but in other, specific cuts. Moreover, he had shown them to an expert—but the latter "was not interested at all." Then, Marina Viktorovna went with Shternberg to the small pilot plant on Polyanka ul. where the appropriate cuts were stored. She described that historical moment—the moment of scientific discovery—as follows: "to our surprise, the twin structure was completely absent in the appropriate cuts. The day was sunny, and it was light and very warm in the room. I remembered about the upper Curie point (24°C). We took a microscope and went downstairs to the cold cellar. There, we saw the desired structure in the prepared cuts. The disappearance of twins at the transition through the Curie point made me certain that we were on the right track."

Detailed investigations performed by Chernyshova would later show that the twin components are the regions of spontaneous polarization (domains) and that the twin structure is observed only in a certain temperature range. Later, on the basis of the obtained data, V.L. Indenbom carried out a theoretical analysis of the results of optical study of domains in Rochelle salt crystals, which contributed to the development of the theory of ferroelectrics, and also proved the relationship between the domain pattern and arrangement of dislocations.

However, the existence of dislocations had been actively debated for a long time. This concept had been proposed by Western researchers, and, in the context of the struggle against cosmopolitanism, which was topical quite a short time ago, the objections to this idea were not only purely scientific. The atmosphere was highly electric.

In 1954, M.V. Klassen–Neklyudova and T.A. Kontorova published, in *Uspekhi Fizicheskikh Nauk* (*Advances in Physical Sciences*), a critical response to a review by Cottrell. This response contained objections against Taylor's suggestion, which lay at the basis of Cottrell's review, that the existence of a regular lattice of steady-state dislocations formed as a result of thermal fluctuations in crystals. But, at the same time, it was Klassen Neklyudova, specifically, who in her laboratory initiated a wide experimental study aimed at detecting dislocations in crystals. Her success was complete. Dislocations in alkali halide crystals were observed for the first time by A.A. Urusovskaya, who used selective etching. V.L. Indenbom and G.E. Tomilovskiĭ saw optical arrays of dislocations oriented along slip lines in ruby in polarized light with high resolution. In silicon crystals with low dislocation density, V.L. Indenbom and V.I. Nikitenko revealed birefringence rosettes, i.e., stresses around single dislocations. Thus, the discussion was closed, and dislocation-based concepts were acknowledged in the Soviet Union.

One day, Fersman asked Marina Viktorovna, "And what has the mistress herself been doing?"

By that time, "the mistress" had written the monograph *Mechanical Twinning of Crystals* (1960), which

was published soon after in the United States. This book, which became a classic, considers the processes of mechanical twinning and related phenomena: the formation of reoriented regions in crystals under the action of high temperatures (martensite transformations, recrystallization twins), electric fields (ferroelectric domains), and magnetic fields (magnetic domains). This was how studies developed along one of the projected lines.

Simultaneously, the second point of the program was being realized. An undertaking made by Marina Viktorovna in studying the mechanical properties of corundum turned out to be of utmost importance in view of the problem of preparing crystals for quantum electronics, which the Soviet Government was addressing. In the Special Design Bureau of the Institute of Crystallography, a special apparatus was designed and built on which V.P. Regel' and, later, V.G. Govorkov studied the temperature and rate dependences of the plasticity of refractory oxides (ruby, sapphire, garnet). Carrying out the optimization of the annealing conditions (which is important even from a practical point of view), Chernyshova revealed the effect of reversible decoration. Thus, the scientific investigations turned out to be useful for technical applications, which, in turn, stimulated the scientific research. This alliance of experiment and practice was typical of the working style of Marina Viktorovna. The very large amount of data on the study of laser crystals performed at the Institute of Crystallography was partially included in the monograph *Ruby and Sapphire* (1974), edited by M.V. Klassen–Neklyuda and Kh.S. Bagdasarov.

Summing up her own scientific work and the studies of her colleagues at the laboratory she headed, Marina Viktorovna wrote in the unpublished memoirs *The History of the Organization of the Laboratory of Mechanical Properties of Crystals: 1939–1967* that "we have traced and studied slip deformation in crystals in all its stages, from the appearance and motion of individual dislocations to their complex manifestation in the form of irrational twins and kinks. It was shown that absolutely brittle crystals do not exist in nature. The practical results of our studies have been implemented in serial production of technical stones for precise applications, semiconductor devices, and solid state lasers."

This is the result of Klassen–Neklyuda's life and scientific activity. And it is far from being all that was done by Marina Viktorovna, her students, and colleagues. How many deeds, achievements, and people whose fates were intertwined with hers have been left beyond the scope of this article! Marina Viktorovna had an amazing ability to comprehend reality creatively and find in it, first of all, beauty, harmony, and proportionality. Her life was no doubt a great one. Marina Viktorovna once said that, "the greater an artist, the more beauty his eyes can see." These words work especially well in her own case.

It is very pleasant that fond memories of Marina Viktorovna live on in the Institute of Crystallography, her students, and the laboratory she founded, the scientific team of which remains among the undoubted leaders in the science of the mechanical properties and real structure of crystals.

A. E. Smirnov

Translated by Yu. Sin'kov

Crystallography Reports, Vol. 49, No. 3, 2004, pp. 516–518. Translated from Kristallografiya, Vol. 49, No. 3, 2004, pp. 582–584.

MEMORIAL DATA

In Memory of Professor Zinoviĭ Grigor'evich Pinsker, Scientist and Teacher (on the Occasion of His 100th Birthday)

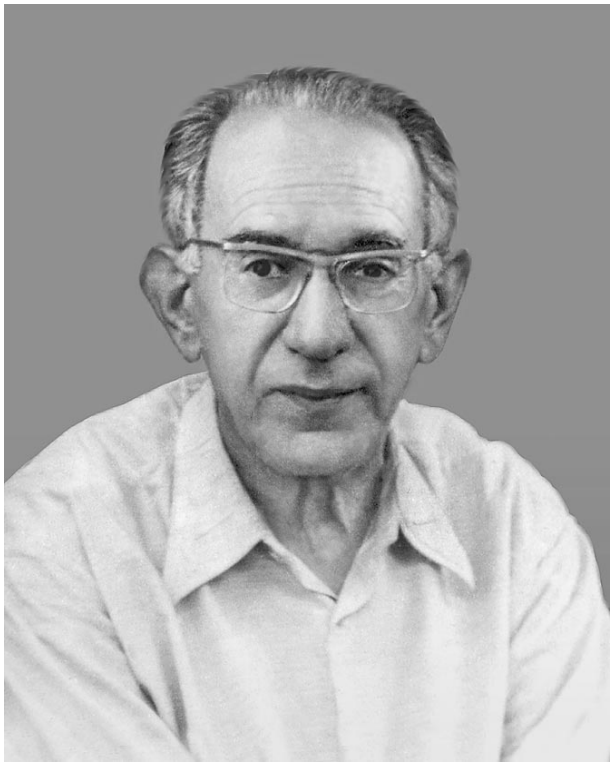

Zinoviĭ Grigor'evich Pinsker, an outstanding scientist and teacher, made a large contribution to the development of one of the important rapidly developing directions of modern physics—diffraction of short electron and X-ray waves.

Pinsker was born on February 13, 1904, in the city of Kherson, Ukraine. In 1920, he graduated from the Commercial school and entered the Faculty of Chemistry of the Bauman technical school (now Technical University). After graduation from the Bauman technical school in 1929, he worked at the Institute of Constructing Materials, where he studied the physics of colloids under the guidance of Prof. B.V. Il'in. In 1932, Pinsker started research in the field of electron diffraction at the All-Union Institute of Mineral Resources. In 1935, he observed experimentally and calculated theoretically the phenomenon of point electron diffraction. In 1936, he designed and constructed the first electron diffraction camera with a rather high resolution. At the same time, he continued experimental and theoretical studies of spot electron diffraction patterns and interpreted these patterns as diffraction from mosaic single crystals, which opened new possibilities for their use in structure analysis of crystals.

In 1936, Academician V.I. Vernadsky invited Pinsker to work at the Biogeochemical laboratory of the USSR Academy of Sciences, where, in 1938, Pinsker successfully defended his Candidate thesis. Pinsker was the first to pay attention to the necessity of developing an independent method—electron diffraction analysis—for structure determination. In 1938–1939, Pinsker and L.I. Tatarinova obtained electron diffraction patterns from layer CdI_2 crystals tilted at a certain angle to an electron beam. Later, these were called oblique texture patterns. Analyzing diffraction patterns from a number of similar layer structures ($CdBr_2$, PbI_2), Pinsker showed that electron diffraction can also be used to study polytypism in layer crystals and determine the mutual arrangement of the layers and, thus, also the atomic structure of crystals. These works, performed in the period from 1941 to 1944, can be considered pioneering experimental studies of polytypism. The above investigations and the theoretical calculations of the contribution of chemical bonds of various types to the lattice energy formed the basis of Pinsker's Doctoral thesis, which he defended in the city of Kazan in 1943.

In 1944, A.V. Shubnikov invited Pinsker to the newly organized Institute of Crystallography of the USSR Academy of Sciences, where Pinsker organized the electron diffraction laboratory. Together with I.I. Yamzin, Pinsker performed precision measurements of reflection intensities on electron diffraction patterns obtained in an electron diffraction camera designed and constructed in the laboratory. These studies showed the applicability of the kinematical theory of electron diffraction to structure analysis of small crystals. Using the same electron diffraction camera, Pinsker's students B.K. Vainshtein and G.I. Distler determined the structures of crystal hydrates of a number of metals and the structures of some polymers.

The investigations performed by Pinsker in the period from 1936 to 1949 were generalized in his famous monograph *Electron Diffraction*, which became an encyclopedia of the knowledge accumulated in the ~20 years since the discovery of electron diffraction. This monograph also showed the perspectives of the use of electron diffraction in various fields of science and technology. The monograph, published in 1949 by the Publishing House of the USSR Academy of Sciences, became the handbook for crystallogra-

1063-7745/04/4903-0516$26.00 © 2004 MAIK "Nauka/Interperiodica"

phers and scientists working in related fields for many years. The English translation of this monograph (Butterworth, London, 1953) increased the prestige of Russian science in the field of structure studies.

In the following years, Pinsker continued developing his well-known school of electron diffraction research. The publications of Pinsker's coworkers and students showed a high level of electron diffraction analysis. Especially important studies were performed by Pinsker's student Vainshtein (later a member of the USSR Academy of Sciences and director of the Institute of Crystallography of the USSR Academy of Sciences), who made an outstanding contribution to the development of Fourier analysis in electron diffraction. Vainshtein was the first to localize hydrogen atoms in organic and inorganic compounds based on the analysis of the Fourier syntheses of electrostatic potential and also made important contributions to other fields of structural electron diffraction and crystallography. B.B. Zvyagin successfully applied electron diffraction to the structural study of clay minerals and developed the methods for analyzing layer structures by oblique-texture electron diffraction patterns. Between the 1950s and 1980s, numerous electron diffraction determinations of the atomic structures of thin films of metal carbides, nitrides, and oxides were performed. Among these compounds were the crystal phases with partial occupancy of some positions and partial disorder not only of the sublattice of light atoms but also in metal sublattices. The deep scientific knowledge and intuition inherent in Pinsker did not allow him to reject the first results obtained in this field despite the fact that they were rather unusual for classical crystallography. Instead, he directed all the efforts of his coworkers and students to make rigorous allowance for all possible artifacts associated with experiments and development of the methods of the interpretation of partly disordered phases up to the refinement of their chemical composition from the syntheses of Fourier potential and creation of crystal chemistry of these compounds. For the first time, electron diffraction analysis was performed at various stages of oxidation, which resulted in the development of the mechanism of oxidation of metals of groups IV–VIII at the atomic level. This resulted in the formulation of new concepts in some fields of crystallography, crystal chemistry, and materials science. These studies were made by N.V. Troitskaya, V.V. Klechkovskaya, V.I. Khitrova, G.G. Dvoryankina, A.A. Zav'yalova, *et al.*

On the initiative of Pinsker in 1950 S.A. Semiletov started studies of crystal structures of thin films of semiconductors and growth and structure of epitaxial layers of semiconductor compounds. These investigations played an important role in the development of microelectronics. Historically, electron diffraction was the first efficient method of obtaining qualitative information on the structural perfection of various substrates and films necessary for epitaxial technology. These investigations were performed with the participation of Pinsker, G.A. Kurov, V.V. Vasil'ev, A.A. Tikhonova, E.V. Rakova, *et al.* Using electron diffraction analysis, S.A. Semiletov, R.M. Imamov, L.I. Man, R.V. Baranova, *et al.*, determined and refined the crystal structures of numerous binary and ternary semiconductors and refined their chemical compositions and conditions of formation and existence.

Pinsker deeply understood the phenomenon of electron diffraction. He predicted that new information on the processes occurring in thin films would be obtained using the kinematic methods of recording diffraction patterns—simultaneous motion of an object and a photographic plate. On his initiative, such studies were started in the 1950s and were successfully continued by G.A. Efendiev, R.B. Shafizade, and I.R. Nuriev at the Institute of Physics of the Azerbaijani Academy of Sciences. The method of kinematic electron diffraction based on continuous recording of intensities allowed one to study the processes of structural, polymorphous, and concentration transformations, ordering, crystallization, etc.

Pinsker also stimulated the development of gas electron diffraction in this country: in his remarkable monograph *Electron Diffraction*, published in 1949, he reviewed the structural studies of free molecules in a vapor jet. In 1950, the first gas electron diffraction camera was designed and constructed at the Department of Physical Chemistry of the Chemistry Faculty of Moscow State University (P.A. Akishin, L.V. Vilkov, L.G. Rambidi, and V.P. Spiridonov). At present, there are several laboratories engaged in gas electron diffraction studies in Russia. The results obtained in these laboratories are highly esteemed by the international commmunity. Gas electron diffraction has become an independent structural method.

It is well known that a considerable contribution to electron diffraction intensities may come from dynamical effects. Therefore, the allowance made for dynamical scattering in diffraction analysis was thoroughly studied by Pinsker, V.V. Udalova, Imamov, A.S. Avilov, *et al.* Today, F.N. Chukhovskiĭ, V.L. Vergasov, and L.A. Aleksanyan are beginning to develop an analytical approach to taking into account the dynamical scattering and its purposeful use in diffraction analysis.

In 1960s, Pinker became interested in X-ray dynamical scattering in ideal crystals. In his fundamental monograph *Dynamical Scattering of X-rays in Crystals*, published in 1974, Pinsker generalized an enormous number of his own results and published data on the theory of X-ray scattering in transparent and absorbing crystals, including the formation of moiré patterns. In this monograph, he systematically stated the theory of dynamical scattering of X-rays. In 1978, this monograph was also translated into English. Preparing the edition of his new monograph *X-ray Crystal Optics* (1982), Pinsker revised some chapters of the first edition (1974) and reviewed, with the participation of M.V. Kovalchuk and É.K. Kov'ev, the results

obtained by the experimental diffractometric and interferometric methods. This monograph also included a detailed statement of multibeam diffraction and theory of scattering by elastically deformed crystals (in coauthorship with A.M. Afanas'ev, V.G. Kohn, and Chukhovskiĭ). Pinsker played an active part in the development of the dynamical theory of X-ray scattering and new directions of development associated with X-ray optics, structure-sensitive methods of diagnostics of the structure of subsurface layer and nanostructures, etc., at the Institute of Crystallography. The research work was accompanied by pedagogical activity. From 1946 to 1957, Pinsker was the head of the Department of Crystallography, and then a professor at Gorky (now Nizhni Novgorod) and Moscow State Universities. Under Pinsker's guidance, the crystallographers of Gorky University began studying nitrogenation processes and structures of nitrides of technologically important metals by electron diffraction (S.V. Kaverin). The characteristic features of Pinsker's scientific style was the drive to penetrate the essence of scientific problems, industriousness, a high level of experimental studies, the ability to select and teach students, and stimulation and support of new directions of research.

Pinsker gave much of his time to preparation of scientific material. Among his students, there are more than 15 doctors and 40 candidates. Electron diffraction laboratory was rather popular among scientists of many countries. Many of Pinsker's students are continuing successful scientific work. Imamov, Kovalchuk, Klechkovskaya, and Avilov now head their own laboratories at the Institute of Crystallography and are engaged in studies related to the diffraction physics of short X-ray and electron waves, X-ray optics, inorganic and organic nanostructures, and X-ray and electron diffractometry. One of Pinsker's students—Kovalchuk—is a correspondent member of the Russian Academy of Sciences and the director of the Institute of Crystallography.

Pinsker's scientific works brought him world recognition and numerous decorations and honorary titles, among which was the highest award of the USSR Academy of Sciences in the field of crystallography—the Fedorov prize. For his great contribution to the development of Russian crystallography and preparation of scientific material, he was awarded the order "Sign of Honor" and the title of Honorary Scientist of the Russian Federation.

Pinsker was a member of the editorial board of the journal *Kristallografiya* from the very beginning of its existence. For many years, he was also a member of the editorial board of *Acta Crystallographica*.

Pinsker was an invited lecturer at numerous national and international meetings. He participated in International Congresses of Crystallographers from 1957. In 1966, he served as the chairman of the Program Committee of the Seventh International Congress of Crystallographers in Moscow. For three terms, he was a member of the Commission on Electron Diffraction of the International Union of Crystallography. Pinsker possessed the best qualities of a classical scientist and was a man of principles. These qualities were complemented with a kind and delicate way of relating people around him.

Prof. Pinsker will always be remembered by his coworkers and students. His name is written in the history of the Institute of Crystallography and world science.

M. V. Kovalchuk
Corresponding Member
of the Russian Academy of Sciences
R. M. Imamov
Doctor of Physics and Mathematics
V. V. Klechkovskaya
Doctor of Physics and Mathematics
e-mail: klechvv@ns.crys.ras.ru

Translated by L. Man

Crystallography Reports, Vol. 49, No. 3, 2004, p. 519. Translated from Kristallografiya, Vol. 49, No. 3, 2004, p. 585.

OBITUARIES

Andreĭ Vladimirovich Zalesskiĭ (June 18, 1930–October 26, 2003)

Andreĭ Vladimirovich Zalesskiĭ, a leading researcher at the Institute of Crystallography of the Russian Academy of Sciences and a doctor of physics and mathematics, died suddenly on October 26, 2003.

The entire scientific career of Zalesskiĭ was closely related to the Institute of Crystallography. Immediately after graduating from the Moscow Institute of Steel and Materials in 1954, he entered the Institute of Crystallography and worked there until the end of his life.

Zalesskiĭ's research was mainly focused on the magnetic properties of crystals. In 1962, he defended his Candidate's dissertation. This was one of the first studies in the Soviet Union devoted exclusively to ferrite single crystals, the growing of which had been developed by that time at the Institute of Crystallography.

For many years, Zalesskiĭ carried out fundamental studies of magnetism using the methods of nuclear magnetic resonance and nuclear quadrupole resonance. He developed a new analytical method—NMR spectroscopy of domain boundaries, which makes it possible to determine the internal magnetic structure of domain boundaries. Zalesskiĭ defended his Doctoral dissertation on this subject in 1985.

Zalesskiĭ made a significant contribution to the studies of high-temperature superconductors and materials with giant magnetoresistance (lanthanum manganites). In the course of studying NMR spectra on lanthanum nuclei, he revealed phase layering in these materials. These results were repeated abroad only much later.

A short time ago, Zalesskiĭ obtained new and interesting results when he investigated a particular class of materials—ferroelectromagnets. He discovered the existence of a long-period incommensurate magnetic structure described by an anharmonic cycloid in the $BiFeO_3$ ferroelectromagnet. For these studies, Zalesskiĭ was awarded first prize at the Session on Magnetism of the Scientific Council of the Russian Academy of Sciences in 2003.

Zalesskiĭ also had begun to study new magnetic structures that are observed at low temperatures in lithium cuprate $LiCu_2O_2$, in particular, the so-called quasi-two-dimensional ladder structure.

All the studies that Zalesskiĭ carried out were devoted to the most important problems of the physics of magnetic phenomena. He was also the author of the chapter "Magnetic Properties of Crystals" in the book *Modern Crystallography* and published several reviews on applying the NMR method to the study of domain boundaries and the real structure of magnetic crystals.

Zalesskiĭ was an excellent physicist–experimenter and high-class radioengineer who was capable of designing very complex apparatuses with his own hands. However, he never limited himself to scientific research alone. His distinctive features were his high intellect, the widest range of interests, and erudition in many fields. Zalesskiĭ's everlasting devotion to science was sincerely respected by his colleagues. His benevolence, generosity, straightforwardness, and sincerity always attracted other people to him.

We will always remember him in our hearts.

Translated by Yu. Sin'kov

1063-7745/04/4903-0519$26.00 © 2004 MAIK "Nauka/Interperiodica"

Crystallography Reports, Vol. 49, No. 3, 2004, pp. 520–521. Translated from Kristallografiya, Vol. 49, No. 3, 2004, pp. 586–587.

OBITUARIES

Vladimir Alekseevich Shamburov (June 25, 1920–December 1, 2003)

Vladimir Alekseevich Shamburov, a leading researcher at the Institute of Crystallography of the Russian Academy of Sciences and a candidate of technical sciences, died on December 1, 2003. Vladimir Alekseevich was one of the oldest researchers at the Institute of Crystallography, having worked there for 56 years.

Shamburov was born on June 25, 1920, in the town of Sarapul (Udmurtiya). He graduated from the Moscow Institute of Geodesy, Aerial Photography, and Cartography (Faculty of Optics and Mechanics) and entered a postgraduate course at the Institute of Machine Building of the Academy of Sciences of the Soviet Union. In 1950, he defended his candidate's dissertation in technical sciences.

Shamburov entered the Institute of Crystallography in 1947 and began to work at the laboratory headed by A.V. Shubnikov along with G.G. Lemmleĭn, M.V. Klassen–Neklyudova, E.V. Tsinzerling, N.V. Vedeneeva, M.A. Chernysheva, and other researchers. These people—the founders of the Institute of Crystallography—set the highest standards of research and attitude to work, which made it possible to solve a number of applied problems and meet the needs of the war industry of the USSR, as well as develop a number of new branches of science. Shamburov belonged to the main group of this unique scientific community.

The scientific interests of Shamburov were in the fields of classical crystal optics, electrooptics, and making optical instruments. He made a significant contribution to the development of these fields of science.

Shamburov played a key role in the development of a new line of research—crystal electrooptics—in our country. Shamburov designed and implemented in series production a number of electrooptical light modulators and gates for generation of laser single pulses and developed new methods and devices for continuous and discontinuous electrooptical laser-beam scanning. These devices were used by Shamburov in carrying out about ten defense developments that had been approved by the Presidium of the Academy of Sciences of the Soviet Union, including the development of the first domestic radar. Giant laser single pulses were obtained in our country for the first time using modulators and gates that had been developed specifically by Shamburov.

In the field of classical crystal optics, Shamburov obtained a number of new results, investigating the processes of propagation and transformation of polarized light in absorbing crystals. He contributed to the development of new methods for studying the parameters of natural waves with the use of the Poincaré sphere method. In analyzing the Maxwell equations, he discovered a previously unknown property of the irreversibility of all the parameters of propagation and polarization of natural waves upon reversal of their wave normals in naturally gyrotropic absorbing crystals belonging to low-order systems. He obtained, for the first time, a matrix solution to the general problem of transmission of a light wave through a crystal plate with regard to multiple reflections from the plate boundaries. Shamburov was interested in fundamental problems. In his last works, he analyzed and tried to refine modern theories of natural gyrotropy and the possible types of natural waves in crystals.

One of Shamburov's distinctive features was his rare ability to use the effects of transformation of light in crystals to develop new principles and original designs of devices for spectral, microscopic, polarization, X-ray, and electrooptical studies of various types of crystals and for the construction of apparatus for controlling the parameters of laser radiation. Many of these devices and systems were widely used in practice, implemented in series production, and protected by

1063-7745/04/4903-0520$26.00 © 2004 MAIK "Nauka/Interperiodica"

inventor's certificates. These developments were extremely diverse: from electrooptic modulators and gates and fundamental technical solutions and units for the first domestic precise automatic spectropolarimeters to prototypes of new laser telescopic collimating sights for small arms and polarizers, lenses, and prisms for very wide use. About 50 methods and devices developed by Shamburov in the course of his work at the Institute of Crystallography are protected by inventor's certificates and patents.

Shamburov's studies that were aimed at practical application of crystals of Iceland spar in science and technology are of particular interest. These studies were related to his work at spar deposits in Évenkiya. Overcoming difficulties on the way to various deposits, Shamburov managed to find specifically those crystals that were most appropriate for a particular system. He was the first to switch on a laser in Évenkiya. With the use of this laser, he implemented a new method of concentrating crystals of Iceland spar, which proved to be less time-consuming and more exact. To meet the needs of the local population, he designed an optical sight for hunting rifles.

Shamburov's studies were distinguished by their innovative spirit, fundamental statement of problems, and elaborate solutions. He tried to inculcate his style of working in his young colleagues, and four candidate's dissertations were defended under his supervision.

Shamburov's scientific activity was highly valued: he was awarded the government medal *For Valiant Labor*, golden and silver medals of the Exhibition of National Economy Achievements, and the highest award of the Institute of Crystallography—the Shubnikov prize (1992). Shamburov was also awarded the medal *For the Defense of Moscow.*

Modest and simple in his personal life, Shamburov was a very wise and brilliant man who was truly devoted to science and deeply attached to it. He was persistent in his search for scientific truth and had an independent mind. Shamburov's range of interests outside of science was very wide and, in different periods of his life, expanded from gliding and motor sports to questions of philosophy and religion and even beekeeping. His life, which began in the 20th and ended in the 21st century, was rich in events and he had a lot to tell about: well-remembered meetings with Esenin, Raĭkh, Krupskaya, Rykov, and Stanislavsky in his childhood; then, when he was a teenager, life in Tuva—hunting and the customs and traditions of the people living there—later, the images of P.L. Kapitsa, A.V. Shubnikov, and other well-known scientists: all in all, different periods in the history of our country.

Shamburov was greatly respected by all the people who dealt with him. He was intelligent, kind-hearted, and quiet; always kept his word; and had a strong sense of self-respect. He came from the Russian intelligentsia, and the features characteristic of this social group—their specific attitude to the world, natural gifts, and democratic nature—were intrinsic to him. Shamburov will always be fondly remembered by those who were privileged enough to know him.

Translated by Yu. Sin'kov

Crystallography Reports, Vol. 49, No. 3, 2004, pp. 522–523. Translated from Kristallografiya, Vol. 49, No. 3, 2004, pp. 588–589.

INFORMATION

Letter to the Editor

B. N. Kolodiev

Received January 15, 2004

In 2000, the second, revised and supplemented edition in three volumes of the book *Synthesis of Minerals* [1] was completed. In the first chapter of the second volume, it is stressed that the scientific and technical data presented in the book are original (see page 5). The authors of the first chapter, "Yttrium Aluminum Garnet" (S.A. Smirnova, L.I. Kazakova, and O.A. Egorycheva), note on page 19 that "they failed to find any data on the activating centers Eu^{2+} and Yb^{2+} in $Y_3Al_5O_{12}$ crystals in the literature" and that they were the first, "apparently, to obtain such centers when growing garnet single crystals containing the aforementioned ions." It looks as if these authors specifically were the first to obtain yttrium aluminum garnet (YAG) crystals containing the aforementioned activating centers. On page 18, it is noted that, in order to obtain jewelry garnets, "a special technique was developed, which makes it possible to implement heterovalent isomorphism in the YAG structure by the scheme $Y^{3+} \longleftrightarrow R^{2+} + Me^{4+}$, where R is a rare-earth metal and Me is a tetravalent metal. In order to conserve the electroneutrality of YAG molecules, tetravalent… hafnium was used as a compensator." Again, there are no references to the original works of the researchers who were actually the first to develop this processing procedure.

It is also noted on page 19 that "optical absorption centers in blue and green YAGs (containing Eu^{2+} and Yb^{2+} ions, respectively) were investigated… The measurements were performed in the frequency range 2000–50000 cm^{-1} at 100 and 300 K… In the optical spectra, along with the forbidden transitions within the 4*f* configuration, which are typical of rare-earth elements, transitions to the mixed configurations $4f^{k-1}5d$ and so on are also observed. These transitions, allowed by the rule $\Delta L = -11$, manifest themselves in the form of wide strong bands in the relatively long-wavelength spectral region. The positions of the bands due to the $f \longrightarrow d$ transitions in the spectrum of $Y_3Al_5O_{12}$ may differ of those in the spectrum of MeF_2… These transitions can be identified as the interconfiguration transitions $4f^7$–$4f^6(^7F)5d$ and $4f^{14}$–$4f^{13}(^2F)5d$ from the ground states $^8S_{7/2}(Eu^{2+})$ and $^1S_0(Yb^{2+})$ to the two split 5*d* levels of the *l* and *t* types." A chapter with the same cited content was also in the first edition [2].

However, none of these results are original. In fact, "simultaneous doping" of blue and green YAG crystals by "Eu (Yb) ions of different valence" during their growth was first performed a long time ago, and the results were published in [3–5]. This can be seen even from the titles of [3–5] and the last names of all the authors (given in the References by a complete list as an exception from the Editorial Guidelines). The optical spectra of blue (doped with Eu^{2+} ions) and green (doped with Yb^{2+} ions) YAG crystals in the range 400–50000 cm^{-1} [4] at 300 and 100 K were measured and interpreted for the first time in 1982 [3]. These spectra were first reported in [5], where it was said that "the charge deficit upon the heterovalent substitution $Y^{3+} \longrightarrow Eu^{2+}(Yb^{2+})$ was compensated by adding HfO_2 into the blend." The spectra in the figure reported in [5] verify the simultaneous presence of both divalent and trivalent Eu and Yb ions in $Y_3Al_5O_{12}$ crystals. The presence of wide strong absorption bands related to Eu^{2+} ions (380 and 550 nm) and Yb^{2+} ions (390 and 650 nm) in the spectra of "YAG crystals that were not subjected to any external actions" was noted in [3, 5]. These bands were attributed to the parity-allowed ($\Delta L = -1$) $f \longrightarrow d$ dipole transitions, which "can be used for sensitization of the emission of Eu^{3+} (Yb^{3+}) ions." In the approximation of the known diagrams of energy levels and transitions between these levels for rare-earth ions (TR^{2+} and TR^{3+}) [6], it was specified in [3, 4] that the wide bands are due to the "interconfiguration transitions $4f^7 \longrightarrow 4f^6(^7F)5d$ and $4f^{14} \longrightarrow 4f^{13}(^2F)5d$ from the ground states $^8S_{7/2}(Eu^{2+})$ and $^1S_0(Yb^{2+})$ to the two *e*- and *t*-type levels split by the strong crystal field." The values of this splitting amount to ~8100 and 10400 cm^{-1} for Eu^{2+} and Yb^{2+} ions, respectively [5].

Concerning the fine-structure lines in the spectrum of the YAGs under consideration, they originate from Yb^{3+} and Eu^{3+} ions and are due to the forbidden transitions within the 4*f* configuration. These are "transitions between the Stark levels of the ground ($^2F_{7/2}$) and excited ($^2F_{5/2}$) states of Yb^{3+} ions and between the levels of the ^7F multiplet of Eu^{3+} ions in YAGs" [5]. This is in agreement with the data of [7] and [8] on other garnet crystals.

The processing procedure noted in the first chapter of the aforementioned book [1], which allows one to synthesize blue (doped with Eu^{2+} and Eu^{3+} ions) and green (doped with Yb^{2+} and Yb^{3+} ions) YAGs was for the first time described by Akhmetov *et al.* in inventor's certificates [9, 10].

1063-7745/04/4903-0522$26.00

Thus, the above-cited data from [1] on the methods of fabrication of blue and green garnets, as well as the data on the absorption bands in the spectra of Eu : YAG and Yb : YAG garnets and their interpretation, are not original. They had been published before by other authors. In [1], Smirnova, Kazakova, and Egorycheva published the data of [3, 5, 9, 10] without referring to the basic publications [3, 5] on the synthesis and optical spectra of garnets doped with the noted impurities (grown in the All-Russia Research Institute of Synthesis of Mineral Raw Materials) or to the authors of these papers. In addition, Kazakova has published a new paper [11] in which the growth of green YAGs, their spectra, and interconfiguration transitions are again described. And again, the data were taken from the same works of Kolodieva *et al.* [3, 5] and no references to these publications or their authors were given.

It was shown in [3–5, 9, 10] that, in the grown Eu : YAG (doped with Eu^{2+} and Eu^{3+} ions) and Yb : YAG (doped with Yb^{2+} and Yb^{3+} ions) crystals, the volume distribution of Eu^{2+} and Yb^{2+} ions (which are, as is well known, color centers) is uniform. This is evidenced by not only the visually uniform blue and soft green colors of Eu : YAG and Yb : YAG crystals, respectively, but also by the good reproducibility of the intensities of the absorption bands in spectra measured from arbitrarily chosen regions of a crystal. The concentrations of growth activating centers Eu^{2+} and Eu^{3+} (Yb^{2+} and Yb^{3+}) in these YAGs can be controlled. Moreover, these concentrations and the intensities of the absorption bands do not change with time. even after heating of crystals up to 1000 K, which is indicative of high stability of the obtained centers [5]. The results of [3, 5] and the data on the mutual positions of the absorption and excitation bands in the spectra of Eu^{3+}, Eu^{2+}, Yb^{3+}, and Yb^{2+} ions in various crystal matrices suggest that the study of the processes of energy transfer between Eu (Yb) ions of different valence in YAG crystals may reveal new or improve already known lasing effects.

REFERENCES

1. *Synthesis of Minerals*, 2nd ed. (VNIISIMS, Aleksandrov, 1998), Vol. 2.
2. *Synthesis of Minerals* (Nedra, Moscow, 1987), Vol. 2.
3. A. P. Andreev, S. F. Akhmetov, G. L. Akchmetova, A. G. Davydchenko, A. B. Dubovskiĭ, S. N. Ivanov, B. N. Kolodiev, S. V. Kolodieva, M. I. Samoĭlovich, and S. A. Smirnova, in *Abstracts of the VII All-Union Symposium on Spectroscopy of Crystals Activated by Ions of Rare-Earth and Transition Metals* (RTP Leningr. Inst. Yad. Fiz., Leningrad, 1982), p. 85.
4. A. P. Andreev, S. F. Akchmetov, G. L. Akchmetova, A. G. Davydchenko, B. N. Kolodiev, S. V. Kolodieva, and M. I. Samoĭlovich, in *Abstracts of XIII International Congress and General Assembly International Union of Crystallography* (Hamburg, 1984).
5. A. P. Andreev, S. F. Akhmetov, G. L. Akchmetova, B. N. Kolodiev, S. V. Kolodieva, and M. I. Samoĭlovich, *Abstracts of the VIII All-Union Feofilov Symposium on Spectroscopy of Crystals Activated by Ions of Rare-Earth and Transition Metals* (UPI, Sverdlovsk, 1985), Part 1, p. 100.
6. M. A. El'yashevich, *Spectra of Rare-Earth Metals* (Gostekhteorizdat, Moscow, 1953).
7. P. A. Arsen'ev and E. F. Kustov, *Elements of Quantum Electronics*, Part 1: *Monocrystals of Garnets: Methods of Production, Spectroscopic and Laser Parameters* (Mosk. Énerg. Inst., Moscow, 1973).
8. Kh. S. Bagdasarov, G. A. Bogomolova, D. N. Vylegzhanin, *et al.*, Dokl. Akad. Nauk SSSR **216**, 1247 (1974) [Sov. Phys. Dokl. **19**, 358 (1974)].
9. S. F. Akhmetov, G. L. Akhmetova, S. V. Kolodieva, *et al.*, USSR Inventor's Certificate No. 1225287 (15 December 1985).
10. S. F. Akhmetov, G. L. Akhmetova, S. V. Kolodieva, *et al.*, USSR Inventor's Certificate No. 1274356 (August 1, 1986).
11. L. I. Kazakova, Tr. VNIISIMS **16**, 7 (2000).

Translated by Yu. Sin'kov